CENTRAL RESEARCH LIBRARY

ORNL-5046

Cy 3

Health Physics DIVISION

MARTIN MARIETTA ENERGY SYSTEMS LIBRARIES
3 4456 0359432 2

Annual Progress Report

TO VAULT

Period Ending June 30, 1975

LIBRARY
REFERENCE COPY

OAK RIDGE NATIONAL LABORATORY
CENTRAL RESEARCH LIBRARY
CIRCULATION SECTION
4500N ROOM 175
LIBRARY LOAN COPY
DO NOT TRANSFER TO ANOTHER PERSON
If you wish someone else to see this report, send in name with report and the library will arrange a loan.
UCN-7969 (3 9-77)

OAK RIDGE NATIONAL LABORATORY
OPERATED BY UNION CARBIDE CORPORATION • FOR THE U.S. ATOMIC ENERGY COMMISSION

Printed in the United States of America. Available from
National Technical Information Service
U.S. Department of Commerce
5285 Port Royal Road, Springfield, Virginia 22161
Price: Printed Copy $10.60; Microfiche $2.25

This report was prepared as an account of work sponsored by the United States Government. Neither the United States nor the Energy Research and Development Administration, nor any of their employees, nor any of their contractors, subcontractors, or their employees, makes any warranty, express or implied, or assumes any legal liability or responsibility for the accuracy, completeness or usefulness of any information, apparatus, product or process disclosed, or represents that its use would not infringe privately owned rights.

ORNL-5046
UC-41 – Health and Safety

Contract No. W-7405-eng-26

HEALTH PHYSICS DIVISION
ANNUAL PROGRESS REPORT

For Period Ending June 30, 1975

J. A. Auxier, Director
D. M. Davis, Assistant Director
J. E. Turner, Associate Director

SEPTEMBER 1975

OAK RIDGE NATIONAL LABORATORY
Oak Ridge, Tennessee 37830
operated by
UNION CARBIDE CORPORATION
for the
ENERGY RESEARCH AND DEVELOPMENT ADMINISTRATION

MARTIN MARIETTA ENERGY SYSTEMS LIBRARIES
3 4456 0359432 2

Reports previously issued in this series are as follows:

ORNL-2384	Period Ending July 31, 1957
ORNL-2590	Period Ending July 31, 1958
ORNL-2806	Period Ending July 31, 1959
ORNL-2994	Period Ending July 31, 1960
ORNL-3189	Period Ending July 31, 1961
ORNL-3347	Period Ending July 31, 1962
ORNL-3492	Period Ending July 31, 1963
ORNL-3697	Period Ending July 31, 1964
ORNL-3849	Period Ending July 31, 1965
ORNL-4007	Period Ending July 31, 1966
ORNL-4168	Period Ending July 31, 1967
ORNL-4316	Period Ending July 31, 1968
ORNL-4446	Period Ending July 31, 1969
ORNL-4584	Period Ending July 31, 1970
ORNL-4720	Period Ending July 31, 1971
ORNL-4811	Period Ending July 31, 1972
ORNL-4903	Period Ending July 31, 1973
ORNL-4979	Period Ending July 31, 1974

Contents

FOREWORD ix

SUMMARY xi

PART I. EMERGENCY TECHNOLOGY

1. STRATEGIC DEFENSE 1
   - National Survival After a Nuclear Attack 1
   - Soviet Civil Defense Studies 5
   - Best Shelter for Critical Industry Workers 6
   - Expedient Life-Support Equipment for Shelters 7

2. REACTOR STUDIES 14
   - National Security and Nuclear Power 14
   - Nuclear Energy Centers 15
   - Nuclear Reactor Complexes in Strategic War 24
   - Perspectives on the Terrorist Problem for Nuclear Power 28
   - Effects of Natural Disasters on the NEC 30
   - Effects of Plutonium Aerosols 45
   - Electromagnetic Pulse Effects on Nuclear Power Plants 49

PART II. ASSESSMENT AND TECHNOLOGY

3. DOSIMETRY INTERCOMPARISON STUDIES 53
   - Nuclear Accident Dosimetry 53
   - Personnel Monitoring Intercomparison 53
   - International Intercomparison of Environmental Dosimeters under Field and Laboratory Conditions 55

4. HEALTH PHYSICS RESEARCH REACTOR AND ACCELERATOR OPERATIONS 57

5. DOSIMETRIC APPLICATIONS OF PARTICLE-TRACK ETCHING 59
   - Spark Counting of Particle Tracks in Mica 59
   - Spark Counting of Neutron-Induced Recoil-Particle Tracks 62
   - Transfer Dosimeters for Fast-Neutron Sources 62

6. EXOELECTRON AND THERMOLUMINESCENCE DOSIMETRY WITH BeO 64
Objectives 64
Light Response and Radiation Sensitization of BeO 64
Bank of Standardized BeO Ceramic Dosimeters 64
Hydration Effects and the Performance of Exoelectron Dosimeters in the Field 65
TL Dosimetry 66
Applications 67

7. DISTRIBUTION OF ENERGY LOSSES OF LOW-ENERGY PROTONS IN HYDROCARBON GASES 69

8. DEVELOPMENTS IN ALPHA SPECTROMETRY WITH LIQUID SCINTILLATORS 72

9. DOSIMETRY FOR TERRESTRIAL GAMMA-RAY SOURCES 75

10. DOSIMETRY FOR HUMAN EXPOSURES 79
Liaison Dosimetry Studies 79
In Vivo Dose Estimates for Atomic Bomb Survivors 83
Radiation Exposure to Atomic Bomb Survivors Residing in the United States 88
Transmission of Photons through Common Shielding Media 89

11. APPLICATION OF ALAP CONCEPT TO LIGHT-WATER REACTORS 93

12. HEALTH PHYSICS ASPECTS OF FUSION POWER 96
Neutron Activation Products 96
Localized Tritium Behavior 97
Global Tritium Circulation 97

13. PUBLIC HEALTH AND DEMOGRAPHIC STATISTICS 100

PART III. BIOLOGICAL AND RADIATION PHYSICS

14. ATOMIC AND MOLECULAR PHYSICS 103
Electron Attachment to SO_2 in High-Pressure Gases 103
Long-Lived Parent Negative Ions Formed via Nuclear-Excited Feshbach Resonances. Part IV: A Systematic Study of NO_2-Containing Benzene Derivatives 105
Threshold-Electron Excitation and Compound-Negative-Ion States of Aromatic Hydrocarbons 107
Linking of Existing Data on Electron-Molecule Interactions in Gases with Those in the Liquid Phase 108
Slowing Down of Subexcitation Electrons in Polyatomic Gases 108
Electron Mobilities in High-Pressure Gases ("Quasi-Liquids") 109
Measurement of the Mobility of Excess Electrons in Liquids 109
Potential Energy Function of an Excess Electron in a NonPolar Liquid 111
Electron Mobilities in Gases and Liquids 112

Photophysics of Aromatic Hydrocarbons 113
Synthesis of Electron-Molecule Interactions with Benzene and Benzene Derivatives 113
Spin-off of our Basic Studies on Electron Attachment to, and Elastic and Inelastic Electron Scattering from, Polyatomic Molecules 113

15. PHYSICS OF LIQUIDS AND SURFACES 114
Photon Scattering from Cylinders 114
Collective Electronic Oscillations in Liquids 116
Thickness of Contamination on the ORMAK Liner 117
Electron Energy Losses in Liquids 118

16. PHYSICS OF SOLIDS AND MACROMOLECULES 120
Optical Properties of Solid Sodium and Lithium from Ellipsometric Measurements 120
Coupling of Photons and Surface Plasmons at Interfaces of Known Profile 121
Photoemission from Aluminum 125
Electron Attenuation Lengths in Carbon Films 127
Optical and Dielectric Properties of Bovine Plasma Albumin Between 2 and 82 eV 128
Optical and Dielectric Properties of Polystyrene Between 2 and 82 eV 131
Feasibility Studies of Monitoring the First Wall in ORMAK by Optical Measurements 132
Soft X-ray Emission from Insulators 134

17. GENERAL PHYSICS 136
Pion Beam Dosimetry 136
Estimated W Values for Negative Pions in Nitrogen and Argon 136
Monte Carlo Treatment of Multiple Coulomb Scattering in Pion-Beam Dose Calculations 139
Surface-Plasmon Excitation in X-ray Inelastic Scattering on Spherical Voids in Metals 142
Theory of the Linear Response Function of a Model Insulator 144
Application of the Model Insulator Theory to Al_2O_3: The Low-Energy End of the Electron Slowing-Down Spectrum 146
Scattering of Electromagnetic Waves by Cylinders: Excitation of Surface-Plasmon Modes 148
Energy Loss of Swift Proton Clusters in Solids 151
A Statistical Approach to the Evaluation of Electron Inelastic Mean Free Paths in Solids 153
Tabulation of Electron Interaction Parameters in Al and Al_2O_3 154

PART IV. CHEMICAL PHYSICS AND SPECTROSCOPY

18. CHEMICAL PHYSICS STUDIES 157
Negative-Ion Formation in Organic Molecules 157
Negative-Ion Formation in $Fe(CO)_5$ and $Ni(CO)_4$ 159
Collisional Ionization of Na, K and Cs by CO_2, COS, and CS_2: Molecular Electron Affinities 160
Abnormally Large Electron Affinities for Some Hexafluoride Molecules 161
π-Electron Affinities for Organic Molecules 163

Gas Phase Laser-Ion Spectroscopy 163
Studies of Dissociative Ionization by Electron Impact 165
Ionization Potentials of Organic Donor Molecules 169
Reactions of Electronically Excited Atoms 169
Kinetic Energy Production from Unimolecular Dissociations 170
Optical and Electrical Measurements on Organic Semiconductors 171
Level Shifts from Coulomb Interaction of Atoms in a Gas 171
Rotational Resonance in Low-Energy Electron-H_2 Scattering 172

19. ATOMIC PHYSICS AND LASER RESEARCH 174
Resonance Ionization Spectroscopy 174
Energy Pathways and Jesse Effects in Helium 182
Energy Transfer 185
Laser Applications 192
Analytical Applications 193

PART V. MEDICAL PHYSICS AND INTERNAL DOSIMETRY

20. METABOLIC MODELS FOR ESTIMATION OF INTERNAL RADIATION EXPOSURE RECEIVED BY HUMAN SUBJECTS FROM THE INHALATION OF NOBLE GASES 197

21. TABULATIONS OF AVERAGE DOSE EQUIVALENT DUE TO RESIDENCE OF RADIONUCLIDES IN BODY ORGANS OF AN ADULT 205

22. VARIATION OF THE ABSORBED FRACTION WITH SHAPE AND SIZE OF THE THYROID 207

23. DOSE TO THE BLADDER 214
Introduction 214
The Bladder Model 214
Activity in the Bladder 216
Dose from Photons 216
Results for Photon Dose 217
Surface Dose from Electrons and Beta Particles 217

24. PRACTICAL CONSIDERATION FOR COMPUTING THE DOSE TO THE BLADDER 219

25. METABOLIC MODEL FOR WHOLE-BODY AND GASTROINTESTINAL-TRACT RETENTION OF ^{141}Ce IN A HUMAN INFANT 221

26. THE DOSIMETRY OF ^{241}Pu RECONSIDERED 222

27. A COMPUTER PROGRAM FOR ESTIMATING MICROCURIE-DAYS OF A RADIONUCLIDE IN THE ORGANS OF THE HUMAN BODY 225

28. A SEMITHEORETICAL APPROACH TO EXCRETION AND RETENTION OF VARIOUS IONS 230

29. ABSORBED DOSE DURING BREAST X-RAY THERAPY 233

30. EFFECT OF SOURCE ORGAN SIZE ON ABSORBED FRACTION DISTRIBUTION 234

31. NUCLEAR-POWERED CARDIAC PACEMAKERS 239
Background 239
Environmental Assessment 239
Benefit Assessment 243
Summary 245

32. VARIATION OF CALCULATED ORGAN DOSE RATES FROM A PACEMAKER AS A FUNCTION OF BODY SIZE 247

33. AGE FACTORS FOR DOSE RATES FROM AN INFINITE CLOUD OF A PHOTON EMITTER 249

34. JOINT RESEARCH WITH THE COMPARATIVE ANIMAL RESEARCH LABORATORY 253

35. SOME OPERATING CHARACTERISTICS OF TISSUE-EQUIVALENT PROPORTIONAL COUNTERS 254

36. HUMAN PHANTOM PLOTTING ROUTINE 256

37. MATERNAL, FETAL, AND PEDIATRIC PHANTOMS 259

38. AN OUTLINE OF EXPERIMENTAL PROGRAMS USING THE MR. ADAM PHANTOM 262

PART VI. OFFICE OF EDUCATION AND INFORMATION

39. EDUCATION AND VOCATIONAL TRAINING 265

40. INFORMATION ACTIVITIES AND DISSEMINATION 267
Health Physics Information System 267
Solid-State Dosimetry Information Dissemination 268

THESES, PAPERS, PUBLICATIONS, AND LECTURES

THESES 269

PAPERS 270

PUBLICATIONS 274

LECTURES 282

MISCELLANEOUS STAFF ACTIVITIES

ACADEMIC APPOINTMENTS 287

SERVICE IN PROFESSIONAL ORGANIZATIONS 287

GUESTS AND TRAINEES 288
Faculty Institute Participants 288
Faculty Research Participant 289
Students 289
Foreign Guests 289

ORGANIZATION CHART 291

Foreword

This annual report covers the research activities of the Health Physics Division between August 1, 1974, and June 30, 1975, and reflects a shifting of the annual information meeting from October to September. As in the past, the Division's work in applied health physics is reported separately by calendar year. The latest report, for 1974, is ORNL-5055.

Several administrative changes were made in the Division during the year. The fundamental physical research efforts in the Radiation Research and Development Section, including proton interaction with noble gases, and the Fundamental Health Physics Research Section were divided into two sections – the Biological and Radiation Physics Section (H. A. Wright, Chief) and the Chemical Physics and Spectroscopy Section (W. R. Garrett, Chief). In addition, the remainder of the Radiation Research and Development Section was combined with assessment and analysis studies to form the Assessment and Technology Section under D. G. Jacobs. Due to the death of J. C. Hart, the Education and Information Section became the Office of Education and Information under the leadership of J. E. Turner, Associate Director.

As will be seen in this report, programs of the Health Physics Division have continued to grow, and there has developed an increasing sense of excitement and productivity. The highlights are described in the opening summary, and detailed descriptions of the work are presented in the six parts of this report. The reader is invited to contact the individual investigators concerning any part of the work reported. Numerous references to the open literature are given, and a list of the Division's publications is included.

Included in the expanding research of the Division is a strong program in laser physics. The work relates both to fundamental processes and to the application of lasers in analytical work. The environmental health physics program in the Division has grown most rapidly during the past year and now encompasses work ranging from routine monitoring activities to instrumentation to epidemiologically oriented research. Collaborative investigations in many disciplines with individual researchers and groups outside the Laboratory have continued to increase, and the number of post-doctoral participants and graduate students has increased markedly.

As is evident from the above, the Division continues its broad approach to health physics–an approach that ranges from basic research to the day-to-day practice of radiation protection and industrial safety. The Division's programs will remain dynamic and responsive to the needs and goals of the Laboratory, ERDA, and the nation.

Summary

PART I. EMERGENCY TECHNOLOGY

1. Strategic Defense

Suppose that, due to relocation of population from high-risk areas and protective measures against radiation from fallout, 90% of the U.S. population survives a hypothetical nuclear attack of magnitude consistent with current international agreements. Can the population survive the postattack situation in which major cities are destroyed, including food warehouses and processing plants, and transportation is restricted by radiation from fallout? An overview of the problem is displayed by computer graphic techniques, and a possible solution to the starvation problem is shown by a transport model for grain stocks by surviving aircraft and trucks.

Continuing research of U.S.S.R. publications regarding civil defense has revealed no evidence of a decreasing Soviet interest. On the contrary, constant upgrading of their CD program is given a great deal of attention. New efforts noted this year include construction and utilization of training facilities which will give the entire population the opportunity to perform CD tasks under simulated emergency conditions. Also, Soviet planners are working out problems of storing and distributing food grains – a prime concern in survival planning.

A *case study* was made of the Knoxville–Knox County industrial area to determine the best methods for sheltering *workers in critical industries* which would continue to operate during a nuclear confrontation which has escalated to an urban evacuation. The alternatives by order of cost effectiveness are (1) *tactical evacuation,* (2) expedient construction of covered trench *blast shelters,* (3) expedient modification of existing structures, (4) precrisis construction of blast shelters. Recommendations to implement the alternatives include pilot studies of tactical evacuation and improvement of expedient blast shelter construction and modification instructions.

Research was continued on survival techniques, with particular emphasis on life-support equipment which could be built during a crisis by average Americans using readily available materials. These include means for carrying and storing water, means for cooking with minimum fuel in austere shelters, shelter sanitation equipment, shelter furnishings, and an accurate, reliable homemade fallout survey meter. The most exciting of these is the fallout meter. To make it, all that is needed is a used No. 2½ can, aluminum foil, nylon thread such as dental floss, a 1-ft ruler or stick, coat-hanger wire, two paper clips, a scrap of nylon cloth, household-grade transparent plastic, and bits of home-roasted Sheetrock wallboard (dehydrated gypsum). The roasting produces dehydrated gypsum, an excellent drying agent to keep the humidity very low and constant inside the instrument. This simple homemade fallout meter can measure the radiation dose accurately enough for a person to identify fallout radiation fields from background levels up to 6 R/hr with an accuracy of about 20%. Still to be determined is what fraction of American families can successfully follow illustrated instructions for building and using this instrument.

2. Reactor Studies

As part of the national Nuclear Energy Center site survey, we are studying the effects of national security considerations, of terrorist or sabotage threat, and of natural disasters on the NEC. Work has been started on the methods and costs of recovery from major accidents under the NEC siting concept.

In the analysis of the national security aspects of Energy Center siting, the definition of national security has turned out to be a problem. We are proposing the definition: "National security is the capacity of the government to neutralize threats to the lives, safety, and property of its citizens." By this definition the national security problems of nuclear power are two: (1) incidents which could generate political pressures to

delay the development or increase the cost of nuclear power and (2) the accumulation of large surface concentrations of fission products which could add significantly to the damage done to this country by a nuclear war.

Reactor complexes of about 5000 MW(e) and up will be strategic targets by the year 2000 solely on the basis of their economic productivity. Attacks concentrating on energy or electric power could include much smaller plants. By the year 2000, the projected number of reactors, reprocessing plants, and associated temporary (ten-year) waste storage will have a fission product inventory that could add substantially to the fallout from a nuclear attack and complicate and delay postattack recovery. One year after an attack on nuclear facilities in the year 2000, the residual fallout would be equal to that of an additional 30,000 megatons of 50% fission explosives arriving at the time of the attack. This additional fallout would increase the average residual dose rate at one year by a factor of 6 over that from the anticipated weapons.

Studies of the psychological motives of terrorists have identified a group of motives connected with the desire for power. While much more destructive tactics are economically and technically within the means of terrorists, theft or seizure of plutonium or armed occupation of a reactor is more consistent with their inferred motives.

Nuclear power generation stations built in Nuclear Energy Centers will be no more vulnerable to natural disasters than similar stations located at dispersed sites. However, due to the high concentration of power lines and cooling towers, the probability of damage by one tornado is slightly higher. But, by separating the cooling towers in an NEC as much as possible (e.g., 1000 yd apart) the vulnerability of a generating system based upon the NEC can be reduced below that of a comparable system based on dispersed sites.

One other difference between the siting options is that some dispersed system reactors may be sited in higher seismic risk areas than the NEC if there is sufficient water to operate the dispersed reactors without cooling towers.

There is concern in some quarters that the high rate of heat release at an NEC may trigger thunderstorms and/or tornadoes. The maximum practical dispersal of cooling towers is indicated in order to reduce this possible hazard.

The quantitative effects of inhaled $^{239}PuO_2$ aerosols are calculated and compared with occupational exposure data. Calculated effects on the U.S. male work force and the U.S. population are presented for cases in which each member of the population has the same exposure to the aerosol. The effects of cigarette smoking are compared with the effects of a lung burden of $^{239}PuO_2$. One microgram of ^{239}Pu retained in the lungs is estimated (by extrapolation of animal data) to produce an excess death rate in 40-year-old males that is one-fourth of the excess rate attributed to average smoking.

A high-altitude nuclear detonation produces a very intense short-duration electromagnetic pulse (EMP) which can cover a large portion of the nation. It is possible that EMP-induced electrical surges in instrumentation, control, and power lines of nuclear power plants could lead to serious consequences. A preliminary analysis of the EMP effects on modern pressurized-water reactor (PWR) plants has been performed as a first step to determine if EMP is a serious problem for nuclear power plants. We found that the most likely consequence of EMP for PWR plants is an unscheduled shutdown. EMP may also prolong the shutdown period by the unnecessary activation of certain safety systems. It is also possible but not likely that numerous EMP's can temporarily interrupt the removal of the residual heat from the reactor. However, no damage to the reactor is expected, since the prepared plant can quickly start the steam-driven auxiliary feedwater pump without the use of electrical controls.

PART II. ASSESSMENT AND TECHNOLOGY

3. Dosimetry Intercomparison Studies

One of the most important aspects of this program in dosimetry has been the planning and conducting of studies and workshops in dosimetry standardization techniques and detector response intercomparisons. During this year, the first intercomparison of personnel monitors in low-intensity radiation fields at the Health Physics Research Reactor was completed. Participants in this study included representatives of foreign and domestic laboratories as well as private companies. The series will continue, with the second study planned for late 1975. In 1973, a small-scale intercomparison of environmental dosimetry systems was conducted at ORNL. The results of the experiment revealed the existence of inadequacies in many systems. Therefore, another, more sophisticated experiment was conducted in Texas in 1974. This field experiment was conducted under realistic conditions near Houston during the period July through September and was designed to assess the capability of dosimetrists to detect (with a high degree of accuracy) the intensity of natural

background under harsh environmental conditions. Results of this experiment are given in the text.

4. Health Physics Research Reactor and Accelerator Operations

The specific objective of this group is the maintenance and operation of the section's radiation facilities, which are used as tools in the areas of research, such as dosimetry, radiation biology, and other radiation effects studies, and for nuclear safety.

The Health Physics Research Reactor (HPRR) continues to play an important role in the efforts to correlate radiation dose with biological effects. Scientists from the ORNL Biology Division, UT-ERDA Comparative Animal Research Laboratory, and several other laboratories comprise the list of most frequent users. In addition, the HPRR is also used for nuclear engineering studies and for nuclear safety through the dosimetry intercomparison studies, which are designed to evaluate nuclear accident dosimetry systems.

Most of the operation of the DOSAR Low Energy Accelerator has continued in support of an experiment designed to determine the stopping of protons, in the energy range of 50 to 150 keV, in tissue-constituent gases.

5. Dosimetric Applications of Particle-Track Etching

Our recent work in particle-track registration in thin foils has been centered in three areas: (1) spark counting of particle tracks in mica, (2) spark counting of neutron-induced recoil particle tracks, and (3) the development of a neutron detector, suitable for making an accurate measurement of fast-neutron fluences, that can be transferred through the mail for intercomparison purposes.

We have demonstrated the feasibility of determining the density of fission-fragment tracks in inorganic material such as natural muscovite mica by the spark-counting technique. This development is important from the standpoint that trace quantities of ^{239}Pu may be detected through neutron-induced autoradiography without suffering from the disadvantages of organic polymers such as registration of recoil nuclei and damage from ultraviolet radiation and high temperatures. Optimum conditions for spark counting the thin mica were determined; it was found that the ~10-μm perforations could be counted with essentially 100% efficiency and that the reproducibility of repeated measurements was generally within ±5%. Recoil nuclei which are registered in organic polymers, in particular cellulose nitrate, and which result from the direct interaction of neutrons with the organic, have been counted successfully by the spark-counting technique. A series of experiments was performed with monoenergetic neutrons in the range 2.2 to 15.5 MeV. Results with the commercially available Kodak Pathé LR-115 were found to be reproducible to within 10%. Work has continued on a small-scale effort to develop or evaluate techniques for making accurate measurements of fast-neutron fluences for applications such as monitoring neutron beams for medical irradiations. Using fissile radiators with thin polycarbonate foils as detectors, it has been found that determinations of track densities in foils etched under carefully controlled conditions may be made by two persons independently with a reproducibility within ±5%.

6. Exoelectron and Thermoluminescence Dosimetry with BeO

The research and application studies using BeO ceramic for TSEE dosimetry have expanded to include TL dosimetry. A combined TSEE-TL technique is now used routinely and permits discrimination between the weakly and strongly penetrating components in mixed radiation fields with a single detector. The method produced promising results for the monitoring of radon.

The TL characteristics of BeO have been studied in considerably more detail, and a potentially valuable method of sensitizing the detectors to red light has been discovered. The betterment of our understanding of the TSEE process has concentrated on hydration effects, particularly those likely to be met under field conditions.

A bank of 500 BeO disks for TL and TSEE studies has been processed. The distribution of the individually calibrated detectors to groups in 14 countries should accelerate the acceptance, or rejection, of these novel dosimeters in radiation monitoring and bring better order into the diverse basic researches.

7. Distribution of Energy Losses of Low-Energy Protons in Hydrocarbon Gases

Measurements of the energy loss distributions of low-energy protons in several hydrocarbon gases were made possible by improved data-taking procedures and better techniques for correcting the data for accelerator fluctuations. Incident proton energies ranged between 51 and 153 keV, with the exact energy chosen so that stopping powers could be quoted at even energies. Gas pressures were chosen to provide a 40% loss in the mean energy of the proton beam. For an energy loss of this magnitude, the mean energy of the protons after

traversing the stopping medium and the second and third moments will describe the proton energy distribution. These values were calculated from the data for comparison with theoretical values. The energy loss data will also be used to evaluate the applicability of Bragg additivity of stopping powers for protons in this energy range.

8. Developments in Alpha Spectrometry with Liquid Scintillators

A program to optimize and simplify the chemical procedures and electronic apparatus used for liquid scintillation counting of alpha emitters has resulted in a number of improvements. It was found that reproducible results could not be obtained unless the chemical used to extract the alpha emitter from the sample into the scintillator was carefully purified. An alternative scintillator was studied with some success in an effort to reduce the amount of light being absorbed by the scintillator. A careful evaluation showed that only a small loss in counts occurred when an electronic discrimination method was used to suppress background counts. Chemical procedures were modified to allow the first stages of sample preparation to use well-known ion exchange techniques rather than solvent extraction. A combination of reflector geometry, photomultiplier tube, preamplifier, and amplifier was found that provided the best pulse height with background suppression. Preliminary work was also done on a simplified circuit for background suppression.

9. Dosimetry for Terrestrial Gamma-Ray Sources

Dose rates from natural radionuclides and ^{137}Cs in soils of the Oak Ridge area have been determined from in situ and core-sample measurements. Core-sample measurements were done by using conventional soil coring and gamma spectroscopy with an NaI detector. In situ gamma measurements were made in the field with a self-contained mobile unit that included a 4096-channel analyzer and a 55-cm^3 GeLi detector system designed for these measurements. The GeLi crystal is mounted on the bottom of the cryostat in a down-looking configuration, so the detector will not be shielded from the gamma radiation coming from the earth. The angular dependence and gamma-ray counting efficiency of this detector were measured.

In situ spectra were analyzed by a computer program which was written to identify and assign energies to peaks, integrate areas under peaks, and calculate radionuclide concentrations based on a uniform distribution in the soil. The assumption of uniform distribution was adequate only for natural radionuclides, but simple corrections were applied for man-made radionuclides distributed on the surface or exponentially with depth in the soil.

10. Dosimetry for Human Exposures

Depth-dose distributions in the body from gamma rays and neutrons are being investigated as functions of the energy and angular distributions of the incident radiation. Results of these studies have important applications in radiation therapy, design of dosimeters, shielding evaluation, and liaison studies with the Atomic Bomb Casualty Commission (ABCC) in Japan. During the latest liaison study, data which can be used to make estimates of the dose to some organs and tissues of survivors were presented to the ABCC. Examples are presented to show that these liaison studies can refine current estimates of risk derived from the ABCC's epidemiological studies by factors of 2 or more. Although the emphasis was on estimating dose to specific organs and tissues of atomic bomb survivors, some time has been devoted to older, but still important, items in the liaison studies with the ABCC. These are (1) the radiation exposure received by survivors now residing in the United States, (2) the epicenter of the Nagasaki weapon, (3) the shielding factors for survivors exposed in concrete buildings and other heavily shielded structures, and (4) the unknown radiation exposure cases in major study samples of the ABCC. Summaries are given of progress made in several phases of these liaison dosimetry studies by the ABCC and ORNL.

11. Application of ALAP Concept to Light-Water Reactors

The application of the as-low-as-practicable (ALAP) philosophy to radiation exposure of workers at light-water reactors (LWR's) has recently received increased attention. The purpose of this project is to investigate the means by which occupational exposure at operating LWR's can be reduced to the lowest practicable levels. Eight such facilities have been studied in phase I of the project to identify significant sources of exposure and to determine the magnitude of the exposures. A complete site review consists of compiling information from safety analysis reports, plant technical specifications, and radiation exposure records and then making an on-site visit for discussions with plant personnel, observation of procedures, and measurement of radiation levels. In phase II, specific problem areas are being studied in depth with regard to corrective measures to

reduce exposure. Information has been collected on solving the problem of exposure from valve maintenance and repair. These corrective measures will be evaluated with respect to ease of application and cost effectiveness. The results of this study will serve as technical backup for the preparation of regulatory guides.

12. Health Physics Aspects of Fusion Power

We have begun studies in three areas concerning potential health physics problems attendant to the development of fusion power. The first area, which contains perhaps the greatest number of unknowns, is that of neutron activation products. Activation products (with greater than 30-day half-life) have been identified which would result from using the principally discussed materials. Available data necessary to construct metabolic models are being collected. In many cases, few human data are available and animal data are inadequate.

The second topic is localized tritium behavior. A computer transport code has been modified to allow determination of the conservatism introduced in dose calculations by assuming that all of the tritium released into the atmosphere is in the form of water vapor. For a given set of meteorological conditions, the principal variables are the conversion rate of tritium gas to tritiated water and the environmental half-time of tritiated water vapor in the atmosphere.

The third topic under study addresses the global effects of tritium releases. A multicompartment generalized model of global hydrologic cycling is being used as a basis for determining the relative effects of alternative modes of tritium discharge on the collective dose to the world population. The compartments are assumed to mix instantaneously and uniformly and to interact with each other in linear fashion. Initial results indicate that uniform discharges of tritiated water into the atmosphere may result in as much as an order of magnitude less collective dose on a global basis than uniform discharges into the surface waters.

13. Public Health and Demographic Statistics

A study has been initiated to determine the feasibility of collecting public health and radioactive effluent data and applying these data to assess the impact of nuclear facilities on surrounding populations. Several sources of public health statistics are being evaluated with regard to the type and availability of information and the practicality of combining data from these sources. In addition, consideration is being given to determining the best statistical methodology. The Oak Ridge area is being used in a pilot study to determine the adequacy of existing records and to evaluate current methods of statistical treatment. Mortality information from the Tennessee Department of Public Health is being correlated with radiation exposures from the radioactive effluents of Oak Ridge nuclear facilities. Quantitative data are available for both aquatic and atmospheric discharges for recent years and can be estimated from records kept during earlier years. This pilot study will be used to develop a viable model which will be useful in achieving the long-range objective of the program, which is to establish a health and mortality profile for a proposed nuclear power plant site.

PART III. BIOLOGICAL AND RADIATION PHYSICS

14. Atomic and Molecular Physics

Our work on quasi-liquids (high-pressure gases), aiming at linking together knowledge on electron-molecule interactions in gases and liquids, continued with emphasis on a detailed study of electron attachment to SO_2 in dense gases. Additionally, existing data on electron capture and drift in gases have been related to those in liquids, and two new pieces of apparatus – one for the measurement of electron capture and drift in dense gases and the other for similar studies in liquid media – have been constructed. Theoretically, in this area we focused attention on the long-range potential energy function describing the interaction of an excess electron with a molecule in a dielectric liquid. Furthermore, we synthesized in a coherent fashion, critically evaluated, and discussed experimental and theoretical work on electron motion through aromatic vapors and also on the excitation and ionization, resonant negative ion states, and negative ions of benzene and its derivatives.

As part of our effort to extend our understanding of fundamental processes on radiation (ionizing and nonionizing) interaction from simple to complex molecules, we undertook a comprehensive and systematic study of organic molecules of biological and toxicological significance. To this end a series of 40 NO_2-containing benzene derivatives have been investigated with mass spectrometric methods. All these molecules were found to form long-lived (lifetimes $> 10^{-6}$ sec) parent negative ions. The lifetimes of these ions were measured, and their relation to molecular structure, intramolecular charge transfer, and intramolecular complexing was treated theoretically. Additionally, threshold electron excitation and compound-negative-ion resonant states, as well as photoluminescence processes in aromatic molecules, have been investigated, and the

slowing down of subexcitation electrons in polyatomic gases has been studied. In the latter study, mobilities, mean fractional energy losses per collision, stopping rates, and thermalization times for subexcitation electrons in polyatomic gases have been determined as a function of mean electron energy.

Finally, a program has been initiated to apply the basic knowledge we have obtained on electron attachment to and elastic and inelastic electron scattering from polyatomic molecules to improve the breakdown strength of high-voltage dielectrics.

15. Physics of Liquids and Surfaces

Experiments have been initiated on the scattering of light from cylinders. An He–Ne laser beam is incident on aluminum-coated glass cylinders as small as 5 μ in diameter. The scattered light intensity shows structure due to excitation of surface electronic states. Application to understanding of electronic behavior of macromolecules and to detection of cylindrically shaped pollutants of the atmospheric and aquatic environments is anticipated.

The optical and dielectric functions of the alkanes tetradecane and heptadecane have been obtained in a joint effort between the Physics Department, University of Tennessee, and ourselves. Optical absorption characteristics out to 26 eV show that these alkanes in the liquid state have characteristics similar to both lower and higher alkanes in the vapor and solid states respectively. However, our liquids show a maximum in the energy loss function at 21 eV which is similar to that in pump oils DC-704 and -705, glycerol, and liquid water and is similarly explained as due to excitation of a collective electronic resonance.

A cooperative program with the Thermonuclear Division involves studies of the feasibility of optically monitoring the thicknesses of deposits on the inner liner of ORMAK. A prototype device has been designed and installed on ORMAK which involves shining a laser beam through windows in the outer vacuum wall and liner onto the inner surface of the liner. When this has been calibrated, it should yield the thicknesses of the deposits from a measurement of the reflectance. The feasibility studies which preceded the design of the device are described in Chap. 16 of this report. This work complements and supplements studies on the liner being performed by personnel of the Metals and Ceramics Division.

Equipment is being constructed and assembled to measure energy losses of electrons scattered from the surfaces of various low-vapor-pressure liquids whose electronic behavior has been studied. For example, for pump oils DC-704 and -705 and/or glycerol, we will investigate whether or not collective electronic states are excited as predicted from optical data. We will look particularly for evidence of surface-plasmon states similar to those reported by Powell for liquid metals.

16. Physics of Solids and Macromolecules

In this program we are undertaking a study of some of the fundamental properties of solids and macromolecules. Photons with energies extending from the infrared to the soft-x-ray region are used to obtain reflectance, transmittance, and photoelectron yield. Such data can be analyzed to yield the optical and dielectric functions associated with the bulk material, electron attenuation lengths in the material, and surface roughness parameters. Interpretation is in terms of energy levels in the solids and macromolecules and photon-electron, photon-plasmon, electron-electron, and electron-phonon interactions. Applications include studies of solar cell material, photosynthetic processes in chloroplasts, chemical and radiation assaults to biological materials such as DNA, basic processes involved in coal technology, and electron mean free paths in communications materials. High-energy electrons are also used to excite single electron transitions and collective electron oscillations in solids, yielding information complementary to that obtained from the optical measurements. In each case the emphasis is on understanding the fundamental processes involved through the study of relatively simple materials.

This year we have obtained the optical properties of solid sodium and lithium in the range of photon energies from 0.6 to 3.8 eV by ellipsometric techniques. This is preparatory to obtaining the optical properties of liquid lithium, using the same techniques. A comparison of the data for solid and liquid lithium will test theories on disordered systems, and the data for liquid lithium will also have a direct practical application in the design of fusion reactors.

As an extension of our previous work on surface roughness, we have measured the specular reflectance from several diffraction gratings with different groove profiles and then analyzed the data in terms of the known periodic "roughness" of the grating profile.

Electron attenuation lengths in solids are known to be small in the energy range from 10 to 100 eV, and hence their accurate determination is difficult. At the same time, the values of these electron attenuation lengths in both metals and insulators are of great importance, both theoretically in solid-state physics and practically

in connection with solid-state devices used in communications systems. We have used various photoelectric yield techniques to obtain values of electron attenuation lengths in aluminum and carbon. We are currently analyzing the sensitivity of each method with the hope of learning how to get completely consistent and reliable values of electron attenuation lengths for 10- to 100-eV electrons in both metals and insulators.

Studies of the optical properties of materials of biological interest, initiated in the Physics of Tissue Damage program, have been continued with the measurement of the optical properties of bovine plasma albumin (a protein) and of polystyrene over the range of photon energies from 2 to 82 eV. These data yield information on the molecular excitations in bovine plasma albumin and in polystyrene. Most important, these data indicate that ionizing radiations traversing either material show a high probability of exciting collective electron oscillations, or plasmons, with an energy of ~21 eV. This same result has been seen for all the solid and liquid organic materials (as well as for water) studied in our laboratory and at the University of Tennessee over the past few years. Thus plasmon creation represents an extremely important mechanism for energy absorption in biological materials and should be a significant factor in track structure models.

During this reporting year we undertook to examine the feasibility of monitoring the first wall in ORMAK (Thermonuclear Division, ORNL) by optical measurements. Calculations of the normal-incidence reflectance as a function of the thickness of a contaminant layer on a gold substrate showed that a monolayer or two of a contaminant on the gold produces a measurable change in the reflectance at a suitably chosen photon energy. A knowledge of the nature of the contaminant, in addition to the reflectance, is required in order to obtain the contaminant film thickness. Uncertainties concerning the nature of the contaminant coupled with scattering problems may prohibit calculations of the exact film thickness by this method, but it should provide a qualitative, if not quantitative, monitor of the surface conditions. A monitoring device which has been designed and installed on ORMAK is described in Chap. 15 of this report.

Soft-x-ray emission spectra have been obtained for evaporated films of LiF, LiCl, and LiBr. To overcome the perturbations of the spectra due to halogen evolution, each point on each spectrum was obtained on a fresh film evaporated in situ. Independently measured photoelectron spectra and optical gap data used in conjunction with our soft-x-ray emission spectra lead to the identification of prominent peaks in the spectra at 61.0, 60.5, and 59.6 eV for LiF, LiCl, and LiBr, respectively, as due to the radiative decay of core-level excitons.

17. General Physics

The work of the General Physics Section seems to divide naturally into two broad categories: (1) the interaction of charged particles with matter and (2) the interaction of photons with matter. Although the work described here is basically theoretical physics, it is closely related to experimental programs at ORNL and elsewhere and has direct applicability for areas as diverse as cancer radiotherapy and nondestructive testing.

Interaction of charged particles with matter. In our theoretical dosimetry program, the computer code PION-1, written for the transport of pions through matter, has been further improved and now appears to contain an adequate treatment of all the physical processes important for applications to cancer radiotherapy. Several calculations have been made of dose distributions from pion beams.

Recent interest in the use of negative pions for cancer radiotherapy has resulted in the necessity for development of pion dosimetry. The use of ionization methods for dosimetry requires a knowledge of W, the average energy required to produce an ion pair. Although W values have been measured for most common types of radiation in many gases, its value for the complex radiation fields that occur from pion irradiation has not. We have made a study to estimate the value of W in nitrogen and argon for the radiation resulting from pion capture stars as well as the value in the plateau and peak dose region for a pion beam typical of those proposed for therapy treatments.

As a charged particle penetrates matter, it undergoes a large number of small-angle scattering events due to Coulomb forces. This multiple Coulomb scattering markedly affects the patterns of dose deposition that can be obtained with pion beams, largely determining the extent to which observed dose can be localized in a tumor region. Because of the large number of scattering events, direct collision-by-collision simulation in Monte Carlo computer codes is not feasible. Three analytic procedures for simulating multiple Coulomb scattering in Monte Carlo codes have been studied, and one has been selected that gives an adequate treatment for radiotherapy applications and that is reasonably efficient in terms of computer running time.

A great deal of effort has gone into the study of the interaction of electrons with matter. Our interest here

centers around differential inelastic interaction probabilities for low-energy electrons in matter and such derived quantities as mean free path, stopping power, and range. Most of these calculations take as a starting point the dielectric response function of a given material, $\epsilon(k, \omega)$, which describes the response of the material to a momentum transfer $\hbar k$ and energy transfer $\hbar\omega$. While this function calculated for the electron gas model has been used quite successfully in understanding the properties of metals as a class, calculations of the dielectric response function for semiconductors, semimetals, and insulators usually deal with specific solids. We have derived a dielectric response function for a model insulator which should prove to have a similarly wide applicability in describing the valence-band electrons in insulators. This general model may be made to apply to specific insulators by a proper choice of the adjustable parameters of the theory. The model insulator theory has been applied in a simplified form to Al_2O_3 by assuming that all valence-band electrons have the same binding energy and determining adjustable parameters such that the imaginary part of the dielectric response function in the zero-momentum-transfer limit agrees with experimental optical data. Encouraging results have been obtained even with this very simple form of the model insulator theory.

The electron gas model for the response of conduction electrons in metals is limited to some extent by the assumption of a uniform electron density. We have been examining a statistical method for the evaluation of low-energy-electron inelastic mean free paths which incorporates the relative simplicity of the electron gas model. The response of the conduction electron at some point in the metal is taken to correspond to an electron gas of density equal to the electron density at that point. The electron inelastic mean free path calculated for a given density is then averaged over the distribution of electron densities in some appropriate volume of the metal. Relativistic Hartree-Fock methods have been used to calculate the electron density distribution in space for silver and gold. Low-energy-electron mean free paths obtained using this statistical procedure agree reasonably well with experimental results for low-energy electrons, considering the difficult experimental problems involved.

The differential cross sections for excitation of electrons to the continuum from the inner shells of aluminum and oxygen atoms by incident electrons have been computed from tabulated generalized oscillator strengths (K shell of O; L shell of Al) and hydrogenic form factors (K shell of Al). This information will be combined with an electron gas treatment of the conduction-band electrons in aluminum metal and the model insulator theory for the response of valence-band electrons in the insulator Al_2O_3 to describe the most important processes by which electrons lose energy in these materials. This information will be used to tabulate mean free paths, stopping power, and range for electrons over an energy range of ~10 eV to 10 keV. These tabulations should be useful to workers in many areas.

A theory has been developed to account for the energy loss of swift proton clusters in solids. Energy loss measurements in transmission experiments on carbon and gold foils with ~100-keV/nucleon H_2^+ and H_3^+ beams reveal that protons moving in spatially correlated clusters have effective charge numbers significantly larger than unity. Qualitatively, as the molecule enters the target, the valence electrons are stripped and the atomic ions move apart under the influence of Coulomb repulsion. The energy loss of the cluster thus is some intermediate value between what is predicted for a point charge corresponding to the sum of the charges of the atomic ions and that for the completely separated atomic ions, depending on the time spent in the target. A linear response theory treatment has been used to derive an effective charge for the cluster as a function of dwell time in the target. The theory takes account of the motion of the particles in the cluster, the distribution of internuclear distances in the cluster on entering the target, and the coherent dynamic response of the target electrons. Quantitative agreement is found between theoretical predictions and the measurements of cluster energy loss for H_2^+ and H_3^+ beams.

Interaction of photons with matter. In our continuing study of collective states in solids and their role in energy transport processes, we have been examining numerically the equations describing the scattering of light by cylinders and the excitation of surface-plasmon modes on the cylinders. We have developed a computer program to calculate the extinction, scattering, and absorption efficiencies for a plane wave of arbitrary angle of incidence on a right circular cylinder. We are now able to calculate these quantities for a cylinder of arbitrary complex dielectric function with a cylinder radius less than about 2 μ. Calculations using a complex dielectric function describing an electron gas of a density corresponding to the density of conduction-band electrons in aluminum show peaks in the scattering efficiency corresponding to the excitation of various surface-plasmon modes on the cylinder. These efforts are designed to complement experimental work carried out in the Physics of Liquids and Surfaces Section.

Void formation in a solid subjected to neutron irradiation may cause serious deterioration in the mechanical strength of the material. Nondestructive diagnostic techniques are needed in this area. Our earlier calculation of surface-plasmon excitation on spheres has been reexamined and revised to describe the excitation of surface plasmons on voids in x-ray inelastic scattering. The response of the medium in which the voids are located is described by a free-electron-gas model. Intensity measurements and energy analysis of the scattered x rays should reveal information on, for example, void density, void size distribution, etc. We are encouraging experimental work along these lines to determine the usefulness of the theory for practical studies of void formation in metals.

PART IV. CHEMICAL PHYSICS AND SPECTROSCOPY

18. Chemical Physics Studies

A number of new and some very dramatic results have been obtained in our continuing studies of the physical and chemical properties of molecular negative ions. With the unique crossed-beam, charge-exchange technique for studying properties of molecular negative ions, studies of chemi-ionizing collisions of sodium, potassium, and cesium atoms with both organic and inorganic molecules have revealed abnormally large electron affinities for several hexafluoride molecules (more than 4.5 eV) and the first observation of a thermal-energy gas-phase collisional ionization process between ground-state reactants (a new kind of chemi-ionization). Detailed experimental studies of alkali-atom scattering by linear triatomic molecules have contributed greatly to our understanding of molecular collision physics. Here we find linear molecules which produce negative ions only after undergoing extreme distortions into a "bent" configuration. A new and potentially very useful method for predicting electron affinities of polyatomic organic molecules of the simple conjugated hydrocarbon type has been developed. The semiempirical theoretical method gives results which are in extremely good agreement with experimental data from molecular beam experiments.

Our detailed studies of molecular dissociative ionization by electron impact have been extended to include polyatomic as well as simple diatomic molecules. The kinetic energy information on various dissociative products provides unique input to questions involving "hot" atoms or ions in atmospheric physics or radiation chemistry studies.

In addition to studies of attachment to and excitation and ionization of atoms and molecules by electron impact, we have also studied reactions of highly excited atoms with unexcited molecules to produce positive and negative ion pairs and with other atomic species to form ionic species through associative ionization. Other properties of highly excited molecular species have been further elucidated through an extension of a theoretical study of unimolecular decompositions. Close agreement has been obtained with recent experimental data. Our experience in electron transfer mechanisms, electron affinity, and ionization potential determinations has been brought to bear on a cooperative study with other divisions of the Laboratory of highly conducting organic charge-transfer salts. Initial studies of TTF-TCNQ salts, mentioned last year, have been extended to studies of ionization potentials and electron affinities of a number of other organic donor-acceptor molecules. Additional optical and electrical conductivity measurements have been made on TTF-TCNQ and other charge-transfer salts over a wide range of temperatures.

Finally, theoretical studies have been made of level shifts of spectral lines which result from Coulomb interactions of neighboring atoms in a high-pressure gas and of rotational resonances in low-energy electron scattering by molecular hydrogen. The first theoretical confirmation has been obtained of the presence of a rotational resonance in the elastic scattering by molecular hydrogen of electrons with energies below the first inelastic rotational threshold. Certain experimental data have been rationalized on the basis of rotational resonances for the last five or more years. The present study has confirmed long-standing speculations on such phenomena.

19. Atomic Physics and Laser Research

This year our research program on energy pathways reached an exceptional level of excitement through new scientific accomplishments and through recognized applicability of the research to several first-order practical problems. We developed a new method for the study of quantum-selected excited species. The method (called resonance ionization spectroscopy, RIS) involves saturated photoionization of excited states, making possible the measurement of the absolute number of states by accurate and sensitive ionization means. RIS impacted our study of the energy pathways following pulsed proton excitation of gases by making possible direct measurement of metastable- and resonance-state populations with laser pulses combined with proton pulses in an ionization chamber.

Research on energy pathways in the noble gases has been a major program for the understanding of the interaction of radiation with matter, and knowledge from this area of physics research has been directly translatable, for instance, to radiation chemistry research and to gas discharge and other plasma devices. Currently, we see two other important applications of these studies, both of which (atmospheric pollution characterization and laser research and development) are now being pursued as an integral part of this program.

Atmospheric pollution characterization. Energy stored in noble gases will seek out trace quantities of impurities and either ionize these (Jesse effect) or cause them to fluoresce. Thus, very sensitive analytical systems are possible simply by looking at characteristic emission from impurities mixed with an irradiated noble gas. This year we have obtained energy transfer rates for several excited atomic and excimer states of both helium and argon to various atmospheric pollutants. Also, we have developed new facilities for the characterization of pollutants through their emission spectra (500 to 10,000 Å).

Laser research and development. ERDA has programmed considerable effort into the development of high-power gas lasers for controlled fusion and isotopic enrichment applications. Several of the major approaches under way in the Laser Research and Technology Division of the Los Alamos Scientific Laboratory can utilize the research results which we obtain on energy pathways for specific laser systems; hence, our program now derives financial support from LASL. Our research can be utilized directly for the development of excimer lasers, including those involving noble gases and metal vapors. Thus we have developed heat pipe facilities and other equipment necessary for the study of metal vapors with our pulsed proton (3-MV Van de Graaff) accelerator. Time-resolved emission studies will also be made on quantum-selected atomic precursors of the metal vapors. Another laser system of considerable promise is the energy transfer laser; this year we made time-resolved emission studies on one example, the $Ar\text{-}N_2$ system.

Resonance ionization spectroscopy can, in principle, be utilized with ionization detectors (Geiger-Mueller counters, proportional counters, and other one-electron detectors) to make possible the detection of one atom in a large-volume sample. We have started a program on "one-atom detection" aimed at demonstrating this ultimate analytical sensitivity. Our current research in this area includes a broad study of laser-induced background and a study of a combination of laser beams fired directly into a gas-flow proportional counter. Future applications of one-atom analytical devices may include (1) aerial survey of atmospheric pollution and of mineral and oil deposits, (2) detection and characterization of new elements, (3) measurement of extremely slow chemical reaction rates, (4) measurement of very slow diffusion of species through materials such as reactor vessels, (5) detection of sputtering products associated with radiation damage, and (6) vapor pressure measurements of the metals.

PART V. MEDICAL PHYSICS AND INTERNAL DOSIMETRY

(Chapters 20–38)

The report of the Section continues to illustrate the merging of the several disciplines which comprise this research area, although internal dosimetry remains the firm basis of much of our research. The Section has attempted to meet the continuing demands placed on the dose-estimation program through additional refinements to the computer codes and models used to produce these estimates.

The annual progress report contains a large number of papers on metabolic modeling and dose estimation. We have attempted to provide data applicable to some of the more practical problems faced by the health physicist. One of the highlights is the paper by Bernard and his colleagues on the noble gases. This paper develops metabolic models needed for estimation of dose equivalent from exposure to noble gases. The models are based on published data on exhalation of ^{222}Rn by a human subject. The variation of absorbed dose with shape and size of the thyroid is also a timely study. The thyroid is quite variable in size and shape. Dose estimates are required for use in environmental impact statements, etc., and a range of sizes and shapes (corresponding to various age groups) must be considered in order to put these dose estimates in the proper perspective.

The extension of internal dosimetry research into the area of nuclear medicine is apparent also in our progress report. Two papers on the continuing study of the bladder and excretion patterns illustrate this point. We also propose a semitheoretical approach to the retention and excretion of various ions based on the results of a continuing study in cooperation with the Radiochemistry Group in the Division. In addition, we report on two studies related to the development and use of nuclear-powered cardiac pacemakers.

Other aspects of our research are shown in the papers on exposure of children to an infinite cloud of a photon

emitter, the effect of source-organ size on the absorbed fraction distribution, and the development of improved mathematical models for a one-year- and five-year-old child. The remaining papers reflect our interest in x-ray diagnosis and therapy, dosimetry for neutron therapy, and other aspects of internal dosimetry (e.g., the cooperative research program with the Comparative Animal Research Laboratory).

PART VI. OFFICE OF EDUCATION AND INFORMATION

(Chapters 39, 40)

The Division's Faculty Institute in Applied Health Physics was started in the summer of 1974. Under this program, which was undertaken in recognition of the nation's growing need for technologists trained in health physics at the bachelor's level, up to ten participants spend ten weeks in the Division during the summer. Nine faculty members from different colleges and universities participated during 1974 in anticipation of implementing undergraduate courses in health physics at their home institutions. The Institute provides supplemental training, experience, and educational materials for college faculty to teach undergraduate health physics. A follow-up survey of the first year's participants indicates that the Institute was successful in increasing the number of institutions where formal undergraduate health physics training is, or soon will be, available.

The Division has continued its teaching, training, and research relationships with Oak Ridge Associated Universities, the University of Tennessee, and a number of other universities at home and abroad.

The Health Physics Information System has developed rapidly. During this year the structuring of the data base and format has been finalized in consultation with the Division's staff and the Laboratory's Energy and Information divisions. A number of requests for health physics information on a range of topics were answered.

Part I. Emergency Technology

C. V. Chester

1. Strategic Defense

G. A. Cristy C. M. Haaland C. H. Kearny Ruby N. Thurmer

NATIONAL SURVIVAL AFTER A NUCLEAR ATTACK

C. M. Haaland

Introduction

It is becoming widely conceded among "thinkers about the unthinkable" that the Soviet Union would not attack the U.S. with nuclear weapons without first activating their extensive civil defense plans, which involve the massive evacuation of population from urban areas. Such large-scale movement would quickly become evident to the U.S. through many channels, and if it were combined with an obvious escalation of military activity and political tension, it is believed by many defense officials that an effective evacuation could be carried out in the U.S. during the same time period. The planning required to make this evacuation effective has come to be known as Crisis Relocation Planning (CRP) within the Defense Civil Preparedness Agency (DCPA), and the general philosophy of crisis relocation and preparation for threatening nuclear attack has been adopted by Secretary of Defense Schlesinger, as described in his report to Congress on February 5, 1975.

One of our tasks in the Emergency Technology Section is to define the nature and scope of plans for taking care of the needs of the people after a nuclear attack, assuming that most of the urban population has been relocated to low-risk areas before the attack, and that protection from the radiological hazards of fallout has been provided. The magnitude of the nuclear attack on the U.S. is assumed to be consistent with the current SALT limitations, which are to extend through the year 1985. Through effective execution of CRP, we are to assume that over 90% of the U.S. population is expected to escape the direct effects of nuclear weapons and will be protected against the harmful effects of fallout. However, most of the urban centers will be destroyed, including their warehouses, storage facilities, communication and transportation centers, industrial plants, hospitals, and social service centers. Furthermore, the movement of people and goods in unattacked areas may be hampered in many places by the presence of dangerous radiation from fallout for a few weeks after the attack. Under these circumstances the major problems become those of existence for the evacuated population through threats of starvation, thirst, and disease, exacerbated by breakdown of authority and general loss of morale. Our problem is to determine (1) whether continued existence is possible after a nuclear attack with current CRP, (2) what is required to make existence (survival) possible if it doesn't appear to be possible at present, and (3) what plans can be made to enhance survival and shorten the time-span from nuclear attack until most of the evacuated labor force can be put back to work again. Answers to these questions are being sought under the assumption that the entire nuclear exchange would occur in a few hours or days, with an attack pattern given to us by the DCPA.

An Overview of the Problem

A simplified approach to the first problem mentioned above, namely, whether existence is possible after a nuclear attack, is to ask whether there will be enough

food and water, assuming lodging facilities exist, to feed the survivors, and if there *is,* how is that food and water distributed geographically in relation to the distribution of the survivors; and if it is poorly distributed, how can it be redistributed?

Water Supply

For most areas designated as reception areas in the U.S., there are abundant water sources. In many localities, local water purification equipment will be overloaded if evacuees and hosts attempt to use water at the precrisis rate of about 100 gal/day per person. Reduction in the use of purified water for bathing and washing will result in an adequate supply of drinking water for nearly all areas. In those few areas where the local water purification equipment will not be adequate to handle the overload, there will be other sources of water from streams and dams which can be purified by mobile emergency water purification units. In the worst case, some people may use water from these sources for drinking without purification, and there is a danger that some of these people may consequently suffer from various dysenteries, typhoid, hepatitis, and other water-borne diseases. In general, there will be enough water such that people will not die of thirst in the postattack situation. There may be a problem in some locations with soluble radioactive components of fallout, such as iodine, which may require special treatment of water by filtration or distillation, or which may be counteracted by prophylactic measures.

Food

In the postattack period, most of the processed food in homes, retail outlets, and wholesalers' warehouses will have either been consumed during the preattack crisis period or destroyed by the attack. Most of the livestock processing plants are located in target areas; hence the livestock food reserve will be largely unusable after the attack. Furthermore, much of the livestock may be killed by radiation from fallout, because little planning is being done to protect them from this hazard.

The major food reserve will therefore reside in unprocessed grains in the postattack situation. The food value of grains in normally covered storage is unaffected by fallout, and most of the U.S. grains are stored on farms, some in privately owned rural elevators, mills, warehouses, and processors, and some in grain terminals. We estimate that less than 20% of the total grain stock will be located in target areas at any one time. Total grain stocks in the U.S. in terms of food supply amounted to about 78 billion man-days or about one year for the U.S. according to the USDA report on October 1, 1974, and about $2\frac{1}{3}$ years on January 1, 1975, including wheat, corn, oats, barley, and soybeans. We assume that 3000 cal/person are required per day, and that an approximate average of 2 lb of grain will supply this caloric requirement. With 20% of the grain stocks destroyed by the attack, there will remain approximately one year's food supply in grains for the surviving 180 million Americans, at the low stock level reported above for October, and about two year's supply at the January stock level. Since most of the U.S. farm area will be arable within a few weeks or months after the attack, regardless of fallout and the time of year of the attack, there will be ample time and opportunity to plant, grow, and reap new harvests before the grain stocks are depleted, assuming that petroleum is available for operating farm machinery. The problem now remains to determine how well the grain stocks are distributed in relation to the distribution of the postattack population.

Distribution of People in the Postattack CRP Situation

In our study the relocated people will be assumed to be distributed according to the plans of the DCPA, which follow fairly closely the computer program called ADAGIO, developed by Leo Schmidt at the Institute for Defense Analyses. This program indicates where people from each urban area should go in order to reach a low-risk area in terms of nuclear weapons effects, and it also evaluates the evacuated area in terms of its hosting ratio and the distance the evacuee must travel (straight-line). The hosting ratio is the number obtained by dividing the number of evacuees in a community by the number of preevacuation inhabitants. We have been provided with a data base which lists the number of evacuees and the initial population by county for the U.S., corresponding to a particular hypothetical attack pattern and level of attack.

Distribution of Grain Stocks

Information on total grain stocks cannot be obtained from USDA for counties in which there are less than three elevators, in order to protect the privacy of individuals in those counties; however, data on the total grains produced per year are available by individual counties for as late as the year 1973. We will assume that, for a part of the year at least, the grains are located within or near the county in which they are produced.

We further assume that the location and availability of grains at the time of the hypothetical attack under consideration can be fairly well represented by the data for 1973. The number of days of food available from all grains for the evacuated population distribution has been listed by county. This listing shows that even though there are adequate grain stocks for the nation to survive, they are not distributed where the people may be located after the cities are evacuated. Furthermore, although the evacuation program ADAGIO will indicate where people should go to avoid a high-risk area, we assume that the grain stocks are not moved during the crisis period, that grain stocks may be located in areas of high fallout contamination, and may not be accessible for movement for many days.

Distribution of Fallout Radiation

The attack pattern given to us by the DCPA was combined with the WSEG-10-NAS fallout model to generate radiation contours at different times after the attack. For simplification of the calculation it was assumed that all weapons were delivered simultaneously and that stratospheric winds, primarily responsible for delivering fallout from surface nuclear bursts, were uniform from the West, resulting in a 25-mph effective wind for computing the arrival of fallout downwind from the bursts. Radiation levels for 3 ft elevation above flat ground were calculated at the centroid of each 0.1° sector of latitude and longitude, and the contours were drawn by a linear interpolation program. Two representative fallout maps for the New England states at H + 48 hr and H + 336 hr (two weeks) are shown in Figs. 1.1 and 1.2 respectively. These maps indicate where movement of grains and people will be hazardous from radiation due to nuclear fallout.

Interstate Highways and Commercial Airports

The computer-drawn map in Fig. 1.3 shows a dot map of the interstate highway system. We also possess a data base showing the location of commercial airports and runways in the New England states. With the maps and listings described so far, especially when produced as transparencies at the same scale, an overview of the essential elements of the problem is presented.

In an actual situation of this nature, distribution of fallout radiation would not be predictable because of the variability of wind patterns and the additional uncertainty introduced by the effects of a large-scale nuclear attack on meteorological conditions. Further-

ORNL-DWG 75-7147

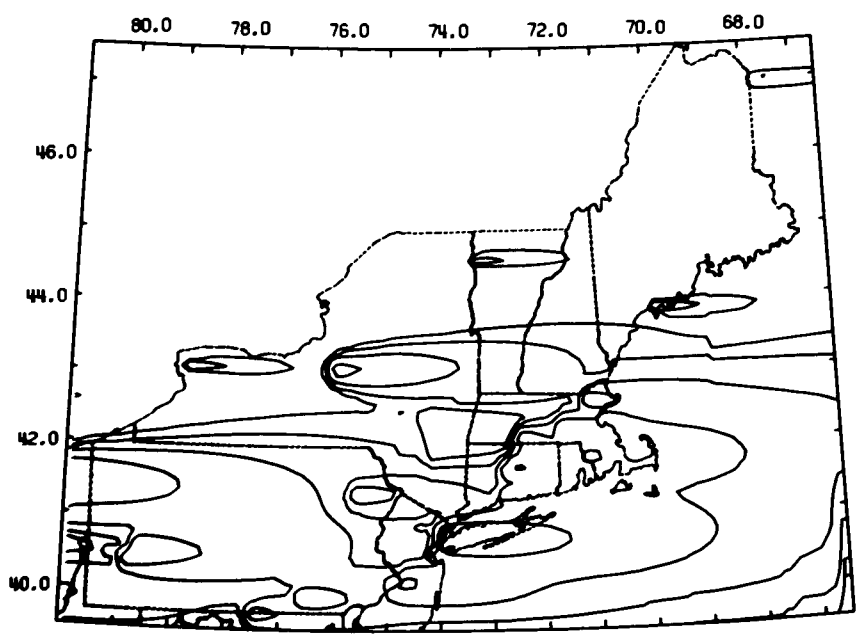

Fig. 1.1. Fallout radiation dose-rate contours for the northeastern United States at 48 hr after a nuclear attack. Dose rates at the contours are 1, 3, 10, 20, 30, and 100 R/hr, beginning at the outermost contour.

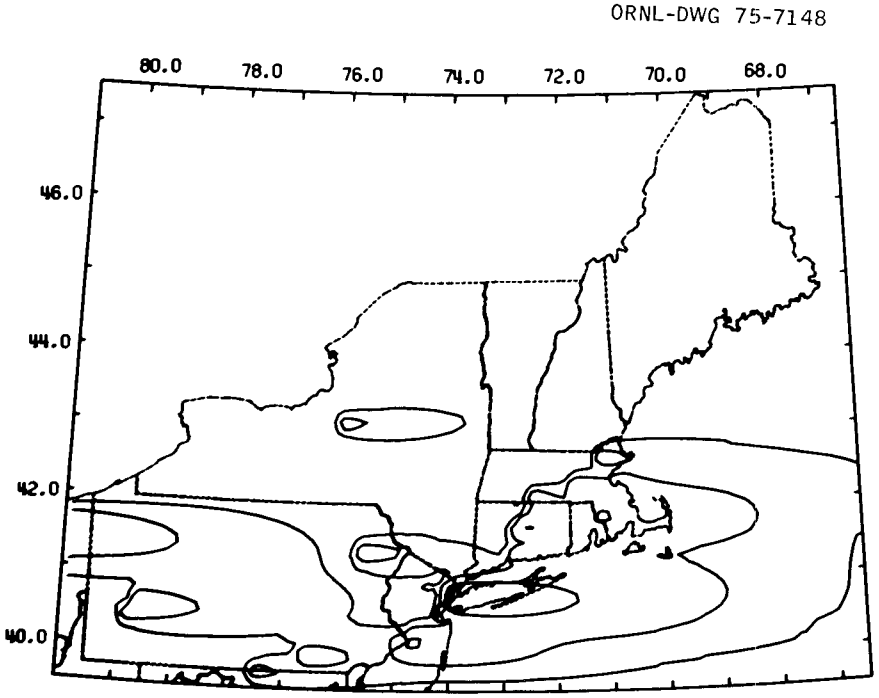

Fig. 1.2. Fallout radiation dose-rate contours for the northeastern United States at 336 hr (two weeks) after a nuclear attack. Dose rates at the contours are 1, 3, 10, 20, 30, and 100 R/hr, beginning at the outermost contour.

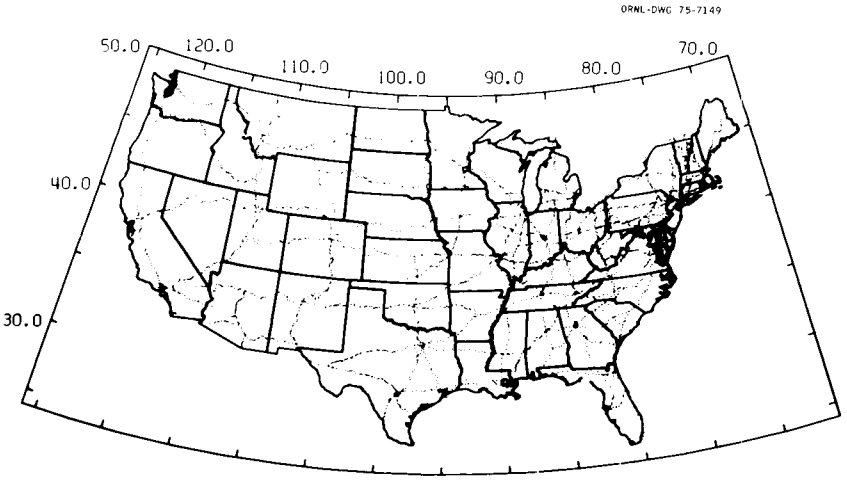

Fig. 1.3. The U.S. interstate highway system represented by a computer-drawn map with dots located at curves in the highways.

more, the actual distribution of the evacuated people may be uncertain. In order to solve the potential postattack food supply problem, it would be highly desirable to map the fallout radiation fields in some manner, perhaps by plane or by automatic field stations reporting upon radio call. The distribution of the evacuated population should be determined during the crisis period before the attack.

After the attack, the locations of destroyed bridges, runways, and railways should be assessed as rapidly as possible, as well as the availability of transport vehicles and operating personnel. A great number of commercial airports and truck terminals will survive the attack, including reserves of petroleum fuels stored at these facilities, as well as the transport vehicles themselves. We also assume that at least 3% of the U.S. and Canadian petroleum refining capacity survives, because it would require over 470 nuclear weapons to destroy 97% of the capacity existing in 266 plants, assuming 80% reliability for each weapon.

At present there are not enough separately targetable weapons in the Soviet arsenal to accomplish this objective in addition to the destruction of other targets which we assume must be rated with higher priority, such as the destruction of military targets and military-industrial complexes. This situation may change rapidly in the near future, as the Soviets replace their current missiles with the larger ones now ready for deployment, and replace the single warheads with MIRV's having much greater accuracy than the present missiles.

Transport Scheduling Model

The elements of the problem, as presented above, of providing adequate nourishment for the relocated population surviving a large nuclear attack can be solved by computer by use of modern linear programming techniques. While such an idealized situation and solution may be hopelessly impossible under actual conditions, it may be useful to go through the idealized calculation to determine whether the redistribution of grain stocks can be accomplished within the restrictions imposed by petroleum limitations. The basic assumptions of the model will be presented here without going into the details of the calculation.

The problem is to establish G days of grain supply in every county within D days after the operation begins, such that the days of grain supply on hand, H, are never less than some minimum, M, no person is exposed to more than R rads of radiation, and the total consumption of fuel, F, is minimized. Movement of grain may be accomplished by truck or aircraft. Trucks must be routed so that the operator receives no more than some level of radiation, to be determined, on the delivery leg of the trip. Aircraft operators are assumed to be exposed to no radiation during the entire trip, except while at their destination, and people may be transported out of a county on the return trip of the aircraft. Note that G will be variable in every county, depending on the population, P, of the county; so when people are transported out of a county, the ultimate grain goal, G, will be reduced, and H will be increased. This double operation of aircraft, hauling grain in and transporting people out, makes them more competitive with trucks, although the fuel penalty per pound-mile is much higher. A model in which trucks will haul people from certain areas will also be considered.

During the entire operation the radiation fields will be decaying in intensity as $t^{-1.2}$; hence at later times in the operation, more and more trucks will be able to operate. We will assume that major highway bridges which have been destroyed in the attack have been repaired or replaced by temporary bridges in a few days after the attack. For the purpose of calculation of fuel consumption, distances for aircraft transportation will be computed as straight-line distances between the geographical centroids of airports. Various truck routes will be postulated to maintain the total radiation exposure to the operator to R rads, with a protection factor of 1.5, and rerouting to avoid radiation fields will be assumed to proceed along the straight-line segments between the geographical centroids of counties. The maximum distance for a one-way trip will be 250 miles for truck (the usual radius of operation) and 1000 miles for aircraft.

We will assume that 20% of the current commercial aircraft force will be available immediately for the emergency airlift of grain, and that 10% more will become available in each of the following three weeks. During the crisis period, both trucks and commercial aircraft should be moved out of target areas. We assume that 30% of the precrisis truck force, by state, will be available for shipment of grains.

The establishment of this model and the calculation of results corresponding to different inputs will provide insight into the problems of whether survival is possible, and what is required to make survival possible. Additional studies are under way to develop plans which would enhance survival and shorten the time to reach a recovery stage.

SOVIET CIVIL DEFENSE STUDIES

Ruby N. Thurmer

Our continuing research of Soviet civil defense activities has revealed no evidence of any lessening of the

effort to prepare their people and industries for defense.

Since 1961, Civil Defense in the U.S.S.R. has been changing in scope and tasks. The nature of the measures carried out has also changed. During World War II the local air defense forces were credited with putting out 90,000 fires, preventing 32,000 serious accidents in critical industries, and disarming or rendering ineffective 430,000 bombs and 2.5 million shells and mines in the Moscow area alone. In 1961 this local air defense system was changed to Civil Defense.

Since that time its functions have increased sharply. Protection of the people is its main goal; however, Civil Defense is also expected to ensure the stable operation of units and branches of the national economy under conditions of war and natural disasters. Its responsibilities include the protection of industry, agriculture, communications, transportation, etc., against "weapons of mass destruction."

The Civil Defense organizations of the U.S.S.R. interact with the armed forces to a very great extent. In fact, both operate under a single military command. Soviet leaders consider Civil Defense an extremely vital part of their defense planning: quite naturally – because upon it depends the continuation of the essential activities of the state under conditions of a contemporary war.

In late 1973, party directives were issued which stipulated that civil defense preparations should be intensified. This increased effort was to be concentrated on bringing civil defense information and skills to the entire population. The manner in which this was to be accomplished was referred to as "practical training exercises." This meant that everyone – workers, students, housewives, and retired persons – was to be included in training classes. These classes were to teach by actual performance the measures necessary to survive a nuclear war.

In 1974 the Communist party directives stated that "site exercises" were to be introduced into the program. This new method means that training centers are being constructed which make it possible to teach such techniques as evacuation, fire fighting, decontamination, rescue and restoration, and shelter building under realistic crisis conditions. It has become apparent that shelters are considered a necessity for the entire population. Many industrial installations already have constructed large-capacity, permanent-type shelters for their employees. Other shelters are constructed in rural and residential areas in the course of the training exercises.

Another development of significance which we have noted is the recent announcement that planners in the U.S.S.R. intend to provide more adequate grain storage facilities throughout the country. They intend to increase their capacity by 2,500,000,000 bu, and this increase alone would result in an allotment of ~10 bu of wheat for every person in the Soviet Union. Additionally, they have declared that these new silos and elevators will be sited in rural, nontarget areas. It appears that the Soviets are getting to the problem of providing food supplies for their population who would survive a nuclear war.

The Communist press regularly emphasizes the importance of upgrading their country's defense capabilities – military as well as civil defense. It stresses their "peace-loving policies, coexistence, and detente" in one breath and their armed forces' ability to deliver a crushing blow to "the aggressive forces of imperialism at any time" in the next.

Again this year we have been able to complete the extensive editing and publication of a translation of the new Russian handbook entitled *Civil Defense, Moscow, 1974,* ORNL-tr-2845. Frequent articles in journals, annual reports, and oral reports to various groups serve to bring the results of our research to the attention of both the general public and influential decision makers. We maintain contacts with the Department of Defense, various Civil Defense officials, members of Congress, and others interested in furthering the cause of survival for the U.S.

BEST SHELTER FOR CRITICAL INDUSTRY WORKERS

G. A. Cristy

One of the serious problems related to the CRP effort of the DCPA is providing adequate shelter for workers in industries which need to continue operating even during a period of international crisis so intense that a strategic evacuation (i.e., crisis relocation) is initiated. A study was performed to determine what needs to be done by CRP planners and industry to provide adequate shelter. The study took the form of a case study of the Knoxville–Knox County industrial area.

A priority list was prepared of Knoxville industries which probably would be expected to continue operating during a crisis period (limited to the period of time between initiation of an evacuation and the detection of an enemy attack or the termination of the evacuation). Visits were made to 31 of the 135 companies on

the priority list. The information gained in those visits forms the basis for the conclusions reached.

Very few blast shelters are available, and few of the structures are of sufficiently strong construction to be considered for upgrading for blast resistance. A manual should be developed which would give guidance to companies who wish to plan for expedient modification of existing buildings. Most of the businesses employ such heavy and complicated machinery that it is impractical to consider relocation of the business to the low-risk areas. On the other hand, there are a significant fraction (25%) who could move part of their operations to low-risk areas, and a smaller group (13%) who have multiple plants which would allow shift of operations from high-risk to low-risk areas.

Many companies, particularly those in industrial park areas, have space available for constructing expedient covered trenches. Structural materials and mechanical earth-moving equipment could be made available through precrisis "mutual aid" agreements. To prepare fully for this alternative, new information on expedient shelter construction (especially blast-resistant covered trenches) needs to be developed and disseminated.

In the higher-blast-threat areas the only alternative seems to be to plan and execute a tactical evacuation plan. With careful preplanning and proper instruction of the workers, coupled with the relatively small number of people who would be in the evacuated area, the workers could drive to the locations where their families are sheltered after a warning of start of hostilities was given. Pilot studies of tactical evacuation are recommended.

The alternatives by order of cost effectiveness are: (1) tactical evacuation, (2) expedient construction of covered-trench blast shelters, (3) expedient modification of existing structures (number capable of such modification is severely limited), (4) precrisis construction of blast shelters.

EXPEDIENT LIFE-SUPPORT EQUIPMENT FOR SHELTERS

C. H. Kearny

The Need

Although the basic requirement for survival in a nuclear attack is an adequately protective shelter, most unprepared Americans also would need several life-support items in order to make their shelter structures habitable, and to improve their chances of surviving during the shelter-occupancy period and beyond. Therefore, during the past several years the writer has devoted almost as much of his civil defense efforts to the design and field testing of expedient life-support equipment for shelters as he has to the development and testing of expedient shelters suitable for crisis construction and use in the principal environments of the United States.[1–4]

For an essentially unprepared population, during a nuclear war crisis, there is certain to be a deficiency of adequately protective shelter space. There would be serious shortages, both of separate expedient shelters built during the crisis and of good shelters in preexisting structures, especially basements. In warm or hot weather, most such below-ground shelters must be provided with forced ventilation; otherwise, the humid heat produced by crowded occupants would, in many cases, rise to lethal levels. The best expedient air pump developed to date is the Kearny Air Pump,[5] so named by the Office of Civil Defense after extensive testing.

Since dependable light can be of critical importance in any long-occupied shelter, the writer has developed and tested several types of expedient lights. The best two types have been described in an ORNL publication.[5]

New or improved items of expedient life-support equipment have been thoroughly or partially tested and will be described in detail in ORNL reports to be issued during the next 12 months. These include (1) a homemade yet accurate fallout survey meter, (2) means for carrying and storing water, (3) means for cooking with minimum fuel in austere shelters, (4) shelter sanitation equipment, (5) shelter furnishings to increase both shelter capacity and comfort.

A Homemade Yet Accurate Fallout Survey Meter

Americans with the best chances of surviving an all-out Soviet nuclear attack – those outside the cities and other targeted areas – probably would have no information concerning, and would have no way of

1. C. H. Kearny, "Hasty Shelter Construction Studies," chap. 21 of *Civil Defense Research Project Annual Progress Report, March 1970–March 1971*, ORNL-4679.
2. C. H. Kearny, "Construction of Hasty Winter Shelters," chapter 14 of *Civil Defense Research Project Annual Progress Report, March 1971–March 1972*, ORNL-4784.
3. G. A. Cristy and C. H. Kearny, *Expedient Shelter Handbook*, ORNL-4941 (Oct. 22, 1974).
4. "Civil Defense Research," in *Health Phys. Div. Annu. Progr. Rep. July 31, 1974*, ORNL-4979, pp. 79–106.
5. C. H. Kearny, How to Make and Use a Homemade, Large-Volume, Efficient Shelter-Ventilating Pump, the Kearny Air Pump, ORNL-TM-3916 (August 1972).

measuring, the dose rate from fallout radiation, either outside or inside their shelters. Before an obviously very threatening crisis develops, very few Americans would buy or maintain conventional fallout monitoring instruments, all of which require batteries. Furthermore, such instruments would not be available in adequate numbers after a nuclear crisis became widely recognized.

Figure 1.4 pictures a man taking a reading with instrument No. 7, one of the first dependable home-made fallout survey meters that can be made using only materials found in millions of American homes. Instruments made like instrument No. 7, one of a number of different designs made and tested by the writer, give promise of being accurate within ±20% in the wide range of gamma dose rates (1 mR/hr to 6 R/hr) concerning which shelter occupants would need to be informed in order to decide when they could leave their shelters for extended excursions, or permanently. This simple instrument probably could be built and used successfully by millions of American families -- provided they are given very thoroughly field-tested, step-by-step illustrated instructions, and have sufficient motivation to study and follow these instructions. The development and field testing of these instructions will require much more work than has been required to date for the conception and development of this fallout survey meter.

Instrument No. 6 (not pictured) may be termed an electroscope-capacitor. It has two aluminum-foil leaves suspended on insulating nylon threads that are connected to the upper edges of its housing can, a standard No. 2½ can. The relative dimensions and positions of the leaves, their supports, and the housing cause instrument No. 6 to be much more stable and easy to read than is the Alvarez Fallout Meter,[6] to which the writer is indebted for ideas. Furthermore, the upper edges of this new instrument's leaves are stiffened with straightened paper-clip wire, both to prevent them from being deformed when they are being charged and to keep the like charges on the fully charged leaves from forcing them too far apart.

The suspended aluminum-foil leaves can be observed through the air-tight clear plastic covering that is taped over the open upper end of the housing can. The air and other things inside the sealed housing can are kept at a very low and constant humidity by small pieces of dehydrated gypsum[7] placed on the bottom of the housing can.

The efficiency of dehydrated gypsum in maintaining very dry and constant humidity inside instrument No. 6 (and also inside similar models) is proven by the fact that, even with leakage and normal background radiation, the change in reading of instrument No. 6 during a 13-hr period was only 1 mm. This change corresponds to a dose rate of 0.21 mR/hr; the dose rate from normal background radiation alone is about 0.02 mR/hr – assuming a normal background radiation of 170 mR/year.

The two insulated aluminum-foil leaves are charged by touching them with the charged strip of insulated aluminum foil of the expedient electrostatic charging device. This frictional device is inside the housing can and is operated by means of the handle of its movable part. This handle is made of coat-hanger wire and protrudes through a snug nail hole in the housing can.

The best electrostatic charging device tested before April 1975 consists of a strip of aluminum foil, insulated as a result of its being connected by nylon threads (such as nylon dental floss) to a small movable frame made of coat-hanger wire. The strip of insulated aluminum foil is charged by rubbing it back and forth on a piece of nylon cloth fixed to a coat-hanger-wire "seat" attached to the inside of the housing can. The aluminum-foil leaves are charged by touching them with the charged aluminum-foil strip. Two nylon stop threads, connected to the sides of the housing can, prevent the leaves from accidently touching the housing can and being discharged accidentally while the instrument is being charged or carried.

The like charges on the stiffened and weighted aluminum-foil leaves cause them to be pushed apart, while the unlike charge on the housing can causes the leaves to be pulled apart. The geometry and relative dimensions of instrument No. 6 are designed so that, as ionizing radiation causes the charges on the leaves to be decreased, the resultant decrease in the forces pulling the leaves apart compensates for the decrease in the horizontal components of the gravitational forces pushing the leaves together. As a result of this approximate balancing of some of the forces acting on the leaves, equal gamma doses produce almost equal decreases in the observed separation of the lower edges of the leaves, as shown by Fig. 1.5.

---

6. The Alvarez Fallout Meter was developed during the Cuban Missile Crisis by L. W. Alvarez of the University of California. It can be made in a few hours with common household materials. However, because its interior and its electrostatic charging devices are exposed to the ambient air, the Alvarez instrument cannot be charged under the humid conditions typical of a long-occupied fallout shelter. Furthermore, it is difficult to manipulate and has several other disadvantages.

7. Dehydrated gypsum can be made easily from ordinary Sheetrock wallboard, by heating pieces of its gypsum in a kitchen oven at 400°F, or higher, for an hour, or in a very hot frying pan for 15 min.

Fig. 1.4. Reading instrument No. 7 by looking straight down so as to observe the separation of the lower edges of the aluminum-foil leaves within the sealed housing can. The observed separation is noted on the scale (which has 1-mm divisions) attached to the top of the clear plastic covering of the housing can. The reader's eye is kept at a constant distance from the leaves by means of the 12-in. ruler, the lower end of which rests on a support attached to the outside of the housing can ½ in. below its upper edge, while its upper end presses against the reader's eyebrow. (Instrument No. 6 is read in the same way.)

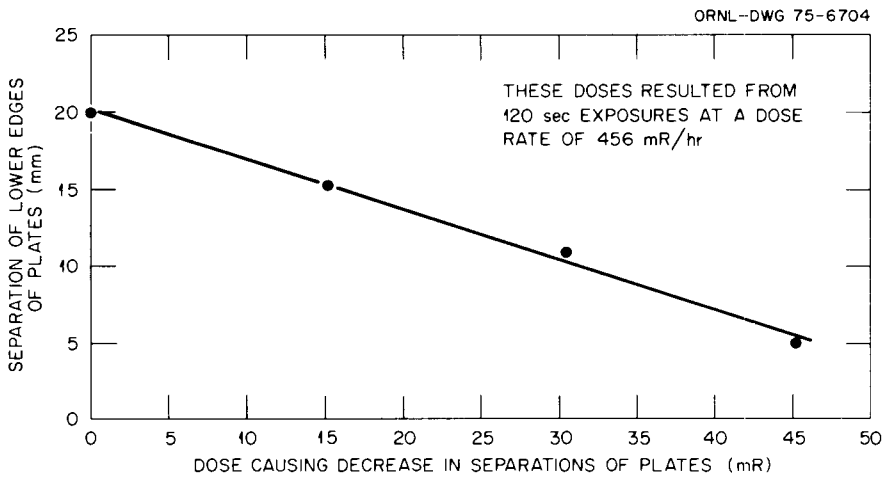

Fig. 1.5. Graph showing the almost straight-line relationship between four 15.2-mR gamma doses to which instrument No. 6 was exposed and the resultant observed separations of the lower edges of its aluminum-foil leaves.

An instrument of this type can be used most advantageously by charging it while inside a good shelter, and then exposing it for periods specified by tables and/or graphs that would be glued to its housing can. The tables and/or graphs would give dose rates for each of the specified exposure periods, corresponding to observed decreases in the separation of the leaves. For example, if a 30-sec exposure of instrument No. 6 outside a shelter results in a decrease of 10 mm in the apparent separation of its leaves, the outside dose rate is ~ 3.6 R/hr; if a 30-min exposure results in a decrease of 10 mm, the outside dose rate is ~0.06 R/hr, that is, ~ 60 mR/hr.

Fortunately, average citizens who will make and use this instrument will have no need to know all the hows and whys of its design and operation. If they follow the instructions and build their fallout meters out of the recommended cans, regular aluminum foil, No. 1 paper clips, and other remarkably standardized American products required, the fallout survey meters they make will be calibrated automatically and permanently – probably for decades if the instrument is kept stored in a sealed metal can with some dehydrated gypsum or other desiccant.

Means for Carrying and Storing Water

If subjected to the heavy, long-lasting fallout dangers that an all-out Soviet attack would cause, few shelters would have enough stored water to last the occupants until they were ready to leave shelter permanently. The most practical expedient means tested to date for carrying water is to line sacks, trouser legs, or pillow cases with larger-diameter plastic garbage or trash bags. With a plastic-lined, water-filled trouser leg or sack carried front and back over a person's shoulder, he can carry 40 to 80 lb of water for miles in relative comfort. Tests have likewise proven that a car can carry hundreds of pounds of water over rough roads, if the water is inside plastic bags used as the waterproof liners of somewhat smaller sacks, pillow cases, boxes, or large cans.

Plastic-lined sacks, boxes, or holes dug in the ground are generally the most available expedient containers in which to store large volumes of water. Field tests have shown that if a hole is dug with a diameter an inch or so smaller than the diameter of its intended plastic liner bag, and if all ends of roots and other sharp objects are first removed from the hole, then 25 gal of water can be stored in a hole with no other lining than an ordinary 30-gal polyethylene trash bag. To protect stored water from contamination by fallout particles or dissolved radionuclides in downward-percolating rainwater, holes or pits used for water storage should be provided with rainproof earth-covered roofs, like those of a small covered-trench shelter.

Up to hundreds of gallons of water can be stored in a pit lined with ordinary 4-mil polyethylene film. From such a storage pit, a below-ground shelter can be supplied with running water by making a siphon out of a garden hose.

From the above-outlined field tests, one can conclude that even the most economical civil defense preparations of a family or a community should include the stockpiling of large plastic bags and rolls or sheets of

4-mil polyethylene film for expedient water transport and storage.

Means of Cooking With Minimum Fuel in Austere Shelters

Although lack of adequate water is likely to be of life-or-death importance long before starvation endangers all but the youngest of shelter occupants, having a means to cook efficiently is likely to prove important. Figure 1.6 shows an expedient Bucket-Stove, the most efficient expedient stove developed and tested to date for use both during the shelter-occupancy period and the very difficult following months. Instructions have been field tested that enable average citizens to make and use this Bucket-Stove, using only common household tools, a metal bucket, coat-hanger wire, metal from a can, and a medium-sized cooking pot.

When burning small pieces of dry wood or twisted paper in this Bucket-Stove, only about 7 oz of fuel are needed to boil 3 qt of water, or to boil 3 qt of soaked grain or beans covered with water. And if an expedient Fireless Cooker has been readied – a job that takes a person having the proven instructions and materials only about 15 min to complete – then no additional fuel is required to thoroughly cook even 3 qt of water-covered grain, beans, or tough meat. The Fireless Cooker keeps the food so near boiling temperature for hours that it cooks thoroughly. Furthermore, a Bucket-Stove can quickly be moved to whichever shelter

Fig. 1.6. Expedient bucket stove. The adjustable damper slides on its attached clamp springs made of coat-hanger wire. The lidded pot is supported on two coat-hanger wires. The movable coat-hanger-wire grate holds the fuel: frequently replaced small pieces of wood, or twisted pieces of paper.

opening is serving for the air-exhaust opening, depending on wind direction.

Shelter Sanitation Equipment

The most practical means so far tested to enable most occupants of expedient shelters to dispose of human wastes is for several persons to defecate in a piece of plastic, or in a plastic bag, then to tie the excrement inside the plastic so that flies cannot reach it, and finally to toss the package outside – preferably into a pit. Flies cannot reach the packaged excrement to lay their eggs or contaminate their feet, but are attracted for days by the gases escaping from the package. By thus attracting the flies to packages outside the shelter, the occupants of shelters lacking insect screen or netting over their openings would be spared harassment, and flies can easily be killed by the thousands if an effective stomach poison[8] is available.

Urine is best collected in a bucket, and occasionally poured outside. Odors inside the shelter can be minimized by placing containers of human wastes near the shelter's air-exhaust opening and using a Kearny Air Pump to pump air through the shelter when wind velocities outside are too low. Keeping a tightly tied plastic cover over the large can or bucket that temporarily holds excrement or urine helps control odors. Odor problems also can be lessened by venting through a hose the gases that are produced in such containers when they are closed, by keeping one end of the hose outside the shelter.

Expedient Furnishings to Increase the Capacity and Comfort of Shelters

Shelter space provided with adequate forced ventilation can accommodate many more occupants if they are able to sleep at night in two or three tiers and to sit comfortably during the day in the same space. A promising expedient means to attain this objective is for each shelter occupant to sleep in a boatlike Bedsheet-Hammock made by folding and tying a double-bed sheet in a novel manner, so as to make a short, boatlike hammock that it is almost impossible to fall out of (see Fig. 1.7). Expedient hammock ropes can be made easily from strips of cloth. In the daytime, each occupant quickly converts his hammock into a comfortable suspended chair – if he can follow illustrated instructions that must be made clearer than the first set the writer produced.

The failure of the first two test subjects to be able to follow what the designer thought were clear instructions for making and using this Bedsheet-Hammock and suspended chair is another illustration of the necessity of thoroughly proof-testing all instructions for the making and using of survival items.

Conclusions and Recommendations

1. During an escalating crisis, the wide distribution of illustrated step-by-step written instructions for making the above-mentioned expedient life-support items would significantly increase the number of survivors if a nuclear attack did occur.

2. Even if the likelihood of a nuclear war is small, Americans would be well advised to keep on hand detailed instructions for making and using expedient shelters and the life-support items needed to make them more effective.

3. Since during a crisis sufficient time is unlikely to be available to build all of the needed items of life-support equipment in addition to essential expedient shelters, prudent citizens should build and store at least some of these very inexpensive items – especially a Kearny Air Pump and a homemade fallout survey meter – before a crisis occurs.

4. Realistic field testing of expedient shelters and life-support equipment should be continued, including the planned blast testing of 15 ORNL shelters of six expedient types during Defense Nuclear Agency's planned surface detonation of 1,200,000 lb of conventional explosive at White Sands Missile Range.

---

8. The best tested poison for this purpose is "Super Die-Fly," which contains 0.46% 2,2-dichlorovinyl dimethylphosphate (DDVP) in a sugar base and is manufactured by Farnam Companies, 8701 N. 29th St., Omaha, Nebraska 68112.

Fig. 1.7. Expedient bed-sheet hammock, slung from the roof poles of an aboveground crib-walled shelter. The roof of this shelter is only 42 in. above the floor, yet one boatlike hammock enables two men to sleep comfortably where only one could sleep otherwise.

2. Reactor Studies

P. R. Barnes R. O. Chester R. R. Davis
C. V. Chester G. A. Cristy R. W. Manweiler[1]

NATIONAL SECURITY AND NUCLEAR POWER

C. V. Chester

In most discussions of military or paramilitary action against any class of facilities, the phrase "national security" is usually invoked, and usually without definition or question. We have found it a difficult term to define in most contexts in such a way that the definition is readily accepted by interested persons. "Provide for the common defense" is the traditional phrase but is inexplicit in some situations. We will nevertheless propose the following definition: "National security is the capacity of the government to neutralize threats to the lives, safety, or property of its citizens."

"Neutralize" is used in the military sense to mean "render ineffective," often but not always by physical destruction, and can include "deter" and "stalemate." "Safety" subsumes "health" and "freedom," since the former must be threatened in order for the latter two to be threatened. The *will* to resist threats is a necessary part of the capacity. It follows that anything that erodes the will to neutralize threats reduces national security.

The first line of defense against external threats is the Department of Defense and its armed services. The capacity of the armed services to neutralize threats, measured in response time and size of threat, is dependent on the economic resources that can be allocated to the Department of Defense. This in turn depends on the size and health of the national economy. An unhealthy economy can directly threaten the safety and property of the citizens. Obviously, anything that adversely affects the economy can be a threat to national security.

It is in this line that most considerations of the national security aspects of energy development lie. Events that could result in further delays in the development of energy production facilities adversely affect national security. In addition to the effect on the economy, foreign control of a critical component, oil, of our present energy supply gravely reduces the capacity of our government to cope with threats from this quarter.

Nuclear power has some unique assets and special problems from the standpoint of national security. It is totally independent of foreign imports. To the contrary, exports of U.S. reactors, fuel, and instruments are a positive contribution to our balance of payments.

The relatively small mass of fuel required for reactors makes nuclear electric generators immune to protracted nationwide labor disputes in the coal or transportation industries.

The national security problems of nuclear power stem from the fission products generated, the plutonium produced, and the popular fear of both.

Possibly the major national security problem of the nuclear industry is the assurance of the prevention of plutonium diversion and its coercive use as an illegal nuclear explosive. The technical aspects of an actual diversion have been adequately discussed by Ted Tayor and others (*Nuclear Theft: Risks and Safeguards,* Ballinger, Cambridge, Mass.). The difficult part of the problem is maintaining such assurance in the safeguards program that an extortion attempt involving a false claim of a nuclear explosive can be readily diagnosed. Overreacting or incompetent handling of this type of threat will invite imitation and provide political pressure for additional controls, delays, and expense on the development of nuclear power.

A similar, principally political problem is that of terrorist action against an operating power reactor. It is theoretically possible for a well-armed and trained

1. Department of Physics, Ursinus College, Collegeville, Pa.

squad to overwhelm the defenses of a large nuclear power station. If members of the attack force have been carefully instructed and rehearsed by someone personally familiar with all the safety systems on that station, they can disable enough systems to induce an uncontained meltdown of the reactor. The ensuing loss of generating capacity and the threat to the safety of a few hundred (or even a few thousand) residents downwind do not constitute a threat to national security, which we assert is the *capacity* of the government to deal with the problem. The threat would be from the ensuing public outcry against nuclear power, which could well delay or even stop the development of this energy source, with the consequent impact on economic growth.

A more likely occurrence, and nearly as damaging politically, would be the armed seizure and occupation of a nuclear station by some dissident group, followed by political demands and threats of a meltdown. Unless this group had very detailed inside information, it is unlikely that they could cause irreversible core damage if they were dislodged quickly. They would present a painful dilemma to the authorities and give much ammunition to the opponents of nuclear power.

The development of the nuclear industry will result in the development of a large inventory of fission products retained above ground in a finite number of locations, most in the populous eastern half of the country. By the year 2000, this inventory would have the potential to increase by a factor of 5 or 10 the residual (one year later) fallout from a nuclear war, seriously complicating and delaying postattack recovery. While a war is extremely unlikely, the existence of this vulnerability could affect crisis negotiations by which international disputes are settled without war. If the vulnerability were unique to the United States, it would seriously degrade our bargaining position if both sides had access to computations that indicated that our opponent would recover from our attack in less than five years but we would not recover from his attack in 20 years.

NUCLEAR ENERGY CENTERS

G. A. Cristy R. R. Davis

One development recommended by the proposed federal energy research and development program (1973) relates to construction of nuclear energy centers (NEC). An NEC is conceived as a site which contains many nuclear power plants (of the order of 10 to 40) plus supporting fuel-cycle facilities. The rationale for such clustering of reactors is based on the idea that they will permit more rapid increases and greater economy in electric generating capacity for one or more of the following reasons:

1. a major reduction in time required to site reactors and to bring them on-line because the site selection, environmental impact studies, licensing procedures, and the public acceptance efforts would be combined;
2. reduction in time and cost of construction through use of a relatively stable and technically sophisticated construction force with specialty in the construction of nuclear reactors;
3. more efficient operations from added flexibility and the ability to share costs for some support facilities;
4. confinement of fission products, plutonium, and wastes to a single location.

The Energy Reorganization Act of 1974 requires the Nuclear Regulatory Commission (NRC) to report to Congress by October 11, 1975, on its evaluation of the NEC concept. The NRC report will include recommendations regarding feasibility and practicality of locating the majority of new nuclear power reactors in "Power Parks" (i.e., NEC) which would have from 10 to 40 power reactors and other facilities of the nuclear fuel cycle (e.g., fuel reprocessing plant, fuel fabrication plant, high-level solid waste storage).

The NRC established assumptions and ground rules for the NEC site survey study and contracted with ORNL to provide certain information[2] for the NEC site survey report.

The work being done by the Emergency Technology Section to provide information for NRC's report involves four topics:

1. national defense (nuclear attack threat),
2. sabotage or terrorist activities,
3. natural disaster,
4. recovery from major accidents.

Progress reports on the first three topics are included later in this chapter. Recovery from major accidents will be reported at a later date.

In each of the four cases a comparison is being made between the NEC concept and the alternate siting method which assumes a continuation of present dispersed siting, limiting the number of reactors to four on any one site. The comparison is made to determine

2. *Nuclear Energy Center Site Survey,* Nuclear Regulatory Commission, Office of Special Studies, NUREG-75/018, March 13, 1975.

whether any adverse or beneficial effects will result in choosing the NEC siting alternatives. An attempt will be made to estimate the additional cost or effort required to reduce any adverse effects to the level of the dispersed siting alternate.

Assumptions and Ground Rules

Site selection criteria for NEC. One task group of the NEC site survey project (from the Energy Division) is performing a rough screening of potential sites for nuclear energy centers. The goal of the rough screening is to select three typical or surrogate sites – one coastal, one inland, and one remote. The site criteria established by the NRC are extensive; so for brevity and clarity, only those criteria which directly affect our study are included here. They are:

1. Ten to forty reactors, each with a nominal 1200-MW(e) generating capacity (reactors to be built in clusters of four reactors with at least 2½ miles between clusters).
2. One-third of the reactors will be BWR's, the remainder will be PWR's. Assumed thermal efficiency is one-third.
3. Exclusion area will be sized to permit 1 acre of exclusion area per megawatt (electric) of generating capacity.
4. Cooling towers are assumed to be either natural draft or mechanical draft, using an open (i.e., wet) cycle. Natural-draft towers are assumed to be designed for maximum loads from 120-mph winds at 30-ft elevation and 195-mph winds at 400-ft elevation.
5. A fuel reprocessing plant and a fuel-element fabrication plant are assumed on site.
6. All radioactive wastes will be processed and stored on site. The high-level liquid wastes will be calcined to solid waste and stored in above-ground, air-cooled containers similar to those proposed by WASH-1539.[3]

Description of surrogate site. Only one surrogate site has been selected at this time – the inland site on Kentucky Lake. The major elements of the surrogate site are on the layout shown in Fig. 2.1.

Dispersed site alternative. For purposes of comparing with the assumed NEC option, a list was prepared of the location and selected characteristics of the presently operating, authorized or proposed reactor sites. This list was augmented by adding assumed locations of additional sites which, with the assumed expansion (to four reactors) of existing dispersed sites, would provide the projected generating capacity for the year 2000.

Cooling Towers

Background. The NEC will generate a substantial amount of waste heat that requires dissipation [e.g., a 48,000-MW(e) park would release 96,000 MW of thermal energy]. Cooling towers dissipate the waste heat by breaking the water into small droplets and cooling them in a draft of air (coolant). This process causes some of the hot water to be evaporated and some of the droplets to be entrained in the coolant. Drift eliminators are installed in the towers for the removal of the entrained water before it escapes from the top of the tower; that which does escape is known as drift.

Mechanical-draft towers incorporate fans to force or pull air past the water droplets to cause cooling, whereas the natural-draft tower uses the chimney effect created by the difference in density between the warm moist air inside the tower and the colder denser air outside to move the cooling air.

Characteristics of natural-draft and mechanical-draft cooling towers which are of concern to our study are included here primarily for reference to the state of the art. Specifically we are interested in the mechanical stability of hyperbolic cooling towers, some comparisons between types of flow, a comparison between natural- and mechanical-draft towers, the problem of drift, and the effect that the loss of a cooling tower has on generating capacity.

Mechanical stability of hyperbolic cooling towers. Hyperbolic cooling towers have only recently been employed in the United States. Before 1960 no actual construction had begun on the towers. Today the structures are widely used and are reaching heights of more than 500 ft. The hyperbolic towers are thin-shelled structures with a height-to-base ratio of approximately 4 to 3. Figure 2.2 shows a typical cross section.

The mechanical stresses that a tower of this height experiences need careful analysis. Characteristically, thin-shelled structures fail by a buckling of the shell, which then causes a catastrophic localized failure of the reinforcement. This was the actual triggering mechanism for the collapse of the only towers which have failed – the Ferrybridge towers in England (Fig. 2.3). The Ferrybridge towers had only one layer of steel reinforcement and a constant shell thickness of 5 in.

3. *Draft Environmental Statement – Management of Commercial High Level and Transuranium-contaminated Radioactive Waste,* WASH-1539, September 1974.

ORNL-DWG 75-8092

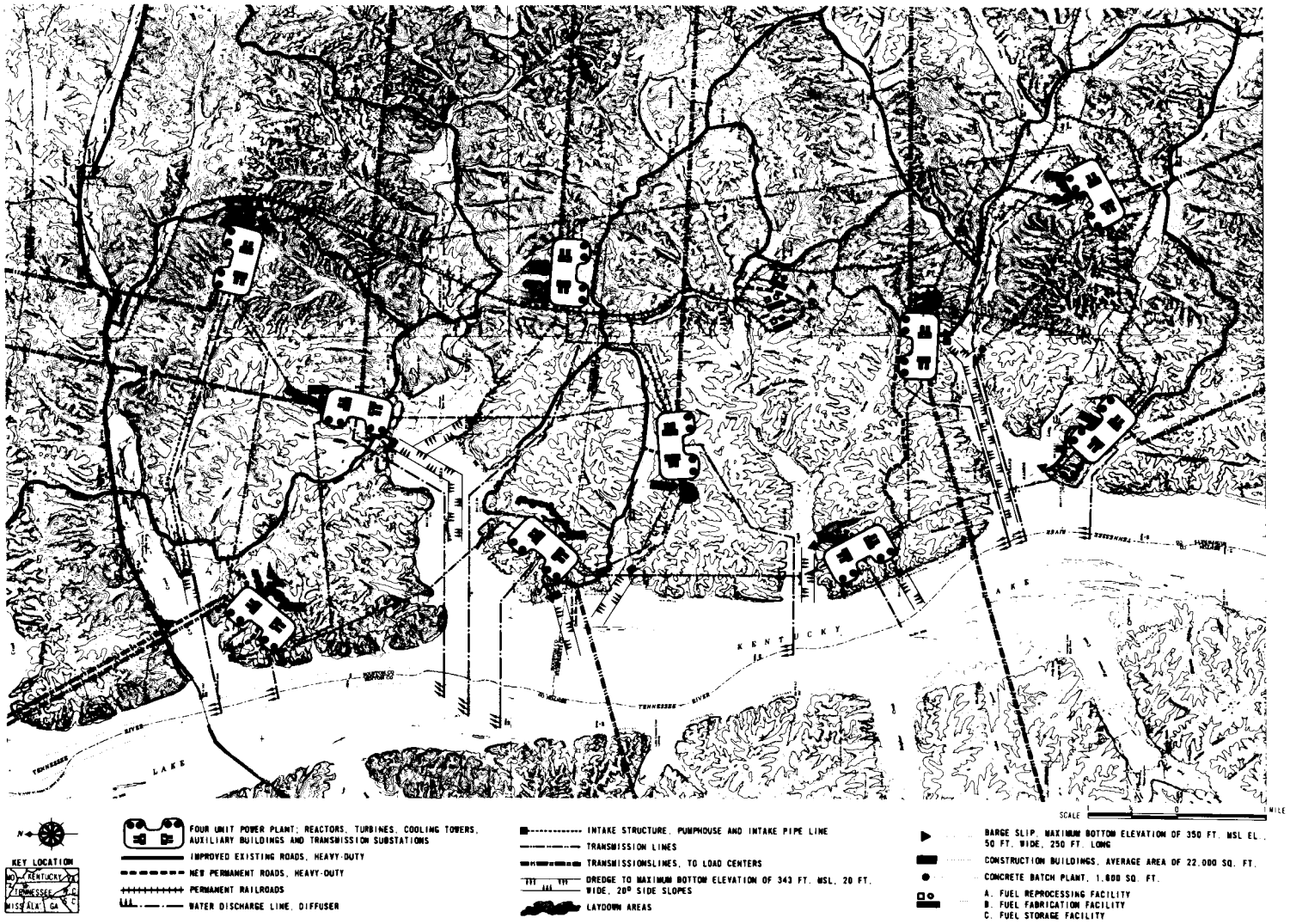

Fig. 2.1. Kentucky Lake NEC surrogate site.

Since the Ferrybridge collapse, designers have reevaluated the stresses due to wind loading and now are careful to design the towers strong enough to prevent buckling.

Wind loading. Wind velocity is seen to increase with altitude. For heights up to 1000 ft, Eq. (1) is utilized to find the dynamic pressure exerted by the wind on the structure at any level h:

$$q = [0.00256(V_{30})^2] \left(\frac{h}{30}\right)^{2/7} , \qquad (1)$$

where V_{30} is the wind velocity at 30 ft, obtained from a map of annual extreme wind velocities by Thom.[4] Equation 2 gives the local pressure (force) at any point at height h:

$$P = qC_p , \qquad (2)$$

4. H. C. S. Thom, "New Distribution of Extreme Winds in the United States," *Journal of Structural Division Proceedings of American Society of Civil Engineers*, ST7, pp. 1787–1801, July 1968.

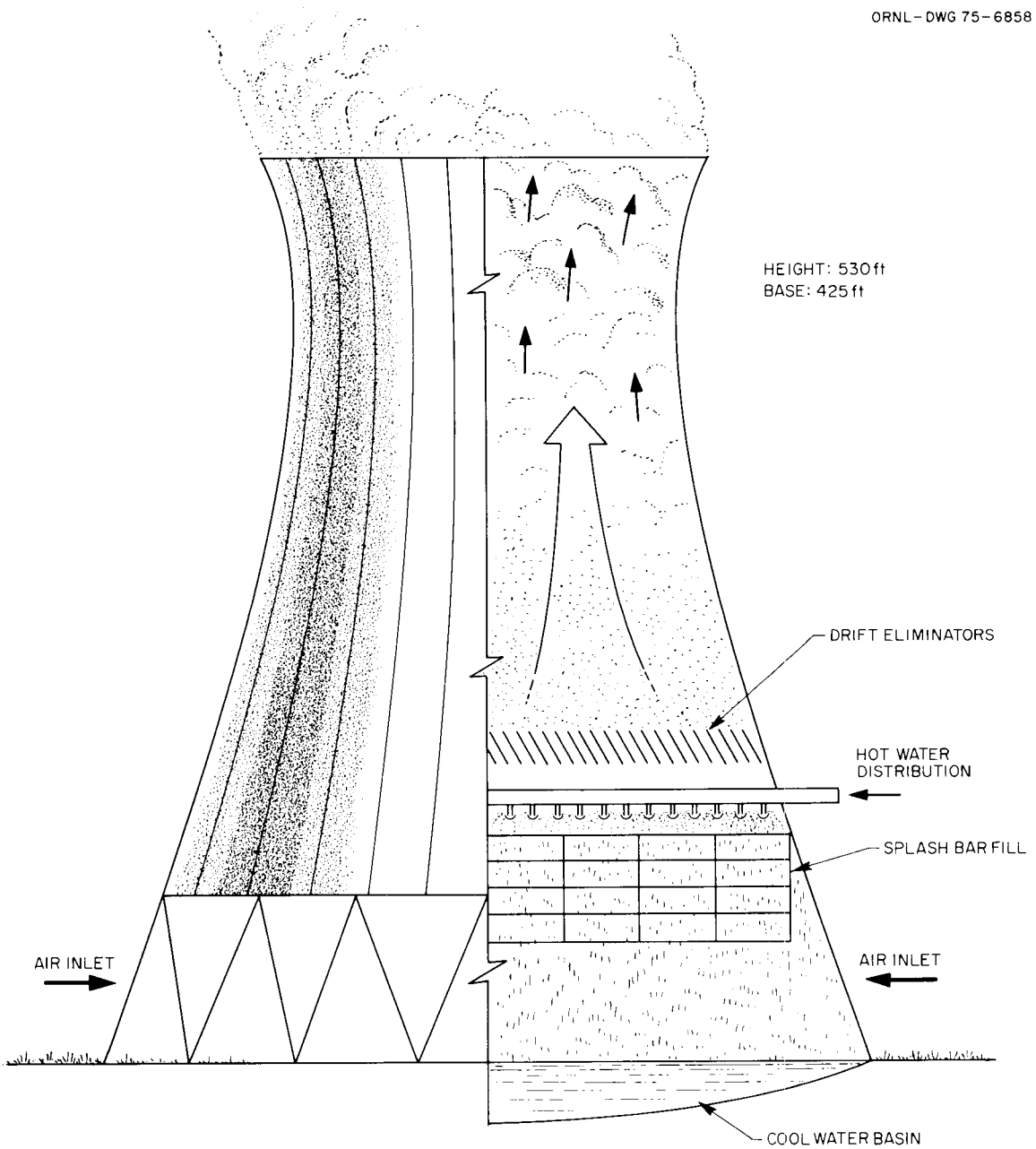

Fig. 2.2. Hyperbolic cooling tower.

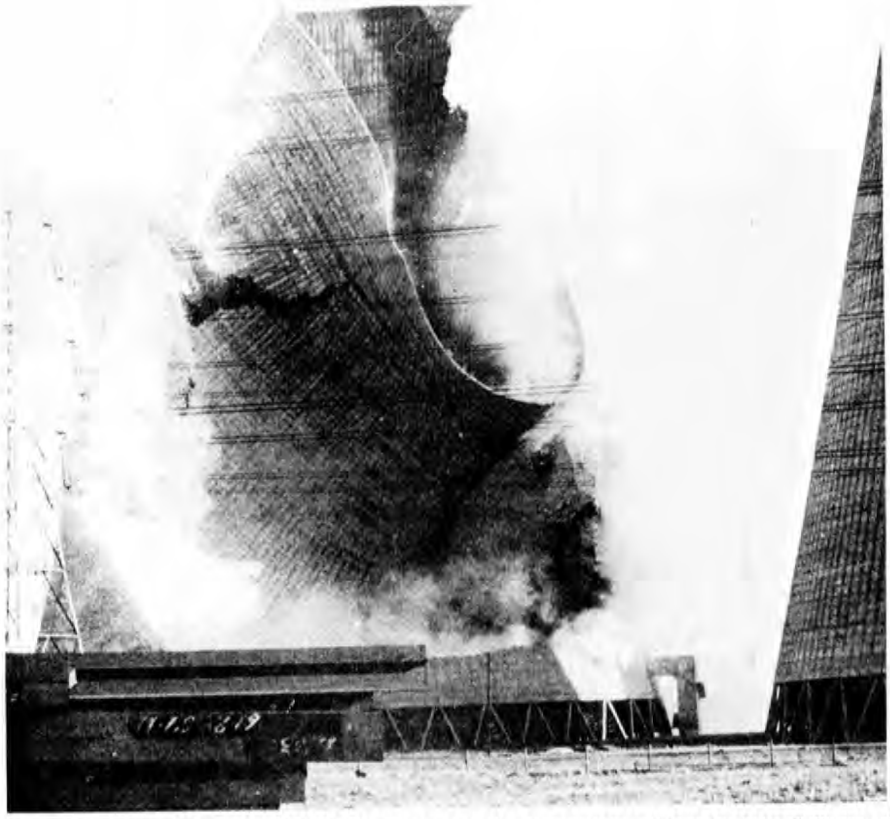

Fig. 2.3. No. 2A cooling tower from west. SOURCE: *Report of the Committee of Inquiry into Collapse of Cooling Towers at Ferrybridge, Monday 1 November 1975*, Central Electricity Generating Board, Sudbury House, 15 Newgate Street, London, E.C.1.

where C_p is a wind coefficient obtained from Table 2.1. The coefficient C_p varies with angle (θ) from the wind direction and with surface roughness. By observing Fig. 2.4 it is evident that a constant pressure is not exerted completely around the structure (variation of C_p). Only part of the tower actually undergoes a positive pressure; the rest is in a state of suction (negative pressure). Wind tunnel tests on Plexiglas models have shown that rough (surface) structures exhibit lower pressures than the smooth structures (Fig. 2.4). Therefore on actual towers vertical fluted ribs or spoilers have been incorporated to reduce these negative pressures.

From Fig. 2.4, it is observed that the maximum C_p is obtained at an angle of 75° from the point of contact of the wind. Since the local pressure is proportional to C_p, a point at this location on the structure will experience the maximum local pressure. Using the criteria cited by the U.S.N.R.C. for the 30-ft wind, the tower experiences a force of −71.2 psf at a height of 530 ft; similar calculations on a point 265 ft up the tower yield −58.4 psf.

To design for this variation in force due to wind loading, the constant reinforcement and concrete thick-

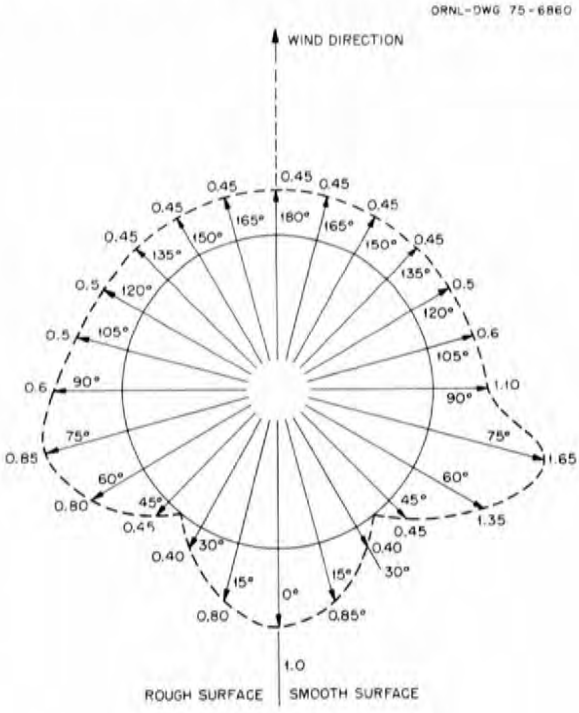

Fig. 2.4. Wind force distribution.

Table 2.1. Wind coefficients

θ (deg)	C_p Smooth surface	C_p Rough surface
0	+1.0	+1.0
15	+0.85	+0.80
30	+0.40	+0.40
45	−0.45	−0.45
60	−1.35	−0.8
75	−1.65	−0.85
90	−1.10	−0.6
105	−0.6	−0.5
120	−0.5	−0.5
135	−0.45	−0.45
150	−0.45	−0.45
165	−0.45	−0.45
180	−0.45	−0.45

ness used in the Ferrybridge towers are no longer employed. Figure 2.5 illustrates the variations in shell thickness and reinforcement pattern of a typical hyperbolic cooling tower.

Overturning. The characteristic shape of the hyperbolic towers provides a high resistance to overturning. From ref. 5, the maximum overturning moment due to wind for a 345-ft-high tower with a base of 290 ft is 290,000 kip-ft. This is resisted by 22,100 kips of self weight. The moment of self weight above the leeward edge of the tower is approximately 22,100 kips × 145 ft = 3,210,000 kip-ft. This incorporates a safety factor of 11 against overturning. Even though this is shown for a 345-ft-high tower, analysis conducted by TVA on towers of heights to approximately 500 ft show similar results. As previously stated, the mode of failure of thin-shelled structures is buckling which results in a localized failure of the shell. The Ferrybridge towers, 375 ft high, collapsed with no overturning (Fig. 2.3). Figure 2.6 shows that most of the debris is located inside the base of the structure.[6]

To date, analysis of hyperbolic towers to heights of approximately 550 ft is well understood. Towers of greater heights need more careful analysis before industry is ready to accept them.[7] It has been proposed by manufacturers to surpass the 550-ft mark. Currently, research is being conducted to fabricate these towers from steel, thus to reduce construction time and also provide the added strength at greater heights.

Types of natural-draft towers. Depending on the particular requirements for a natural-draft tower, the designer will arrange for either a counterflow or a crossflow movement of the air past the falling water. In a counterflow tower the water moves down and the air moves up; in a crossflow tower the water moves down and the air moves horizontally.

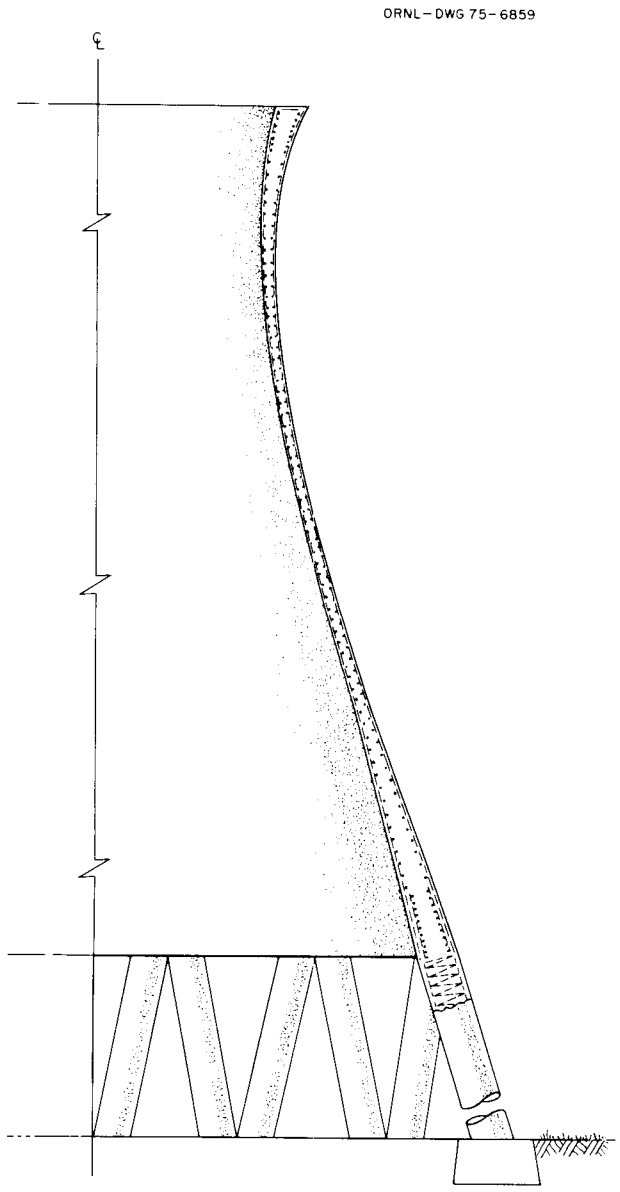

Fig. 2.5. Reinforcement layout of shell, typical.

5. German Gurfinkel and Adolf Walser, "Analysis and Design of Hyperbolic Cooling Towers," *Journal of the Power Division Proceedings of the American Society of Civil Engineers*, p. 148, June 1972.

6. Central Electricity Generating Board, "Report of the Committee of Inquiry into Collapse of Cooling Towers at Ferrybridge, Monday, 1 November, 1955," Subdury House, London, E.C.I., England.

7. Private communication, Bob Barney, TVA, to R. R. Davis, ORNL, on "Hyperbolic Cooling Towers."

In a counterflow tower, the "fill," that is, the material in the tower that breaks up the water into fine droplets, is located in the base of the tower. As the water is cooled by the air circulating around the droplets, the fill plus the water causes a significant loss of draft in the tower.

In a crossflow tower, the fill is located at the base of the tower, on the outside. As the air flows through the water, it meets little resistance because of the fill and thus has a lower loss of draft. Therefore, the crossflow tower will have a higher cooling performance than a counterflow tower of equal height. Because of this the crossflow tower is usually shorter in height than the counterflow tower for a specified cooling performance. The crossflow tower is superior to the counterflow tower in handling heavy loads of water with long cooling ranges and close approaches to the wet-bulb temperature.

Mechanical-draft cooling towers. The height of fill that can be incorporated in a mechanical-draft tower is set by the height of the tower. The only variable in

Fig. 2.6. Ferrybridge C power station, debris in cooling tower No. 1A. SOURCE: *Report of the Committee of Inquiry into Collapse of Cooling Towers at Ferrybridge, Monday 1 November 1975*, Central Electricity Generating Board, Sudbury House, 15 Newgate Street, London, E.C.1.

cooling capacity is in the draft of air flowing through the tower. This can be accomplished by varying the fan speed or replacing the fan motor with a larger one.

The main reason for choosing a mechanical-draft tower over the hyperbolic tower is one of initial capital investment and land availability. By 1970 values, the dollar investment of a mechanical-draft (wet) tower was $1.7 million, whereas the cost of a natural-draft (wet) tower was $4.2 million. These costs relate to an 800-MW(e) station.[8] However, since the natural-draft tower operates on the chimney effect and the mechanical draft requires forced-air cooling (i.e., large fans), the maintenance and operating costs of the mechanical towers should be considered.

TVA has postulated that assuming the life of the structures to be 40 years, the mechanical-draft tower will cost about 5% less. In actuality the life of a mechanical-draft tower is approximately 40 years, whereas a hyperbolic tower could conceivably last forever.

Because of the close proximity to the ground, the drift released by the mechanical-draft towers will be kept in the immediate vicinity of the plant, depending upon the surrounding terrain, which could be of major importance.

TVA utilizes the mechanical-draft cooling tower at its Browns Ferry Station. The towers occupy an area of 45.5 ft^2 per MW(t) dissipated. This does not include the exclusion area around the towers.

A natural-draft tower capable of providing the cooling of a 1250-MW(e) reactor utilizes 37.6 ft^2/MW(t) without exclusion area. Since the mechanical-draft tower is a class III structure, it can be designed to withstand the required wind loadings (i.e., up to 120 mph) with little difficulty.

Drift. The water lost from a tower as liquid droplets entrained in the exhaust air is known as drift. The objective of installing drift eliminators is for the removal of the entrained water droplets from the exhaust air. For the measurement of the entrained water vapor that escapes the drift eliminators, a cyclone separator is utilized. The most effective method of drift elimination involves a combination of direct impingement and rapid changes in the direction of the air stream which is accomplished by the geometric arrangement of the blades. This depends not only on the individual blade size and shape, but also its spacing, pitch, number of rows, and the ability of the blades to drain moisture. In addition to these criteria, minimum resistance to air flow must be maintained.

A typical drift sensor is shown in Fig. 2.7. TVA specified that the drift measured at the top of the tower not exceed 0.01% of the flow rate. Using the criteria of the Hartsville Station, a water flow rate of 450,000 gpm accounts for a water release of 45 gpm as the maximum allowable. The drift is composed of all sizes of water droplets; therefore they will be dispersed over a large area. The area covered depends upon their release point (height) and the wind velocity at the time.

By the use of Figs. 2.8 and 2.9, information can be obtained as to the size and quantity of a particular droplet released from the natural-draft tower and its corresponding fall velocity. With this information, Fig. 2.10 is obtained and can be extrapolated to involve any droplet size.

Droplets smaller than 100 μ have fall velocities extremely low, indicating that the weight of these small drops has a minor influence on their dynamic behavior. Thus, their path and position will be primarily governed by aerodynamic forces, most important of which are wind, buoyancy of the exhaust plume, and turbulence in the atmosphere. Plume buoyance and vertical atmospheric turbulence will tend to keep these small droplets in suspension for an extended period. The smaller droplets will essentially follow the plume path, and their concentration at any point downwind will be ultimately governed by atmospheric dispersion. If the ambient air is cold, the exhaust air is rapidly cooled and becomes supersaturated. The moisture released upon condensation is sufficient to cause some fogging in the area around the NEC. Natural-draft towers by virtue of their height of release tend to reduce the incidences of fogging. The small drift droplets that remain entrained in the exhaust vapor act as condensation nuclei and tend to grow in size as long as this supersaturated condition remains and therefore do not effect localized fogging.

Effect of cooling tower loss on generating capacity. In the event of severe damage to a cooling tower, the effects on the power generation capability of the center depend upon the alternate piping configuration incorporated into the main condenser heat removal system. These alternates are known as the open, crosstie, and closed configurations. In the open system (i.e., once-through cooling), the hot water (coolant) is simply discharged back into its source (lake, pond, river, etc.). Because of recent changes in environmental water quality standards, this system will not be considered an alternative for the NEC. The crosstie system uses a series of valves to divert the flow from the faulty tower to a tower being used by an adjacent reactor (or reactors). When this situation occurs the reactors must reduce their output power, the amount depending upon

8. R. D. Woodson, "Cooling Towers," *Sci. Amer.* **224**, 70–79 (1971).

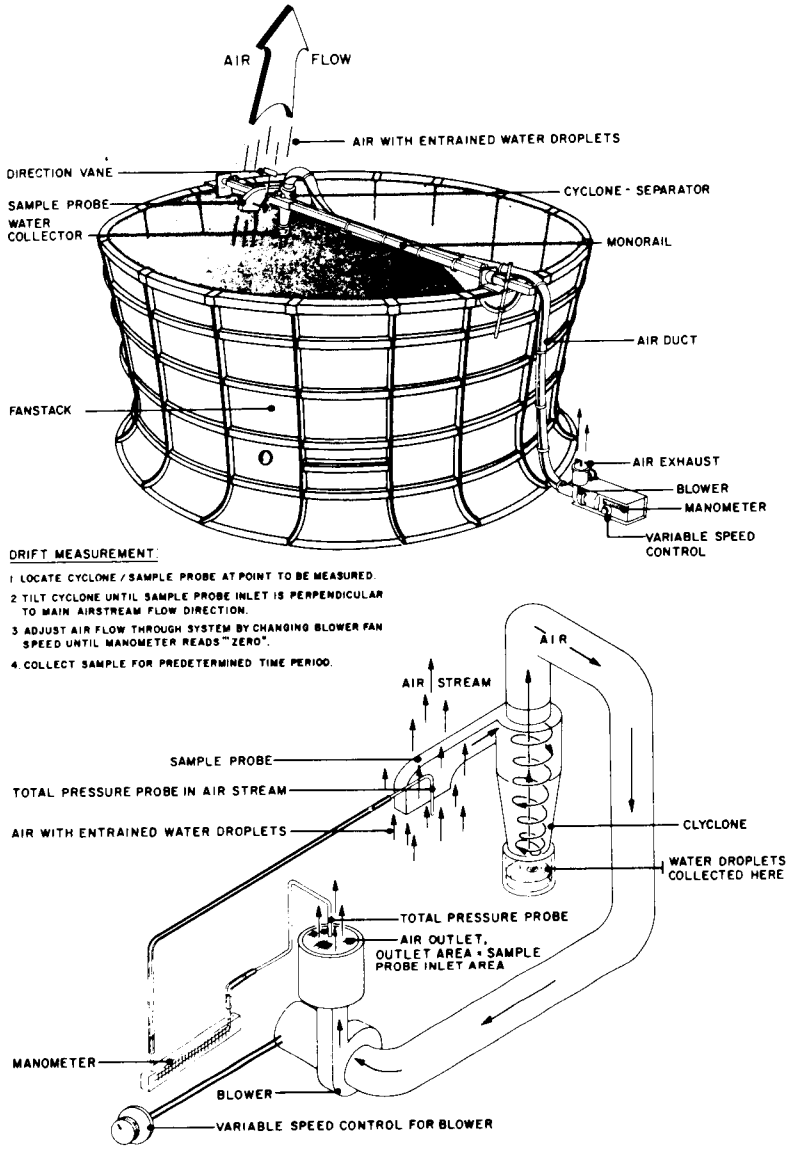

Fig. 2.7. Drift measurement schematic diagram. SOURCE: Ecodyne Cooling Products Division of Ecodyne Corporation, Santa Rosa, California, January 1973.

the wet-bulb temperature at the time. In a study conducted by TVA, it was found that in the winter two reactors using a single tower could operate between 75–85% of total power, and in the summer they would be limited to between 55–65% of total power. In the closed system there is no alternative in the event of the loss of the cooling sink, except to shut the reactor down and repair the tower.

Examples of plants operating under these various systems follow:

1. open – TVA Browns Ferry (initially),
2. crosstie – proposed for TVA Sequoyah Station,
3. closed – TVA Hartsville Station.

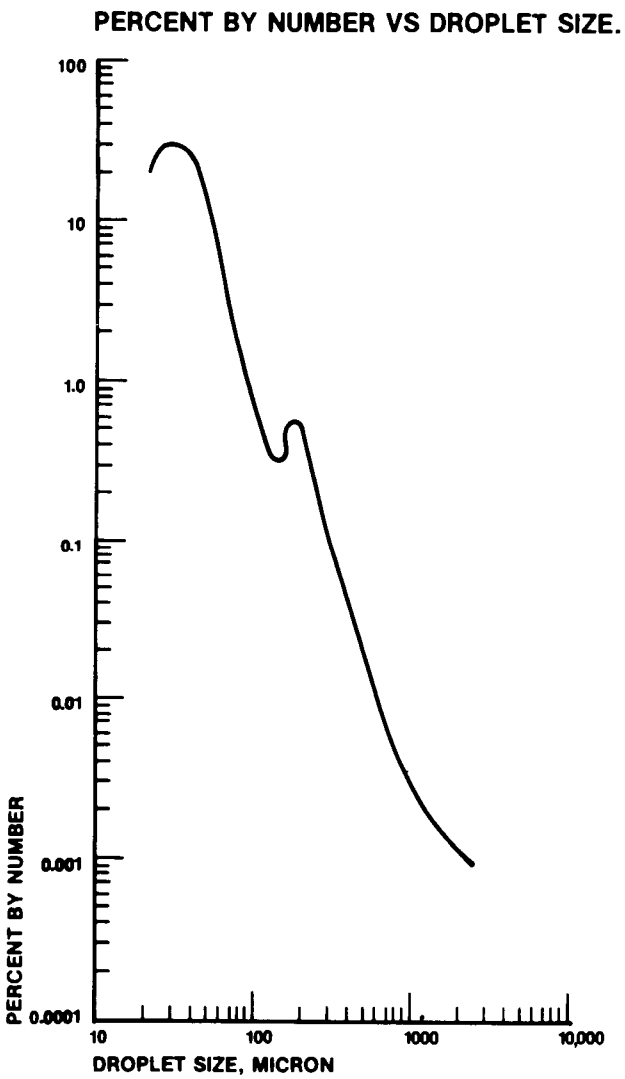

Fig. 2.8. Percent by number vs droplet size. SOURCE: Ecodyne Cooling Products Division of Ecodyne Corporation, Santa Rosa, California, January 1973.

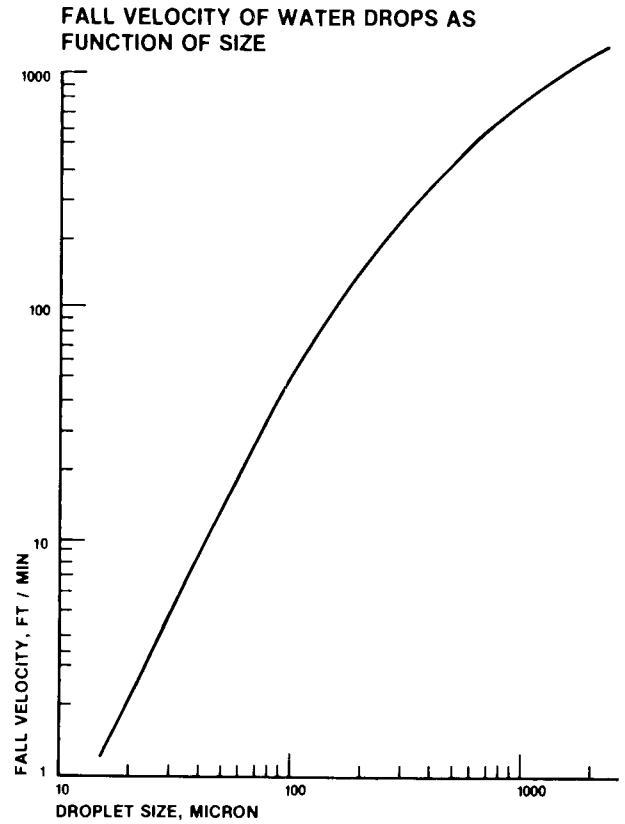

Fig. 2.9. Fall velocity of water drops as function of size. SOURCE: Ecodyne Cooling Products Division of Ecodyne Corporation, Santa Rosa, California, January 1973.

NUCLEAR REACTOR COMPLEXES IN STRATEGIC WAR

C. V. Chester

In a world in which forces armed with large strategic nuclear weapons exist, the consequence of large-scale construction of nuclear power plants is a legitimate question. There are at least two parts to this question:

1. Would reactors be targets in a nuclear war?
2. If they are targets, what are the consequences of an attack on them, including the impact on the postattack recovery efforts of the nation?

Different aspects of these questions have been raised by several concerned parties. Unfortunately, many discussions contain more emotional reaction than informed analysis.

The question of targeting reactors cannot be answered with certainty without access to the top-secret war plans of the potential attacker. Even then the unknown reliability and untested battle performance of his forces add uncertainty to the conclusions.

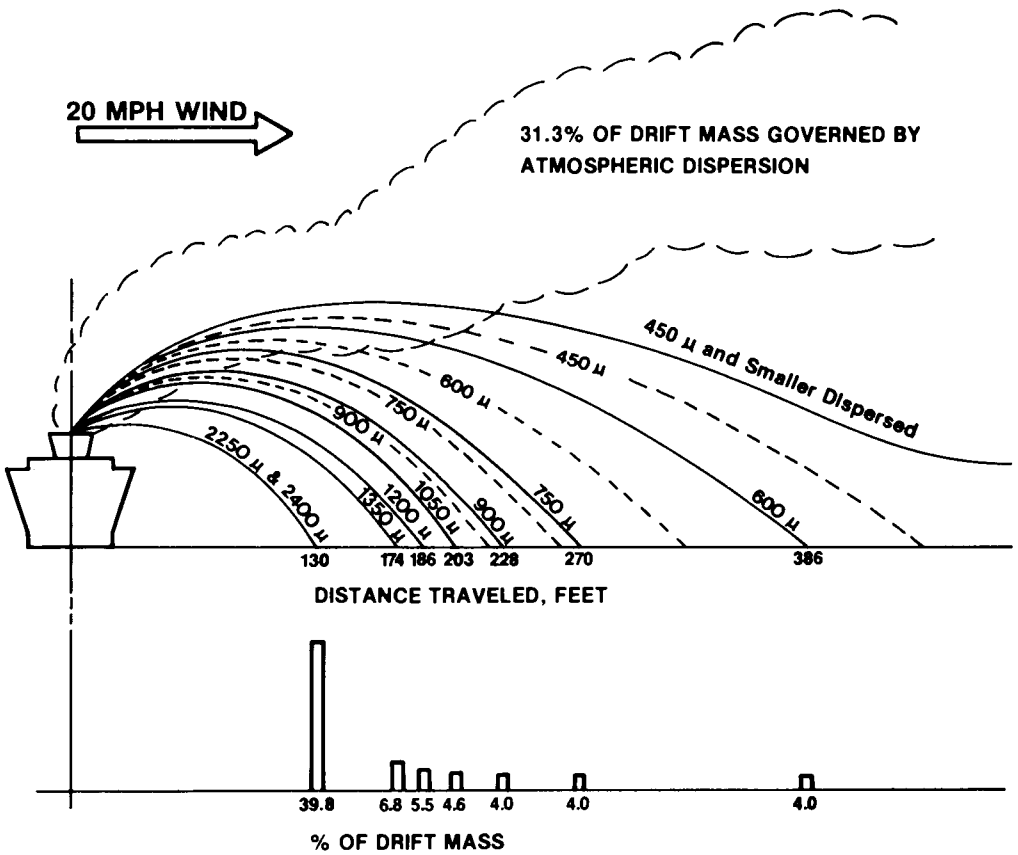

Fig. 2.10. Cooling tower drift pattern. SOURCE: Ecodyne Cooling Products Division of Ecodyne Corporation, Santa Rosa, California, January 1973.

However, reactors, and especially reactor complexes, can be compared in economic value with other portions of our economic system. If we have a rough idea of the size of the attacker's strategic payload, and make some reasonable assumptions as to how much of it is allocated to industrial targets, it is feasible to reach some conclusions as to the priority of different size reactor complexes as purely economic targets.

MVA Density

It is assumed here that an industrial attack would be designed to destroy the maximum amount of economic productivity measured as manufacturing value added (MVA). To keep the calculation simple, it will be assumed that within the scale of strategic weapon effects, MVA is colocated with the population. Specifically it is assumed to have the same density distribution as the 1970 U.S. population. If we use a per capita annual gross national product of $10,000 (for the year 2000), multiplying the population density in persons per square mile by 10,000 gives an MVA density distribution in annual dollars per square mile. Figure 2.11 is the curve obtained by plotting the population density of each 0.4° quadrangle against the cumulative area. The population density multiplied by the annual per capita MVA and the area covered per megaton equivalent gives a measure of the MVA destroyed in order, starting with the most valuable and moving down the curve.

The MVA of a reactor is taken as the value of the electricity produced. For an ideal 1000-MW(e) reactor operating 7000 hr (out of 8760) per year and selling the power at $0.01/kWhr, the MVA is $70,000,000/year. A quadruple installation of 1200-MW(e) reactors has an MVA of $336,000,000, equal to that of a town of 33,600 economically average people in the year 2000.

Megaton Equivalents

It is convenient to express the size of a strategic force in megaton equivalents. These are defined as the sum of the yields of the warheads, each raised to the $^2/_3$ power. The sum is proportional to the area which can be destroyed, and it is very nearly proportional to the total

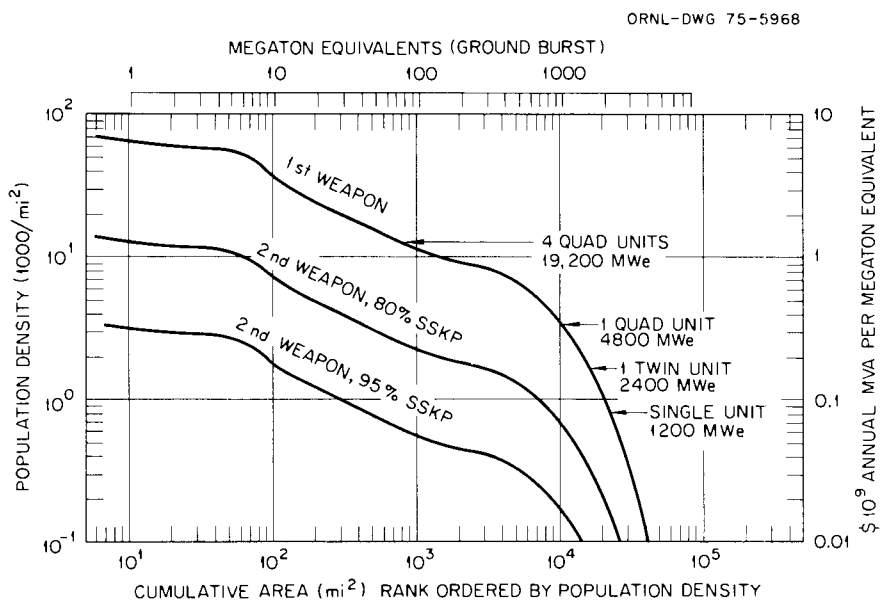

Fig. 2.11. Population and MVA density vs cumulative area.

payload weight of the force, regardless of how the payload is subdivided.

A discussion in these terms minimizes the effect of errors in assumptions as to the extent to which multiple independently targeted reentry vehicles (MIRV's) are introduced into the force in question.

The target area that is assumed destroyed by a megaton equivalent depends on the hardness assumed for the structures to be destroyed. For most urban-industrial targets, 10 psi is adequate for destruction. One megaton equivalent will cover an area of 21.2 sq miles if burst at optimum height. Ground-bursting the weapon reduces the area covered by almost a factor of 2, to 10.2 sq miles; however, it covers thousands of square miles with lethal fallout.

From these considerations, it can be seen in Fig. 2.11 that from an economic standpoint, a ground burst that could destroy four quadruple units in a power park would become an attractive target for the 75th megaton equivalent. A single quadruple unit would be a target for the 1000th ground-burst megaton equivalent. A single 1200-MW(e) unit would be a target for the 2200th ground-burst megaton equivalent. By comparison, this is the approximate MVA rank of a 160,000-barrel-per-day oil refinery. Attacks designed to produce bottlenecks in the economy by concentrating on energy production would assign much higher priorities to targets of these values.

Present and Projected Soviet Forces

The composition of the present Soviet strategic force, based on unclassified sources, is given in Table 2.2. The total is about 4500 megaton equivalents. If they carry out improvements permitted under the SALT and Vladivostok agreements, and presently under testing or preliminary deployment, the force will increase to about 5000 megaton equivalents. It would be reasonable to assume that over the next two decades there will be significant improvements in delivery accuracy and reliability. These improvements will permit the use of fewer weapons for any given target, making weapons available to attack targets of progressively lower value. One possible future configuration of the Soviet force is given in Table 2.3.

Kill Probability and Reliability

At the present stage of technology, there is no dependable method of determining whether a strategic weapon has destroyed its intended target in the time likely to be available for decisions in a nuclear war. Therefore, an estimate is made of the single-shot kill probability (SSKP) for each weapon against a given type of target. These probabilities usually assume arriving weapons and are a function of target hardness, weapon yield, and delivery accuracy. They may be based on launched weapons, which include an addi-

Table 2.2. 1974 Strategic offensive forces of the Soviet Union

	1974 force	Payload megatons	15-psi area per booster (sq miles)	Total warheads	Total megatons	Total area	Megaton equivalents
SS-7, 8	220	5	38.4	220	1100	8,450	
SS-9	300	20	95.0	300	6000	28,500	
SS-11	950	1	12.6	950	950	11,970	
SS-13	60	1	12.6	60	60	750	
						49,670	3942
SSN-5	27	1	12.6	27	27	340	
SSN-6	512	1	12.6	512	572	6,457	
SSN-8	72	1	12.6	72	72	903	
				2140	8720	7,700	611
						57,368	4553

Table 2.3. Assumed year-2000 Soviet strategic force[a]

Missile	No.	MIRV's	Yield (megatons)	Megatons$^{2/3}$	Accuracy[b] (nautical miles)	K[c]	Total warheads	Total megatons	Total Megatons$^{2/3}$	Total K
SS-18	313	6	1	1	0.1	100	1878	1878	1878	187,800
SS-19	1007	3	0.56	0.68	0.1	68	3021	1692	2054	205,438
SS-13	60	1	1	1	0.7	2	60	60	60	120
SS-8	109	1	5	2.9	1.5	0.4	109	545	316	142
SSS-N-8	910	1	1	1	0.5	4	910	910	910	3,640

[a]Adapted from R. L. Leggett, "Two Legs Do Not a Centipede Make," *Armed Forces J. Int.* **112**(6), 30 (February 1975).
[b]Circle of equal probability (CEP).
[c]$K = \text{yield}^{2/3}/(\text{CEP})^2$ for each warhead.

tional factor of system reliability, assumed in this discussion.

When programming the attack on a sequence of targets of progressively lower value, at some distance down the sequence, when the value of the next target is numerically less than that of the most valuable target times the kill probability, it is advantageous to allocate the next weapon at the first target again. A little further down the sequence, when the value of the next target times the system reliability is less than the second most valuable target, that target receives a second missile. This process continues so that the force is allocated to maximize damage to the target value. For sufficiently low value of reliability and wide range of target value, a third or fourth weapon may be assigned to the high-value targets by the same process.

The curves in Fig. 2.11 show the assignment of second weapons for 80 and 95% reliable systems. (The second weapon curve for the 95% reliable system is very close to the third weapon curve for the 80% reliable system.) For example, a target with an MVA density of $0.16 billion per megaton equivalent, equal to a twin 1200-MW(e) reactor unit, would rank as the target for the 1600th 100% reliable ground burst one megaton equivalent. If a 95% reliable system were being used, the 12 highest value megaton equivalent target areas would be assigned a second weapon before the twin unit. If an 80% reliable system were used, the targets of the first 350 megaton equivalents would be allocated a second weapon, and the eight highest a third.

The point is that even relatively high values of reliability, such as 80%, can add significantly to the weapons required to attack a target system.

It was correctly asserted in the 1960's and early 1970's that reactors were not attractive targets. Most installations were small, 1000 MW(e) or less, weapon system reliabilities were probably assumed significantly less than 80%, and the Soviet strategic forces were smaller than they are now.

From the 1980's through the end of the century the situation will be quite different. The throw weight of the force will increase slightly, and the accuracy and reliability can be assumed to increase very significantly. The technology exists to increase accuracy to the point

where a warhead can be delivered on (or in) the outer containment vessel, requiring a circle of equal probability (CEP) of less than 100 ft. Electro-optical terminal guidance has typical CEP's in the range of a few feet or less. It is theoretically possible to monitor the boost phase of an ICBM, especially if it is not under attack, and detect any malfunctions leading to significant inaccuracy. It is theoretically possible to retarget a reserve missile if a malfunction is detected. In this way an effective reliability on the order of 0.95 or better might be achieved.

Fallout Maximization vs Fallout Minimization

Maximization of fallout severely retards economic recovery and enormously complicates the difficulty of supporting military operations. The penalty for maximizing fallout is a reduction by a factor of about 2 in area covered by the blast. Soviet strategic forces are sufficiently large that this reduction can be easily afforded. Soviet policy has demonstrated a preference for long-term solutions to foreign problems and is not noticeably restricted by humanitarian considerations. It is, therefore, at least possible that an attack maximizing fallout might be designed. It is the purpose of this study to analyze the consequences of such an attack, the role nuclear power might play, and the consequences for such an attack in the year 2000 of policy decisions being considered now.

The curves in Fig. 2.12 show gamma energy vs time for a 1-megaton fission weapon, the equilibrium core of a PWR, and the inventory associated with a 5-ton-per-day fuel reprocessing plant. The reactor cores can make a very sizable contribution to the fallout problem, especially if the situation one year after the attack is considered. One year after shutdown, an average 1000-MW(e) reactor core delivers about 7.4 times the gamma energy of a 1-megaton fission weapon one year after detonation. By the year 2000, it is anticipated that about 850 1000-MW(e) reactors will be in operation. Perhaps the gamma energy equivalent to another 1770 cores would be in reprocessing or temporary (five-year) high-level waste storage. If added to the fallout, the aggregate might increase the residual activity after one year by an amount equivalent to 30,000 megatons of 50% fission weapons. By the year 2020, the available above-ground activity can add fallout equivalent to an attack of more than 60,000 megatons.

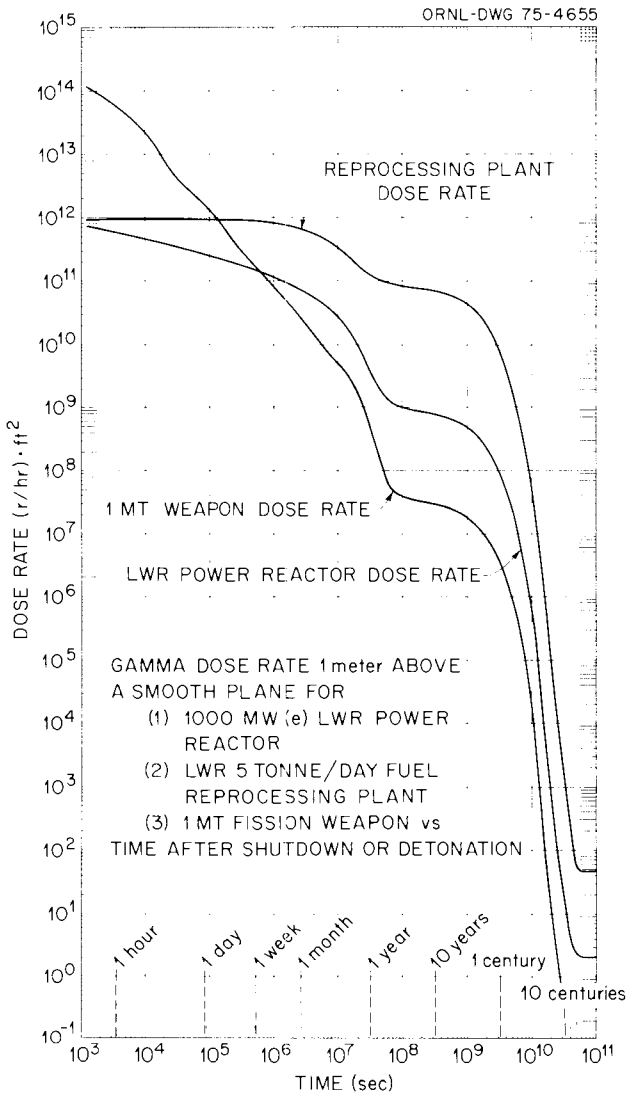

Fig. 2.12. Dose rate vs time for a reprocessing plant, 1-megaton weapon, and LWR reactor core.

PERSPECTIVES ON THE TERRORIST PROBLEM FOR NUCLEAR POWER

C. V. Chester

Terrorist Motivation

Many apparently senseless acts of violence by terrorists can be understood, and even predicted, in terms of the motivation of the terrorist. This should be useful in considerations of the terrorist problem for the nuclear industry.

Terrorism is a transaction involving the terrorist, the victim, and the spectator. The real target is the spectator, and the victim is merely a means to an end. F. G. Harris, M.D.,[9] identifies four elements in the motives of the terrorist:

1. Assertion of masculinity by imposition of will on others by use of force.
2. Depersonalization: that is, identification as an anonymous member of a large (and powerful) group.
3. Intimacy (with authority). By this Dr. Harris refers to the direct negotiation by the terrorist with high officials, for example, the governor, a general, the president. It constitutes recognition of the power of the terrorist by some universally recognized authority.
4. Magic of bloodshed. The ancient mystical concept of blood sacrifice that has appeared in the history of virtually every culture.

The common denominator of these motives is the boost of ego by assertion of power. While this general phenomenon is common in political and corporate life, it is the use of illegal force and violence that makes it a special problem.

Nonnuclear Options for the Terrorist

If a terrorist group should choose to maximize destruction and/or death as the means to demonstrate its power, there are a number of technical approaches that could be very effective. That they have not been used may give some insight into the constraints on terrorists.

Incendiaries. Some incendiaries have been used by terrorists, notably Molotov cocktails. Notably absent has been coordinated use of several incendiaries and simultaneous sabotage of the sprinkler system.

Controlled fragment mines. Mines of the claymore type are easily constructed, very effective, and were used very effectively in Vietnam. They have not been used much outside Vietnam.

Fuel-air explosives. Accidental gas explosions adequately demonstrate the potential of this technique. No application has been made.

Ammonium nitrate–fuel oil (ANFO). An explosive made from fertilizer-grade prilled ammonium nitrate and fuel oil is readily available in ton quantities at a modest price (~$120/ton). It was used to destroy the Army Mathematics Center at the University of Wisconsin at Madison a few years ago. A truck filled with the explosive and detonated in a crowded downtown area could kill several hundred people.

Chemical weapons. The chemical literature abounds with preparations for chemicals with an LD_{50} of a milligram or two. Commercial insecticides are available with 10% or more of this toxicity. One pound of the latter per 1000 design occupants introduced into a building ventilation system would be fatal to all those present. No application has been made.

Biological weapons. It is theoretically possible for a small group to cause millions of fatalities using biological weapons. The necessary information is distributed in the open literature. However, considerable technical skill is required to work safely with these materials. Some threats of this type of attack have been received by authorities, but in all cases the party involved was far from having the competence to make good. In many cases this was apparent from the communication.

It would be difficult to imagine anything more terrifying than the random introduction of botulism toxin into commercial food channels.

Observed and expected practices. The weapons used are usually bombs of conventional explosives and automatic weapons. The principal tactics are bombing of buildings of some symbolic importance, bank robbery (usually to finance the organization), and political kidnapping. All of these are consistent with the motive of demonstrating power, and exacting public acknowledgment of that power, in addition to other political demands.

Surreptitious theft or armed seizure of a strategic quantity of plutonium would be completely consistent with the demonstrated tactics and inferred motives of terrorists. Surreptitious use of plutonium (or other toxic agent) as a toxic aerosol would be inconsistent with behavior observed to date.

Armed seizure of an operating nuclear power reactor is similar to a kidnapping or airline hijacking in terms of the immediate ego rewards. The reactor is defended (as are banks), which would make the operation somewhat more dangerous if good tactics were not used.

In this country under the present political climate, terrorism as a means of solving problems is attractive to people of usually very limited ability. In contrast in the Mideast, the Palestinian movements have been able to attract some educated people with ability. As long as the political conditions in this country do not motivate

9. F. G. Harris, letter of Sept. 30, 1974, to R. H. Ichord, House Committee on Internal Security, published in Part 4, p. 4420 of Hearings before the Committee on Internal Security, H.R. 93rd Congress, 2nd session, July 30, August 1, 15, and 20, 1974.

technically able people to join violent movements, the technical complexities surrounding nuclear facilities should provide them a great deal of protection.

The problem will arise if a terrorist organization should recruit a disaffected employee of an installation. In this case the inside information on security personnel, procedures, and physical facilities could provide the motive as well as the opportunity for an attack. This would be especially true if the outsiders percieved some loophole (real or imaginary) in the defenses.

EFFECTS OF NATURAL DISASTERS ON THE NEC

G. A. Cristy

The NRC requires[10] that "structures, systems, and components important to safety" be designed to withstand the effects of natural phenomena such as earthquakes, tornadoes, hurricanes, floods, tsunamis, and seiches "without loss of capability to perform their safety function." Such structures are defined by Regulatory Guide 1.29 and designated Seismic Category I.

Effects of Tornadoes

General. The significant properties of tornadoes are:

1. geographical distribution of frequency of occurrence,
2. rotational wind speed,
3. translational wind speed,
4. pressure drop across the tornado,
5. rate of pressure drop,
6. radius of maximum rotational wind speed.

The latest and most accurate data on these six parameters have been assembled and published[11] by the AEC Office of Regulation (now NRC). The regulatory position on design for resistance to tornadoes is as follows:

"1. Nuclear power plants should be designed to withstand the Design Basis Tornado (DBT). The values of the parameters in Table I[12] for the appropriate regions of Figure 1[12] are generally acceptable to the Regulatory staff for defining the DBT for a nuclear power plant. Sites located near the general boundaries of adjoining regions may involve additional consideration.

"2. If a DBT proposal for a given site is characterized by less conservative values for the parameters than the

10. General Design Criterion 2, "Design Bases for Protection Against Natural Phenomena" of "General Design Criteria for Nuclear Power Plants" Appendix A to CFR part 50, *Licensing of Production and Utilization Facilities,* U.S. Nuclear Regulatory Commission, Washington, D.C.

11. "Technical Basis for Interim Regional Tornado Criteria," WASH-1300 (UC-11), USAEC Office of Regulation, May 1974.

12. Table I of ref. 13 is included in this report as Table 2.4, and Fig. 1 of ref. 13 is included as Fig. 2.13.

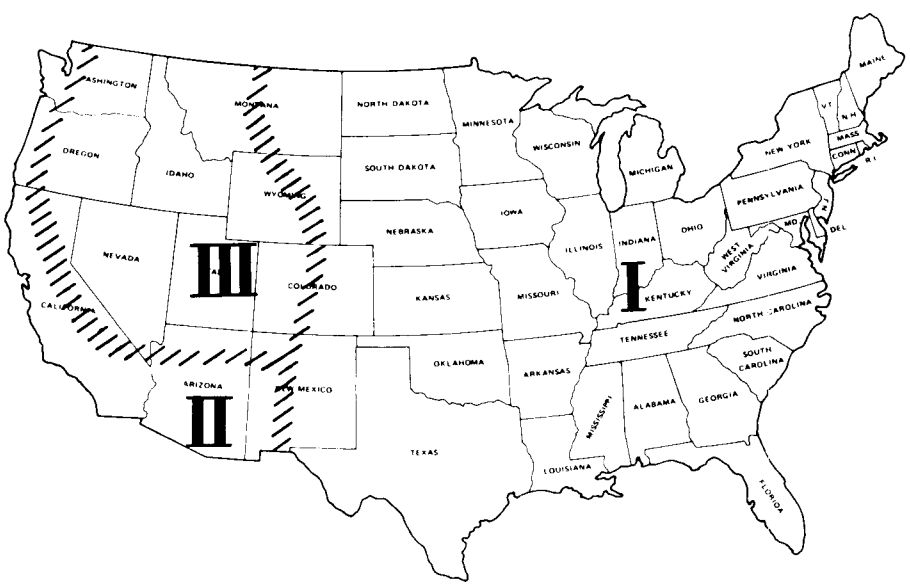

Fig. 2.13. Tornado intensity regions. Source: "Technical Basis for Interim Regional Tornado Criteria," WASH-1300, USAEC Office of Regulation, May 1974.

Table 2.4. Design basis tornado characteristics[13]

Region	Maximum wind speed[a] (mph)	Rotational speed (mph)	Translational speed (mph)		Radius of maximum rotational speed (ft)	Pressure drop (psi)	Rate of pressure drop (psi/sec)
			Maximum	Mimimum[b]			
I	360	290	70	5	150	3.0	2.0
II	300	240	60	5	150	2.25	1.2
III	240	190	50	5	150	1.5	0.6

[a]The maximum wind speed is the sum of the rotational speed component and the maximum translational speed component.

[b]The minimum translational speed, which allows maximum transit time of the tornado across exposed plant features, is to be used whenever low travel speeds (maximum transit time) are a limiting factor in design of the ultimate heat sink. The ultimate heat sink is that complex of water sources, including associated retaining structures, and any canals or conduits connecting the sources with, but not including, the intake structures of nuclear reactor units. Regulatory Guide 1.27 (Safety Guide 27), "Ultimate Heat Sink," describes a basis that may be used to implement General Design Criterion 44 of Appendix A to 10 CFR Part 50 with regard to the ultimate heat sink.

regional values in Table I, a comprehensive analysis should be provided to justify the selection of the less conservative design basis tornado."[13]

The Regulatory Guide recognizes the fact that the present data are much too meager and on the whole less quantative than desired for design calculation purposes. Recognition of this need for better data resulted in the initiation of a systematic method of collecting engineering data in 1971. Fugita[14] developed a rating scale called the FPP scale for tornadoes based on intensity and size. All tornadoes since January 1971 have been rated on the FPP scale and are compiled by the National Weather Service in Kansas City, Missouri. As these data are collected and compiled, our knowledge of tornado phenomena will be greatly increased, and perhaps before the first NEC is in operation much better data will be available to evaluate the hazard of tornadoes to the NEC.

Design of structures to resist tornado damage is beyond the scope of this report, but readers interested in the subject are referred to articles in *Nuclear Safety*[15,16] and an ASCE paper.[17]

The probability (P_t) that a tornado will strike a particular location during one year is defined[18] by

$$P_t = \bar{\eta}\,(a/A)\ ,$$

where

$\bar{\eta}$ = average number of tornadoes per year,

a = average area of damage of a single tornado,

A = total area in which the tornado frequency has been determined.

The tornado strike probability for each 5° square in the contiguous United States is shown in Fig. 2.14. The probability of a tornado strike varies widely over the United States. However, for any specific NEC site, the probability of a strike will be essentially the same per reactor as it would be for the competing dispersed site case except in some very special cases (e.g., a nuclear energy site located in a low strike probability area but serving load centers predominantly in a high strike probability zone, such as a remote site on the northern tip of Michigan serving load centers in Chicago and Detroit).

Cooling towers. Hyperbolic cooling towers have been built to be structurally sound in winds as high as 110 mph (at 30-ft standard elevations). However, it has been

13. Regulatory Guide 1.76, *Design Basis Tornado for Nuclear Power Plants,* USAEC Directorate of Regulatory Standards, April 1974.

14. T. T. Fugita, "Proposed Characterization of Tornadoes and Hurricanes by Area and Intensity," The University of Chicago Satellite and Mesometeorology Research Project Paper No. 91, February 1971.

15. P. L. Doan, "Tornado Considerations for Nuclear Power Plant Structures," *Nucl. Safety* **11**(4), 296–308 (1970).

16. J. R. McDonald, K. C. Mehts, and J. E. Minor, "Tornado-Resistant Design of Nuclear Power-Plant Structures," *Nucl. Safety* **15**(4), 432–39 (1974).

17. ASCE Paper 3269, "Wind Forces on Structures," final report of the Task Committee on Wind Forces, Committee on Loads and Stresses, Structural Division, American Society of Civil Engineers.

18. H. C. S. Thom, "Tornado Probabilities," *Monthly Weather Rev.* **91** (10–12), 730–36 (1963).

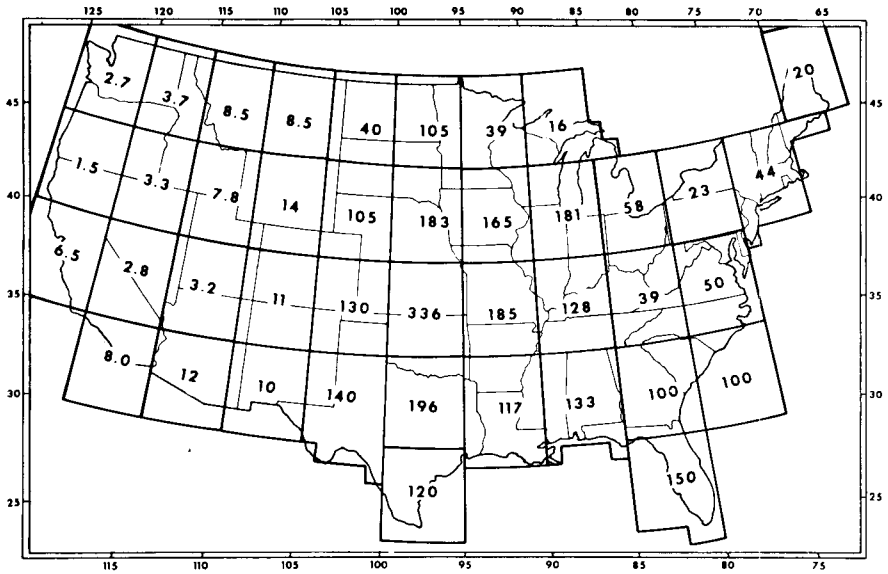

Fig. 2.14. Tornado strike probability within 5° squares in the contiguous United States. Units are 10^{-5} times probability per year. Source: "Technical Basis for Interim Regional Tornado Criteria," WASH-1300, USAEC Office of Regulation, May 1974.

estimated[19] that the cost of a cooling tower would be increased by a factor of 8 if it were designed to withstand tornado wind velocities and tornado-generated missiles. Therefore, it is assumed that whenever a cooling tower is subjected to a tornado, it will be damaged to the point where it cannot be used until it has been repaired.

For the purpose of this report it will be assumed that loss of one cooling tower will result in the loss of generating capacity of one 1200-MW reactor. This is a conservative assumption, since it is possible (except in extremely hot weather) to use three cooling towers for four reactors and have little or no loss in generating capacity, provided the quad unit[20] has been provided the necessary interconnecting piping.

For the Tennessee surrogate site area, the annual strike probability (P_t) is 128×10^{-5} (see Fig. 2.14). The probability (P_m) of one of the quad units being struck in the assumed 50-year life (m) can be calculated as follows:

$$P_m = 1 - (1 - P_t)^m ,$$

$$P_{50} = 1 - (0.99872)^{50}$$

$$= 1 - 0.935 = 0.065 \quad (\text{or } 6\tfrac{1}{2}\%).$$

The probability defined by Thom[18] is a point probability and theoretically applies equally to every point in a single geographic area. However, the development of the probability contains an implicit assumption of no interaction between the points. When multiple points such as the four cooling towers of a single quad unit (or of a single dispersed site) are considered, the probability of damage is more complicated. The annual probability of at least one of the four cooling towers being damaged is, of course, $4P_t$. But the probability of more than one being damaged depends on the distance between cooling towers, the direction from one cooling tower to the other, and the width of the damage zone produced by the tornado.

The layout of the quad units within the surrogate site (Fig. 2.13) was based upon the conceptional layout of TVA's proposed Hartsville plant. It shows two pairs of cooling towers, with the towers of each pair only 200 ft apart and the two pairs about 1200 ft apart. The towers thus make a line of cooling towers 2600 ft (1200 yd) long. The probability distribution of path width given by Thom[18] shows that there is less than 2% probability of all four towers being damaged by one tornado – provided the path of the tornado is perpendicular to the line of towers. On the other hand, if the tornado path is in the direction of the line of towers, the probability that all four will be damaged is 90%.

The probability that a tornado traveling perpendicular to the line of towers will damage two (given that one is struck) will be very close to 50%. Therefore, the weighted average of probability of damage to two towers (given that one is struck) will be at least 50%.

19. Personal communication – Wayne Bowman, TVA, and R. R. Davis, ORNL.

20. "Quad units" are compact assemblies of four reactors and their supportive facilities assumed to be used in the layout of an NEC (see Fig. 2.13).

It is obvious that the present surrogate site configuration is not optimum from the standpoint of minimizing the threat of damage from tornadoes. By arranging the four cooling towers in a square pattern with at least 1000 yd between towers, the probability of a second tower being hit, by a tornado that has already struck one, drops to about 2%, while the probability of the same tornado striking more than two is negligible.

The optimum spacing from the standpoint of tornadoes is more expensive than the present practice, so an economic balance needs to be made to compare the present cost of the increased capital investment and the estimated present cost of the hazard (approximately 3% probability that two units will be hit during the lifetime of the plant). One advantage of the NEC site option may be that it will provide enough space to permit the greater spacing, whereas the dispersed sites may not.

The probability of a tornado striking a single reactor site within the same geographic area will be exactly the same as for the NEC. Therefore, the only increased probability of damage of the NEC over the dispersed siting is just the probability that more than one quad unit will be damaged by the same tornado. The probability of two reactor sites of the dispersed siting option being struck by the same tornado is too low to be seriously considered.

The NEC siting criteria require that quad units be spaced at least $2\frac{1}{2}$ miles apart. Therefore, any tornado of less than $2\frac{1}{2}$ miles in length could not strike two quad units. Using the distribution of path lengths of tornadoes reported by Thom,[18] and assuming the tornado is moving in the direction established by the location of two quad units $2\frac{1}{2}$ miles apart, the weighted probability of the one tornado striking the second quad unit was calculated to be approximately 0.20 (20%).

Calculating the probability that a tornado which strikes one quad unit is moving in the direction to strike another unit is more complicated. As a first approximation we calculated that probability as follows:

1. The tornado path direction and frequency as reported by Thom[18] is shown in Table 2.5.
2. Using the mean path width from ref. 18 of 200 yd, the maximum angular variation of direction possible for a single tornado to strike a second quad unit is 200/4400 = 0.045 radian.
3. Each direction indicated in Table 2.5 represents 45° or $\pi/4 = 0.785$.
4. Using the surrogate site as an example, the direction from each quad unit to each of the others was obtained. Then using the Table 2.5 values as weighting factors, a weighted average probability was obtained that a second reactor would lie in the same direction that the tornado was moving. This weighted average was 0.026 (2.6%).

Table 2.5. Tornado path direction and frequency

Toward	Percent
NW	1.3
N	5.6
NE	63.1
E	15.0
SE	13.8
S	1.2
Total	100.0

Combining the probability that the tornado is moving in the right direction for striking a second quad unit and the probability that the path length includes two units, the probability that a second unit will be struck (given that one has been struck) is $0.20 \times 0.026 = 0.0052 = 0.5\%$. Recapitulating, the 50-year probability that one quad unit would be struck is $6\frac{1}{2}\%$, and the probability that two units will be struck by a single tornado is

$$0.065 \times 0.005 = 0.0003 = 3 \times 10^{-4} = 0.03\% .$$

Power transmission systems. The switching and relay stations of the power system are vulnerable to the effects of tornadoes, but there should be no difference in the hazard by virtue of the fact that they are located in the NEC. If a tornado passed through the NEC, the damage to the switching gear or transformers would be extensive.

Clustering nuclear reactors into nuclear energy centers requires that an extensive transmission system be built to carry all of the power to the loads. An idea of the complexity of the system may be gained by a study of the layout of the surrogate site (shown in Fig. 2.1).

The transmission towers are normally designed to withstand the highest winds (except tornadoes) that have been experienced in the area where they are to be used. Typically, TVA towers are designed for 110-mph winds. Designing for tornado wind velocities is considered to be too expensive. With an annual strike probability of 1.85×10^{-3} (for the Tennessee area), a power company would have to repair or replace, on the average, two towers each year for each 1000 towers in

use. TVA engineers report[21] that they do not have tornado damage every year, but sometimes they lose quite a large number in one year (e.g., 96 transmission towers damaged at the Huntsville, Alabama, site by one tornado).

Using the surrogate site layout, an estimate was made of the probability of damaging more than one "external" transmission line (i.e., a line from the NEC to a load center[22]). The surrogate site has 34 miles of external transmission lines which will have a total of approximately 150 transmission towers. Therefore, the annual probability (P_s) that any single tower is hit by a tornado with winds exceeding the design wind speed of the tower is

$$P_s = P_i P_a = 0.35 \times 1.28 \times 10^{-3} = 4.5 \times 10^{-4} ,$$

where P_i = probability of the tornado wind speed exceeding the value i (in this case i = 110) taken from Fig. 5 of ref. 11, P_a = annual probability of a tornado striking the point, taken from Fig. 2.1 for the area including the Tennessee surrogate site location. With 150 towers in the NEC, the annual probability of at least one external line being shut off because of tornado damage is $150 \times 4.5 \times 10^{-4} = 0.0675$ or $6\frac{3}{4}\%$.

The probability that a second external transmission line would be damaged by the same tornado was estimated using the distribution of path lengths from Fig. 1 of ref. 11. The average minimum distance between adjacent external transmission lines is just over 3 miles. The maximum probability that a second line would be damaged was found to be 18%.

The annual probability of more than one external transmission line being put out of service by tornadoes is

$$0.0675 \times 0.18 = 0.012 .$$

This corresponds to a recurrence interval (R) of

$$R = 1/0.012 = 82 \text{ years} .$$

One caveat must be made at this point. Probability is a powerful tool (and about the only one for this problem), but it can give misleading results if the data are insufficient. Consider these facts:

1. The annual point probability reported in ref. 11 was based upon 1955–1967 tornado frequency from Pautz;[23] the 1953–1962 path length and width data were from Thom[18] and were calculated as an average over 5° squares.
2. For the Tennessee area the point probability is 128×10^{-5}, and for Alabama it is 133×10^{-5}. These two 5° squares cover most of the TVA service area. The point probability for the TVA area should be about 130×10^{-5}. We just showed that the probability of a single tower being hit by a tornado with wind speed exceeding the design speed of 110 mph is 45×10^{-5}.
3. TVA records for the 18-year period 1957–1974 show[21] that the yearly rate of towers lost to tornadoes has been 0.128 per 100 miles of line. On the basis of 4.4 towers/mile this gives

   $$0.128/440 = 29 \times 10^{-5} \text{ per tower} .$$

   This is very close to the predicted rate (45×10^{-5}).
4. If the year 1974 were excluded, the resulting 17-year period would show only 0.024 tower lost per year per 100 miles, or a point probability of only 5×10^{-5}. This would suggest that the predicted value was conservative by at least an order of magnitude.

Summary. The threat to the NEC from tornadoes can be evaluated only by statistical methods. The data base presently available is rather narrow (about 13 years) but is probably adequate to show trends. The national interest in nuclear power expansion and in tornadoes will undoubtedly result in frequent updating of the tornado statistics and will give designers more accurate design criteria. The more accurate data may even reduce the design wind speed requirements.

To the best of present knowledge, tornadoes will not cause loss of containment (i.e., the risk of loss of containment is less than 10^{-7}). Based on the Tennessee surrogate site location, the following probabilities have been calculated:

21. Personal communication – Sam Simon, supervisor of line maintenance, TVA, to R. R. Davis, ORNL, May 8, 1975.

22. The damage to interconnecting transmission lines was not included, since they will have enough redundancy to avoid losing the power from more than one quad unit, and it is assumed that the strike of a tornado within the NEC will damage some part of one quad unit enough to require a shutdown of the unit.

23. M. E. Pautz (ed.), "Severe Local Storm Occurrences, 1955–1967," U.S. Department of Commerce, Environmental Science Services Administration (ESSA) Tech Memo WBTM-FCST-12, September 1969.

1. Probability that any one cooling tower will be severely damaged by a tornado within its (assumed) 50-year life = $6\frac{1}{2}\%$.
2. Probability that any one cooling tower will be severely damaged by a tornado in any one year = 128×10^{-5}; recurrence interval = 780 years.
3. Probability that two cooling towers within the same quad unit will be damaged at the same time during the (assumed) 50-year life with layout as shown in Fig. 1 of ref. 11 = $3\frac{1}{4}\%$.
4. Probability that two cooling towers within the same quad unit will be damaged during the (assumed) 50-year life with optimum spacing (i.e., 1000 yd apart) = 0.1%.
5. Probability that two quad units will be struck by a single tornado = 0.03%.
6. Probability of losing the switching or relay station to a tornado during the 50-year life of the NEC is $6\frac{1}{2}\%$.
7. Annual probability of at least one external line being shut off because of tornado damage = $6\frac{3}{4}\%$.
8. Annual probability of two external lines being shut off because of tornado damage = 1.2%.

The only increased probability of loss due to tornadoes by virtue of being in the NEC is the 0.03% probability of two cooling towers not in the same quad unit being struck by the same tornado and the 1.2% probability that two transmission lines would be shut off by a single tornado. This increased damage would increase the loss of power only from 4% to 8% of the generated power within the NEC. If the cooling towers within quad units were spaced at least 1000 yd apart, the total vulnerability of the NEC to tornadoes would be reduced to less than the vulnerability of dispersed sites if the dispersed sites had cooling towers spaced according to present practice.

Effects of Hurricanes and Other High Winds (Other Than Tornadoes)

Adverse effects of hurricanes and other high winds other than tornadoes can be prevented by designing all structures, including cooling towers and transmission towers, strong enough to resist the winds. It should be noted that the requirement for building class I structures to withstand the design tornado makes such structures invulnerable to hurricanes. Designing cooling towers and transmission towers to hurricane wind standards can be done but is so costly that a coastal site for the NEC may not be economically feasible, although individual dispersed stations can and have been built there (but without cooling towers).

The accepted method for establishing a design wind speed for a specific site requires the use of Thom's[24] annual extreme fastest mile wind speed maps.

The wind speed maps (Figs. 2.15–2.17) are actually wind speed probability maps. Each map gives the wind speed contours for a specific mean recurrence interval defined by

$$R = \frac{1}{1 - F(x)},$$

where R is the mean recurrence interval in years, $F(x)$ is the probability of the extreme wind speed not exceeding the value x during one year. The wind probability maps were created by Thom[24] from meteorological data of approximately 150 airport or open-country stations over a 21-year period. The extreme wind values are adjusted to a standard 30-ft elevation, assuming a $1/7$ power relation:

$$V_z = V_{30}\,(Z/30)^{1/7},$$

where

Z is the height above ground,

V_z is the wind speed at height Z,

V_{30} is the wind speed at 30 ft.

The wind maps represent a mixed population of nontropical and tropical storms. The relatively small frequency of tropical storms compared with other storms does not greatly affect the distribution.

Use of the wind probability maps in establishing a design wind speed at a specific location involves taking a reading off two different maps, plotting a line on the Frechet distribution chart (Fig. 2.18), and reading a design wind speed from the chart. This makes it difficult to compare alternate sites rapidly. Therefore, we have prepared a list of wind speed values for a number of sites (Table 2.6), to form the basis for preparing a map which shows the wind speed required for design, assuming that one is willing to accept a 95% probability that no wind will exceed that value during the (assumed) 50-year life of the plant. The recommended values shown in Table 2.7 were used to prepare the wind speed design map (Fig. 2.19).

24. H. C. S. Thom, "New Distribution of Extreme Winds in the United States," *Journal of Structural Division Proceedings of ASCE*, ST7, pp. 1787–1801, July 1968.

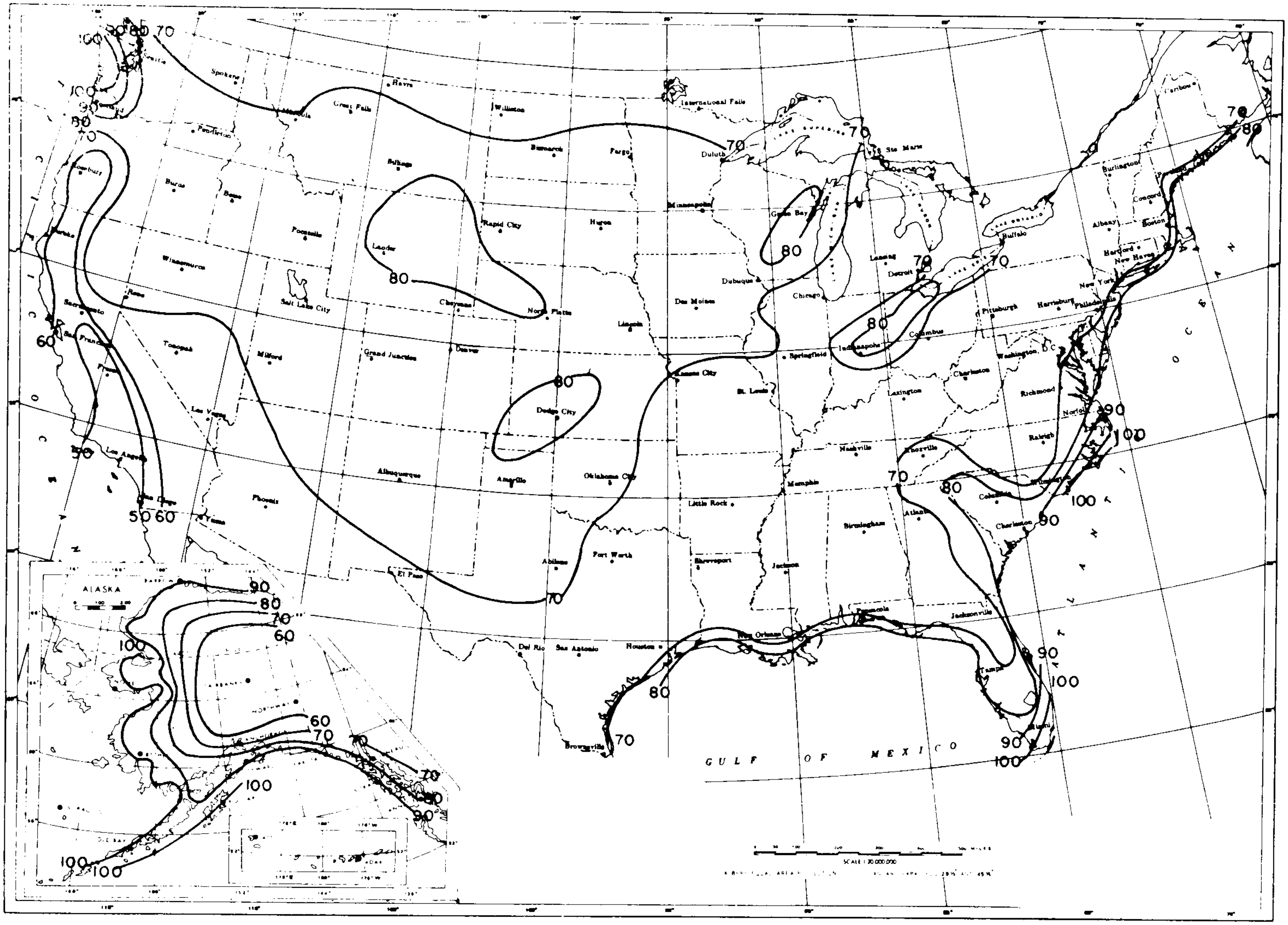

Fig. 2.15. Basic wind speed in miles per hour. Annual extreme speed 30 ft above ground, 25-year mean recurrence interval. This material is reproduced from *American National Standard Building Code Requirements for Minimum Design Loads in Buildings and Other Structures,* A58.1-1972, copyright 1972 by the American National Standards Institute, copies of which may be purchased from the American National Standards Institute at 1430 Broadway, New York, N.Y. 10018.

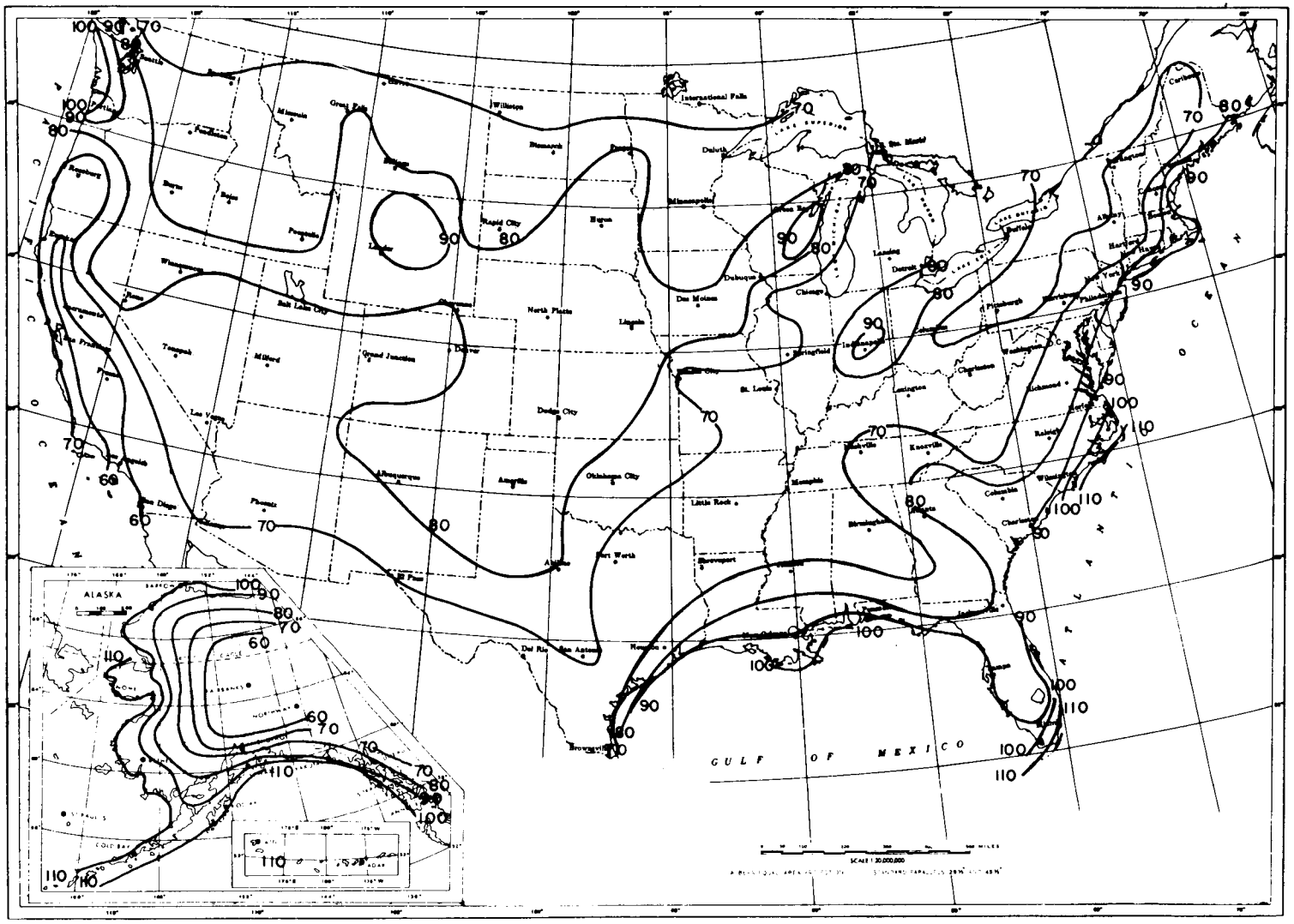

Fig. 2.16. Basic wind speed in miles per hour. Annual extreme fastest-mile speed 30 ft above ground, 50-year mean recurrence interval. This material is reproduced from *American National Standard Building Code Requirements for Minimum Design Loads in Buildings and Other Structures,* A58.1-1972, copyright 1972 by the American National Standards Institute, copies of which may be purchased from the American National Standards Institute at 1430 Broadway, New York, N.Y. 10018.

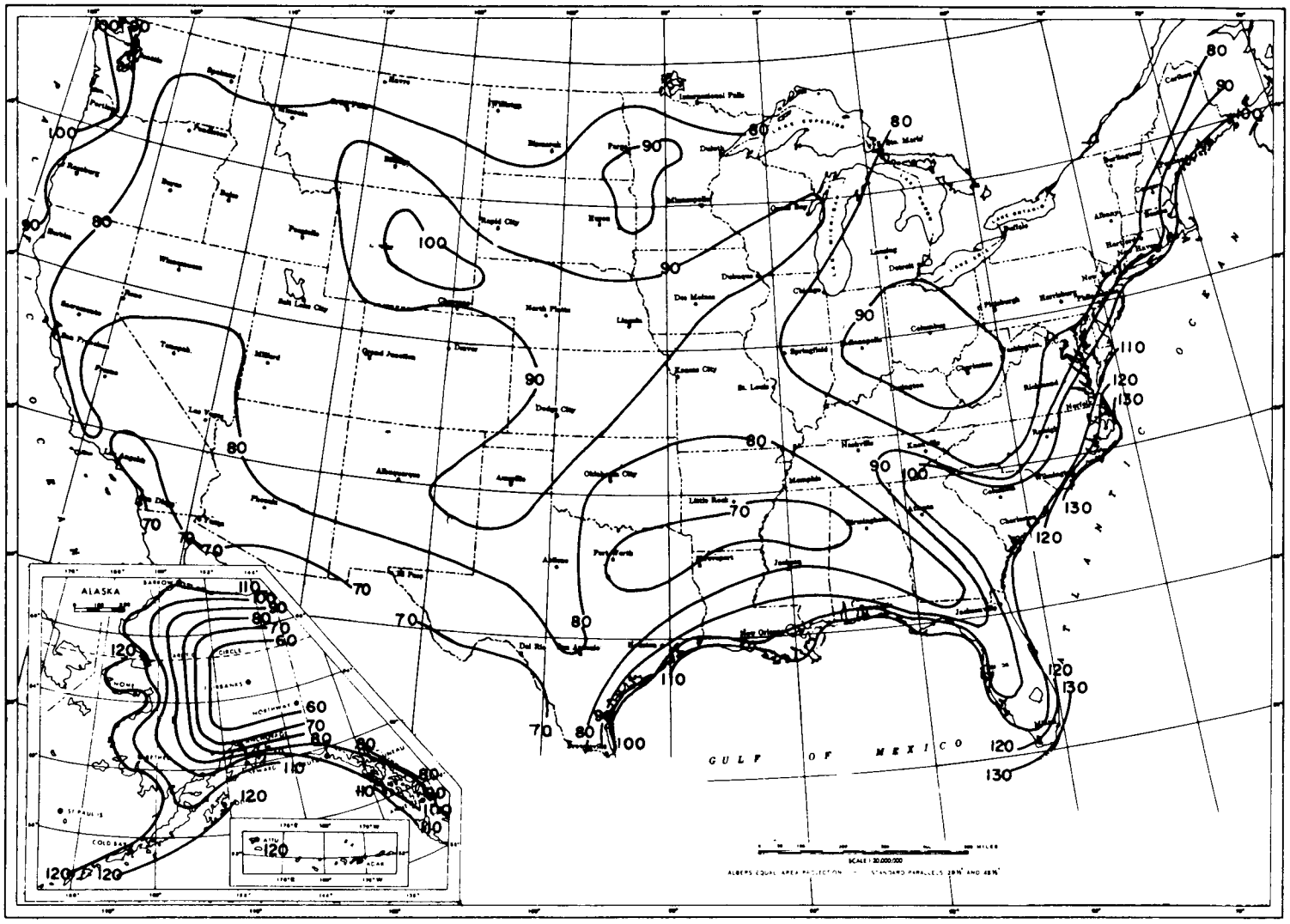

Fig. 2.17. Basic wind speed in miles per hour. Annual extreme fastest-mile speed 30 ft above ground, 100-year mean recurrence interval. This material is reproduced from *American National Standard Building Code Requirements for Minimum Design Loads in Buildings and Other Structures,* A58.1-1972, copyright 1972 by the American National Standards Institute, copies of which may be purchased from the American National Standards Institute at 1430 Broadway, New York, N.Y. 10018.

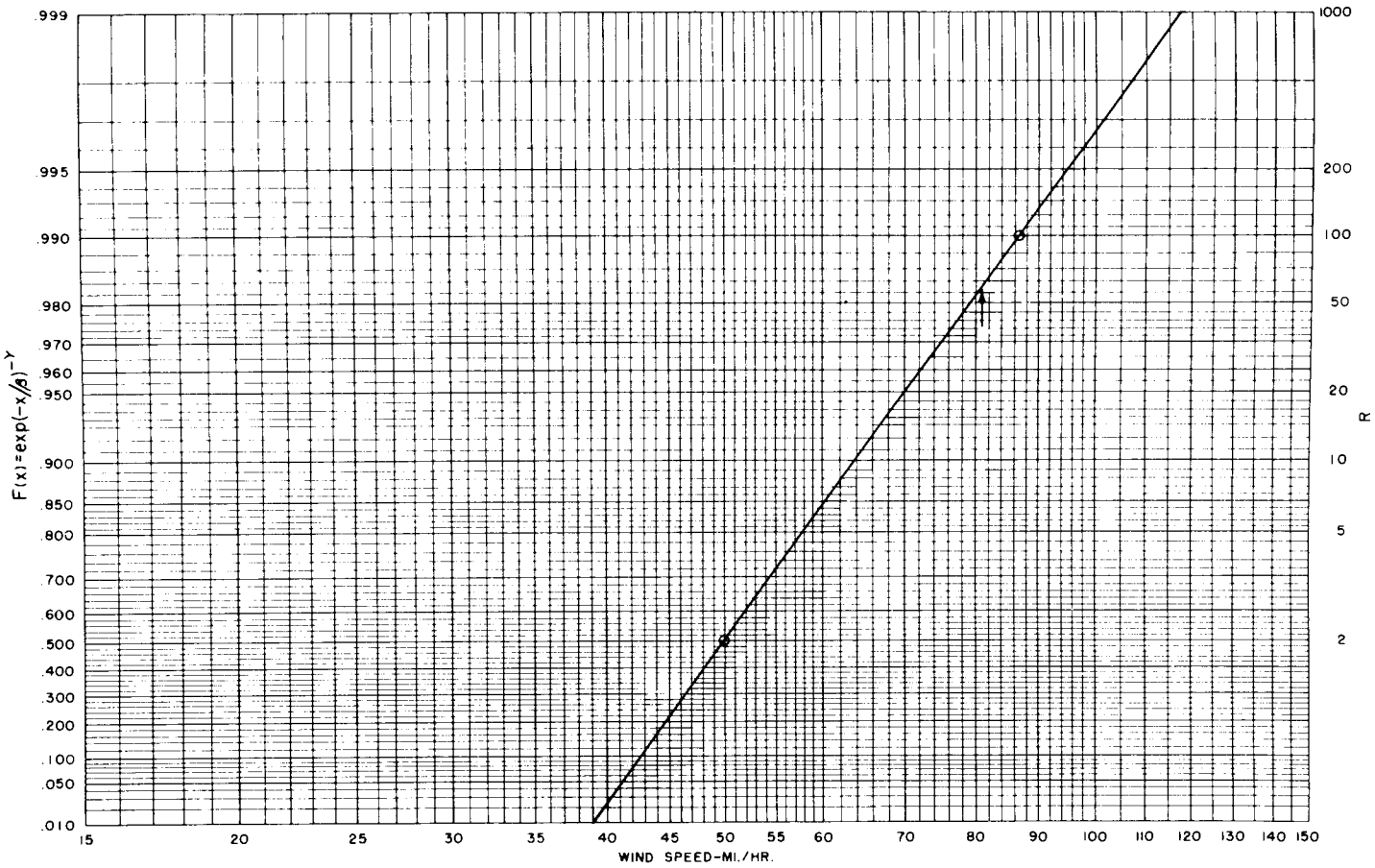

Fig. 2.18. Maximum-value probability paper, Fréchet distribution. Source: H. C. S. Thom, "New Distributions of Extreme Winds in the United States," Paper No. 6038, p. 1795, *Journal of the Structural Division, Proceedings of the American Society of Civil Engineers,* July 1968.

Table 2.6. Design wind speeds

Location	$F(x) = 0.90$	$F(x) = 0.99$	$F(x) = 0.999$
Key West, FL	82	130	200
Key Largo, FL	82	130	200
Beaufort, NC	80	130	205
Buxton, NC	84	130	197
Kitty Hawk, NC	83	130	199
Porpano Beach, FL	80	120	174
Wilmington, NC	78	120	130
Columbia, NC	75	120	185
Elizabeth City, NC	76	120	190
Virginia Beach, VA	74	120	190
Naples, FL	73	110	164
Norfolk, VA	70	110	170
Pensacola, FL	60	110	200
Galveston, TX	72	110	165
Charleston, SC	75	110	158
Pilottown, LA	70	110	170
Group 1 – West Coast			
Portland, OR	80	100	124
Elma, WA	80	100	124
Group 2 – Rocky Mountain Area			
Lander, WY	73	100	135
Torrington, WY	70	100	140
Group 3 – Eastern U.S. and Gulf Coast			
Portland, ME	70	100	140
Jacksonville, FL	60	100	140
Corpus Christi, TX	70	100	140
Abbeville, LA	73	100	135
Tampa, FL	70	100	140
Group 1 – West Coast			
Seattle, WA	65	90	125
Eugene, OR	60	90	130
Orick, CA	60	90	130
Group 2 – Central States and Rocky Mountains			
Cheyenne, WY	73	90	110
Santa Rose, NM	73	90	110
O'Niell, NB	68	90	119
Wausau, WI	65	90	125
Fargo, ND	73	90	110
Sioux Falls, SD	68	90	119
Brainerd, MN	68	90	119
Group 3 – Eastern U.S. and Gulf Coast			
Lexington, KY	55	90	145
Houston, TX	60	90	130
Richmond, VA	58	90	135
Philadelphia, PA	60	90	130
New York City, NY	60	90	130
Lake City, FL	53	90	150
Durham, NC	55	90	145

Table 2.6. (continued)

Location	$F(x) = 0.90$	$F(x) = 0.99$	$F(x) = 0.999$
Group 1 – Eastern U.S. and Gulf Coast			
Caribou, ME	55	80	112
Hartford, CT	58	80	107
Charlottesville, VA	54	80	115
Springfield, IL	56	80	113
Muskegon, MI	70	80	102
Jackson, MS	55	80	112
Jennings, FL	55	80	112
Gadsden, AL	54	80	115
Group 2 – West Coast			
Berkeley, CA	50	80	122
Wenatchee, WA	55	80	112
Group 3 – Central States and Rocky Mountains			
Springfield, MO	60	80	105
San Antonio, TX	55	80	112
Jamestown, ND	70	80	102
Group 1 – West Coast			
Los Angeles, CA	55	70	88
Group 2 – Central States and Rocky Mountains			
Tuscon, AZ	56	70	86
Eagle Pass, TX	57	70	85
Laredo, TX	56	70	86
Weatherford, TX	60	70	81
Group 3 – Eastern U.S. and Gulf Coast			
Pine Bluff, AR	57	70	85
Shreveport, LA	56	70	86
Tuscaloosa, AL	55	70	88

Table 2.7. Recommended contour designations

Present contours on 100-year recurrence maps	Contours to be put on new map[a]		
	West Coast	Central States and Rocky Mountains	Eastern U.S. and Gulf Coast
130	N.A.	N.A.	200
120	N.A.	N.A.	185
110	N.A.	N.A.	170
100	130	140	150
90	120	120	140
80	110	110	110
70	85	85	85

[a]The 100-year recurrence map contours were renumbered to produce a 1000-year recurrence map (the design wind speed map, Fig. 2.19).

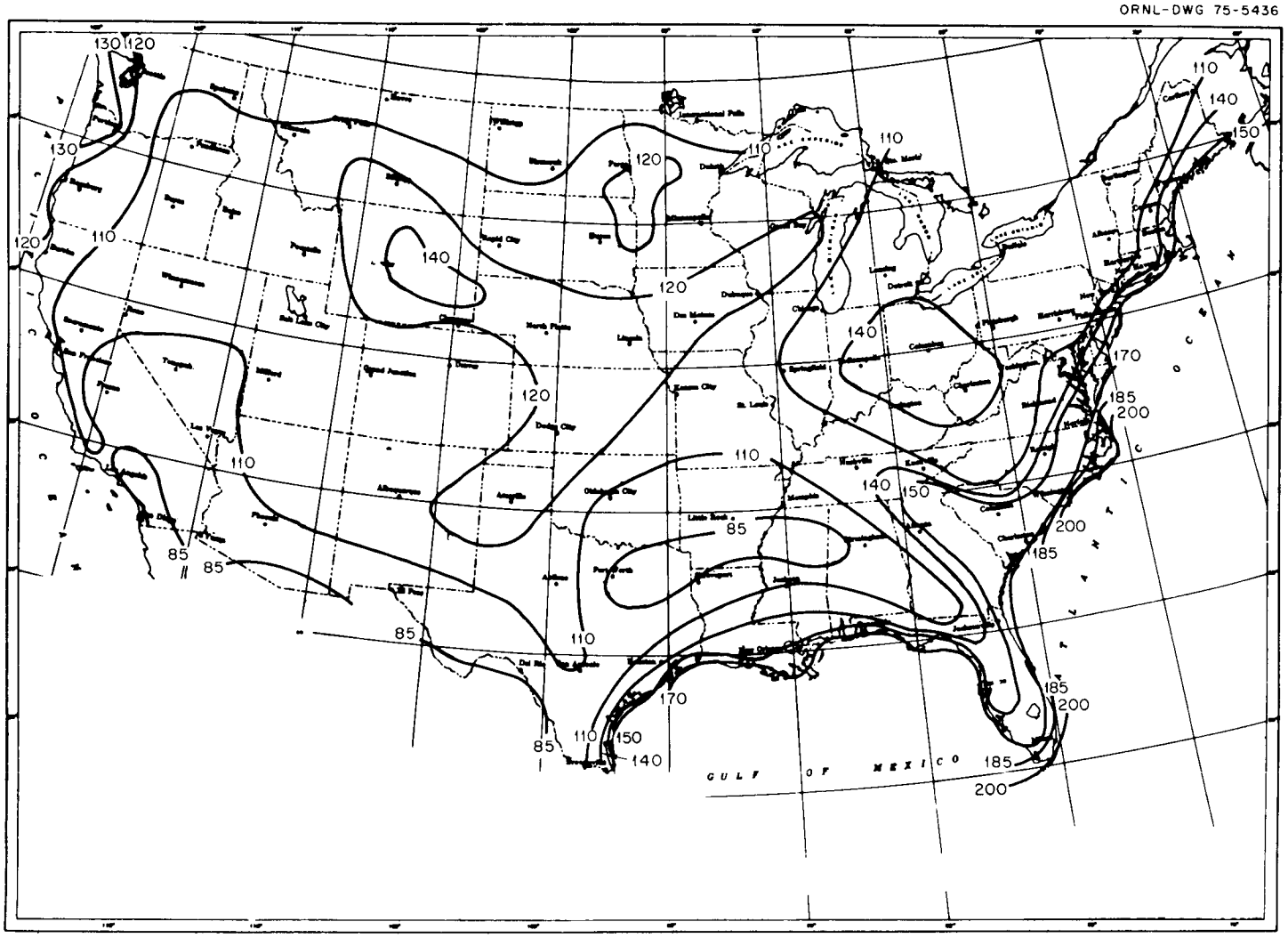

Fig. 2.19. Wind speed design map.

In Table 2.6 the values of the wind speeds listed under $F(x) = 0.90$ were read directly from the ten-year recurrence map, and the wind speeds for $F(x) = 0.99$ were read from the 100-year recurrence maps. The values in the column $F(x) = 0.999$ were obtained by plotting the first two values on the Frechet distribution paper (Fig. 2.18) and reading the values off the extrapolated line connecting those points.

The rationale for use of the $F(x) = 0.999$ is as follows: The probability of no extreme wind exceeding the value x in the first m years of the lifetime of a plant is

$$P_m = 1 - [F(x)]^m ,$$

or, solving for $F(x)$,

$$1 - F(x) = 1 - (1 - P_m)^{1/m} .$$

Assuming the design criteria to be that the design wind will have no more than a 5% probability of being exceeded in 50 years,

$$P_m = 0.05 ,$$

$$m = 50 .$$

Therefore,

$$1 - F(x) = 1 - (0.95)^{1/50} = 1 - 0.999 ,$$

$$F(x) = 0.999 .$$

Incidentally,

$$R = \frac{1}{1 - F(x)} = \frac{1}{1 - 0.999} = 1000 \text{ years}$$

(i.e., the design criteria is equivalent to a 1000-year mean recurrence interval). Conversely, the wind probability maps represent the following probabilities of the wind speed of x being exceeded at least once in 50 years:

Recurrence level (years)	Probability (%) of x being exceeded in 50 years
10	99.5
25	87.0
50	63.6
100	31.5

Effects of Earthquakes and Tsunamis

The effects of earthquakes and earthquake phenomena have been extensively discussed in the literature and are carefully considered in every application for permit to build and operate a nuclear power plant.

The most comprehensive treatment of the subject has been published by Lomenick et al.,[25] and an extensive bibliography is available.[26]

The seismic and geologic siting criteria[27] are extensive and detailed. The major item of concern to this study is the requirement that the nuclear power plant structures, systems, and components important to safety be designed to withstand the effects of earthquakes without loss of capability to perform their safety function. More specifically, these criteria define a "safe shutdown earthquake" (SSE) as that earthquake which is based upon an evaluation of the maximum earthquake potential, considering the regional and local geology and seismology and specific characteristics of local subsurface material (i.e., historical earthquakes and evidences of prehistorical earthquakes must be used to predict the maximum earthquake that might happen at some time in the future). It is that earthquake which produces the maximum vibratory ground motion for which certain structures, systems, and components are designed to remain functional to assure integrity of the reactor coolant pressure boundary, the capability to shut down the reactor and maintain it in a safe shutdown condition, and the capability to prevent or mitigate the consequences of accident which could result in potential off-site exposure. The structures, systems, and components which must remain functional during an SSE are defined in Regulatory Guide 1.29 and designated Seismic Category 1. They do not include the cooling towers or the power lines (other than auxiliary systems for on-site electric power supplies). The operating basis earthquake (OBE) is defined as the maximum intensity earthquake which the power station can "reasonably"[28] expect to experience at least once during its lifetime. The maximum vibratory ground motion of the OBE shall be at least one-half the maximum vibratory ground motion of the SSE. The reactor and all its associated systems are required to

25. T. F. Lomenick et al., *Earthquakes and Nuclear Power Plant Design,* ORNL-NSIC-28 (July 1970).

26. *An Indexed Bibliography of Literature on Seismic Considerations in the Siting of Nuclear Facilities,* ORNL-NSIC-88.

27. "Seismic and Geologic Siting Criteria," *Fed. Regist.* 38(218), Nov. 13, 1973.

28. Unfortunately, "reasonably" is not quantitatively defined.

remain operational (i.e., must be able to generate power during an OBE). However, this requirement does not extend to the cooling towers or the power transmission system.

The major earthquake-induced phenomena to be considered are faults, vibrations, and tsunamis. The available earthquake data for the U.S. have been collected and published[29] by the National Oceanic and Atmospheric Administration. Although this publication lists all recorded earthquakes of intensity V or greater (modified Mercalli scale), it cautions that "exact seismological information has been available for less than 70 years." This listing is limited to location, maximum intensity, and approximate felt area. Another source of information helpful for establishing general earthquake criteria is the seismicity zoning maps in ANSI A58.1 – 1972 (p. 55),[30] which establishes four seismic zones (3, 2, 1, 0) based on the history of the frequency of occurrence of the earthquake. The highest magnitude earthquake would be in zone 3 and is successively halved for zones 2, 1, and 0. Although much effort is being expended in the U.S. on prediction of location, time, and intensity of earthquakes, no reliable method is yet available.

Only a very few strong-motion accelerograph records are available at present, mostly made by the U.S. Coast and Geodetic Survey. Because so few accurate measurements have been made, designers must make highly conservative estimates of ground motion. Actual experience with large structures in great earthquakes is limited to the San Francisco earthquake of 1906, the Tokyo-Yokohama earthquake of 1923, the Alaska "Good Friday" earthquake of 1964, and the Caracas earthquake in 1967. No structure of the type used for nuclear reactors has ever been subjected to an intense earthquake.

The chief engineering problem is to determine how to use the existing records of strong motion to estimate the ground motion likely to occur at sites where only magnitude and intensity data exist. At present there are no widely accepted correlations of magnitude and intensity. Herschberger[31] has shown that there is poor correlation between maximum acceleration and intensity. For this reason it is difficult to assign realistic ground motion values for the SSE to reactor sites. The current method consists, in general, of evaluating strong ground motions from small nearby shocks as well as large earthquakes. It is generally assumed that the largest earthquake that may affect the area will be no larger than the maximum magnitude shock recorded or estimated (from geologic structure) that occurred in the general vicinity of the site. If an active fault lies relatively near (e.g., within 200 miles), it is assumed that earthquakes up to a size commensurate with the length of the fault can occur along it.

Once the vibratory ground motion related to the SSE has been assigned, the design of the Seismic Category I structures follows well-established procedures. Although the structures which have been designed by the accepted seismic procedures have not been subjected to any severe earthquakes, some have been subjected to minor earthquakes[32] and some have been tested using high explosives to simulate earthquakes.[33] Although all the responses of nuclear power-plant components to earthquake vibrations are not completely known, it does appear that present design practices are adequate, even conservative. Although present NRC regulations do not require that cooling towers remain operational under earthquake conditions, it should be noted that the cost of the failure of a cooling tower could be great. Not only is the cooling tower a very expensive structure, but the resulting shutdowns of the power plant and the consequent loss of revenue could be disastrous.

Design of hyperbolic cooling towers for low-intensity earthquakes should pose no serious problems. Gurfinkel and Walser[34] report that tall towers designed for 100-mph basic wind velocity may be capable of resisting earthquake effects of 0.05*g* maximum ground acceleration with 2% damping. Gupta and Schnobrich[35] have shown that it is feasible to design

29. J. T. Coffman and C. A. Von Hake, *Earthquake History of the United States,* publication 41-1, revised ed. (through 1970), National Oceanic and Atmospheric Administration, Boulder, Colo., 1973.

30. "Building Code Requirements for Minimum Design Loads in Buildings and Other Structures," American National Standards Institute ANSI-A58.1 – 1972.

31. J. Herschberger, "A Comparison of Earthquake Acceleration with Intensity Ratings," *Bull. Seismological Society of America* 32(3), 171 (June 1974).

32. C. B. Smith, "Power Plant Safety and Earthquakes – Nuclear Safety and Earthquakes," *Nucl. Safety* 14(6), 568–96 (1973).

33. C. B. Smith and R. B. Mattiesen, "Simulating Strong-Motion Earthquake Effects on Nuclear Power Plants," *Nucl. Safety* 13(2), 114–21 (1972).

34. German Gurfinkel and Adolf Walser, "Analysis and Design of Hyperbolic Cooling Towers," *Journal of the Power Division Proceedings of the American Society of Civil Engineers,* p. 148, June 1972.

35. A. K. Gupta and W. C. Schnobrich, "Seismic Analysis and Design of Hyperbolic Cooling Towers," meeting preprint 2190, ASCE National Structural Engineering Meeting, Cincinnati, Ohio, April 22–26, 1974.

hyperbolic cooling towers to withstand earthquakes with up to 1.0*g* horizontal acceleration. Since the cooling towers and the electrical systems should be designed to survive the OBE, and since present design procedures are dependable, there should be no difference in risk of power loss from earthquakes between the NEC and the dispersed siting. Only if the earthquake exceeds the OBE will there be any damage. Because of the conservatism required in establishing the OBE (and the SSE), the probability of experiencing an earthquake greater than an OBE should be very low. That is, the recurrence level should be 1000 years or greater.

In the unlikely event that an earthquake greater than the OBE does occur, all reactors would automatically shut down. By NRC regulations, they would not be put into operation again until the operator has proven that there has been no damage to Seismic Category I structures.

The only restrictions on the NEC by earthquake threat that can be foreseen is in site selection to assure that the OBE is small enough to permit construction of cooling towers strong enough to resist the earthquake. This restriction would not apply to some dispersed sites if sufficient water is available at the site to permit elimination of the cooling towers.

Tsunamis present essentially no problem to an NEC. The only part of the United States subject to tsunami action is the west coast. The largest recorded run-up was only 16 ft, except for a single (reportedly questionable) report[25] of a 50-ft rise at Gaviota, California, in 1812. Run-up heights in Japan, Chile, the Hawaiian Islands, and Alaska have exceeded 30 ft. Protecting the NEC west coastal site (if any) by the same methods used for individual sites (i.e., wave defense adequate for maximum expected run-up and protection of offshore cooling-water structures) will assure there will be no difference between NEC and dispersed siting due to tsunamis.

Effects of Floods

Regulatory Guide 1.59 (August 1973) and its Appendix completely specify the methods required to calculate the probable maximum flood (PMF). Since all Seismic Category I buildings and structures must be protected against the PMF to the point of remaining functional, the rest of the plant can readily be protected from the same flood. There should be no difference between the NEC and the dispersed siting option regarding flooding.

EFFECTS OF PLUTONIUM AEROSOLS

R. O. Chester

The objective of the following calculations is to obtain a realistic estimate of the number of radiation-induced lung cancers in a population that inhales a $^{239}PuO_2$ aerosol.

Plutonium-239 inhalation results in a radiation dose to the lungs that produces an additional risk of lung cancer. The additional risk is expressed as the number of additional or excess annual deaths from lung cancer per rem to the lung.[36]

In addition, biological processes transport part of this lung burden of plutonium to other parts of the body, resulting in radiation doses that produce an additional risk of cancer in those other parts. For a lung burden inhaled over a short period compared with one year, the radiation dose to various organs, including the lungs, is not all received instantly, but because of the time required for biological transport processes is received as depicted in Fig. 2.20.[37,38]

To obtain the number of radiation-induced cancers to be expected in an exposed population, the radiation dose to the lungs must first be calculated. Dose to the lungs is equal to the lung burden times the dose commitment. The lung burden is proportional to the total amount of plutonium inhaled, which is proportional to the breathing rate times the exposure time. The dose commitment is the total dose received over a specified time interval. The dose commitment is a function of age at exposure and mass of the lungs and has been calculated using the model of the ICRP Task Group on Lung Dynamics.[39] The dose commitment results are summarized in column 1 of Table 2.8, and the relative breathing rate is given in column 2. For the members of a population having the same exposure conditions, the lung dose is proportional to the breath-

36. National Academy of Sciences, National Research Council, *The Effects on Population of Exposure to Low Levels of Ionizing Radiation*, NP-19638, report of the Advisory Committee on the Biological Effects of Ionizing Radiation, Washington, D.C., November 1972.

37. B. R. Fish, O. W. Keilholtz, W. S. Snyder, and S. D. Swisher, *Calculation of Doses Due to Accidentally Released Plutonium from an LMFBR*, ORNL-NSIC-74 (November 1972).

38. R. O. Chester, *Biological Dose and Radiological Activity from Nuclear Reactor or Nuclear Weapon Fission Products*, ORNL-4996 (December 1974).

39. Task Group on Lung Dynamics (P. E. Morrow et al.), "Deposition and Retention Models for Internal Dosimetry of the Human Respiratory Tract," *Health Phys.* **12**, 173–207 (1966).

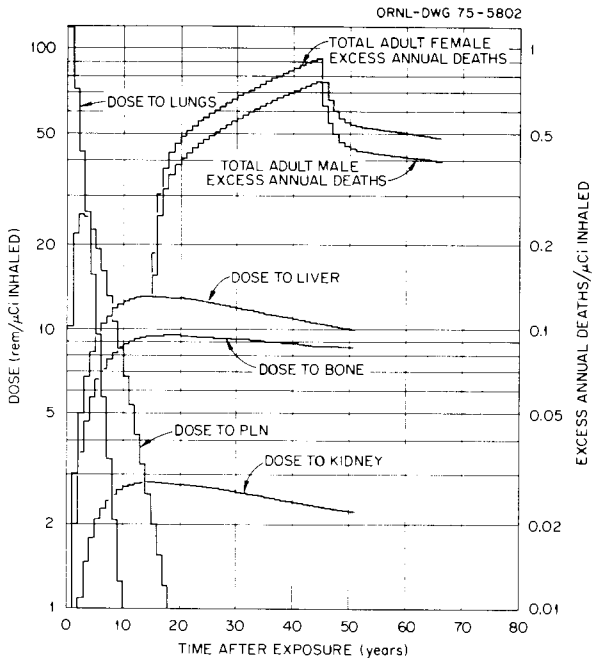

Fig. 2.20. Effects of ^{239}Pu inhalation in a single exposure.

ing rate times the dose commitment for each individual, that is, the product of columns 1 and 2.

Next, the additional risk of lung cancer from exposure to radiation must be known. This number has been estimated and is presented in column 3 of Table 2.8. The estimate applies to low levels of irradiation, possibly less than a few hundred rems to the lungs. The proposed model for cancer induction specifies a latent period following the irradiation during which there is no apparent effect. Then, for a specified number of years, or plateau period, a fraction of the irradiated population dies of cancer of the target organ. The fraction that dies is assumed proportional to the dose to the target organ. The proportionality constant is the additional risk of cancer and is different for different organs. The calculated excess annual deaths in an adult male from radiation-induced lung cancer is shown in Fig. 2.21. Also shown is the total death rate from lung, liver, and bone cancer.

Using the above information, the excess annual deaths during the plateau period can be calculated for a population with the members having the same exposure conditions. For example, if the exposure is such that a

Table 2.8. Effects of ^{239}Pu inhalation

Age at exposure (years)	Dose commitment to lungs[a] (rems/μCi dep.)	Breathing rate[a] (m^3/hr)	Excess annual deaths/rem (lung cancer)[b]	Excess annual deaths/μCi ^{239}Pu dep. in lungs[c]	Excess annual death for same exposure[d]
Newborn	8210	0.033	$(1.3/5)/10^6$	$2.1/10^3$	$0.07/10^3$
1	5510	0.16	$(1.3/5)/10^6$	$1.4/10^3$	$0.24/10^3$
10	2340	0.62	$1.3/10^6$	$3.0/10^3$	$2.0/10^3$
20 (male)	1540	0.99	$1.3/10^6$	$2.0/10^3$	$1.8/10^3$
20 (female)	1230	0.95	$1.3/10^6$	$1.6/10^3$	$1.6/10^6$

[a]Data taken from NSIC-74, Table 6.3. It should be noted that the dose commitment is given to age 70, but since the unciliated lung surfaces clear with a half-life of about 500 days and the ciliated surfaces with a half-life of about one day, ½ the dose commitment is received in 1 year and 90% in 4 years.

[b]The source for this column is the BEIR report, Table 3-2. The numbers represent the absolute risk of lung cancer. The model for this cancer is a 15-year latent period following low-level exposure during which no excess lung cancer is evident. The latent period is followed by a 30-year plateau period during which there is an elevated constant cancer risk. The excess lung cancer risk is assumed to return to zero at the end of the plateau period. The long-term lung cancer cure rate is assumed negligible.

[c]$$\frac{\text{excess annual lung cancer deaths}}{\mu\text{Ci } ^{239}\text{Pu deposited in lungs}} = \text{dose commitment to lungs (rems)} \times \frac{\text{excess annual deaths (lung cancer)}}{\text{rem}} .$$

[d]The amount of plutonium in the lungs = aerosol concentration × breathing rate × exposure time. Therefore, for the same aerosol concentration and exposure time the amount is proportional to the breathing rate. The numbers in this column are obtained by assuming the same exposure time and aerosol concentration for everyone and such that a 20-year-old male has 1 μCi ^{239}Pu deposited in his lungs. For example, a 20-year-old female would have 0.88/0.95 = 0.92 μCi deposited in her lungs. The excess annual deaths in the 20-year-old female population under these exposure conditions would be 2.0/1000 × 0.88/0.95 = 1.8/1000.

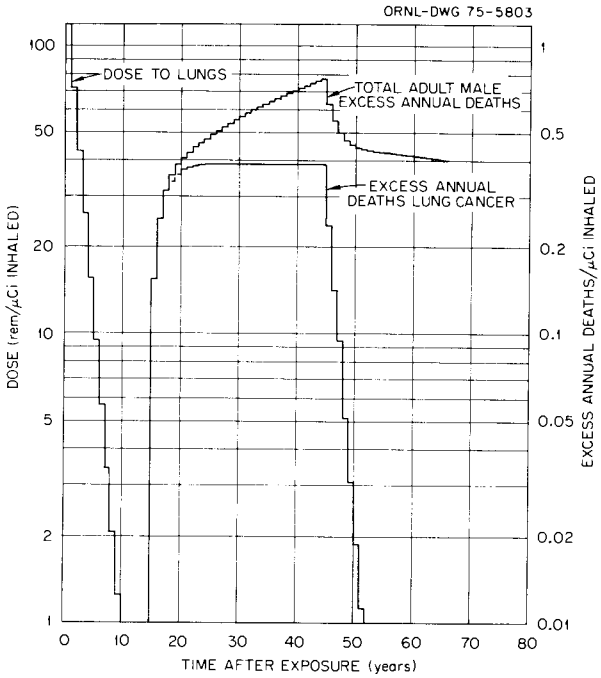

Fig. 2.21. Effects of ^{239}Pu inhalation in a single exposure.

20-year-old adult male receives a total lung burden of 1 μCi of ^{239}Pu, the excess annual death values given in column 5 of Table 2.8 are calculated. This calculation assumes an exposure time that is short compared with one year. Interpolating between the values presented in column 5 and assuming the 20-year-old results apply to the 20-year-old and older population, the numbers in column 5 can be applied to any population whose age and sex distribution and death rate from all other causes is known. For example, the results are given in Fig. 2.22 for the U.S. population[40] and in Fig. 2.23 for the adult male work force,[40] assuming exposure such that an adult male receives a lung burden of 1 μCi of ^{239}Pu. The results for the male work force are replotted twice, once in Fig. 2.24 for comparison with occupational exposures[41] and once in Fig. 2.25 for

40. U.S. Bureau of the Census, *Statistical Abstract of the United States: 1971,* 92d ed., Washington, D.C., 1971.

41. United States Atomic Energy Commission, Division of Operational Safety, *Operational Accidents and Radiation Exposure Experience Within the United States Atomic Energy Commission 1943–1970,* WASH-1192, Washington, D.C., 1971.

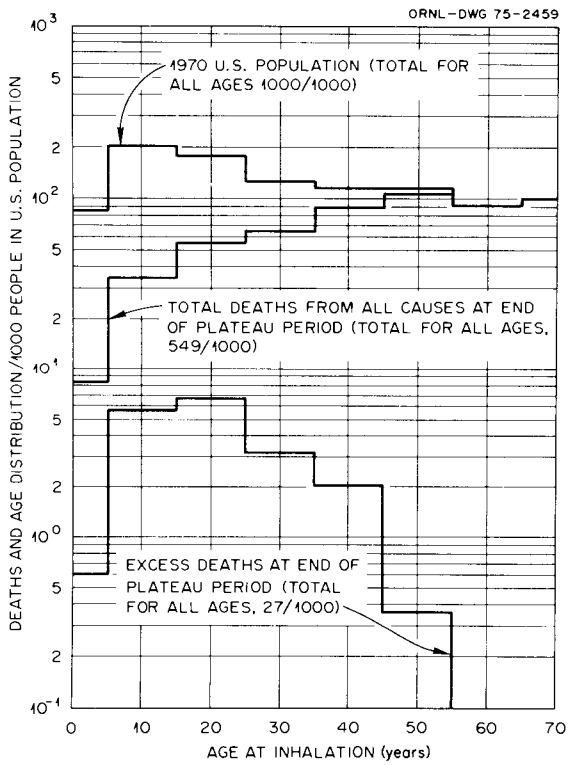

Fig. 2.22. Effects of ^{239}Pu inhalation on 1970 U.S. population. Adult male has 1 μCi deposited in lungs; others have same exposure time.

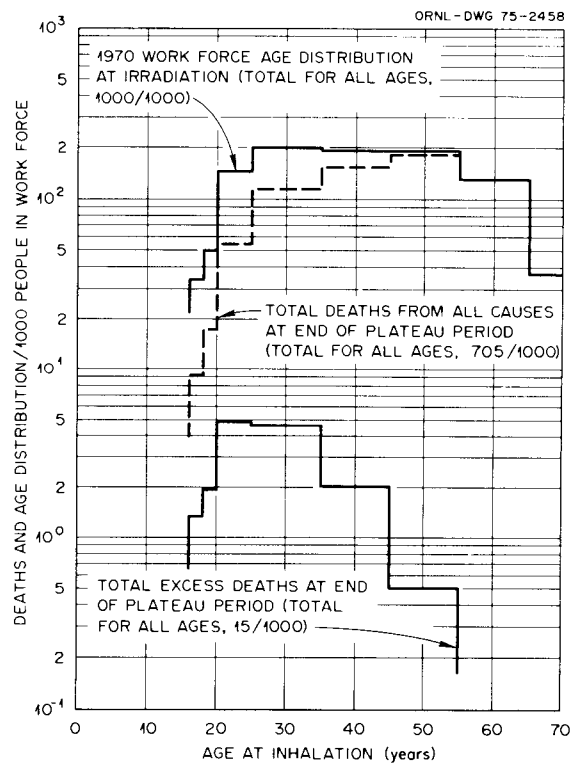

Fig. 2.23. Effects of ^{239}Pu inhalation on 1970 U.S. labor force. Adult male has 1 μCi deposited in lungs; others have same exposure time.

comparison with death rates from cigarette smoking.[42] Figure 2.25 presents the total death rate of cigarette-smoking males, nonsmoking males, and nonsmoking males with a ^{239}Pu lung burden.

The reportable incidents are all for members of the male work force employed at facilities where plutonium is routinely handled. This work force, which has the most opportunity for accidental inhalation, has had only a few members exposed, and these exposures have resulted in relatively small lung burdens.

42. U.S. Department of Health, Education, and Welfare, *Smoking and Health,* Public Health Service Publication No. 1103, report of the Advisory Committee to the Surgeon General of the Public Health Service, Washington, D.C., 1964.

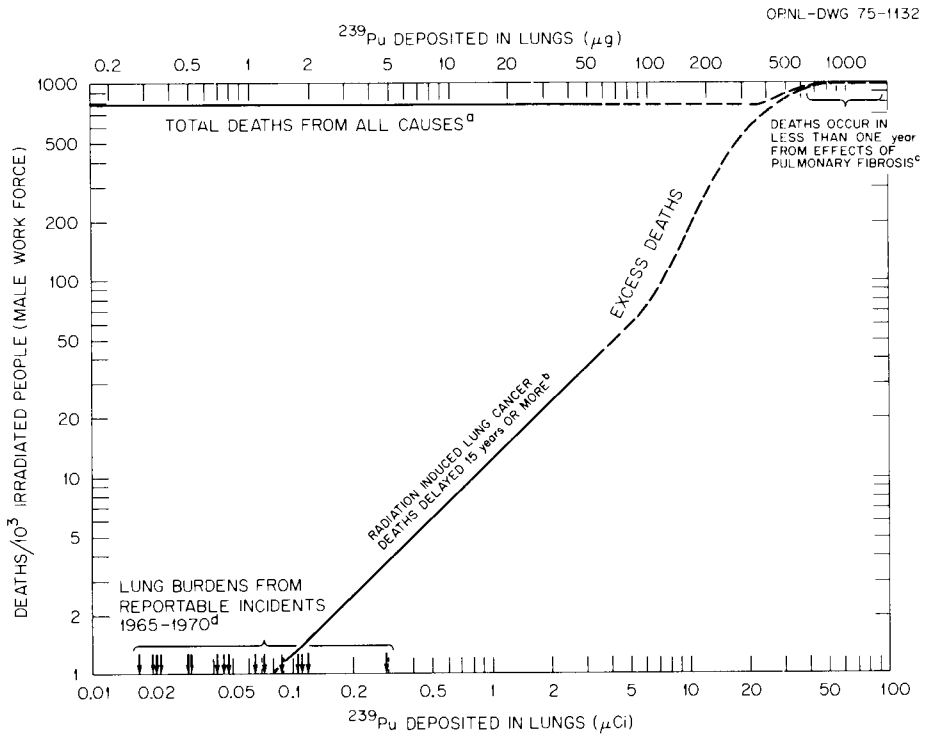

Fig. 2.24. Deaths in male work force, if irradiated, vs ^{239}Pu lung burden. (*a*) Total deaths from all causes include excess deaths from ^{239}Pu inhalation and deaths from all other causes during the time period in which the radiation-induced deaths occur. Deaths from all other causes were calculated from the 1970 male labor force and death rate statistics given in Table 71 and 328 in the *Statistical Abstract of the United States, 1971.* (*b*) Plutonium-239 inhalation results in a radiation dose to the lungs that produces an additional risk of lung cancer. Estimates are made of this risk in Appendix II.A.f. of the BEIR report using both animal and human exposure data. The graph solid curve was calculated using the absolute risk of 1.3×10^{-6} death per year per rem, a 15-year latent period, and a 30-year plateau. The total numbers of lung cancers induced in the male labor force by the end of the 30-year plateau are plotted. (c) Large lung burdens of $^{239}PuO_2$ ($\gtrsim$0.06 μCi per gram of lung tissue, 1 mg/man) cause death from the effects of pulmonary fibrosis, generally within a year. See, for example, W. J. Bair and D. H. Willard, "Plutonium Inhalation Studies IV," *Radiat. Res.* **16,** 811–21 (1962). The dashed section of the "excess deaths" curve is an estimated interpolation between the 15 or more years delayed and the one year or less causes of death. (*d*) Reportable incidents are defined and listed in WASH-1192. Both ^{238}Pu and ^{239}Pu curie lung burdens are plotted. Since the half-life of insoluble PuO_2 particles in the lungs is much less than the respective 3.3×10^4- and 8.9×10^6-day radiological half-lives, the 57-Mev and 53-Mev effective energies in the lung tissue lead to dose rates of 3.82 and 3.55 rems/μCi-day (20-year-old female, BEIR Table 6.7). Therefore the same curie lung burdens of the two isotopes should produce very nearly the same effects. For a given curie lung burden the weight lung burdens for the two isotopes are different (^{239}Pu, 15.8 μg/μCi; ^{238}Pu, 0.0578 mg/μCi).

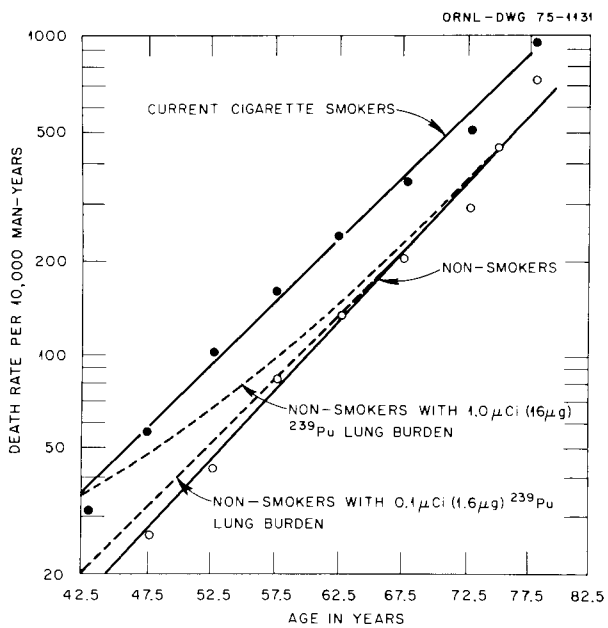

Fig. 2.25. Death rate (logarithmic scale) plotted against age. Prospective study of mortality in U.S. veterans. Adapted from Public Health Service Publication No. 1103.

ELECTROMAGNETIC PULSE EFFECTS ON NUCLEAR POWER PLANTS

P. R. Barnes R. W. Manweiler[1]

Introduction and Conclusions

Nuclear power plants are designed to minimize the probability of serious accidents which would damage the plant or endanger the community. Since the probability of a multiple failure involving two or more components is extremely small, protection is normally provided against a single-failure accident. This is accomplished by the use of redundant instrumentation and protection channels and safety-related equipment. However, the probability of a multiple failure due to the effects of nuclear electromagnetic pulse (EMP) has not been considered in the failure analysis. The probability of an EMP-caused multiple failure is not necessarily small, since all parts of the system are subjected to the failure mechanisms at the same time.

In this study[43] a preliminary analysis of the EMP effects on modern pressurized-water reactor (PWR) plants has been performed as a first step to determine if EMP is a serious problem for nuclear power plants. The Sequoyah plant near Chattanooga was used as a model of modern PWR plant. Two EMP threats were considered in the analysis, a single high-altitude EMP and multiple high-altitude EMP's. We found that the most likely consequence of EMP for PWR plants is an unscheduled shutdown. EMP may also prolong the shutdown period by the unnecessary activation of certain plant safety systems. It is also possible but not likely that numerous EMP's can temporarily interrupt the removal of the residual heat from the reactor.

High-Altitude EMP

High-altitude EMP is produced by a nuclear detonation at an altitude near or above 50 km. The gamma radiation from the nuclear burst interacts with the atmosphere to generate a Compton electron current. This Compton current is the source for the intense electromagnetic pulse. Due to the large area of the source current, high-altitude EMP can cover a large portion of the country which is completely free from the other nuclear weapon effects. Typical areas of coverage for a megaton-range weapon detonated at a height of burst of 100 and 400 km are shown in Fig. 2.26. As shown, most of the United States can be covered by a single exoatmospheric burst.

The short-duration EMP fields are very intense. The amplitude of the electric field pulse is on the order of 50 kV/m. The time history of an EMP is characterized by a very short rise time of about 10 nsec and an exponential-type decay with a time constant on the order of 200 nsec. A double exponential is often used to describe the EMP waveform. An example of a double-exponential EMP time history is shown in Fig.

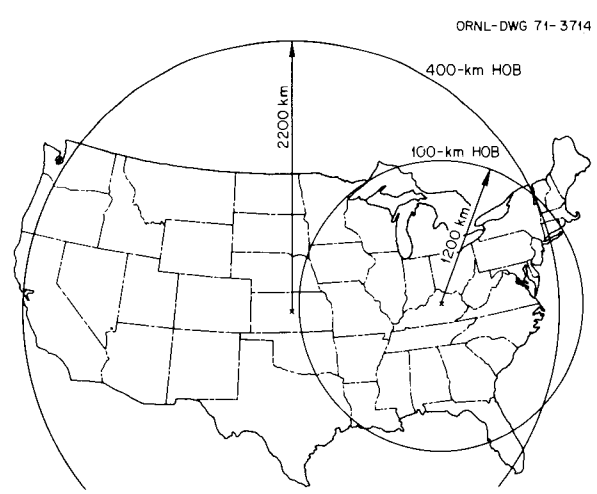

Fig. 2.26. Area of coverage of EMP from high-altitude detonations.

43. P. R. Barnes and R. W. Manweiler, *The Effects of Nuclear Electromagnetic Pulse (EMP) on Nuclear Power Plants*, ORNL-5029 (July 1975).

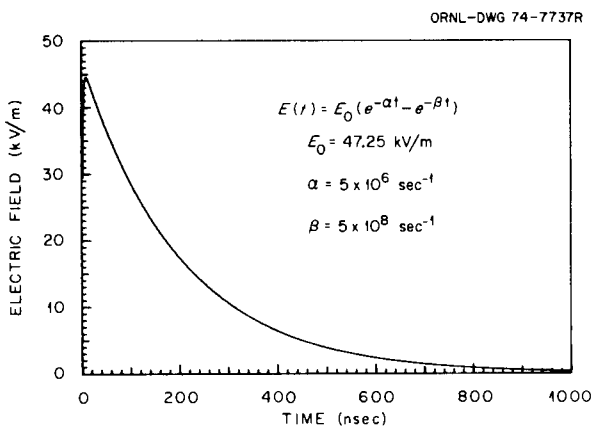

Fig. 2.27. Double-exponential EMP time history.

2.27. The fast rise time implies a wide excitation bandwidth, and the high intensity implies significant energy content in a broad range of the electromagnetic spectrum. A portion of this energy will couple to the many instrumentation, control, and power cables of nuclear power plants.

EMP-Induced Surges

Any conductor exposed to the EMP fields performs as an inadvertant antenna by receiving EMP energy. This results in electrical transients of magnitudes comparable with near-average lightning surges. The rise time of an EMP surge is generally much shorter than that of a lightning surge. For a long line with a length of hundreds of meters, the rise time is on the order of 100 nsec. For shorter lines the rise time is much shorter. Many solid-state components are especially vulnerable to these fast-rising EMP surges, due to the significant energy at high frequencies. The fast-rising surges also present special protection problems.

The instrumentation, control, protection, and power lines of nuclear power plants will have EMP surges induced in them. Most of these lines are shielded to some extent from the EMP by the plant building and cable runs. Some lines such as the instrumentation, control, and protection lines have additional shieldings provided by the conduit or cable trays and cable shields. The effects of shielding reduce and modify the EMP surges received by the cables. We found that the EMP shielding of the Sequoyah control building is at least 20 dB.

The off-site power lines have no appreciable shielding. The EMP surges induced on power lines have been considered in a previous report.[44] An example of an EMP voltage surge from line to ground on the off-site power source is shown in Fig. 2.28. The peak voltage of about 5 MV is induced after about 200 nsec. The waveform decreases to near 1 MV after 10 μsec.

The intrabuilding instrumentation, protection, control, monitoring, and power lines will be subjected to attenuated EMP fields. The nuclear instrumentation system (NIS) lines have a high degree of shielding to minimize electromagnetic noise interference. The total EMP shielding is at least 150 dB. This reduces the peak current of the EMP surge to the order of 0.2 mA. An example of the expected NIS EMP surge is shown in Fig. 2.29. Notice that the rise of the surge is much slower than that of the EMP waveform we have discussed. Also, the surge has a relatively long duration. These effects are the result of the shielding and cable length.

---

44. J. H. Marable, P. R. Barnes, and D. B. Nelson, *Power System EMP Protection,* ORNL-4958 (March 1975).

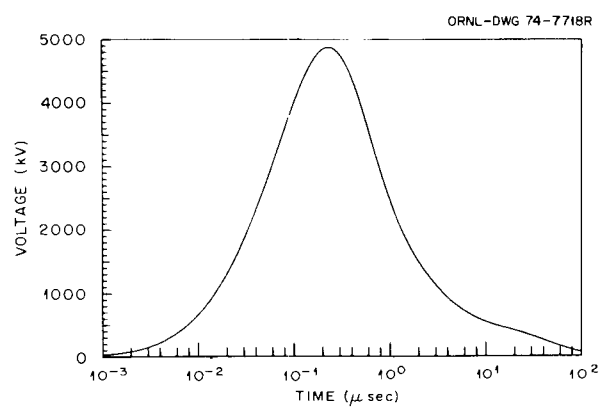

Fig. 2.28. EMP voltage surge on an infinite line 10 m above the earth.

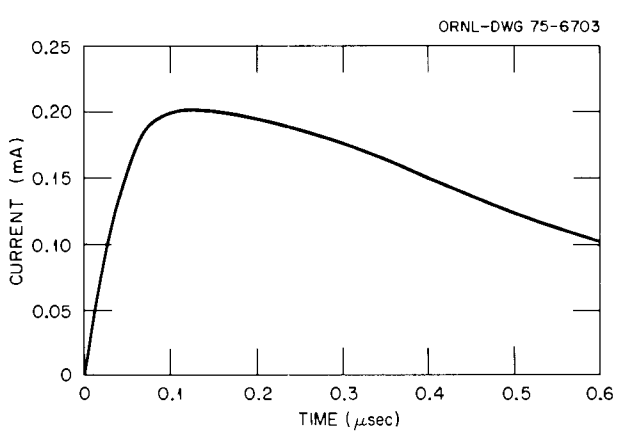

Fig. 2.29. EMP noise on the NIS sensor cable.

Shielded lines used for protection,[45] process variable instrumentation, control, and monitoring each have about the same level of shielding and will have EMP surges with peaks on the order of 200 mA. Intrabuilding power lines and unshielded protection and control lines will have EMP surges with peaks that range from 100 to 1000 A.

EMP Surge Effects

The EMP surges that will couple to the instrumentation sensor lines will not likely damage electronic components. They may activate trip circuits, however. EMP surges in the NIS lines could cause a "power-rate" trip in each of the four channels and scram (shut down) the reactor. Also, EMP surges may heat up the resistance temperature detectors and cause an "over-temperature" reactor scram.

The EMP surges coupled to the NIS output and power circuits will not likely be a problem to the NIS, since they are isolated by electrostatically shielded transformers. Such shielded transformers are not used with the process variable instrumentation power supplies, however, and solid-state components may be damaged by EMP power-line surges. If several of the power supplies were damaged and lost power, a reactor scram would likely result.

The reactor protection system logic trains are protected from transients on the input and output lines by the isolation afforded by their input and output relays. In addition, these logic circuits are also protected by surge suppression diodes and filters. The power supplies for the reactor protection system are not protected by electrostatically shielded transformers, and solid-state components may be damaged by EMP power-line surges. Such damage would likely scram the reactor. EMP surges in the plant electrical ground system may also cause the reactor protection to generate a scram signal, since it has a history of ground system noise problems.

EMP surges in the control lines may upset tne logic in the logic circuits of the reactor control system. If this should occur, special circuits in the reactor control system would detect the logical upset and stop all automatic control rod motion.

Multiple EMP's could result in a loss of electrical power. The EMP voltage surges in the preferred off-site power lines will have peaks on the order of a megavolt. These surges will occur on all of the lines throughout the power grid. Flashovers on these lines and in the switchyards will likely initiate breaker action to disconnect the off-site power from the plant. Also, the entire grid is likely to become unstable if subjected to multiple EMP's.[46] This would result in a blackout (loss) of off-site power.

EMP surges in the intrabuilding power circuits may trigger circuit breakers to disconnect large motors. Also, EMP-initiated flashovers near the main feeder circuits could cause a loss of emergency backup generator power by an "over-current" trip. If such a trip occurred twice at the Sequoyah plant, personnel would have to be sent to the generator building to reset the generators. The generator building is about 1200 ft from the control building.

EMP power-line surges may also cause a loss of emergency battery power used for instrumentation and control. These solid-state battery systems have a history of problems with lightning surges, even though they are protected by lightning arresters. The battery systems in the Sequoyah plant are not even protected against lightning, since it is unlikely that lightning surges could penetrate into the building.

Consequences and Countermeasures

In considering the consequences of EMP, we assume that the plant is operating at full power, the operator is unaware of EMP effects, and no special EMP protection has been provided for the plant. The most likely consequence of EMP is a reactor scram. This may occur from EMP surges in the instrumentation, protection, and control systems. A loss of off-site power due to multiple EMP's will also cause a scram. The operator may also cause a scram by responding to alarms falsely activated by EMP. A loss of power to the large motors by circuit breakers responding to EMP surges may also scram the reactor. The relatively large number of independent EMP events that can possibly cause a scram makes it a likely possibility.

The false activation of safety systems is another possible consequence of EMP. This can occur from EMP effects on the reactor protection system but is more likely to occur from the loss of power to large pump motors. This could cause a change in the reactor coolant pressure and initiate the safety injection system.

---

45. We have considered the instrumentation systems separately, even though they are normally considered as part of the reactor protection system.

46. R. W. Manweiler, *The Effects of Nuclear Electromagnetic Pulse on the Synchronous Stability of the Electric Power Transmission and Distribution Systems,* ORNL-4919 (in preparation).

The loss of instrument and control power due to numerous EMP surges is a remote but important possibility. If the plant is not properly prepared, such a loss could interrupt the removal of the residual heat from the reactor.

In considering EMP protection for nuclear power plants, it is important to ensure the safety of the public and the plant. It is not necessary to ensure the continued operation of the plant in an intense multiple EMP environment. To provide this kind of protection would be very difficult and costly.

The countermeasures we propose will greatly reduce the probability of serious damage to PWR plants without significantly increasing the cost of the plant. They are as follows:

1. All plants should be equipped with a nonelectrical auxiliary feedwater pump which can be operated without control power.
2. Plant operators should be informed about EMP effects.
3. If an EMP event is suspected, check out all important systems.
4. Install EMP surge protection on the emergency battery systems.
5. Employ shielded transformers whenever possible.
6. Use a separate ground for the reactor protection system.

These recommendations will also increase the protection of the plant against damage by lightning, switching, and electromagnetic interference transients as well as general failures in electrical and control power.

Part II. Assessment and Technology

D. G. Jacobs F. F. Haywood

3. Dosimetry Intercomparison Studies

K. Becker W. F. Fox
G. de P. Burke[1] T. F. Gesell[2]
H. W. Dickson F. F. Haywood
D. R. Ward[3]

For several years, this research section has conducted a very successful program in dosimetry standardization and intercomparison. The initial effort consisted of a program in nuclear safety whereby criticality monitors were tested for three different reactor spectra at the HPRR (Health Physics Research Reactor). In 1973 a small-scale intercomparison of environmental dosimetry systems was conducted as a part of our continuing program. This led, subsequently, to a more elaborate study (reported later) under more realistic conditions. In 1974 the regular dosimetry intercomparison program was expanded. An additional study was organized for the purpose of comparing the response of personnel monitors exposed to low levels of neutrons and gamma rays from the three standard radiation fields used for the routine program.

NUCLEAR ACCIDENT DOSIMETRY

The eleventh in the series of Nuclear Accident Dosimetry Intercomparisons was held during the period July 29 to August 9, 1974. A major effort has been to invite representatives from NRC licensees, as well as ERDA contractors. However, the number of participating licensees has been small to date. A list of participants and dosimetry results are given in Table 3.1.

In April, one representative from the section participated in the Fourth IAEA Dosimetry Intercomparison Study, which was held at the Harwell Training and Education Center, Harwell, England. Laboratories from the following countries were represented: Canada, Denmark, France, Germany, Hungary, India, Italy, Japan, Poland, United Kingdom, the United States, and Yugoslavia. The Harwell study was the final portion of the organized coordinated program in nuclear accident dosimetry. This program, which was patterned after that in the Health Physics Division, was designed to provide information useful to developing nations.

PERSONNEL MONITORING INTERCOMPARISON

An intercommunication of personnel monitoring dosimeters was conducted at the Dosimetry Applications Research Facility (DOSAR) during the period May 14–16, 1974. Ten independent laboratories and companies participated in an intercomparison of neutron and gamma-ray dosimeters used for routine personnel dosimetry. The dosimeters, which were sent through the mail, were exposed at the HPRR to the same three "standardized" radiation fields that have been used for the past several years for intercomparing nuclear accident dosimeters. In addition, a 14-MeV neutron field

1. ERDA, Health and Safety Laboratory, New York, New York.
2. School of Public Health, University of Texas, Houston, Texas.
3. Neutron Physics Division.

Table 3.1. Eleventh Nuclear Accident Dosimetry Intercomparison Study: summary of results

Group	Pulse 1		Pulse 2		Pulse 3		Pulse 4	
	D_n	D_γ	D_n	D_γ	D_n	D_γ	D_n	D_γ
				Tissue kerma (rads)				
BCL	77	66	430				110	16
Y-12 (1)	70	48.6	325	70			121	16
Y-12 (2)	74		308				137	
DOW	62.8	110	402	159	126	73.5		
ILL	49	46	410	57			161	13.4
SLA (1)	55	53	356	60	147	19		
SLA (2)	48		343		175			
K-25	62		347				115	16
ORNL	46.2	51	372	59	160	18	162	12.4
NOL	55.7	64.5	329	114	59.6	46.1		
Mean	60.0	62.7	362	86.6	133	39	134	14.8
Standard deviation	11.0	22.2	40.3	41.6	45.1	26	22.9	1.7
				Yield (number of fissions) $\times 10^{-16}$				
	7.1		9.3		9.9		9.7	

was used as a fourth exposure configuration, using a small Phillips neutron generator (sealed tube).

The reactor was operated in a steady-state mode at a power level of 1 W for a length of time necessary to produce an exposure to the dosimeters that would be in a dose range likely to be encountered in personnel monitoring. The neutron generator was operated in a similar manner to obtain a similar level of personnel dose. Since dose equivalents of a few hundred millirems are commonly encountered, this level was selected. In order to produce this condition, a free-air tissue kerma of approximately 40 millirads was selected for the neutron component; and the reactor operating time was calculated based on this value. The resultant reactor runs were performed as shown in Table 3.2.

All badges were placed on water-filled trunk portions of Bomab phantoms at 3 m in the case of the reactor exposures and at 1 m in the case of the 14-MeV exposure. When shields were used, they were placed at 2 m.

A summary of the results is presented in Table 3.3. It is reasonable to expect a more favorable agreement between the several participating laboratories if the results of experimental devices and nonroutine dosimeters are ignored or if a selective data-handling technique is used. For example, if the extreme data points are excluded, the resultant average dose-equivalent estimates are 385 ± 98, 444 ± 162, and 405 ± 64 millirems respectively. Also, if the upper and lower extremes are excluded from the 14-MeV results, the average neutron dose equivalent becomes 311 ± 107 millirems.

The results of the intercomparison show widely varying dose estimates having, for example, standard deviations of neutron dose equivalents ranging from 44 to 103%. This suggests that more effort should be expended on measurement techniques and dose conversion factors.

Table 3.2. Exposure parameters for personnel monitoring intercomparison

Run No.	Shield	Power (watts)	Time (min)	Fissions
1	Unshielded	1	5.0	9.25×10^{12}
2	Steel	1	13.9	2.57×10^{13}
3	Lucite	1	26.4	4.90×10^{13}

Table 3.3. Summary of results

Exposure condition	Neutron dose equivalent (millirems)	Gamma dose equivalent (millirems)
Bare reactor	438 ± 193[a]	24.6 ± 4.6[a]
Steel-shielded reactor	540 ± 345	18.4 ± 4.3
Lucite-shielded reactor	662 ± 679	74.5 ± 13.9
14 MeV	515 ± 486	365 ± 159

[a]One standard deviation.

INTERNATIONAL INTERCOMPARISON OF ENVIRONMENTAL DOSIMETERS UNDER FIELD AND LABORATORY CONDITIONS[4]

One of the prime purposes of time-integrated measurements of external environmental radiation is the estimation of population exposures, particularly in areas with abnormal radiation levels and in the environs of nuclear facilities. With the increasing concern about the possible effects of very low radiation levels, this subject attracts more attention. The first step of an environmental monitoring program is usually the measurement of local exposure levels with a network of stations that are situated outdoors about 1 m aboveground. A network is needed because the time-averaged environmental gamma-radiation level varies substantially from one location to another, mostly due to differences in the concentration of naturally radioactive nuclides in the upper layer of the soil.

In 1972 and 1973, evidence was accumulating that the results of various laboratories, undertaking measurements with different detectors at the same location, did not always agree within the assumed accuracy of the detectors. In a pilot intercomparison study at ORNL in 1973, for example, the detectors of five groups from three countries were exposed simultaneously to the same background radiation; but the findings varied substantially. Therefore, during a USAEC Workshop Environmental Radiation in New York early in 1974, an ad hoc committee was formed to carry out a more comprehensive and systematic intercomparison.

Fifty-six sets of six detectors each from 41 laboratories representing 11 countries were mailed to and from Houston, Texas, where the detectors were exposed for three months (July to September 1974) as follows: two in an unprotected space out-of-doors 1 m aboveground; two in an air-conditioned shielded area with a known, low exposure rate; and two as the second group, but with an additional exposure of 30 mR. Evaluation of the dosimeters provided information on the calibration accuracy, the accuracy of field measurement, and transit exposure.

A graphical presentation of the distribution of the results of all dosimeters exposed to 30 mR in the laboratory is given in Fig. 3.1. Fifty-nine percent of the detectors fell within ±10%, 80% within ±20%, and 89% within ±30% of the expected value. In Fig. 3.2, which represents the field measurements, the two sets of photographic films and one TSEE set are not included because these detectors did not provide any data. The average of the readings of the TLD's (16.2 mR) agrees within 0.9% with the ionization chamber reading. Of all the TLD's, 34% fell within ±10% of the accuracy, 74% within ±20%, and 85% within ±30%. The standard deviation of all the field exposures (±26%) was significantly higher than that of the laboratory exposures (±16%), probably because of the harsher climatic conditions and lower exposure levels involved.

It can be seen in Fig. 3.3 that the correlation between transit exposure and round-trip distance is very poor. Obviously, in many cases, only a fraction of the transit exposure can be attributed to the increased cosmic radiation exposure in high-flying aircraft (assuming travel by the shortest route). At least in the cases of some unusually high values, the detectors apparently received additional radiation from some other source,

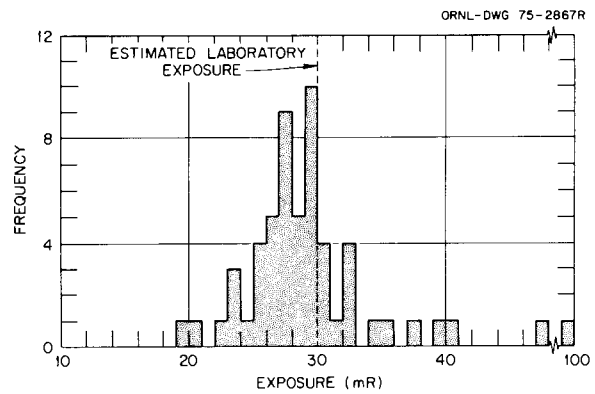

Fig. 3.1. Frequency distribution of the exposures measured with all detectors in the laboratory tests.

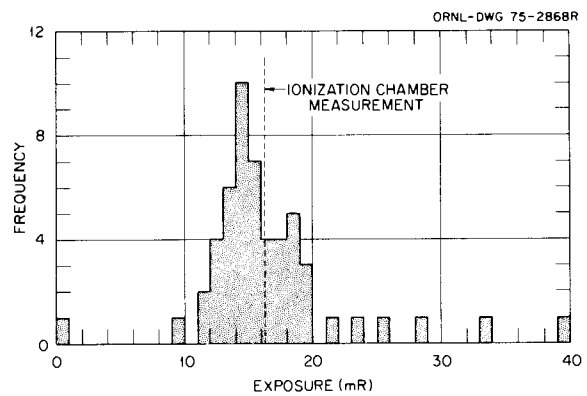

Fig. 3.2. Frequency distribution of the exposures measured with the thermoluminescence dosimeters (excluding films and TSEE).

4. For details, see T. F. Gesell, G. de P. Burke, and K. Becker, ORNL-TM-4487, 1975.

such as transport or storage, together with radioisotope shipments. The exposures received while flying the estimated round-trip distances at 55° geomagnetic latitude during solar minimum, at a speed of 885 km/hr and at three different altitudes, are indicated by the solid lines in Fig. 3.3.

There was also no significant difference in the relative performance of LiF:mG,Ti; $CaSO_4$:Dy,Tm; and CaF_2:Mn; but CaF_2:Dy exhibited a larger standard deviation than the others, probably due to the difficulties associated with its pronounced low-temperature glow peak. Although the overall results of this intercomparison were reasonably good, it is evident that some participants must substantially improve their procedures and/or calibration techniques before they will be able to produce sufficiently reliable results. (A few participants over- or underestimated both laboratory and field exposures by as much as 15 to 20 mR.) Further intercomparisons of this type are anticipated. It can be hoped that this experiment and possible future intercomparisons will have a beneficial effect on the state-of-the-art in this field.

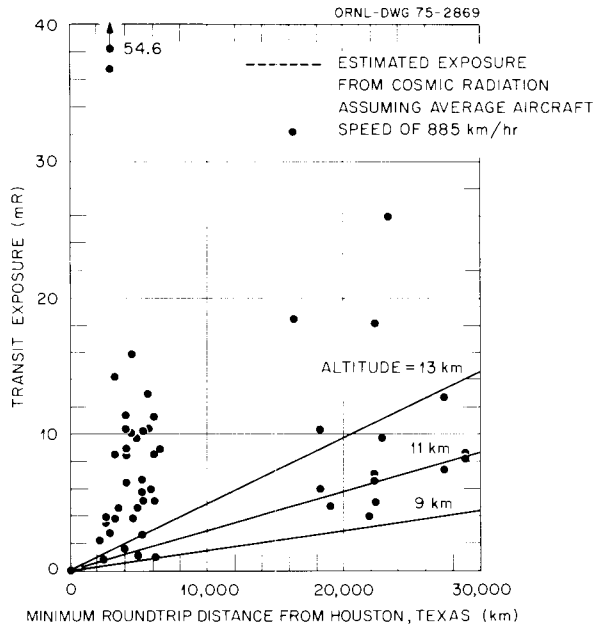

Fig. 3.3. Transit exposures of detectors mailed to and from testing area.

4. Health Physics Research Reactor and Accelerator Operations

D. R. Ward[1]
F. F. Haywood
L. B. Holland[1]
H. W. Dickson J. E. Jackson
W. F. Fox C. P. Littleton[2]

The principal research tool for the Dosimetry Applications Research Facility (DOSAR) is the Health Physics Reactor (HPRR). This reactor is an unshielded and unmoderated assembly that provides mixed neutron and gamma-ray fields over a wide range. It is a powerful tool for research in dosimetry, radiobiology, and other radiation-effects studies requiring coexistent neutrons and gamma rays. Frequently, monoenergetic neutrons, photons, and charged particles are required for experiments in dosimetry and radiobiology. These needs are filled through the use of a low-energy positive-ion accelerator (DLEA).

For over ten years, the HPRR has been used for testing and standardizing activities on a national and international scale. In this respect, many items such as criticality alarm systems, nuclear accident dosimeters, and numerous other passive dosimetry systems related directly to radiobiology research and dosimetry intercomparisons, have been irradiated. Biological systems that are typically irradiated include plants, seeds, mice, rats, cells in culture, small animal organs, etc. Some important continuing radiobiology experiments that have been reported earlier include the relative biological effectiveness (RBE) for intestinal crypt cell survival under differing conditions, grain plant mutant studies, incidence of neutron-induced tumors in rats, lens opacity studies, early embryo death in mice, and studies of the effect of neutrons on flowering plants and food crops.

Use of the HPRR for training purposes continues. For the fourth year, a class from the University of Tennessee, Nuclear Engineering Department, conducted a comprehensive series of experiments designed to study the kinetic behavior of a fast reactor. Also, the HPRR is used for studies associated with the Health Physics Division's Summer Faculty Institute in Applied Health Physics. The principal users of the HPRR are given in Table 4.1.

A report is being prepared (ORNL-TM-4898) which describes a system for monitoring the HPRR core with respect to its full complement of uranium. During the first reactor startup of each operating day, readings are taken of control rod positions, core temperature, core height, and reactor power. By comparing this information with data taken earlier under controlled conditions, the operator can confirm that the full core fuel loading is still present. This "running check" is made while the reactor is being taken to the power level required by the experimental program, and there is no requirement for the reactor to be operated at zero

1. Neutron Physics Division.
2. Instrumentation and Controls Division.

Table 4.1. Principal users of the HPRR

User group	Percent of total time	
	1973	1974
Radiation Research and Development	48.1	22.4
Biology Division	20.0	22.2
UT–Nuclear Engineering	9.6	18
University of Louisville	7.1	8.9
Comparative Animal Research Laboratory	6.7	6.3
Civil Aeromedical Institute	2.8	4.7
Dosimetry Intercomparisons	1.6	7.7
Others	4.1	9.8

power for the specific purpose of checking the fuel loading.

A more accurate check is made every three months or whenever the running check needs reinforcement. The more accurate check is made under controlled conditions and with the pulse rod and regulating rod at their limits of travel.

Both types of checks have been demonstrated to be sensitive enough to detect the absence of the smallest piece of easily removable HPRR core fuel, which weighs 112 g.

This safeguards activity is considered adequate for this reactor, but it is still in the proposal stage and has not been accepted formally by laboratory management.

5. Dosimetric Applications of Particle-Track Etching

Klaus Becker J. S. Jun[1] M. Abdel-Razek[2]

SPARK COUNTING OF PARTICLE TRACKS IN MICA

The simple automatic counting of fission-fragment, alpha-particle, and recoil-nuclei tracks in thin (~ 5 to 20 μm) foils of organic polymers, such as polycarbonates or cellulose nitrate, by an electrical discharge method commonly called "spark counting" is widely used today for neutron dosimetry, the quantitative determination of trace quantities of alpha emitters, fissile elements, etc. Organic foils have a relatively high sensitivity, not only to charged particles [depending on the polymer and its treatment, particles with a linear energy transfer (LET) exceeding 1–4 MeV-cm^2/mg can be recorded], but also to chemically damaging agents such as uv light and a large variety of chemicals. Due to their low melting point, rapid fading of latent tracks prior to etching takes place at temperatures higher than 50 to 100°C. Temperatures above ~ 150°C permanently destroys most foils.

Inorganic detectors, on the other hand, have a much higher de facto threshold for particle detection of approximately 15 MeV-cm^2/mg and often are chemically and thermally much more resistant. It has been shown that the track density in one organic material, mica, can also be determined by conventional spark-counting techniques.[3] Several mica types were found to be suitable, but for the more detailed investigations, a type of natural muscovite called "Ruby Angolan Mica"[4] was selected. This material cleaves easily into large thin sheets of uniform thickness and has, therefore, been widely used as a counter window in pre-Mylar days.

Although in this study fission fragments from thin sources of natural uranium, ^{252}Cf, and ^{239}Pu have been used, other particles of sufficient LET and energy could also be counted by this method. There is an optimum mica thickness for such experiments. If the mica layer is too thick, some fission fragments will not fully penetrate the layer. Surface etch pits will result instead of sparkable perforations. If the mica layer is too thin, it becomes extremely fragile during etching and easily breaks during transfer to and from the spark counter. It was found that a weight of about 2 to 3 mg/cm^2, corresponding to a thickness of about 7 to 14 μm, gives the most satisfactory results.

Muscovite mica is chemically very inert, but treatment for about 6 to 7 hr in concentrated (~48%) HF at 22°C, or about 3 hr at 40°C, produces fairly large (~10 μm) rhombic perforations that can be sparked with a good efficiency at about 440 to 540 V Fig. 5.1). As can be seen in Fig. 5.2, the exact shape of the sparking "plateau" depends somewhat on the etching time, but repeated sparking of the same sample does not result in increases of the spark count. Unlike organic foils, no "presparking" at an increased voltage is required for cleaning out the insufficiently etched perforations. Sparking above 600 to 700 V tends to produce multiple sparkings ("burns") and microscopic evidence of beginning damage to the mica. Under optimized conditions, sparking permits an essentially 100% counting efficiency; and even etch pits spaced closer than the diameter of the evaporated Al layer are counted separately. If the etch-pit density becomes too high, however, exhaustion of the metal supply on the aluminized Mylar electrode leads to electrically insulated "islands"; and the counting efficiency begins to drop, as is the case with organic foils (Fig. 5.3).

The etch-pit "background" in unexposed and unheated samples (mostly due to spontaneous fission of

1. IAEA Fellow, on leave from KAERI, Seoul, Korea.
2. Physics Department, University of Tennessee, on leave from Atomic Energy Establishment, Cairo, Egypt.
3. K. Becker, *Nucl. Instr. Meth.*, in press.
4. Asheville Schoonmaker Mica Co., 900 Jefferson Avenue, Newport News, Va.

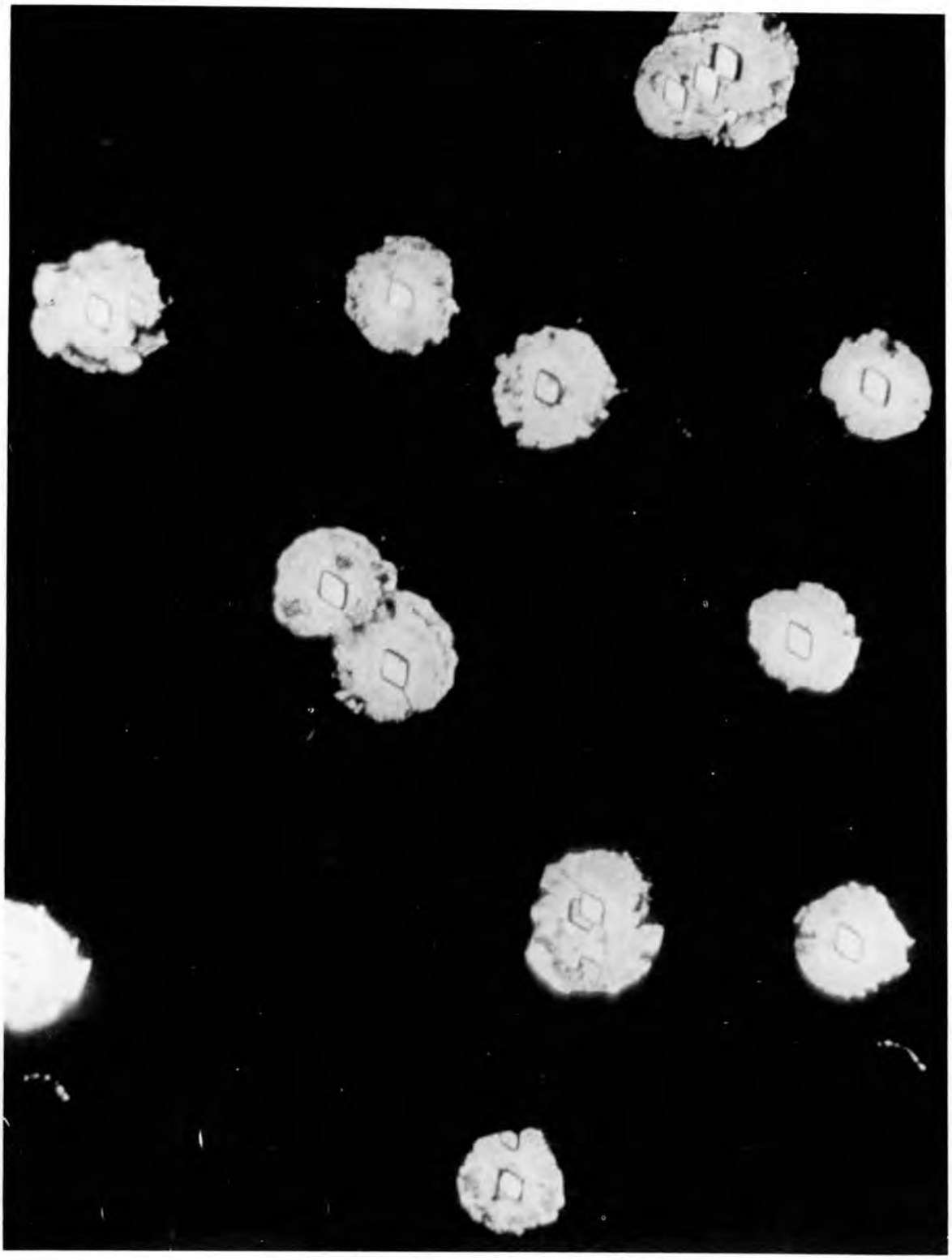

Fig. 5.1. Halos produced by evaporation of the very thin metal layer on aluminized Mylar by electrical discharges (sparks) through the rhombic perforations at fission fragment impact locations in mica.

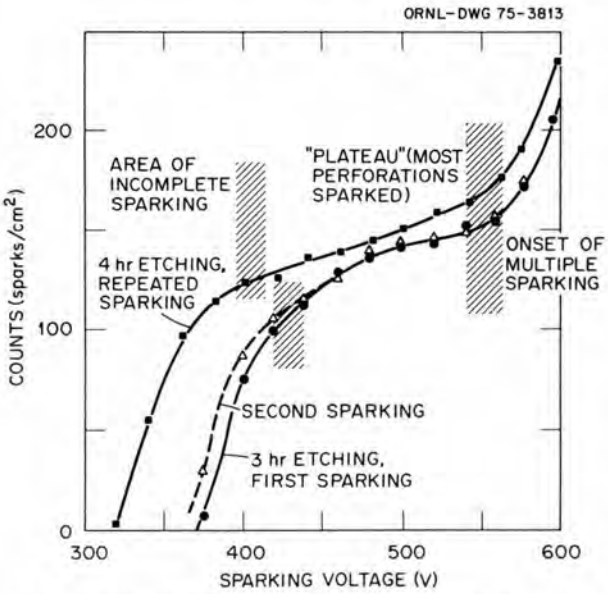

Fig. 5.2. Spark count as a function of sparking voltage in 1 cm^2 (electrode diameter) muscovite mica ~7.1 μm thick (2.0 mg/cm^2), preannealed for 100 min at 800°C, then exposed in contact with 40 nCi of ^{239}Pu to about 5×10^{13} fast fission neutrons per square centimeter and etched for different times in concentrated hydrofluoric acid at 40°C.

constituent natural uranium) is fairly high, about 8.4 etch pits/mm^2. A pre-etching thermal treatment of 20 hr at 500°C was insufficient to anneal these latent tracks. A 20-hr heating to 1000°C, on the other hand, damaged the mica substantially. A standard pre-exposure annealing for ~100 min. at about 750 to 800°C was adopted for routine applications, such as neutron-induced autoradiography (NIAR) of fissile elements.[5] The natural uranium content of the mica, although higher than in polymers, did not disturb experiments employing fast neutron fluences as high as ~10^{14} neutrons/cm^2. A "background" of only a few sparks per square centimeter was thus induced, permitting the detection of small amounts of fissile materials by NIAR with fast neutrons (Fig. 5.4).

The method for integrating measurement of very low fluences of high-LET particles described here offers advantages in studies involving mica itself, for example, in dating or in determining its uranium content and/or distribution. This method can also be employed in heavy-charged-particle detection or neutron dosimetry work at high temperatures (up to about 500 to 700°C)

5. K. Becker and D. R. Johnson, *Science* **167**, 1370 (1970).

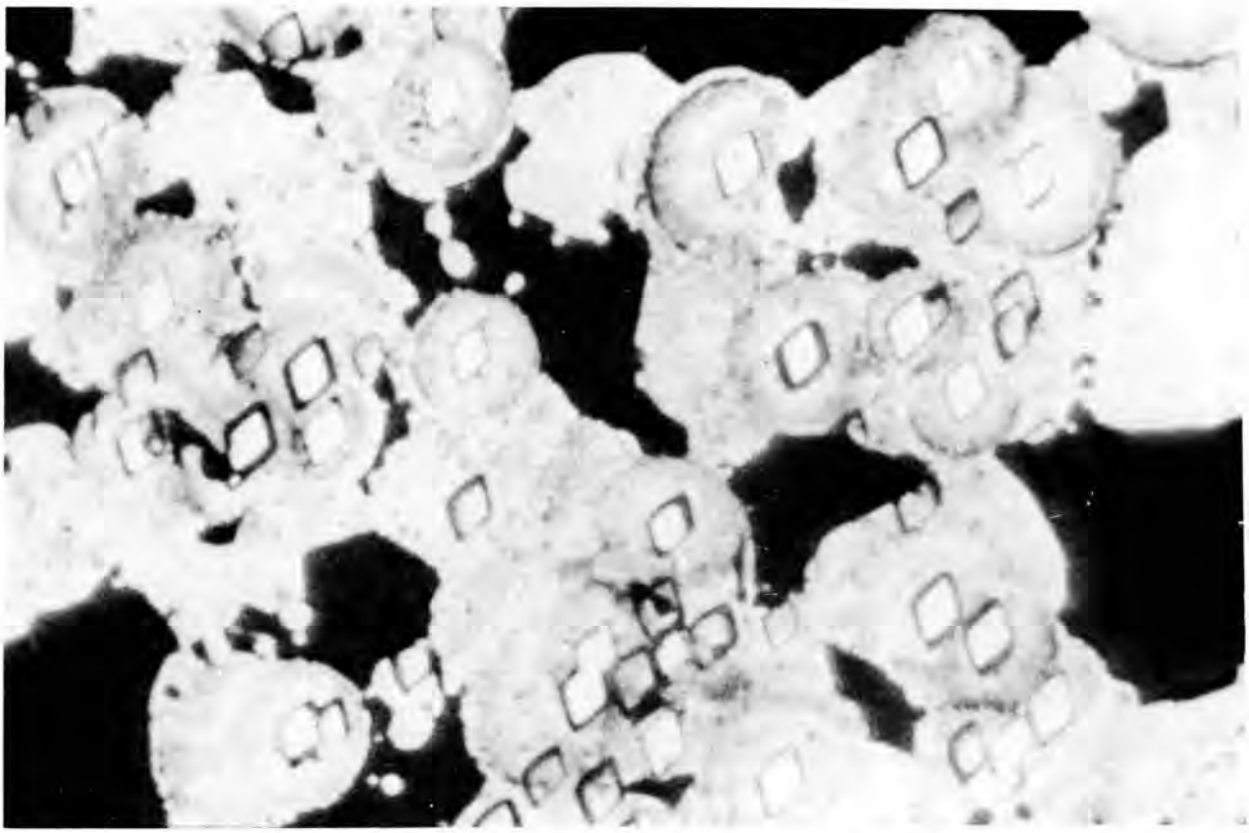

Fig. 5.3. Incomplete spark counting of perforations at high perforation densities due to the exhaustion of aluminum and electrical insulation of unsparked islands.

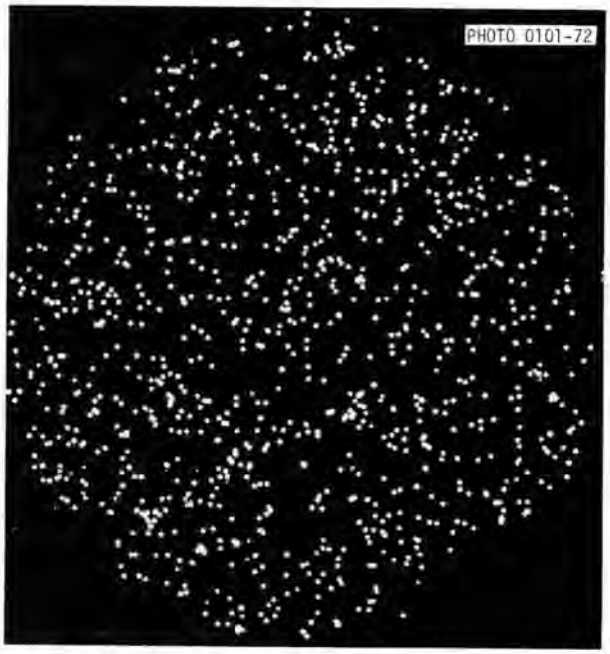

Fig. 5.4. Neutron-induced autoradiograph (NIAR) of ~40 nCi of ^{239}Pu, electroplated as a spot 6 mm in diameter on a metal carrier, after exposure to 5×10^{14} fission neutrons.

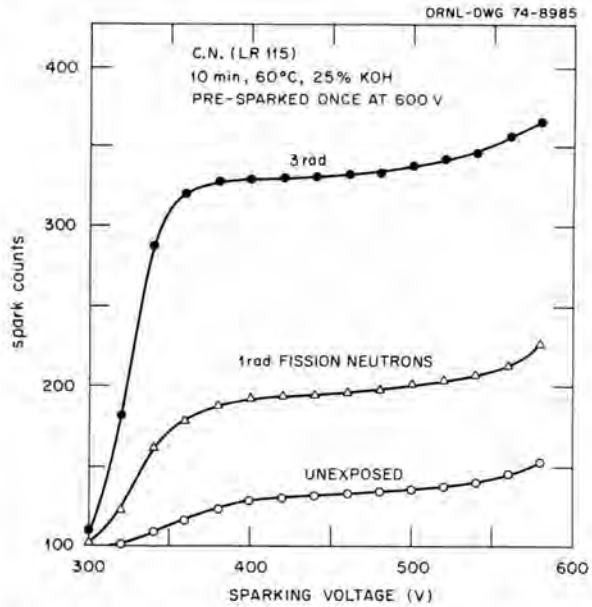

Fig. 5.5. Neutron-induced recoil-particle-track spark counts as a function of sparking voltage for the LR 115 cellulose nitrate foil etched for 10 min at 60°C in 25% KOH, presparked once at 600 V.

or in the presence of a large number of reactive chemicals or physical agents, such as intense uv light, which would badly damage or destroy organic detectors. More importantly, it permits discrimination against low-LET particles, for example, the induced recoil particles in fast-neuton NIAR. Such recoil-particle tracks have been shown in previous studies with organic foils to yield sparkable tracks, as well as changes in the foils' etching properties, thus interfering with the detection of low fission-fragment densities after exposure to a fast-neutron fluence. One application, namely the selective detection of trace amounts of ^{239}Pu in the presence of natural uranium, is of particular interest and will be studied further. Obviously, other methods for automatic perforation counting in thin organic foils based on the penetration of uv light, alpha particles, electrons, dyestuffs, chemicals, etc. or on the detection of changes in the electrical conductivity can also be applied in the case of mica and may, in some cases, have advantages over spark counting.

SPARK COUNTING OF NEUTRON-INDUCED RECOIL-PARTICLE TRACKS

This study, which has already been described in part in last year's Annual Report, was completed in 1974.[6] In particular, optimum conditions for etching and sparking have been established for a number of foils. As an example, the results obtained with an 8-μm commercial cellulose nitrate foil (Kodak Pathé LR 115, strippable) with fission neutrons are given in Fig. 5.5. In another experiment, foils have been exposed with monoenergetic neutrons of different energies at Brookhaven National Laboratory (Fig. 5.6). There is a strong energy dependence of sensitivity and an effective registration threshold around 2 MeV, which restricts the practical usability of this method for routine fast-neutron monitoring. Also, the reproducibility of recoil-particle-track etching did not exceed 10% due to small fluctuations in foil thickness and/or sensitivity or to variations in the etching conditions. Etching and evaluation of "controls" with every batch helped to reduce this problem.

TRANSFER DOSIMETERS FOR FAST-NEUTRON SOURCES[7]

Work on this subject under a Research Agreement with IAEA continued in 1974. Concerning the repro-

6. K. Becker and M. Abdel-Razek, *Nucl. Instr. Meth.* **124**, 557 (1975).

7. K. Becker and J. S. Jun, *Phys. Med. Biol.*, in press.

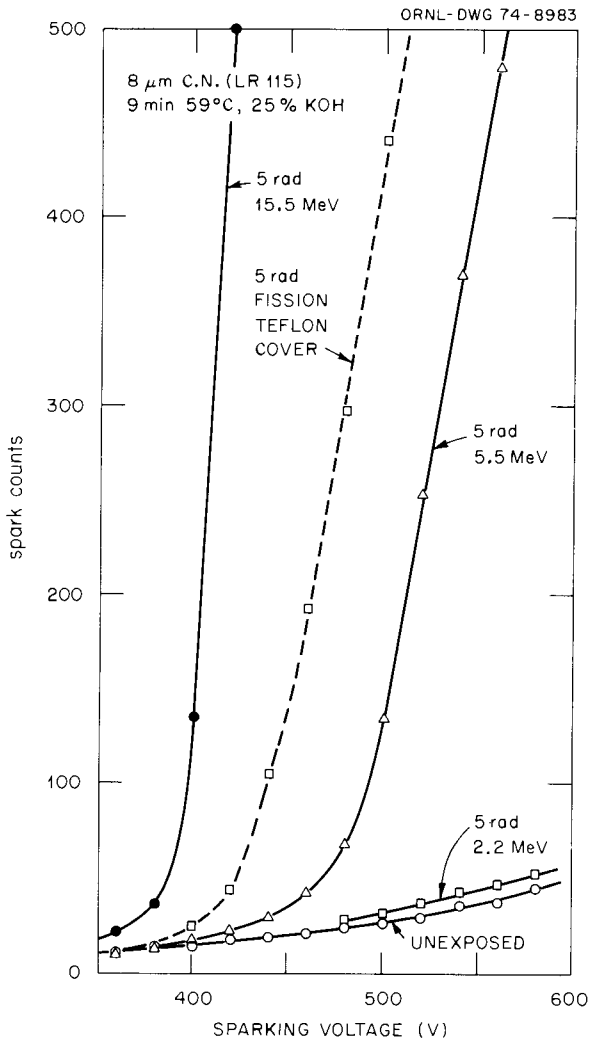

Fig. 5.6. Neutron energy dependence of response in cellulose nitrate for first sparking.

ducibility of spark counting, one has to distinguish between three levels of reproducibility:

1. repeated spark counting of the same foil can be done with a reproducibility as high as ±1 to 2 sparks;
2. for the reproducibilities in the counting of a series of foils that have been exposed and etched under identical conditions, in-set standard deviations of 2 to 4% can be obtained under carefully controlled conditions;
3. the long-term set-to-set reproducibilities depend strongly on the constancy of etching and sparking conditions, the batch-to-batch consistency, and history of the foils, etc. It may be difficult to obtain reliably a reproducibility of $< 5\%$.

The independent visual counting of the foils by two persons gives results that also agree well within ± 5%. As visual counting is equally fast and does not require a spark counter and constant etching conditions, this method may actually be preferable for the high track densities encountered in transfer dosimetry. In other experiments involving higher neutron energies, it has been found, however, that the agreement between different observers was not as satisfactory. The main reason is the increasing average radius and number of the recoil-particle tracks. Overlapping size distributions introduce some ambiguity into the visual counting procedure. One method to reduce the size distribution of the fission-fragment etch pits consists of placing a "collimator" spacer plate with cylindrical holes between the radiator and detector foil. In combination with glass detectors, which do not register recoil-particle tracks, well-defined etch pits of rather uniform size are thus obtained which are easy to count at a low magnification.

6. Exoelectron and Thermoluminescence Dosimetry with BeO

K. Becker L. Huskey[2]
J. S. Cheka[1] G. D. Kerr
K. Crase[1] J. S. Jun[3]
R. B. Gammage

OBJECTIVES

Beryllium oxide is one of the most potentially useful materials, in the tissue-equivalent range, as a solid-state integrating dosimeter. We seek to exploit its use both as a thermally stimulated exoelectron (TSEE) and as a thermoluminescent dosimeter (TLD), particularly in situations where other types of integrating dosimeters are nonexistent or inadequate. This material also exhibits unique characteristics in its response to nonionizing radiation.

LIGHT RESPONSE AND RADIATION SENSITIZATION OF BeO

Further experiments have been carried out concerning the previously observed response of TSEE detectors based on ceramic BeO (Thermalox 995) to uv light, which was found to depend on the irradiation history of the sample. This effect is obviously of interest for at least two reasons, namely, the potential use of such detectors for uv dosimetry and the "spurious" signals it can cause in radiation dosimetry.

A sensitization treatment has been developed which consists essentially of exposure of the detectors to a high gamma-radiation dose (about 10^3 to 10^6 rads), followed by a temperature treatment sufficient for the complete annealing of the dosimetry traps but insufficient to anneal the very deep trapping levels, for example, 1 hr at 500 to 600°C. The sensitization thus obtained for gamma radiation amounts to a factor of about 7. Because the background signal is also increased, the practical value of the sensitization for radiation dosimetry is limited.

The sensitivity to visible light and uv, however, is increased several hundred times (values up to 750 were measured). The wavelength dependence of the sensitization depends on the preirradiation level, as well as on the temperature treatment. With an optimized combination of both, detectors can be made sensitive enough to respond even to a few minutes of exposure to red darkroom illumination. Very few simple image storage systems are known to respond to red light. Also, the effect leaves room for basic studies concerning the underlying machanism, which is probably an optically stimulated electron transfer from a high-temperature trapping level to the "dosimetry peak" at ~300°C.

BANK OF STANDARDIZED BeO CERAMIC DOSIMETERS

The calibration work for the TSEE of a batch of 500 BeO disks, with identical histories of preparation, sensitization, and stabilization, has expanded to TLD. A single detector exposed to 20 mR ^{60}Co has a constant response within a standard deviation of (σ) of ±4% when reading the TL or the TSEE. The intragroup σ value in the mean TL or TSEE response of a large batch of detectors is about ±15%.

Detectors have been distributed to 27 groups in 14 countries. The purposes are to allow interlaboratory comparison of readers, to gauge the practical applica-

1. Consultant.
2. ORAU undergraduate research trainee, Defiance College, Ohio.
3. IAEA Fellow, on leave from KAERI, Seoul, Korea.

tions in a more logical manner, and to bring better order into the diverse, basic researches. The aim is to accumulate the findings and communicate them to all the participants.

HYDRATION EFFECTS AND THE PERFORMANCE OF EXOELECTRON DOSIMETERS IN THE FIELD

Thin-layer elements and high-sensitivity BeO:Li are used by Brown[4] and Boros,[5] respectively, for measuring depth dose distribution, dose across interfaces of bone–tissue, and radiation leakage from teletherapy units at the μR level. While the stability and reliability of these unique dosimeters can now be controlled under laboratory conditions, by these workers and ourselves, the reverse is sometimes the case under field conditions. When exposed to the elements, hydration of the surface is the root problem. From the fading characteristics of BeO:Si, shown in Fig. 6.1., one expects favorable performance, provided liquid water does not form on the surface. Below the dewpoint, or in a frost, conditions are favorable for wetting to occur. The result is excessive fading and often a change in detector sensitivity. The latter problem is correctable by a washing and annealing treatment.

This untoward behavior explains the failure of unprotected dosimeters in long-term field tests on the Gulf Coast and in Oak Ridge during the humid summer months. For satisfactory use, the detectors must be protected from "misting" or "frosting over" or must be used in controlled environments.

The sensitivity and the structure of the glow curve change with the state of hydration, as illustrated in Fig. 6.2. An increase in drying temperature increases the exoelectron output and modifies the peak shape, particularly at the leading edge. (The initial preparation of the ceramic BeO involves sensitization at ~1300°C followed by immersion in water; the final step is to dry the detector.) Problems occur with the use of very high drying temperatures to enhance the sensitivity; the scatter in the sensitivities of a batch of detectors is increased and longer times are required for equilibration with atmospheric moisture. After a drying at 800°C, for example, the TSEE sensitivity has two components – one stable and the other decaying exponentially with a half-life of about 20 min.

Our experiences have led to the following recipe of drying and annealing treatments in the production of high-sensitivity, stable BeO:Si dosimeters. Drying is affected at 500 or 600°C for 1 hr. Subsequent annealings, when required, are at 350 to 400°C for 5 min. Residual signals disappear rapidly at these temperatures. (At 350°C, the time needed for complete

4. L. D. Brown, *Proc. 4th Int. Conf. Lumin. Dosimetry* **2**, 551 (1974).
5. L. Boros, ibid., **2**, 769 (1974).

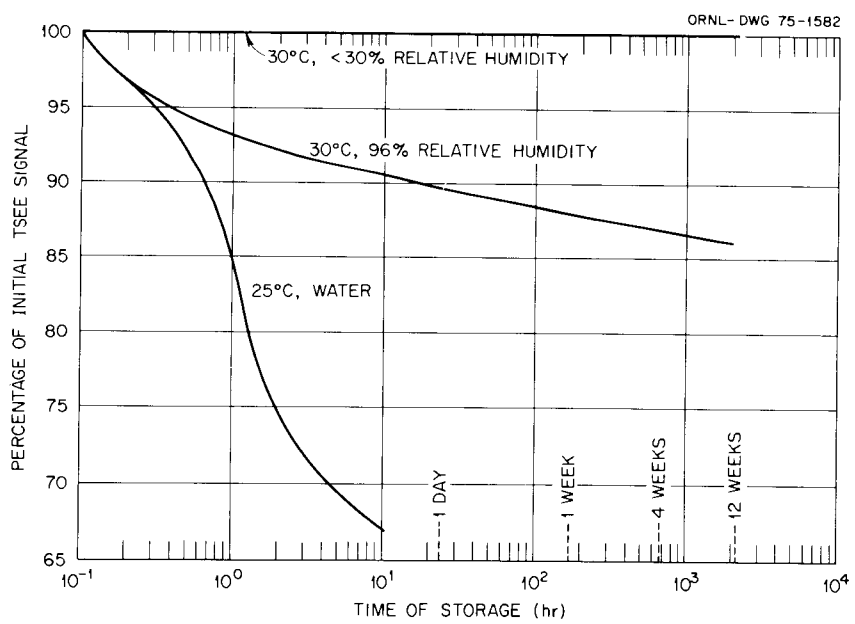

Fig. 6.1. Fading of the TSEE signal from irradiated BeO dosimeters of Thermalox 995 as a function of storage conditions.

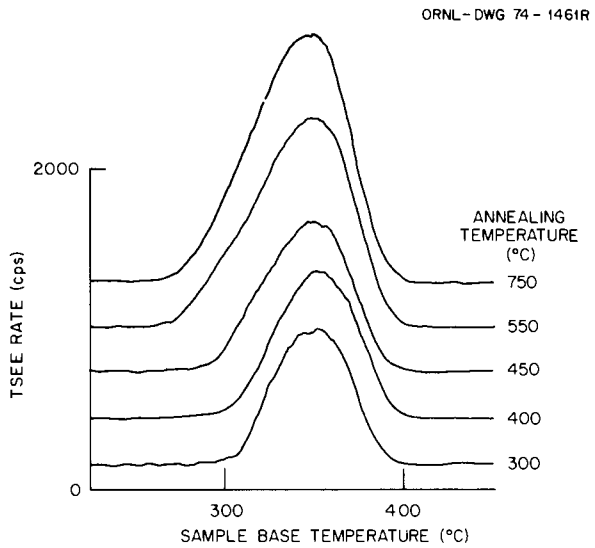

Fig. 6.2. TSEE emission curves from a surface-hydrated BeO ceramic detector (Thermalox 995) as a function of the drying temperature.

annealing is 5 min.) Neither the annealing temperature nor the maximum temperature achieved during reading should exceed the drying temperature; otherwise, the sensitivity will be permanently altered.

TL DOSIMETRY

Several types of commercially available ceramic BeO have been evaluated for thermoluminescence and combined TL–TSEE. The ceramic Thermalox 995 is superior in nearly all respects and is the only one with well-separated, clearly resolvable TL and TSEE glow peaks. A thin surface region, which is rich in impurities, suppresses spurious emissions of both light and exoelectrons. Without its stabilizing influence, separate or combined TL and TSEE measurements cannot be made.

The characteristics important for TLD are as follows: (1) the luminescence is maximum at 260 nm for each type of ceramic (Fig. 6.3); (2) with a reader having an S-13, uv-sensitive photomultiplier tube, the lower practical exposure limit is 1 mR, with supralinearity starting at 10R; (3) only 10% fading after three months at 30°C and 90% relative humidity (Fig. 6.4), but rapid bleaching of 50% in 30 min. in laboratory fluorescent lighting (Fig. 6.5); and (4) an energy dependence of response similar to that of LiF TLD (Fig. 6.6).

A photon counting system is being mounted into a TSEE reader that is operating as a proportional counter. This will reduce further the lower limit of TL sensitivity and will facilitate the ease with which combined TL–TSEE measurements are made.

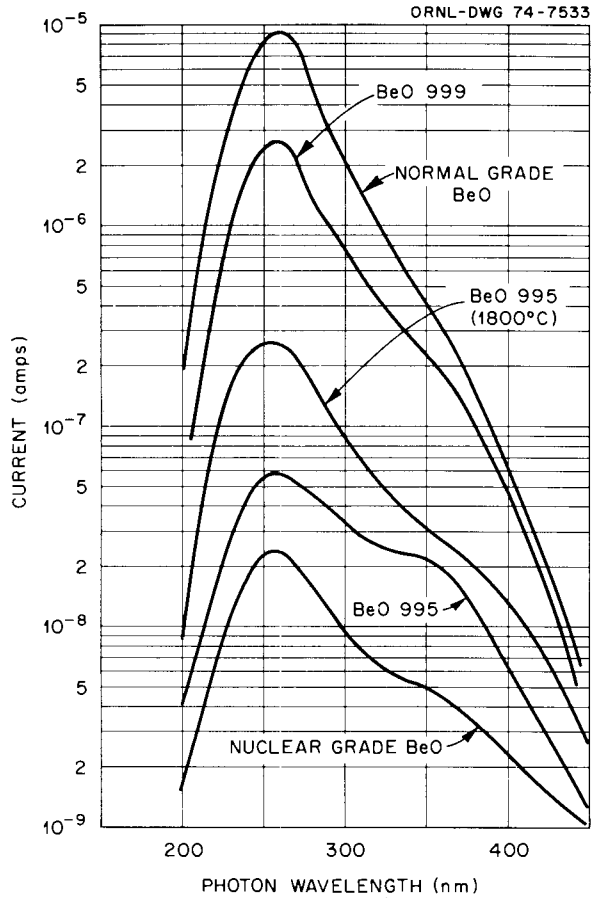

Fig. 6.3. Luminescence induced by electron bombardment of several types of ceramic BeO. Measurements made by E. T. Arakawa, Biological and Radiation Physics Section, Health Physics Division.

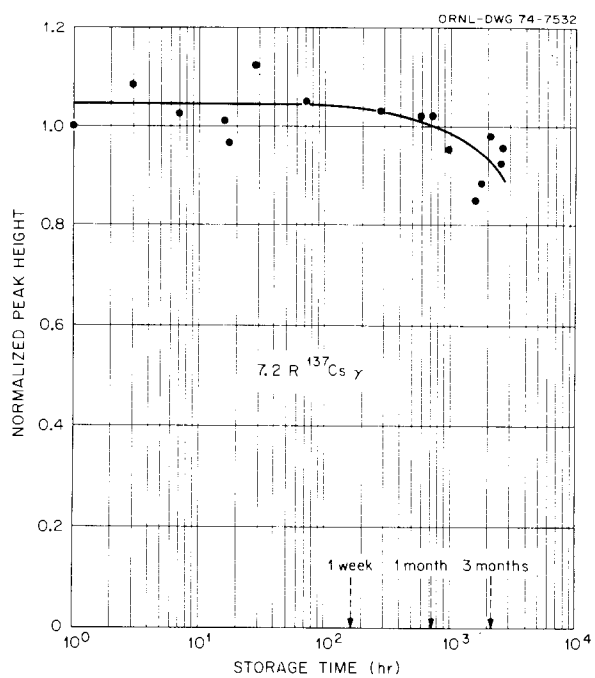

Fig. 6.4. Fading of the TL (167°C peak) from Thermalox 995 stored at 30°C and 90% relative humidity.

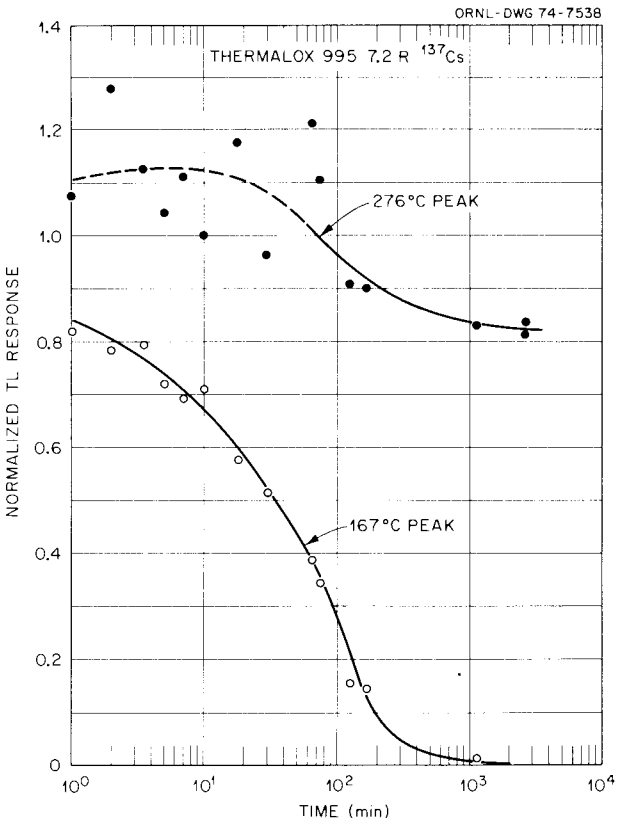

Fig. 6.5. Fading of the TL signals from Thermalox 995 exposed to laboratory fluorescent light of normal intensity.

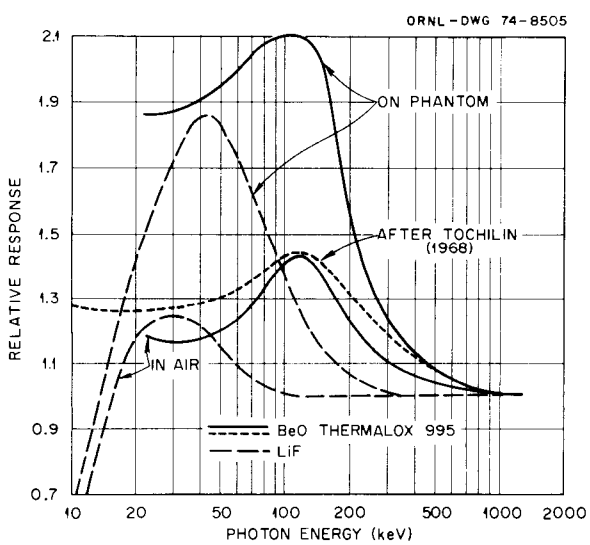

Fig. 6.6. TL response of Thermalox 995 and LiF 100 as a function of photon energy, normalized to unity at 1.25 MeV. LiF data supplied by D. Hankins, Health Physics Division, LASL.

APPLICATIONS

The monitoring of tritium beta rays or other weakly penetrating beta-emitting radionuclides, such as ^{14}C, in the presence of photon radiations is a particularly attractive practical application. Exposures to high levels of tritium, which cause exoelectron saturation effects in the TSEE reader, give no significant TL response. A complete discrimination between the beta and photon exposure is therefore possible after an exposure in a mixed radiation field.

An exploratory study of the use of BeO dosimeters in radon monitoring has been made. The principle of making combined TL and TSEE readings that can be used to discriminate between the exposures to photon and alpha radiations in a mixed field is typified by the glow curves in Fig. 6.7. The exposure to alpha rays was made with the BeO disk 1 mm above a small ^{230}Th source (0.097 μCi) emitting 4.7-MeV alpha particles. The gamma-ray exposures were made using a calibrated ^{60}Co source. The TSEE sensitivity is about 10 counts per alpha particle incident on the BeO and about 1000 counts per milliroentgen ^{60}Co per square centimeter of emitting BeO surface. There is similar high TSEE and low TL sensitivity to the beta radiations emitted by the radon daughters ^{214}Pb and ^{214}Bi.

The extremely dusty atmospheres and high humidities encountered in uranium mines necessitate protection of the emitting surface of the BeO disk. To do this, thicknesses of Mylar foil have been used to cover the BeO surface. The normalized TSEE response for ^{230}Th alpha rays after passage through varying thicknesses of Mylar is shown in Fig. 6.8. For radon monitoring a single layer of commercially available 0.25-mil-thick Mylar foil will have sufficient rigidity to protect the BeO disk without compromising the high sensitivity of the TSEE dosimeter.

The head of a radon progeny dosimeter employing a track detector (and developed at Oak Ridge) has been adapted to accept 12.5-mm-diam BeO ceramic disks. The detector is 1 cm from the filter which catches the aerosols and is protected by the thin Mylar cover. The results subsequently obtained are shown in Fig. 6.9 in terms of working level-liters; one working level-liter is the minimum sensitivity. At a pumping speed of 0.1 liter/min, this is equivalent to $^1/_6$ working level-hour. The generally accepted requirement for a personal dosimeter is a sensitivity of 1 working level-hour or less.

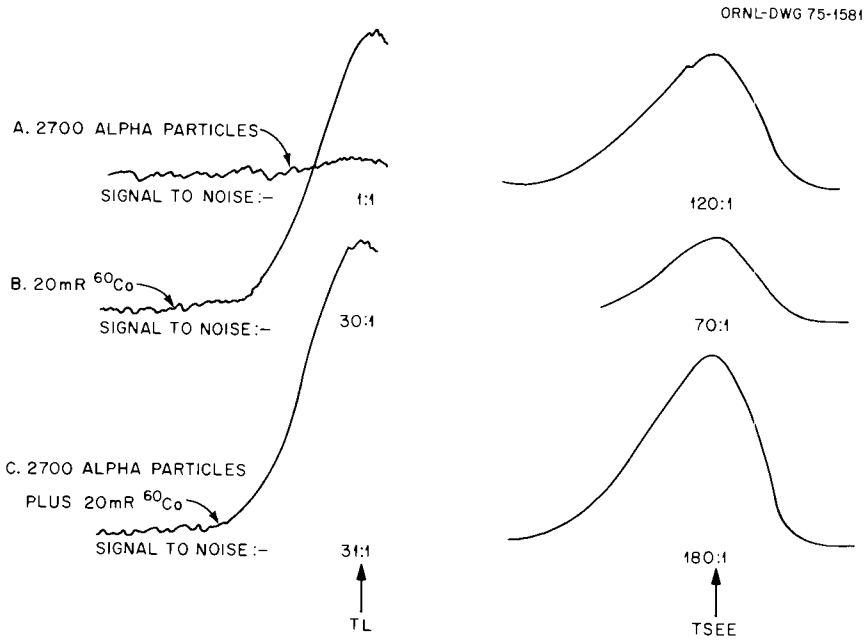

Fig. 6.7. TL and TSEE readings from the same Thermalox 995 BeO detector exposed to (*A*) alpha particles from a ^{230}Th source, (*B*) ^{60}Co gamma radiation, and (*C*) both alpha and gamma radiation exposures. The TL signals are measured at maximum intensity (peak height), the TSEE signals by integration of pulses. The TSEE background signal is 200 pulses.

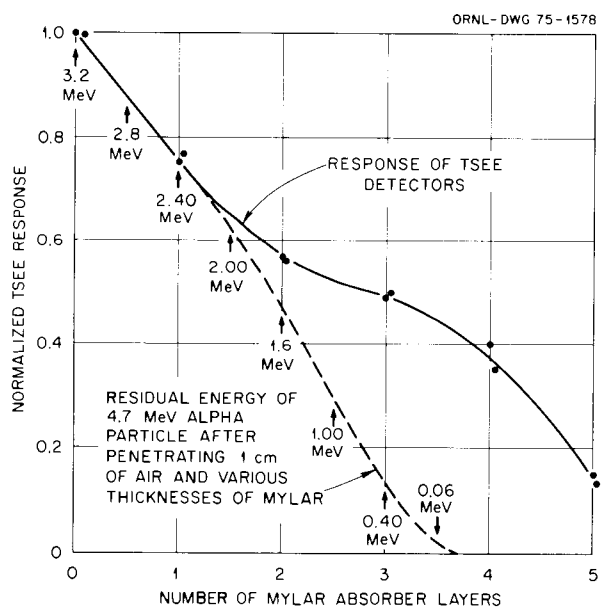

Fig. 6.8. Normalized TSEE response of a Thermalox 995 BeO detector, 1 mm above a ^{230}Th source emitting alpha particles of energy 4.7 MeV, as a function of the number of layers of Mylar foil (0.00038 cm thick) covering the BeO surface.

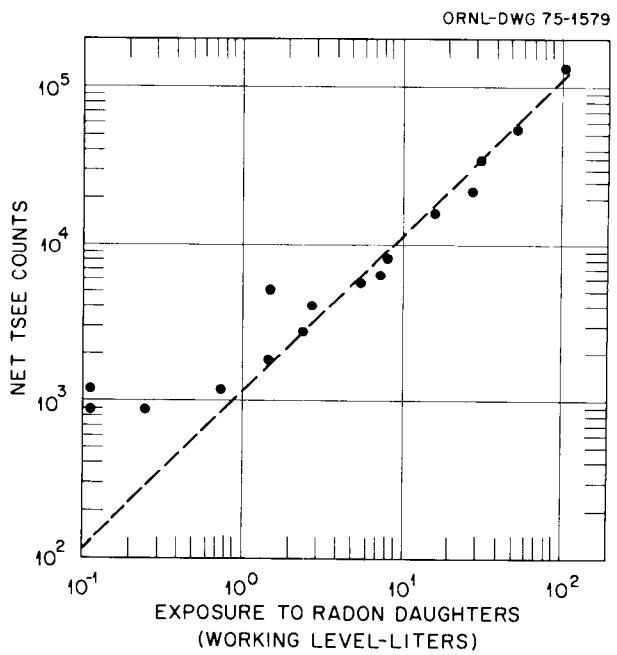

Fig. 6.9. TSEE response of six detectors of Thermalox 995 BeO after the exposure to radon-daughter-containing atmospheres. Below 1 working level-liter, background effects cause deviations from the linearity of response.

7. Distribution of Energy Losses of Low-Energy Protons in Hydrocarbon Gases

J. H. Thorngate W. S. Shinpaugh

The distribution of proton stopping in hydrocarbon gases, first described in the 1973 Annual Report,[1] is entering the final phases of data acquisition. Protons with energies between 50 and 150 keV are provided by the DOSAR Low Energy Accelerator (DLEA). A number of problems have arisen because the combined energy resolution of the electrostatic analyzers is less than 0.2%; so small shifts in accelerator voltage result in the loss of transmitted beam. For the first data, taken with H_2, fluctuations in machine output were recorded by digitizing the current wiping off on the input aperture of the electrostatic analyzer used to measure the energy spectrum of the protons emerging from the gas cell. The digitizer did not have sufficient sensitivity for measurements with heavier gases because of their larger scattering cross sections; so a vibrating-reed electrometer was installed. This arrangement was used for a second measurement with hydrogen and with methane. Sufficient data were obtained by using this technique to allow three consecutive measurements at each point in each of three separate runs. Having nine values for each data point allows reasonable statistical interpretation of the data.

As data were accumulated, it became obvious that even this normalization was inadequate because reproducibility of the ratio of the output and normalizing currents was no better than ±10% for a large series of measurements at the same analyzer settings. This method of normalization records only protons that do not go through the aperture into the analyzer; thus small changes in the position of the proton beam can result in an increase in the normalization current while at the same time decreasing the transmitted current. A better measurement of normalization was provided by installing an electrode mounted in the analyzer box between the input aperture and the deflection plates. This electrode was designed to intercept a portion of the top or either side of the beam. Normalization within ±3% was obtained by intercepting a portion of the beam on the side toward the outer (positive) deflector plate. The electrode was also useful for aligning the apparatus to the proton beam, because it measured only current that had come through all the apertures in the system. A test to measure induced charge without intercepting the beam did not work as well since it sensed the total beam, not just that part transmitted through the analyzer.

Further data will be taken with ethyne (acetylene), ethene (ethylene), ethane, propyne (methyl acetylene), propene (propylene), propane, propadiene (allene), and cyclopropane. Several of these gases will also provide direct information on Bragg additivity at low proton energies. For example, propyne and propadiene both have the empirical formula, C_3H_4, and additivity implies that they have the same stopping power. Similarly, propene and cyclopropane are both C_3H_6.

The energy loss distribution can be described in terms of central moments. The nth central moment is defined as

$$A_n = {}_0\int^{\infty}(E - \langle E\rangle)^n F(E, s)dE ,$$

where the mean energy of the protons after they have traversed the stopping medium, $\langle E\rangle$, is defined by the equation

$$\langle E\rangle = {}_0\int^{\infty} EF(E, s)dE .$$

$F(E, s)$ is the energy loss distribution, which is a function of proton energy, E, and the thickness of the

1. J. H. Thorngate, "Spectrometric Dosimetry," *Health Phys. Div. Annu. Progr. Rep. July 31, 1973,* ORNL-4903, pp. 46, 47.

stopping medium, s. Payne[2] shows that when $[E(s = 0) - \langle E \rangle] \gtrsim 3\%$ of $E(s = 0)$, only the mean energy and the second and third central moments are required to describe the distribution. Thus the gas pressures used in this experiment were chosen, on the basis of a preliminary run, to give a 4% energy loss at each energy. Data were recorded for five proton energies (51, 76.5, 102, 127.5, and 153 keV); so the mean energies of the proton spectra emerging from the gas cell were 49, 73.5, 98, 122.5, and 147 keV. These values allow the stopping powers to be given at the even energies 50, 75, 100, 125, and 150 keV.

The energy of the charged particles transmitted by the electrostatic analyzer changes 57.5 eV for each 2-V change in the potential between the electrodes, but the resolution of the analyzer is about 60 eV at 50 keV and increases to 175 eV at 150 keV. Therefore, data were taken at 2-V increments at 50 keV, 4-V increments at 100 keV, and 6-V increments at 150 keV. Ten-volt increments were used at 75 and 225 keV because only mean energy loss was measured at these energies. Typical energy loss distributions for protons of 51, 102, and 153 keV in hydrogen are shown in Figs. 7.1 to 7.3. The mean energy loss, dE/dx, and the second and third central moments are given in Table 7.1. The dE/dx values are about 4% lower than those of Reynolds et al.,[3] probably due to the refinements available for this experiment. A small amount of almost any contaminant will raise the values. The large uncertainties exist because these are the original hydrogen data. As the order of the central moment increases, its uncertainty will increase because the calculation depends more on those data which are hardest to measure, near the limits of the distribution.

Data taken so far have produced nothing unusual; the theoretical values have not yet been calculated. Ultimately, theories by Bohr,[4] Livingston and Bethe,[5] and Symon[6] will be used to calculate the expected central moments of the distributions.

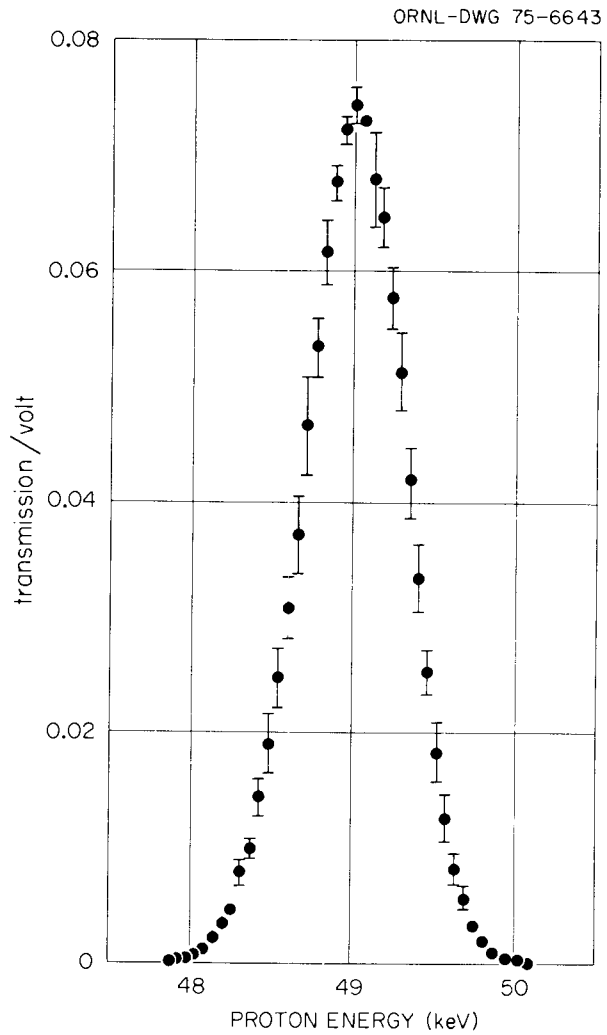

Fig. 7.1. Proton spectrum resulting when 51-keV protons traverse sufficient hydrogen to lose 4% of their energy.

2. M. G. Payne, *Phys. Rev.* **185**, 611 (1969).
3. H. K. Reynolds, D. N. F. Dunbar, W. A. Wenzel, and W. Whaling, *Phys. Rev.* 92, 742 (1953).
4. N. Bohr, *Phil. Mag.* **30**, 581 (1965).
5. M. S. Livingston and H. A. Bethe, *Rev. Mod. Phys.* 9, 261 (1937).
6. K. R. Symon, Thesis, Harvard University, 1948, unpublished.

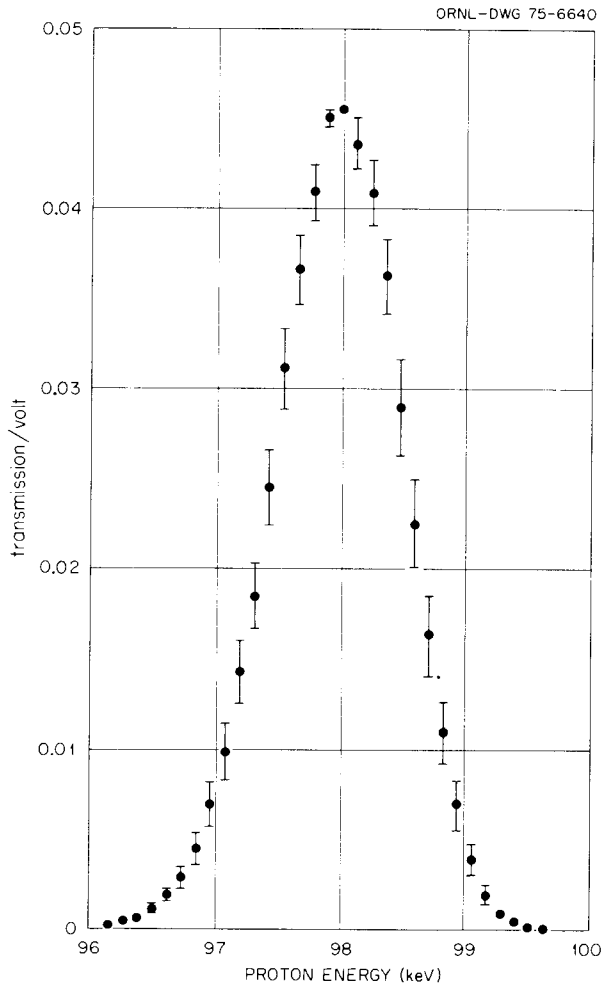

Fig. 7.2. Proton spectrum resulting when 102-keV protons traverse sufficient hydrogen to lose 4% of their energy.

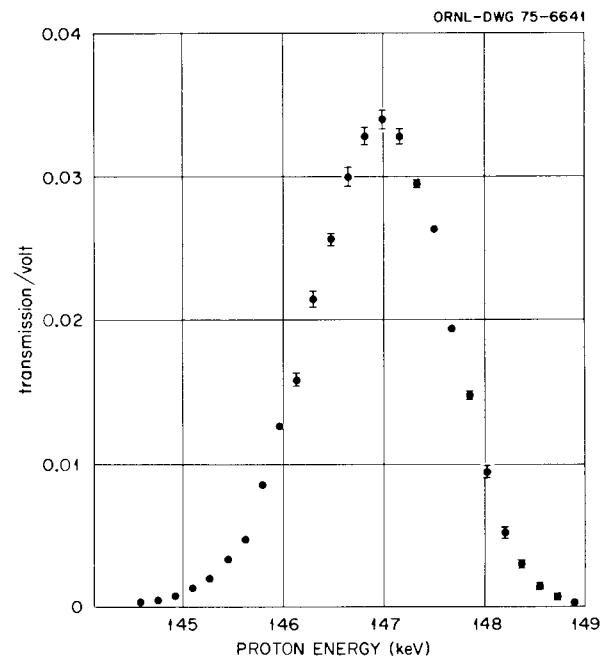

Fig. 7.3. Proton spectrum resulting when 153-keV protons traverse sufficient hydrogen to lose 4% of their energy.

Table 7.1. Typical values for the energy loss distribution of low-energy protons in hydrogen

E (keV)	$E - \langle E \rangle$ (keV)	$\frac{dE}{dx}$ (keV–cm^2/mg)	Second central moment	Third central moment
50	2.02 ± 0.02	(3.71 ± 0.03) × 10^6	(9.9 ± 0.4) × 10^{-2}	– (5.5 ± 2.2) × 10^{-3}
75	3.04 ± 0.04	(3.60 ± 0.04) × 10^6		
100	4.06 ± 0.06	(3.30 ± 0.05) × 10^6	(2.56 ± 0.07) × 10^{-1}	– (2.6 ± 0.8) × 10^{-2}
125	5.15 ± 0.09	(2.98 ± 0.06) × 10^6		
150	6.08 ± 0.01	(2.71 ± 0.01) × 10^6	(4.7 ± 0.6) × 10^{-1}	– (8.0 ± 1.9) × 10^{-2}

8. Developments in Alpha Spectrometry with Liquid Scintillators

J. H. Thorngate W. J. McDowell P. T. Perdue D. J. Christian

Liquid organic scintillators, combined with solvent extraction techniques, provide a sensitive means to measure small amounts of alpha-emitting heavy metals.[1,2] Moreover, pulse-shape discrimination procedures can reduce the background from pulses produced in the scintillator by electrons to below 0.01 count/min.[3] Recently, an effort was conducted to optimize both the detection system and the solvent extraction process. The scope of the program was limited to bone and tissue samples, because the Medical Physics and Internal Dosimetry Section of the Health Physics Division was interested in measuring plutonium in such samples.

Work on the chemical processes stressed developing techniques that would increase reproducibility. A major finding was that the extractant used (di-2-ethylhexyl phosphoric acid, HDEHP) must be carefully prepared and purified. This produced extractions that were more uniform and complete, typically 98% of the plutonium extracted with a ±2% variation. Also, purified HDEHP is water clear, so that it absorbs less of the light produced in the liquid scintillator, resulting in improved pulse-height resolution.

Earlier work had arrived at an optimum scintillator comprised of 180 g per liter of naphthalene and 3.6 g per liter of PBBO [2-(4′-biphenyl)-6-phenylbenzoxazole] in toluene with 80 g per liter of HDEHP as the extractant. However, absorption by naphthalene may interfere with optimum light transmission, so a brief test was made using a scintillator consisting solely of PBBO in purified tetralin (1,2,3,4-tetrahydronaphthalene). The results indicate that this scintillator may be a possible alternative for use with faster photomultipliers to improve pulse-shape discrimination. Such tubes generally have the peak in their efficiency at a shorter wavelength than do slower tubes. This comparison is shown in Fig. 8.1.

A detailed study was made to determine what part of the alpha counts were lost when pulse-shape discrimination was used to suppress the background. In a series of

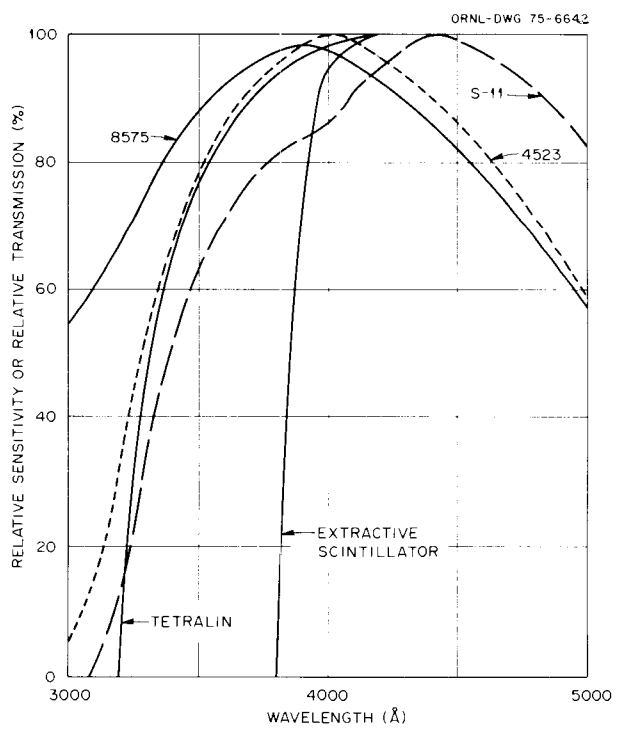

Fig. 8.1. A comparison of the transmission of light as a function of wavelength for the extractive scintillator and tetralin. Also shown are the relative efficiencies of 4523 and 8575 and S-11 response photomultiplier tubes.

1. W. J. McDowell and L. C. Henley, *An Evaluation of the Possibility of Detecting and Identifying Alpha Emitters in Low-Count-Rate Samples Using Some Low Liquid Scintillation Counting Techniques,* ORNL-TM-3676 (March 1972).
2. W. J. McDowell, D. T. Farrar, and M. R. Billings, *Talanta* **21**, 1231 (1974).
3. J. H. Thorngate, W. J. McDowell, and D. J. Christian, *Health Phys.* **27**, 123 (1974).

over 200 measurements, the alpha peak was diminished by 2 to 4%. Somewhat greater losses occurred when low-level samples or high backgrounds were encountered. Considerable care must be taken in measurements of this type to ensure that the scintillation sample is well deoxygenated, since even small amounts of oxygen can suppress that part of the pulse that provides the information necessary for pulse-shape discrimination. These effects can be observed over periods as short as a few hours if the sample is not sealed. A commercial compound, Vitride, can be used to scavenge oxygen, but it was found to discolor the scintillator after about 24 hr. Moreover, the Vitride will turn a scintillation solution bright yellow without HDEHP.

Because considerable use is made of ion exchange techniques for extracting transuranics from samples, a technique was devised for placing the solutions washed from the columns into the liquid scintillator. It turned out that the procedures necessary are similar to preparing samples separated by solvent extraction. A series of bone samples, run using ion exchange, gave a yield of plutonium of 93% with a ±7% uncertainty.

A number of tests were conducted to select the detector and the associated electronics to maximize both the pulse-height and pulse-shape response. To provide a wide range of pulse-height response, a sample was prepared by putting natural thorium into the scintillator. After careful deoxygenation this sample was sealed to provide long-term stability. One factor studied was the photomultiplier tube. The performance of an 8575, a fast tube widely used for nuclear counting, was compared with the 4523 used in the original counter. Increasing the high voltage applied to the photomultiplier improved pulse-height resolution somewhat, but with a decrease in the quality of the pulse-shape data.

Several combinations of preamplifiers and linear amplifiers were compared. As expected, the best pulse-height resolution was obtained by using a low-noise, charge-sensitive preamplifier; but the best combination of pulse-shape and pulse-height response was obtained by using an integrating preamplifier designed here.[4] Source-follower and emitter-follower preamplifiers gave poorer response for both parameters. A double-delay-line amplifier, used with minimum integration, gave the best pulse-shape response with little loss of pulse-height response when compared with more sophisticated active-filter amplifiers.

A figure of merit is useful for making quantitative comparisons of widely differing data. For pulse height, a value was calculated by taking the reciprocal of the sum of the ratios of the full width at half maximum to the centroid of the peak for the four major peaks in the thorium data. Pulse-shape comparisons were based on the relation $(A_e/A_a)(P_a/V)D$, where A_e is the area of the electron-produced time distribution, A_a is the area of the alpha, P_a is the peak of the alpha distribution, V is the valley between the distributions, and D is the separation of the centroids of the distributions. This figure of merit gives a higher weight to a good peak-to-valley ratio and separation when the number of electrons recorded is high compared with the number of alpha particles. This compensates for the improvement in separation that occurs when a pulse-height discriminator is used to eliminate the response to the electrons below the lowest alpha peak, a change that does not represent any intrinsic improvement in the detection system.

Data were also taken for a number of different reflector-sample-holder systems. The reflectors can be described by the geometry of the reflection surface and whether they held the sample so that it was viewed end-on or side-on by the photomultiplier tube. They are illustrated in Fig. 8.2: (*a*) hemispherical, side viewing, (*b*) spherical, end viewing, (*c*) conical (semiparabolic), end viewing, (*d*) modified hemispherical, end viewing, (*e*) two photo tubes, side viewing, and (*f*) a special side viewing unit that had a cylindrical reflector surface immediately around the sample. In every case the insides are coated with reflecting paint, and the void is filled with silicone fluid. Figure 8.2*a* shows how the

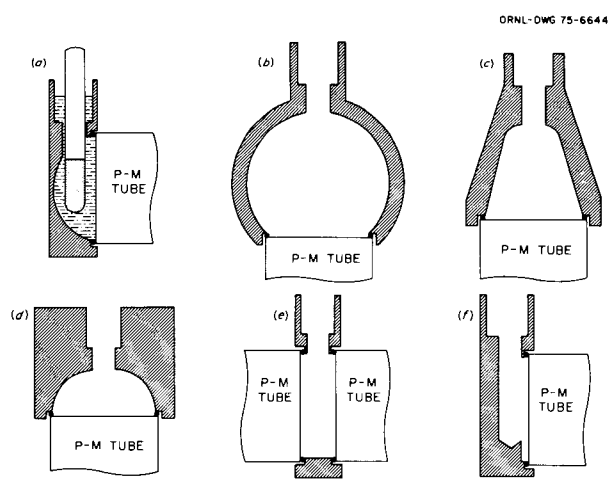

Fig. 8.2. Cross sections of the reflector–sample-holder geometries studied in this work. They are described in more detail in the text.

4. D. J. Christian and J. H. Thorngate, *A Compact Electronic System for an Improved Alpha Air Monitor*, ORNL-TM-4346 (September 1973).

sample vial fits into a reflector. Generally, the findings were that side viewing was superior to end viewing and that reflector geometry and source position had a marked effect on the pulse-height response, although these variables produced much smaller changes in pulse shape.

Because the pulse-shape apparatus used for this counting is quite complicated, preliminary design was done on a simplified pulse-shape discrimination circuit. Used in conjunction with the optimum reflector, photomultiplier, preamplifier, and amplifier, and with the improved chemical techniques, it should result in a relatively simple means of measuring low levels of alpha-emitting materials from biological samples. A detailed report of all of these findings is under preparation.

9. Dosimetry for Terrestrial Gamma-Ray Sources

S. A. Abdullah[1]
H. W. Dickson G. D. Kerr
M. F. K. Miah[1] P. T. Perdue

Dose rates from natural radionuclides and ^{137}Cs in soils of the Oak Ridge area have been determined from in situ and core sample measurements. Information on soil composition, density, and moisture content and on the distribution of cesium in the soil was obtained from the core samples. Measurements of radionuclide concentrations in the samples were made with a 4 X 4 in. NaI detector. Gamma-ray spectroscopy using a lithium-drifted germanium (GeLi) detector has been applied to the determination of radionuclide concentrations in soil and the associated gamma dose rates above the earth plane.[2-5] An unshielded GeLi detector placed about 1 m above the earth detects gamma radiation from an area of about 100 m^2.

For our in situ gamma measurements, a spectrometer system consisting of a 55-cm^3 GeLi detector and a 4096-channel analyzer was used. The detector, shown in Fig. 9.1, is specially designed for in situ measurements. The GeLi crystal is mounted on the bottom of the cryostat in a down-looking configuration so the container will not shield gamma radiation from the earth. This represents a substantial improvement over our previous detector geometry which included a GeLi crystal mounted at a right angle to the tip of the cryostat and, consequently, was partially shielded by the cryostat. The new design provides a nearly uniform 2π detector. Angular dependence of the detector, as measured using standard sources at 10° intervals, showed less than 10% variation through 180°. Variation occurring at large angles has little influence on actual in situ counting applications. Table 9.1 gives the measured angular dependence of the detector.

The GeLi detector was obtained commercially to specifications; however, a supporting stand (see Fig. 9.1) was designed and fabricated at ORNL. The tripod stand is made of light-weight aluminum tubing. Each leg is independently adjustable using a worm-gear arrangement with a locking mechanism. The stand may be erected on nearly any terrain at the desired height and leveled using three bubble levels located one over each leg on the detector supporting ring. The GeLi detector mounted to a matching support ring is then placed on the stand and checked for final alignment.

The counts recorded by the spectrometer in the total energy peak, n_e, are given for a semi-infinite mono-energetic source of uniform distribution in the soil by the expression

$$n_e(E_\gamma) = \frac{4\pi S k(E_\gamma)}{\mu_s} E_2(\mu_a D) ,$$

where $k(E_\gamma)$ is the efficiency of the detector in counts per gamma ray multiplied by the distance squared, D is the source-to-detector distance, μ_s and μ_a are the attenuation coefficients of soil and air respectively, E_2 is a second-order exponential integral, and S is the concentration of emitters in the soil in photons per cubic centimeter.

The detector was calibrated by using several gamma sources covering the energy range from 121.9 to 1836.0

1. Alien guest.
2. L. R. Anspaugh, P. L. Phelps, G. W. Huckabay, P. H. Gudiksen, and C. L. Lindeken, *Methods for the in Situ Measurements of Radionuclides in Soil,* UCRL-74061 (1972).
3. J. A. Auxier, D. J. Christian, T. D. Jones, G. D. Kerr, P. T. Perdue, W. H. Shinpaugh, and J. H. Thorngate, *Contribution of Natural Terrestrial Sources to the Total Radiation Dose to Man,* ORNL-TM-4323 (September 1973).
4. H. L. Beck, J. DeCampo, and C. Gogolak, *In Situ Ge(Li) and NaI(Tl) Gamma-Ray Spectrometry,* HASL-258 (September 1972).
5. H. W. Dickson, G. D. Kerr, P. T. Perdue, and S. A. Abdullah, "Environmental Radiation Measurements Using in Situ and Core Sampling Techniques," *Proceedings of Eighth Midyear Topical Symposium of Health Physics Society, Knoxville, Tenn., Oct. 21–24, 1974.*

Fig. 9.1. GeLi detector mounted on field support.

keV. Values of k were determined for all these sources, and a power function was fitted to the data to give $k(E_\gamma)$ for all energies from 100 to 2700 keV which covers all the naturally occurring gamma radiation from the earth. Since uniform deposition of radionuclides in the soil was assumed for natural emitters, the factor R giving counts per photon per cubic centimeter from the soil was calculated by using the equation

$$R = \frac{4\pi k(E_\gamma)}{\mu_s} E_2(\mu_a D)$$

for a number of energies from 100 to 3000 keV (see Table 9.2). Values of R for the energies in the data were found above 200 keV by a Gaussian backward interpolation technique. The resulting factors were used to determine the gamma rays emitted per cubic centimeter of soil for each observed energy. By including the gamma abundance, a concentration in picocuries per cubic centimeter could be found.

A computer program was prepared to facilitate the analysis of the large amount of data. The 4096 channels of data for each spectral measurement are punched onto paper tape. Upon return to ORNL the paper tape is read onto the user's disk area at the computer center. The user edits the file and loads it onto magnetic tape which is recalled at a remote terminal, and a FORTRAN file is written using the data. The FORTRAN program VGAPE.F4 operates on this data file to find peaks, integrate under the peaks, assign

Table 9.1. Measured angular dependence of GeLi detector response relative to 0° position

Angle (deg)	Energy (keV)								
	122	279	511	662	898	1173	1274	1332	1836
0	1.000	1.000	1.000	1.000	1.000	1.000	1.000	1.000	1.000
10	0.946	1.021	0.975	0.986	0.995	0.990	1.022	0.968	0.945
20	0.900	1.010	0.942	0.989	0.963	0.941	1.001	1.002	1.021
30	0.937	0.942	0.910	0.993	0.947	1.001	0.981	0.966	1.024
40	1.038	0.978	0.935	0.969	0.959	0.973	0.991	0.998	0.990
50	0.988	1.015	0.917	0.959	0.946	0.955	0.933	0.956	1.011
60	0.984	1.020	0.907	0.973	1.018	0.975	0.975	0.975	0.998
70	1.079	0.991	0.936	0.970	1.022	0.984	0.976	0.976	0.965
80	0.934	1.043	0.911	0.928	0.993	0.991	1.013	0.972	1.013
90	0.962	1.029	0.935	0.979	1.024	0.977	0.985	0.942	1.042

Table 9.2. Ratio R of counts in photopeak to gamma rays emitted per cubic centimeter of soil

E_γ (keV)	$\mu_a D$	$E_2(\mu_a D)$	μ_s (cm^{-1})	k (counts per gamma per cm^2)	R (counts per gamma per cm^3)
	$\times 10^{-3}$				
100	1.72	0.9883	0.2672	0.750	17.43
150	1.89	0.9873	0.2256	0.525	14.44
200	2.04	0.9865	0.2032	0.462	14.09
300	2.20	0.9856	0.1744	0.352	12.42
400	2.26	0.9853	0.1560	0.275	10.91
500	2.27	0.9852	0.1430	0.211	9.13
600	2.26	0.9853	0.1320	0.169	7.92
800	2.21	0.9856	0.1161	0.126	6.73
1000	2.14	0.9859	0.1040	0.098	5.81
1500	1.96	0.9869	0.0840	0.065	4.75
2000	1.82	0.9877	0.0730	0.053	4.50
3000	1.61	0.9890	0.0594	0.041	4.28

energies based on calibration information, and to calculate soil concentrations using predetermined detector parameters.

In general, the in situ measurements have been made near the perimeter monitoring stations around ORNL. In addition, an interesting in situ measurement was conducted at TVA's Bull Run power plant. The GeLi detector was placed on the coal reserve pile at this plant. This coal pile essentially constituted an infinite source, since it was approximately 50 ft deep and extended for well over 125 ft in any direction from the detector location. The results of this measurement are presented in Table 9.3. The dose rates were obtained by using conversion factors determined by Beck et al.[4]

Table 9.3. In situ measurement at Bull Run site

Series	Radionuclide	Concentration (pCi/cm^3)	Dose rate (microrads/hr)
Uranium	Pb-214	1.08 ± 0.08	
	Bi-214	1.08 ± 0.05	
		av 1.08 ± 0.04	1.17 ± 0.04
Thorium	Tl-208	0.76 ± 0.06	
	Pb-212	1.14 ± 0.09	
	Ac-228	0.90 ± 0.09	
		av 0.90 ± 0.04	1.52 ± 0.08
Potassium	K-40	4.44 ± 0.08	0.47 ± 0.01
		Total	3.16 ± 0.09

10. Dosimetry for Human Exposures

J. A. Auxier F. F. Haywood T. D. Jones G. G. Warner[3]
J. S. Cheka[1] G. D. Kerr D. L. Solomon[2] H. Yamada[4]

Objectives of these studies are to investigate human radiation exposures from gamma-ray and neutron fields and to establish improved physical dosimetry for correlations between observed biological effects and radiation dose. Emphasis is currently on investigations of dose distribution and dose to specific organs and tissue of human-type phantoms as functions of the energy and angular distributions of the incident radiation. These dosimetry studies and liaison studies with the Atomic Bomb Casualty Commission (ABCC) in Japan will result in significant refinements in estimates of radiation exposure risks, RBE values of neutrons, and relationships of biological effect vs radiation dose derived from medical and epidemiological studies of atomic bomb survivors. In addition to the importance of these studies in the establishment of radiation protection criteria, the studies of dose to organs and tissues of the body as functions of the energy and angular distributions of incident gamma rays and neutrons have important application in areas such as radiotherapy, the evaluation of shielding in shelters, and the design of dosimeters.

LIAISON DOSIMETRY STUDIES

The latest liaison dosimetry study trip to the ABCC was from August 20, 1974, to September 17, 1974.[5] During this trip, important new data were presented to the ABCC. These data dealt with depth-dose distributions which can be used to make in vivo (organ and tissue) dose estimates for atomic bomb survivors.[6] The need for these data has been emphasized in several recent and authorative reports by the Advisory Committee on the Biological Effects of Ionizing Radiation (BEIR) of the National Academy of Sciences–National Research Council and the United Nations Scientific Committee on the Effects of Atomic Radiation (UNSCEAR).[7,8]

In reviewing data available on the effects of radiation on man, the BEIR report acknowledged the importance of both the medical and epidemiological studies of the ABCC and the T65D system of estimating radiation dose to survivors developed at ORNL by stating:

> Some of the most useful data available for the evaluation of the late effect of radiation on man come from the Atomic Bomb Casualty Commission: The population of A-bomb survivors is large and received doses ranging from the trivial to the near lethal: estimated doses are available for almost all; the population is relatively unselected (except for mortality at the upper end of the dose range), in contrast to series arising from therapy administered for pre-existing disease or from occupational exposure.[9]

To stress uncertainties in estimates of effects of low-level radiation exposures, shortcomings of both the epidemiological and dosimetric data of all studies were discussed in detail in both reports. In discussing the estimated doses to atomic bomb survivors, the BEIR report states:

> These dose estimates, drawn from the ABCC data, are of air doses to the mother. The degree of attenuation of the dose in

1. Consultant.
2. Biometrics Unit, Cornell University, Ithaca, N.Y.
3. Computer Sciences Division.
4. Department of Statistics and Epidemiology, Atomic Bomb Casualty Commission, Hiroshima, Japan.
5. G. D. Kerr, *Report of Liaison Studies with the Atomic Bomb Casualty Commission, Hiroshima, Japan, August 20, 1974 to September 17, 1974,* ORNL-TM-4830 (February 1975).
6. T. D. Jones, J. A. Auxier, J. S. Cheka, and G. D. Kerr, *Health Phys.* 28, 367 (1975).
7. Advisory Committee on the Biological Effects of Ionizing Radiation, *The Effects on Populations of Exposure to Low Levels of Ionizing Radiation,* National Academy of Sciences–National Research Council, Washington, D.C., November 1972.
8. United Nations Scientific Committee on the Effects of Atomic Radiation, *Ionizing Radiation: Levels and Effects,* United Nations, New York, 1972.
9. Ref. 7, p. 100.

reaching the fetus would depend on such factors as fetal age; e.g., the younger the fetus, the greater the attenuation. An equation to allow for this attenuation in computing fetal dose has not been formulated.[10]

The mean dose shown in Column 11 is usually the relevant tissue dose, but for the A-bomb survivors, it is the whole-body, free field, or "air" dose. Attenuation factors for atomic bomb survivors have not been published, and hence no effort is made here to provide tissue doses, which might be 60 to 70 percent of the dose given in rads, depending on the tissue and the proportions of neutron and gamma radiation.[11]

The UNSCEAR report states:

> It must also be clearly borne in mind that absorbed doses, particularly to deep tissues, are difficult to obtain from the kerma estimates available, and the fact that a substantial neutron contribution was received by the survivors at Hiroshima introduces additional complications owing to the higher biological effectiveness of neutrons relative to gamma rays.[12]

Techniques developed by the Health Physics Division of ORNL to specify the radiation exposure to a survivor are the basis of the so-called tentative 1965 dose (T65D) assignments for most of the 117,000 survivors in the master files of the ABCC. The quantity originally used in these techniques was a "first-collision" absorbed dose (i.e., the kinetic energy deposited locally by ionizing particles produced by gamma-ray and neutron interactions in a small mass of biological tissue). According to more recent recommendations of the International Commission on Radiological Units and Measurements,[13,14] the "first collision" concept of radiation dose should now be referred to as kerma (kinetic energy released in material, tissue in this case) in free air, or simply "tissue kerma in free air."

Because the survivor was replaced by a small mass of biological tissue in the T65D assignments of radiation exposure to survivors, references to these estimates as "whole body" doses in the literature have been misleading. The *irradiation* of atomic bomb survivors was, however, "whole body" in comparison with so-called "partial body" irradiation in therapeutic x-ray beam exposures. Due to multiple scattering (or multiple collisions) and absorption (or attentuation) of radiation by the body, the absorbed dose to organs and tissue of the body or to the whole body (usually interpreted to mean the average absorbed dose to the body) of a survivor was different from his or her T65D assignment of tissue kerma in free air. In general, the absorbed dose to organs and tissues is less than the tissue kerma in free air, the reduction for neutrons being greater than that for gamma rays.

Table 10.1. Estimates of absorbed dose to the breasts and fetus of an atomic bomb survivor

Ratio of absorbed dose to tissue kerma in free air

	Breasts	Fetus
D_γ/K_γ	0.80	0.42
$D_{n,p}/K_n$	0.55	0.14
$D_{n,\gamma}/K_n$	0.045	0.077

Estimates of the absorbed doses to the breasts of women survivors and to survivors exposed in utero were made at the request of the ABCC for immediate use in their studies. These estimates, shown in Table 10.1, give the absorbed dose from heavy charged particles ($D_{n,p}$) and gamma rays ($D_{n,\gamma}$) produced by neutrons incident on the body and from gamma rays (D_γ) incident on the body of a survivor in terms of the T65D assignments of the tissue kerma in free air from neutrons (K_n) and gamma rays (K_γ) for survivors.

Absorbed doses to the fetus, which are given in Table 10.1, were obtained by combining calculations of the distribution of absorbed dose in a homogeneous phantom of radius 12 cm and length 60 cm with information on fetal size[6] and distance from the front skin surface to the center of the uterus[15] at the different stages of fetal development. In the first trimester of fetal development, the fetus and slightly enlarged uterus remain centrally located at an average distance (or penetration depth for the incident radiation) from the front skin surface of the abdomen to the center of the uterus of about 8 cm. In the second trimester, the fetus and greatly enlarged uterus move upward and forward, decreasing the average penetration depth to a minimum of about 6 cm, but in the third trimester, the greatly enlarged fetus and uterus settle back down in the body, increasing the average penetration depth to about 8 cm. Because of small variations in

10. Ref. 7, footnote on p. 76.

11. Ref. 7, "Definitions and Notes to Accompany Reference Tables Summarizing Quantitative Data on Carcinogenic Effects of Ionizing Radiations," pp.195–99.

12. Ref. 8, Annex H, p. 404.

13. International Commission on Radiological Units and Measurements, *Physical Aspects of Irradiation,* National Bureau of Standards Handbook 85, U.S. Government Printing Office, Washington, D.C., Mar. 31, 1964.

14. International Commission on Radiation Units and Measurements, *Radiation Quantities and Units,* ICRU Report 19, July 1, 1971.

15. A. Tabuchi, T. Kawaishi, M. Hirata, S. Nakagawa, H. Yoshinaga, S. Antoku, and T. Sunayashiki, "Exposure Dose by Diagnostic X-Ray in Obstetrics, and Some Consideration on the Lowering of Such Doses," *Hiroshima Daigaku Igakubu Zasshi* 12(1.2) (February 1965) (in Japanese).

the penetration depth from the front skin surface to the center of the uterus, which was assumed to be the center of the fetus, and because of small variations in the distribution of absorbed dose at these penetration depths, the variations in average absorbed dose to the fetus obtained by integrating the absorbed dose distribution over the volume of the fetus and dividing by the volume of the fetus were also small. Due to the small variations in these calculations of absorbed dose to the fetus for the first, second, and third trimesters and some uncertainties involved in the calculations, the use of the one set of values given in Table 10.1 seems reasonable for all stages of fetal development. The absorbed doses to the breasts of women given in Table 10.1 are based on the assumption that the tissue at greatest risk lies at a penetration depth of 1 cm below the skin surface. This is consistent with the assumption used in estimating the absorbed dose to the breasts of women who were subjected to multiple fluoroscopies during artificial pneumothorax for pulmonary tuberculosis.[16]

These estimates are of great interest at present because of new dose-specific analyses of breast cancer being made at the ABCC and the Jablon-Stewart controversy over the risk of radiation exposure to a fetus. In brief, this controversy arose because the number of "radiogenic cancers" predicted by the Stewart-Kneale formula, derived from an epidemiological study involving fetal diagnostic x-ray exposures in England, simply did not occur among Japanese children exposed in utero.[17] Estimates of absorbed dose to a fetus given in Table 10.1 are less, especially for neutrons, than the "conservative assumption" used by Jablon and Kato that the absorbed dose to the fetus was one-half of the mother's T65D assignment of tissue kerma in free air, for both neutrons and gamma rays (i.e., $D_\gamma/K_\gamma = 0.5$ and $D_n/K_n = (D_{n,p} + D_{n,\gamma})/K_n = 0.5$); but the difference may not be great enough to resolve this controversy. Other factors that could be responsible for the discrepancies between the two studies have been discussed by Stewart[18] and Jablon[19] and some third parties (see, for example, the UNSCEAR report[20] and the BEIR report[21]).

The immediate importance of estimates of the absorbed dose to the breasts and other organs of survivors can be demonstrated by the following example. Estimates of absolute risk of breast cancer from studies of tubercular women in Nova Scotia subjected to repeated chest fluoroscopy for artificial penumothorax, women in New York State given localized x-ray treatment for acute partum mastitis, and women atomic bomb survivors are, respectively, 8.4, 6.0, and either 2.9 (RBE of 1 assumed for neutrons) or 1.8 (RBE of 5 assumed for neutrons), in units of deaths or cases per million women per year per rem.[22] In summarizing these data, the BEIR report states, "If an RBE of 1 for the neutron component at Hiroshima is assumed, the absolute risk from the studies are remarkably close. For example, if it is assumed that a factor of 2 can be applied to correct deaths from, to incidence of, breast cancer in Japanese women, then the estimated values of the absolute risk, in case/10^6 women/year/rad, are 6.0 for the Japanese study." But, "If an RBE of 5 for the neutron component in Hiroshima is assumed, then neither the absolute nor relative risk estimates for the Japanese would appear to agree with those of the two western studies." The above estimates of risk from the ABCC studies are, of course, based on the radiation exposure of women in terms of tissue kerma in free air. If they are recalculated on the basis of the absorbed dose to the breasts given in Table 10.1, they become approximately 3.8 (RBE of 1) and 2.7 (RBE of 5) deaths per million women per year per rem. If the factor of 2 is used to convert these estimates to cases of breast cancer, as in the BEIR report, estimates of risk based on absorbed doses to the breast of Japanese women survivors become 7.6 (RBE of 1) and 5.4 (RBE of 5) cases per million women per year per rem, and both estimates are in agreement with the two Western studies. In general, use of tissue kerma in free air, rather than absorbed dose to a tissue or organ of interest, will tend to underestimate the absolute risk and the RBE of neutrons.

Liaison dosimetry studies by the ABCC and ORNL are now moving into a new phase in which correlations of medical effects with estimates of absorbed dose to critical organs for each effect will provide better estimates of risk associated with gamma-ray and neutron exposures and of radiation quality (RBE) of neutrons. Future studies are expected to add factors of 2 or more to some current estimates of risk based on

16. Ref. 7, pp. 141–43.
17. S. Jablon and H. Kato, "Childhood Cancer in Relation to Prenatal Exposure to Atomic-Bomb Radiation," *Lancet* **2**, 1000 (1970).
18. A. Stewart, "The Carcinogenic Effects of Low Level Radiation. A Reappraisal of Epidemiologists Methods and Observations," *Health Phys.* **24**, 223 (1973).
19. S. Jablon, "Comments on the Carcinogenic Effects of Low Level Radiation. A Re-appraisal of Epidemiologists Methods and Observations," *Health Phys.* **24**, 257 (1973).
20. Ref. 8, pp. 427–28.
21. Ref. 7, pp. 160–66.
22. Ref. 7, pp. 136–44.

tissue kerma in free air. For example, the absolute risk of leukemia from studies of survivors in Nagasaki is 0.56 case per million persons per year per rem.[23] Based on some preliminary calculations at ORNL and some other data from the literature,[24] the absorbed dose to bone marrow is of the order of half the tissue kerma in free air for these survivors, who were ten years of age or older and were exposed almost entirely to gamma radiation. Therefore, an estimate of absolute risk based on absorbed dose to bone marrow would be of the order of 1 case per million persons per year per rem. An estimate of this order is, of course, in better agreement with estimates of 0.9 to 1.3 and of 1.2 cases per million persons per year per rem from studies of adult spondylitic and menorrhagia patients, respectively.[23] In Hiroshima, the survivors also received significant radiation exposures from neutrons, as well as gamma rays. Hence, the magnitude of the increased absolute risk of leukemia based on absorbed dose to red bone marrow, rather than tissue kerma in free air, will be even greater in Hiroshima than in Nagasaki, and the RBE's for neutrons derived from the leukemia studies in the two cities will be larger than current estimates.[25]

In a recent report, it is stated:

> Undoubtedly the most useful data available for evaluation of the late effects of radiation on man come from the Atomic Bomb Casualty Commission (ABCC). We regard the continued study of this unique population as essential to the elucidation of risk estimates for carcinogenic effect of radiation on man. Not only is the population under study of a large size (over 100,000 individuals) and irradiated for other than medical reasons (which often introduces uncertainty into the interpretation of data from patients), but, also, the survivors received irradiation at all ages and in doses ranging from a few rads to near lethal levels. Many important questions remain to be answered in connection with these A-bomb survivors, which have a direct bearing on our estimation of the risk to human populations from exposure to radiation at or near background levels.
>
> Estimated excess cancer rates are derived from observations on survivors of Hiroshima and Nagasaki averaged over the period 1960 to 1970. We do not know whether the excess cancer death rates of these survivors will rise, remain the same, or decrease during the coming years.
>
> We would estimate that definitive answers to these questions will take a further 20 to 30 years of follow-up by the ABCC and could refine present risk estimates down by a factor of 2 or up by a factor of 3 to 4.[26]

As demonstrated by the examples on leukemia and breast cancer, use of in vivo doses in estimating risks from the ABCC studies will result in refinements equal in magnitude to those deemed important by this panel. Moreover, correlations of observed medical effects with in vivo doses are a necessity in interpreting differences in dose-specific analyses and deriving valid RBE's for neutrons from data for the two cities.

The estimates of absorbed dose to organs of survivors must be age dependent; that is, they must be applicable to survivors who were adult males, adult females, or juveniles at the time of bombing. Mathematical representations of adults and various age groups of juveniles being developed by the Medical Physics and Internal Dose Section will be modified to make them applicable to atomic bomb survivors. Some reports with information needed to modify these phantoms for use in the liaison dosimetry studies have been obtained from staff members of the ABCC. Calculations with these heterogeneous phantoms will supplement, but not necessarily replace, the depth-dose curves presented to the ABCC during the latest liaison study trip. The depth-dose curves will still be important in assessment of absorbed dose at a given point of interest, such as the isthmus of the thyroid, where benign and neoplastic nodules commonly occur.

In vivo dose estimates from neutron irradiation are much more difficult to obtain than those from gamma rays, because more interaction and scattering models are required in transport codes for the phantoms. For this reason, a technique is being investigated for obtaining absorbed doses by calculating chord length distributions for specific critical organs.

Although the emphasis is on in vivo dosimetry, some time was devoted to older, but still important, phases of the liaison dosimetry studies. These include (1) the radiation exposure received by survivors residing in the United States, (2) the epicenter of the Nagasaki weapon, (3) the shielding factors for survivors exposed in concrete buildings and other heavily shielding structures, and (4) the unknown T65D exposure cases in major study samples of the ABCC. Summaries are given in this section of progress made in several phases of the liaison dosimetry studies.

---

23. Ref. 7, Table A-7, p. 117.

24. C. E. Clifford and R. A. Facey, "Changes in Acute Radiation Hazards Associated with Changes in Exposure Geometry," *Health Phys.* 18, 217 (1970).

25. Ref. 7, pp. 100–106.

26. Ad Hoc Panel of the Committee on Nuclear Science, *Research Needs for Estimating the Biological Hazards of Low Doses of Ionizing Radiations,* National Research Council–National Academy of Sciences, Washington, D.C., 1974. pp. 28–30.

IN VIVO DOSE ESTIMATES FOR ATOMIC BOMB SURVIVORS

As reported last year,[27] depth-dose curves were obtained for exposure analogs of the spatially dependent radiation fields in Hiroshima and Nagasaki. These were based on computer-simulated analog exposure situations which in turn depend on transport calculations and on experimental data from the laboratory and the Nevada test site. As expected, the in vivo dose assignments for atomic bomb survivors are complex and require many data that are applicable on a marginal basis; however, most possible variations due to the questionable data are damped by the intraphantom transport processes. Since much of the dose to an in vivo organ appeared to have been delivered by photons at energies where dependence on atomic number is important, it was recommended that calculations for the four-element homogeneous tissue medium not be applied to predict doses to bone or red bone marrow.[28] An additional problem arises because the depth-dose curves are difficult to apply to organs that were irradiated nonuniformly. This situation may be illustrated by the red bone marrow system, for which it is difficult to assign a mean "in vivo dose." The problems caused by assigning a mean exposure value to a nonuniformly irradiated organ are being investigated through the application of a CHORD (critical human organ radiation dosimetry) concept.

The CHORD concept depends on probability density distributions $p\{l\}\,dl$ of length l. These CHORD length distributions are to be used as "weighting" factors for integrations over a "multicollision" depth curve derived from the source geometry of interest. A specific $p\{l\}\,dl$ distribution is obtained by assuming that the "critical organ" of distributed mass is simply a volume of constant density; for each differential unit of mass dm, chosen by Monte Carlo techniques, the minimum distance l to the closest irradiated air-tissue interface is uniquely determined. This process is continued until $p\{l\}\,dl$ is well known statistically.

In radiology, the dose at a penetration depth of 5 cm is often chosen to describe the exposure of the red bone marrow. However, for photon irradiation this approximation is often in error by a factor of 2;[29] it is expected to be even worse for neutron irradiation. This rule tends to retain popularity in spite of its inaccuracy, because the red marrow is distributed widely in the skeleton and the "5-cm rule" is simple to remember and easily applied. For an organ such as the red bone marrow, having distributed mass exposed to a source of radiation where dose-vs-depth curves are known for single energies, existing "multicollision" depth-dose curves can be used in a simple moment-type computation according to

$$M\{D(t)_{\mathrm{RM}}\} = \frac{\int_E [\int_l D(t, E, l)\, p\{l\}\, dl]\; \rho\{E\}\, dE}{\int_l p\{l\}\, dl \;\; \int_E \rho\{E\}\, dE}$$

$$= \frac{\sum_{i=1}^{n} \sum_{j=1}^{m} D(t, E_i, l_j)\, p\{l_j\}\, \Delta l_j\, \rho\{E_i\}\, \Delta E_i}{\sum_{i=1}^{n} \rho\{E_i\}\, \Delta E_i \;\; \sum_{j=1}^{n} p\{l_j\}\, \Delta l_j}. \tag{1}$$

In Eq. (1), $M\{D(t)_{\mathrm{RM}}\}$ is the mean dose to the red marrow for a specific type of radiation denoted by t; $D(t, E, l)$ is taken from the existing "multicollision" depth-dose distributions for a monoenergetic source energy E at a penetration depth of l which is the distance of a differential unit of mass, dm, from the closest irradiated air-tissue interface; and $dP\{l\} = p\{l\}\,dl$ is the differential probability density function of length. Although l must be computed according to the geometrical distribution of mass, dm, it is stochastically independent with respect to other variables in the equation. Calculations for other organs would be done in the same fashion, and the red marrow was chosen only to illustrate the method. If depth-dose information is available for the spectrum of interest, then the expected dose can be obtained by simply integrating Eq. (1) over l. Once Eq. (1) has been solved, the expected dose could be related back to a specific l, but it is obvious that l cannot remain invariant for different irradiation situations.

For the past several years, many depth-dose distributions, usually in the form of graphs or equations, have been developed. Generally, these investigations have explored depth-dose sensitivity, in homogeneous media, to the variation in important physical parameters. Some of the more important physical parameters are the spatial distribution of the radiation about the source, the degree of collimation, the type of radiation,

27. *Health Phys. Div. Annu. Progr. Rep. July 31, 1974*, ORNL-4979.

28. T. D. Jones, J. A. Auxier, J. S. Cheka, and G. D. Kerr, "In-Vivo Dose Estimates for A-Bomb Survivors Shielded by Typical Japanese Houses," *Health Phys.* **28**, 367 (1975).

29. T. D. Jones, J. A. Auxier, W. S. Snyder, and G. G. Warner, "Dose to Standard Reference Man from External Sources of Monoenergetic Photons," *Health Phys.* **24**, 241 (1973).

the energy distribution of a given type, the medium of irradiation, and the geometry of the medium.

In radiation protection, low-level population exposures, or studies of dose-specific effects,[30] there are usually "critical organs," which are either more radiosensitive or more important in the traditional genetic reproductive structure. These critical organs may include blood, red bone marrow, developing fetus, thyroid gland, cervix, prostate gland, portions of bone, testes, ovaries, lenses of the eyes, etc. The specific organ choices usually conform to committee recommendations for radiation protection of progeny or regions of possible neoplastic soft tumors, bone sarcomas, etc. These CHORD probability distributions should be applicable to common types of radioactive particles, microwaves, and even other electromagnetic radiations.

In addition to the CHORD density functions from a 2π isotropic source analog for the Japanese atomic bomb studies, additional calculations of CHORD distributions for anterior-posterior, posterior-anterior, and 4π isotropic exposure of reference-man-type calculational analog phantoms would complement the existing depth-dose and depth-dose-equivalent information. The absorbed-dose index D_I and dose-equivalent index H_I for the standard 30-cm sphere as recommended by ICRU Report 19[14] would become even less useful for radiation protection. By using these CHORD probability density functions plus standard "multicollision" dose vs depth curves, a health physicist could easily and quickly estimate values of exposure to biological organs of interest. It is becoming apparent that significant calculational and experimental efforts will soon be directed to the estimation of organ exposures due to microwave irradiations. The use of $p\{l\}\,dl$ distributions should simplify microwave dosimetric calculations; CHORD $p\{l\}\,dl$ distributions could be easily programmed or hard-wired into the logic of minicomputers or microcomputers interfaced to instruments of detection.

Thus, it is sufficient to say that the problem introduced by nonuniform irradiation of critical organs in the atomic bomb survivors is expected to be solved by the CHORD concept. As for the difficulty introduced by different chemical compositions of bone marrow and bone tissue, the doses from neutron irradiation are expected to be obtainable from an application of CHORD length density functions, because the hydrogen density abundance is not greatly different between bone and standard soft tissue. In vivo dose calculations are under way for photon irradiations. Because the Compton, pair-production, and photoelectric interaction processes are often strongly influenced by the magnitude of the mean atomic number,[29] the Monte Carlo transport method is being employed. These Monte Carlo simulated irradiations of a reference-man-type phantom in a spatially dependent radiation field present some new sampling difficulties.

For Monte Carlo simulated irradiation of a detector[31] immersed in a spatially dependent field of radiation, the points of entrance of the irradiating particles may be selected uniformly according to differential units of surface area. Each position of entrance should then be either accepted or rejected according to the comparison of the magnitude of a pseudorandom number, chosen between zero and unity, with an evaluation of a probabilistic model, derived from the angular fluence intensities of the irradiating field about the point of interest. A method of "particle-current-to-fluence" conversion for instruments of detection or for Monte Carlo simulated irradiation was published previously[32] and is applicable to radiation analogs discussed here. This probabilistic model of the angular fluence intensities, $P\{\theta, \phi\}$, should be selected so that the relative responses for different directions are linear, and, for economy, a value of unity indicates the direction of the maximum irradiating fluence. For an isotimic surface defined by $f(X, Y, Z)$ = constant, it is often convenient to select points of entrance randomly but nonuniformly with either surface area or angular fluence intensity and to additionally modify the probabilistic model in order to take this into account. This modification of $P\{\theta, \phi\}$ by $M\{\theta, \phi\}$ yields a new density function

$$E\{\theta, \phi\} = M\{\theta, \phi\}\, P\{\theta, \phi\} \tag{2}$$

and describes the expectation probability of a particle's acceptance.

A density function $M\{\theta, \phi\}$, which helps to describe the "fate" of a point, may be determined from a comparison of differential arc lengths when irradiated areas are determined by the magnitudes of the arc lengths. Such is the case for most surfaces used to approximate a bioorganism for computer simulations

30. Studies of dose-specific effects include those based on the atomic bomb survivors, the ankylosing spondylitics, large animal experiments, etc.

31. In this paper, "detector" indicates any irradiated surface and can mean a dosimeter or a bioorganism but *not* a point of detection as it often does in neutron physics.

32. T. D. Jones, "Particle Current to Fluence Conversion for Instruments of Detection and for Monte Carlo Simulated Radiation Transport," *Health Phys.* 28, 451 (1975).

and for almost all sensitive volumes of instruments of detection.

For an arbitrarily shaped curve described in polar coordinates by $S(\rho, \lambda)$, the differential arc length dS relative to a differential change in the angle of rotation $d\lambda$ may be expressed as

$$dS/d\lambda = [\rho^2 + (d\rho/d\lambda)^2]^{1/2} . \tag{3}$$

The normalization of the $M\{\lambda\}$ distribution requires the determination of all roots of $d^2S/d\lambda^2$ and an investigation as to which root yields the maximum value of $dS/d\lambda$. This Max $[dS(\lambda)/d\lambda]$ then becomes the normalizing factor of the probabilistic density function denoted by $M\{\lambda\}$. In order to obtain $d^2S/d\lambda^2$ and then evaluate the Max $[dS(\lambda)/d\lambda]$, it is necessary to express ρ as a function of λ and to form $d\rho/d\lambda$.

This technique is most profitably illustrated for the practical case of an elliptical cylinder where

$$\rho^2 = \frac{A^2B^2}{A^2 \sin^2 \lambda + B^2 \cos^2 \lambda} \tag{4}$$

and

$$\frac{dS}{d\lambda} = \frac{\rho[A^4B^4 + (B^2 - A^2)^2\rho^4 \cos^2 \lambda \sin^2 \lambda]^{1/2}}{A^2B^2} = \frac{\rho^3}{A^2B^2}(B^4 \cos^2 \lambda + A^4 \sin^2 \lambda)^{1/2} . \tag{5}$$

In order to obtain the density function for the probabilistic schema, it is necessary to compute

$$M\{\lambda\} = \frac{dS(\lambda)/d\lambda}{\text{Max } [dS(\lambda)/d\lambda]} \tag{6}$$

for each and every point of entrance.

From Eq. (5),

$$\frac{1}{AB(A^2 - B^2)}\left(\frac{d^2S}{d\lambda^2}\right) = (\sin \lambda \cos \lambda)[(A^2 + B^2) \times (A^2 \sin^2 \lambda + B^2 \cos^2 \lambda) - 3(B^4 \cos^2 \lambda + A^4 \sin^2 \lambda)] \times (B^4 \cos^2 \lambda + A^4 \sin^2 \lambda)^{-1/2} \times (A^2 \sin^2 \lambda + B^2 \cos^2 \lambda)^{-5/2} . \tag{7}$$

Zeros of Eq. (7) occur when

$$\sin \lambda = 0 , \tag{8}$$

which implies $\lambda_1 = 0$ or π,

$$\cos \lambda = 0, \tag{9}$$

which implies $\lambda_2 = \pm\pi/2$,

and

$$(A^2 + B^2)(A^2 \sin^2 \lambda + B^2 \cos^2 \lambda) - 3(B^4 \cos^2 \lambda + A^4 \sin^2 \lambda) = 0 . \tag{10}$$

If

$$f = B/A , \tag{11}$$

then roots of Eq. (10) are found when

$$\lambda_0 = \text{arc sin} \left\{ f\left[\frac{1 - 2f^2}{2(1 - f^4)}\right]^{1/2} \right\} \tag{12}$$

and

$$\frac{dS(\lambda_0)}{d\lambda} = \frac{Af(\sin^2 \lambda_0 + f^4 \cos^2 \lambda_0)^{1/2}}{(\sin^2 \lambda_0 + f^4 \cos^2 \lambda_0)^{3/2}} , \tag{13}$$

which is then compared with A and B from roots (8) and (9) in order to select the Max $[dS(\lambda)/d\lambda]$. Equation (12) breaks down for a narrow range of λ, and in this region the normalizing factor becomes either A or B. This method of obtaining the normalizing factor is similar conceptually to that used by Dillman[33] in the infinite isotropic cloud calculations, although the applications and results are somewhat different.

The preceding probability density function modification is usually applied to cases where the differential units of surface are proportional to differential arc lengths, and in these cases the points of entry are usually predicted easily from a systematic determination of the upper limits of integration of

$$R_i = \frac{1}{A}\int_{X_l, Y_l, Z_l}^{X_u, Y_u, Z_u} da(X, Y, Z) = \frac{1}{A}\int_{\rho_l, \lambda_l, Z}^{\rho_u, \lambda_u, Z} da(\rho, \lambda, Z) , \tag{14}$$

where R_i is a pseudorandom number, uniform on the net interval zero to unity, A is the total surface area of the detector, and da is a differential unit of surface

33. L. T. Dillman, *Health Phys.* 27, 571 (1974).

area.[32] Unfortunately, Eq. (14) is sometimes difficult to solve for the upper limits of integration – for example, when the irradiated surface is not "well defined" by differential arc lengths; hence, one must resort to other means. One such alternative technique is to select a random distribution of points on a selected surface, project these points on the surface exposed to the irradiating particle so that there is an isomorphism of points between the two surfaces, and apply Monte Carlo techniques according to a probability density function.

An example of the application of this principle is the determination of points of entrance uniformly on the lateral surface area of a frustum of a right elliptical cone defined by

$$\frac{X^2}{(A^2/C^2)(Z+C)^2} + \frac{Y^2}{(B^2/C^2)(Z+C)^2} = 1. \qquad (15)$$

Equation (15) for $A = 20$, $B = 10$, $C = 100$, and $-80 \leqslant Z \leqslant 0$ is used to simulate the combined two legs of a person for the reference-man phantom[34] which is used for computer experiments involving spatially dependent radiation fields.

To sample uniformly with surface area, one is tempted to choose Z from a density function obtained from the ratios of perimeters in a plane parallel to $Z = 0$:

$$P\{Z\} \doteq \frac{(\sqrt{2}\,\pi/C)(Z+C)(a^2+b^2)^{1/2}}{\sqrt{2}\,\pi\,(a^2+b^2)^{1/2}}\ ; \qquad (16)$$

however, this is equivalent to sampling between planes at Z and $Z + dZ$. This method may yield usable results but is basically incorrect because the strip of differential area between Z and $Z + dZ$ is of variable width. In order to obtain the density function for use in our probabilistic model, let us assume that we have a function $f(X, Y, Z)$ and corresponding surface normal vector defined by

$$\mathbf{N}_f = \frac{\partial f}{\partial X}\hat{\mathbf{i}} + \frac{\partial f}{\partial Y}\hat{\mathbf{j}} + \frac{\partial f}{\partial Z}\hat{\mathbf{k}} \qquad (17)$$

and that $f(X, Y, Z)$ can be projected on another surface $g(X, Y, Z)$ which has a surface normal vector defined by

$$\mathbf{N}_g = \frac{\partial g}{\partial X}\hat{\mathbf{i}} + \frac{\partial g}{\partial Y}\hat{\mathbf{j}} + \frac{\partial g}{\partial Z}\hat{\mathbf{k}}\ . \qquad (18)$$

34. W. S. Snyder, M. R. Ford, G. G. Warner, and H. L. Fisher, Jr., MIRD Pamphlet No. 5; *J. Nucl. Med.*, Suppl. No. 3 **10** (August 1969).

The surface $g(X, Y, Z)$ is arbitrary but must be defined so that it is possible to select points randomly and uniformly within its bounds and that $\mathbf{N}_f \cdot \mathbf{N}_g$ does not vanish. If we consider a differential unit of area da_f on $f(X, Y, Z)$ and its corresponding differential projection $da_{f,g}$ on $g(X, Y, Z)$, then

$$\begin{aligned} da_{f,g} = da_f\,[&(\partial f/\partial X)(\partial g/\partial X) \\ &+ (\partial f/\partial Y)(\partial g/\partial Y) + (\partial f/\partial Z)(\partial g/\partial Z)] \\ &\times [(\partial f/\partial X)^2 + (\partial f/\partial Y)^2 + (\partial f/\partial Z)^2]^{-1/2} \\ &\times [(\partial g/\partial X)^2 + (\partial g/\partial Y)^2 + (\partial g/\partial Z)^2]^{-1/2}\ , \end{aligned} \qquad (19)$$

or, more simply, $da_{f,g} = da_f \cos\lambda$, where λ is the angle between surface normals. If $\cos\lambda$ does not vanish, then

$$da_f = da_{f,g}/\cos\lambda\ . \qquad (20)$$

In order to apply this technique, it is necessary to determine the minimum value of $\cos\lambda$ so that

$$1 \leqslant \frac{1}{\cos\lambda} \leqslant \frac{1}{(\cos\lambda)_{\min}}\ . \qquad (21)$$

The density function for the probabilistic model is then obtained from

$$(\cos\lambda)_{\min} \leqslant \frac{(\cos\lambda)_{\min}}{\cos\lambda} \leqslant 1 \qquad (22)$$

and becomes

$$M\{\lambda\} = \frac{(\cos\lambda)_{\min}}{\cos\lambda}\ . \qquad (23)$$

For a spatially dependent field, the direction of travel of the ith irradiating particle (i.e., $\mathbf{D}_i = U_i\hat{\mathbf{i}} + V_i\hat{\mathbf{j}} + W_i\hat{\mathbf{k}}$, must be selected so that the angle θ_i, determined by the velocity vector $\mathbf{D}_i$ and the surface normal $\mathbf{N}_i$, is from a distribution that varies with differential units of subtended solid angle according to the $M\{\theta, \phi\}$ modification.[35] The surface normal vector $\mathbf{N}$ for any point (X_i, Y_i, Z_i) on an isotimic surface where the partial derivatives $\partial f/\partial X$, $\partial f/\partial Y$, and $\partial f/\partial Z$ exist and are continuous is found to be

$$\mathbf{N} = \mathbf{grad}\, f = \frac{\partial f}{\partial X}\hat{\mathbf{i}} + \frac{\partial f}{\partial Y}\hat{\mathbf{j}} + \frac{\partial f}{\partial Z}\hat{\mathbf{k}}\ ; \qquad (24)$$

35. θ in this algorithm is not necessarily defined in the same way as θ in the $M\{\theta, \phi\}$ distribution.

so, for the ith particle,

$$\mathbf{N}_i \cdot \mathbf{D}_i = |\mathbf{N}_i| \cos \theta_i \,, \tag{25}$$

or

$$[(\partial f/\partial X)_i^2 + (\partial f/\partial Y)_i^2 + (\partial f/\partial Z)_i^2]^{1/2} \cos \theta_i$$
$$= U_i(\partial f/\partial X)_i + V_i(\partial f/\partial Y)_i + W_i(\partial f/\partial Z)_i \,. \tag{26}$$

If θ_i, ψ_i, and ϕ_i are defined as in Fig. 10.1, then θ_i and ψ_i must be selected according to the angular distribution of the radiation field of interest. [For any isotropic-type field, θ_i = arc cos R_n and $\psi_i = 2\pi R_m$, where R_n and R_m are pseudorandom numbers.[32]] The angle ϕ_i is determined from

$$\phi_i = \text{arc sin} \left\{ \frac{(\partial f/\partial Z)_i}{[(\partial f/\partial X)_i^2 + (\partial f/\partial Y)_i^2 + (\partial f/\partial Z)_i^2]^{1/2}} \right\} , \tag{27}$$

ORNL-DWG 75-276

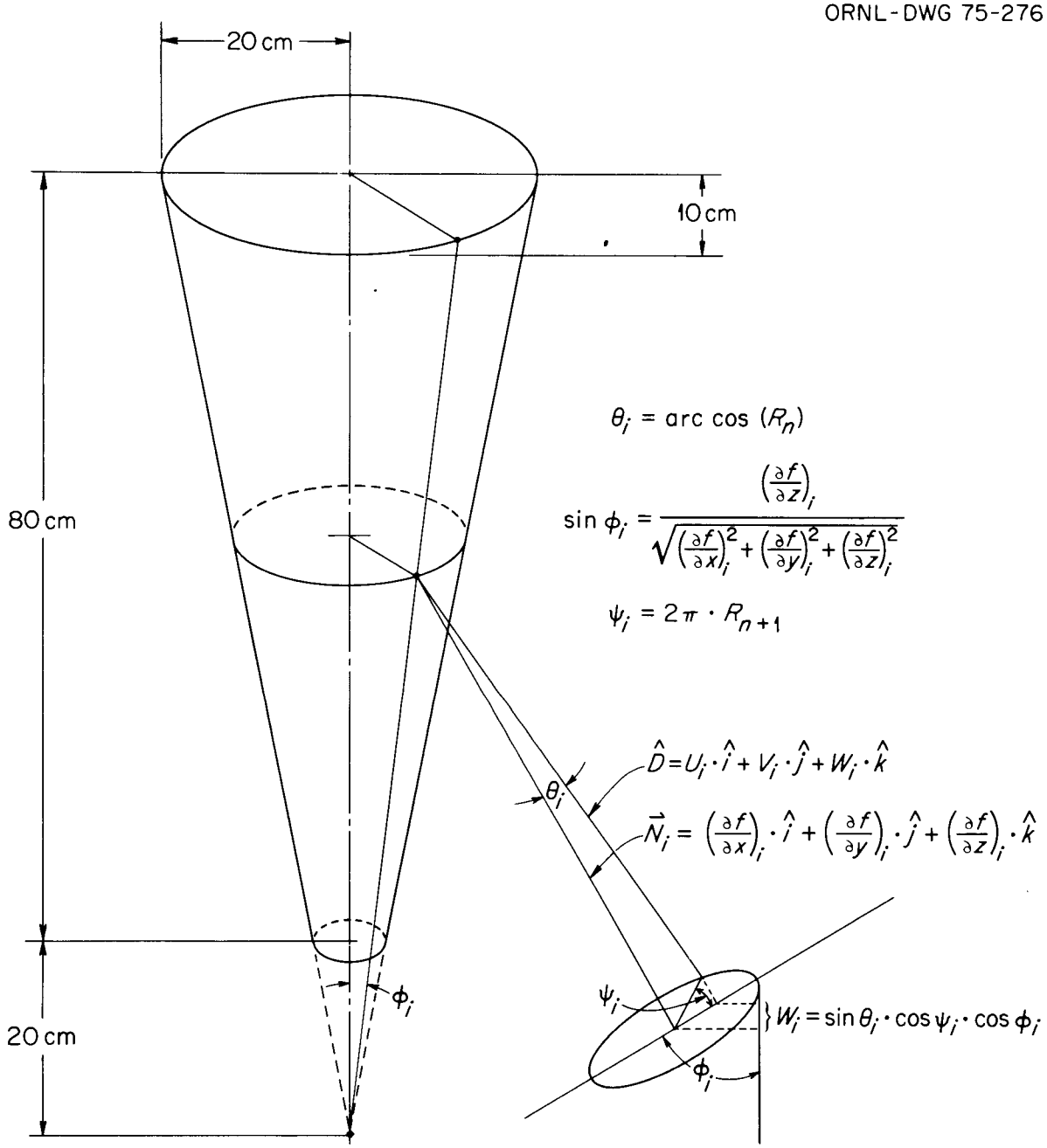

Fig. 10.1. Surface normal vector and particle incidence on a right elliptical cone.

and Fig. 10.1 shows that

$$W_i = \sin\theta_i \cos\psi_i \cos\phi_i \,. \tag{28}$$

Now if

$$\alpha_i = \cos\theta_i \times [(\partial f/\partial X)_i^2 + (\partial f/\partial Y)_i^2 + (\partial f/\partial Z)_i^2]^{1/2} \tag{29}$$

is substituted into Eq. (26), it can then be solved for U_i, yielding

$$U_i = \frac{\alpha_i - V_i(\partial f/\partial Y)_i}{(\partial f/\partial X)_i} \,. \tag{30}$$

Substitution of Eq. (30) into

$$U_i^2 + V_i^2 + W_i^2 = 1 \tag{31}$$

yields

$$V_i^2\,[(\partial f/\partial X)_i^2 + (\partial f/\partial Y)_i^2] + V_i[-2\alpha_i(\partial f/\partial Y)_i^2] + \alpha_i^2 + (W_i^2 - 1)(\partial f/\partial X)_i^2 = 0\,, \tag{32}$$

and the solution yields two values of V_i. The choice of one of these values must be determined from the amount of the radiation incident from below the horizon relative to the amount incident from above the horizon for the given horizontal angle of interest.

RADIATION EXPOSURE TO ATOMIC BOMB SURVIVORS RESIDING IN THE UNITED STATES

A study of radiation exposure to atomic bomb survivors residing in the United States was started in 1973 at the request of the USAEC. These survivors consist of Japanese-Americans trapped in Japan during the war, Japanese wives of U.S. servicemen, Japanese immigrants to the United States after the war, and some American servicemen who were prisoners of war in Nagasaki.

In 1973, information of variable quality on 69 survivors was obtained from Dr. Thomas Noguchi, Chief Medical Examiner-Coroner for the County of Los Angeles. This information was analyzed in cooperation with the ABCC during a liaison study trip.[36] Preliminary radiation exposure estimates were made for 44 of these 69 survivors. Based on these preliminary results, the USAEC decided to extend the study to include additional survivors in the Los Angeles and San Francisco areas.

In the early phases of this larger study, emphasis was on obtaining reliable information on as many survivors in these two areas as possible.[37] Efforts of voluntary bilingual interviews were coordinated by Dr. Noguchi and Dr. Francis J. Curry, Director, and Dr. Lorraine Smookler, Assistant Director, Department of Public Health for the City and County of San Francisco. The response was greater than anticipated, due in part to attention given to the study by news media on the West Coast. Estimates of the number of survivors in the United States have been increased from 500 to 1000.

Presently, we have information on over 300 survivors in our files. This information is in the form of questionnaires completed by the survivors with the voluntary help of bilingual survivors. The questionnaires are used to identify each survivor, to establish his approximate location at the time of bombing, and to search the master files of the ABCC for additional pertinent information on him. Searches of the files of the ABCC have been completed on 267 survivors. Of these, 123 were listed in their files, and T65D dose estimates were available for 32. Emphasis at present is on completing T65D dose estimates for the other 235 in this group of 267 survivors.

During trips to the West Coast in November of 1974 and March of 1975, H. Yamada has helped the survivors establish their exact location at the lime of bombing by using old maps and aerial photographs of Hiroshima and Nagasaki. Shielding histories were also prepared for those exposed close to the hypocenters of the two weapons. Interviews with the survivors were arranged by several chapters of the Committee of Atomic Bomb Survivors in the United States. These included the Los Angeles, San Francisco, San Jose, and Sacramento chapters. In addition to these areas, survivors have been interviewed in Fresno, California; Denver, Colorado; Salt Lake City, Utah; and Amarillo, Texas.

The difficult task of estimating building attenuation factors for survivors exposed in concrete and other heavily shielded structures has been completed, and the T65D estimates are now being completed for those exposed in houses and more lightly shielded structures. A report summarizing results for the group of 267 will be completed in mid-1975. These results are needed by physicians treating survivors and are important as

36. *Health Phys. Div. Annu. Progr. Rep. July 31, 1973*, ORNL-4903, pp. 1–2.

37. *Health Phys. Div. Annu. Progr. Rep. July 31, 1974*, ORNL-4979, pp. 187–90.

supporting evidence for proposed federal and state legislation providing medical aid to some qualified survivors.

TRANSMISSION OF PHOTONS THROUGH COMMON SHIELDING MEDIA

For narrow-beam monochromatic photon irradiation of a slab of shielding material, the uncollided fluence $\phi(x)$ at a penetration depth x into the shield may be expressed as $\phi(x) = \phi_0 e^{-\mu x}$, where ϕ_0 is the uncollided fluence at the front of the shield and μ is the linear attenuation coefficient of the shielding medium. Broad-beam irradiation produces a scatter component that increases the fluence and consequently causes a dose buildup over the uncollided values of a narrow-beam geometry, which loses all of its scatter component. The dose (exposure, fluence, or kerma) buildup factor is defined as the ratio of the dose due to the entire fluence to that arising from the unscattered fluence,[38] so that it is possible to describe kerma at depth x according to $K(x) = K_0\, B(G, S, M)\, e^{-\mu x}$, where K_0 denotes the kerma value, usually in air or biological tissue, at the position of the front of the shield except in its absence. The attenuation coefficient μ is representative of the shield. The numerical difference between the buildup computed for air and that for tissue is small.[39] The real issue is often academic, and, for this reason, some investigators prefer air[38,40] while others prefer tissue. In many instances it would be even more convenient to base the buildup on the medium of irradiation, in which case the magnitude of the difference may become significant. The functional form of the buildup is represented by $B(G, S, M)$, where G, S, and M indicate functional responses due to geometry, source parameters, and medium of irradiation, respectively.

For this work, slabs of shielding media were assumed to be irradiated normally by broad beams of monochromatic photons. The kerma buildup factors for iron and water from Goldstein and Wilkins[38] and for ordinary concrete from Chilton[41] were interpolated and extrapolated as functions of energy in order to span the range of the energy spectrum from a typical thermonuclear weapon at 1200 m and from fission product gamma rays.[42] Extrapolation often is a deceptive process; however, only small amounts of the kerma contributions occur outside the end points of Goldstein's buildup tabulations. The buildup factors in ordinary concrete appear to be known with less certainty than those for iron and water; therefore, our estimated buildup factors shown in Fig. 10.2 were based on Chilton's results.[41] Kerma buildup factors for polymeric wood cellulose, $(C_6H_{10}O_4)_n$, for a spherical boundary about a point isotropic source were calculated by Clark;[43] however, a search of the literature revealed no buildup factors for broad normal irradiation of wood or cellulose. If Compton, pair-production, and photoelectric interactions are assumed to occur according to Z, Z^2, and Z^5 respectively,[44] then total doses

38. H. Goldstein and J. E. Wilkins, Jr., *Calculations of the Penetration of Gamma Rays,* NYO-3075, Nuclear Development Associates (1954).

39. F. H. Clark and D. K. Trubey, for *Nucl. Appl.* 4, 37–41 (1968).

40. A. B. Chilton, "Buildup Factors for Point Isotropic Gamma Ray Sources in Infinite Medium of Ordinary Concrete," *Nucl. Eng. Design* 6, 205–12 (1967).

41. A. B. Chilton, *Engineering Compendium on Radiation Shielding,* ed. by R. G. Jaeger et al., Springer-Verlag, New York, 1968, vol. I, pp. 210–26.

42. J. A. Auxier et al., *Nuclear Weapons Free-Field Environment Recommended for Initial Radiation Shielding Calculations,* ORNL-TM-3396 (1972).

43. F. H. Clark, "Gamma-Ray Buildup Factors for Sand, Air, and Wood (Cellulose)," *Nucl. Appl.* 6, 588–93 (1969).

44. R. D. Evans, *The Atomic Nucleus,* McGraw-Hill, New York, 1955.

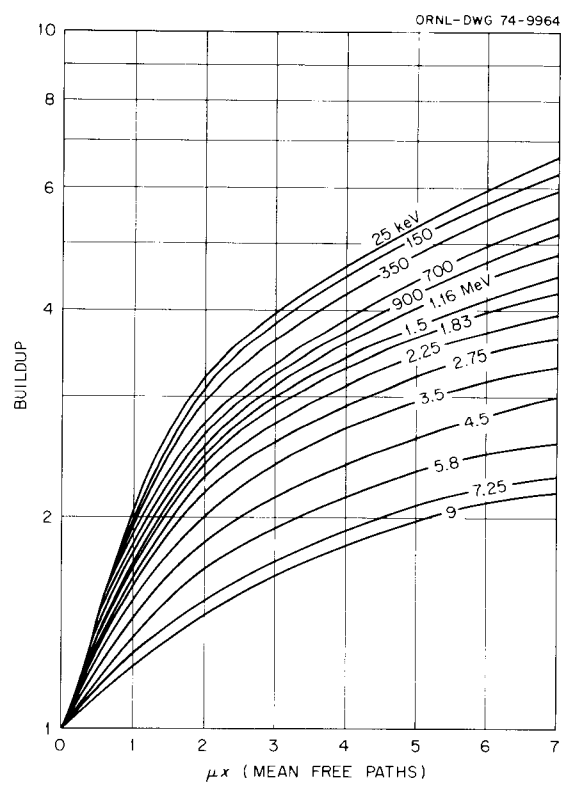

Fig. 10.2. Exposure buildup factors for broad beams of monoenergetic photons normally incident on ordinary concrete.

(kerma values) dependent on these quantities are not greatly different for water and cellulose; so buildup correction factors for broad normal irradiation of water relative to a point isotropic source in an infinite water medium were applied to Clark's buildup factors for cellulose. These factors are given in Fig. 10.3. Cellulose is listed as having a specific gravity of 1.27 to 1.61,[45] but these calculations assumed a value of 0.64, which corresponds to the specific gravity of longleaf pine.[45]

A search of the literature revealed no applicable buildup factors for soil; however, buildup factors in silicon dioxide from a point isotropic source were available.[43] The chemical composition of ordinary soils can vary significantly from silicon dioxide. However, it is expected that major differences in attenuation coefficients are due to the greater density of silicon dioxide (2.65); it appears that the transmission factors for silicon dioxide should be fairly representative of ordinary soils if they are normalized to a mean specific gravity of 1.60. Since buildup factors for normal incidence on silicon dioxide were not available, Table 10.2 was constructed. It shows the ratio of the broad-beam buildup factor to the corresponding point isotropic factor as a function of energy, penetration depth in mean free path lengths, and atomic number for

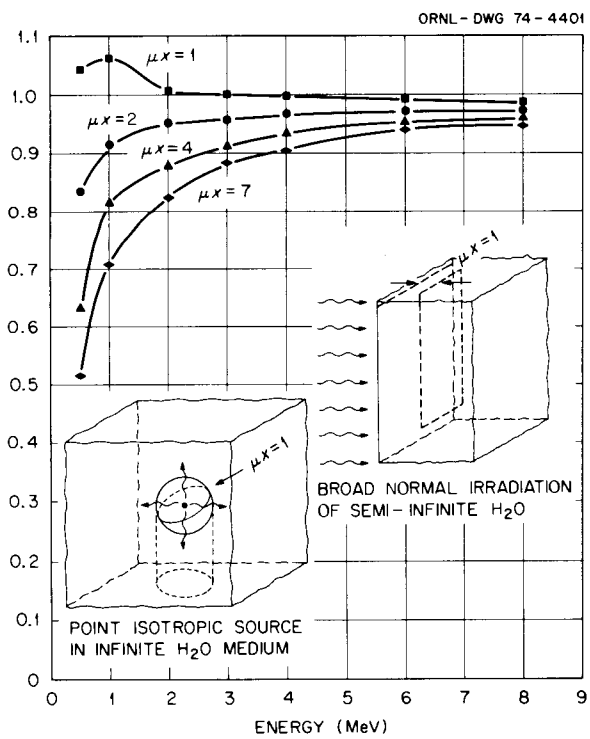

Fig. 10.3. Photon dose buildup from broad normal irradiation of H_2O relative to that from a point isotropic source in H_2O.

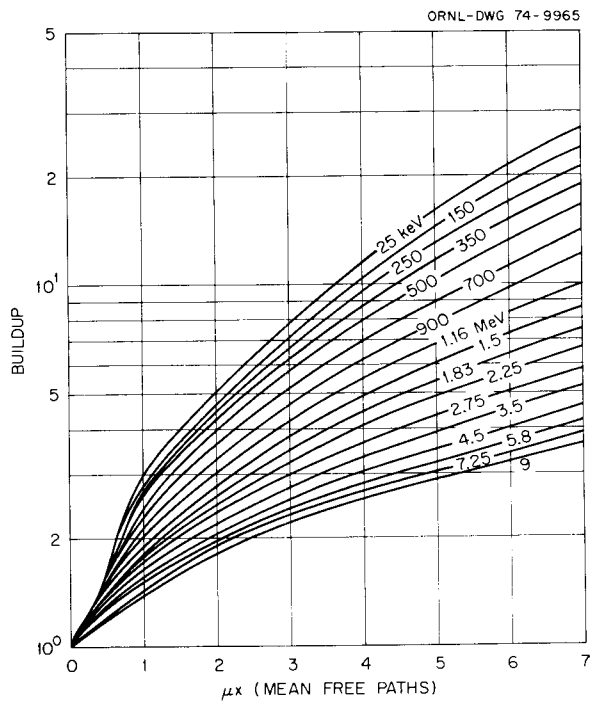

Fig. 10.4. Estimated exposure buildup factors for broad beams of monoenergetic photons normally incident on SiO_2.

Z ranging from 3.33 to 92. It appears that the buildup factors are not strongly dependent on Z except for the lower energies and greater penetration depths.

Table 10.2 also indicates that the ratios for concrete are not in line with those for other media; for applications requiring precise estimates of transmission, the buildup factors for ordinary concrete[41] should be checked. For most shielding applications, however, Chilton's results should be sufficient. Point-isotropic-to-broad-beam conversion factors based on Table 10.2 were applied to Clark's buildup factors[43] in order to obtain the values given in Fig. 10.4.

The transmission of gamma rays in terms of kerma through iron, water, wood, silicon dioxide, and ordinary concrete for selected monochromatic sources was computed.[46] In addition, the transmission averaged over the typical fission product and thermonuclear spectra was computed according to

$$T_x = \frac{\Sigma k(E)\, T(E, x)\, \Delta E}{\Sigma k(E)\, \Delta E},$$

45. *Handbook of Chemistry and Physics*, Chemical Rubber Company, Cleveland, Ohio, 1961.

46. T. D. Jones and F. F. Haywood, *Transmission of Photons through Common Shielding Media*, ORNL-TM-4728 (1975).

Table 10.2. Ratio of the broad-beam buildup factor to the corresponding point isotropic buildup factor as a function of energy, penetration depth, and material with increasing atomic number

Material	$\mu x = 1$	$\mu x = 2$	$\mu x = 4$	$\mu x = 7$
		0.5 MeV		
Water	1.04	0.84	0.63	0.52
Concrete[a]	0.85	0.73	0.47	0.30
Fe	1.05	0.95	0.81	0.71
Sn				
U	1.00	0.98	0.98	0.96
Mean[b]	1.03 (0.99)	0.92 (0.88)	0.81 (0.72)	0.73 (0.62)
		1 MeV		
Water	1.06	0.91	0.82	0.71
Concrete	0.91	0.83	0.59	0.40
Fe	1.03	0.95	0.85	0.77
Sn	1.01	0.97	0.91	0.84
U	0.99	0.98	0.96	0.93
Mean	1.02 (1.00)	0.95 (0.93)	0.88 (0.83)	0.81 (0.73)
		2 MeV		
Water	1.01	0.95	0.88	0.82
Concrete	0.95	0.91	0.72	0.53
Fe	0.96	0.97	0.91	0.84
Sn	1.01	0.98	0.93	0.87
U	1.00	0.99	0.96	0.94
Mean	1.00 (0.99)	0.97 (0.96)	0.92 (0.88)	0.87 (0.80)
		3 MeV		
Water	1.00	0.96	0.91	0.88
Concrete	0.96	0.92	0.76	0.58
Fe	1.02	0.99	0.95	0.90
Sn				
U	1.00	0.99	0.96	0.92
Mean	1.01 (1.00)	0.98 (0.96)	0.94 (0.90)	0.90 (0.82)
		4 MeV		
Water	1.00	0.97	0.93	0.90
Concrete	0.96	0.91	0.76	0.60
Fe	1.02	0.98	0.97	0.94
Sn	1.01	0.99	0.95	0.89
U	1.01	0.99	0.97	0.92
Mean	1.01 (1.00)	0.98 (0.97)	0.96 (0.92)	0.91 (0.85)
		6 MeV		
Water	0.99	0.97	0.95	0.94
Concrete	0.92	0.85	0.73	0.57
Fe	1.01	0.99	0.96	0.92
Sn	1.01	1.00	0.96	0.89
U	1.02	1.01	0.98	0.93
Mean	1.01 (0.99)	0.99 (0.96)	0.96 (0.92)	0.92 (0.85)
		8 MeV		
Water	0.99	0.97	0.96	0.95
Concrete	0.89	0.82	0.70	0.56
Fe	1.00	0.99	0.97	0.94
Sn				
U	1.01	1.00	0.97	0.92
Mean	1.00 (0.97)	0.99 (0.94)	0.97 (0.90)	0.94 (0.84)

Table 10.2 (continued)

Material	$\mu x = 1$	$\mu x = 2$	$\mu x = 4$	$\mu x = 7$
		10 MeV		
Water				
Concrete	0.92	0.83	0.71	0.59
Fe	1.02	1.01	1.00	0.97
Sn	1.02	1.02	0.99	0.94
U	1.01	1.01	0.98	0.94
Mean	1.02 (0.99)	1.01 (0.97)	0.99 (0.92)	0.95 (0.86)

[a]Values for ordinary concrete are based on those of A. B. Chilton, *Engineering Compendium on Radiation Shielding*, ed. R. G. Jaeger et al., Springer-Verlag, New York, 1968, vol. 1, pp. 210–26.

[b]Value in parentheses in average; other value excludes concrete.

where T_x is the transmission in terms of kerma from the spectrum at depth x and $T(E, x)$ is the monochromatic transmission of kerma $k(E)$ for energy E at depth x. Transmissions of photons from fission products and from the thermonuclear spectrum are shown in Figs. 10.5 and 10.6.

Under shielding conditions, the densities of iron, water, and ordinary concrete are, for the most part, controlled by temperature and are not expected to vary significantly over the usual temperature range of ambient air. The densities of soil and construction-grade wood are also affected by moisture and can vary by about a factor of 2. Thus, for certain applications, it might be desirable to adjust the penetration depths shown as abscissas; for example the penetration in wood having a different specific gravity can be obtained by scaling according to the ratio of densities, $\rho/0.64$.

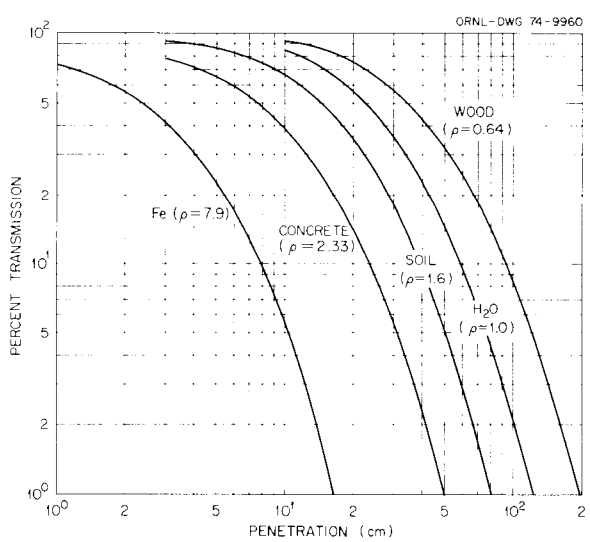

Fig. 10.5. Transmission of photon kerma from fission product gamma rays.

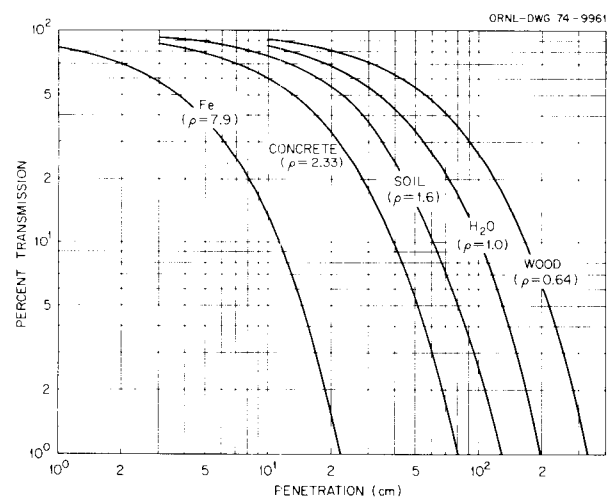

Fig. 10.6. Transmission of photon kerma from a typical thermonuclear weapon at 1200 m.

11. Application of ALAP Concept to Light-Water Reactors

H. W. Dickson M. P. Kanduc[1] W. D. Cottrell

Recently much attention has been given to reducing exposures to the general population in the vicinity of operating nuclear power plants. An exposure objective quantity is now specified by 10 CFR 50 at the site boundary. The population dose within a 50-mile radius of a new 1000-MW(e) plant is in the range of 10 to 100 man-rems. Unfortunately, occupational exposures at these plants have not received the same attention, and only now are they being examined as carefully under the as-low-as-practicable (ALAP) philosophy. In 1973, plant exposures[2] ranged from a low of 74 man-rems at Pilgrim to a high of 5134 man-rems at Indian Point, where a great deal of special maintenance and repair took place. There is also a trend, especially noticeable at boiling-water reactors (BWR's), toward increasing occupational exposure as the plants get older. Furthermore, the average number of persons exposed at each plant has been increasing. There is no good basis for predicting future occupational exposure; however, the present data are sufficient to make it clear that something must be done to reduce these exposures.

The current work is aimed at application of the ALAP concept to exposure of workers at light-water reactors (LWR's). The purpose of this program is to investigate the means by which the radiation exposure of workers at operating LWR's can be reduced to the lowest practicable levels. Several operating LWR's are being visited to identify significant sources of exposure and to determine the magnitude of the exposures. As these sources are identified, work will concentrate on specific problem areas, and attempts will be made to determine the most practicable methods for reduction of such exposures. The results will serve as technical backup for preparation of regulatory guides.

Having established criteria for selecting nuclear power stations to be reviewed in depth, the schedule in Table 11.1 was arranged. Site reviews began with a review of general plant characteristics, radioactive waste systems, maintenance and refueling schedules, radiation protection staff, exposure records, and special problem areas specific to the plant. Most of this took place prior to the actual onsite visit by studying the safety analysis report, technical specifications, exposure records, etc. At the site, the review consisted of discussions with supervisory, maintenance, and radiation protection personnel; determination of the latest plant modifications; examination of the most recent exposure records; surveys of radiation exposure levels with survey instruments and integrating dosimeters (such as TLD's and pocket ionization chambers); and observation of routine and special maintenance that was being performed.

The study was divided into four phases, which overlap in time. Phase 1, which is nearing completion, deals with a preliminary overview of the problem, including reviews of records and site visits to identify significant problem areas. In phase II, specific problem areas will be studied in depth with regard to corrective measures to reduce exposure. These corrective measures will be evaluated with respect to ease of application and cost effectiveness. A suggested sequence of corrective measures, including alteration of both hardware and operating procedures, will be developed, and a cost–benefit comparison will be made to determine the extent to which the sequence should be implemented. Recommendations will be made regarding design considerations for new facilities. Phase III will consist of providing technical assistance in the drafting of regulatory guides as the specific problem areas are evaluated and corrective action recommended. Phase IV will be an extension of the study to other nuclear facilities including, but not necessarily limited to, high-temperature gas-cooled reactors, fuel reprocessing plants, and breeder reactors.

1. IAEA Fellow.
2. T. D. Murphy, *A Compilation of Occupational Radiation Exposures from Light Water Cooled Nuclear Power Plants*, WASH-1311, May 1974.

Table 11.1. Site visits

Site	Dates	Plant status	Reactor type
Browns Ferry – Unit 1	Dec. 16–20, 1974	Routine operation	BWR
Unit 2		Power testing	BWR
Big Rock Point	Jan. 22–27, 1975	Planned outage	BWR
Yankee Rowe	Feb. 10–14, 1975	Routine operation	PWR
Turkey Point – Unit 3	Mar. 3–7, 1975	Routine outage	PWR
Unit 4		Routine operation	PWR
San Onofre	Mar. 20–22, 1975	Refueling outage	PWR
Dresden – Unit 1	Mar. 31–Apr. 3, 1975	Extended outage	BWR
Unit 2		Extended outage	BWR
Unit 3		Routine operation	BWR
Zion – Unit 1	Apr. 2, 1975	Routine operation	PWR
Unit 2			
Ginna	Apr. 21–25, 1975	Refueling outage	PWR

A number of significant problem areas at LWR's have been identified, such as refueling (head removal, installation, and fuel handling); handling of radioactive waste; in-service inspections; and inspection, repair, and maintenance of particular components, such as recirculation pumps, valves, and steam generators. Data supporting these conclusions came from exposure records at nuclear power plant sites and from discussions with health physics and maintenance personnel at these plants. Thus far, the study has also revealed a serious communication problem that exists among the major parties in the nuclear industry, including architectural-engineering firms, nuclear steam supply system vendors, utilities, and the Nuclear Regulatory Commission. The result of the communication problem has been the incorporation of similar design errors into several generations of nuclear plants. There also exists a lack of understanding or, in some cases, a misunderstanding of what ALAP really means and how ALAP philosophy should be applied.

The extent of exposure during outages has been emphasized in several reports.[2–4] A reasonable estimate of the fraction of the total exposure occurring during outages is two-thirds. Some individual plants vary in this respect, showing a range of 27 to 97% in actual studies, but these represent extremely unusual cases. Some typical examples of jobs and exposures incurred during refueling outages are shown in Tables 11.2 and 11.3.

Table 11.2. Dose for refueling outage at Pilgrim Nuclear Power Station (ref. 3)

Job	Dose (man-rems)
Valve repair	28
Insulation removal and replacement	20
Control rod drive removal	8
Vessel internals inspection	10
Reactor head removal and replacement	29
Nondestructive testing inspection	7
Total for outage	121

Table 11.3. Dose for partial refueling outage at Big Rock Point Nuclear Power Station

Job	Dose (man-rems)
Valve repair	3.7
Insulation removal and replacement	6.4
Control rod drive work	2.5
Reactor head removal and replacement	6.0
In-service weld inspection	9.0
Routine refueling	2.1
In-core probe work	1.2
Total for outage	50.3

While most information gathered was general in nature, an in-depth study was conducted on valve maintenance and repair. The early identification of valves as a significant problem area caused special

3. C. A. Pelletier, L. Simmons, M. Barbier, and J. H. Keller, *Compilation and Analysis of Data on Occupational Radiation Exposure Experienced at Operating Nuclear Power Plants,* AIF NESP Report, September 1974.

4. R. F. Decker, J. H. Morgan, and R. L. Morgin, *Radiation Protection Coverage Winter 1973-4 Refueling/Maintenance Outage: Pilgrim Nuclear Power Station,* General Electric Report NEDC 12518, June 1974.

emphasis to be placed on this problem. In one case, valve work resulted in approximately 40% of the exposure during a refueling outage. This is much greater than the maximum of 16% of the annual dose found by Pelletier;[3] however, the accounting system used was significantly different. In the Pelletier study, some of the exposure from valve work was assigned to other categories, such as in-service inspection, radioactive waste-handling systems, main coolant loop work, etc.

Some of the valves that have been identified as causing significant exposure include pressurizer spray valves, boric acid evaporator valves, steam drum valves, relief valves, primary check valves, main steam isolation valves, cleanup demineralizer drain valves, residual heat removal system valves, and pump suction and discharge valves. In many cases, nearby sources contributed most of the exposure received in performing in-place valve repair. One good example of this is the pressurizer spray valves; here the pressurizer is the source of exposure and not the valve. In some of these cases, better placement of valves or the isolation of valves in shielded cubicles would result in considerable dose reduction. Valves located adjacent to the regenerative heat exchangers in some Westinghouse PWR's are examples of this situation.

Other ways to reduce exposure include extensive use of new, longer-lasting packing materials and flexatallic gaskets where appropriate. Also, the replacement of packed valves with packingless types, such as bellows seal valves, has helped. More attention needs to be given to the design and fabrication of valves and valve parts used in nuclear applications. While valves in a nuclear power plant must meet the same specifications required in a conventional power plant, there are additional considerations that must be made for nuclear plants. Better specifications of valve internals would simplify maintenance procedures and would reduce the time spent in high radiation fields. Either the utilities have not insisted upon these specifications or the valve vendors have not provided them. Many maintenence supervisors are forced to gradually build up a file of pertinent data on individual valves in order to be able to perform efficient maintenance on them.

Work is continuing on identifying means of reducing valve exposures. In addition, similar analyses of several other systems and components are being started in order to provide guidance for specific regulatory guides relating to keeping exposures in light-water power plants as low as practicable.

12. Health Physics Aspects of Fusion Power

C. E. Easterly R. L. Shoup[1]
J. W. Poston[1] R. S. Booth[2]
F. H. Clark[2]

Much of the technical progress in the program on health physics aspects of fusion power is qualitative at this time due to the scoping nature of the early parts of the program. Efforts in this project have been directed along three lines: (1) neutron activation products, (2) localized tritium hazards, and (3) global tritium circulation.

NEUTRON ACTIVATION PRODUCTS

During normal operation of a controlled thermonuclear reactor (CTR), tritium will be the major effluent. Under accident conditions or after normal shutdown and subsequent dismantling of a fusion reactor during maintenance operations, other radioisotopes – the activation products – become increasingly important. Activation products are produced when high-energy neutrons interact with the primary structural and coolant materials.

It is still uncertain as to which materials will be used for structural components of fusion reactors, but niobium, vanadium, aluminum (sintered aluminum products), and stainless steel have been suggested for first-generation CTR's. A breeder blanket immediately adjacent to the primary containment will most likely contain lithium or a lithium salt with lithium or a lithium–beryllium salt used as a coolant. Activation of such materials with energetic neutrons will lead to the production of radionuclides not commonly encountered in fission reactors. A list of significant activation products with half-lives greater than 30 days is presented in Table 12.1.

Vogelsang et al.[3] have predicted that during the period 1 year to 100 years after shutdown, the inventories of activation products in a CTR will be on the same order of magnitude as the fission and activation products produced in a comparable LMFBR. Hence, there may exist a significant source of potential exposure to radiation workers and the general population. Kulcinski[4] has indicated the existence of certain strategic

Table 12.1. Summary of significant activation products

Activation product	Half-life
^{26}Al	7.3×10^5 y
^{45}Ca	163 d
^{49}V	331 d
^{51}Cr	27.7 d
^{53}Mn	3.7×10^6 y
^{54}Mn	312 d
^{55}Fe	2.7 y
^{59}Fe	44.6 d
^{57}Co	271 d
^{58}Co	71.3 d
^{60}Co	5.27 y
^{59}Ni	8×10^4 y
^{63}Ni	100 y
^{91}Nb	Long
^{92m}Nb	2×10^7 y
^{93m}Nb	12 y
^{94m}Nb	2×10^4 y
^{95}Nb	35 d
^{93}Mo	3×10^3 y
^{93}Zr	9.5×10^5 y
^{95}Zr	65.5 d
^{99m}Tc	2.13×10^5 y

1. Medical Physics and Internal Dosimetry Section.
2. Instrumentation and Controls Division.
3. W. F. Vogelsang, G. L. Kulcinski, R. G. Lott, and T. Y. Sung, *Nucl. Technol.* 22, 379 (1974).
4. G. L. Kulcinski, "Fusion Power – An Assessment of the Potential Impact in the U.S.A.," *Energy Policy*, pp. 104–125 (June 1974).

structural materials for use in fusion reactors. The use of refractory metals, such as niobium or vanadium, for structural materials in CTR's may mean that the United States will be dependent, almost entirely, on foreign sources for these metals. Thus recycling of the metals used in a CTR may be necessary. With recycling, the potential for exposure of occupational personnel, as well as members of the general population, will be increased. Hence there is a need to collect the necessary data to assess the potential radiologic hazards associated with exposure to the radionuclides likely to be produced. This collection has recently begun.

In constructing a metabolic model for aluminum, it has been necessary to use data on rats and to rely on information obtained on metabolism of gallium, which is in the same classification in the periodic chart. Based on these data, the uptake is estimated to be about 10^{-3}; however, this is somewhat lower than that indicated for reference man or in some of the reference literature cited in the reference man report.[5] Calculations based on this small amount of data give a maximum permissible concentration (MPC) of about 10^{-9} $\mu Ci/cm^3$ of air for the radioisotope ^{26}Al. In addition, the lower large intestine has been identified as the critical organ for ingestion and the red marrow as the critical organ when inhalation is the mode of entry into the body.

The situation is much the same if the element niobium is considered. There appear to be no data on the metabolism of radioactive niobium in man and very little information on stable niobium. In a recent study, Furchner and Drake[6] compare the metabolism of niobium in the mouse, rat, monkey, and dog. Their studies show preferential retention in bone – a tenfold higher concentration compared to the whole-body average. In the absence of data on the metabolism of niobium in man, these data have been employed in the derivation of a retention equation for use in dosimetric evaluations.

Several studies using a number of niobium compounds and small animals indicate a gastrointestinal (GI) absorption of 1% or less. However, the observed level of urinary excretion and balance data on stable niobium in humans indicate a GI absorption of at least 60% of dietary niobium. Thus the incorporation of radioactive niobium into the food chain could be a significant exposure pathway. It is also significant to point out that in calculations for many of the isotopes of niobium, the critical organ is often the red marrow or the testes.

The situation of scarce and conflicting data is much the same for many of the other elements of potential importance to fusion power. In general, little human data are available and, in some cases, little animal data. Much of the intake and excretion data published in the reference man report[5] is based on studies of a few individuals or a survey of institutional diets.

LOCALIZED TRITIUM BEHAVIOR

Tritium is the only radionuclide likely to be released from fusion reactors during routine operations that will be an important potential contributor of radiation exposure to the public. Tritium may be released either in the form of tritiated gas (T_2) or tritiated water (HTO). Tritium released as T_2 will be converted eventually to HTO through oxidation and isotopic exchange reactions that occur in the atmosphere. The maximum permissible concentration in air (MPC_a) of T_2 is two orders of magnitude higher than the MPC_a for HTO since HTO is more readily absorbed and retained in the body. Because of this higher relative hazard from HTO and the necessity for conservatism in environmental assessments, tritium is usually assumed to be released exclusively as HTO.

The purpose of this study is to determine how much conservatism is introduced into the assessment of a tritium release when this release is assumed to be HTO but was actually T_2. The time-dependent, atmospheric diffusion code ACRA-II has been modified to include chemical conversion from T_2 to HTO as a first-order reaction. For an initial release as T_2, concentrations of T_2 and HTO are calculated as a function of time after release and distance from the release point. These concentrations are converted to potential doses to man with appropriate dose rate factors. Doses can be calculated for typical meteorological conditions with the reaction rate for conversion of T_2 to HTO and the environmental half-time of HTO in the atmosphere as parameters. If initial calculations justify further refinement, doses will also be calculated for the case in which the reaction rate for conversion of T_2 to HTO is a function of the T_2 concentration.

GLOBAL TRITIUM CIRCULATION

A multicompartment generalized model of global hydrologic cycling is being used as a basis for determining the relative effects of alternative modes of tritium

5. International Commission on Radiological Protection, *Reference Man*, ICRP Publication 23, Pergamon Press, London, 1975.

6. J. E. Furchner and G. A. Drake, *Health Phys.* 31, 173 (1971).

discharge on the collective dose to the world population. The current principal modes of discharge from nuclear facilities are into the atmosphere in the form of tritiated gas or tritiated water and into the surface waters in the form of tritiated water. A block diagram of the generalized cycle used is shown in Fig. 12.1. The compartments are assumed to mix uniformly and instantaneously and to interact with each other in a linear fashion. A set of linear, homogeneous, differential equations is solved for an initial set of conditions (for example, input of tritiated water into a compartment or compartments) and evaluated for the relative compartmental distributions at subsequent times. The equations are also evaluated for a continuous input, as in the case of a continuous discharge of tritium into the environment.

The volumes of the earth's compartments are taken from Todd[7] and for man, a population of 5×10^9 people is used for the year 2000. Most of the transfer coefficients between the earth's compartment are taken from Todd.[7] However, the deep ocean exchange rate is based on an advection rate of 1.4×10^{-5} cm/sec, as determined by Bieri et al.,[8] and the groundwater exchange rate is based on a diffusion rate of 4×10^{-6} cm^2/sec. The transfer coefficients to and from man are based on water balance data from the reference man report.[5] For the base case, the food intake is taken to be 5% from the ocean and 95% in equilibrium with the vadose water; the water supply is assumed to be 80% from surface waters and 20% from wells (deep ground). In order to have well-behaved solutions to the differential equations, it is necessary to make minor adjustments to the rates so that no water is gained or lost in any compartment.

The solution to the base case (actually six separate cases) is presented in Table 12.2. Conditions for this case are the numerical values of Fig. 12.1 and contin-

7. D. K. Todd (ed.), *The Water Encyclopedia*, Water Information Center, Port Washington, New York, 1970, p. 62.

8. R. H. Bieri, K. Minor, and E. D. Goldberg, *J. Geophys. Res.* 71, 5243 (1966).

ORNL-DWG 75-6367

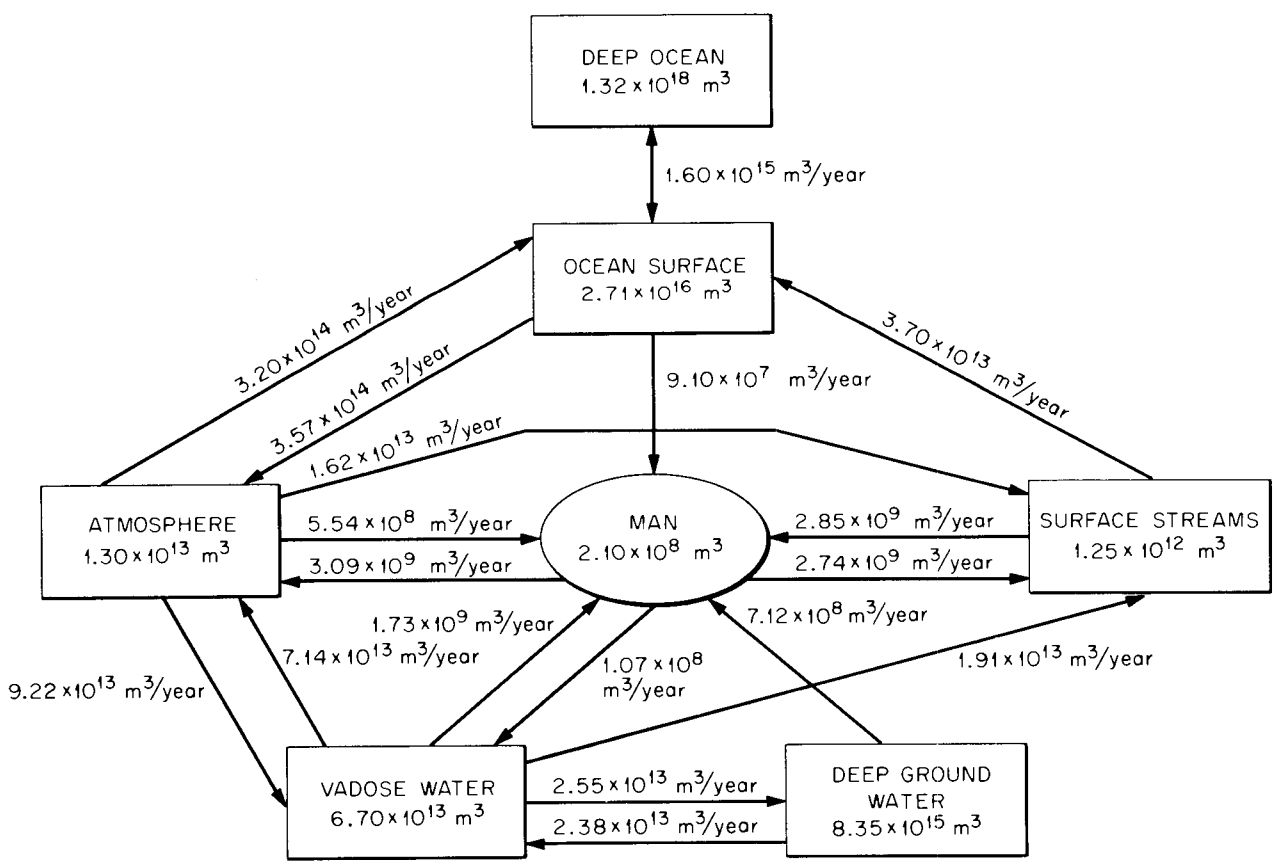

Fig. 12.1. Global hydrologic cycle with respect to man.

uous injection of tritiated water into each compartment separately. The equations were solved to determine the relative fraction of tritiated water present in man's compartment at the end of 1, 25, 50, and 100 years as a function of the compartment of injection. It is seen that by the end of 25 years, equilibrium is essentially attained. In order to determine the sensitivity to those transfer rates for which there is some uncertainty, a case was run for 30% additional rainfall on the ocean surface. The relative percents of tritium in each compartment after the continuous injection of tritiated water into the two principally used modes, the atmosphere and surface waters, are presented in Table 12.3 for the base case and for the case of 30% additional rainfall. Here, the change for the compartments was about 15% maximum. A sensitivity check was also performed for another uncertain transfer rate, vadose to deep groundwater; a change in order of magnitude for this coefficient resulted in about 15% difference in the resulting fraction in the man compartment for both armospheric and surface-water tritium discharge.

The numerical collective doses to man have not yet been determined as a function of curies discharged into the various compartments. However, it is evident from the data presented on the relative quantities of tritium arriving in man's compartment that uniform discharges of tritiated water into the atmosphere may result in as much as an order of magnitude less collective dose, on a global basis, than uniform discharges into the surface waters.

Table 12.2. Relative contribution to global collective dose as a function of discharge mode

Compartment of tritium discharge	Relative collective global dose to man after continuous discharge for:			
	1 year	25 years	50 years	100 years
Atmosphere	0.1	0.2	0.2	0.2
Vadose water	0.3	0.4	0.4	0.4
Deep groundwater	0.002	0.03	0.03	0.04
Surface waters	1.0	1.0	1.0	1.0
Ocean surface (75 m)	0.001	0.01	0.02	0.02
Deep ocean	5×10^{-7}	0.0002	0.0003	0.0003

Table 12.3. Relative percent of tritium in each compartment after 100 years' continuous injection into the atmosphere and surface waters

	Base case		30% additional rainfall onto ocean surface	
	Atmosphere	Surface water	Atmosphere	Surface water
Atmosphere	0.22	0.022	0.18	0.023
Vadose water	0.87	0.090	0.72	0.091
Deep groundwater	5.6	0.57	4.6	0.58
Surface water	0.017	0.19	0.014	0.19
Ocean surface	46.0	49.0	47.0	0.49.0
Deep ocean	47.0	50.0	48.0	50.0
Man	0.0000025	0.000015	0.0000021	0.000015

13. Public Health and Demographic Statistics

C. E. Easterly P. N. Ritchey[2] A. S. Loebl[1]
C. H. Patrick[1] D. L. Solomon[3] J. P. Hickey

A study has been undertaken to determine the feasibility of collecting public health data required to assess the impact of nuclear facilities on neighboring populations. The program consists of several components. One involves the identification of sources of public health statistics already available and an assessment of the difficulties involved in combining data from several such sources. To date, the Tennessee Department of Public Health, the National Center for Disease Control, and the National Center for Health Statistics have been contacted to determine what types of data they collect and their availability.

A second aspect of the program concerns assessment of the availability of the statistical theory and methodology required to detect very small effects. A pilot study is being carried out in which the impact of the Oak Ridge facilities on the mortality characteristics of the nonworker segment of the surrounding population is being analyzed. By attempting to apply the available statistical methodology to these data, the shortcomings of the techniques can be identified, and appropriate modifications can be made. The operations at Oak Ridge have been chosen because the facilities are long established and because historical data are available for gaseous and liquid effluents from which radiation doses can be estimated. Furthermore, present and former employees can be identified, enabling separate consideration of the workers and the population-at-large. Mortality information is being obtained from the Tennessee Department of Public Health on post- and prenatal deaths; these data will be correlated with estimated radiation exposures resulting from releases of radioactive effluents from the Oak Ridge facilities. Data from more distant regions of the state are also being collected to be used for statistical controls.

Another component of the long-range objectives of the program is the establishment of a health and mortality profile for a proposed nuclear power plant site. This will serve as a benchmark against which to measure these characteristisc after several years of operation.

For this study, the methodology developed will use as input data radiation release data and the individual death records by cause and the location of residence of the deceased. Additionally, the Census of Population data will be used for specific demographic characteristics to measure the population at risk and for specific socioeconomic variables to control for important environmental conditions. The radiation release data incorporate meteorological and hydrological information in order to determine exposure levels by location within the state. The program methodology utilized will attempt to ensure that spurious correlation is minimized and that significant control variables are included.

Individual records of mortality by Tennessee counties for 1949 through 1972 are being analyzed. Census data for 1960 and 1970 for each Tennessee county will be used to standardize mortality rates and to control spurious association in the analyses undertaken. The methodological framework to be utilized is currently being determined by a team consisting of health physicists, epidemiologists, demographers, and statisticians. Dose rates for each county are being estimated from release data of the Oak Ridge facilities and meteorological information for the region. An extensive literature review is continuing on two fronts: (1) a review of the relationship between radiation dose and mortality, especially the methodology used in such studies, and (2) a review of the social and economic correlates of mortality in order to properly control factors that might induce a spurious correlation between radiation dose and mortality. Initial analyses will be undertaken in FY 1976, applying the methodology

1. Energy Division.
2. ORAU.
3. Temporary employee on leave from Cornell University.

with appropriate control variables as determined by the research effort completed in FY 1975.

Table 13.1 presents the major dimensions to be encompassed in the Oak Ridge pilot study. The focus of the study will be the 1960 and 1970 mortality experience of population subgroups in Tennessee counties. Data availablility for these years permits the most rigorous analysis of the association between radiation level and mortality. The control variables will function to standardize the data and to reduce the likelihood of spurious association between the major variables.

An epidemiologist is to provide input on the determination of "relevant causes/complications" in the mortality–radiation relationship, with special reference to causes of death related to specific nuclides. For examination of fetal deaths, information will be collected on relevant dimensions of history in gestation (e.g., multiple births, length of pregnancy, and date since penultimate delivery), for both control and pathological contexts.

Dose estimates will be made for all potential pathways resulting from gaseous and liquid releases. Radioactive materials have been released from the confines of ORNL (the principal source of past radioactive releases) into both the aquatic and the atmospheric environs since the beginning of the Laboratory in 1943. Quantitative data are available for both aquatic and atmospheric discharges for recent years. Generally, they become less reliable with increasing age and are not explicitly available for the first decade.

The geography of the ORNL environs limits aquatic releases to the White Oak Drainage Basin. In principle, all radioactive releases into the aquatic system can be monitored at that point when they leave the boundaries of restricted access, that is, White Oak Dam. Considerable effort has been spent since 1956 in accumulating the aquatic release data for the Clinch River Study. It is not likely that more reliable determinations of releases could be made; hence the results of the Clinch River Study will be used in specifying the liquid source term for those years which it covers. Aquatic release data are readily available for the remaining several years.

Data for the early years apparently were estimated by tracing back old health physics records on daily gross beta measurements and estimating counting efficiencies and daily flows. Chemical analyses were made only infrequently; so, on the basis of analyses made from 1949 to 1958, ^{90}Sr activities have been estimated for the years 1944 to 1948. No additional radionuclide breakdown has been attempted for those years.

Gaseous effluent release data are more difficult to organize than those for liquid effluents. There was no single discharge point for monitoring, and an attempt to use health physics records to estimate gaseous releases does not appear to be practical. The approach that has produced the most useful information is personal contact with individuals who worked in the various buildings or who were connected with the particular process in question.

Initial efforts in quantifying the gaseous effluents have been centered around one of the principal sources of releases from the Oak Ridge facilities, the RaLa project. Records of curie quantities of end product are available, and these are used as a basis for back calculations. Information on average fuel rod burnup, average cooling time prior to processing, and the chemical process steps is being correlated with known quantities of end product to calculate the quantities of radionuclides released.

There are only a few substantial sources of historic releases of radioactive materials and many minor ones. Initial dose calculations will be made subsequent to quantification of the principal sources. The dose calculations will be made using presently available computer codes and methodology.

The calculated doses are expected to be quite small relative to natural background, perhaps several percent, and of about the same magnitude as the changes in background from one location to another. Hence, a new approach that is significantly different from those previously used will be attempted for correlation between dose and mortality rate. This new approach will take advantage of the knowledge that certain radionuclides can be accumulated in various organs. Therefore, doses to specific organs will be correlated with deaths from malignancies of these organs.

Table 13.1. Major dimensions to be encompassed in the Oak Ridge pilot study

Independent variables
Radiation exposure: Dose calculations with special reference to specific radionuclides
Control variables (from census data)
1. County values for extent of urbanization, industrial mix, age and race composition, socioeconomic level, net migration
2. Demographic variables, including sex, color, age, residence (rural/urban), state of birth (native/nonnative), marital status, occupation
Dependent variables (from death certificates)
1. Fetal deaths by "relevant" dimensions of history in gestation and parental characteristics
2. Infant deaths (< 1 year) by sex, color, residence "relevant" underlying causes, complications
3. Post-infant deaths by sex, color, residence, "relevant" underlying causes, complications

Part III. Biological and Radiation Physics

H. A. Wright R. N. Hamm

14. Atomic and Molecular Physics

L. G. Christophorou

V. E. Anderson[1]
J. K. Baird
Ada E. Carter
J. G. Carter
J. T. Cox
C. E. Easterly
Kathy S. Gant[2]
M. Grant[3]
Q. A. Huynh[2]
D. R. James[3]
J. P. Johnson[2]
D. L. McCorkle
C. Metcalfe[2]
M. Pace[4]
D. Pittman
J. Rademacher[2]

ELECTRON ATTACHMENT TO SO_2 IN HIGH-PRESSURE GASES[5]

Sulphur dioxide is an abundant atmospheric pollutant, and an elucidation and identification of its reaction pathways in the atmosphere are greatly significant. In assessing its effects and role in atmospheric physicochemical reactions, we need to know its behavior toward slow electrons. In collaboration with a sister program at the Physics Department of the University of Tennessee, the attachment of slow ($\lesssim$10-eV) electrons to SO_2 embedded in N_2 (300–25,000 torr), C_2H_4 (200–15,000 torr), and Ar (500–2000 torr) gases has been investigated. At electron energies $\lesssim$0.5 eV, SO_2^- is formed via a nuclear-excited Feshbach resonance mechanism. The rate for its formation is strongly dependent both on the density and the nature of the gaseous medium, as can be seen clearly from the data shown in Figs. 14.1 and 14.2.

The data in Fig. 14.1*b* were used to determine absolute electron attachment cross sections in the manner described by Christophorou et al.[6] These are shown in Fig. 14.3 and are seen to possess two maxima at 0.06 and ~0.28 eV, attributed to electron capture into vibrational levels of SO_2^-. Reaction schemes consistent with the observed density dependences of the attachment rate have been proposed and discussed. On the basis of these the probability of stabilization of SO_2^{-*} in collisions with C_2H_4 and N_2 is found to be ~60 times larger for C_2H_4 than for N_2. The autodetachment lifetime of SO_2^{-*} at thermal energies is estimated to be $\gtrsim 2 \times 10^{-10}$ sec. Experimental evidence has been provided suggesting that SO_2^{-*} is radiatively stabilized with a rate of $\sim 1.8 \times 10^8$ sec^{-1}, in addition to being stabilized collisionally.

At higher energies (~4–10 eV) SO_2 attaches electrons dissociatively. The cross section for dissociative attachment to SO_2 is shown in Fig. 14.4 and is seen to have a primary maximum of 5 eV and a secondary one at ~8 eV.

1. On loan from the Computer Sciences Division.
2. Graduate student.
3. Postdoctoral Fellow from the University of Tennessee.
4. Consultant.
5. J. Rademacher, L. G. Christophorou, and R. P. Blaunstein, *J. Chem. Soc. Faraday II* **71**, 1212 (1975).
6. L. G. Christophorou, D. L. McCorkle, and V. E. Anderson, *J. Phys. B* (Atom. Molec. Phys.) **4**, 1163 (1971).

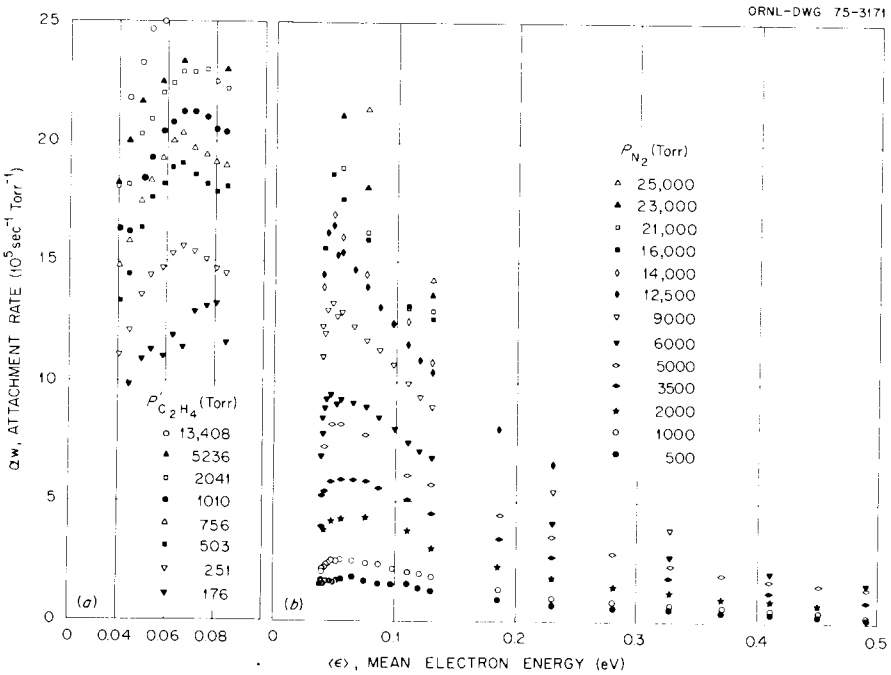

Fig. 14.1. Attachment rate for SO_2 in C_2H_4 and N_2 as a function of the mean electron energy, $\langle\epsilon\rangle$, at the indicated total pressures.

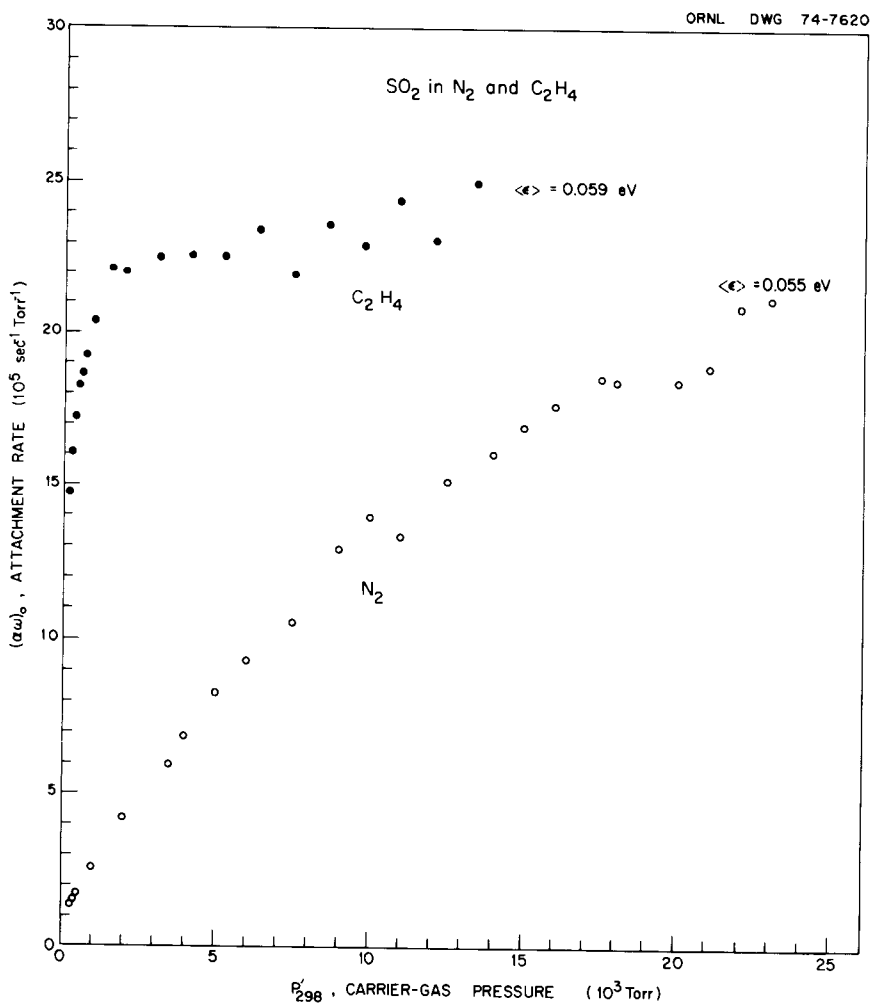

Fig. 14.2. Attachment rate for SO_2 in C_2H_4 and in N_2 as a function of carrier-gas pressure for approximately the same value of $\langle\epsilon\rangle$ (~0.06 eV).

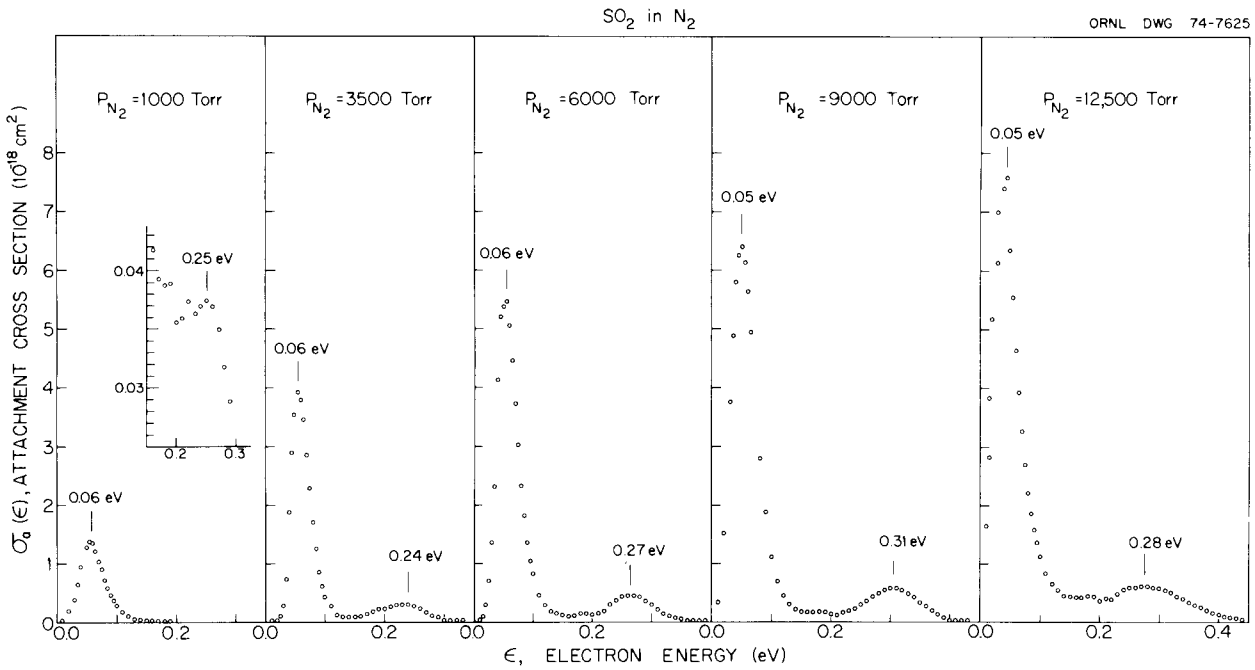

Fig. 14.3. Attachment cross sections as a function of electron energy for SO_2 in N_2 at the indicated nitrogen pressures.

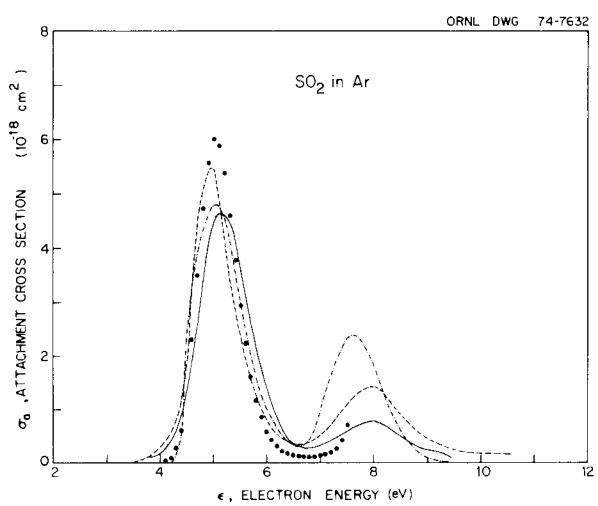

Fig. 14.4. Attachment cross section for SO_2 in Ar obtained by Rademacher, Christophorou and Blaunstein (ref. 5) using the swarm-unfolding (ref. 6) and the swarm-beam (ref. 7) techniques and their data on $\alpha w(\langle\epsilon\rangle)$. (•) swarm-unfolding analysis. (——), (- - - - -), (– . – . – .) swarm-beam analysis using the $\alpha w(\langle\epsilon\rangle)$ data of ref. 5 for SO_2 in Ar and the negative ion yields reported, respectively, by Kraus on O^- and SO^- from SO_2 (ref. 8), by Lifshitz et al. on O^- from SO_2 (ref. 9), and by Harland and Thynne[10] on O^- from SO_2 (ref. 10).

LONG-LIVED PARENT NEGATIVE IONS FORMED VIA NUCLEAR-EXCITED FESHBACH RESONANCES. PART IV: A SYSTEMATIC STUDY OF NO_2-CONTAINING BENZENE DERIVATIVES[11]

As part of our effort to study comprehensively organic structures of biological and toxicological significance, we studied 40 NO_2-containing disubstituted (substituents NO_2 and X) benzene derivatives with a time-of-flight mass spectrometer. These were all found to capture thermal and near-thermal energy electrons forming long-lived (lifetimes $\tau > 10^{-6}$ sec) nuclear-excited Feshbach resonant states.

7. L. G. Christophorou, R. N. Compton, G. S. Hurst, and P. W. Reinhardt, *J. Chem. Phys.* **43,** 4273 (1965).
8. K. Kraus, *Z. Naturforsch.* **16a,** 1378 (1961).
9. C. Lifshitz, J. Agam, A. Weinberg, D. Kantor, U. Shainok, and M. Péres, *Int. J. Mass. Spectrom. Ion Phys.* **11,** 243 (1973).
10. P. Harland and J. C. J. Thynne, *J. Phys. Chem.* **74,** 52 (1970).
11. J. P. Johnson, D. L. McCorkle, L. G. Christophorou, and J. G. Carter, *J. Chem. Soc. Faraday II* (in press).

The lifetimes of the parent negative ions were determined from plots of $-\ln (N^-/N^T)$ vs t, where N^T is the number of ions formed at $t = 0$ (the beginning of the drift space), and N^- is the number of ions which have not autoionized after they have traveled for a time t along the flight tube of the time-of-flight mass spectrometer. The lifetime data are summarized in Table 14.1.

In the present as well as in previous studies,[12,13] τ was found to decrease greatly with increasing electron energy ϵ for a number of negative ions. The variation of τ with ϵ observed in the present study for m-nitroacetophenone and m-nitrobenzonitrile is shown in Fig. 14.5, along with the negative ion current as a function of electron energy.

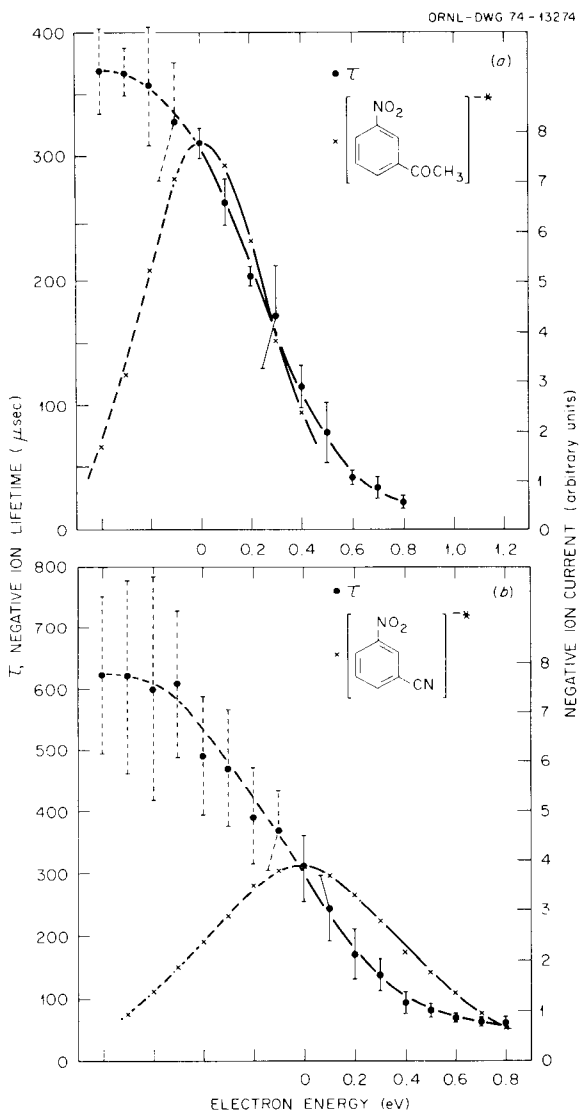

Fig. 14.5. Dependence of the negative ion lifetime and negative ion current for the m-$C_6H_4NO_2COCH_3^{-*}$ and m-$C_6H_4NO_2CN^{-*}$ metastable ions on the incident electron energy.

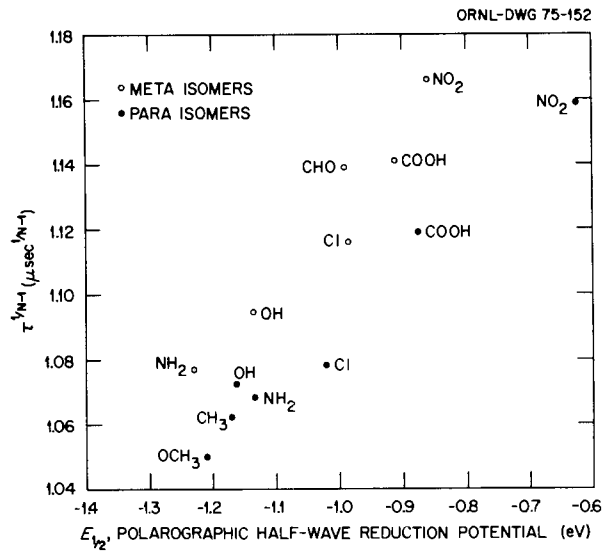

Fig. 14.6. $\tau^{1/(N-1)}$ vs $E_{1/2}$, the polarographic half-wave potential of the NO_2-containing benzene derivatives. (○) meta isomers; (•) para isomers. The compounds are identified by the second substituent X. The number of vibrational degrees of freedom N was taken equal to $3n - 6$, where n is the number of atoms in the molecule.

The parent negative ion autodetachment lifetimes were found to increase with increasing value of the polarographic half-wave potential of these molecules as might be expected theoretically. This is shown in Fig. 14.6. They were also found to depend on the electron donor-acceptor properties of the substituent X and the intramolecular interaction between NO_2 and X. When, in addition to NO_2, the second substituent X is also an electron acceptor (molecules above the dotted line in Table 14.1), the ions have lifetimes about ten times longer than when the ions contain an X which is an electron donor. In this connection, CNDO-2 molecular orbital calculations on the neutral molecules have shown that when X is an electron acceptor, the magnitude of τ correlates with the amount of π-electron charge removed from the benzene ring, while τ is little affected by the amount of π-electron charge donated to the benzene ring by X when X is an electron donor, as shown in Fig. 14.7. Similar calculations on the negative ions of 12 para-substituted compounds indicated an

12. P. M. Collins, L. G. Christophorou, E. L. Chaney, and J. G. Carter, *Chem. Phys. Lett.* **4**, 646 (1970).

13. L. G. Christophorou, A. Hadjiantoniou, and J. G. Carter, *J. Chem. Soc. Faraday II, Part III* **69**, 1713 (1973).

Table 14.1. Lifetimes of long-lived parent negative ions of NO_2-containing disubstituted benzene derivatives

Compound	X	Lifetime (10^{-6} sec)		
		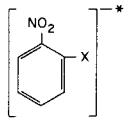	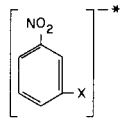	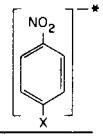
Nitroanisole	OCH_3	16	52	10
Nitrobromobenzene	Br	18	21	10
Nitrofluorobenzene	F	17	28	10
Nitrophenol	OH	460[a,b]	31[b]	14[b]
Nitrochlorobenzene	Cl	17	47[c]	14
Nitrotoluene	CH_3	13[d]	19[d]	14[d]
Nitroaniline	NH_2	46[b]	21[b]	15[b]
Nitrobenzene	H			18[c]
Nitrothiophenol	SH			23
Nitrobenzaldehyde	CHO	395	205	47
Nitrobenzoic Acid	COOH		338	142
Nitro-α,α,α-trifluorotoluene	CF_3	200	187[a]	143
Nitroacetophenone	$COCH_3$	189	310[a]	196
Nitrobenzonitrile	CN	209	315[a]	205
Dinitrobenzene	NO_2	463	537	421

[a]Lifetime found to decrease with increasing electron energy.

[b]A. Hadjiantoniou, L. G. Christophorou, and J. G. Carter, *J. Chem. Soc. Faraday II* **69**, 1691 (1973).

[c]W. T. Naff, R. N. Compton, and C. D. Cooper, *J. Chem. Phys.* **54**, 212 (1971).

[d]L. G. Christophorou, J. G. Carter, E. L. Chaney, and P. M. Collins, *Proc. IVth Int. Congress of Rad. Res. (July 1970)*, vol. 1, Physics and Chemistry, Duplan and Chapiro (eds.), Gordon and Breach, London, 1973, pp. 145–59.

increase in the ring π-electron charge by 0.2 to 0.3 electron unit when X is an electron donor and by 0.4 to 0.7 electron unit when X is an electron acceptor, as shown in Fig. 14.8. At thermal energies the lifetimes for the ions of *o*-nitrophenol, *o*-nitrobenzaldehyde, and *o*-nitroaniline were found to be 460, 395, and 46 μsec respectively, that is, much longer than those (14, 47, and 15 μsec respectively) for the ions of the respective para isomers. The strong enhancement in the lifetimes of the former ions is attributed to the intramolecular interaction (complexing) between the substituents NO_2 and X at the ortho position.

The results of this investigation lead to the conclusion that all NO_2-containing benzene derivatives form long-lived parent negative ions at thermal and epithermal energies, unless a fast dissociative attachment process is energetically possible. They also provide an insight into the details of electron attachment to polyatomic molecules and suggest that the degree of intramolecular charge transfer between a substituent and the benzene ring, as well as the extent of intramolecular complexing between the substituents around the benzene periphery, may be inferred from the measured values of τ.

THRESHOLD-ELECTRON EXCITATION AND COMPOUND-NEGATIVE-ION STATES OF AROMATIC HYDROCARBONS

The three-ring aromatic hydrocarbon molecule phenanthrene was investigated with our threshold-electron excitation spectrometer. Energy-loss spectra of phenanthrene indicated the existence of three peaks below 2 eV which were tentatively assigned to compound negative ion states. Other energy-loss processes were due to excitation of electronic states. The hydrocarbons furan and thiophene were also investigated. The overall quality of the spectra obtained with these compounds, however, was poor because of rapidly deteriorating electron gun characteristics after introduction of the sample. One compound negative ion resonance was observed in thiophene below 1 eV.

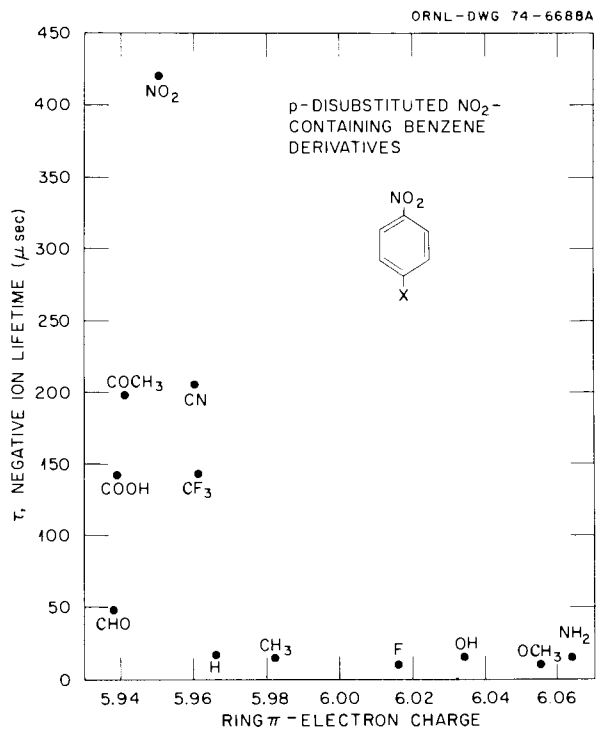

Fig. 14.7. τ vs ring π-electron charge for the neutral para-disubstituted NO_2-containing benzene derivatives. The compounds are identified by the second substituent X (nitrobenzene by H).

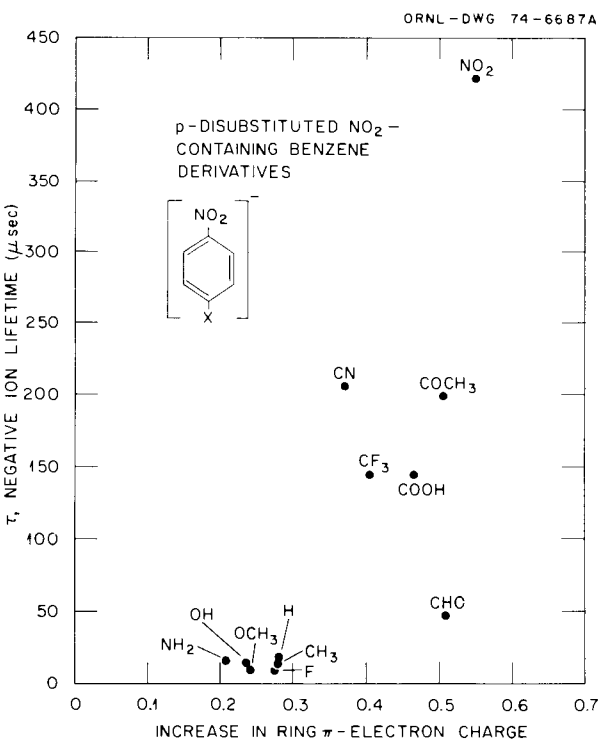

Fig. 14.8. τ vs increase in ring π-electron charge for the parent negative ions of para-disubstituted NO_2-containing benzene derivatives. The compounds are identified by the second substituent X (nitrobenzene by H).

LINKING OF EXISTING DATA ON ELECTRON-MOLECULE INTERACTIONS IN GASES WITH THOSE IN THE LIQUID PHASE

Our earlier successful linking of existing gaseous data on electron attachment in gases to electron attachment to molecules in liquids has been refined and extended from aqueous media to other nonpolar liquids. Gaseous information on the negative-ion lifetime, resonance energies (in both attachment and scattering), electron affinity, and cross-section functions has been found useful in predicting electron-molecule reaction rates in liquid media. In Fig. 14.9 we present our recent finding that R_{eaq} (the hydrated electron-molecule reaction rate) decreases with increasing energy of the lowest compound-negative-ion or dissociative attachment resonant state. A discussion of this work can be found in a recent paper by Christophorou.[14]

SLOWING DOWN OF SUBEXCITATION ELECTRONS IN POLYATOMIC GASES[15]

Electron drift velocities and lateral diffusion coefficients for a number of polyatomic gases have been employed to determine mobilities, mean fractional energy losses per collision, stopping rates, and thermalization times as a function of mean electron energy, $\langle\epsilon\rangle$. The energy dependence of the electron mobility for a number of hydrocarbons is shown in Fig. 14.10. The electron mobility is seen to vary considerably from one molecule to another, generally possessing a maximum between $(3/2)\,kT$ and ~0.2 eV. In contrast, the mobility for molecules with significant dipole or quadrupole moments continues to increase beyond 0.2 eV.

In Fig. 14.11 the mean fractional energy loss per collision as a function of $\langle\epsilon\rangle$ is presented. It shows distinct maxima which indicate that direct excitation of deformation, bending, and torsional modes is an important energy loss process for slow electrons. The water molecule shows significant rotational excitation at very low energies.

The stopping rate – the rate at which the electron loses energy in collisions with molecules – increases rapidly with $\langle\epsilon\rangle$ above the thermal energy and gradually levels off beyond a few tenths of an electron volt, as can be seen from the data in Fig. 14.12; it varies considerably from one molecule to another, particularly below ~0.2 eV. Estimates of thermalization times are presented in Fig. 14.13; they are seen to depend strongly on the gaseous medium and to be relatively

14. L. G. Christophorou, *Chemical Reviews* (in press).
15. L. G. Christophorou, K. Gant, and J. K. Baird, *Chem. Phys. Lett.* **30**, 104 (1975).

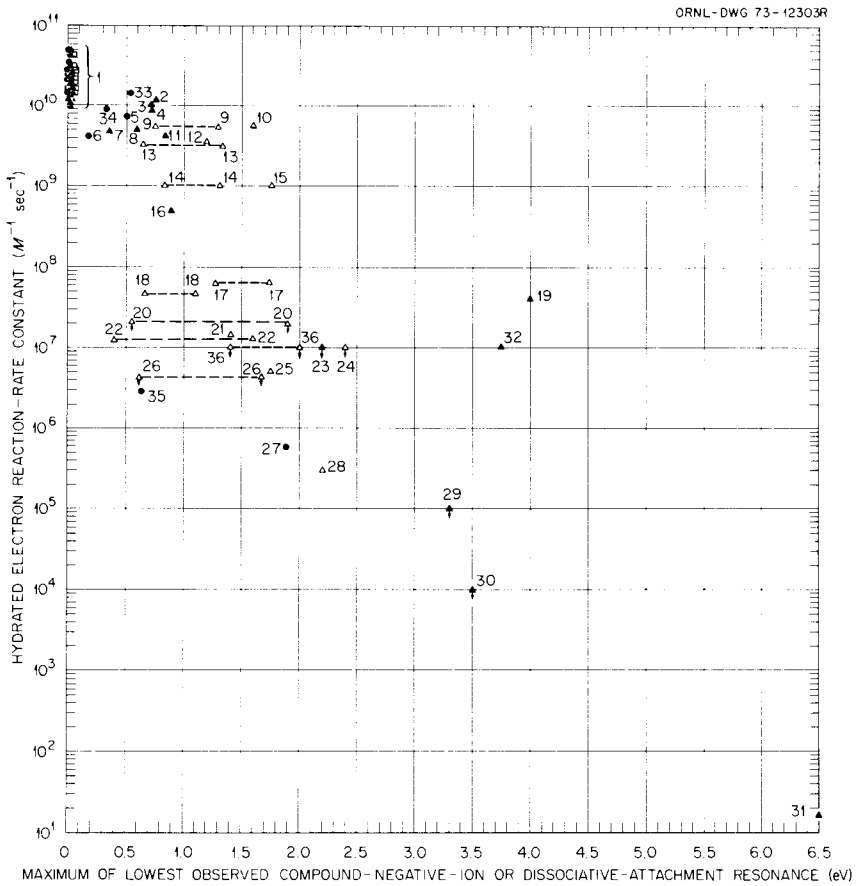

Fig. 14.9. Hydrated electron reaction rate constant against the position of the lowest observed compound-negative-ion or dissociative attachment resonance.

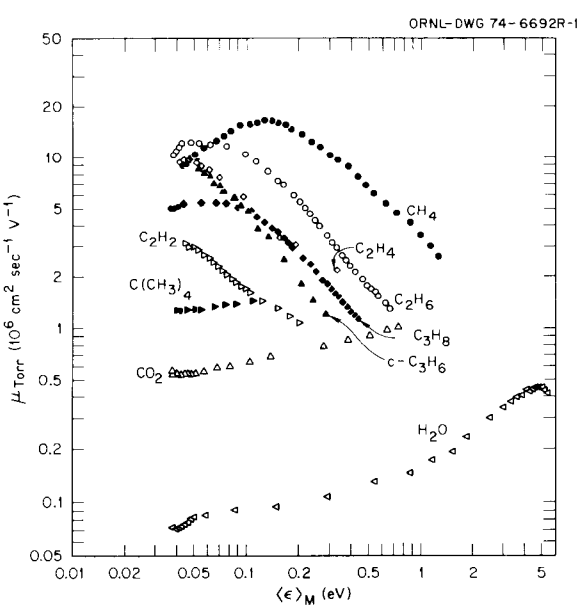

Fig. 14.10. Electron mobility μ_{torr} vs mean electron energy $\langle\epsilon\rangle_M$.

independent of $\langle\epsilon\rangle$ above ~0.1 eV, suggesting that they are critically affected by interactions in the subexcitation energy region.

ELECTRON MOBILITIES IN HIGH-PRESSURE GASES ("QUASI-LIQUIDS")

The construction of a new apparatus for the measurement of electron mobilities in dense gases up to ~80 atm and 450°C has progressed well and nears completion. Fabrication of the chamber, building of gas handling and purification manifolds, and purchase of the furnace have been completed. Similarly, auxiliary equipment (such as a nanosecond pulsed light source, a high-temperature pressure-measuring transducer, and a signal analyzer) has been purchased and tested.

MEASUREMENT OF THE MOBILITY OF EXCESS ELECTRONS IN LIQUIDS

Construction of the apparatus for the measurement of the mobility of excess electrons in liquids described in

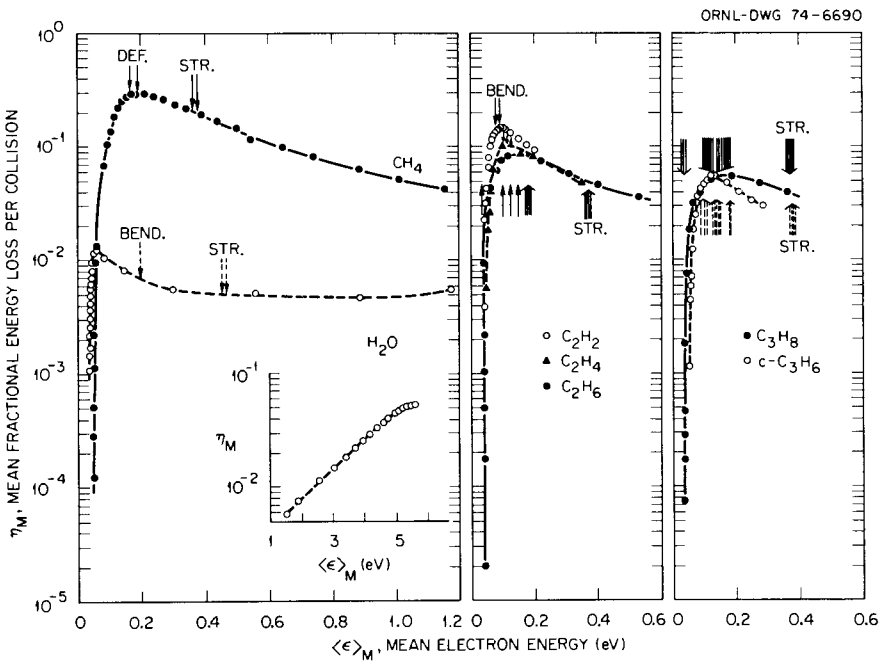

Fig. 14.11. Mean fractional energy loss per collision, η_M, as a function of mean electron energy, $\langle\epsilon\rangle_M$.

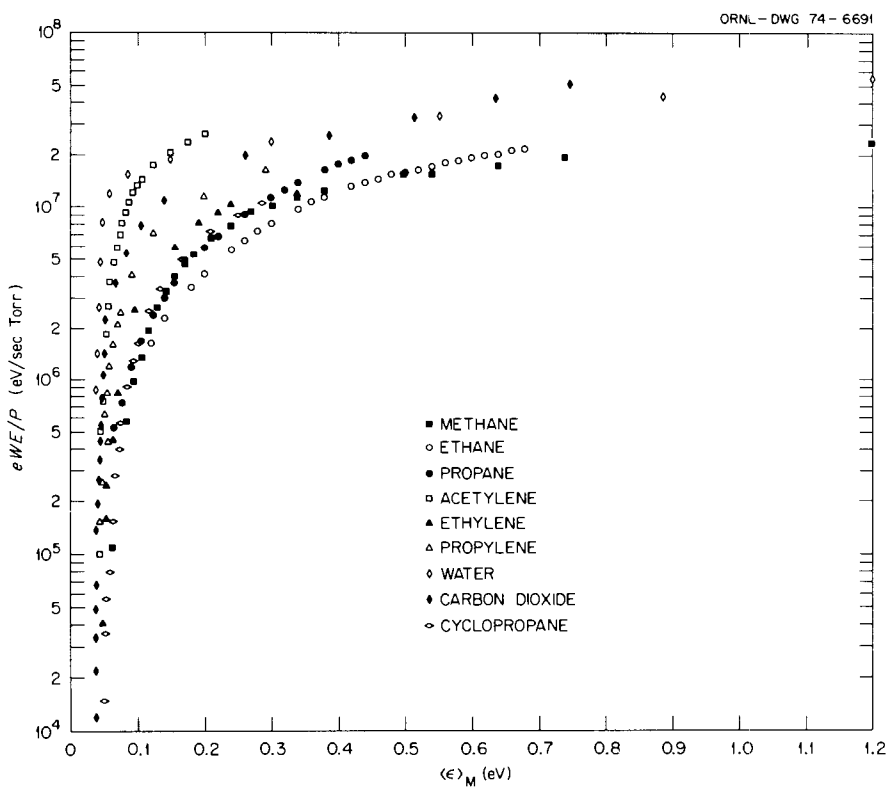

Fig. 14.12. Stopping rate (P = 1 torr), ewE/P, vs mean electron energy $\langle\epsilon\rangle_M$.

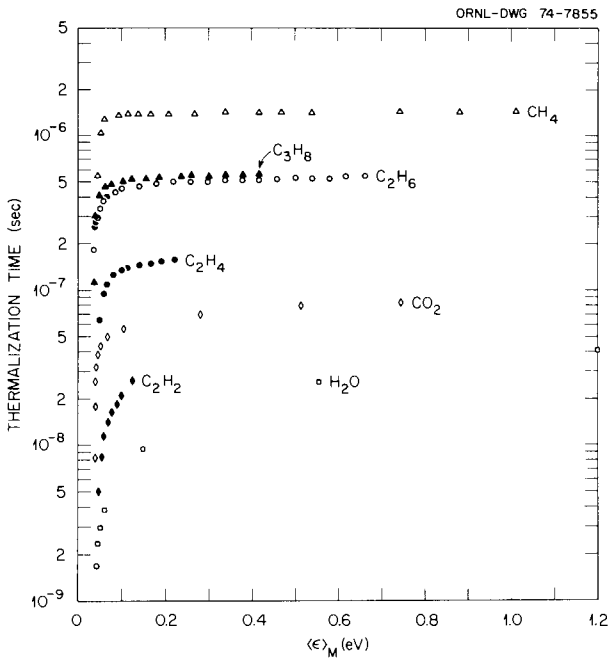

Fig. 14.13. Thermalization times (P = 1 torr) as a function of mean electron energy for a number of polyatomic molecules.

last year's annual report is complete, and the debugging of the electronic equipment and the purification of the sample liquids have begun. By use of molecular sieves and 14 cycles of freeze-pump-thaw at three different temperatures, we have obtained a sample of benzene with an intrinsic conductivity of approximately 10^{-14} $\text{ohm}^{-1}\ \text{cm}^{-1}$. The present purification system is being improved by the addition of a step in which the benzene is brought in contact with Na-K alloy.

POTENTIAL ENERGY FUNCTION OF AN EXCESS ELECTRON IN A NONPOLAR LIQUID

In last year's annual report, we presented the calculation of a long-range polarization potential function describing the interaction of an excess electron with the molecules of a liquid. Briefly, the electron was taken to be a point charge, and a molecule in the liquid was regarded as a point electrical dipole at the center of a spherical cavity embedded in a uniform dielectric of dielectric constant ϵ. The point dipole was induced by the local electric field generated by the electron. The calculation of the potential energy of the electron proceeded in analogy with Onsager's theory[16] of the local electric field in a dielectric liquid. If r is the distance of the electron of charge q from the center of the cavity, $u = \alpha/a^3$, where α is the polarizability of the molecule, and a is the radius of the cavity, then the leading term of the potential function is

$$V(r) = -\frac{1}{2}\frac{\alpha q^2}{r^4}F(\epsilon)\,, \tag{1}$$

where $F(\epsilon)$ is the screening function given by[17]

$$F(\epsilon) = \left(\frac{1}{u\epsilon}\right)\left[\frac{u(\epsilon+2)-(\epsilon-1)}{(2\epsilon+1)-2u(\epsilon-1)}\right]. \tag{2}$$

By comparison, the screening function $F_L(\epsilon)$ calculated by Lekner[18] and used by Springett, Jortner, and Cohen[19] is

$$F_L(\epsilon) = (\epsilon+2)/3\epsilon\,. \tag{3}$$

Plots of $F_L(\epsilon)$ and $F(\epsilon)$ for various values of u are shown in Fig. 14.14.

One may note that there is a value of ϵ at which $F(\epsilon)$ goes through zero. Physically, this means that the fringing of the electric field at any point in the dielectric due to the presence of the cavity is just canceled by the electric field due to the induced dipole. Consequently, neither the presence of the cavity nor the induced dipole is felt at the position of the electron. This behavior of the screening function may have important implications for understanding the mobility of excess electrons in compressed gaseous and liquid argon. Jahnke, Meyer, and Rice[20] have shown experimentally that at fixed pressure, the electron mobility in argon goes through a maximum at a number density of 0.012 atom/Å^3. One interpretation of this effect may be that the electron-atom scattering cross section in argon goes through zero at this density. Since the cross section is proportional to the square of the screening function, this interpretation is in accord with the behavior of $F(\epsilon)$ shown in Fig. 14.14, since ϵ depends upon the number density.

To test this proposition, it is necessary to determine the free parameter u for argon. This can be done by analyzing data on the dependence of the dielectric

16. L. Onsager, *J. Amer. Chem. Soc.* **58**, 1486 (1936).
17. The function published in last year's annual report contains an algebraic error that has been corrected.
18. J. Lekner, *Phys. Rev.* **158**, 130 (1967).
19. B. E. Springett, J. Jortner, and M. H. Cohen, *J. Chem. Phys.* **48**, 2720 (1968).
20. J. A. Jahnke, L. Meyer, and S. A. Rice, *Phys. Rev.* **A3**, 734 (1971).

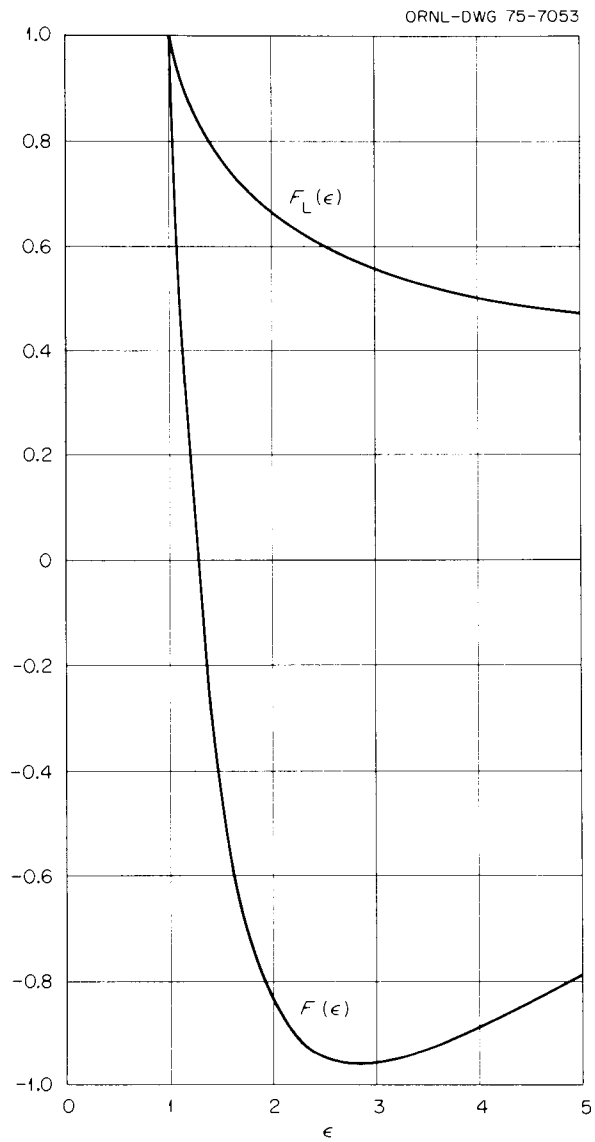

Fig. 14.14. The screening functions $F(\epsilon)$ and $F_L(\epsilon)$ for various values of u (see text).

constant on density in accordance with the Böttcher-Onsager formula[21]

$$\frac{12\pi N\epsilon}{(\epsilon-1)(2\epsilon+1)} = \frac{1}{\alpha} - \frac{1}{a^3}\left(\frac{2\epsilon-2}{2\epsilon+1}\right), \tag{4}$$

where N is the number density. We have used the dielectric data of Michels, Ten Seldam, and Overdijk[22] for compressed gaseous argon to estimate α and a. This follows from fitting the right-hand side of Eq. (4) to the quantity $(2\epsilon - 2)/(2\epsilon + 1)$ by the method of least squares in which $1/\alpha$ and $1/a^3$ are interpreted as linear least-squares parameters. The results are summarized in Table 14.2. By combining Eqs. (2) and (4), one calculates that the number density N_0 at which $F(\epsilon)$ is zero is

$$N_0 = \left(\frac{4\pi}{3}a^3\right)^{-1} . \tag{5}$$

Using the least-squares values of a determined from the data of Michels et al., we obtained values for N_0 as shown in Table 14.2. The values of N_0 are remarkably close to the critical density at which the electron mobility is a maximum.

Before the explanation proposed above is adopted, one needs to consider also the short-range interaction of the electron with the Hartree field of the argon atom. It is the sum of this interaction and the long-range polarization interaction given by Eq. (1) which determines the scattering cross section, and which must go through zero at the density 0.012 atom/Å^3. The next goal of our efforts is thus to include this short-range interaction in the theory.

ELECTRON MOBILITIES IN GASES AND LIQUIDS

Our measurement of electron mobilities in low-pressure gases for which similar measurements have been or are being made in the corresponding liquids continued. The effects of electron trapping, autoionization, molecular geometry and sphericity, rotational and vibrational energy levels, and microscopic molecular characteristics on the mobility of slow electrons through gases and liquids have been and are being investigated. In polar liquids, electrons are much slower than in the corresponding gases (due, predominantly to the effect of electron trapping), but for spherical molecules such as tetramethyl silane, electrons are more mobile (about 45 times) than in the corresponding low-pressure gases. This finding is similar to that we reported earlier for methane, neopentane, and the heavier-rare-gas atoms. An explanation of this latter behavior has been suggested,[23] but more work is needed. Additionally, the effect of the static polarizability, α, on electron motion in gaseous and liquid linear hydrocarbons has been

21. C. J. F. Böttcher, *Theory of Electric Polarization*, vol. 1, 2nd ed., Elsevier, New York, 1973.

22. A. Michels, C. A. Ten Seldam, and S. D. J. Overdijk, *Physica (Utrecht)* **17**, 781 (1951).

23. L. G. Christophorou, *Int. J. Radiat. Phys. Chem.* **7**, 205 (1975).

Table 14.2. Calculated properties of argon

Temperature (°K)	a (Å)	α (Å^3)	N_0 (Å^{-3})
298	2.70 ± 0.03	1.6421 ± 0.0007	$(1.21 \pm 0.04) \times 10^{-2}$
398	2.58 ± 0.02	1.6373 ± 0.0005	$(1.40 \pm 0.04) \times 10^{-2}$

investigated. The mobility decreases with α for both gases and liquids, but the decrease is much faster for the latter.

PHOTOPHYSICS OF AROMATIC HYDROCARBONS

Our research in this area has continued with emphasis on the fluorescence emission from higher excited π-singlet states. Special emphasis has been given to separating the emission from the second excited π-singlet state from that originating from the vibrationally excited first excited π-singlet state. To this end the fluorescence spectra of 1,12-benzoperylene were measured as a function of temperature in various solvents.

SYNTHESIS OF ELECTRON-MOLECULE INTERACTIONS WITH BENZENE AND BENZENE DERIVATIVES

As part of our effort to extend our basic understanding of fundamental processes on radiation (ionizing and nonionizing) interaction from simple to complex molecules, we have been synthesizing – in collaboration with a sister program at the Physics Department of the University of Tennessee – knowledge on slow-electron interactions with benzene and its derivatives. Experimental and theoretical work on electron motion through and on ionization and excitation, resonant negative ion states, and negative ions of benzene and its derivatives has been synthesized in a coherent fashion, critically evaluated, and discussed. Benzene and its derivatives remain the common building blocks of many biomolecules and relate to many biologically and genetically important structures. The synthesis of this knowledge will certainly lead us to a better understanding of these basic organic molecules and their interaction with slow electrons. This understanding, in turn, could serve as a prototype for bigger organic structures.

SPIN-OFF OF OUR BASIC STUDIES ON ELECTRON ATTACHMENT TO, AND ELASTIC AND INELASTIC ELECTRON SCATTERING FROM, POLYATOMIC MOLECULES

Our basic studies in this area indicated that the number and energies of electrons triggering the breakdown process in gaseous (and liquid) dielectrics can be controlled by the use of appropriate substances in multicomponent mixtures. Our new findings on electron attachment and scattering indicated that indeed the breakdown strength of high-voltage dielectrics can be greatly improved. It is hoped that this work will lead not only to better but also cheaper dielectrics for high-voltage transmission, transformers, and switches. Aided by Laboratory "seed money," we have completed construction of necessary equipment and are currently testing "model" systems.

15. Physics of Liquids and Surfaces

R. D. Birkhoff
L. C. Emerson[1]
J. C. Ashley R. A. MacRae[2]
J. M. Heller[2] L. R. Painter[2]

PHOTON SCATTERING FROM CYLINDERS

In last year's Annual Report, we reported briefly on attempts to calculate the scattering of light from a dielectric cylinder. This work was initiated in order to verify theoretically the results of Miziumski,[3] who directed a helium–neon laser beam at an aluminized glass fiber some 58 μ in diameter. Miziumski reported structure in the reflectance curve at near-glancing angles of incidence which he attributed to excitation of surface plasmons of high order. Our preliminary calculations failed to find agreement with Miziumski's data. In addition, our prediction from optical measurements that DNA molecules in the form of a thin film should exhibit a large collective electron or plasmon response to ionizing radiation made us wonder if the DNA molecule by itself might support such a collective electronic excitation. The rich π-electron density in DNA is slightly reminiscent of the conduction electron density in a thin metallic layer around a dielectric cylinder.

Cylindrical geometry has been little explored as to its electromagnetic response as compared with planar and spherical geometries because of inherent mathematical complexities. A literature survey showed that in theoretical papers by Kerker et al.,[4] Ashley and Emerson,[5] and Pfeiffer, Economou, and Ngai[6] there seems to be an inadequate understanding of the experimental results of Miziumski. Thus we have attempted to reproduce experimentally Miziumski's results, using improved techniques with smaller diameter aluminum cylinders and thus lower order and presumably more prominent plasmon excitations.

The experimental problem combines features of geometrical optics, diffraction, and surface-plasmon physics in an interesting way. The unscrambling of these different effects poses challenging experimental problems, which we have attempted to solve as follows. The thicknesses of the fibers (some as small as 5μ in diameter) were measured, using Fraunhofer diffraction when a He–Ne laser beam was directed along a normal to the cylinder axis. For oblique incidence the scattering pattern from the fiber is a hollow diverging cone of radiation coaxial with the fiber axis and containing the unscattered laser beam in its circumference. A screen placed normal to the axis of the fiber reveals a brilliant red circle of light, which sometimes shows discontinuities or striations if the surface of the minute fiber is not uniform. In order to minimize experimental artifacts due to the motion of various parts of the apparatus, we rotated only the fiber, reflecting the scattered light off a plane mirror onto a concave mirror, which, in turn, focused the light onto a photomultiplier detector. A light trap absorbed the unscattered part of the incident laser beam, and a slit could be interposed over the surface of the concave mirror so that only the portion of the reflected light diametrically opposite from the laser spot was recorded. The system can be used with or without this slit and with or without polarizers in the laser beam. A schematic of the geometrical arrangement is shown in Fig. 15.1.

Miziumski proposed a simple model for the excitation of surface waves on a cylinder. When the component of the photon momentum k lying along the cylinder axis is

1. Now transferred to Metals and Ceramics Division.
2. Consultant.
3. C. Miziumski, *Phys. Letters* **40A,** 187, 1972.
4. M. Kerker, D. Cooke, W. A. Farone, and R. A. Jacobsen, *J. Opt. Soc. Am.* **56,** 487 (1966).
5. J. C. Ashley and L. C. Emerson, *Surface Sci.* **41,** 615 (1974).
6. C. A. Pfeiffer, E. N. Economou, and K. L. Ngai, *Phys. Rev. B* **10,** 3038 (1974).

ORNL DWG 75-7079

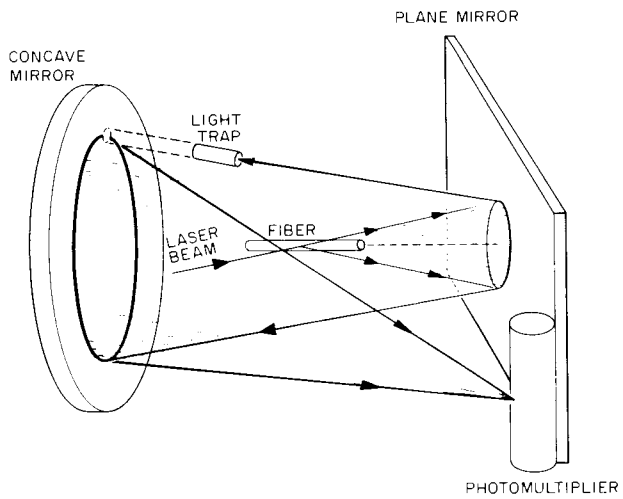

Fig. 15.1. Schematic of optical system for photon scattering. Laser beam crosses fiber and reflects off plane mirror into light trap. Light reflected from fiber into a hollow core of radiation is reflected by plane mirror and focused by concave mirror onto photomultiplier.

added to the momentum of the surface k_s, a resonant condition exists if the vector sum equals the surface-plasmon momentum k_p. This condition may be expressed by

$$(k \cos \beta)^2 + k_s{}^2 = k_p{}^2 \ , \qquad (1)$$

where β is the angle between k and the cylinder axis. If we introduce $k = 2\pi/\lambda$, the surface-plasmon dispersion relation $k_p = k\sqrt{\epsilon/(\epsilon + 1)}$, where ϵ is the dielectric function of the cylinder material, and the cyclic boundary condition $n = 2\pi a/\lambda_s = ak_s$, then

$$\cos^2 \beta = \left(\frac{\lambda}{2\pi}\right)^2 (k_p{}^2 - k_s{}^2) = \frac{\epsilon}{\epsilon + 1} - \left(\frac{n}{a}\right)^2 \left(\frac{\lambda}{2\pi}\right)^2 \ . \qquad (2)$$

Equation (2) shows that for a given surface coating and wave length (ϵ fixed), a resonant condition will exist at various angles β for various integers n depending on the radius of the cylinder a. For example, calculations from this equation showed that there should be 12 resonances between 0 and 12° for an aluminized fiber 10 μ in radius. The data shown in Fig. 15.2 taken at a point on the focal circle diametrically opposite from the unscattered laser beam show such resonances. We have been unable to make a comparison with the more complete Ashley-Emerson theory because of the theoretical difficulties in computing Bessel functions of large arguments. However, we are now working to make this calculation possible while at the same time concentrating on making the cylinders smaller in diameter in

ORNL-DWG 75-7080

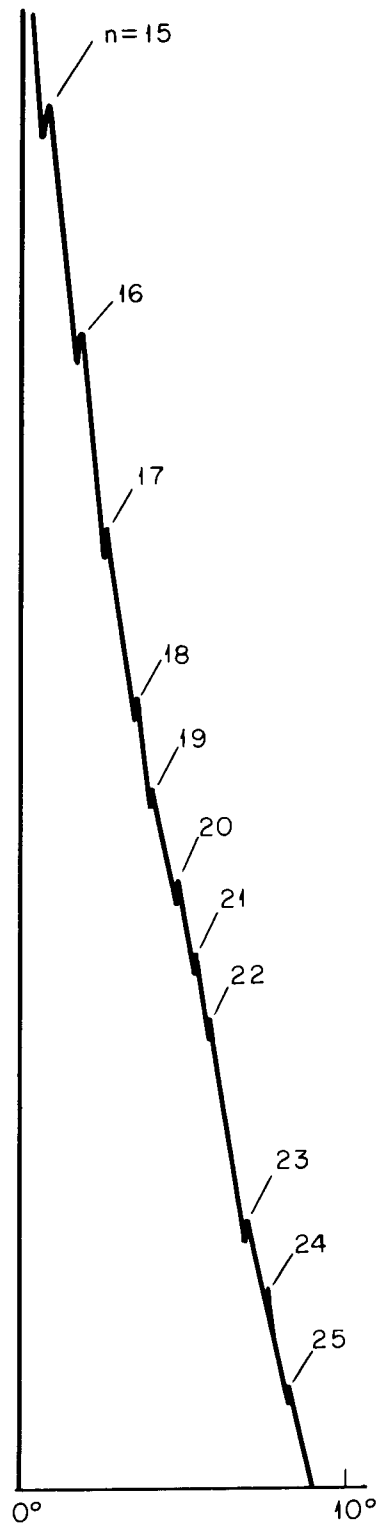

Fig. 15.2. Light scattered from fiber as a function of angle between fiber and laser beam. Discontinuities in light intensity are attributed to excitation of surface plasmons. Orders from n = 14 to 25 are seen.

order to make these resonance effects occur in a lower order and hence occur more prominently. We wish to caution against taking the data of Fig. 15.2 too seriously since they are difficult to reproduce, and this experiment abounds in experimental artifacts. A "giant slingshot" method has been devised to draw the fibers to smaller diameters. The present slingshot, which is 24 ft long, is being extended to 50 ft.

Although our principal interest in this research is in understanding basic surface properties of dielectrics and metals in cylindrical form, there are many potential applications. For example, the fiber optics field is a very large and rapidly growing one which offers important applications to communication systems. Our fibers are an order of magnitude or more smaller in diameter than those being studied at Bell Labs and elsewhere. Likewise, our studies will help in understanding the propagation of electromagnetic waves in and on dielectric cylinders. So far, we have been able to make fibers 5 μ in diameter, but a 1-μ size does not seem impossible. At this diameter, the cylinder is of the same size as a living cell, and this suggests using it as a probe to touch, move, illuminate, or irradiate a cell. It is well known that asbestos fibers are quite prevalent in some atmospheric and aquatic environments. It may be possible to monitor ambient air or water for such cylindrical fibers by making use of the unique conical reflection pattern, as noted above. Finally, on the molecular scale, we would like to see if we can detect the generation and absorption of surface waves in the π-electron systems in macromolecules such as DNA.

COLLECTIVE ELECTRONIC OSCILLATIONS IN LIQUIDS

In a cooperative project with Prof. L. R. Painter and Dr. J. M. Heller, Jr., of the Physics Department, University of Tennessee, we have obtained optical and dielectric data on a number of liquids over the past few years. For several low or relatively low vapor pressure liquids, we have been able to extend our investigations out to about 26 eV photon energy. Low vapor pressure is a requirement for measurements at these higher energies because of optical absorption in the vapor surrounding the liquid contained in an open dish. Previously, dielectric functions had been obtained for the silicone diffusion pump oils DC-704 and DC-705, glycerol, and water. During the last year, we decided to look at the liquids normal tetradecane ($C_{14}H_{30}$) and normal heptadecane ($C_{17}H_{36}$). The measurements were made with the unique vacuum uv instrument at the University of Tennessee, and the analysis was carried out jointly with our staff at ORNL. Near-normal-incidence (15°) reflectance measurements were analyzed by a Kramers-Kronig method to yield the optical parameters n and k, the refractive index and extinction coefficient, respectively. The near-normal reflectance and the optical constants are shown in Fig. 15.3. The absence of π electrons in the alkanes defers the onset ($k > 0$) of optical absorption to almost 8 eV. In Fig. 15.4, we have plotted the real and imaginary parts of the dielectric functions and the energy loss functions for these two alkanes. As found for all liquids studied previously, the energy loss function, which is proportional to the probability that an energetic electron will lose energy in a medium, shows a maximum at around 21 eV. This prominent feature is thought to be associated with an electron energy loss which causes excitation of a collective electronic plasma oscillation. The simple formula for the plasma frequency of a free electron gas predicts a plasma oscillation at about 16.6 eV for an electron density corresponding to that in the alkanes. The electrons are not free, of course, and thus the peak in the energy loss function will usually occur at a different energy. Where collective effects are small, the peak will occur at the same energy (or energies) as the maximum (or maxima) in ϵ_2, that is, at 7 and 12 eV

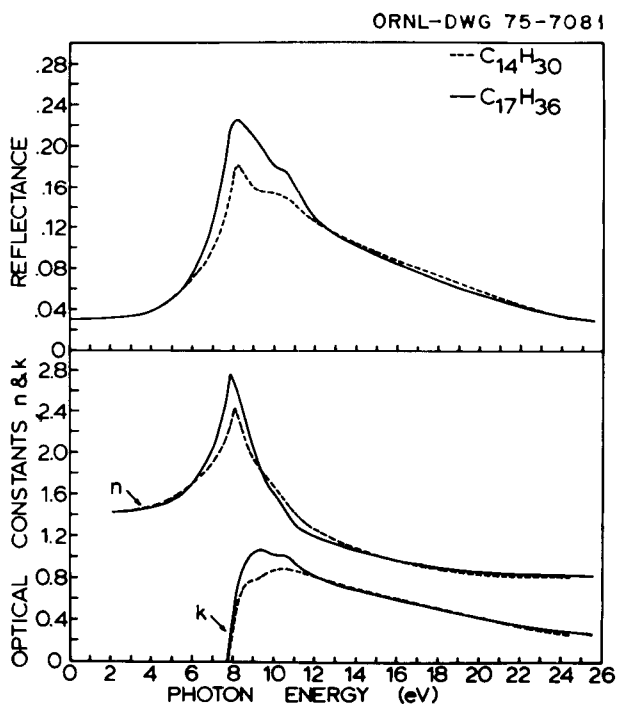

Fig. 15.3. Reflectance and optical functions for tetradecane and heptadecane. The optical functions shown are n, the index of refraction, and k, the extinction coefficient.

in these alkanes. The observation that the peak in the calculated loss function is at 21 eV instead is taken to imply that collective effects are important in the absorption of energy by liquid alkanes from ionizing radiation. That is, the absorptions at 7 and 12 (due to $\sigma-\sigma^*$ transitions of the C-H and C-C bonding electrons) give rise to a broad peak in the calculated loss function at 21 eV, predicting that collective effects can occur at this energy.

The cross sections for optical absorption per molecule obtained from the data of Fig. 15.3 and from the literature are shown in Fig. 15.5 for *n*-butane vapor, *n*-tetradecane liquid, and *n*-hexacosane solid. Not unexpectedly, the curves are very similar, differing primarily in magnitude. In Fig. 15.6 we have plotted the maximum value of this optical absorption cross section as a function of molecular weight for all alkane data we have been able to find. Here, the lower molecular weight materials are in the vapor phase, the intermediate are in the liquid phase, and the highest are in the solid phase. It is clear that the state of condensation of the alkane makes no difference in this maximum optical absorption cross section and that it is simply proportional to the length and molecular weight of the molecule.

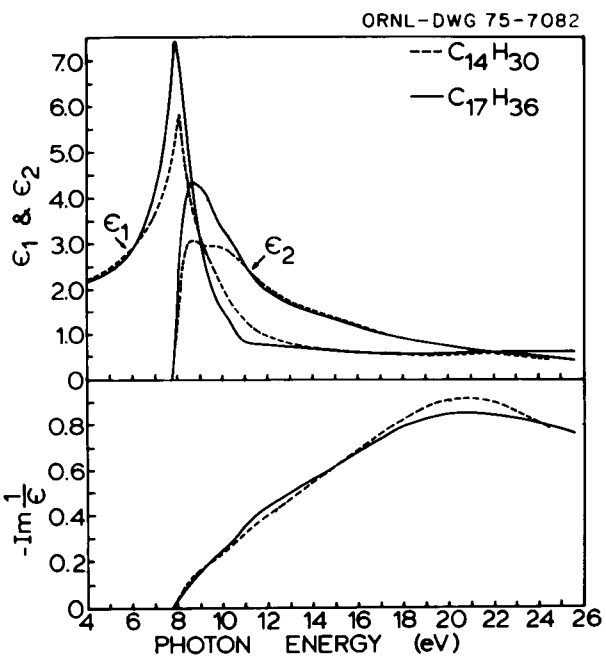

Fig. 15.4. The dielectric functions for tetradecane and heptadecane. The real and imaginary parts of the dielectric function, ϵ_1 and ϵ_2, are given as functions of photon energy. The imaginary parts of the reciprocal of the dielectric function, ϵ, are shown in the lower figure.

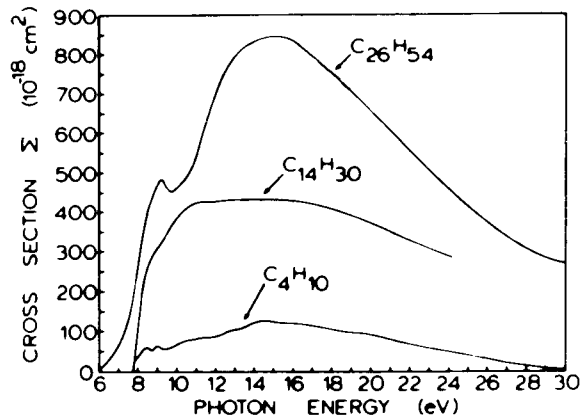

Fig. 15.5. Cross sections for optical absorption for hexacosane (solid), tetradecane (liquid), and butane (vapor).

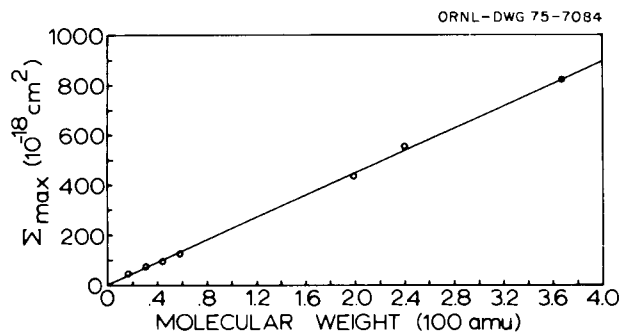

Fig. 15.6. Maxima of the optical absorption cross sections for various alkanes as a function of molecular weight. Lower weights are for vapors, intermediate for liquids, and largest for a solid. The state of condensation does not affect the maximum cross section.

The energy loss functions for all liquids that have been reported are shown in Fig. 15.7. Aside from the structure due to π electrons in the pump oils at 7 eV, the curves are remarkably simple, all showing a maximum at around 21 eV. As has been reported previously,[7] this loss represents the principal mechanism by which energetic electrons lose energy in nonmetallic liquid media. The significance of this finding to radiation chemistry has been the subject of much discussion that is still going on, but no conclusions have yet been reached.

THICKNESS OF CONTAMINATION ON THE ORMAK LINER

In a cooperative program with the Thermonuclear Division, we have been attempting to evaluate the

7. J. M. Heller, R. D. Birkhoff, and L. R. Painter, *J. Chem. Phys.* 62(10), 4121–4124 (May 15, 1975).

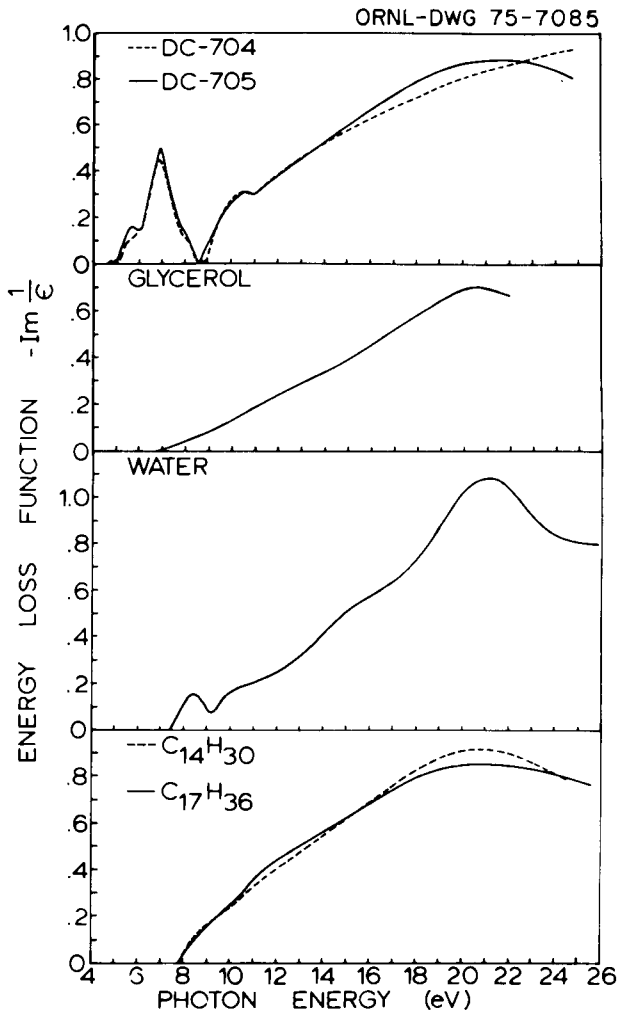

Fig. 15.7. Energy loss functions for several liquids. All liquids exhibit a broad maximum at about 21 eV, which is attributed to excitation of a collective electronic oscillation.

thickness of the contaminant layer on the ORMAK liner, since it is thought that impurities from this layer might affect the discharge characteristics of this Tokamak system. The results of theoretical calculations on the reflectance of the liner surface as a function of the thickness of carbon or other contamination are reported in Chapter 16 of this Annual Report.

A low-power helium–neon laser has been used in an optical arrangement as shown in Fig. 15.8. The laser beam was directed through the outer vacuum wall and through the inner liner into the inner wall section of the liner. We attempted to measure the reflectance of the liner by collecting the light returning back through the liner and vacuum wall windows. As shown, this light strikes a paper screen and is viewed with a mirror attached to the outer wall of the vacuum system. Reflected light has been detected but with relatively poor efficiency, and attempts are now being made to improve the system.

This work complements and supplements studies on the liner being performed by personnel of the Metals and Ceramics Division.

ELECTRON ENERGY LOSSES IN LIQUIDS

The recent prediction of collective electronic excitations or plasmons in the liquids water, glycerine, pump oils, and the alkanes has given rise to the questions: (1) Can these plasmons be excited by an energetic electron beam? (2) Will a surface plasmon state be excited also? Little work has been reported on electron energy losses in liquids since the pioneering work of Powell.[8] In these experiments, Powell used an 8-kV electron beam that was reflected from liquid and solid metals at various angles of incidence. The energy losses experienced by the beam were noted at each angular deflection of the electrons. Powell discovered that at near-glancing incidence, surface plasmons were generated by the beam, whereas as incidence approached the normal direction, losses to volume plasmon excitation were found. No observations on nonmetallic liquids have ever been reported. It is our intention to repeat essentially the Powell experiment on various low vapor pressure liquids, including the silicon pump oils and possibly glycerine. The possibility that surface-plasmon waves can be supported at the vacuum–liquid interface needs to be studied, since it is related to our work on surface waves on dielectric cylinders. In getting this experiment under way, we have located a suitable vacuum system, a high-voltage supply, and an electron gun and gun supply, and we have initiated construction of a spherical electrostatic analyzer for low-energy electrons.

8. C. J. Powell, *Phys. Rev.* **175**, 972 (1968).

ORNL DWG 75-7086

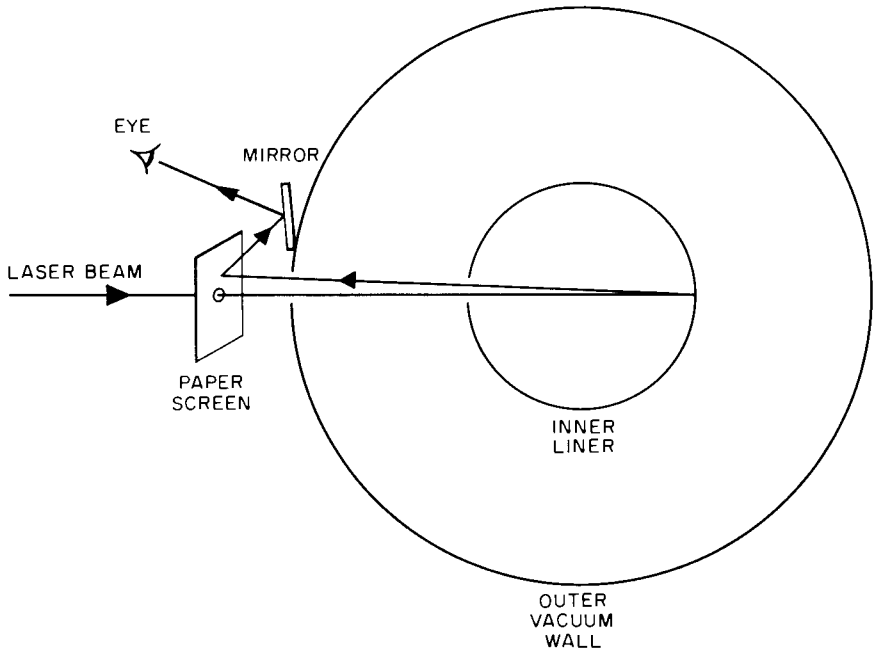

Fig. 15.8. Optical arrangement for locating reflected laser beam from ORMAK liner.

16. Physics of Solids and Macromolecules

E. T. Arakawa T. A. Callcott[1] R. N. Hamm
R. D. Birkhoff J. T. Cox T. Inagaki[2]
A. J. Braundmeier[1] Sung-I Juan[1]
C. E. Wheeler[3] Mary W. Williams

OPTICAL PROPERTIES OF SOLID SODIUM AND LITHIUM FROM ELLIPSOMETRIC MEASUREMENTS

The optical properties of the alkali metals in both the solid and liquid forms are of considerable theoretical and practical interest. Over the past several years, we have undertaken a systematic study[4,5] of the optical properties of solid alkali metals in the photon energy range from 4 to 10.7 eV. This includes energy regions of major interest for these materials, ranging over intra- and interband transitions and the volume plasmon energies. In these studies a solid thick film of an alkali metal was deposited on the flat surface of a transparent semicylinder substrate, and reflectance as a function of photon angle of incidence was measured at the substrate–metal interface. The real and imaginary parts of the complex refractive index, $\tilde{n} = n + ik$, were then obtained by a least-squares fit of the data to Fresnel's equations. Relative values of k were also obtained from transmittance measurements on thin alkali metal films on transparent substrates of uniform thickness.

We are now concentrating our efforts toward the precise measurement of the optical properties of simple liquid metals. Presently, there are theoretical predictions for disordered systems which have not been checked out experimentally. Thus one reason for studying liquid metals is to find a "simple" disordered system for which existing theories can be checked. A comparison of the optical properties of solid and liquid lithium, using the same experimental techniques, should provide a good test of these theories. In addition, the optical properties of liquid lithium will be required in the design of fusion reactors in which a "wetted" first wall of liquid lithium will be used.

Although lithium is the simplest of the alkali metals from the theoretical point of view, experimentally it is difficult to work with. Especially below ~6 eV, widely differing values[6] have been reported for the optical properties n and k of solid lithium; the values depend on many factors, including the thickness and structure of the films. However, there were existing, generally accepted, values for the optical properties of solid sodium in the literature. In order to get the maximum sensitivity, we decided to measure the optical properties of both solid and liquid lithium in the infrared to visible range (0.6 → 3.8 eV), using ellipsometric techniques. In preliminary observations, which were designed to check out our techniques and the interpretation of our data, we deposited a thick layer of sodium on the base of a quartz prism and analyzed the reflectance at the quartz–sodium interface, using standard ellipsometric techniques. The values obtained for the optical conductivity, $\sigma = nk\omega/2\pi$, are shown in Fig. 16.1 as a function of photon energy $\hbar\omega$. This figure shows that we have reproduced very closely the optical conductivity reported by Smith.[7] Using the same equipment, we obtained the σ vs $\hbar\omega$ for solid lithium and compared it with the three different curves published by Mathewson and Myers[8] (see Fig. 16.2). Curve A was obtained

1. Consultant.
2. Postdoctoral Fellow.
3. Graduate student.
4. J. C. Sutherland, R. N. Hamm, and E. T. Arakawa, *J. Opt. Soc. Amer.* **59**, 1581 (1969).
5. U. S. Whang, E. T. Arakawa, and T. A. Callcott, *Phys. Rev. B* **6**, 2109 (1972).
6. E. T. Arakawa et al., *Health Phys. Div. Annu. Progr. Rep. July 31, 1974*, ORNL-4979, pp. 125–128; T. A. Callcott and E. T. Arakawa, *J. Opt. Soc. Amer.* **64**, 839 (1974).
7. N. V. Smith, *Phys. Rev. Lett.* **21**, 96 (1968); *Phys. Rev.* **183**, 634 (1969).
8. A. G. Mathewson and H. P. Myers, *Phil. Mag.* **25**, 853 (1972).

from measurements on a lithium film 12 hr after deposition on a quartz substrate, and curve B was obtained from measurements on the same film six and one-half days later. Curve C was obtained from measurements on a lithium film on a sapphire substrate. In the Mathewson and Myers study, the films were deposited onto substrates cooled with liquid nitrogen, and then measurements were made at the vacuum–lithium interface. Our films were deposited on quartz at room temperature, and then the measurements were made at the quartz–lithium interface. The magnitude of the conductivity for the four curves is in general agreement, but the positions of the minima, and hence their possible interpretation, show significant differences from each other. It has been suggested[8] that the differences in curves A to C may be associated with differences in the crystalline phase. If this be true, our results may correspond to an average of the different crystal structures. Further study is needed on the possible effects on the optical properties of different substrate materials and of the substrate temperature. In addition, the optical properties of some of our lithium films were found to change with time, and this requires further investigation.

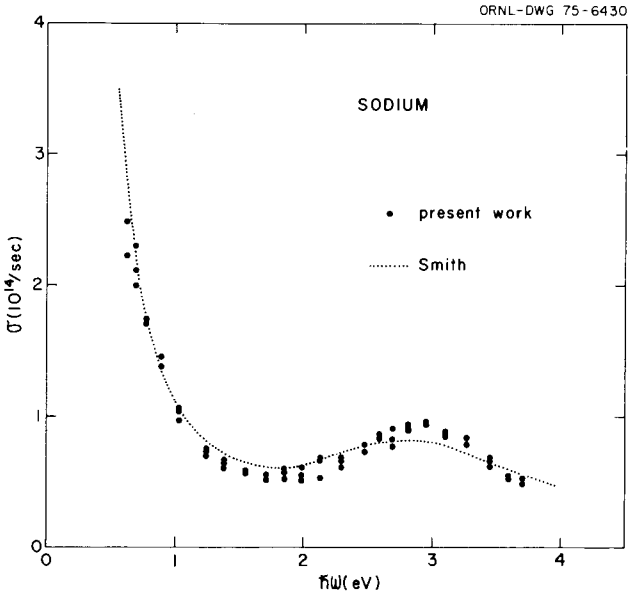

Fig. 16.1. Optical conductivity of solid sodium vs incident photon energy.

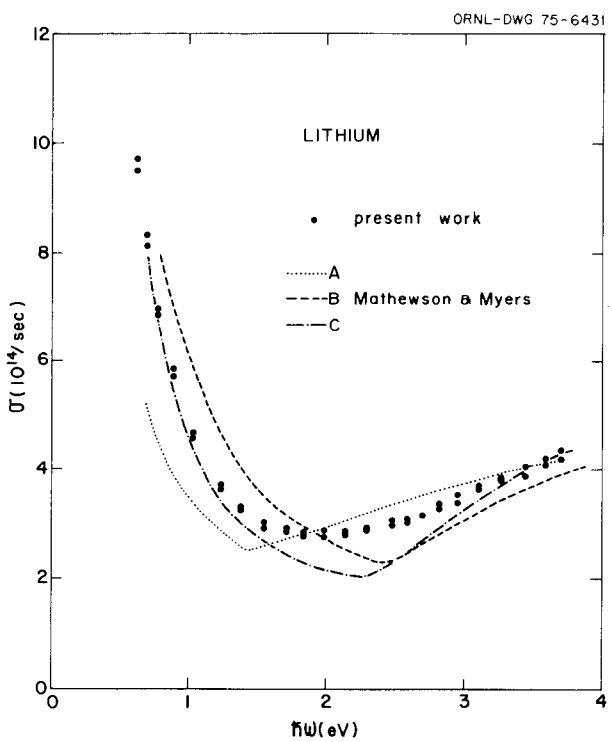

Fig. 16.2. Optical conductivity of solid lithium vs incident photon energy.

In Table 16.1 the parameters defining the optical properties of solid sodium and lithium obtained from the data presented in Figs. 16.1 and 16.2 are compared with the previously published parameters. For a nearly free-electron model of a metal,

$$n^2 - k^2 = 1 + 4\pi N\alpha_1 - \frac{4\pi\eta e^2}{m^*\omega^2}\,, \qquad (1)$$

where N is the number of ions per unit volume, α_1 is the polarizability of a single ion modified slightly by interband transitions, η is the density of free carriers, and m^* is the average optical effective mass of a conduction band electron. A plot of $(n^2 - k^2)$ vs $1/\omega^2$ should be linear. It was found that plots of the data of Figs. 16.1 and 16.2 showed linear portions in the infrared and in the visible to uv energy regions. The effective masses, calculated from the slopes of these plots, are given for these two energy regions in Table 16.1.

COUPLING OF PHOTONS AND SURFACE PLASMONS AT INTERFACES OF KNOWN PROFILE

The coupling of photons and surface plasmons at metallic diffraction grating surfaces has been investigated extensively in our laboratory in the past.[9] At that

9. E. T. Arakawa et al., *Health Phys. Div. Annu. Progr. Rep. July 31, 1969,* ORNL-4446, pp. 188–196; *July 31, 1970,* ORNL-4584, pp. 82–83.

Table 16.1. Effective electron masses of solid sodium and lithium at room temperature

	m^*/m	
	Infrared	Visible and uv
Sodium		
Present work	1.07	1.08
Ives and Briggs[a]		1.01
Hodgson[b]	1.08	
Mayer and Hietel[c]	1.27	1.17
Smith[d]	1.13	1.07
Palmer and Schnatterly[e]		1.00
Monin and Boutry[f]		1.07
Sutherland et al.[g]		1.06
Lithium		
Present work	1.61	1.56
Hodgson[h]		1.57
Bösenberg[i]		1.47
Mathewson and Myers[j]	1.7 (A)	
	1.33 (B)	
	1.33 (C)	
Callcott and Arakawa[k]		1.42 ~ 1.28

[a]H. E. Ives and H. B. Briggs, *J. Opt. Soc. Amer.* **27**, 181 (1937); M. H. Cohen, *Phil. Mag.* **3**, 762 (1958).
[b]J. N. Hodgson, *J. Phys. Chem. Solids* **24**, 1213 (1963).
[c]H. Mayer and B. Hietel, *Optical Properties and Electronic Structure of Metals and Alloys,* edited by F. Abelès North-Holland, Amsterdam, 1966, p. 47.
[d]N. V. Smith, *Phys. Rev. Lett.* **21**, 96 (1968); *Phys. Rev.* **183**, 634 (1969).
[e]R. E. Palmer and S. E. Schnatterly, *Phys. Rev. B* **4**, 2329 (1971).
[f]J. Monin and G. A. Boutry, *Phys. Rev. B* **9**, 1309 (1971).
[g]J. C. Sutherland, R. N. Hamm, and E. T. Arakawa, *J. Opt. Soc. Amer.* **59**, 1581 (1969).
[h]J. N. Hodgson, footnote *c*, p. 160.
[i]J. Bösenberg, *Phys. Lett. A* **41**, 185 (1972).
[j]A. G. Mathewson and H. P. Myers, *Phil. Mag.* **25**, 853 (1972).
[k]E. T. Arakawa et al., *Health Phys. Div. Ann. Progr. Rep. July 31, 1974,* ORNL-4979, pp. 125–128; T. A. Callcott and E. T. Arakawa, *J. Opt. Soc. Amer.* **64**, 839 (1974).

time, we studied the effect on the surface-plasmon dispersion relation of different metal and dielectric coatings on the grating surface by monitoring the radiative decay of surface plasmons into the diffraction orders. Any dependence on groove profile was not considered in these studies. Very recently there have been several theoretical treatments of the effect of groove profile on the absorption of photons in grating surfaces. We have undertaken a systematic experimental investigation of the effect of groove profile on the specular reflectance from metallic diffraction gratings and have compared our experimental results with a newly developed theory proposed by Elson and Ritchie (General Physics Group, Health Physics Division).

Excitation of surface plasmons by photons requires the conservation of both energy and wave vector (or momentum) parallel to the surface. For a grating surface, wave-vector conservation requires that the surface-plasmon wave vector $\mathbf{K}_{sp}$ and the component of the photon wave vector parallel to the surface $\mathbf{K}_p \sin\theta$, where θ is the photon angle of incidence, satisfy

$$\mathbf{K}_{sp} = \mathbf{K}_p \sin\theta + N\mathbf{g}, \tag{2}$$

with N a nonzero integer and $\mathbf{g}$ a vector parallel to the surface but perpendicular to the grooves and of magnitude $2\pi/d$, where d is the groove spacing. Excitation occurs only for p-polarized photons when the

plane of incidence (defined by $\mathbf{K}_p$ and the normal to the surface) is perpendicular to the grooves; for this case $\mathbf{K}_{sp}$ and $\mathbf{K}_p \sin\theta$ are collinear although they may be opposite in direction for negative N. A theoretical treatment by Elson[10] gives the probability for this excitation process as $P_0 = \sum_N \Delta_N$, with

$$\Delta_N = 8\pi^2\lambda^{-2}|S_N|^2\,\epsilon_2|(1-\epsilon)|^2\cos\theta|2\sigma_N{}^2-\epsilon|$$

$$\times\,|[(\sigma_N{}^2-1)(\sin^2\theta-\epsilon)]^{1/2}-\sigma_N\sin\theta|^2$$

$$\times\,\{\mathrm{Re}(\sigma_N{}^2-\epsilon)^{1/2}\cdot|(\sin^2\theta-\epsilon)^{1/2}-i\epsilon\cos\theta|^2$$

$$\cdot|(\sigma_N{}^2-\epsilon)^{1/2}+\epsilon(\sigma_N{}^2-1)^{1/2}|^2\}^{-1}\quad . \qquad (3)$$

S_N is the Nth coefficient of the Fourier transform of the groove profile, while λ is the wavelength of the incident photon; $\epsilon = \epsilon_1 + i\epsilon_2$ is the dielectric function of the metal coating of the grating; and $\sigma_N = \sin\theta + N\lambda/d$. This expression, Eq. (3), was derived from a first-order perturbation treatment of the boundary value problem using the magnetic vector potential, a transformation to relative coordinates, and a dyadic Green's function. Elson and Ritchie[11] employed similar techniques for a randomly rough surface but used the Hertz vector potential instead of the magnetic vector potential. In the derivation of Eq. (3), the wavelength of the incident photons was assumed to be much larger than the groove depth. In order to be able to use Eq. (3) when this approximation may not be satisfied, we have calculated the probability, P, of photon–to–surface-plasmon conversion assuming[12]

$$P = 1 - e^{-P_0} = 1 - e^{-\sum_N \Delta_N}. \qquad (4)$$

When using this expression, the probability, P, never exceeds unity and reduces to P_0 when P_0 is small.

Experimental curves of reflectance vs angle of incidence were recorded for aluminum-overcoated replica gratings with different known groove spacings and groove profiles. At an angle θ, such that Eq. (2) is satisfied, resonance surface-plasmon absorption results in a dip in reflectance at that angle of incidence. These dips were studied as a function of the angle between the grating rulings and the plane of incidence, polarization of the incident photons, and wavelength from 2400 to 6500 Å. Equation (3) gives the probability of surface-plasmon excitation where this is greatest, that is, with 90° between the grating rulings and the plane of incidence, and for p-polarized light. Most of our data were obtained for these conditions.

Representative experimental data and the corresponding quantities calculated from Eq. (3) are given in Fig. 16.3. Reflectance vs photon angle of incidence is given for several fixed values of the photon wavelength. For a given wavelength the upper curve shows the experimental reflectance on an arbitrary scale, and the lower curve shows a calculated quantity, P_N. The wavelength of the incident photons was chosen so that the angular separation of dips in reflectance for different N was a maximum with the result that $1 - \exp(-P_0)$, from Eq. (4), became $1 - \exp(-\Delta_N) \equiv P_N$. Since the maximum value of P_N should correspond to the minimum of the dip in reflectance, the convention was adopted of plotting P_N increasing downward. The integers next to each dip indicate the appropriate N value in Eq. (2).

Fitting the curves to the experimental reflectance vs angle of incidence data involved use of the Fourier coefficients appropriate to the groove profile to calculate P_N. In these calculations the dielectric functions appropriate to the aluminum overcoating were treated as adjustable parameters; ϵ_1 was adjusted so that the angular position of the dips corresponded to experiment, and ϵ_2 was adjusted until the angular half widths of the dips agreed with experiment. It is seen in Fig. 16.3 that having made the positions of the minima and the angular half widths correspond, the experimental and theoretical curves agree very well. The experimental curves are not symmetrical about the positions of the minima, and this is predicted correctly by the theory. In addition, the relative depths of the dips at different angular positions for a given wavelength are predicted fairly well. These calculations seem to indicate a general confirmation of Elson's theory, assuming that an "effective" dielectric function, ϵ, is used for the metal overcoating of the diffraction grating. From observations on several gratings, the probability for surface-plasmon excitation in grating surfaces has been shown to increase with increasing groove depth for fixed groove spacing and to increase with decreasing groove spacing for fixed groove depth.

The values of ϵ required to fit the theoretical to the experimental reflectance vs angle of incidence curves indicate considerably more damping in the aluminum overcoatings on the grating surfaces than in bulk aluminum. This is reflected in the dispersion curve for a given grating. The frequency, ω, of nonradiative surface

10. J. M. Elson, private communication.
11. J. M. Elson and R. H. Ritchie, *Phys. Status Solidi (B)* **62**, 461 (1974).
12. J. M. Elson and R. H. Ritchie, ORNL-TM-3752.

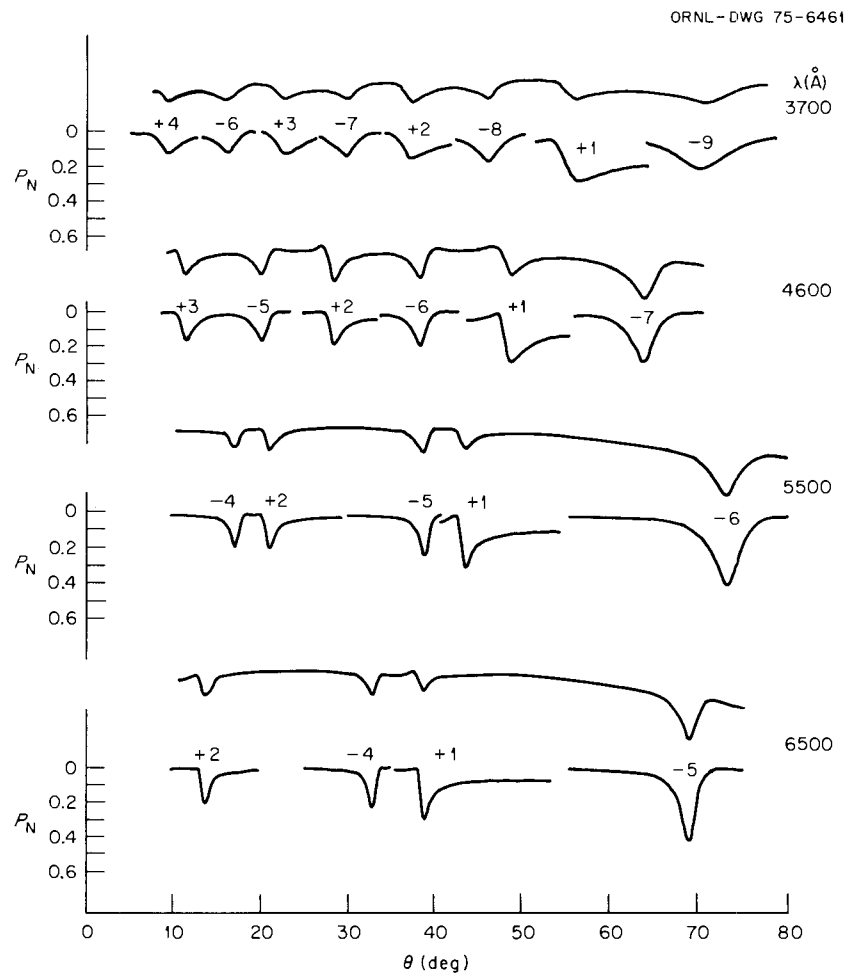

Fig. 16.3. Experimental reflectance (arbitrary units) and calculated probability (P_N) of surface-plasmon excitation for a grating for four different wavelengths. The integer next to each dip indicates the appropriate N in Eq. (16.2). Experiment and calculations are for p-polarized light and for 90° between the grating rulings and the plane of incidence.

plasmons at a smooth, planar, metal vacuum boundary is related to its wave vector, **K**, by

$$\mathbf{K} = \frac{\omega}{c}\sqrt{\frac{\epsilon}{\epsilon + 1}} . \tag{5}$$

Since the effective dielectric functions of the aluminum grating surfaces are not those of bulk aluminum, this implies that the dispersion relation for a grating is different than that for a planar surface of the same metal. This problem would be rather difficult to treat theoretically. We have assumed Eq. (5) to be valid for the grating or rough surface with ϵ set equal to the effective dielectric constant obtained by the reflectance vs angle of incidence fitting procedure. Preliminary analysis of our data indicates results for aluminum-overcoated gratings similar to those reported in the literature for silver-overcoated gratings[13] and for surface plasmons on randomly rough silver surfaces.[14,15] Compared with that for a smooth aluminum surface, the surface-plasmon dispersion curve, $\hbar\omega$ vs **K**, for a given groove depth or surface roughness is shifted to higher **K** values, the amount of the shift increasing with increasing groove depth of the grating surface. This implies a slowing down of the phase velocity of the surface plasmons on grating surfaces compared with a planar surface. In addition, we see a broadening of the reflectance dips with increasing groove depth, which

13. I. Pockrand, *Phys. Lett. A* **49**, 259 (1974).
14. A. J. Braundmeier, Jr., and E. T. Arakawa, *J. Phys. Chem. Solids* **35**, 517 (1974).
15. D. Hornauer, H. Kapitza, and H. Raether, *J. Phys. D* **7**, L100 (1974).

implies a stronger radiative damping of the surface plasmons by coupling to light via the periodicity of the surface.

Investigations need to be continued along two lines: (1) we need to consider the effect of nontriangular groove profiles on P_N when comparing the experimental and theoretical variations of reflectance with angle of incidence, and (2) we need to investigate further the meaning of the values of the effective ϵ obtained by our fitting procedure in relation to a theoretical dispersion curve for the grating surface.

PHOTOEMISSION FROM ALUMINUM

Photoemission measurements reported last year[16] have been extended to higher energies, and an extensive analysis of all of the data has been carried out.[17] Samples consisted of thin films of aluminum evaporated onto the plane face of an MgF_2 semicylinder. These samples were prepared in situ in an ion-pumped ultrahigh vacuum system for which the pressure was $\sim 3 \times 10^{-7}$ torr during evaporations and $\sim 2 \times 10^{-9}$ torr during measurements. Film thickness was determined by measuring the normal incidence transmission at a wavelength of 5480 Å, and in experiments where the film thickness was an important parameter, the thickness determination was checked with an optical interference microscope after the film was removed from the chamber. A prism monochromator with a high-pressure mercury–xenon lamp as source was used for excitation at photon energies below 5.2 eV. A 0.5-m Seya monochromator with a hydrogen discharge lamp as source was used for excitation for photon energies between 7.7 and 10.2 eV.

Both yields and energy distributions of emitted electrons have been measured. The total photo yield as a function of incident angle of *p*-polarized light for photon energies below 5.2 eV have been presented previously[16] and analyzed in terms of volume and surface photoemission processes. Only (35 ± 10)% of the yield observed at the plasmon peak could be accounted for by the volume process. The remaining 65% of the yield was attributed to the surface emission process. The higher energy data shown in Fig. 16.4 are the angular yields produced by the partially polarized light from the Seya monochromator incident on a 120-Å aluminum film. At 10.2 eV the light is predominantly *s*-polarized,[18] and the film is thinner than that used for the lower energy data, resulting in a far less spectacular resonance peak. Analysis of these curves in terms of volume and surface photoemission processes is inconclusive due to the large and somewhat uncertain percentage of *s*-polarized light in the exciting beam. However, some additional evidence for surface emission may be obtained from an examination of the energy distribution curves (EDC's) of photoemitted electrons. We can examine the curves for evidence of scattered electrons, which should be produced by the volume process but not by the surface process. In Fig. 16.5, we display EDC's made at three photon energies with photons normally incident from vacuum and with photons incident through the substrate both normally and at the resonance angle. For each energy the curves are normalized at the high-energy shoulder of the distributions. The relative amount of scattering ex-

ORNL-DWG-74-3256

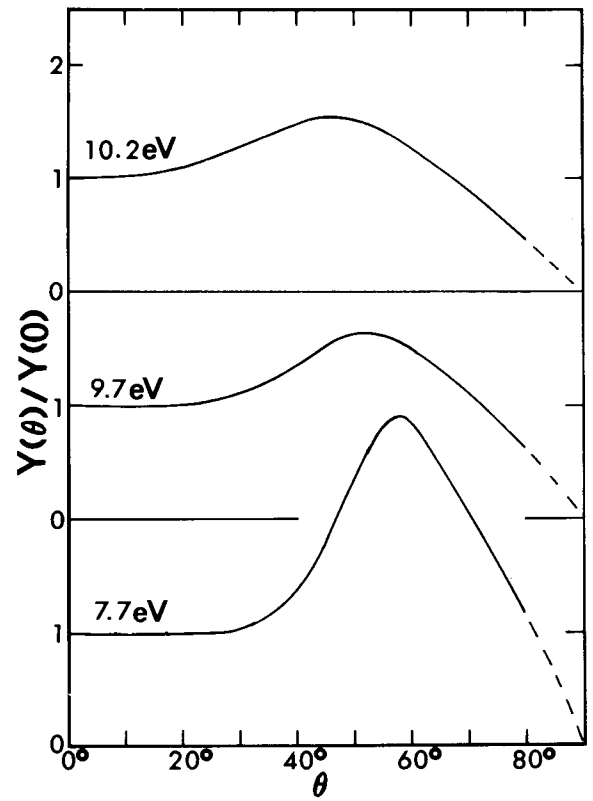

Fig. 16.4. Total photoyield vs incident angle of partially polarized photons of energies between 7.7 and 10.2 eV. Curves normalized to yield at normal incidence.

16. E. T. Arakawa et al., *Health Phys. Div. Annu. Progr. Rep. July 31, 1974,* ORNL-4979, pp. 129–132.

17. T. A. Callcott and E. T. Arakawa, *Phys. Rev. B* **11**, 2750 (1975).

18. W. F. Hanson and E. T. Arakawa, *J. Opt. Soc. Amer.* **56**, 124 (1966); J. J. Cowan, E. T. Arakawa, and L. R. Painter, *Appl. Opt.* 8, 1734 (1969).

pected from the volume process for each angle of excitation may be estimated from plots of energy density $\eta(y)$ vs y such as those plotted in Fig. 16.6, using parameters appropriate to 5.2-eV photons incident on a 160-Å film. Profiles calculated for other photon energies have the same characteristic features. EDC's were taken on thin aluminum films (~160 Å) in order to obtain sufficiently large yields for energy analysis with photons normally incident through the substrate. It can be seen (Fig. 16.6) that for normal incidence, the energy density decreases nearly exponentially away from the surface of incidence. At the plasmon resonance, it is reversed and has a profile very similar to that produced by photons incident from vacuum. At angles ~5° below the peak, the theory predicts a minimum in the photoemission which we have not observed experimentally. Clearly, relatively more electrons are produced away from the emission surface for photons normally incident through the substrate, and such excitation should produce the strongest scattering peak. The volume process should produce comparable scattering for the other two angles of excitation. In all cases (Fig. 16.5), the scattering peak is largest for photons normally incident through the substrate, as expected. The experimental curves indicate that there are significantly fewer scattered electrons in the plasmon-resonance photoemission than in free-surface photoemission. Though by no means conclusive, the EDC's are at least consistent with the existence of a strong surface emission at the resonance angle.

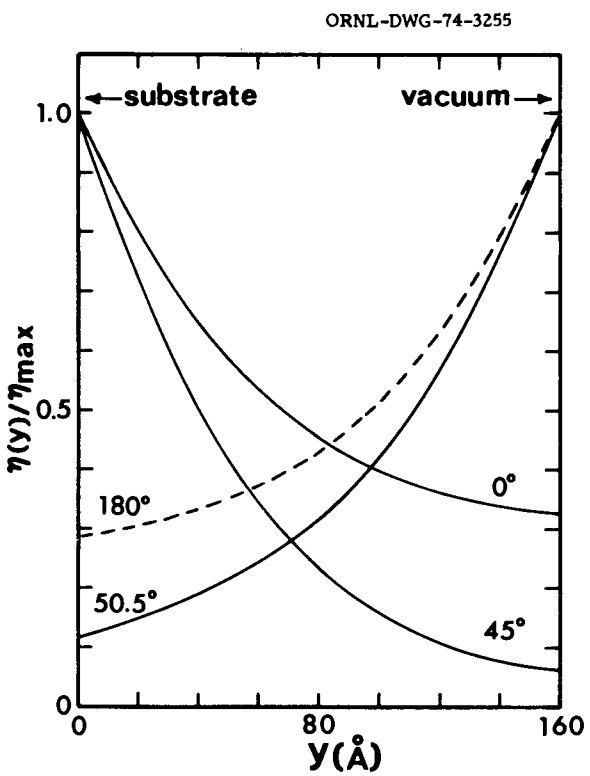

Fig. 16.6. Normalized energy densities in a 160-Å aluminum film for different angles of incident light. The curve for photons incident normally through the substrate is labeled by 0°. The plasmon-resonance angle is 50.5°.

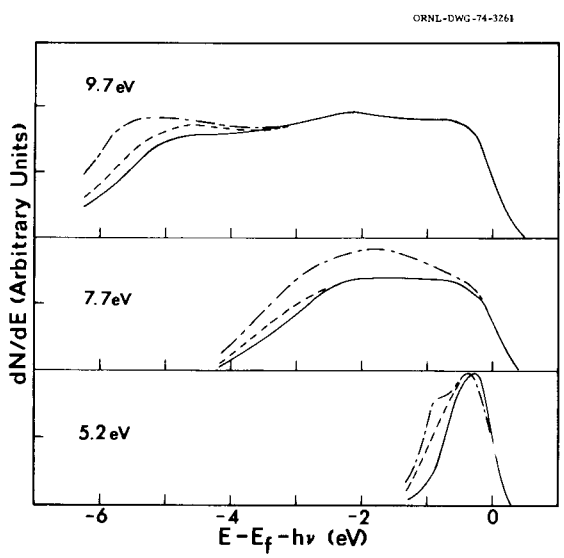

Fig. 16.5. Energy distributions measured with photons incident at the plasmon angle (solid line), normally through the substrate (dot-dashed line), and normally from vacuum (dashed line). Each set of curves is labeled with the incident photon energy.

The ratios of yields from aluminum with light normally incident from vacuum and through the MgF_2 substrate have been presented previously.[16] Analysis of these and additional data for the escape depths for the volume process have yielded values ranging from (45 ± 15) Å for 5.0-eV electrons to (20 ± 10) Å for 8.2-eV electrons.

For electrons near threshold, the measured escape depth or attenuation length, L, can be directly compared with an electron mean free path. In Fig. 16.7, we compare our values of the attenuation lengths with those measured by other workers and with the electron–electron scattering lengths calculated by Ashley and Ritchie[19] for a free-electron gas with the density of aluminum. Our value of the attenuation length at 5.0 eV is in good agreement with the value obtained by Kanter[20] from direct measurements of the

19. J. C. Ashley and R. H. Ritchie, *J. Phys. Chem. Solids* **26**, 1689 (1965).

20. H. Kanter, *Phys. Rev. B* **1**, 522 (1970).

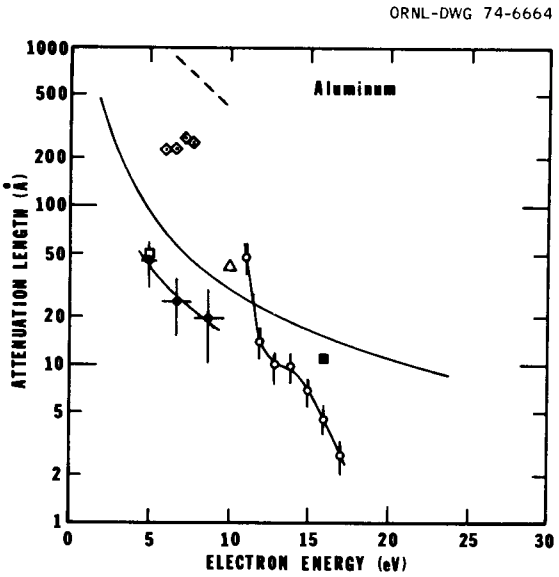

Fig. 16.7. Attenuation lengths for electrons in aluminum as a function of energy above the Fermi level. Solid circle, our data; diamond with dot, Pong et al. (ref. 22); dashed line, Wooten et al. (ref. 23); open square, Kanter (ref. 20); open circle, Gesell (ref. 24) from total yield; solid square, Gesell from $Y(\theta)/Y(0)$; solid line, theory of Ritchie and Ashley with exchange correction. Bars through solid and open circles indicate estimated limits of error due to experimental uncertainties.

attenuation of electron beams by thin foils. Both these values at 5.0 eV are, however, lower than values obtained by Feuerbacher, Godwin, and Skibowski,[21] Pong, Sumida, and Moore,[22] and Wooten, Huen, and Stuart[23] from analysis of photoemission data for photon energies between 5 and 10 eV. These latter analyses were made using assumptions appropriate to the volume emission process, and they neglect surface emission. It seems probable to us that surface emission contributes in an important way to their yields and that their values are consequently too high. The presence of emission via the roughness-coupled surface photoeffect would affect our determination of yield in the opposite way and would lead to erroneously small values.

Gesell has determined attenuation lengths in the immediately higher photon energy range by the analysis of total yield using L as an adjustable parameter.[24] Thus any unaccounted-for process that increases (or decreases) yield increases (or decreases) the value of L determined. The value of L Gesell determined at the surface-plasmon energy is significantly higher than the other values he obtained, presumably due to enhanced yield produced by the roughness-coupled surface-plasmon excitation. Above 15 eV, his values are thought to be too low; here the yield is depressed by the introduction of a new energy loss process in which electrons lose energy by exciting surface plasmons as they approach the sample surface. Our values of L join satisfactorily to the values Gesell found in the intermediate region between 11 and 14 eV, where neither of the above processes are important, and to the single value he obtained at 16 eV from an analysis of the angular yield ratio $Y(\theta)/Y(0)$ at this energy.

ELECTRON ATTENUATION LENGTHS IN CARBON FILMS[25]

Electron attenuation lengths, L, of photoexcited electrons in thick vapor deposited carbon films have been reported previously[26] over the range of photon energies from 20 to 64 eV. These values were derived from measurements of the total photoelectric yield, $Y(\theta)$, as a function of photon angle of incidence, θ. For a small extinction coefficient, k (<0.1), and a refractive index, n less than unity, the ratio $Y(\theta)/Y(0) = G(\theta)$ vs θ curves were analyzed to yield n and L. For each photon energy the position of the maximum of $G(\theta)$ vs θ, which occurs in the vicinity of θ_c, where $\theta_c = \sin^{-1} n$, yields a value of n while the magnitude of $G(\theta_c)$ is sensitive to both k and L. We measured k independently and hence obtained values of n and L by this method. As a consistency check, we compared the values of n obtained from reflectance and from photoelectric yield measurements on similar samples and obtained very good agreement. However, even though this consistency check was satisfactory, we still questioned the high values of L (~ 150 to 50 Å) obtained in the photon energy region of 20 to 30 eV. We thus decided to obtain values of L from measurements of the photoelectric yield, $Y(t)$, as a function of carbon film thickness, t. A wedge-shaped carbon film was deposited on a glass slide, and the metrical thickness as a function

21. B. D. Feuerbacher, R. B. Godwin, and M. Skibowski, *Z. Phys.* **224**, 172 (1969).

22. W. Pong, R. Sumida, and G. Moore, *J. Appl. Phys.* **41**, 1869 (1970).

23. F. Wooten, T. Huen, and R. N. Stuart, in *Optical Properties and Electronic Structure of Metals and Alloys,* edited by F. Abelès, North-Holland, Amsterdam, 1966, p. 333; T. Huen and F. Wooten, *Solid State Commun.* **9**, 871 (1971).

24. T. F. Gesell, Ph.D. Thesis, University of Tennessee, 1971; T. F. Gesell and E. T. Arakawa, *Phys. Rev. Lett.* **26**, 377 (1971).

25. Research sponsored in part by the Defense Nuclear Agency, under subtask TA040, but does not reflect endorsement by the sponsor.

26. E. T. Arakawa et al., *Health Phys. Div. Annu. Progr. Rep. July 31, 1974,* ORNL-4979, pp. 128, 129.

of position on the slide was obtained from a combination of transmittance and independent interferometric measurements. The experimental apparatus described previously[26] was used. In the same way as for the $Y(\theta)$ vs θ measurements, the carbon films were deposited in vacuum and exposed to the atmosphere on being transferred to the apparatus used for photoelectric measurements; then the values of $Y(t)$ were obtained with the experimental chamber pumped down to $\sim 2 \times 10^{-7}$ torr. For each constant incident photon energy, a $Y(t)$ vs t curve was plotted. Some representative curves of $Y(t)$ vs t for carbon on glass are shown in Fig. 16.8. It was found that for each photon energy from 10 to 64 eV, there was a rapid increase in $Y(t)$ in the vicinity of t = (10 to 15) Å with saturation of $Y(t)$ above this thickness. The complete analysis of photoelectric yield

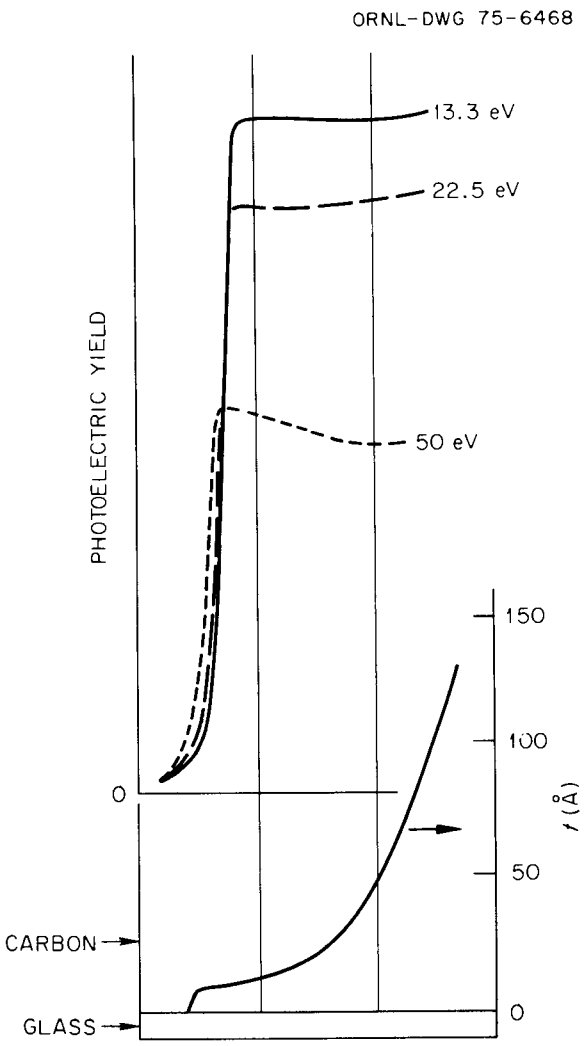

Fig. 16.8. Photoelectric yield vs carbon film thickness for constant incident photon energies.

measurements from such thin films is very complicated, requiring a knowledge of the homogeneity of the films and their effective optical properties in addition to a knowledge of the factors affecting the electron transport properties. Although a complete analysis of our $Y(t)$ vs t data for carbon has not yet been attempted, the values of L for photoexcited electrons in carbon appear to be much smaller in the region of 20 to 40 eV than the ones obtained[26] from the observations of $Y(\theta)$ vs θ. A theoretical analysis of the $Y(\theta)$ vs θ method has since been undertaken which showed that although reliable values of n can be obtained from $G(\theta)$ vs θ, to obtain L to ±1 Å requires that k be known to within ~1%. The uncertainty in the independently measured k values was much greater than this, leading to very large uncertainties in the calculated L values.

Electron attenuation lengths are known to be small in the region of 10 to 100 eV, and hence their accurate determination is difficult. At the same time, the values of these electron attenuation lengths in both metals and insulators are of great interest. We thus regard this as a continuing project. For the $Y(\theta)$ vs θ method, we plan to investigate various techniques whereby we can obtain extinction coefficients, k, to a higher accuracy than presently attainable since we have shown that the uncertainties associated with the values obtained for L are directly related to the uncertainties in the input values of k. For the $Y(t)$ vs t method, we plan to prepare and measure films of gold in ultrahigh vacuum for comparison with preliminary data already obtained on gold wedges prepared in vacuum but then exposed to air on transfer to the apparatus used to measure $Y(t)$ vs t. Gold is simpler to work with than carbon and should provide a check on the reliability of the experimental $Y(t)$ vs t curves obtained for carbon. Furthermore, experimental and theoretical studies of the electron attenuation lengths and the related electron mean free paths for gold have been reported in the literature. Data on the effective optical properties of gold as a function of film thickness are also available for evaporated gold films prepared under various conditions. A complete analysis of the $Y(t)$ vs t data for gold should thus be possible, providing a check on the reliability of this method. Ultimately, we hope to get completely consistent and reliable values of L in both metals and insulators.

OPTICAL AND DIELECTRIC PROPERTIES OF BOVINE PLASMA ALBUMIN BETWEEN 2 AND 82 eV

Studies of the optical properties of macromolecules of biological interest, which were initiated in the

Physics of Tissue Damage program, have been continued. The complex refractive index, $\tilde{n} = n + ik$, of dry films of bovine plasma albumin has been determined for incident photon energies from 2 to 82 eV. The techniques used were very similar to those used previously[27] to determine the optical properties of DNA over this energy range. The experimental details associated with obtaining the reflectance and transmittance measurements are identical with those described in ref. 27.

The dry films of bovine plasma albumin were obtained by dissolving bovine plasma albumin in distilled water, putting a few drops of the solution on the substrate, and allowing the water to evaporate at room temperature. To measure the extinction coefficient, k, for photon energies from 2 to 10 eV, a wedge of solid bovine plasma albumin was formed on a CaF_2 disk by inclining the disk just before the film started to solidify. Five positions on this film were selected for transmission measurements. Near-normal incidence reflectance at these positions showed good interference patterns in the photon energy region from 2.1 to 5.9 eV (6000 to 2100 Å), indicating that the thickness variation in the area illuminated by the incident light was small. From the interference patterns and the values of refractive index, n, which were determined by critical-angle measurements on a solid film deposited on a sapphire semicylinder, the thicknesses, d, were calculated at the five positions. The extinction coefficient of the bovine plasma albumin was then obtained from observations of transmittance, T, as a function of thickness for selected photon energies in the 2-to-10-eV range. It was assumed that $T = \exp(-4\pi kd/\lambda)$, where λ denotes wavelength. A plot of $\ln(1/T)$ vs d for a given λ yielded a straight line with a slope of $4\pi k/\lambda$ and hence a value of k at that photon energy. For the transmission measurements in the region between 8 and 82 eV, albumin films were made on ultrathin films of polystyrene supported by a fine-mesh nickel screen. Polystyrene was selected as the substrate material mainly because of its mechanical strength, surface smoothness, and good affinity to solid albumin. Although polystyrene absorbs strongly in the regions of 6.4 and 16 eV, the polystyrene films used showed greater than 25% transmission over the whole energy range. The thin films of polystyrene were made by dissolving polystyrene in a mixture of benzene and cyclohexane and then placing a single drop of this solution on a clean water surface and allowing the solvent to evaporate. The film was then lifted from the water surface on the nickel mesh screen. Before use, the films were checked for uniform thickness by measuring transmittance for a constant photon energy at different positions on the films. For those polystyrene films found to be uniform, half of each film was then covered with a small amount of the aqueous solution of albumin and the water allowed to evaporate. The transmittance, T, of these albumin films was assumed to be given by $T = I/I_0 = \exp(-4\pi kd/\lambda)$, where I and I_0 are the light intensities transmitted through the covered and uncovered parts of the polystyrene film respectively. In order to make measurements of k by this method, the bovine plasma albumin films had to be very thin, and it was impossible to measure their thickness. Hence the k values obtained by this method were normalized to those obtained for the films on CaF_2 in the overlapping region from 8 to 10 eV. As is well known, proteins show an absorption around 4.43 eV (2800 Å) due to aromatic side chains. Since this absorption band was too weak to be observed in the film deposited on CaF_2, additional transmission measurements were obtained for a 4.247-μ-thick film deposited on a sapphire substrate. This thick film was also used to determine the density of the albumin film. A known area was dissolved in water, and the mass was calculated from the absorptance measured at 2800 Å. The calculated density was 1.14 g/cm^3.

As previously mentioned, the refractive index, n, in the photon energy region from 2 to 5.5 eV, where bovine plasma albumin is nearly transparent, was obtained from critical-angle measurements. The n values above 5.5 eV were obtained by a Kramers-Kronig analysis of the k values from 2 to 82 eV. For each photon energy, E, $n(E)$ was determined from

$$n(E) = 1 + \frac{1}{2\pi}\int_0^\infty \frac{E'k(E')}{E'^2 - E^2}\,dE' .$$

It was assumed that k is zero in the region below 2 eV and, for the region above 82 eV, the values of k at 70 and 82 eV were linearly extrapolated to zero k at ~90 eV. Errors in the calculated n values due to these assumptions should be small. However, larger errors in n could result from uncertainties in the k values above 10 eV due to the normalization procedure used in determining these data. Since the n values determined by critical-angle measurements in the 2-to-4-eV region were considered accurate, the values of k above 10 eV were adjusted so that the n values between 2 and 4 eV from the Kramers-Kronig analysis agreed with those from the critical-angle measurements.

27. E. T. Arakawa et al., *Health Phys. Div. Annu. Progr. Rep. July 31, 1974*, ORNL-4979, pp. 149–151.

From the values of n and k thus obtained, the complex dielectric function, $\epsilon = \epsilon_1 + i\epsilon_2$, where $\epsilon_1 = n^2 - k^2$ and $\epsilon_2 = 2nk$, and the energy loss function $-\mathrm{Im}(1/\epsilon)$ were calculated from 2 to 82 eV.

The real and imaginary parts of the refractive index and the dielectric function and the energy loss function for dry, solid bovine plasma albumin are shown as functions of incident photon energy in Figs. 16.9, 16.10, and 16.11 respectively.

The extinction coefficient, k, shown in Fig. 16.9, exhibits maxima at 4.4, 6.4, 7.6, and 14.0 eV and shoulders at ~5.5 and ~9.7 eV. The small band at 4.4 eV has been attributed to π-electron transitions in aromatic side chains.[28] The peak at 6.4 eV has been established to be the $\pi^0 - \pi^-$ ($NV_\perp$) band, which shows exciton splitting at 6.02 and 6.56 eV in α-helical polypeptides. The shoulder at 5.5 eV has been assigned to the $n-\pi^-$ transition and is widely used in the conformational analysis of proteins and polypeptides in optical rotary dispersion and circular dichroism studies. However, Barnes and Rhodes[29] have proposed another interpretation for this band as composed of the $n-\pi^-$ band and a "mystery" band that has recently been observed in the amide monomer. The small peak at 7.6 eV may have the same origin as the peak found in aliphatic homo-polypeptides, over whose assignment considerable controversy exists in the literature.[30] Absorption studies on a series of homo-polypeptides have shown that the intensity of this band is as sensitive to the conformation as the $\pi^0-\pi^-$ band. Pysh[31] has carried out a theoretical analysis of the absorption intensity for various conformations and has obtained results that describe the experimental data quite well. The absorption data on aliphatic amino acids[32] have suggested, however, that the intensity is also affected

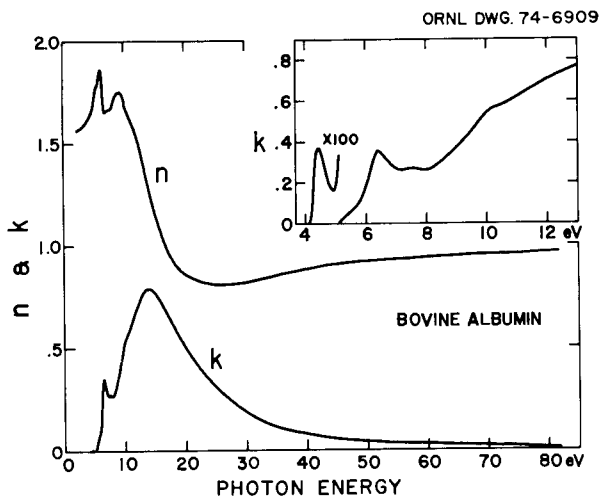

Fig. 16.9. Real and imaginary parts of the complex refractive index of a dry film of bovine plasma albumin as a function of incident photon energy.

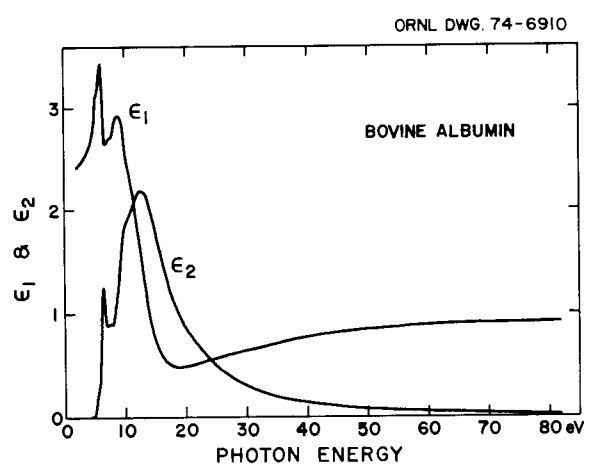

Fig. 16.10. Real and imaginary parts of the dielectric function of a dry film of bovine plasma albumin as a function of incident photon energy.

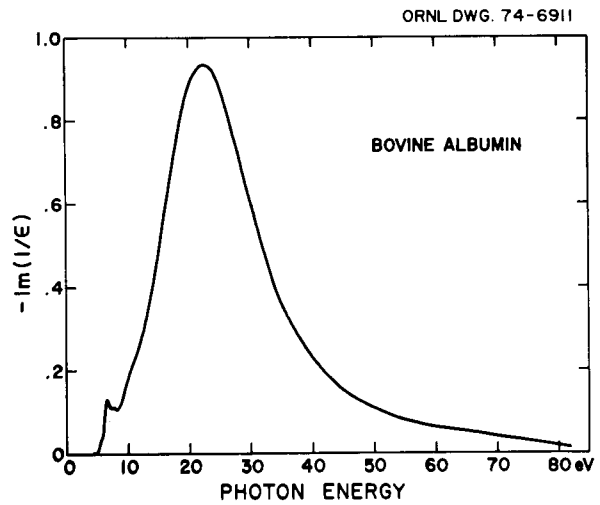

Fig. 16.11. Energy loss function of a dry film of bovine plasma albumin as a function of incident photon energy.

28. For a complete survey, see G. D. Fasman (Ed.), *Poly-α-Amino Acids*, Marcel Dekker, New York, 1967. M. A. Stahmann (Ed.), *Polyamino Acids, Polypeptides and Proteins*, University of Wisconsin Press, Madison, 1962.

29. D. B. Barnes and W. Rhodes, *J. Chem. Phys.* **48**, 817 (1969).

30. C. R. McMillin, W. B. Rippon, and A. G. Walton, *Biopolymers* **19**, 589 (1973); M. A. Young and E. S. Pysh, *Macromolecules* **6**, 790 (1973), and references therein.

31. E. S. Pysh, *J. Chem. Phys.* **52**, 4723 (1970).

32. T. Inagaki, *Biopolymers* **12**, 1353 (1973).

by the species of the side chain group. In regard to the shoulder found at ~9.7 eV, possible transitions[33] predicted in this region are $n'-\pi^-$, $n-\sigma^*$, and $\pi^+-\pi^-$ (NV_2). Studies on oriented films of polypeptides with polarized light may be of help for assignment of this band. The strong peak in k at 14.0 eV appears to arise mainly from σ-electron transitions, since a peak has been observed at nearly the same position for a wide variety of organic materials.[34]

Bovine plasma albumin is a typical globular protein, and the absorption spectrum obtained in these studies is of fundamental importance in the quantitative analysis of radiation effects on the macromolecule over the extended energy range from 2 to 82 eV. In addition, however, our data yield the energy loss function $-\mathrm{Im}[1/\epsilon(E)]$ which describes the probability that a high-energy charged particle will lose energy, E, in exciting single electron transitions or collective electron oscillations, on traversing the protein film. The separation in energy between the peak in ϵ_2 and the corresponding peak in $-\mathrm{Im}(1/\epsilon)$ is a measure of the degree of collective behavior that the system exhibits.[35] Examination of Figs. 16.10 and 16.11 shows that, up to ~10 eV, structures in $-\mathrm{Im}(1/\epsilon)$ are displaced very little from the corresponding structures in ϵ_2 and hence the system shows little collective behavior at these energies. However, the pronounced peak in $-\mathrm{Im}(1/\epsilon)$ at 22.7 eV is shifted considerably from the corresponding peak in ϵ_2 at 12.8 eV, indicating considerable collective behavior of the π and σ electrons.

The oscillator strength for bovine plasma albumin, calculated in the same way as for DNA,[27] approaches unity for high photon energies, implying that almost all of the loosely bound electrons participate in the optical transitions observed below 82 eV.

OPTICAL AND DIELECTRIC PROPERTIES OF POLYSTYRENE BETWEEN 2 AND 82 eV

For a large macromolecule, such as DNA,[27] we were able to make thin self-supporting films on a fine nickel mesh. For a smaller macromolecule, such as bovine plasma albumin, making thin self-supporting films proved impossible, and polystyrene was used as a substrate (see preceding section, this chapter).

Polystyrene is one of the most radiation-resistant polymers. It is mechanically strong, can be formed into thin, smooth, homogeneous films, and is transparent in the visible with the uv absorption edge at 4.59 eV (2700 Å). It is an excellent thermal and electrical insulator, with aromatic stabilization. It has many applications; in particular, it is an important material in communications systems, and hence it is important to know what response it does show to ionizing radiations over as large an energy range as possible. Furthermore, it is a chemically simple linear polymer involving phenyl groups; thus it is of interest to compare its properties with those of benzene[36] and of the alkanes.[37]

The characteristic energy loss spectrum of 20-keV electrons has been reported by Swanson and Powell,[38] showing pronounced energy losses at (6.97 ± 0.10) eV and at (21.3 ± 0.3) eV. Previous optical measurements[39] have yielded ample comparison between the calculated energy loss function and the lower electron energy loss peak but little comparison with the higher electron energy loss peak. It was thus decided to measure the optical properties of polystyrene over the energy range from 2 to 82 eV. The techniques used were similar to those for DNA[27] and for bovine plasma albumin (see preceding chapter, this section). The real and imaginary parts of the dielectric function, $\epsilon = \epsilon_1 + i\epsilon_2$, and of the energy loss function, $-\mathrm{Im}(1/\epsilon)$, are shown as functions of incident photon energy in Figs. 16.12 and 16.13 respectively. Pronounced structure is seen in ϵ_2 at 6.2 and 12.5 eV and corresponding structure in $-\mathrm{Im}(1/\epsilon)$ at 7.0 and 21.5 eV. The structure in ϵ_2 at 6.2 eV corresponds to that seen in liquid benzene[36] at 6.5 eV. This is due to a $\pi-\pi^*$ transition attributed to a molecular excitation of the π electrons in the benzene ring. The structure in ϵ_2 at 12.5 eV is assumed to be due to a $\sigma-\sigma^*$ transition, or transitions, comparable with the transitions seen in the alkanes[37] in

33. R. W. Woody and T. Tinoco, *J. Chem. Phys.* **46**, 4927 (1967), and references therein.

34. For example, E. E. Koch and A. Otto, *Chem. Phys. Lett.* **12**, 476 (1972); E. E. Koch and M. Skibowski, *Chem. Phys. Lett.* **9**, 429 (1971); J. T. Shapiro and R. P. Madden, *J. Opt. Soc. Amer.* **58**, 771 (1968); J. M. Heller, Jr., R. D. Birkhoff, M. W. Williams, and L. R. Painter, *Radiat. Res.* **52**, 25 (1972).

35. E. T. Arakawa et al., *Health Phys. Div. Annu. Progr. Rep. July 31, 1974*, ORNL-4979, pp. 140–143.

36. M. W. Williams, R. A. MacRae, R. N. Hamm, and E. T. Arakawa, *Phys. Rev. Lett.* **22**, 1088 (1969).

37. J. M. Heller, R. D. Birkhoff, and L. R. Painter, *J. Chem. Phys.* **62**, 4121 (1975).

38. N. Swanson and C. J Powell, *J. Chem. Phys.* **39**, 630 (1963).

39. J. G. Carter, T. M. Jelinek, R. N. Hamm, and R. D. Birkhoff, *J. Chem. Phys.* **44**, 2266 (1966); W. L. Buck, B. R. Thomas, and A. Weinreb, *J. Chem. Phys.* **48**, 549 (1968); J. T. Shapiro and R. P. Madden, *J. Opt. Soc. Amer.* **58**, 771 (1968); S. Onari, *J. Phys. Soc. Jap.* **26**, 500 (1969).

the (8–12) eV range of energies. The difference in energy between the positions of corresponding peaks in ϵ_2 and $-\mathrm{Im}(1/\epsilon)$ indicates the degree of collective behavior associated with the peak in $-\mathrm{Im}(1/\epsilon)$.[35] Thus the peak in $-\mathrm{Im}(1/\epsilon)$ at 7.0 eV indicates that high-energy charged particles traversing the polystyrene have a high probability of losing 7.0 eV of energy to a hybrid excitation of the π electrons, which shows mainly molecular excitation and very little collective behavior. Conversely, the 21.5-eV peak in $-\mathrm{Im}(1/\epsilon)$ shows highly collective behavior of both the π and σ electrons. The calculated peaks in $-\mathrm{Im}(1/\epsilon)$ are seen to correlate well with the peaks measured by Swanson and Powell[38] in the characteristic electron energy loss spectrum.

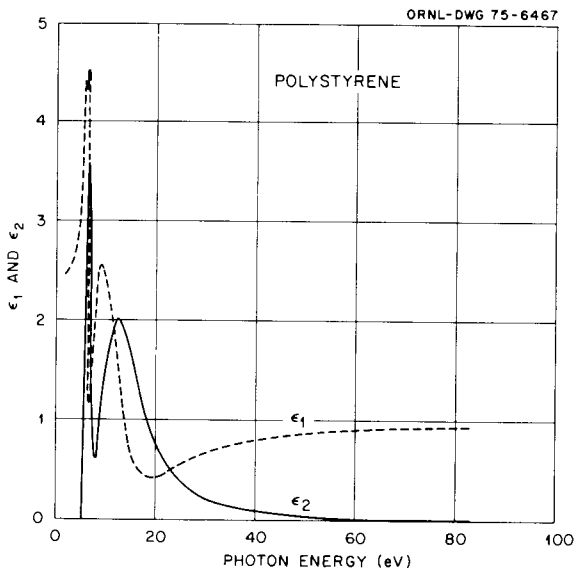

Fig. 16.12. Real and imaginary parts of the dielectric function of polystyrene as a function of incident photon energy.

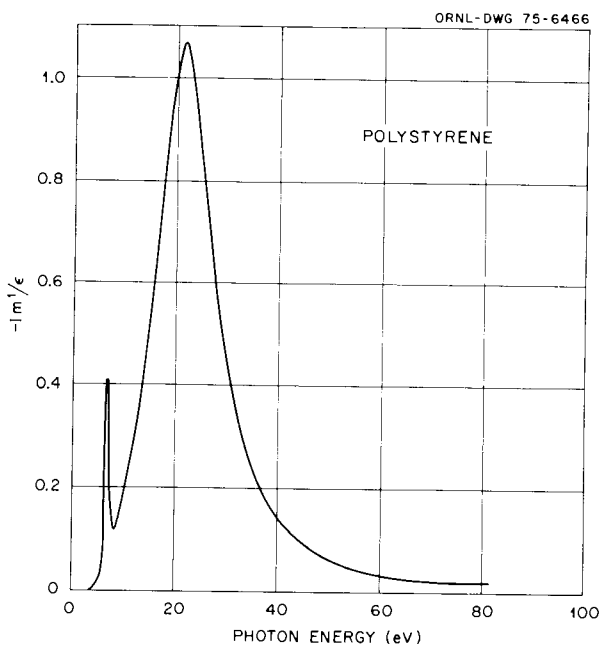

Fig. 16.13. Energy loss function of polystyrene as a function of incident photon energy.

Several materials of biological interest, (i.e., water and many organic molecules in the liquid and solid states) have now been studied in our collaborative programs[27,37] here and at the University of Tennessee. In each case, prominent structure has been found in the calculated energy loss function, $-\mathrm{Im}(1/\epsilon)$, in the vicinity of 21 eV. Analysis of the spectra for the dielectric functions and the corresponding loss function, as done here for polystyrene, indicates a high degree of collective electron behavior in each case. Since the energy loss function is proportional to the probability that a high-energy charged particle will lose energy to the medium, this represents an extremely important mechanism for energy absorption in these materials. In particular, the importance of collective electron oscillation (plasmon) creation at this energy and its nonlocalized nature is significant in track structure models and calculations for ionizing radiation.

FEASIBILITY STUDIES OF MONITORING THE FIRST WALL IN ORMAK BY OPTICAL MEASUREMENTS

A study of the feasibility of using optical measurements to monitor a portion of the gold liner, forming the first wall in ORMAK, for the effective thickness of the contaminant layer on the gold was undertaken this year. Since it was thought that the predominant contaminant is carbon, we calculated the specular reflectance expected theoretically for electromagnetic radiation of various photon energies incident on carbon films of various known thicknesses on a gold substrate. The specular reflectance for normal incidence was calculated using Fresnel's equations and optical properties of gold and carbon taken from the literature.[40] In these calculations, it was assumed that the gold is homogeneous, isotropic, and semi-infinite, with a perfectly planar interface with vacuum (zero thickness of carbon) or with the carbon. Likewise, we assumed the carbon to be homogeneous, isotropic, and uniform in

40. H. J. Hagemann, W. Gudat, and C. Kunz, "Optical Constants from the Far Infrared to the X-Ray Region: Mg, Al, Cu, Ag, Au, Bi, C, and Al_2O_3," Report No. DESY SR-74/7, May 1974.

thickness and to have perfectly planar interfaces with the gold and with vacuum. The results of these calculations are shown in Fig. 16.14. It can be seen that for this idealized case of carbon contamination on gold, even a few angstroms of carbon thickness can be detected directly by measurement of the normal incidence reflectance at a properly chosen photon energy although, in practice, for very thin layers the homogeneity condition breaks down and an "effective" thickness would be obtained. As a direct check on these calculations, a single reflectance vs thickness curve for carbon on gold was determined experimentally. A thick, smooth evaporated gold film was deposited on a glass slide and then overcoated with various known thicknesses of evaporated carbon. Reflectance vs thickness was then obtained for a photon energy of 2.3 eV. These measurements are shown in Fig. 16.15 and demonstrate the feasibility of using this method to determine the thickness of a carbon contaminant layer on a smooth gold substrate.

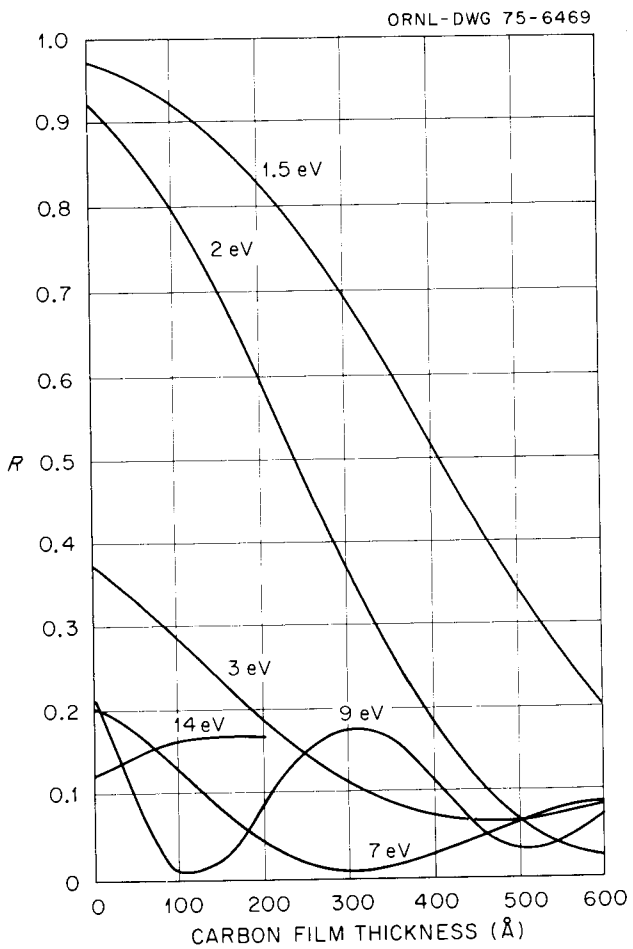

Fig. 16.14. Calculated reflectance vs contaminant film thickness for carbon on gold for selected incident photon energies.

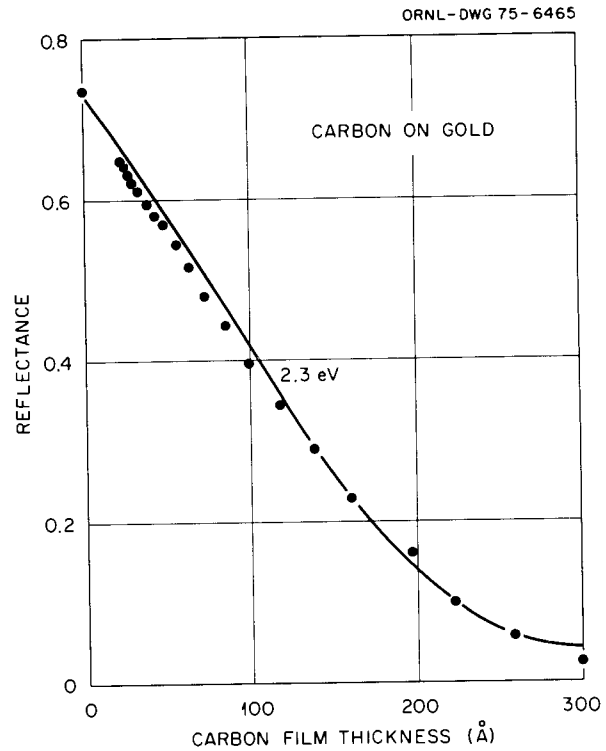

Fig. 16.15. Calculated reflectance vs film thickness for carbon on gold compared with experimental values for a photon energy of 2.3 eV.

Transmission measurements were also performed on a lens that had been used in ORMAK. Although the lens was not expected to show the same contaminant layer as the liner, its measurement had value as a test case. Experimental observations of transmittance were obtained at 4500 and 5400 Å, and theoretical curves of transmittance vs film thickness were calculated by the same techniques as described above. Assuming the contaminant layer to be carbon on glass, we calculated the film thickness, t, to be (440 ± 30) Å. Auger analysis, by others, of the contaminant layer later indicated that C, Fe, W, and O were present. Using optical constants from the literature, transmittance vs thickness curves were obtained for Fe_3O_4 on glass and Fe (or W) on glass. For Fe_3O_4 on glass, t = (690 ± 120) Å, and for Fe (or W) on glass, t = (110 ± 5) Å. These observations illustrate several important facts. Assuming homogeneous materials and perfectly planar interfaces, it is essential to know the constituents of the contaminant layer and the corresponding effective complex refractive index in order to calibrate the system. The large, estimated errors in thickness, Δt, for the film on

the lens are indicative of incorrect input variations of complex refractive index with photon energy rather than of experimental errors in the measured transmittance. If the system is fully defined except for the contaminant film thickness, the accuracy with which this can be obtained for a given accuracy of the reflectance measurements depends on the nature and thickness of the contaminant layer, on the nature of the substrate, and on the choice of photon energy.

Examination of the calculated reflectance vs carbon film thickness curves, shown in Fig. 16.14, leads us to suggest that initially measurements should be made using a He–Ne laser for which the photon energy is 1.96 eV. The reflectance for this photon energy drops monotonically from over 90% for no carbon to approximately 2% for a 600-Å-thick film. Similar characteristics are anticipated for other possible contaminant layers assuming ideal conditions, as in the calculations for carbon on gold. In reality, the gold liner in ORMAK is not mirror-like to the eye, and there is appreciable surface roughness and hence some diffuse scattering of the incident light. The calibration will have to be determined experimentally, and for this it will be necessary to know the nature of the contaminant layer. Films of the same composition as the contaminant layer in ORMAK will have to be deposited on a liner sample and the reflectance measured as a function of known film thickness. Such measurements will give a better approximation to the actual conditions in ORMAK, and hence a better calibration, than any values we could calculate assuming a smooth gold substrate. It is anticipated that the variation of reflectance with film thickness will be less than that indicated by the ideal values calculated for a smooth gold substrate. However, the system should be sufficiently accurate for use as a monitor of surface contamination thickness.

Finally, it was pointed out that to measure very thin contaminant layers or small changes in the thickness of the contaminant layer, it might be necessary to use ellipsometric techniques to obtain the desired information.

Some preliminary experimental investigations of the ORMAK liner are described in Chapter 15 of this report.

SOFT X-RAY EMISSION FROM INSULATORS

The soft x-ray emission spectrum of LiF obtained previously[41] using cleaved LiF crystals has been repeated for evaporated films of LiF. As observed previously, the specimen changed on electron beam bombardment such that within a few minutes the surface looked metallic. Correspondingly, the main K_α emission peak shifted from that of Li^+ in LiF at 46.5 eV to that for pure Li at 54.3 eV. In the initial spectrum obtained before the Li buildup can occur, we now see a peak at 61.0 eV, with a magnitude ~10% of the main emission peak. This is indicated clearly in our present data in Fig. 16.16, whereas it was barely seen in the emission spectra obtained previously[41] for LiF. The difference arises from the way in which the initial spectrum was obtained in each case. For the cleaved LiF reported previously, the crystal was cleaved, mounted in the apparatus, and bombarded with electrons. Each soft x-ray emission spectrum was scanned continuously with time, the time recorded on each spectrum being the average time for that spectrum from the beginning of the bombardment. It took 1 to 2 min to obtain each spectrum. For the evaporated LiF, each point on the spectrum corresponds to a fresh film. With the monochromator set to record a given photon energy, a LiF film was evaporated in situ and the photon intensity recorded when the electron beam was first turned on. This process was repeated until the whole spectrum was obtained. The x-ray emission peak at 61 eV is thought to be due to the radiative decay of a core-level exciton in LiF. Until recently the soft x-ray absorption spectra of various alkali halides reported in the literature were interpreted in terms of band structure alone, dismissing the possibility of core-level

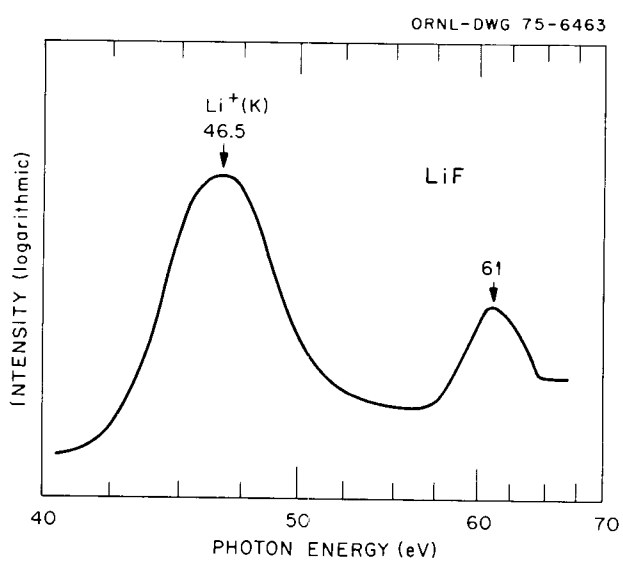

Fig. 16.16. Li^+ K emission spectrum of an evaporated film of LiF.

41. E. T. Arakawa et al., *Health Phys. Div. Annu. Progr. Rep. July 31, 1974*, ORNL-4979, pp. 132, 133.

exciton states. The use of optical gap data in conjunction with the soft x-ray absorption spectra has led to a new interpretation of the x-ray absorption spectra in which some structure is associated with core-level excitons.[42,43]

From various observations, including independently measured x-ray photoelectron spectra and optical gap data, it has been determined, as outlined by Pantelides,[42] that in LiF the top of the valence band lies 50.8 eV above, and the bottom of the conduction band 64.4 eV above, the Li 1s level. It is seen that these numbers are consistent with our emission spectrum for LiF, which is shown in Fig. 16.16. Thus the emission seen at 61.0 eV occurs in the band gap and must represent a direct observation of the radiative decay of a core-level exciton. Data obtained in the same way for evaporated films of LiCl and LiBr are shown in Figs. 16.17 and 16.18 respectively. Calculations[42] identical to those for LiF have set the bottom of the conduction band in LiCl at 62.3 eV and in LiBr at 61.8 eV. The peaks in the emission spectra of LiCl at 60.5 eV (Fig. 16.17) and of LiBr at 59.6 eV (Fig. 16.18) thus originate in core-level excitons. The progression of exciton peak energies seen in our emission spectra (i.e., 61.0 eV in LiF, 60.5 eV in LiCl, and 59.6 eV in LiBr) is very similar to the variation of peak energies seen in the absorption spectra reported by Pantelides[42] (i.e., 61.9 eV in LiF, 60.8 eV in LiCl, and 60.4 eV in LiBr).

Other emission peaks seen in Fig. 16.17 correspond to Li^+ in LiCl at 49.5 eV (K_α emission) and Cl^- in LiCl at 184 eV ($L_{23}M_1$), with a second order at 92 eV. The peaks in Fig. 16.18 correspond to Li^+ in LiBr at 51.4 eV (K_α emission) and Br^- in LiBr at 65 eV ($M_{4,5}$) and 114 eV (M_2M_4).

42. S. T. Pantelides and F. C. Brown, *Phys. Rev. Lett.* **33**, 298 (1974); S. T. Pantelides, *Phys. Rev. B* **11**, 2391 (1975).

43. W. Gudat, C. Kunz, and H. Petersen, *Phys. Rev. Lett.* **32**, 1370 (1974).

Emission spectra were also obtained for evaporated films of Li_2SO_4 and $LiNO_3$. These spectra did not show exciton peaks. Neither did they show the rapid changes with time seen in the halogens.

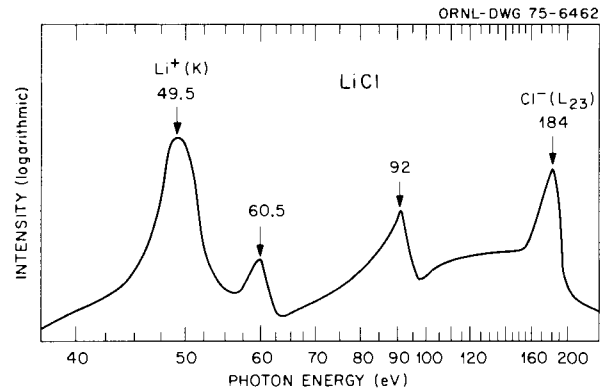

Fig. 16.17. Soft x-ray emission spectrum of an evaporated film of LiCl.

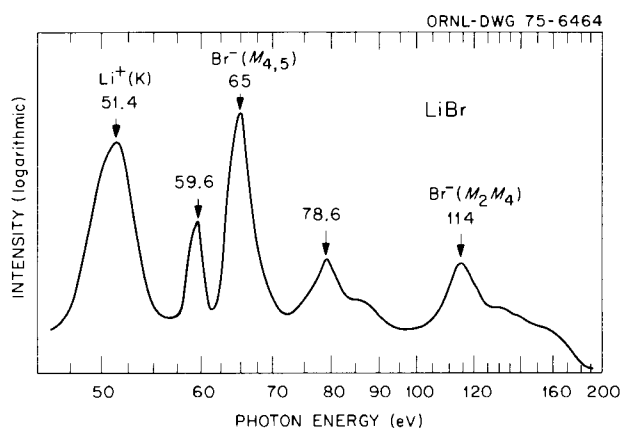

Fig. 16.18. Soft x-ray emission spectrum of an evaporated film of LiBr.

17. General Physics

R. H. Ritchie J. C. Ashley
V. E. Anderson[1] T. L. Ferrell[2] J. Neufeld[2] J. E. Turner
Werner Brandt[2] R. N. Hamm C. J. Tung[3] H. A. Wright

PION BEAM DOSIMETRY

The computer code PION-1, which has been discussed in previous annual reports, has been further improved and now appears to contain an adequate treatment of all of the physical processes important for applications to cancer radiotherapy. A complete description of the code is currently being prepared for publication.

Several calculations have been made of dose distributions from pion beams. The results of one set of calculations, made at the request of a group at the Los Alamos Scientific Laboratory, are shown in Fig. 17.1. The curves display the effects on depth-dose patterns in tissue of changing the momentum spread of a negative pion beam. The calculations were made for a uniform, circular, parallel pion beam of radius 2 cm. In each case the mean momentum was 171.5 MeV/c, which corresponds to a nominal range of 20 cm. The curves show the dose that would be measured with an axial circular cylindrical detector the same size (2 cm radius) as the beam and 2 mm thick. It is seen that, as the momentum spread increases, the peak dose decreases and the position of the peak dose shifts toward the surface. The curve for zero percent spread was calculated for a monoenergetic pion beam and indicates the degree to which the width of the peak dose region is determined by multiple scattering, range scattering, and nuclear capture stars.

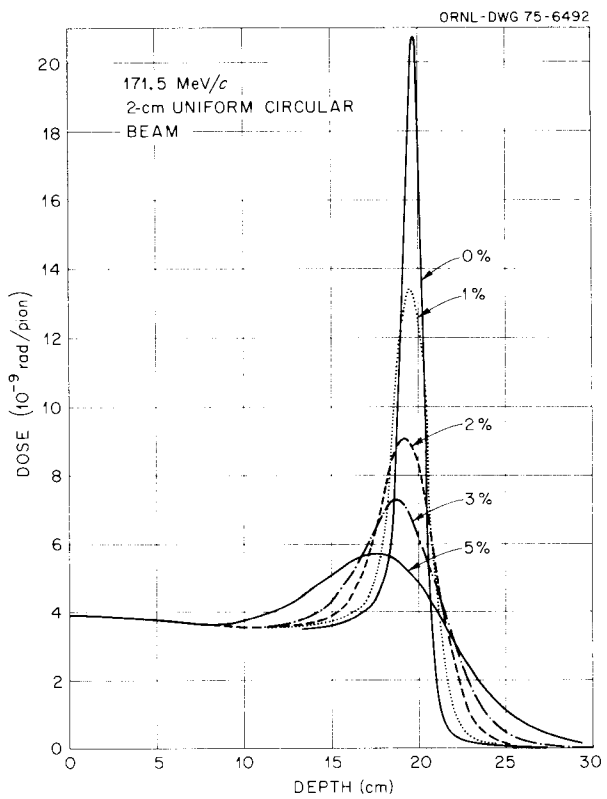

Fig. 17.1. Absorbed dose produced by uniform circular (2 cm radius) beams of negative pions as a function of depth in tissue. The curve labeled 0% results from a monoenergetic beam with momentum 171.5 MeV/c. For the other cases the momentum distribution of the beam is Gaussian and such that one-half of the particles have momentum within the indicated percentage of the mean.

ESTIMATED W VALUES FOR NEGATIVE PIONS IN NITROGEN AND ARGON

Because of the availability now of high-intensity negative pion beams for radiobiology and radiotherapy, interest in pion dosimetry has intensified. Knowledge of W, the average energy required to produce an ion pair, underlies the use of ionization methods to measure radiation dose. While W has been measured for the most common types of radiation in many gases, its value for pions has not. The present work provides estimates of

1. Computer Sciences Division.
2. Consultant.
3. Graduate student.

W for nitrogen and argon, based on a combination of calculations and available experimental data.

The number-energy spectra of fragments produced from capture of negative pions by oxygen, nitrogen, and carbon have been calculated by Guthrie, Alsmiller, and Bertini.[4] These computed spectra are consistent with available measurements.[5,6] Except for alpha particles, W-value data for multiply charged ions are sparse. In a recent interview, Dennis[7] summarizes measurements of W for a number of ions in nitrogen, carbon dioxide, argon, and several hydrocarbon gases. The most extensive data are available for nitrogen and argon, which were chosen for the present study.

Dennis[7] reports the values shown in Fig. 17.2 for nitrogen. Measurements have been made with protons and alpha particles over the entire range of energies shown. Data are also available for nitrogen ions between 25 keV and 608 keV and for carbon ions between 25 keV and 50 keV. In Fig. 17.2 we have drawn smooth curves through the data points for helium, carbon, and nitrogen ions. Dennis gives the values W_β = 34.6 eV/ip (electron volts per ion pair) and W_α = 36.39 eV/ip for high-energy beta and alpha particles in nitrogen gas. The curve for nitrogen has been extrapolated (dashed portion) to energies beyond which experimental measurements are available, based on use of the universal reduced velocity-squared parameter, $E/MZ^{4/3}$, where E is the energy of the ion, M its mass, and Z its atomic number. This parameter is the same for a 537-keV alpha particle and a 10-MeV nitrogen ion, for which the extrapolated value W_N = 38.5 eV/ip was assumed. Data for the other nuclear fragments produced by pion capture in tissue – namely, boron, beryllium, and lithium ions, tritons, and deuterons – are scant. Curves for these ions could also be constructed, based on the reduced velocity-squared parameter, and drawn smoothly between the curves in Fig. 17.2. However, these other ions were treated collectively in the calculations.

Figure 17.3 shows a similar plot for argon gas. The values of W are generally smaller than those for nitrogen. The data for argon indicate that W is the same for nitrogen, helium, and hydrogen ions at energies as low as about 0.5 MeV.

Based on Figs. 17.2 and 17.3 and the spectra of Guthrie et al.,[4] numerical calculations of W were carried out. The results are given in Table 17.1. The values of W_C, W_N, and W_O represents the average energies required to form an ion pair in nitrogen or argon gas by the ions produced when a stopped negative

4. M. P. Guthrie, R. G. Alsmiller, Jr., and H. W. Bertini, *Nucl. Instrum. Methods* **66**, 29 (1968), erratum, *Nucl. Instrum. Methods* **91**, 669 (1971).

5. P. H. Fowler and V. M. Mays, *Proc. Phys. Soc.* **92**, 377 (1967).

6. H. L. Anderson, E. P. Hincks, C. S. Johnson, C. Rey, and A. M. Segar, *Phys. Rev.* **133**, B392 (1964).

7. J. A. Dennis, *Radiat. Eff.* **8**, 87 (1971).

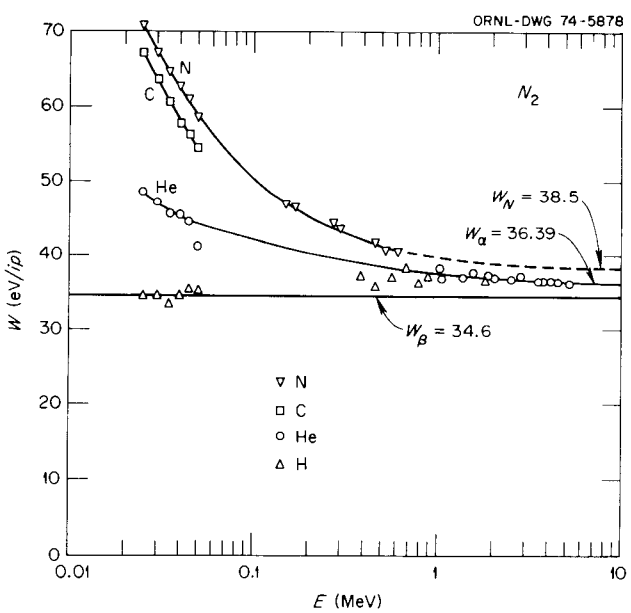

Fig. 17.2. W values for ions stopped in N_2 as functions of their initial energy E. Dashed curve shows extrapolation of data used in the present work for nitrogen ions.

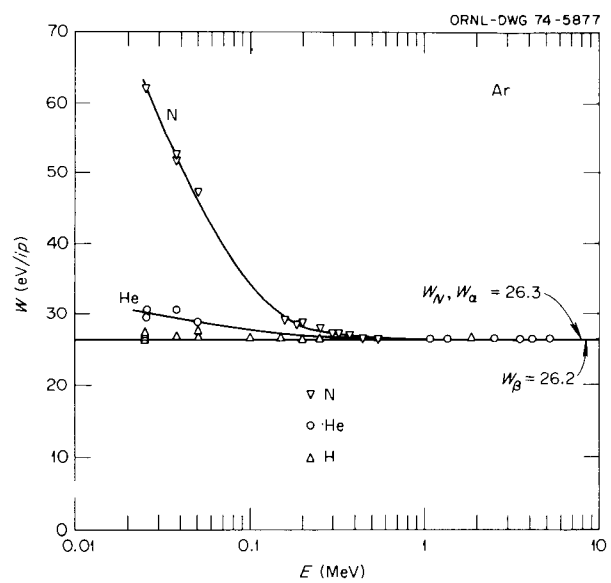

Fig. 17.3. W values for ions stopped in Ar as functions of their initial energy E.

Table 17.1. Calculated W for ionization in nitrogen and argon gas following capture of negative pions by elements in soft tissue and W averaged over tissue elements
Values in electron volts per ion pair

	N_2	Ar
W_C	36.40	26.30
W_N	36.42	26.30
W_O	36.44	26.30
W_{TISSUE}	36.43	26.30

pion is captured by a carbon, nitrogen, or oxygen nucleus. The values of W_{TISSUE} represent the energies when the capturing carbon, nitrogen, and oxygen nuclei are present in the relative atomic abundance with which they occur in soft tissue (C, 0.2594; N, 0.0370; O, 0.7036). In computing the values of W_{TISSUE}, it was assumed that the capture probability is proportional to Z, as described by the Fermi-Teller[8] capture rule.[9]

Since only a few measurements of W have been made at low energies, it is important to see what effect the energy dependence of W may have on dosimetric measurements with negative pions. To this end, the calculations were repeated with an energy-independent value of W for each type of ion. Specifically, values at 10 MeV were assumed to apply at all energies. The results for nitrogen are shown in Table 17.2. Comparison with Table 17.1 indicates that neglecting the energy dependence of W introduces an error of only about 0.1% for nitrogen. The error for argon is much less. This finding is not strongly dependent on the actual values of W assumed at 10 MeV. These results indicate that the energy dependence of W is not critical for the dosimetry of negative pions in tissue-like materials.

Additional computations were made for an experimental pion beam used in previous work.[10] The pions had a Gaussian momentum distribution with a mean of 176 MeV/c and a spread of 2%. The beam was parallel, nonuniform, and elliptic in shape with major and minor axes of 7 cm and 6 cm and was incident on a water target. The absorbed dose was calculated as a function of depth in thin circular volume elements of radius 3 cm centered along the beam axis. Pion depth-dose curves are characterized by two regions, a plateau and a peak. For the beam studied, the plateau extends from the surface to a depth of about 15 cm, beyond which the peak occurs with a maximum at 21 cm. Beyond this peak, the dose falls virtually to zero at a depth of 25 cm.

Table 17.2. W for nitrogen gas computed under assumption of energy independence
Values in electron volts per ion pair

W_C	36.38
W_N	36.39
W_O	36.40
W_{TISSUE}	36.39

Table 17.3. W estimated for nitrogen gas in plateau and peak regions of typical pion depth-dose curve

Particle type	Relative dose (%)		W (eV/ip)
	Plateau	Peak	
Pion (direct ionization)	89	38	36.3
Protons	4	27	36.3
Heavy particles	6	30	37.4
Neutrons	1	5	37.4
Average W			
Plateau			36.38
Peak			36.69

Values of W for nitrogen gas, calculated in the plateau and peak regions of this beam, are given in Table 17.3. Contributions to dose made by various types of particles[11] were weighted by the W values for capture by oxygen (Table 17.1). Table 17.3 indicates that, when nitrogen is used in an ionization chamber, the value of W may increase about 0.3 eV/ip in the peak, relative to the plateau – a difference of approximately 1%. Since these changes were determined by taking differences, they are not very sensitive to systematic errors in the individual numbers used in the calculations. When argon is used, even less difference in W between the plateau and peak regions is expected.

In summary, W values estimated for stopped negative pions are given in Table 17.1. This work indicates that the energy dependence of W amounts to only about 0.1% in measuring the dose delivered in tissue by stopped pions. The calculations also indicate that W

8. E. Fermi and E. Teller, *Phys. Rev.* 72, 399 (1947).

9. If this rule is ignored, the computed value of W_{TISSUE} is different by less than 10^{-4} eV/ip.

10. J. E. Turner, J. Dutrannois, H. A. Wright, R. N. Hamm, J. Baarli, A. H. Sullivan, M. J. Berger, and S. M. Seltzer, *Radiat. Res.* 52, 229 (1972).

11. These contributions are shown individually in Fig. 6 of ref. 9. The muon and electron contamination of the actual experimental beam was not included in the estimates made here. Its inclusion would have little effect.

changes by only about 1% between the plateau and peak regions for a typical pion beam. A summary of this work has been submitted for publication.[12]

MONTE CARLO TREATMENT OF MULTIPLE COULOMB SCATTERING IN PION-BEAM DOSE CALCULATIONS

As a charged particle traverses matter, it undergoes a large number of small-angle scattering events due to the long-range Coulomb interaction with atomic nuclei. This multiple Coulomb scattering, which occurs almost continuously, markedly affects the patterns of dose deposition that can be obtained with pion beams. Indeed, for therapeutic applications, multiple scattering largely determines the extent to which the absorbed dose from pions can be localized in a tumor region.

The question arises of how to represent multiple Coulomb scattering in Monte Carlo calculations for pion beams. Because of the large number of scattering events, direct collision-by-collision simulation based on the Rutherford scattering cross section is not feasible. Instead, an analytic procedure must be devised to represent this effect. Three such procedures were investigated, as described below, and one was selected and incorporated in PION-1. Theoretical predictions were compared with results obtained by using the empirical formulas of Fowler and Perkins[13] for the lateral spread of pion beams in tissue due to multiple Coulomb scattering.

1. Single scatter at surface of target. In the first calculation it was assumed that each pion is deflected through some angle as it enters the surface of the target; thereafter, the pion travels in a straight line. For each incident pion the angle was chosen from a distribution that gives the correct empirical distribution of lateral track displacements in the stopping region. This simple procedure, which uses only 38 sec of computer time for 10,000 incident pions,[14] gives the correct peak-to-surface dose ratio for the typical pion beams we have studied. However, it causes the beam to spread too much between the surface and the peak.

Calculations were performed for a pencil beam of 82-MeV pions incident on tissue of unit density. All nuclear reactions and range straggling were "turned off" in order to study the effects of multiple scattering alone. Each pion traveled exactly the same distance, 20.2 cm, and came to rest. The empirical distribution of projected lateral displacements at a depth of 14 cm is shown by the crosses in Fig. 17.4. The calculated projected distribution, determined by tabulating the relative number of pions with displacement between 0 and 2.4 cm in 0.1-cm intervals, is shown by the circles. Both distributions are relative and have unit height at $y = 0$. The results show clearly the extent to which this simplified, single-deflection representation exaggerates multiple scattering at intermediate depths between the surface and the peak (near 20.2 cm).

While perhaps useful in special cases, the single-deflection method is unnecessarily crude and inadequate for many applications.

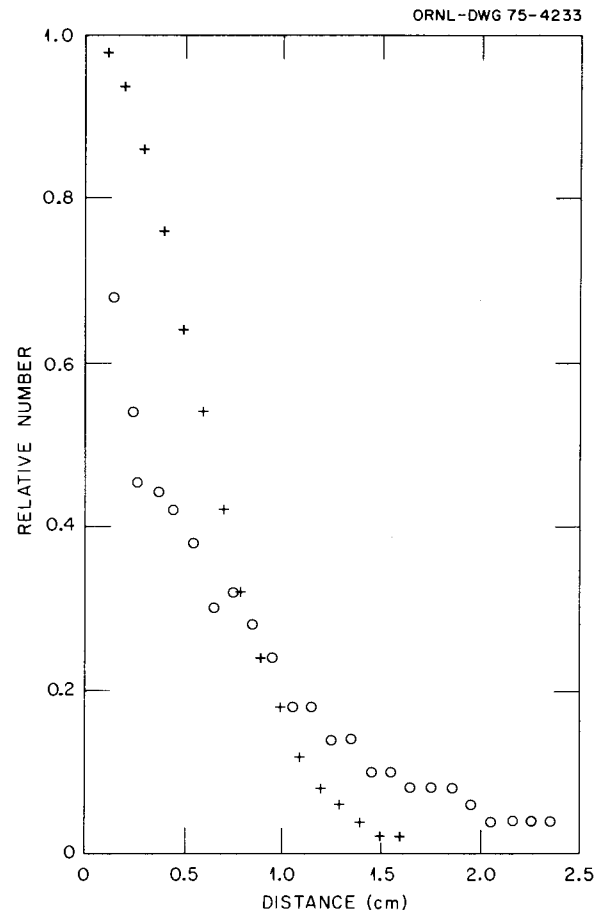

Fig. 17.4. Empirical (crosses) and calculated (circles) distributions of projected lateral displacements at a depth of 14 cm in a tissue target bombarded by a pencil beam of 82-MeV pions (range, 20.2 cm). A single deflection at the surface of the target was assumed in the calculations.

12. J. E. Turner, H. A. Wright, and R. N. Hamm, submitted to *Health Physics.*
13. P. H. Fowler and D. H. Perkins, *Nature* 189, 524 (1961).
14. IBM 360 model 91.

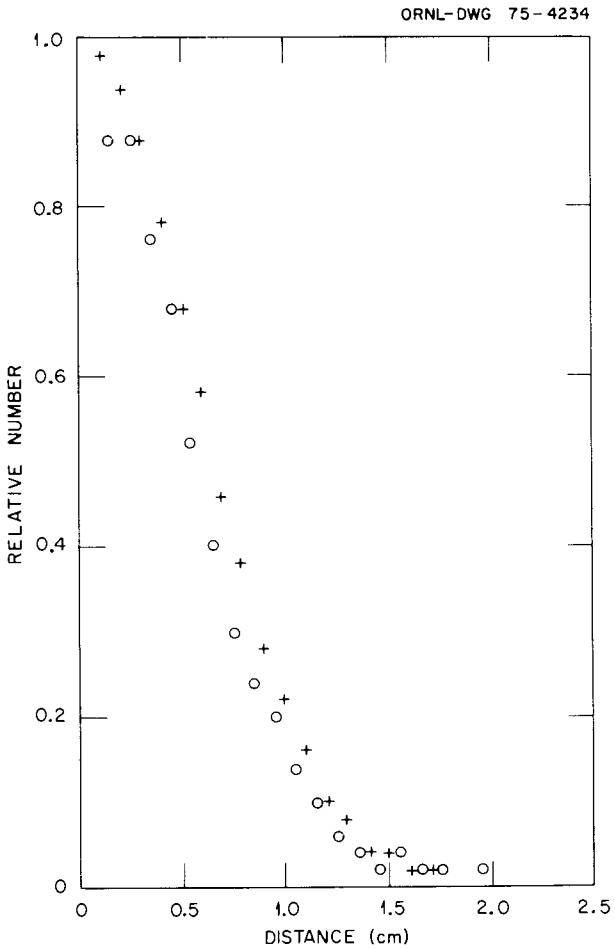

Fig. 17.5. Empirical (crosses) and calculated (circles) distributions of projected lateral displacement at a depth of 14 cm in a tissue target bombarded by a pencil beam of 82-MeV pions. Multiple scattering was computed at successive scattering distances s = 1 cm by use of angular distributions only.

2. Use of angular scattering distributions only. Bichsel[15] has given formulas, based on Molière's theory,[16] which describe the angular distribution of an initially parallel beam of charged particles after penetrating a thin foil of variable thickness s. Using Bichsel's tabulations, we performed calculations for a pencil beam of 82-MeV pions by letting each pion be deflected after each centimeter of travel in the target. Figure 17.5 shows the calculated projected lateral displacement distributions (circles) for the 82-MeV pencil pion beam at a depth of 14 cm. The displacements fall generally below the Fowler-Perkins empirical values (crosses) except at large displacements. Since Bichsel's compilations apply to thin foils, improvement in the computation of multiple scattering is expected when the scattering distance is reduced. Calculations were also performed with scattering at intervals of s = 0.5 cm and s = 0.1 cm, with some improvement. The computer running time for 10,000 incident pions is increased from 113 sec to 190 sec in going from s = 1 cm to s = 0.5 cm.

As a practical trade-off between physical reality and running time, further calculations have indicated that using Bichsel's tabulations with suitably adjusted parameters and s = 1 cm gives a good overall compromise to use for pion dose calculations. This formalism has been incorporated into PION-1. As described next, little improvement, if any, is noted with the more detailed joint angle-displacement distribution.

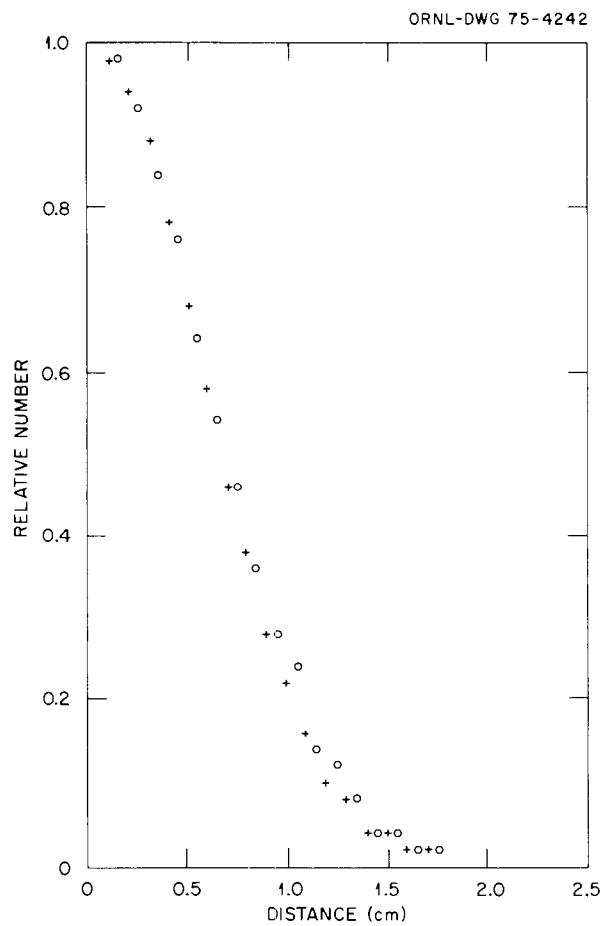

Fig. 17.6. Empirical (crosses) and calculated (circles) distributions of projected lateral displacement at a depth of 14 cm in a tissue target bombarded by a pencil beam of 82-MeV pions. Multiple scattering was computed by use of joint angular-lateral displacement distributions at path intervals of 1 cm.

15. Hans Bichsel, p. 8 in *American Institute of Physics Handbook,* 3d ed., ed. by Dwight E. Gray, McGraw-Hill, New York, 1972.

16. G. Molière, *Z. Naturforsch.* **3A,** 78 (1948).

3. Use of correlated angle-displacement distributions. Rossi[17] presents a formula for the distributions of lateral displacements and projected angles at a given depth. The joint angle-displacement distribution was applied to the pencil beam of 82-MeV pions. Results of the calculation are shown in Fig. 17.6, where it is seen that the agreement with the empirical fit is good. The computer running time of 179 sec exceeds the 113 sec needed when only the angular distributions are used every centimeter of travel. Comparison of the two methods indicates that the simpler treatment of multiple Coulomb scattering with Bichsel's tabulations is adequate for many applications.

Results of a realistic sample case show the effect of multiple Coulomb scattering. Calculations were performed for a uniform, circular (radius = 2 cm), parallel beam of pions incident normally on the end of a tissue cylinder. The pions were given a Gaussian momentum distribution with a mean of 153 MeV/c (energy = 67.8 MeV; range in tissue = 15.0 cm) and a momentum spread of 2% (i.e., 50% of the pions had momentum within ± 2% of the mean). The absorbed dose from 10,000 pions was calculated as a function of position in the target, and the code ISODATA[18] was used to compute and plot isodose contours. The calculations in this section were performed with nuclear reactions, range straggling, and secondary particle transport included, both with and without multiple scattering.

The isodose contours with multiple scattering "turned off" are shown in Fig. 17.7. The calculated contour levels range from 0.18×10^{-7} rad/pion down to 0.10×10^{-9} rad/pion, as indicated. The pions are incident

17. Bruno Rossi, *High-Energy Particles*, p. 569, Prentice-Hall, Inc., New York, 1952.

18. V. E. Anderson, R. N. Hamm, J. E. Turner, H. A. Wright, R. G. Alsmiller, Jr., and T. W. Armstrong, ORNL-TM-4296 (February 1974).

ORNL-DWG 74-6437

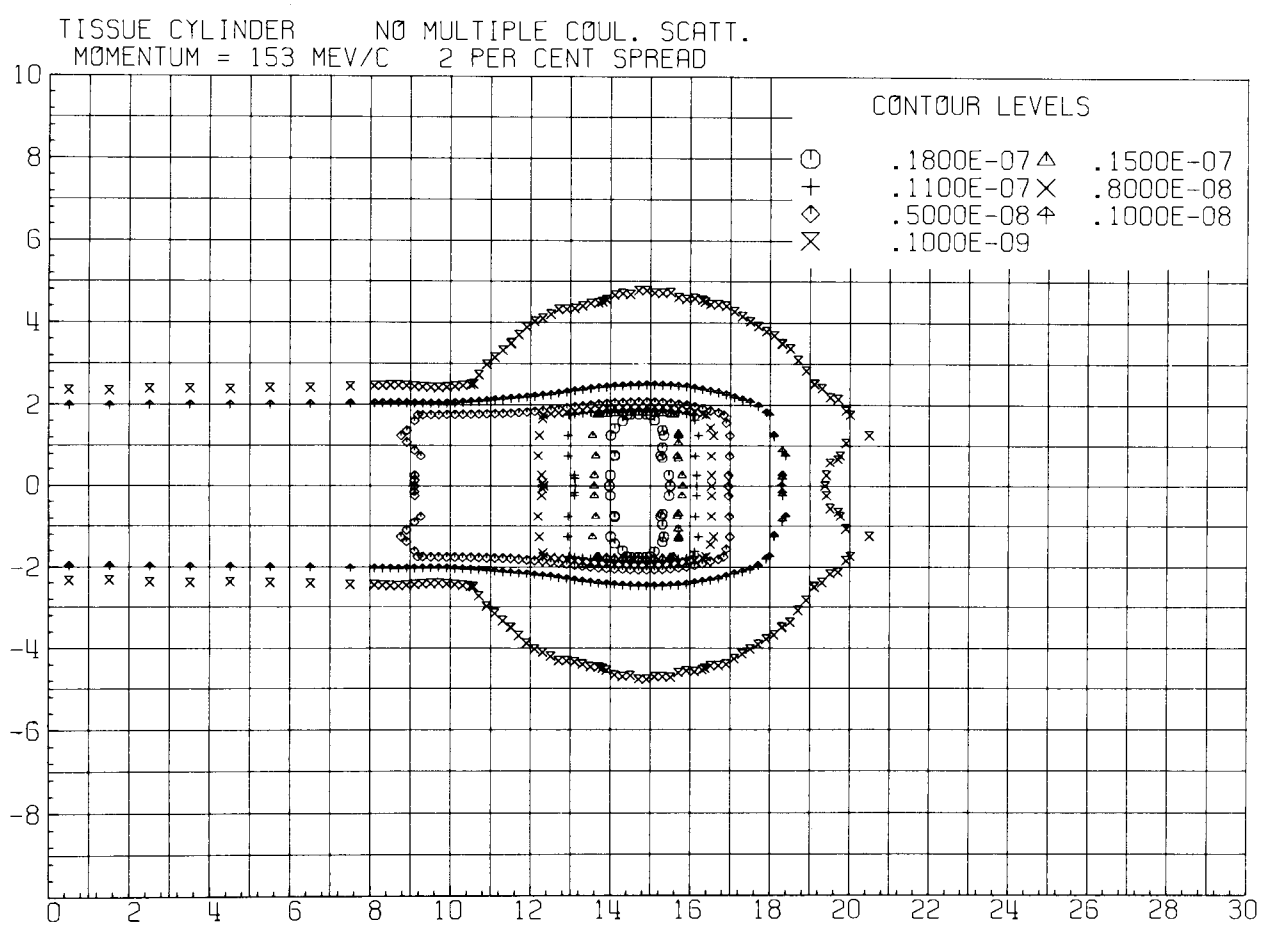

Fig. 17.7. Isodose contours for typical pion beam with multiple scattering neglected.

from the left parallel to the beam axis at 0 and cover a circular area of radius 2 cm seen edge on in the figure. Because the beam is uniform and the target homogeneous, the contours have cylindrical symmetry about the beam axis. Distances are shown in centimeters. With no multiple scattering, each incident pion travels straight ahead until it interacts with a nucleus or comes to rest. The dose contours spread only slightly as the beam penetrates the target. In the peak region the contours fall off rapidly on both sides at a distance of about 2 cm from the axis. The dose falls by a factor of 18 in less than 1 cm.

The corresponding dose contours when multiple scattering is included are shown in Fig. 17.8. The high-dose region is much smaller than before. The same lateral drop-off in dose by a factor of 18 occurs over a distance of about 3 cm. The spreading of the beam as it enters the target is also evident. As this example illustrates, multiple Coulomb scattering can limit severely the degree to which a concentrated therapeutic dose can be delivered to a localized tumor region.

A report of this work is being prepared for publication.[19]

SURFACE-PLASMON EXCITATION IN X-RAY INELASTIC SCATTERING ON SPHERICAL VOIDS IN METALS

The production of voids in metals, under neutron irradiation for example, may lead to serious deterioration in the mechanical strength of the material. Nondestructive testing methods are needed to determine density of voids, size distribution, etc. We have per-

19. R. N. Hamm, H. A. Wright, and J. E. Turner, submitted to the *Journal of Applied Physics.*

ORNL-DWG 74-6438

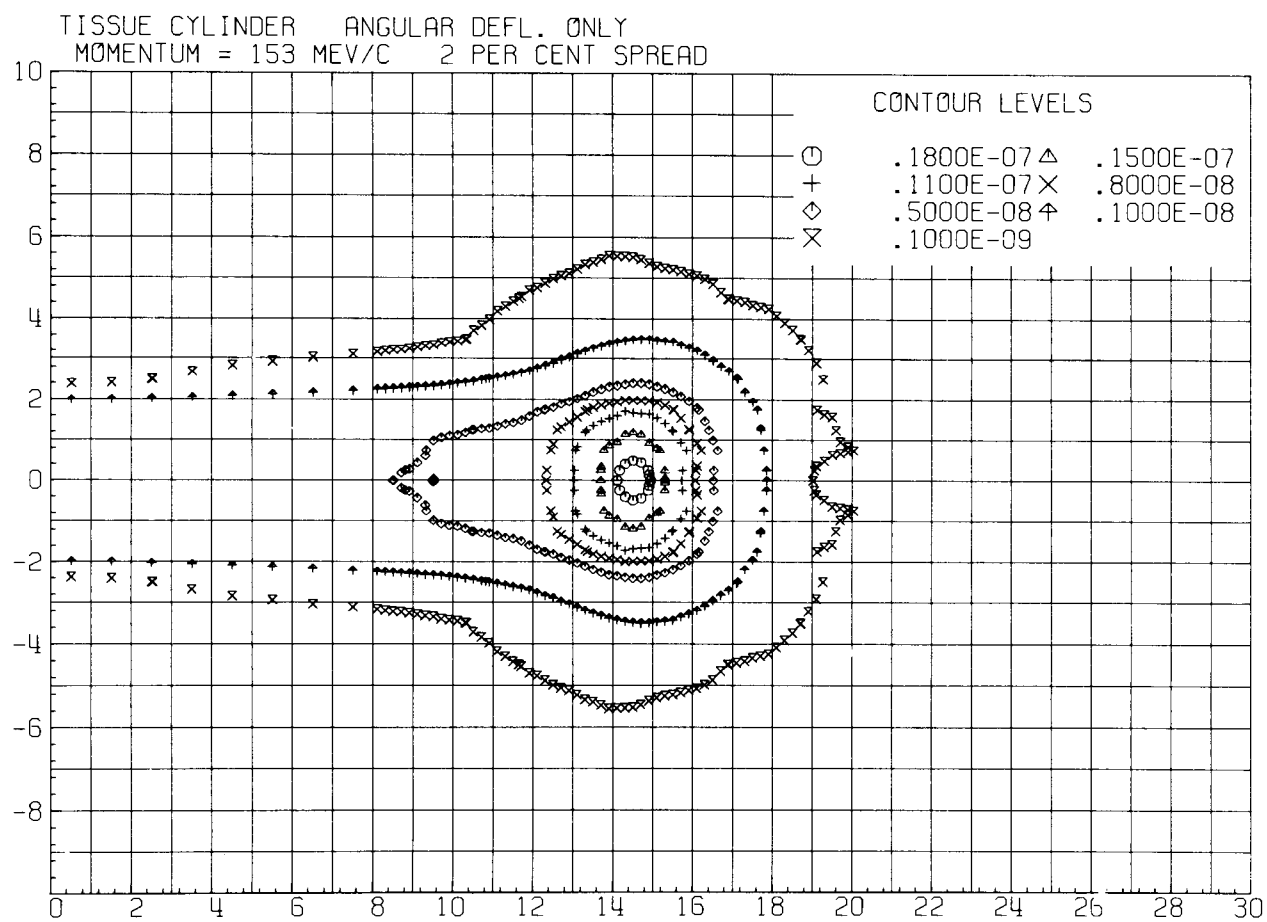

Fig. 17.8. Isodose contours for typical pion beam with multiple scattering included.

formed a theoretical calculation of the excitation of surface plasmons in x-ray inelastic scattering on spherical voids in a metal which may have direct relevance to this problem.

We consider a system composed of voids distributed at random in a metal. The number of voids per unit volume is assumed to be so small that the scattering from each void is not influenced by the presence of the other voids. The theoretical calculation then reduces to the calculation of the cross section for x-ray inelastic scattering from a single void in the metal.

The model chosen to represent the response of the metal to perturbations is the classical free-electron gas treated in the hydrodynamical approximation.[20] For the case of x-ray photons with frequency much greater than the plasma frequency, the interaction Hamiltonian is given by

$$V' = \frac{e^2}{2mc^2}\int d^3r\, n(\mathbf{r})\, \mathbf{A}(\mathbf{r}) \cdot \mathbf{A}(\mathbf{r}) \ , \qquad (1)$$

where $\mathbf{A}(\mathbf{r})$ is the vector potential of the photon field and $n(\mathbf{r})$ is the hydrodynamic density fluctuation operator for the electron gas. For a "void" of radius r_0 containing a material with dielectric constant ϵ_0 embedded in the electron gas, we find

$$n(\mathbf{r}) = -\frac{\delta(\mathbf{r}-\mathbf{r}_0)}{4\pi e}\sum_{l,m,p}\left\{\frac{2\pi\hbar\omega_l}{[l(\epsilon_0+1)+1]r_0^{\,3}}\right\}^{1/2}$$

$$\times\,(2l+1)\,Y_{lmp}(\theta,\varphi)\,(b_{lmp}+b^{\dagger}{}_{lmp}) \qquad (2)$$

in a spherical coordinate system with origin at the center of the void. The delta function $\delta(\mathbf{r}-\mathbf{r}_0)$ indicates that density fluctuations occur only on the surface of the void. The Y_{lmp}'s are real spherical harmonics; b_{lmp} ($b^{\dagger}{}_{lmp}$) is the annihilation (creation) operator for the l, m, p surface-plasmon state. The frequency ω_l depends only on the integer $l = 0, 1, 2, 3, \ldots$, and the dielectric constant of the material in the void through the equation

$$\omega_l^{\,2} = (l+1)\omega_p^{\,2}/[l(\epsilon_0+1)+1] \qquad (3)$$

with ω_p the plasma frequency for the electron gas. An interesting feature here is the existence of a monopole mode corresponding to a uniform charge distribution over the surface of the void. The charge on the void for this mode varies with time at the frequency $\omega_{l=0} = \omega_p$ independent of the dielectric material in the "void."

The cross section can now be calculated using standard methods of quantum mechanics. We find the differential cross section $d\sigma_l/d\Omega$ for exciting a surface plasmon of energy $\hbar\omega_l$ by scattering photons of initial energy $\hbar\omega_s$ into the solid angle $d\Omega$ about the direction of the incident photon beam, for an unpolarized incident beam, to be given by

$$\frac{d\sigma_l}{d\Omega} = \frac{1}{4}\alpha^3 a_0^{\,2}\,\frac{r_0\omega_l(2l+1)^3\,(\omega_s-\omega_l)}{c\,[l(\epsilon_0+1)+1]\,\omega_s}$$

$$\times\, j_l^{\,2}(kr_0)\,(1+\cos^2\theta). \qquad (4)$$

Here k is the momentum transfer to the void (in units of $\hbar$), $\alpha \equiv e^2/\hbar c$, $a_0 \equiv \hbar^2/me^2$, and j_l is the spherical Bessel function of order l. The momentum transfer is related to the scattering angle θ through the equation

$$k^2 = \frac{4\omega_s}{c^2}(\omega_s-\omega_l)\sin^2\frac{\theta}{2} + \frac{\omega_l^{\,2}}{c^2}\,. \qquad (5)$$

In Fig. 17.9 we plot the sum over all modes (only $l = 0, \ldots, 15$ contribute in this case for $0° \leqslant \theta \leqslant 12°$) of the differential scattering cross section for plasmon excitation per void in units of the Thomson scattering

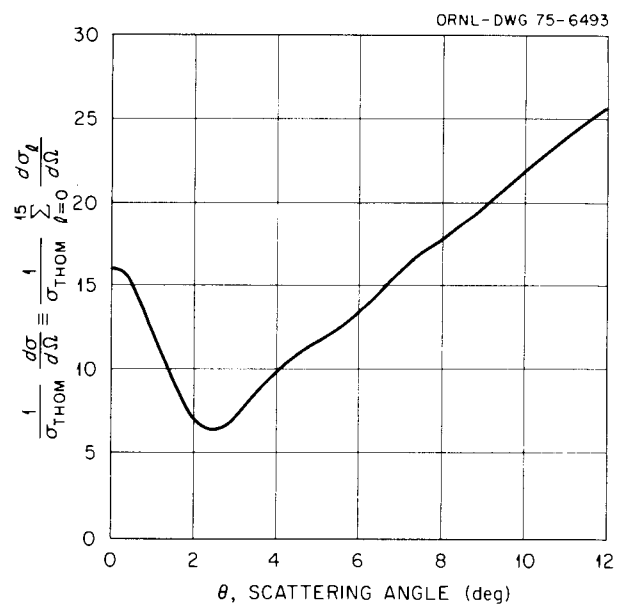

Fig. 17.9. Total differential scattering cross section for exciting surface plasmons on voids in an electron gas (plasma energy $\hbar\omega_p$ = 22 eV) as a function of x-ray scattering angle for 6-keV x rays. The void radius is r_0 = 20 Å, and ϵ_0 = 1.

20. See, for example, R. H. Ritchie and R. E. Wilems, *Phys. Rev.* **178**, 372 (1969).

cross section $\sigma_{THOM} = 8\pi r_c^2/3$ (r_c is the classical electron radius). The plasma energy $\hbar\omega_p$ is 22 eV corresponding to molybdenum, the energy of the x-ray photons is 6 keV, and the void of radius 20 Å is assumed to have vacuum inside (i.e., $\epsilon_0 = 1$). The shape of this curve should describe the scattered intensity as a function of angle in an experiment, and the scattered intensity should be proportional to the density of voids in the sample.

Additional information might also be obtained from an energy analysis of photons scattered at a fixed angle. In Fig. 17.10 we show the differential scattering cross section for the first four surface-plasmon modes for $\hbar\omega_p = 22$ eV, x-ray energy = 6 keV, but with a void radius of 200 Å. Also shown on the figure is a list of the energies of these first four modes. The photon energy loss spectrum for a fixed scattering angle should reveal peaks at these energies with intensities proportional to the cross sections for the modes at that scattering angle. As may be seen from this figure, rather large variations in these intensities may occur as the scattering angle is varied.

We would encourage experimental work to study excitation of surface-plasmon modes on voids. It is not only a problem of intrinsic scientific interest but one which may prove to be of practical value also for the study of void formation in metals.

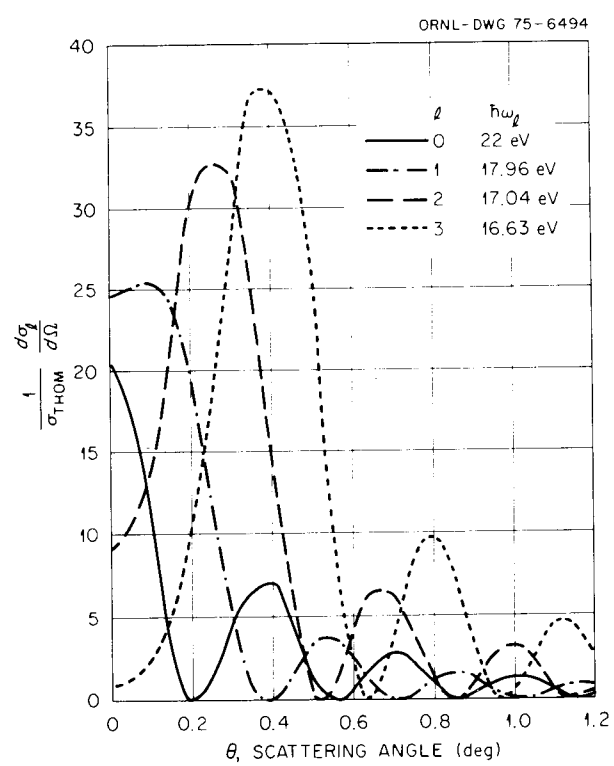

Fig. 17.10. The differential scattering cross section for the $l = 0, 1, 2, 3$ modes as a function of scattering angle θ for $\hbar\omega_p = 22$ eV, $\epsilon_0 = 1$, x-ray energy = 6 keV, and $r_0 = 200$ Å.

THEORY OF THE LINEAR RESPONSE FUNCTION OF A MODEL INSULATOR[21]

Important progress has been made in understanding the properties of metals through study of the electron gas model. Here one ignores the detailed crystalline properties of the metal and concentrates on the dynamic properties of the conduction electrons. From this model, far-reaching conclusions have been drawn about collective modes, screening of impurity charges, and stopping power, to name only a few of the important phenomena in metals which have been treated on this basis.

There have been a few calculations of the dielectric response function of semiconductors, semimetals, and insulators. Most of the recent papers are concerned with the dielectric response function, ϵ, of specific solids. In an effort to develop a similarly simplified model for insulators which retains useful physical information about electronic properties, we have recently derived an expression for the linear response function of a randomly distributed assembly of molecules. This model would be expected to describe best the electronic properties of an insulating liquid.

The theoretical calculation starts with the polarization propagator, $\pi(\mathbf{r}_2, t; \mathbf{r}_1, 0)$, describing the ground-state expectation value for the process of pair creation at $(\mathbf{r}_1, 0)$ followed by destruction of a pair at $(\mathbf{r}_2, t)$. It is defined by

$$\pi(\mathbf{r}_2, t; \mathbf{r}_1, 0) = -\frac{i}{\Omega}\langle\Psi_0|T[\hat{\psi}^\dagger(\mathbf{r}_2, t)\,\hat{\psi}(\mathbf{r}_2, t)\,\hat{\psi}^\dagger(\mathbf{r}_1, 0)\,\hat{\psi}(\mathbf{r}_1, 0)]\,|\Psi_0\rangle\,, \qquad (1)$$

where $|\Psi_0\rangle$ is the exact Heisenberg state vector of the system (we consider only the case $T = 0°K$), Ω is the volume of the system, and $\hat{\psi}(\mathbf{r}, t)$ is the wave destruction operator for electrons at $(\mathbf{r}, t)$. The wave operators may be expressed in occupation number representation as

$$\hat{\psi}(\mathbf{r}, t) = \sum_{\mathbf{l}} \sum_{n \leq n_F}^{\text{OCC}} u_{n\mathbf{l}}(r)\,\hat{a}_{n\mathbf{l}}(t) + \sum_{\mathbf{k}}^{\text{UNOCC}} u_{\mathbf{k}}(\mathbf{r})\,\hat{a}_{\mathbf{k}}(t)\,, \qquad (2)$$

21. Research sponsored in part by the Defense Nuclear Agency, under subtask TA040, but does not reflect endorsement by the sponsor.

where $u_{n\mathbf{l}}(\mathbf{r})$ is the nth single-particle "orbital" on the ion core at position $\mathbf{l}$ and the a's are the usual creation operators. We take electrons to occupy independent orbitals centered on each of the ion cores, neglect overlap of orbitals on different ion cores, and will assume that there are n_F occupied orbitals on each core. With these assumptions we have $u_{n\mathbf{l}}(\mathbf{r}) = u_n(\mathbf{r}-\mathbf{l})$. Although not considered here, we could take a different distribution of orbitals on different cores. The excited states are taken to be OPW (orthogonalized plane wave) orbitals; that is,

$$u_{\mathbf{k}}(\mathbf{r}) = \frac{e^{i\mathbf{k}\cdot\mathbf{r}}}{\Omega^{1/2}} - \sum_{n<n_F} \sum_{\mathbf{m}} \langle n\mathbf{m}|\mathbf{k}\rangle \; u_{n\mathbf{m}}(\mathbf{r}) \,, \tag{3}$$

where $\langle \mathbf{r}|n\mathbf{m}\rangle \equiv u_{n\mathbf{m}}(\mathbf{r})$ and $\langle \mathbf{r}|\mathbf{k}\rangle \equiv e^{i\mathbf{k}\cdot\mathbf{r}}/\Omega^{1/2}$ for brevity. One may easily check that $u_{\mathbf{k}}(\mathbf{r})$ is orthogonal to all bound-state orbitals. The binding energies corresponding to these orbitals will be taken to fit experiment. Since we do not wish to assume that the system possesses any sort of crystal symmetry, it is not appropriate to use Bloch functions to represent electron states.

The Fourier representation of $\pi(\mathbf{r}_2, t; \mathbf{r}_1, 0)$ may be defined as

$$\pi_{\mathbf{q}_1,\mathbf{q}_2}(t) \equiv \int d^3r_1 \int d^3r_2 \, e^{-i(\mathbf{q}_1\cdot\mathbf{r}_1 + \mathbf{q}_2\cdot\mathbf{r}_2)} \, \pi(\mathbf{r}_2, t; \mathbf{r}_1, 0) \;. \tag{4}$$

If we abbreviate Eq. (2) as

$$\psi(\mathbf{r}, t) = \sum_{n,\mathbf{l}} u_{n\mathbf{l}}(\mathbf{r}) \hat{a}_{n\mathbf{l}}(t) \,, \tag{5}$$

Eq. (4) leads to

$$\pi_{\mathbf{q}_1,\mathbf{q}_2}(t) = -\frac{i}{\Omega} \sum_{s,\mathbf{l}} \sum_{u,\mathbf{m}} \sum_{v,\mathbf{p}} \sum_{w,\mathbf{q}} \int d^3r_1 \int d^3r_2 \, e^{i(\mathbf{q}_1\cdot\mathbf{r}_1 + \mathbf{q}_2\cdot\mathbf{r}_2)} \times u^*_{s\mathbf{l}}(\mathbf{r}_2)\, u_{u\mathbf{m}}(\mathbf{r}_2)\, u^*_{v\mathbf{p}}(\mathbf{r}_1)\, u_{w\mathbf{q}}(\mathbf{r}_1) \times \langle \Psi_0 | T[\hat{a}^\dagger_{s\mathbf{l}}(t)\, \hat{a}_{u\mathbf{m}}(t) \hat{a}^\dagger_{v\mathbf{p}}(0)\, \hat{a}_{w\mathbf{q}}(0)] \; |\Psi_0\rangle \;. \tag{6}$$

To proceed, we need to approximate; we take $|\Psi_0\rangle$ to be the state vector of the noninteracting ground state ($|0\rangle$), and we take the state creation and annihilation operators also to have their noninteracting forms. Thus

$$\hat{a}_{s\mathbf{l}}(t) = e^{-i\omega_s t} \hat{a}_{s\mathbf{l}}(0) \equiv e^{-i\omega_s t} \hat{a}_{s\mathbf{l}} \,, \qquad \hat{a}^\dagger_{s\mathbf{l}}(t) = e^{i\omega_s t} \hat{a}^\dagger_{s\mathbf{l}}(0) \equiv e^{i\omega_s t} \hat{a}^\dagger_{s\mathbf{l}} \,, \tag{7}$$

where ω_s is the eigenenergy of an electron in the sth orbital located on any of the ions. We also find it convenient to make the assumption that the positions of the ion cores are completely random. Then we may replace the sum over $\mathbf{l}$ by an integral,

$$\sum_{\mathbf{l}} \to \frac{N}{\Omega} \int d^3 l \,,$$

where N is the number of ion cores in the volume Ω. With these assumptions we find

$$\pi^{(t>0)}_{\mathbf{q}_1,\mathbf{q}_2}(t) = -\frac{iN}{\Omega} \sum_s \sum_{\mathbf{p}} |\langle \mathbf{p} + \mathbf{q}_1 | s\rangle - \sum_n \langle \mathbf{p}|n\rangle \langle n|e^{-i\mathbf{q}_1\cdot\mathbf{r}}|s\rangle|^2 \, e^{-i(\omega_{\mathbf{p}} - \omega_s)t} \times \delta^3(\mathbf{q}_1 + \mathbf{q}_2) \tag{8}$$

for $t > 0$. For the case $t < 0$ it is only necessary to take the complex conjugate of the time-dependent exponential factor in Eq. (8). We now compute the frequency transform of the complete polarization propagator as

$$\pi_{\mathbf{q}_1,\mathbf{q}_2,\omega} = \int_{-\infty}^{\infty} dt \, e^{i\omega t} \, \pi_{\mathbf{q}_1,\mathbf{q}_2}(t) = -\frac{N}{\Omega} \delta^3(\mathbf{q}_1 + \mathbf{q}_2) \sum_s \sum_{\mathbf{p}}{}' \langle \mathbf{p} + \mathbf{q}_1 | s\rangle - \sum_n \langle \mathbf{p}|n\rangle \langle n|e^{-i\mathbf{q}_1\cdot\mathbf{r}}|s\rangle|^2 \times \left(\frac{1}{\omega_{\mathbf{p}} - \omega_s - \omega - i\eta} + \frac{1}{\omega_{\mathbf{p}} - \omega_s + \omega - i\eta} \right) \,, \tag{9}$$

where η is a positive infinitesimal. Furthermore, in case the system has translational symmetry,

$$\pi_{\mathbf{q}_1,\mathbf{q}_2}(t) \to \delta^3(\mathbf{q}_1 + \mathbf{q}_2)\, \pi_{\mathbf{q}_1}(t);$$

in that case the dielectric response function $\epsilon_{\mathbf{q},\omega}$ is given in terms of

$$\pi_{\mathbf{q},\omega} = \int dt \, e^{i\omega t} \pi_{\mathbf{q}}(t)$$

as

$$\epsilon_{\mathbf{q},\omega} = 1 - v_{\mathbf{q}}\pi_{\mathbf{q},\omega} \quad , \tag{10}$$

where $v_{\mathbf{q}} = 4\pi/q^2$ is the Fourier transform of the Coulomb interaction energy. Note that atomic units are being used throughout. Thus we have

$$\epsilon_{\mathbf{q},\omega} = 1 + \frac{4\pi N}{q^2\Omega}\sum_s \sum_{\mathbf{p}} |F_{\mathbf{pq}s}|^2 \times \left(\frac{1}{\omega_{\mathbf{p}} - \omega_s - \omega - i\eta} + \frac{1}{\omega_{\mathbf{p}} - \omega_s + \omega - i\eta}\right) \tag{11}$$

as the dielectric response function for our model insulator, where

$$F_{\mathbf{pq}s} \equiv \int d^3r \frac{e^{-i(\mathbf{p}+\mathbf{q})\cdot\mathbf{r}}}{\Omega^{1/2}} u_s(\mathbf{r}) - \sum_n \int d^3r_1 \frac{e^{-i\mathbf{p}\cdot\mathbf{r}_1}}{\Omega^{1/2}} u_n(\mathbf{r}_1) \int d^3r_2 e^{-i\mathbf{q}\cdot\mathbf{r}_2} \times u_n^*(\mathbf{r}_2)\, u_s(\mathbf{r}_2) \tag{12}$$

is the OPW form factor.

It is reasonable to look at the case where only a single ground-state orbital need be considered. This might be appropriate when all other orbitals are tightly bound. For an s orbital take

$$u_0(\mathbf{r}) = \sqrt{\frac{\alpha^3}{\pi}}\, e^{-\alpha r}$$

as a properly normalized one. Then

$$F_{\mathbf{pq}_0} = 8\sqrt{\frac{\pi\alpha^5}{\Omega}} \left\{ \frac{1}{[\alpha^2 + (\mathbf{q}+\mathbf{p})^2]^2} - \frac{16\alpha^4}{(\alpha^2+p^2)^2(4\alpha^2+q^2)^2} \right\} . \tag{13}$$

The resulting response function is analytically quite manageable; it describes collective states and screening of impurity charges and at present is being used to determine electron inelastic mean free paths and energy loss rates in insulators.

APPLICATION OF THE MODEL INSULATOR THEORY TO Al_2O_3: THE LOW-ENERGY END OF THE ELECTRON SLOWING-DOWN SPECTRUM[22]

The theory described in the preceeding paper yields an analytical expression for the imaginary part of the dielectric response function of a model insulator and has been applied to compute the differential inelastic mean free path of a swift electron interacting with valence-band electrons in Al_2O_3. We assume that the dispersion relation for energetic electrons in the model insulator is given by $\omega_{\mathbf{p}} = \beta\mathbf{p}^2$, where $\beta = 1/2$ if the energetic electron has the bare electron mass, and we consider only one bound state. Instead of using the conventional normalization for the excited-state OPW wave function, we require that the imaginary part of the dielectric response function, $\epsilon^{(2)}_{\mathbf{q},\omega}$, satisfy the usual sum rule:

$$\int_0^\infty \omega\epsilon^{(2)}_{\mathbf{q},\omega}\, d\omega = 2\pi^2 n \quad . \tag{1}$$

Here n is the density of ion cores, and we continue to work in atomic units. We find the sum-rule-constrained $\epsilon^{(2)}_{\mathbf{q},\omega}$ to be given by

$$\epsilon^{(2)}_{\mathbf{q},\omega} = \pi n\Gamma/\beta q\Lambda \quad , \tag{2}$$

where

$$\Gamma \equiv \frac{1}{3}\left\{ \frac{1}{[\alpha^2+(q-p)^2]^3} - \frac{1}{[\alpha^2+(q+p)^2]^3} \right\} - \frac{32\alpha^4}{(\alpha^2+p^2)^2(4\alpha^2+q^2)^2}\left[\frac{1}{\alpha^2+(q-p)^2} - \frac{1}{\alpha^2+(q+p)^2}\right] + \frac{1024pq\alpha^8}{(\alpha^2+p^2)^4(4\alpha^2+q^2)^4} \quad , \tag{3}$$

$$\Lambda \equiv [\omega_B + \beta(q^2+\alpha^2)]\left[\frac{1}{8\alpha^5} - \frac{32\alpha^3}{(4\alpha^2+q^2)^4}\right] \quad , \tag{4}$$

$$p = [(\omega - \omega_B)/\beta]^{1/2} \quad . \tag{5}$$

Here ω_B is the excitation energy of the single bound state. The procedure for using this model dielectric function to represent that of a real insulator will be to consider α and β as adjustable constants and match the optical dielectric function measured for that material. In the "optical limit," $q \to 0$, Eq. (2) becomes

$$\epsilon^{(2)}_{0,\omega} = \frac{512\pi}{3} n \frac{\alpha^7 p^3}{\beta(\omega_B+\beta\alpha^2)(\alpha^2+p^2)^6} \quad . \tag{6}$$

22. Research sponsored in part by the Defense Nuclear Agency, under subtask TA040, but does not reflect endorsement by the sponsor.

We have tried matching $\epsilon^{(2)}_{0,\omega}$ as given by Eq. (6) to the experimental values measured for Al_2O_3 by Arakawa and Williams.[23] Figure 17.11 shows a comparison of these results, where curve A represents the experimental results and curve B is obtained from our model with $\alpha = 0.78$, $\beta = 1/2$, and $\omega_B = 0.3309$. We used a density of 4.05 for corundum and took 15 valence electrons per Al_2O_3 unit. In effect we have assumed that the threshold for excitation of any of the valence electrons is 9 eV. We see that the agreement is quite reasonable. We could obtain excellent agreement by taking a combination of ground-state orbitals.

From the values of α, β, and ω_B determined in the "optical limit," the real part of the dielectric response function, $\epsilon^{(1)}_{q,\omega}$, was computed from $\epsilon^{(2)}_{q,\omega}$ using the Kramers–Kronig relations between the real and imaginary parts of an analytic function. Figure 17.12 shows a plot of the energy loss function, Im $(-1/\epsilon_{q,\omega})$, as a function of energy transfer ω for various values of momentum transfer q from these calculations, where q and ω are measured in atomic units. One sees a prominent plasmon resonance peaking at $\omega \sim 1$ (energy transfer ~ 27.2 eV) when $q \lesssim 1$. As q increases to larger values the loss function peaks at values of ω which increase and approach the quantity $\omega = q^2/2$, the energy-momentum relation of a free electron, as $q \to \infty$. Thus our model displays a smooth transition in response from collective behavior for small q to single-particle behavior for large q.

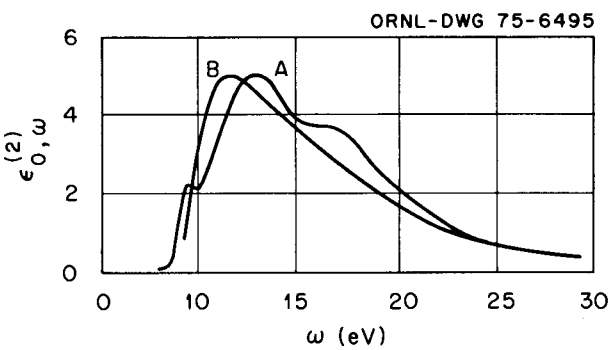

Fig. 17.11. The imaginary part of the dielectric response function of the model insulator in the "optical limit" (curve B) fitted to experimental results for Al_2O_3 (curve A).

The differential inverse mean free path, $d\mu/d\omega$, for an electron of velocity v interacting with a medium of dielectric response function $\epsilon_{q,\omega}$ is given by

$$\frac{d\mu}{d\omega} = \frac{2}{\pi v^2}\int_{v-\sqrt{v^2-2\omega}}^{v+\sqrt{v^2-2\omega}} \frac{dq}{q}\,\mathrm{Im}\left(\frac{-1}{\epsilon_{q,\omega}}\right) . \tag{7}$$

This integral has been evaluated numerically as a function of v using the dielectric response function of a model insulator applied to Al_2O_3. The results may be fitted reasonably well for $v > 4.7$ with a function of the form

$$\frac{d\mu}{d\omega} = f(\omega)\ln(v/v_1) + g(\omega) , \tag{8}$$

where $f(\omega)$ is a function which describes mainly plasmon creation, $g(\omega)$ represents primarily interactions

23. E. T. Arakawa and M. W. Williams, *J. Phys. Chem. Solids* 29, 735 (1968).

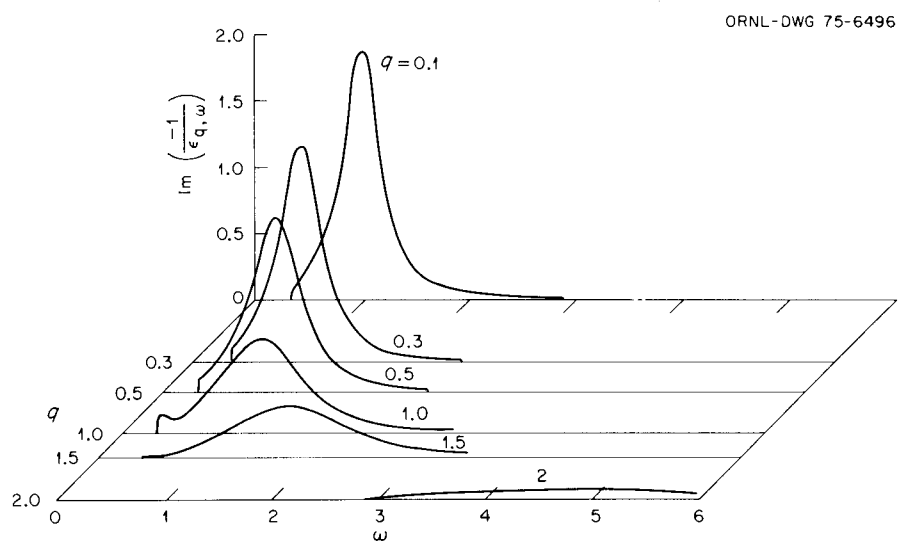

Fig. 17.12. The energy loss function as a function of momentum and energy transfer from the model insulator theory.

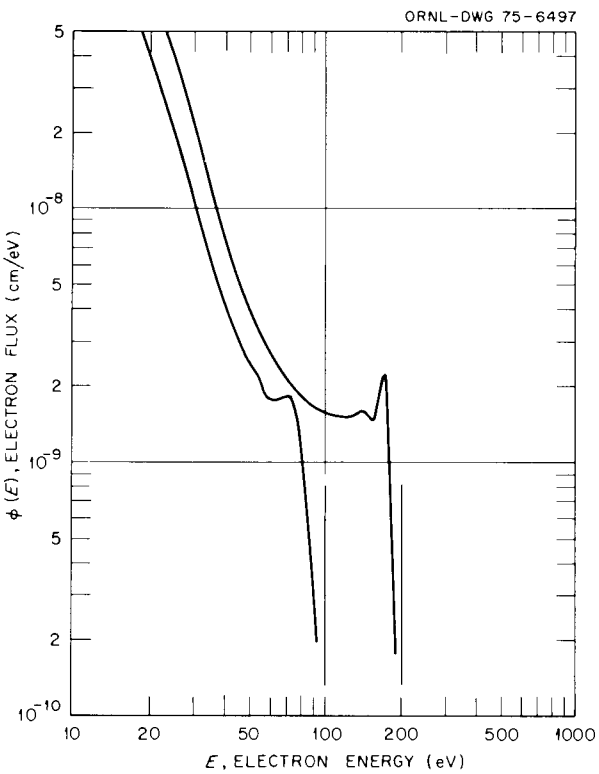

Fig. 17.13. Slowing-down spectrum generated by source electrons of 100 eV and 200 eV due to interaction with the valence band in Al_2O_3.

corresponding to large momentum transfers, and v_1 is an empirically determined constant. For values of $v < 4.7$ the function $d\mu/d\omega$ is stored in tabular form; double interpolation in these tables is carried out in a straightforward way for intermediate values of v and ω.

Figure 17.13 shows some preliminary results of a calculation of electron slowing-down spectra generated in our model insulator by electrons having energies of 100 and 200 eV. One sees a divergence in the flux $\phi(E)$ as the energy E approaches the threshold for excitation in the insulator. At the high-energy end of the spectrum there are several peaks just below the source energy spaced at intervals of ~ 28 eV. These are plasmon loss peaks and represent electrons which are degraded by the creation of one, two, etc., plasmons after being emitted from the source. These calculations are being extended to include inner-shell excitations.

These calculations show that it is possible to fit experimental data on optical dielectric functions of insulating materials using the model insulator theory. The dielectric response function determined in this way may then be used to calculate mean free paths, stopping powers, ranges, slowing-down spectra, etc. This model may thus prove to have wide applicability to the study of dynamic electron properties in insulating substances.

SCATTERING OF ELECTROMAGNETIC WAVES BY CYLINDERS: EXCITATION OF SURFACE-PLASMON MODES

In our continuing study of collective states in solids and their role in energy transport processes, we have been examining numerically the equations describing the scattering of light by cylinders and the excitation of surface-plasmon modes on the cylinders. We have developed a computer program to calculate the extinction, scattering, and absorption efficiencies for a plane wave of arbitrary angle of incidence on a right circular cylinder. The work described here represents a significant extension of the work reported last year on this topic.

The theoretical basis for our calculations is the treatment by Wait[24] of the scattering of a plane wave of arbitrary angle of incidence from an infinitely long circular dielectric cylinder. Consider a plane wave of frequency ω (time dependence $\sim e^{i\omega t}$) and wave vector **k** incident at an angle θ_i from the cylinder axis as shown in Fig. 17.14. The response of the material in the cylinder of radius a to an electromagnetic field of frequency ω is specified by the complex dielectric function $\epsilon(\omega)$, while the response of the medium outside the cylinder is specified by $\epsilon_0(\omega)$. Both materials are assumed to be nonmagnetic. Standard methods from electromagnetic theory are used to calculate the extinction, scattering, and absorption efficiencies.

The scattering efficiency of the cylinder is defined as the ratio of the energy scattered per second per unit length of cylinder to the energy incident per second per unit length. The polarization of the incident plane wave will be specified by λ. For $\lambda = 0$ the electric field of the incident wave is in the plane of incidence formed by **k** and the cylinder axis (P polarization), and $\lambda = 1$ corresponds to the electric field of the incident wave perpendicular to the plane of incidence (S polarization). The scattering efficiency is given by

$$Q_{\mathrm{SCATT},\lambda} = \frac{2}{\epsilon_0^{\frac{2\lambda+1}{2}}(a\omega/c)\sin\theta_i}\left[\,|A_{0,\lambda}|^2 + 2\sum_{n=1}^{\infty}\left(|A_{n,\lambda}|^2 + |B_{n,\lambda}|^2\right)\right], \qquad (1)$$

24. J. R. Wait, *Can. J. Phys.* **33**, 189 (1955).

ORNL-DWG. 74-10511R

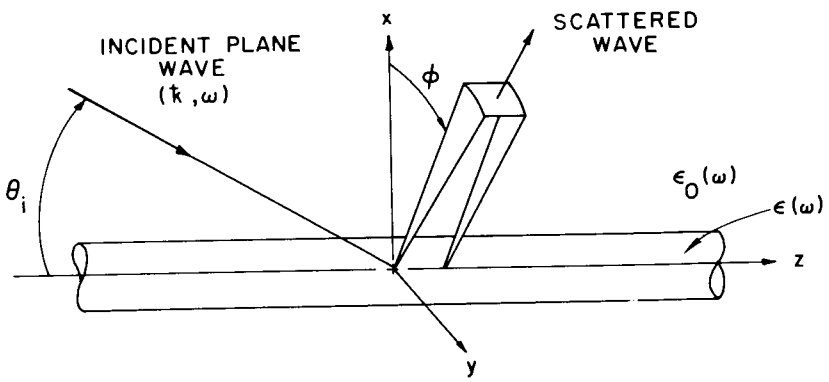

Fig. 17.14. Geometry for the scattering of electromagnetic waves by a cylinder.

where

$$A_{n,\lambda} \equiv \frac{J_n(\mathrm{v})}{H_n^{(2)}(\mathrm{v})} + \frac{2i\,\{h_n(\mathrm{v}) - [\epsilon(\omega)/\epsilon_0(\omega)]^{\lambda}\, j_n(u)\}}{\pi \mathrm{v}^2\,[H_n^{(2)}(\mathrm{v})]^2\, D_n} \quad (2)$$

$$B_{n,\lambda} \equiv \frac{2}{\pi \mathrm{v}^2}\left(\frac{1}{\mathrm{v}^2} - \frac{1}{u^2}\right)\frac{n\cos\theta_i}{[H_n^{(2)}(\mathrm{v})]^2\, D_n} \quad , \quad (3)$$

$$D_n \equiv [h_n(\mathrm{v}) - \frac{\epsilon(\omega)}{\epsilon_0(\omega)}\, j_n(u)]\;[h_n(\mathrm{v}) - j_n(u)] - \left(\frac{1}{\mathrm{v}^2} - \frac{1}{u^2}\right)^2 n^2 \cos^2\theta_i \,. \quad (4)$$

In the above equations we have also used the definitions

$$u \equiv \frac{a\omega}{c}\,[\epsilon(\omega) - \epsilon_0(\omega)\cos^2\theta_i]^{1/2} \quad , \quad (5)$$

$$\mathrm{v} \equiv \frac{a\omega}{c}\,[\epsilon_0(\omega)]^{1/2}\sin\theta_i \quad , \quad (6)$$

$$j_n(u) \equiv \frac{J'_n(u)}{u\,J_n(u)} \quad , \quad (7)$$

where J_n is the Bessel function of the first kind of order n and the prime indicates differentiation with respect to the argument, and

$$h_n(\mathrm{v}) \equiv \frac{H_n^{(2)\prime}(\mathrm{v})}{\mathrm{v}\,H_n^{(2)}(\mathrm{v})} \quad , \quad (8)$$

where $H_n^{(2)}$ is the Hankel function of the second kind of order n.

The extinction efficiency is a measure of removal of energy from the incident electromagnetic field by scattering from the cylinder and absorption in the cylinder. The extinction efficiency is given by

$$Q_{\mathrm{EXT},\lambda} = \frac{2}{\epsilon_0^{(2\lambda+1)/2}\,(a\omega/c)\sin\theta_i} \times \left(\mathrm{Re}\,A_{0,\lambda} + 2\sum_{n=1}^{\infty}\mathrm{Re}\,A_{n,\lambda}\right) \quad , \quad (9)$$

where Re ( ) denotes the real part of ( ). The absorption efficiency is then given by

$$Q_{\mathrm{ABS},\lambda} = Q_{\mathrm{EXT},\lambda} - Q_{\mathrm{SCATT},\lambda} \quad . \quad (10)$$

If the dielectric function of the cylinder is real, $Q_{\mathrm{ABS}} = 0$ and $Q_{\mathrm{EXT}} = Q_{\mathrm{SCATT}}$.

We are now able to calculate these quantities for a cylinder of arbitrary complex dielectric function with a cylinder radius less than about 2 μ. However, to accentuate features due to surface-plasmon excitation, our calculations have been done mainly for the free-electron gas model including a phenomenological damping constant γ. For the dielectric response of the cylinder we use

$$\epsilon(\omega) = 1 - \frac{\omega_p^2}{\omega(\omega - i\gamma)} \quad . \quad (11)$$

In Fig. 17.15 we plot the scattering efficiency as a function of the frequency of the incident P-polarized plane wave in units of the plasma energy. The angle of incidence is $\theta_i = 40°$, $\Gamma \equiv \gamma/\omega_p = 0$ (no damping), and $a\omega_p/c = 1.00$. For an electron gas with a plasma frequency corresponding to that of the conduction band in aluminum, $a\omega_p/c = 1$ implies $a \approx 132$ Å. The curves labeled $n = 0, 1, 2, 3$ represent the contribution to the total from these terms in the sum over n. The $n = 2$ and $n = 3$ resonances indicate rather well-defined surface-plasmon excitations. The $n = 1$ mode produces less well defined structure. Figure 17.16 illustrates the effect of damping in the electron gas. As the damping is increased the structure in the scattering efficiency becomes less pronounced (i.e., the corresponding surface-plasmon modes are less well defined), and the absorption efficiency increases. In Fig. 17.17 we show the results for the scattering efficiency for S- and P-polarized incident plane waves for a larger value of the parameter $a\omega_p/c$. Here we have labeled the peaks corresponding to the $n = 3$ through $n = 9$ surface-plasmon modes. In general, for larger values of $a\omega_p/c$, more peaks are seen in the scattering efficiency spread over a wider range of ω/ω_p values. There is, however, an upper limit on the value of ω/ω_p for which structure will be seen. That value is $\omega/\omega_p = 1/\sqrt{2}$, corresponding to the surface-plasmon energy on a flat surface bounded by vacuum.

We are still limited in our calculations to a value of $a\omega_p/c \lesssim 270$ due to limitations in the routines required for calculating the Bessel functions. This restriction on the calculations has prevented detailed comparison with experimental results, where the parameter $a\omega_p/c$ generally takes on values $\gtrsim 400$ for metals. We hope to be able to extend the range of applicability of our results to larger values of $a\omega_p/c$ to complement experimental work in this area.

The results we have described here are related to, but more detailed than, the calculations of Pfeiffer, Economou, and Ngai[25] on the surface-plasmon modes on a cylinder. They have derived dispersion relations for the

25. C. A. Pfeiffer, E. N. Economou, and K. L. Ngai, *Phys. Rev.* B 15, 3038 (1974).

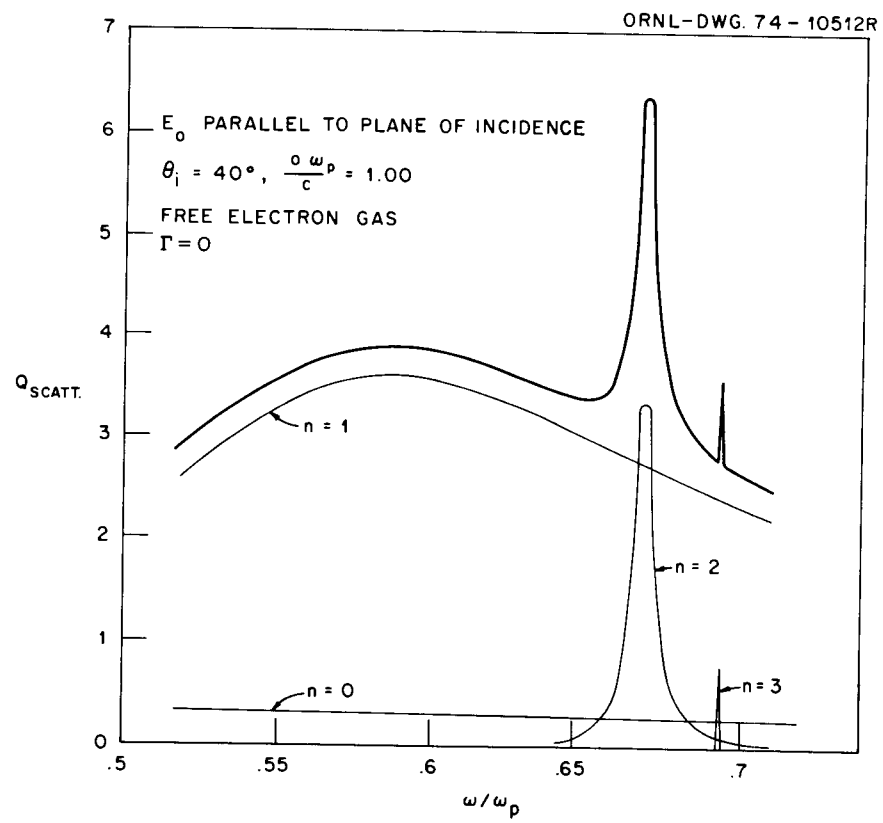

Fig. 17.15. The scattering efficiency as a function of frequency of an incident plane wave. The contributions to the total curve from the $n = 0, 1, 2, 3$ terms in the sum are also indicated.

radiative surface-plasmon modes by searching for minima in the function D_n in Eq. (4). For the sharp, well-defined resonances we find excellent agreement with their calculations. However, for the broader resonances the position where the maximum in the scattering occurs for a given n is shifted from their dispersion relation predictions, due to other terms which enter in the scattering equations. Thus for comparison with experimental measurements of light scattering, the dispersion relations are not sufficient to predict the positions of all peaks, and the full treatment of the interaction of electromagnetic waves with the cylinder is required.

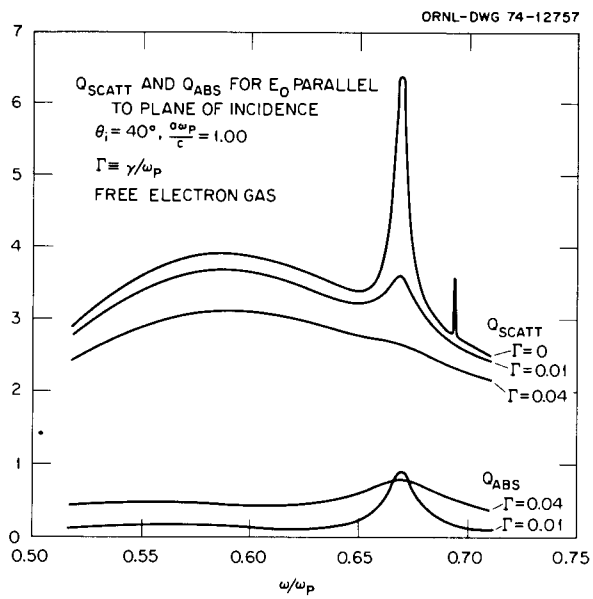

Fig. 17.16. The influence of damping in the electron gas on the scattering efficiency and absorption efficiency for $a\omega_p/c = 1$.

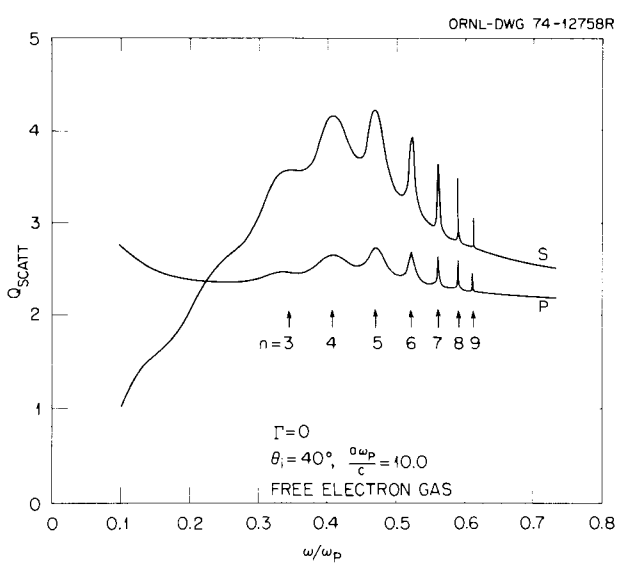

Fig. 17.17. The scattering efficiency as a function of ω/ω_p for $a\omega_p/c = 10$.

ENERGY LOSS OF SWIFT PROTON CLUSTERS IN SOLIDS

Energy-loss measurements in transmission experiments on carbon and gold foils with ~100-keV/nucleon H_2^+ and H_3^+ beams reveal that protons moving in spatially correlated clusters have effective charge numbers significantly larger than unity. This effect may be readily understood qualitatively. Consider a molecule of mass M_c and kinetic energy $E = \frac{1}{2}M_c v^2$ impinging on a solid so that the speed v exceeds $v_0 = e^2/\hbar$. Within a few atomic layers, the valence electrons are stripped, at time $t = 0$, leaving a cluster of spatially correlated atomic ions to penetrate into the target. During penetration, the cluster explodes: The distance between the ions i and j, $R_{ij}(t)$, increases from the initial value, $R_{ij}(0)$, under the influence of Coulomb repulsion. The kinetic energy loss of the cluster per unit distance traversed in the solid, that is, the cluster stopping power $S_c(v)$, in first Born approximation can be written as $S_c(v) = Z_c^2(t)\, S_p(v)$, where $Z_c^2(t)$ is the square of the effective charge number of the cluster and $S_p(v)$ is the proton stopping power. Clearly, if all R_{ij} were shorter than a characteristic small distance, r_{close}, to be determined, the cluster would act as a unified point charge with $Z_c^2(R_{ij} < R_{close}) = (\Sigma Z_i)^2$. When the $R_{ij}(t)$ become longer than a characteristic distance r_{dist}, the ions act independently, so that $Z_c^2(R_{ij} > r_{dist}) = \Sigma Z_i^2$ and the stopping power of the cluster becomes equal to the sum of the stopping powers of its constituents. The measured stopping power will thus be a function of the dwell time of the cluster in a target of thickness D, that is, of $\tau = D/v$.

We have derived $Z_c^2(t)$ using a linear response theory treatment. Let two point charges, $Z_1 e$ of mass M_1 and $Z_2 e$ of mass M_2, proceed with velocity v parallel with the z axis of a cylindrical coordinate system (z, ρ) in a medium characterized by the dielectric function $\epsilon(k, \omega)$. The particles are separated by a vector **R** from 1 to 2, with components (**d**, **b**) in the z and ρ directions respectively. Starting from an initial distance $R(0) \equiv R_0$, the separation has grown under the influence of the force $Z_1 Z_2 e^2/R^2$ to $R(t)$ at the time

$$t = t_0 \{ \xi^{1/2}(\xi - 1)^{1/2} + \ln[\xi^{1/2} + (\xi - 1)^{1/2}] \} \quad ,$$

where $t_0 \equiv (\mu R_0{}^3/Z_1 Z_2 e^2)^{1/2}$ and $\xi \equiv R/R_0$, with μ the reduced mass.

In linear response theory, the particles set up the scalar electric potential

$$\varphi(\mathbf{r}, t) = \frac{e}{2\pi^2 \mathrm{v}} \int d^2\kappa$$

$$\int d\omega \frac{e^{i[\kappa\cdot\rho + (z/\mathrm{v} - t)\omega]}\,(Z_1 + Z_2 e^{-i(\kappa\cdot\mathbf{b} + \omega d/\mathrm{v})})}{(\kappa^2 + \omega^2/\mathrm{v}^2)\,\epsilon(k, \omega)} \qquad (1)$$

where $k^2 = \kappa^2 + \omega^2/\mathrm{v}^2$. The cluster stopping power,

$$S_c = Z_1 e\, \partial\varphi/\partial z|_{\mathbf{r} = \mathbf{v}t} + Z_2 e \partial\varphi|_{\mathbf{r} = \mathbf{v}t + \mathbf{R}(t)},$$

becomes

$$S_c = \frac{2e^2}{\pi \mathrm{v}^2} \int_0^\infty \kappa\, d\kappa \int_0^\infty \frac{\omega\, d\omega}{(\kappa^2 + \omega^2/\mathrm{v}^2)} \times \mathrm{Im}\left(-\frac{1}{\epsilon(k, \omega)}\right)$$

$$\times\, [Z_1{}^2 + Z_2{}^2 + 2Z_1 Z_2\, J_0(\kappa b) \cos(\omega d/\mathrm{v})]\ , \qquad (2)$$

since $\dot{\mathbf{R}} \ll \mathbf{v}$ in the present context. The last term describes the interference caused by the vicinage of the projectiles, with J_0 the zero-order Bessel function of the first kind. At our particle velocities, or under channeling conditions, the target core electrons are ineffective; the stopping power from interactions with the valence electrons dominates, to which Bethe's theory applies. If the valence electrons can sustain well-defined plasmons of energy ω_0, where $\omega_0 = (4\pi e^2 n_0/m)^{1/2}$, one can set $\mathrm{Im}(-1/\epsilon) \cong (\pi/2)(\omega_0{}^2/\omega_k)\,\delta(\omega - \omega_k)$, with $\omega_k{}^2 \cong \omega_0{}^2 + k^4/4m^2$, and Eq. (2) becomes

$$S_c = \frac{e^2 \omega_0{}^2}{\mathrm{v}^2} L \left[Z_1{}^2 + Z_2{}^2 + 2Z_1 Z_2 g \frac{\mathbf{R}\omega_0}{\mathrm{v}} \right]. \qquad (3)$$

In the limit $\mathrm{v} \gg \mathrm{v}_0$, the forefactor with the stopping number

$$L = \int_0^\infty \frac{\kappa\, d\kappa}{\kappa^2 + \omega_k{}^2/\mathrm{v}^2} = \ln \frac{2m\mathrm{v}^2}{\hbar\omega_0} \qquad (4)$$

is equal to the Bethe formula for S_p. We have averaged the interference function $g(\mathbf{R}\omega_0/\mathrm{v})$ over all cluster orientations with the result $G(R\omega_0/\mathrm{v})$ shown in Fig. 17.18. When $R < r_{\mathrm{close}} = \hbar/2m\mathrm{v}$, G is of the order unity and $Z_c{}^2 = (Z_1 + Z_2)^2$. When $r_{\mathrm{close}} < R < r_{\mathrm{dist}} = \mathrm{v}/\omega_0$, G has values close to $1/2$ and varies only slowly with R so that $Z_c{}^2 \cong 1/2\,[(Z_1{}^2 + Z_2{}^2) + (Z_1 + Z_2)^2]$. When $R > r_{\mathrm{dist}}$, G drops sharply to small values and oscillates with decreasing amplitude about zero, giving $Z_c{}^2 = Z_1{}^2 + Z_2{}^2$ as for independent point particles. The oscillations signify the interference between the two wakes of electron-density fluctuations trailing particles separated by more than the screening length v/ω_0. In terms of r_{close} and r_{dist} so obtained, one retrieves Eq. (4) in Bohr's formulation $L = \ln(r_{\mathrm{dist}}/r_{\mathrm{close}})$.

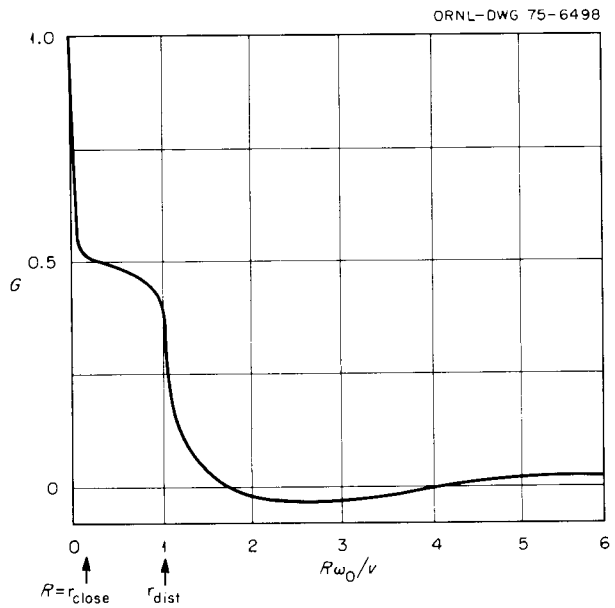

Fig. 17.18. The directionally averaged interference function vs the reduced interparticle distance, with $r_{\mathrm{CLOSE}} = \hbar/2m\mathrm{v}$ and $r_{\mathrm{DIST}} = \mathrm{v}/\omega_0$.

To compare with experimental measurements of energy losses by clusters, the function $G[R(t)\omega_0/\mathrm{v}]$ must be averaged over times up to τ and over the distribution upon entering the target of interproton distances of the cluster. Good quantitative agreement is found with the experimental measurements of the effective charge of $H_2{}^+$ and $H_3{}^+$ ions as a function of dwell time or target thickness.[26]

The phenomenon of dwell-time-dependent stopping powers of ion clusters in solids is important for the prediction of penetration properties. More significantly, it provides quantitative information about the inter-

26. W. Brandt, A. Ratkowski, and R. H. Ritchie, *Phys. Rev. Lett.* 33, 1325 (1974).

ference in clusters between the wakes of electron-density fluctuations trailing charged particles.[27]

A STATISTICAL APPROACH TO THE EVALUATION OF ELECTRON INELASTIC MEAN FREE PATHS IN SOLIDS[28]

The electron gas model for the response of the conduction-band electrons in metals has been used quite widely. The uniform electron density assumed in this model leads to results in many cases which agree quite well with experiment. In the case of aluminum, for example, calculations of electron inelastic mean free paths yield excellent agreement with experiment.

We have been examining various methods of evaluating electron inelastic mean free paths which incorporate the relative simplicity of the electron gas model but which would be applicable to a larger class of materials. A statistical approach, pioneered by Jens Lindhard, has met with considerable success when applied to the calculation of charged-particle energy loss in many different materials.[29,30] Basically the approach involves the assumption that the stopping medium is characterized by a space-varying density of electrons, $n(\mathbf{r})$, and that the contribution of those electrons in a small element d^3r at $\mathbf{r}$ to the stopping process is the same as that of the same number of free electrons in an electron gas at the same density. The total stopping power is computed by averaging over the $n(\mathbf{r})$ distribution appropriate to a given medium.

This procedure has been applied to the computation of inelastic mean free paths in the two metals silver and gold. The inverse inelastic mean free path of an electron of energy E in an electron gas of density n is given in atomic units by

$$\mu(E, n) = \frac{E_F}{\pi E}\int\frac{dk}{k}\int d\omega \, \mathrm{Im}\left(\frac{-1}{\epsilon(k, \omega)}\right) , \qquad (1)$$

where $\epsilon(k, \omega)$ is the linear dielectric response function of the electron gas,[31] E_F is the Fermi energy, and k and ω are the momentum and energy lost by the fast electron to the electron gas. The limits on the double integration are fixed by the energy-momentum relationship of the fast electron and by the properties of the electron gas. In Fig. 17.19 we show the results of numerical calculations using Eq. (1) of the inverse mean free path in reciprocal angstroms as a function of electron kinetic energy in electron volts. The curves corresponding to different uniform densities are labeled by the average interelectron spacing r_s related to the density n through $n^{-1} = 4\pi a_0{}^3 r_s{}^3/3$, where $a_0 = \hbar^2/me^2 = 0.529$ Å.

If we now consider the density to be a function of position, $n(\mathbf{r})$, then $\mu[E, n(\mathbf{r})]$ will vary from point to point in the medium. For a given density distribution we can define an average value of μ as

$$\langle\mu(E)\rangle \equiv \int d^3r \, \mu[E, n(\mathbf{r})] / \int d^3r \quad , \qquad (2)$$

where the integration is over some appropriate volume. To test this statistical procedure we have used electron densities in two metals, silver and gold, computed by a relativistic Hartree-Fock method using the Wigner-Seitz boundary condition. The densities $4\pi r^2 n(r)$ plotted in Fig. 17.20 in atomic units (a.u.) for silver and gold represent, approximately, the number of electrons per unit radius of a spherical shell of radius r centered about each nucleus in the respective metals. These data have been used to average values of $\mu(E, n)$, such as are shown in Fig. 17.19 at fixed E, according to

$$\langle\mu(E)\rangle = \int_0^{r_{WS}} dr\, r^2 \, \mu[E, n(r)] / \int_0^{r_{WS}} dr\, r^2 \quad , \qquad (3)$$

where r_{WS} is the radius of the Wigner-Seitz sphere for a given solid.

Figures 17.21 and 17.22 show the results of this averaging for gold and silver respectively. For the

27. V. N. Neelavathi, R. H. Ritchie, and W. Brandt, *Phys. Rev. Lett.* 33, 302 (1974.

28. Research sponsored in part by the Defense Nuclear Agency, under subtask TA040, but does not reflect endorsement by the sponsor.

29. J. Lindhard, M. Scharff, and H. E. Schiøtt, *Kgl. Dan. Vidensk. Selsk., Mat.-Fys. Medd.* 33, No. 14 (1963).

30. E. Bonderup, *Kgl. Dan. Vidensk. Selsk., Mat.-Fys. Medd.* 35, No. 17 (1967).

31. J. Lindhard, *Kgl. Dan. Vidensk. Selsk., Mat.-Fys. Medd.* 28, No. 8 (1954).

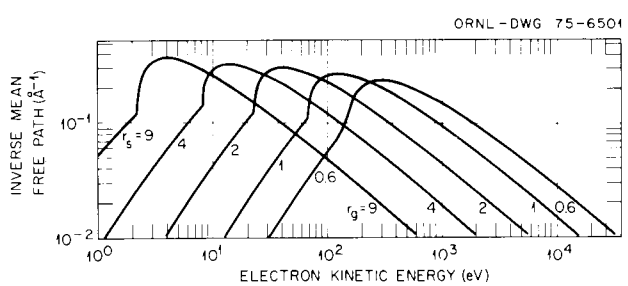

Fig. 17.19. Inverse mean free path of electrons as a function of electron energy for electron gas of several uniform densities.

purposes of comparison we have also shown experimental data which have been obtained for these metals.[32] Reasonable agreement is found, considering the experimental difficulties which attend measurements of $\langle\mu\rangle$ in these energy ranges. We plan to apply this model to other substances for which experimental data exist.

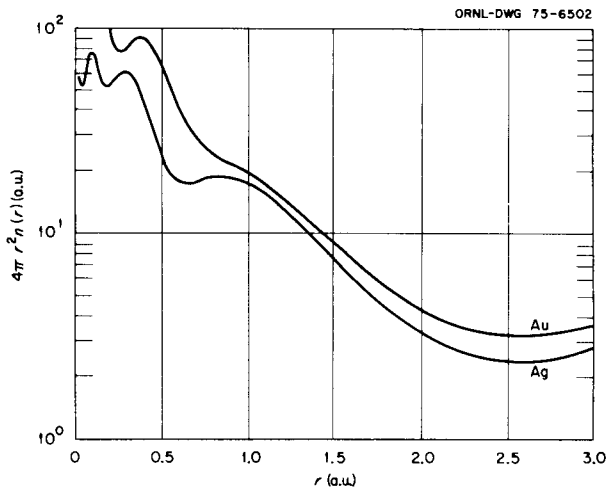

Fig. 17.20. Electron density distribution around ion cores in the metals Au and Ag.

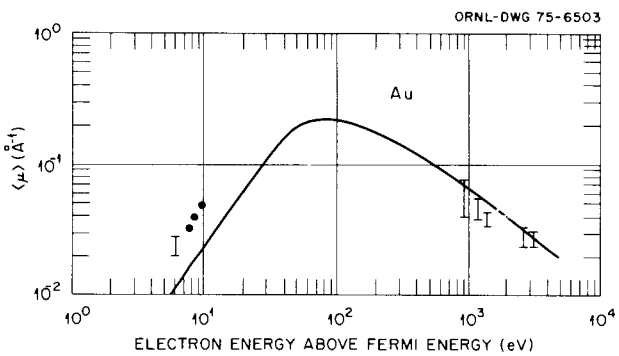

Fig. 17.21. Inverse mean free path of electrons in Au, based on a statistical model.

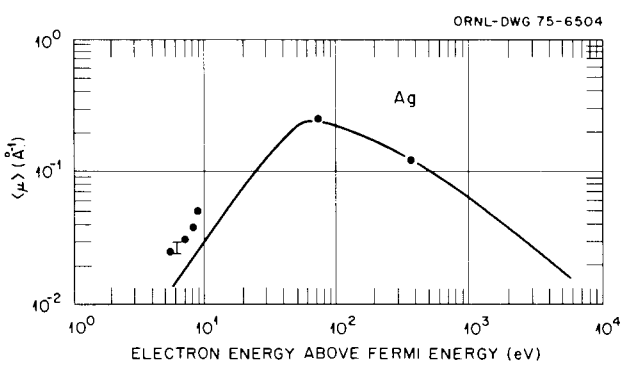

Fig. 17.22. Inverse mean free path of electrons in Ag, based on a statistical model.

TABULATION OF ELECTRON INTERACTION PARAMETERS IN Al AND Al_2O_3[33]

We have begun the theoretical calculations of mean free path, stopping power, and range (in the continuous slowing-down approximation) of electrons in the materials Al and Al_2O_3 for electron energies over the wide range of ~10 eV to ~10 keV. Tables of these interaction parameters will be compiled which should be useful to workers in many areas. The determination of these parameters will be based on currently available theoretical cross sections for the various mechanisms involved in the interaction of electrons with matter. The principal mechanisms determining the interaction parameters are (1) the interaction of electrons with the conduction band in Al and with the valence band in Al_2O_3 and (2) the excitation of electrons into the continuum from the inner shells of the Al and O atoms. Part (1) has been discussed elsewhere in this annual report and in earlier reports. Work with part (2) will be discussed briefly here.

For the case of solids where the excitation of electrons from the inner shells is to states in the continuum, we write the cross section for excitation of an electron from the subshell nl to a continuum energy level between ϵ and $\epsilon + d\epsilon$ as

$$\frac{d\sigma_{nl}}{d\epsilon} = \frac{4\pi a_0^2}{(E/R)(\Delta E/R)} \int_{(Ka_0)_{min}}^{(Ka_0)_{max}} f_{nl}(K, \epsilon)\, d\ln(Ka_0)^2 \quad , \quad (1)$$

where $\Delta E = \epsilon + \epsilon_{nl}^B$ is the energy loss of the incident electron, E is the energy of the incident electron, and ϵ_{nl}^B is the binding energy of the subshell (a positive quantity here). In addition, $a_0 \equiv \hbar^2/me^2$ is the Bohr radius, $R = e^2/2a_0 = 13.6$ eV is the Rydberg energy, and $\hbar\mathbf{K}$ is the momentum transfer. The limits on the integration are given from energy and momentum conservation by

$$(Ka_0)^2_{\substack{max\\min}} = \{2E - \Delta E \pm 2\,[E(E - \Delta E)]^{1/2}\}/R. \quad (2)$$

32. C. R. Brundle, *J. Vac. Sci. Technol.* **11**, 212 (1974).

33. Research sponsored in part by the Defense Nuclear Agency, under subtask TA040, but does not reflect endorsement by the sponsor.

Generalized oscillator strengths for the ionization of L-shell electrons in Al have been calculated by Manson,[34] using a nonrelativistic Hartree-Slater central-field model of the atom for ionized-electron energies from threshold to $128R$. These values have been used as input for numerical evaluation of the integral over momentum transfer in Eq. (1). We now have tables of $(E/\pi a_0^2)d\sigma_{2s}/d\epsilon$ and $(E/\pi a_0^2)d\sigma_{2p}/d\epsilon$ for the values of $\epsilon/R = 0, 0.5, 1, 2, 4, 8, 16, 32, 64$, and 128 and for about 35 values of incident electron energy. As some representative results of these calculations, we have plotted $(E/\pi a_0^2)d\sigma_{nl}/d\epsilon$ as a function of ϵ/R for several values of E for a limited range of ϵ/R in Fig. 17.23 with $nl \rightarrow 2s$ and in Fig. 17.24 with $nl \rightarrow 2p$. The energy loss of the incident electron is given by $\Delta E = \epsilon + 8.715R$ and $\Delta E = \epsilon + 5.947R$ for removing electrons from the $2s$ and $2p$ subshells respectively.

Similar calculations have been done for the $1s$ shell in oxygen. The values of the generalized oscillator strength for excitation to the continuum from the $1s$ shell of O were taken from the work of McGuire.[35]

Generalized oscillator strengths for the K shell in Al are not available using the Hartree-Slater method of Manson or McGuire, partly due to the length of the computer calculations. However, it is widely accepted that for the K shell of Al, hydrogenic calculations should be quite good. Consequently, we have used the form factor calculated using hydrogenic wave functions[36] to determine the cross section of excitation of electrons from the K shell of Al to the continuum.

From the calculated differential cross section per atom, the differential inverse mean free path for the given process is obtained by multiplying the cross section by the density of atoms in the solid under study. The tabulations of this quantity for the inner shells of Al and O and for the conduction band of Al and the valence band of Al_2O_3 form the basic input information of our calculations of mean free paths, stopping powers, and ranges of electrons in Al and Al_2O_3. Further theoretical consideration must be given to the most efficient way to include exchange effects in the calculations. From a practical standpoint we must decide on the most useful format for presentation of the tabulations (units, interval size for incident electron energies, etc.).

34. S. T. Manson, *Phys. Rev. A* **6**, 1013 (1972).
35. E. J. McGuire, Sandia research report SC-RR-70-406.
36. E. Merzbacher and H. W. Lewis in *Handbuch der Physik*, ed. by S. Flügge, Springer-Verlag, Berlin, 1958, p. 166.

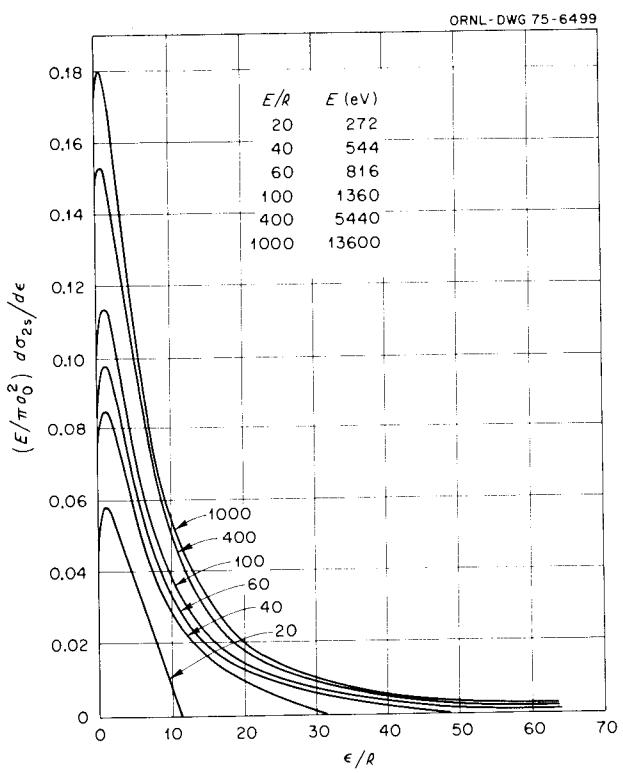

Fig. 17.23. Plot of differential cross section for excitation of an electron from the $2s$ subshell in Al to a continuum energy level ϵ by incident electrons of energy E/R = 20, 40, 60, 100, 400, 1000.

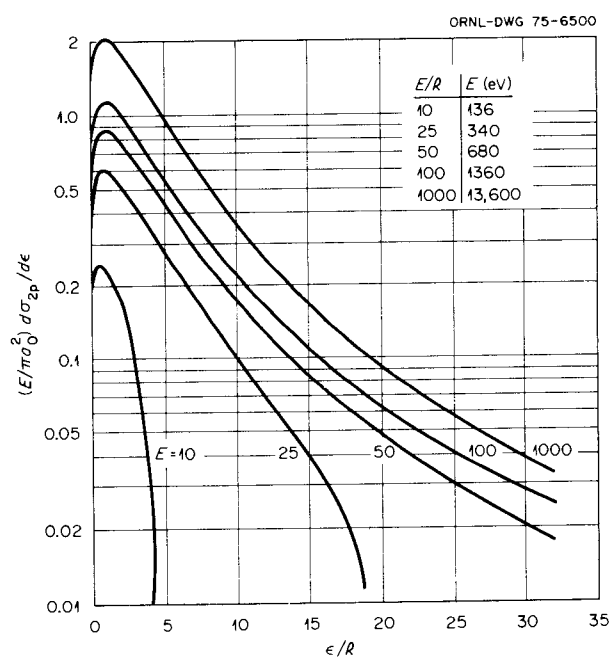

Fig. 17.24. Plot of differential cross section for excitation of an electron from the $2p$ subshell in Al to a continuum energy level ϵ by incident electrons of energy E/R = 10, 25, 50, 100, 1000.

Part IV. Chemical Physics and Spectroscopy

W. R. Garrett

18. Chemical Physics Studies

R. N. Compton

T. A. Callcott[1]
Ada Carter
C. D. Cooper[2]
J. T. Cox
W. F. Frey[3]
W. R. Garrett
C. E. Klots
B. P. Pullen[4]
P. W. Reinhardt
H. C. Schweinler
L. J. Smith[5]
J. A. D. Stockdale
R. J. Warmack[6]
J. M. Younkin[6]

NEGATIVE-ION FORMATION IN ORGANIC MOLECULES

There is considerable interest in the negative-ion properties of organic molecules in the gas phase. However, despite this intense interest, very little is known about organic anions. Perhaps the lack of experimental data can be traced to two reasons: (1) experimental difficulties, or (2) physicists generally prefer to study simpler systems. We have been making steady progress in the area of organic negative-ion physics by employing collision techniques (e.g., low-energy electron attachment, SF_6 scavenger, negative-ion–molecule reactions, and alkali atom collisional ionization experiments). The development of these techniques has allowed us to study bound states, compound states (long- and short-lived), and metastable dissociating negative-ion states. Perhaps the most innovative aspect of our work is the measurement of electron affinities for organic molecules.[7] The collisional ionization technique has been used to measure electron affinities for a number of organic molecules. As an example, Fig. 18.1 shows the relative cross section for the formation of $TCNQ^-$ (tetracyanoquinodimethan) ions formed by collisions with cesium atoms. From the threshold we deduce an

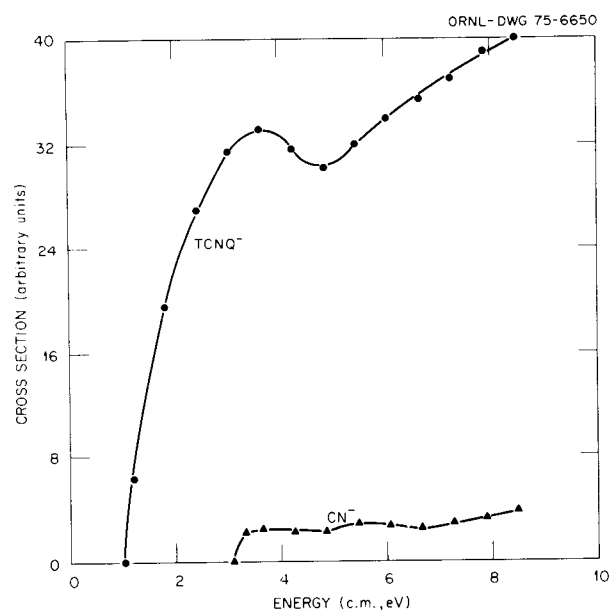

Fig. 18.1. Relative cross sections for the production of tetracyanoquinodimethan (TCNQ) negative ions and CN negative ions resulting from collisions with fast cesium atoms as a function of the energy in the center-of-mass system.

1. Consultant from the University of Tennessee.
2. Consultant from the University of Georgia.
3. Consultant from Davidson College.
4. University Research Participant, ORAU.
5. Southern Colleges University Union Participant from Southwestern University, Memphis, Tennessee.
6. Graduate Student, University of Tennessee.
7. R. N. Compton, P. W. Reinhardt, and C. D. Cooper, *J. Chem. Phys.* **60**, 2953 (1974).

electron affinity of 2.8 ± 0.2 eV. Further data on molecular electron affinities and correlations with molecular orbital energy levels, using Koopmans' theorem, are presented in a later section.

A rather thorough study of negative ion states in parabenzoquinone (PBQ) has been completed and is described herein. The electron affinity of PBQ was measured to be 1.89 ± 0.2 eV, using the collisional ionization technique. Dissociative electron attachment to PBQ produced $C_5H_4O^-$, $C_5H_3O^-$, $C_4O_2H_2^-$, C_2HO^-, and C_2H^-. Our observations show that the cross section for producing the long-lived metastable parent negative ion, $C_6H_4O_2^-$, peaks at 1.4 ± 0.1 eV, which is considerably lower in energy than previously reported.[8] Compound negative ion states were observed at 0.7, 1.35, and 1.9 eV, using the SF_6 scavenger technique (see Figure 18.2). Our electron affinity value coupled with calculated energies of the lowest unfilled orbitals of PBQ permits an assignment of the compound states observed using the SF_6 scavenger technique. Orbital energies of the four lowest unfilled and the four highest filled orbitals of PBQ as calculated by Merrienne-Lafore[9] using a CNDO approximation are shown in Fig. 18.3. A different set of molecular orbital energy values as determined by Kunii and Kuroda[10] using a Parisier-Parr-Pople-SCF (self-consistent field) type of calculation are also included. The molecular orbital designations apply only to the calculations of Merrienne-Lafore.[9] Kunii and Kuroda[11] showed that for a series of molecules, the electron affinity of a molecule is related to the energy of the lowest vacant molecular orbital, ϵ_{LVMO}, by $-\epsilon_{LVMO} - 1.9$ eV. From this relationship (Koopmans' theorem) they predicted an electron affinity of 2.08 eV for PBQ. In Fig. 18.3 the calculated energies of the lowest unfilled molecular orbitals have been shifted so that the lowest vacant orbital coincides with our measured electron affinity of 1.89 eV. The three resonances of lowest energy observed experimentally for PBQ, using the SF_6 scavenger technique, are included in Fig. 18.3. If one associates the 0.70-, 1.35-, and 1.90-eV resonances with the a_u, b_{1u}, and b_{3g} unfilled orbitals of PBQ, the agreement with the theoretical calculations of both

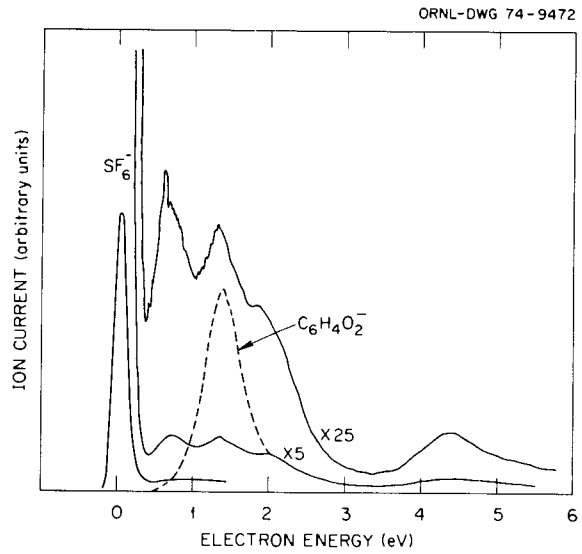

Fig. 18.2. SF_6 scavenger spectrum showing low-lying compound negative ion states in *p*-benzoquinone. The PBQ^- negative ion peak ($C_6H_4O_2^-$) is included as a reference. The retarding potential difference technique was used to obtain an effective electron distribution of 0.2 eV, and the energy scale was calibrated with the krypton energy loss peak at 10.0 eV.

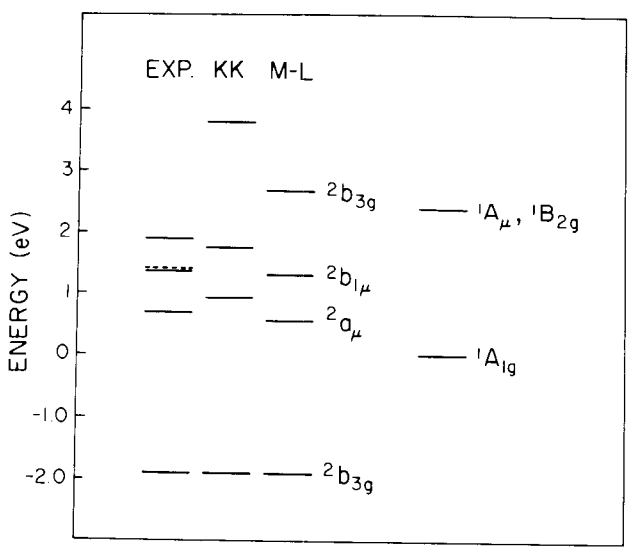

Fig. 18.3. Energies of the observed compound negative ion states of PBQ are placed in the "exp." column. The energies of the lowest unfilled orbitals of neutral PBQ which were calculated by Kunii and Kuroda (ref. 10) and Merrienne-Lafore (ref. 9) are placed in the KK and M-L columns. The energies of these calculated values have been shifted so that the energy of the lowest unfilled orbital of PBQ coincides with the measured electron affinity of 1.89 eV. The lowest excited singlet states, ^1A_u and $^1B_{2g}$, of neutral PBQ are shown on the right side of the diagram.

8. L. G. Christophorou, J. G. Carter, and A. A. Christodoulides, *Chem. Phys. Lett.* 3, 237 (1969); P. M. Collins, L. G. Christophorou, E. L. Chaney, and J. G. Carter, *Chem. Phys. Lett.* 4, 646 (1970).

9. M. F. Merrienne-Lafore, quoted in H. P. Trommsdorf, *J. Chem. Phys.* **56**, 5358 (1972).

10. T. L. Kunii and H. Kuroda (private communication).

11. T. L. Kunii and H. Kuroda, *Theor. Chim. Acta* 11, 97 (1968).

Merrienne-Lafore[9] and Kunii and Kuroda[10] are surprisingly good for the two lowest orbitals. The peaks of the compound states are plotted here because of the difficulty in determining the onset of the resonance (i.e., the 0-0 transition energy). The qualitative agreement shown here supports the theoretical methods used in the calculations and indicates that the energies of the compound states qualitatively correspond to the energy of the unfilled orbitals (i.e., it is not necessary to use configuration interaction in calculating the approximate energy of these states). Thus, the long-lived state at 1.4 eV is interpreted to result from attachment of an electron into a b_{1u} orbital to form a $^2B_{1u}$ state which undergoes an internal conversion process to the ground state $^2B_{3g}$.

NEGATIVE-ION FORMATION IN $Fe(CO)_5$ AND $Ni(CO)_4$

The formation of negative ions from iron and nickel carbonyl was studied in gas-phase collision experiments using both low-energy (0 to 10 eV) electron beams and fast (0 to 40 eV) potassium atom beams. Dissociative electron attachment to $Fe(CO)_5$ and $Ni(CO)_4$ occurs with an extremely high probability for low-energy electrons to produce $Fe(CO)_4^-$ and $Ni(CO)_3^-$. Ions of the type $Fe(CO)_x^-$ (where x = 0 to 3) and $Ni(CO)_x^-$ (where x = 0 to 2) are observed to occur at higher energy. Upper limits to the electron affinity of Fe and Ni were estimated from the threshold for formation of Fe^- and Ni^- to be $\leqslant 0.5 \pm 0.3$ and $\leqslant 1.1 \pm 0.3$ eV respectively. Figure 18.4 shows a low-resolution (~0.5 eV) scan of the various negative ions from $Fe(CO)_5$ as a function of the electron energy. As the electron energy is increased, we see from the figure that progressively more and more CO molecules are ejected from the molecule to form the molecular ion. Figure 18.5 shows a high-resolution (~0.1 eV) electron impact ionization cross section for three of these ion currents. A well-defined structure is seen in the cross sections for producing $Fe(CO)_3^-$ and $Fe(CO)_2^-$ in the energy region between 3 and 5 eV. This structure is attributed to predissociation from an electronically excited state of the $Fe(CO)_4^-$ ion. This appears to be the first clear evidence for predissociation from a negative ion, although there is no reason that negative ion predissociation should not occur. Collisions of fast potassium atoms with $Fe(CO)_5$ yield $Fe(CO)_4^-$ at an energy ~0.4 eV below the ionization potential of potassium, while $Ni(CO)_3^-$ from $Ni(CO)_4$ occurs at ~4.3 eV, the ionization potential of potassium. Figure 18.6 shows sample data for $Ni(CO)_4$. These results imply that dissociative electron attachment is approximately thermoneutral; that is, the electron affinity of the radical is approximately equal to the first CO bond dissociation energy. This may allow for favorable overlap of the neutral and ionic surfaces, which in turn offers an explanation for the large attachment rates observed in these com-

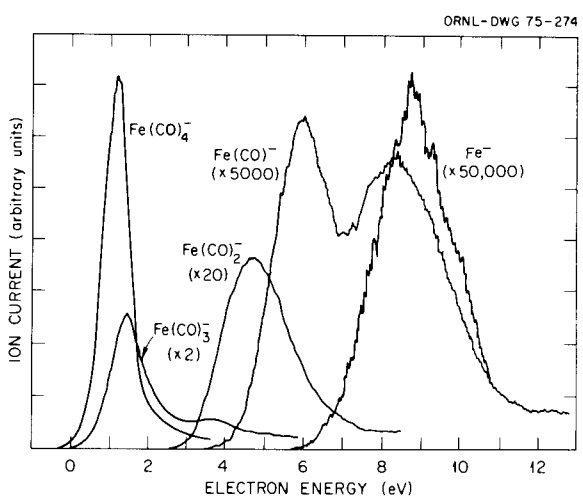

Fig. 18.4. Low-resolution electron impact study of iron pentacarbonyl.

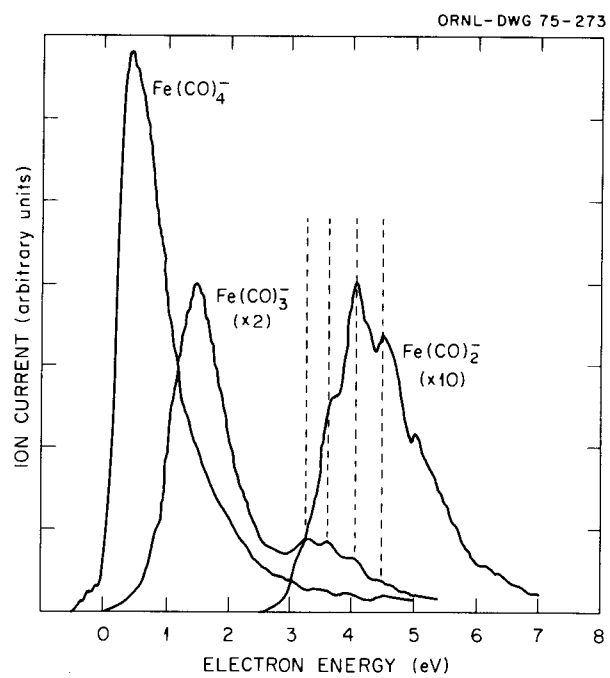

Fig. 18.5. Relative cross sections for the production of negative ions from $Fe(CO)_5$ by low-energy electrons. The structure in the negative ion yields of $Fe(CO)_3^-$ and $Fe(CO)_2^-$ is attributed to predissociation from a compound $Fe(CO)_4^-$ state.

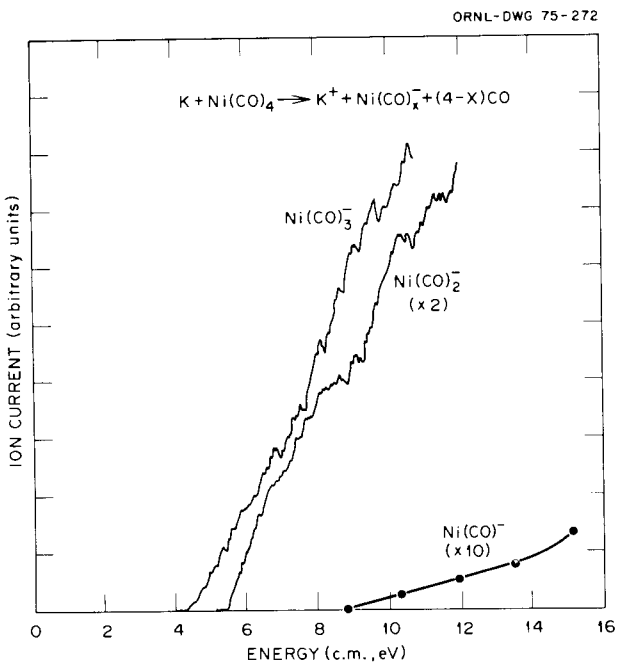

Fig. 18.6. Relative cross sections for the formation of negative ions from nickel carbonyl resulting from collision with fast potassium atoms as a function of the energy in the center-of-mass system.

pounds. The thresholds for the various reaction products are also energetically consistent with the thresholds observed by electron impact. This work clearly shows the utility of studying dissociative negative ion processes with both electron and alkali atom beams.

COLLISIONAL IONIZATION OF Na, K, AND Cs BY CO_2, COS, AND CS_2: MOLECULAR ELECTRON AFFINITIES

Studies of the reactions occurring between beams of alkali metal atoms and molecules are contributing greatly to our understanding of collision physics. In some cases much sought-after molecular electron affinities have been deduced from threshold measurements for the formation of positive and negative ion pairs in such collisions. Alkali atoms have low ionization potentials, and thus the valence electron can easily be transferred from the alkali atom to an acceptor molecule. The reaction sequence is

$$A^0 + M \rightarrow A^+ + M^- . \qquad (1)$$

Lower limits to the electron affinity of M are deduced from measurements of the threshold for the initiation of the above reaction. Alternately, the energy of the incident alkali atom is set above the endothermic reaction threshold, and the energy of the product alkali ion is determined in the forward direction. The electron is generally transferred over large distances (5 to 15 Å), leading to large reaction cross sections in which very little momentum is imparted to the target molecule.

During the past year we have studied the collisions of alkali metal atoms (Na, K, Cs) with the linear triatomic molecules CO_2, COS, and CS_2. (Preliminary results were presented for the electron affinity of CO_2 in last year's annual report.) These molecules provide an extreme test of the collisional ionization technique for determining molecular electron affinities, since the ground states of the molecular anions are greatly distorted from their neutral parent molecules. The C-O bond length, for example, changes from 1.1621 Å for CO_2 to ~1.25 Å for CO_2^-, and the bond angle changes from 180° for CO_2 to ~135° for CO_2^-.[12] Ions with masses corresponding to the parent molecules CO_2, COS, and CS_2 are observed for all collision permutations except for Na colliding with CO_2. Perhaps in this case the collision complex ($Na^+ \,..\, CO_2^-$) does not live long enough for relaxation to the ground state of CO_2^- to occur. The following electron affinities are deduced from measurements of the threshold for the ion-pair production reactions: CO_2 (−0.60 ± 0.2 eV), COS (+0.46 ± 0.2 eV), and CS_2 (1.0 ± 0.2 eV). Table 18.1 summarizes the data obtained for all the collision permutations. The CO_2^- ions were always metastable with respect to autodetachment, and the lifetime ($9 \pm 2 \times 10^{-5}$ sec) was measured to be independent of collision energy over the region of energy studied (threshold to ~20 eV c.m.). As an example of the

12. C. D. Cooper and R. N. Compton, *J. Chem. Phys.* 59, 3550 (1973).

Table 18.1. Electron affinities of some linear triatomic molecules

Molecule	Projectile	Electron affinity (eV)
CO_2[a]	Na	CO_2^- not observed
CO_2	K	−0.68
CO_2	Cs	−0.55
COS	Na	+0.34
COS	K	+0.50
COS	Cs	+0.58
CS_2	Na	+1.2
CS_2	K	+0.9
CS_2	Cs	+1.2

[a]The CO_2^- ions observed were metastable with respect to autodetachment. The lifetime was determined to be $9 \pm 2 \times 10^{-5}$ sec and *independent* of collision energy.

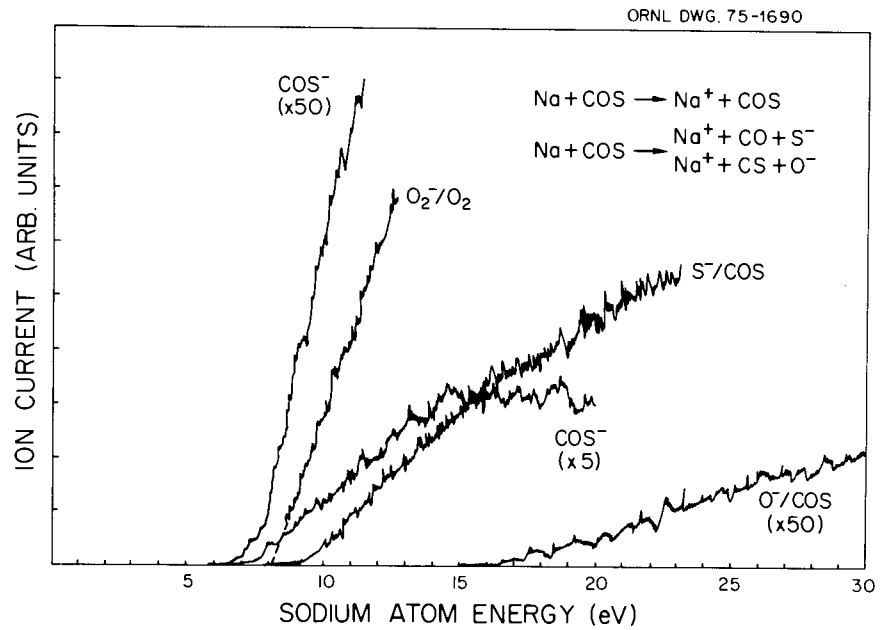

Fig. 18.7. Negative ion yields from carbonyl sulfide produced by collisions with fast sodium atoms as a function of the sodium atom energy. The yield of O_2^- from molecular oxygen is used to calibrate the energy scale.

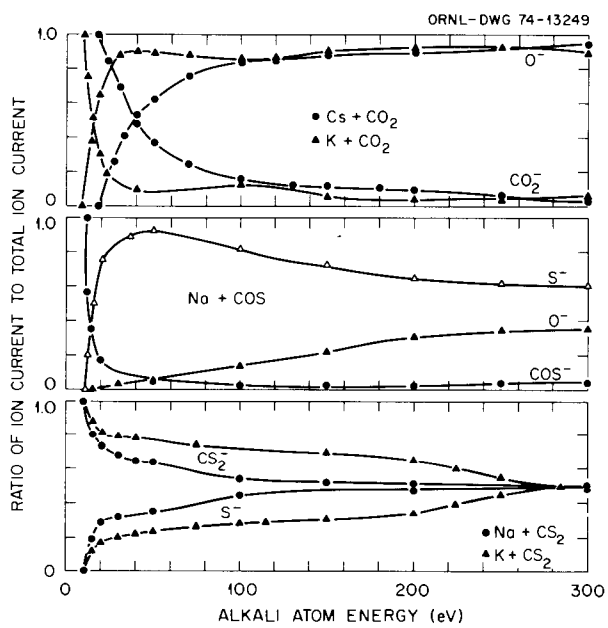

Fig. 18.8. Ratio of individual negative ion current divided by the total negative ion current for collision of alkali atoms with CO_2, COS, and CS_2.

threshold measurements, Fig. 18.7 displays the negative-ion yields produced by collisions of fast sodium atoms with carbonyl sulfide as a function of the sodium atom energy. The fragment ions O^-/CO_2, O^-/COS, S^-/COS, and S^-/CS_2 were detected at a threshold energy consistent with the known energetics of the reactions. Interesting data as to the ratio of the individual negative ion currents divided by the total negative ion currents for collisions of alkali atoms with CO_2, COS, and CS_2 are shown in Fig. 18.8. Data such as these provide insight as to the reaction mechanisms involved.

ABNORMALLY LARGE ELECTRON AFFINITIES FOR SOME HEXAFLUORIDE MOLECULES

Electron affinity values reported for atoms and small molecules (number of atoms $\leqslant 4$) range from approximately -2 to $+4$ eV. Reliable electron affinities for polyatomic molecules are difficult to determine, although estimated values for inorganic and organic molecules are also less than 4 eV. In last year's annual report we presented evidence that the collisions between thermal beams of cesium and tungsten hexafluoride produce the gas phase ions Cs^+ and WF_6^-. Because of the extreme interest in these unique reactions, we have extended these measurements to other alkalis and hexafluorides.

Lower limits to molecular electron affinities are deduced from measurements of the threshold energies for the formation of positive and negative ion pairs from orthogonal crossed-beam reactions of fast alkali atoms (Na, K, Cs) with room-temperature MF_6 molecules; that is,

$$A + MF_6 \rightarrow A^+ + MF_6^- \ . \qquad (1)$$

In some cases the incident alkali atom energy is set above the endothermic reaction threshold, and the energy of the alkali ion is determined in the forward direction. Values determined from the "energy loss" experiments are in good agreement with electron affinities derived from the threshold measurements for SF_6 (0.65 ± 0.2 eV),[13] SeF_6 (3.0 ± 0.2 eV), and TeF_6 (3.2 ± 0.2 eV).[13]

Perhaps the most interesting result from this work is the observation that reactions of thermal cesium ($T \cong 120°C$) and potassium ($T \cong 180°C$) with MF_6 beams at room temperature produce separated A^+ and MF_6^- ion pairs. To our knowledge this is the first observation of a "thermal" energy collisional ionization process between ground-state reactants. The exothermic reactions $A + MF_6 \rightarrow A^+ + MF_6^-$, represented by (A/MF_6), which have been observed are (Cs or K/WF_6), (Cs/ReF_6), (Cs or K/IrF_6), (K/PtF_6), and (Cs/MoF_6). These results imply that $EA(WF_6)$, $EA(IrF_6)$, and $EA(PfF_6)$ are greater than 4.34 eV; $EA(MoF_6)$ and $EA(ReF_6)$ are equal to or greater than 3.89 eV. All collision permutations between alkalis and hexafluorides have not yet been examined. Effects on the collisional ionization reaction due to thermal population of vibrational states of the hexafluoride have not as yet been considered, and thus these limits are uncertain by as much as ~0.4 eV. Rothe et al.[14] have verified our observations of exothermic reactions between cesium and WF_6.

In the case of sodium colliding with WF_6, a reaction threshold was observed from which we obtain an electron affinity for WF_6 of 4.5 eV. Figure 18.9 shows the relative yield of WF_6^- and F^- produced by collisions with fast sodium atoms.

Bartlett[15] has analyzed the oxidizing properties of the third transition-metal hexafluoride molecules and also finds exceptionally large electron affinities. From a Born-Haber cycle involving $O_2^+(PtF_6)^-$, he estimates $EA(PtF_6) \cong 9.3$ eV. We find that reactions of low-energy Na with PtF_6 produce mainly PtF_5^-; PtF_6^- ions are also detected. Collisions of thermal potassium atoms with PtF_6 resulted in both $K^+ + PtF_6^-$ (weak signal) and $(K^+ + F) + PtF_5^-$ (strong signal). The latter reaction is the first observation of a thermal energy dissociative ionization reaction between ground-state reactants, and thus the electron affinity of PtF_5 must be quite large. We can also conclude that $EA(PtF_6) \geqslant 4.3$ eV, which is consistent with Bartlett's estimation.

Endothermic collisional ionization reactions are easy to rationalize from simple covalent-ionic curve crossing considerations. However, for exothermic reactions the ground-state ionic surface must lie below the covalent surface, and therefore the two surfaces do not cross. The initial electron transfer most likely occurs at the

13. R. N. Compton and C. D. Cooper, *J. Chem. Phys.* **59**, 4140 (1973).

14. S. Y. Tang, G. P. Reck, and E. W. Rothe, *Bull. Amer. Phys. Soc.* **19**, 1173 (1974); private communication from E. W. Rothe.

15. Neil Bartlett, *Angew. Chem. Int. Ed. Engl.* **7**, 433 (1968) and private communication.

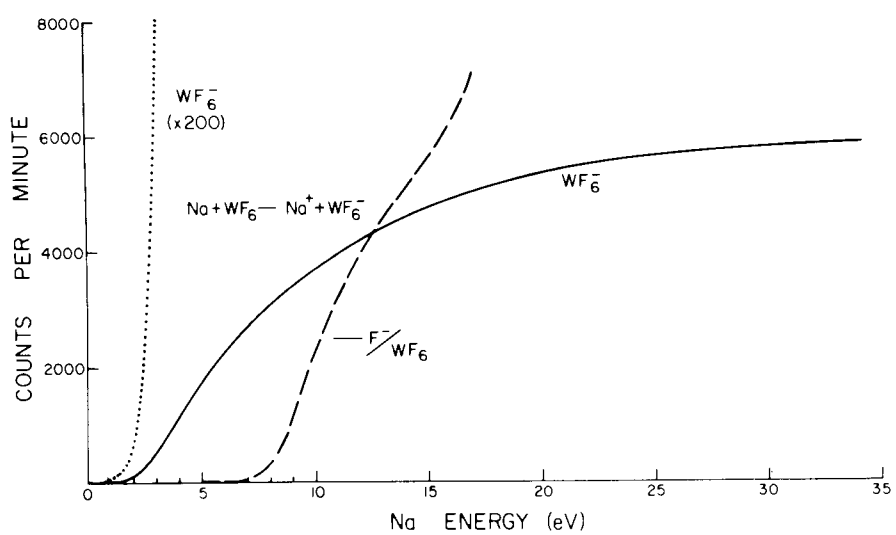

Fig. 18.9. Relative negative ion yields from WF_6 produced by collisions with fast sodium atoms.

crossing of an ionic surface involving a vibrationally or electronically excited MF_6^- ion with the covalent surface.

π-ELECTRON AFFINITIES FOR ORGANIC MOLECULES

The electron affinity of a molecule is defined as the difference in energy between the neutral in its ground state, E^0, and the ion in its ground state, E^-; that is, EA = $E^0 - E^-$. In cases where the ionic surface lies above that of the neutral, a virtual or compound state exists (negative EA); and conversely when the total energy of the negative ion is below that of the neutral, a bound state exists (positive EA). The position and width of a compound state can be studied by electron scattering techniques, whereas the bound states can be studied by photodetachment methods for simple molecules or by the collisional ionization method for polyatomic molecules.

The lowest negative ion state of a simple conjugated hydrocarbon results in the addition of an electron into a π-molecular orbital, and the energy of this vacant orbital is determined by the structure of the molecule. The large variety of conjugated hydrocarbons allows for considerable range in "π-electron affinities," and both bound and virtual states are known to exist. Recent beam experiments have provided reliable electron affinities for both bound[16] and virtual states.[17]

Koopmans' theorem states that the Hartree-Fock energy of the lowest vacant molecular orbital (ϵ_{LVMO}) gives an approximation to the electron affinity. Previous correlations between ϵ_{LVMO} and EA have been made, and one of the more successful was due to Kunii and Kuroda.[11] Along these lines we have calculated energy levels for some conjugated systems containing C, N, and O atoms, using a semiempirical SCF-MO method based upon a variable β-γ modification of the Parisier-Parr-Pople approximation to the Hartree-Fock equation. Figure 18.10 shows an excellent correlation between electron affinities deduced from beam data and the calculated value of ϵ_{LVMO}.

The ground state of $C_6H_6^-$ ($^2E_{2u}$) is degenerate, and the degeneracy is removed upon substitution of one or more nitrogen atoms into the ring.[18] The calculated splitting of the pyridine negative ion state is seen to be

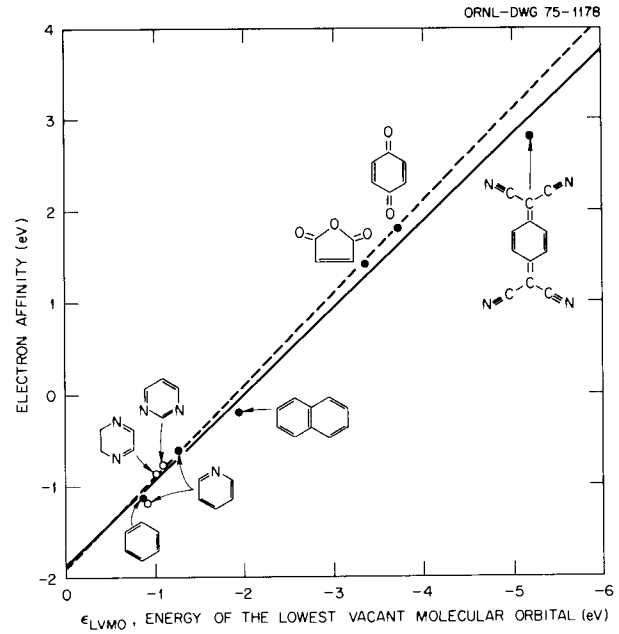

Fig. 18.10. Correlation of the calculated energy of ϵ_{LVMO} and EA determined from beam data. The dashed line results from a previous correlation (ref. 11) using a limited number of molecules with electron affinities between 0 and 0.8 eV. The negative EA values are taken from ref. 17.

in good agreement with experiment. The open circles for pyrazine and pyrimidine are the $\tilde{A}^2A_u$ states reported by Nenner and Schulz,[17] while the ground ^2B states were believed to be bound; however, our calculations predict virtual states. The correlation shown in Fig. 18.10 is used to calculate ground and excited negative ion energy states for other simple conjugated hydrocarbons where experimental data are nonexistent or fragmentary. For example, a compound state is observed as a broad and structureless dip at 1.7 eV in the electron transmission spectra of ethylene. We find the $^2B_{3u}$ state of $C_2H_4^-$ at 1.6 eV. Bound excited states are also predicted for some organics, in particular, organics containing the C≡N subgroup. In Table 18.2 we include semiempirical calculations of electron affinities for a large number of organic molecules. We hope that these calculations will be useful in predicting electron affinities for many complex molecules.

GAS PHASE LASER-ION SPECTROSCOPY

The invention of high-powered tunable dye lasers now makes it possible to study the energy levels of ions

16. A complete tabulation of electron affinity data is in preparation. Partial results can be found in ref. 7.

17. I. Nenner and G. J. Schulz, *J. Chem. Phys.* **62**, 1747 (1975).

18. R. H. Huebner, R. N. Compton, and H. C. Schweinler, *Chem. Phys. Lett.* **2**, 407 (1968).

Table 18.2. Calculated electron affinities from the modified Parisier-Parr-Pople method

Molecule	Electron affinity (eV)	Molecule	Electron affinity (eV)
Acenaphthylene	0.77	Maleic anhydride	1.28
Acridine	0.75	Maleimide	1.15
Acrylonitrile	1.31	Naphthacene	0.84
Adenine	−0.24	Naphthalene	−0.06
Alloxan	1.43	1,5-Naphthyridine	0.43
Aniline	−0.58	1,6-Naphthyridine	0.29
Anthracene	0.49	1,7-Naphthyridine	0.34
Azulene	0.77	1,8-Naphthyridine	0.41
1,2-Benzanthracene	0.42	2,6-Naphthyridine	0.26
1,12-Benzperylene	0.51	2,7-Naphthyridine	0.14
3,4-Benzphenanthrene	0.18	Novacene	1.49
1,2-Benzpyrene	0.64	Octacene	1.43
4,5-Benzpyrene	0.35	Ovalene	0.81
Benzene	−1.07	Oxazole	−2.26
p-Benzoquinone	1.62	Parabanic acid	0.90
Biphenyl	−0.21	Paraphenylenediamine	3.49
Biphenylene	−0.33	Pentacene	1.06
1,3-Butadiene	−0.52	Pentaphene	0.44
Carbazole	−0.35	Perylene	0.71
Chrysene	0.26	Phenanthrene	0.03
Coronene	0.33	Phenazine	1.06
Cytosine	−0.03	Phenol	−0.66
1,2;3,4-Dibenzanthracene	0.34	Picene	0.29
1,2;7,8-Dibenzanthracene	0.33	Purine	−0.08
1,2;5,6-Dibenzanthracene	0.37	Pyrazine	−0.30
3,4;5,6-Dibenzphenanthrene	0.26	Pyrene	0.45
Ethylene	−1.61	Pyridine	−0.70
Fluoranthene	0.63	Pyrimidine	−0.52
Fulvalene	1.73	Pyrrole	−2.39
Fumaronitrile	2.26	Quinazoline	0.30
Furan	−2.40	Quinoline	0.20
Glyoxal	0.94	Quinoxaline	0.51
Guanine	−0.86	Styrene	−0.39
HCN	1.11	TCNE	3.05
Heptacene	1.34	TCNQ	2.96
Heptafulvalene	0.18	*s*-Triazine	−0.54
Hexacene	1.23	Triphenylene	−0.06
Hexahelicene	0.26	Uracil	−0.13
Imidazole	−2.00	Vinylene carbonate	−1.60
Isoquinoline	0.07	Vinylidene cyanide	1.65

in the gas phase. During the past year an experiment has been designed and constructed which will allow us to study photon-ion processes of the following type:

$$h\nu + AB^{\pm} \rightarrow A + B^{\pm} , \quad (1)$$

$$AB^{-} \rightarrow AB + e , \quad (2)$$

$$AB^{-} \rightarrow A + B + e . \quad (3)$$

A schematic diagram of the experimental apparatus is shown in Fig. 18.11. A pulsed electron beam of controllable energy is used to produce negative or positive ions in the source region of a time-of-flight mass spectrometer. The ions are allowed to remain in the ion source for a variable period of time ($0-10^{-3}$ sec) before they are pulsed out down the flight tube of the mass spectrometer. During the ion residence time in the source, monoenergetic photons of variable energy are directed into the source through a Brewster angle window. If dissociation of $AB^{\pm}$ occurs to form $A + B^{\pm}$, a decrease in the $AB^{\pm}$ signal will occur along with an increase in the $B^{\pm}$ signal. Photodetachment reactions (2) and (3) appear as a decrease in the AB^{-} signal. The wavelength dependence of these signals will allow for much new information on ionic energy levels.

ORNL-DWG 75-6405

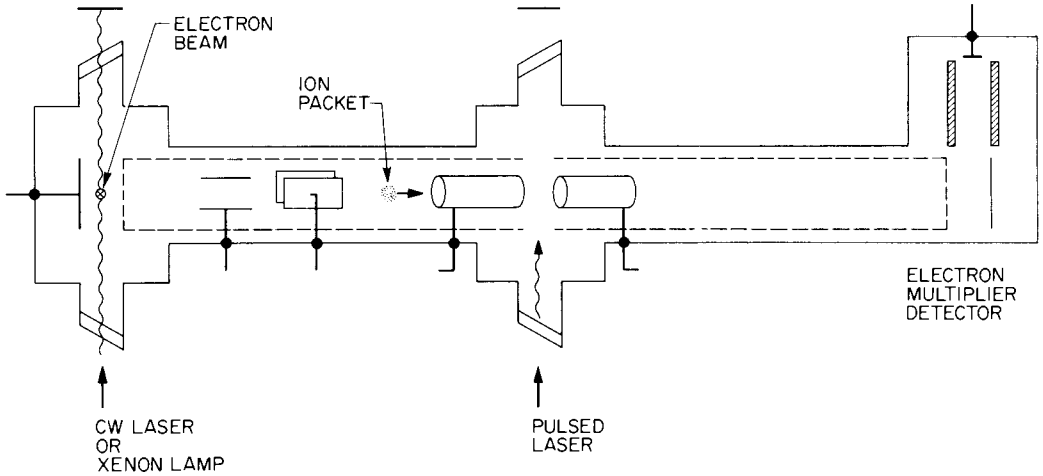

Fig. 18.11. Schematic diagram of crossed-beam photon-ion reaction experiment.

The kinetic energy released in reactions (1) and (3) can be studied by introducing the laser beam at a second point down the ion flight path. An argon ion laser which operates in the cavity dumping made by use of an acousto-optical device is used to synchronize a high peak power pulse of photons to strike one ion packet as it passes a point along the flight path. If photodissociation occurs, the kinetic energy released in the center of mass will result in a broadening of the time-of-arrival distribution of the ion and the neutral peaks. Asymmetries in the dissociation with respect to the polarization vector of the laser light can also be investigated. Collision-induced dissociation or detachment, which might occur in the ion beam before or after the intersection of the ion packet and light pulse, is not a problem in these experiments, since the collision-induced processes are separated from the light-induced processes by using a pre- and post-decelerator lens (see Fig. 18.11). If dissociation occurs as a result of photon absorption, for example, reaction (1), two peaks will be observed in the time-of-flight spectrum in addition to the parent $AB^{\pm}$ peak. We anticipate that these experiments will add much new information to the growing field of gas phase ionic processes.

STUDIES OF DISSOCIATIVE IONIZATION BY ELECTRON IMPACT

Dissociative ionization of sulfur hexafluoride. The crossed-beam method previously described[19] has been used to study electron impact dissociative ionization of SF_6 for electron energies from threshold to 300 eV. Figure 18.12 shows F^+ ion time-of-flight spectra at a number of electron energies for a 1.0-μsec electron beam pulse and a flight distance of 28.7 cm from the beam intersection region to the entrance aperture of the quadrupole mass spectrometer detection system. The spectra were obtained with the electron beam at 90° to the mass spectrometer aperture and have been unfolded to eliminate the transit time through the quadrupole. Figure 18.13 shows F^+ energy spectra derived from the data of Fig. 18.12. The energy spectra are cut off below an F^+ energy of 0.8 eV corresponding to the far tail ($\geqslant$100 μsec) of the time-of-flight distribution. Considerable structure is evident in both time-of-flight and energy spectra. This structure corresponds to the various states of the SF_6^{+*} molecule involved in the dissociation process, and its detailed interpretation requires additional experimental and theoretical work. A general point of interest is that the spectra, even at low electron energies, show a considerable quantity of fast F^+ ions with kinetic energies above 1 eV. The appearance potential for the F^+ ion from this and previous work[20] is $\geqslant$35 eV, much greater than the values for the ions SF_5^+, SF_4^+, and SF_3^+, which are 15.9, 19.5, and 20.4 eV.[20] Since from the known

19. J. A. D. Stockdale and L. Deleanu, *Chem. Phys. Lett.* **22**, 204 (1973). See also *Health Phys. Div. Annu. Progr. Rep. July 31, 1974*, ORNL-4979, p. 117.

20. V. I. Dibeler and F. L. Mohler, *J. Res. Nat. Bur. Stand.* **40**, 25 (1948).

SF_5-F bond strength and the ionization potential of the F atom only 20.1 eV is required for the process

$$e + SF_6 \rightarrow SF_5 + F^+ + e \ ,$$

it follows that at the observed F^+ threshold of 35 eV, 15.5 eV of internal excitation would remain in the SF_5 fragment if the F^+ were produced with near zero kinetic energy. This amount of energy is sufficient for nearly complete dissociation of the SF_5. However, the kinetic energy spectra of Fig. 18.13 indicate that the F^+ ion is, in fact, frequently produced with considerable kinetic energy, which raises the possibility that energy is not shared uniformly between the available vibrational modes in the SF_6^{+*} complex prior to dissociation.

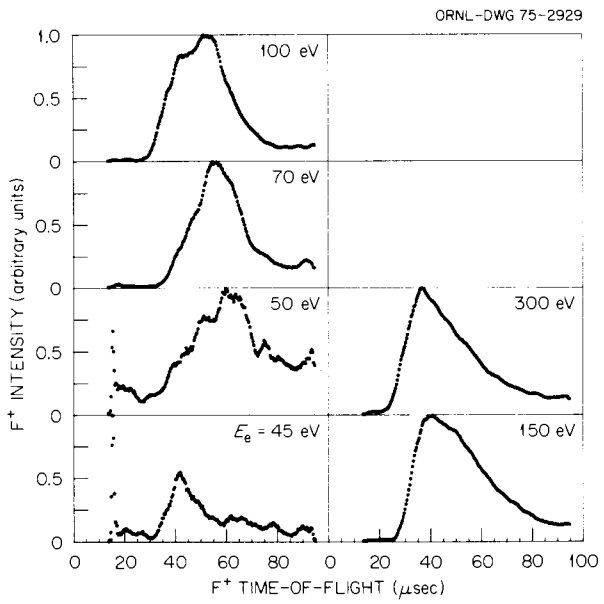

Fig. 18.12. Time-of-flight spectra for F^+ ions produced by electron impact on SF_6. E_e, electron energy. Spectra recorded at 90° to incident electron beam; flight distance, 28.7 cm. Electron beam pulse width, 1.0 μsec. Spectra unfolded to allow for ion transit time through quadrupole mass spectrometer.

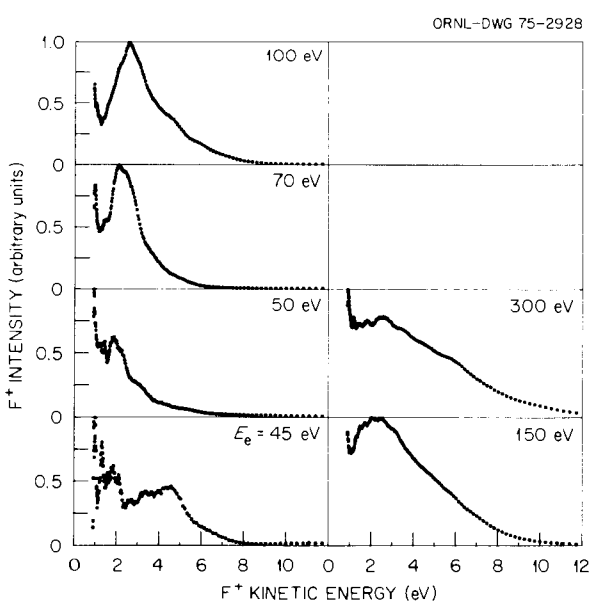

Fig. 18.13. F^+ from SF_6 kinetic energy spectra derived from Fig. 18.12. E_e, electron energy.

Figures 18.14 and 18.15 show angular distributions for F^+ ions of various kinetic energies obtained at electron impact energies of 55 and 100 eV respectively. The distributions are isotropic within the accuracy of the measurements.

Method for obtaining excitation functions in digital form: Application to dissociative ionization of CO_2. For full interpretation of ion kinetic energy spectra such as those shown in Fig. 18.13, it is necessary to obtain ion excitation functions differential in ion energy. These are plots of the intensity of a given ion of

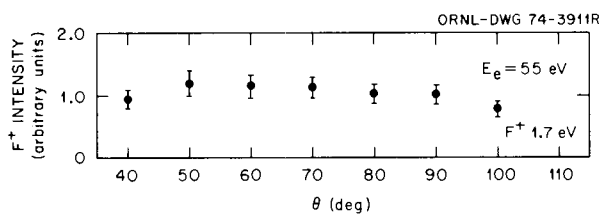

Fig. 18.14. Angular distribution of 1.7-eV F^+ ions from impact of 55-eV electrons on SF_6.

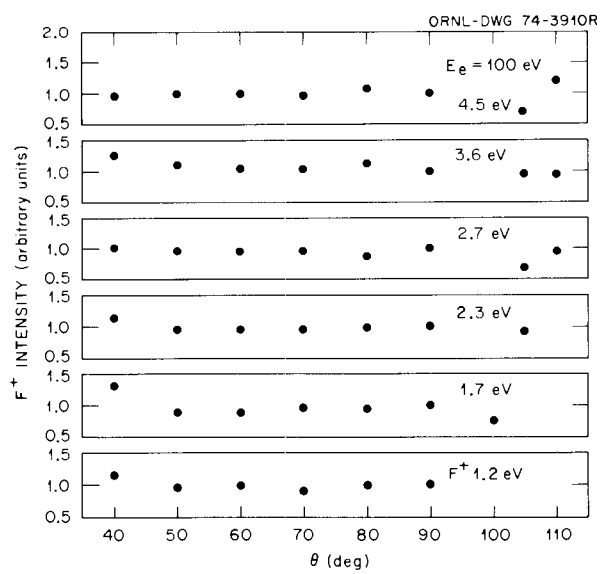

Fig. 18.15. Angular distributions of F^+ ions from impact of 100-eV electrons on SF_6.

a given kinetic energy against the exciting electron energy. Integral excitation functions, plots of total ion current for a particular ion against electron energy, are also used to obtain appearance potentials and calibrate energy scales. This latter measurement is one of the most common and useful in mass spectrometry. Excitation functions are most frequently obtained by an analog method in which the measured ion current is recorded as the electron energy is driven through a predetermined range. It is preferable, however, to obtain excitation functions in digital form. Here each detected ion produces a single count, and the electron energy is repetitively swept over the region of interest many times. In this way the threshold regions of low intensity can be studied in greater detail, and drifts in experimental conditions tend to average out through repeated scanning. Data are also obtained in a form suitable for processing by digital computer.

Figure 18.16 shows schematically an arrangement for obtaining excitation functions in digital form.[21] The ramp generator in the center box produces a pulse which provides the ramp voltage of a sampling time-to-pulse-height converter and also drives an operational amplifier which varies the electron beam energy through an adjustable range. Detected ion pulses are fed to the time-to-pulse-height converter which produces output pulses of amplitude proportional to the electron energy at the instant of detection of the ion. This output is accumulated and stored in a multichannel analyzer. Provided the ramp rise is slow compared with the time of flight of the ions in the pulsed crossed-beam experiment,[19] this arrangement can be used to compile differential excitation functions for ions (as illustrated in Figs. 18.20 and 18.21). Figures 18.17 and 18.18 show excitation functions for the ions O^+ and C^+ produced from CO_2 by electron impact. The data apply to ions of all energies emitted at 90° to the incident

21. J. A. D. Stockdale, B. P. Pullen, and A. E. Carter, *Int. J. Mass Spectrom. Ion Phys.* 17, 241 (1975).

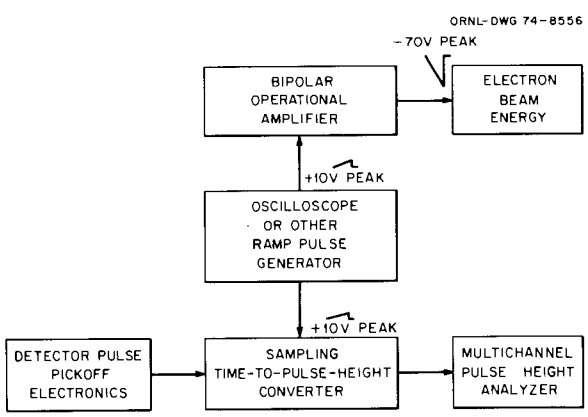

Fig. 18.16. Schematic diagram of electronics for obtaining excitation functions in digital form.

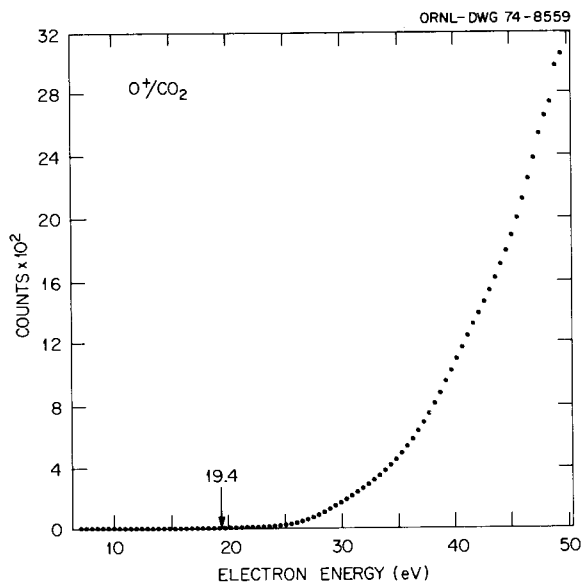

Fig. 18.17. Excitation function (plot of ion counts vs electron beam energy) for O^+ from CO_2 within the electron energy range 0–60 eV. The results are normalized to unit electron beam current. The O^+ ions were detected at 90° to the incident electron beam direction. The experimental data have been smoothed once (see ref. 19).

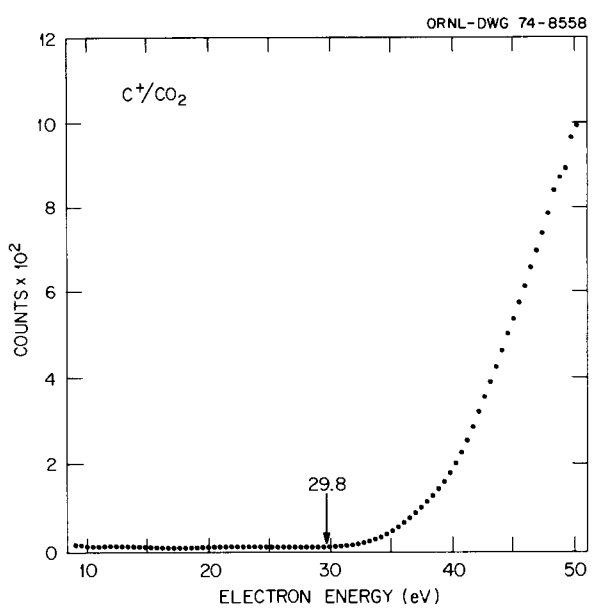

Fig. 18.18. Excitation function for C^+ from CO_2 within the electron energy range 0–60 eV. Experimental conditions were the same as for Fig. 18.17.

electron beam direction. The appearance potential of 19.4 ± 0.3 eV obtained for O^+ probably corresponds to the threshold for excitation of the predissociating $C^2\Sigma_g^+$ state of CO_2^+.[22] The C^+ onset of 29.8 ± 0.3 eV corresponds to total dissociation of the CO_2 molecule:

$$e + CO_2 \rightarrow C^+ + O + O + 2e\ .$$

The process $e + CO_2 \rightarrow C^+ + O_2 + 2e$, which has a threshold of 22.9 eV for zero kinetic energy and zero internal excitation of the products, was not observed under our experimental conditions.

Dissociative ionization of deuterium. Figure 18.19 shows kinetic energy spectra of D^+ ions produced by electron impact on D_2 in the crossed-beam experiment. The D^+ ions were detected at 40° to the incident electron beam direction, and the effect of the 3.0-μsec electron beam gate pulse and the transit time through the quadrupole mass spectrometer detector system have been unfolded. The dashed lines in the figure are previously reported measurements of Van Brunt and Kieffer[23] for a detection angle of 23°. The two sets of measurements are consistent at high D^+ energies. The interesting feature of these observations is the structure observed in the D^+ kinetic energy spectra below the prominent peak at 8 eV from dissociation of D_2^+ via the $^2\Sigma_u^+$ state. Some suggestion of such structure can be seen in the results of Van Brunt and Kieffer,[23] and more sharply resolved peaks have been reported for H^+ from H_2 by Crowe and McConkey.[24]

The appearance potentials for the various structural features are of central concern; Figs. 18.20 and 18.21 show typical excitation functions for D^+ ions of energies ≥0.9 and ≥3.4 eV respectively. Within the accuracy of the measurements, only two onsets can be distinguished with certainty. The low-lying onset in both figures is consistent with formation of D^+ ions through excitation of the ground $^2\Sigma_g^+$ state of D_2^+, which has an asymptotic limit of 18.1 eV. The higher onset is consistent with formation of ions from the $^2\Sigma_u^+$ state of D_2^+. This data and other similar excitation functions do not provide any definite evidence for onsets in the electron energy region lying between the $^2\Sigma_g^+$ and $^2\Sigma_u^+$ states, that is, between approximately 19 and 32 eV in the Franck-Condon region. Since the yield of D^+ ions observed in the excitation functions increases dramatically above 32 eV and the fraction of D^+

22. K. E. McCulloh, *J. Chem. Phys.* **59**, 4250 (1973).
23. R. J. Van Brunt and L. J. Kieffer, *Phys. Rev.* **A2**, 1293 (1970).
24. A. Crowe and J. W. McConkey, *Phys. Rev. Lett.* **31**, 192 (1973).

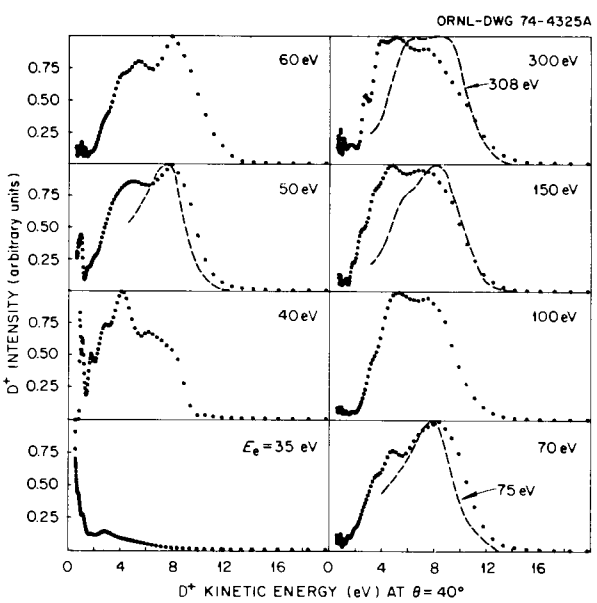

Fig. 18.19. Kinetic energy spectra of D^+ ions produced by electron impact on D_2. E_e, electron energy. Spectra recorded at 40° to the incident electron beam direction. 3.0-μsec electron beam pulse and D^+ ion transit time through detection system have been unfolded. Dashed line, data of Van Brunt and Kieffer (ref. 23) recorded at 23°.

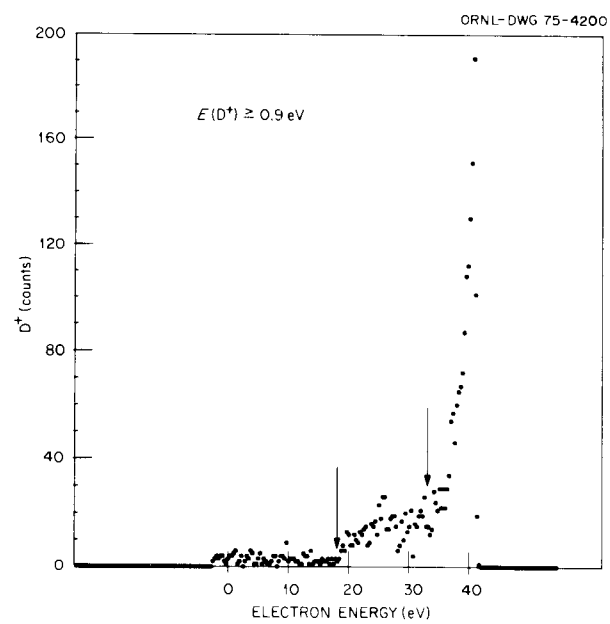

Fig. 18.20. Excitation function for D^+ ions produced by electron impact on D_2. D^+ kinetic energy ≥0.9 eV. Breaks indicated at $18.1\ ^{+1}_{-2}$ eV and 33.0 ± 2.0 eV.

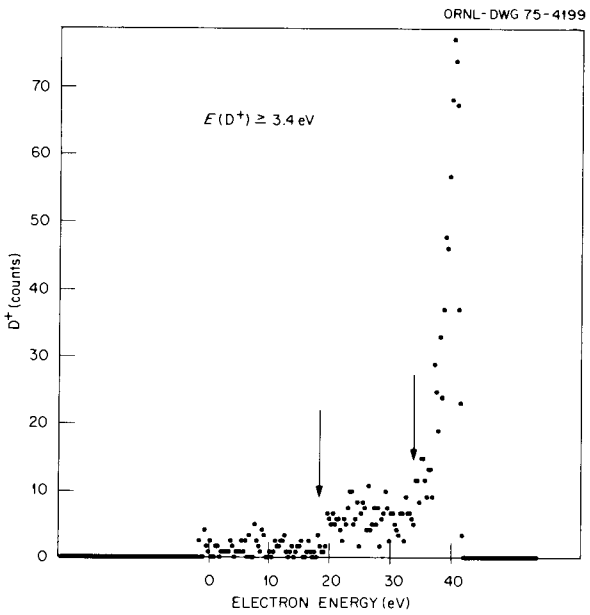

Fig. 18.21. Excitation function for D^+ ions produced by electron impact on D_2. D^+ kinetic energy ≥3.4 eV. Breaks indicated at 18.6^{+1}_{-2} eV and 33.8 ± 3 eV.

ions of anomalous kinetic energy (between the 8-eV $^2\Sigma_u^+$ and zero eV peaking $^2\Sigma_g^+$ associated groups) is quite large, the data suggest onsets for these D^+ ions of near 32 eV. Their origin therefore might be either with the formation of D^+ ions through excitation of D_2^+ states lying above but near the $^2\Sigma_u^+$ state in the Franck-Condon region or with formation of D^+ through decay of doubly excited autoionizing states of D_2 which have excitation thresholds in the same region into the continuum of the $^2\Sigma_g^+$ state.[25,26] Recent calculations by Bottcher[26] indicate thresholds between 28 and 34 eV for excitation of such states.

IONIZATION POTENTIALS OF ORGANIC DONOR MOLECULES

There is much interest in the charge-transfer complexes of organic molecules; a number of these complexes show extraordinary electrical conductivity in the crystalline phase. An important parameter, which affects their stability, structure, and conductivity, is the ionization potential of the electron-donor component.[27] We have determined these ionization potentials for several such donors, using the retarding potential difference modification of the electron impact technique, with a time-of-flight mass spectrometer. These are listed in Table 18.3.

Table 18.3. Ionization potentials for selected donor molecules

Donor molecule	Ionization potential (eV)[a]
TTF (tetrathiofulvalene)	6.95
Heptafulvalene	7.00
TSeF (tetraselenafulvalene)	7.21
Tetraperfluoromethyl (TTF)	8.04
TMPD (tetramethylphenylenediamine)	6.33
DMPD (*n,n'*-dimethylphenylenediamine)	6.84
PD (*p*-phenylenediamine)	7.22

[a]The estimated imprecision is ±0.1 eV.

Although these molecules are usually viewed as electron donors, there are indications of interesting acceptor properties also. Attachment of electrons of extremely low energy of heptafulvalene yields a parent negative ion. Attachment to tetraperfluoromethyl (TTF) shows similar behavior and also dissociative attachment to yield $C_2(CF_3)_2$. Low-energy attachment to TSeF and TTF gives no detectable parent negative ion but extensive decomposition, predominantly yielding a C_2H_2 fragment. These observations suggest a substantial electron affinity for these "donor" molecules.

REACTIONS OF ELECTRONICALLY EXCITED ATOMS

Previous investigations[28,29] of the reactions of highly excited atoms and molecules are being continued; we are interested in particular in species excited to Rydberg-like states lying just below the ionization potential. An example of the reactivity of these states is the process

$$Kr^{**} + CS_2 \rightarrow Kr^+ + CS_2^- .$$

This reaction occurs with a large cross section and hence shows two things: (1) the electron affinity of CS_2 must be positive, and (2) its rate of reaction with low-energy electrons is also large. These studies hence complement other studies of the section.

We have investigated further these reactions with the following technique. A pulse of electrons is used to excite (and ionize) a mixture of, for example, xenon and SF_6. This is followed by a pulsed electric field to

25. A. U. Hazi (private communication, 1974).
26. C. Bottcher, *Proc. Phys. Soc., London (At. Mol. Phys.)* 7, 352 (1974).
27. C. E. Klots, R. N. Compton, and V. F. Raaen, *J. Chem. Phys.* **60**, 1177 (1973).
28. J. A. D. Stockdale, F. J. Davis, R. N. Compton, and C. E. Klots, *J. Chem. Phys.* **60**, 4279 (1974).
29. C. E. Klots, *J. Chem. Phys.* **62**, 741 (1975).

clear out the Xe^+ and SF_6^- ions found by the original electron pulse or by the scavenging of scattered electrons. The buildup in time of additional ions via the process

$$Xe^{**} + SF_6 \rightarrow Xe^+ + SF_6^-$$

is then monitored in the usual way with a time-of-flight mass spectrometer. Even in the absence of SF_6, some Xe^+ will be observed; at least some of the Xe** will be field-ionized by the second electric-field pulse used to sample the ions. We find that (1) the cross section for making Xe** Rydberg states under electron impact is very nearly a step function at threshold; (2) at large electron energies it is equivalent to that for making an Xe** with energy just above the ionization potential, that is, Xe^+ and a slow electron, as observed in trapped-electron experiments;[30] and (3) the cross section for SF_6^- and hence for the Xe reaction is the same. We take this as implying that, although SF_6 apparently reacts with only S-wave free electrons, it can react with Rydberg electrons of all orbital angular momenta.

Of interest also are some nonreactions of Rydberg states. The reactions

$$Ar^{**}, Kr^{**}, Xe^{**} + He \rightarrow HeAr^+, HeKr^+, HeXe^+ + e$$

could not be observed, although energetically allowed. These diatomic ions can be made when the helium atom is initially excited, for example, into its metastable 2^1S, 2^3P states. Likewise the reaction

$$Kr^{**} + Ar \rightarrow KrAr^+ + e$$

does not occur readily, although initial excitation of Ar to a state of energy virtually equal to Kr* readily affords reaction. A pattern seems to be emerging. The initially excited moiety must be the species of higher ionization potential to effect these mixed Hornbeck-Molnar reactions. The reason for this is only poorly understood.

KINETIC ENERGY PRODUCTION FROM UNIMOLECULAR DISSOCIATIONS

Our earlier work on the unimolecular decomposition of species with well-defined energy has focused on the rates of these decompositions.[31] These studies employed a model in which the long-range potential determines the mechanism of fragmentation, with only a small perturbation arising from the short-range forces.

Recent measurements of the kinetic energies of the separated fragments following decomposition of ions in a mass spectrometer offer a nice opportunity to illustrate these ideas. Figure 18.22 shows the kinetic energy distribution of the fragments from the reaction[32]

$$C_6H_5CN^+ \rightarrow C_6H_4^+ + HCN\ .$$

The distribution is approximately that of a two-dimensional Boltzmann gas, although the leading edge, at very low energies, is clearly depleted. The smooth curve is our calculated result, obtained with no adjustable parameters. It reproduces the experimental "histogram" quite well. In particular, the depletion of the leading edge, which in the present model arises from the small perturbation of the short-range forces, is accurately predicted.

This work has been extended to other decompositions where the short-range forces become especially important, and to collision complexes where large angular momenta are involved. In these instances the "depletion" effects assume overriding importance.

30. J. T. Grissom, R. N. Compton, and W. R. Garrett, *Phys. Rev.* **A6**, 977 (1972).

31. C. E. Klots, *Z. Naturforsch.* **27**, 553 (1972).

32. D. T. Terwilliger, J. H. Beynon, and R. G. Cooks, *Proc. Roy. Soc., London* **A341**, 135 (1974).

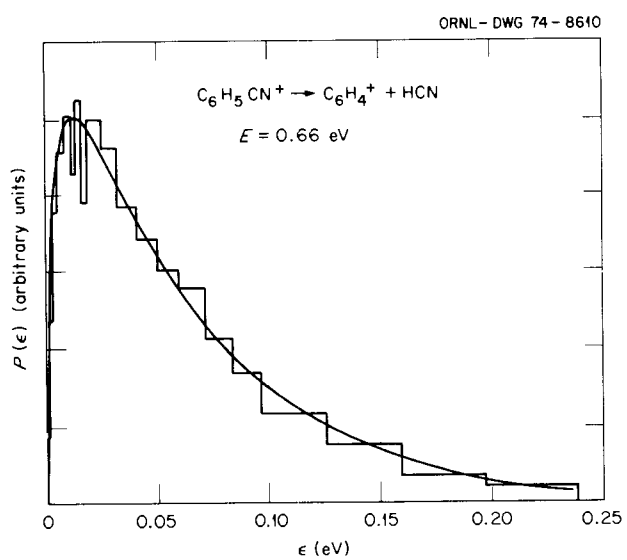

Fig. 18.22. Observed and calculated (smooth curve) kinetic energy distribution for the fragments C_6H_4 + HCN.

OPTICAL AND ELECTRICAL MEASUREMENTS ON ORGANIC SEMICONDUCTORS

Preliminary data were reported last year for the room-temperature reflectance and transmittance of small crystals of TTF-TCNQ (tetrathiofulvalene tetracyanoquinodimethan), using plane-polarized light over the photon energy range 1.5 to 3.2 eV. Experimental techniques have now been improved, and these measurements were repeated from 0.7 to 4.1 eV. The reflectance $R_{\parallel}$ obtained with the electric vector, **E**, incident in the z direction, or direction of the high-conductivity axis, shows a sharp Drude edge in the vicinity of 0.73 eV and marked structure above this energy. The reflectance $R_{\perp}$, corresponding to the electric vector perpendicular to the high-conductivity axis, shows little structure, being close to 10% over the range of photon energies studied. The dc electrical conductivity along the three principal directions in the crystal was also measured as a function of temperature from 4.2 to 300°K. The extremely high conductivity peaks reported by one group of observers have not been seen. The suggestion that a probe misalignment could generate false high peaks was investigated by computer modeling.[33] Although very high conductivity peaks can be generated by computer modeling to fit experimentally misaligned probe data, the temperature dependence of the measured extraordinary peaks can in no way be attributed to simple probe misalignment. We did find the electrical conductivity, σ_z, along the stacking direction to be at least 10^3 times as great at 58°K as that along the other two principal directions. Two forms of TTF-I, orthorhombic crystals of stoichiometry TTF-I_2 and monoclinic crystals of approximate stoichiometry $(TTF)_7$-I_5, were also studied. For orthorhombic TTF-I the TTF molecules are aligned in the x-y plane, allowing resolution of the reflectances Rx and Ry corresponding to the incident electric vector in the x and y directions respectively. For monoclinic TTF-I this alignment is not present. Room-temperature measurements of $Rx + Ry$ over the energy range 0.7 to 5.1 eV on monoclinic TTF-I showed the combined structures obtained independently for Rx and Ry on orthorhombic TTF-I. In addition, for monoclinic TTF-I a Drude-like edge was observed at ~–0.15 eV in Rz. High dc conductivity was observed in monoclinic TTF-I. There was little temperature dependence in σ_z near room temperature; but at 205 to 260°K there was a sudden change to semiconductive behavior, with major hysteresis in σ_z on temperature recycling. For orthorhombic TTF-I the value of σ_z was considerably lower than for the monoclinic TTF-I, and there was no hysteresis. Monoclinic TTF-Br, with a high dc conductivity comparable to that observed in monoclinic TTF-I, showed the sudden change to semiconductive behavior at ~180°K, without hysteresis.

33. R. J. Warmack, T. A. Callcott, and H. C. Schweinler, *Appl. Phys. Lett.* **24**, 635 (1974).

LEVEL SHIFTS FROM COULOMB INTERACTION OF ATOMS IN A GAS

We consider N_a identical atoms in a gas of volume V; each atom has a $J^w = 0^+$ ground state and L excited 1^- levels. The three N_aL excited states are labeled $|\mathbf{R}_I\alpha\nu\rangle$; they have at $\mathbf{R}_I$ partner $\alpha(\alpha = x, y, z)$ of the νth 1^- level, of excitation energy E_ν, and have at all other atomic positions unexcited atoms. The atoms are assumed not to overlap. The Hamiltonian is $H = H^0 + H^{\text{int}}$, where H^0 is the sum of N_a one-atom terms, and H^{int} is the sum of $N_a(N_a - 1)/2$ Coulomb interaction terms. Here the Hamiltonian matrix $\langle\mathbf{R}_I\alpha\nu|H|\mathbf{R}_{I'}\alpha'\nu'\rangle$ is the Kronecker product $G \times \mathcal{E}$ of a $3N_a$ by $3N_a$ "geometrical" matrix G and an L by L "electronic" matrix $\mathcal{E}$. Similarity transformation of H by $\Gamma \times I_L$, where Γ is the matrix of eigenvectors of

$$G[\Sigma(I'\alpha')G_{I\alpha}, I'\alpha'\Gamma_{I'\alpha'}, n = g_n\Gamma_{I\alpha}, n] ,$$

and $I_L = (\delta_{\nu\nu'})$ is the L-dimensional unit matrix, reduces H to $3N_a$ diagonal L by L blocks with zeroes elsewhere. Furthermore, the nth such block of $H - W$ has matrix elements

$$(H - W)_{\nu\nu'} = (E_\nu - W)\delta_{\nu\nu'} + g_n e^2 Z_{\nu 0} Z_{0\nu'}/r_s^3 ,$$

where $-eZ_{\nu 0}$ is the transition moment between the νth excited and ground state of any atom, and r_s (defined by $4\pi r_s^3/3 = V/N_a$) is a scale length introduced to make G and g dimensionless. The determinant of $H - W$ is

$$\prod_n [(\prod_\nu \lambda_{n\nu})(1 + \sum_\nu 1/\lambda_{n\nu})] ,$$

where

$$\lambda_{n\nu} = (E_\nu - W)/(g_n e^2 Z_{\nu 0} Z_{0\nu}/r_s^3) .$$

The secular equation $\det(H - W) = 0$ has a simple graphical interpretation for the energy eigenvalues $W_{n\nu}$ and a surprisingly simple equation for the coefficients of the excited states. All the above can be carried through explicitly if the atomic positions $\mathbf{R}_I$ form a lattice; the states are then the "exciton states" $|\mathbf{k}\, p\nu\rangle$ of

solid-state physics, described by N_a propagation vectors **k**, three polarization indices p, and energy $W_{\mathbf{k}p\nu}$ (which approaches E_ν as r_s gets large). We conclude that for each **k** and ν two transverse excitonic states are shifted downward by about $e^2 Z_{\nu 0} Z_{0\nu}/r_s^3 (g_{\mathbf{k}p} \cong -1)$, and the longitudinal exciton is shifted downward by twice as much. For the argon resonance line this is a shift of about 1 in 10^5 at 1000 torr.

ROTATIONAL RESONANCE IN LOW-ENERGY ELECTRON-H_2 SCATTERING

In a recent theoretical study[34] the existence of rotational resonances was established in low-energy electron scattering by polar molecules. Some of the properties of the phenomenon were elucidated, but the more interesting question of whether such resonances might exist for very simple molecules such as H_2 was not answered. Electron drift velocity experiments on ortho and para H_2 (ref. 35) and an electron beam transmission experiment on H_2 and D_2 (ref. 36) seem to incate the presence of resonant structure in electron scattering cross sections in the energy region below the first vibrational excitation threshold. However, detailed close-coupling results for electron-H_2 scattering[37] have failed to show any theoretical evidence for such proposed resonances.[38]

A theoretical study of low-energy electron-H_2 and D_2 scattering has now been completed. The approach was analogous to that taken earlier in the study of rotational resonances in electron scattering by polar molecules.[34] The calculations were made in the close-coupling approximation,[34,39] utilizing an electron-molecule interaction potential similar to that used successively by Henry and Lane[37] for describing low-energy electron scattering by hydrogen. The object here was to ascertain whether rotational resonances might be sustained by a realistic interaction potential, that is, one which yields cross sections in agreement with available experimental data.

The electrostatic potential which results from integration over electron coordinates has the form

$$V(r_a) = -2(0.583 + 0.5/r_a)\exp(-2.33\, r_a)\,, \qquad (1)$$

where r_a is the distance from nucleus a (Fig. 18.23). A similar expression holds for $V(r_b)$. Terms of the form (1) may be readily expanded in a multipole expansion of the form

$$V(\mathbf{r}) = \sum_{\lambda=0}^{\infty} V_\lambda(r) P_\lambda(\cos\theta_{rs})\,. \qquad (2)$$

In addition to terms of the form (1), a term arising from the permanent quadrupole moment, Q_{zz}, is included in the total interaction potential. This has the form

$$V_2^q(r) = -Q_{zz} r^{-3}\, C(r)\,. \qquad (3)$$

Finally, spherical and quadrupolar distortion terms due to the parallel and perpendicular polarizabilities are included in the semiempirical analytic forms

$$V_0^p(r) = -\frac{\alpha_0 C(r)}{2(r^2 + r_p^2)^2}\,, \qquad (4)$$

$$V_2^p(r) = -\frac{\alpha_2 C(r)}{2(r^2 + r_I^2)^2}\,. \qquad (5)$$

These expressions contain the experimentally determined values $Q_{3z} = 0.49ea_0^2$, $\alpha_0 = 5.5a_0^3$, and $\alpha_2 = 1.38a_0^3$ for the quadrupole moment and the two

ORNL-DWG 70-1081A

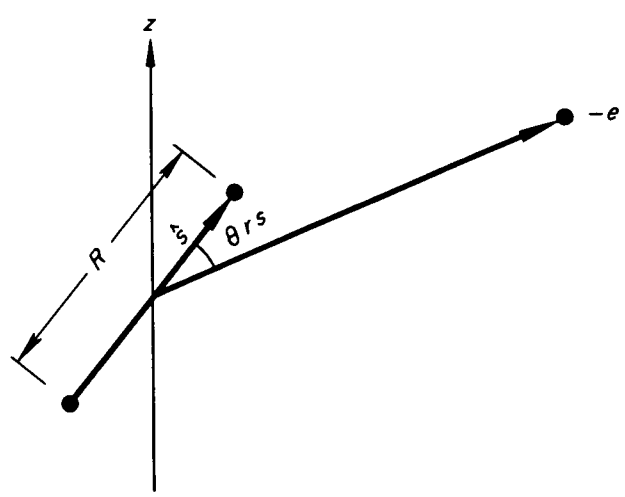

Fig. 18.23. Coordinate system for electron-molecule system.

34. W. R. Garrett, *Phys. Rev.* **A11**, 509 (1975).
35. R. W. Crompton and A. G. Robertson, *Aust. J. Phys.* **24**, 543 (1971).
36. W. Raith and J. E. Land, p. 82 in *Proc. Third Int. Conf. At. Phys.*, Boulder, Colorado, 1972, ed. by S. J. Smith and G. K. Walters, Plenum, New York, 1973.
37. R. J. W. Henry and N. F. Lane, *Phys. Rev.* **183**, 221 (1969).
38. L. Frommhold, *Phys. Rev.* **172**, 118 (1968); W. N. Sams, L. Frommhold, and D. J. Kouri, *Phys. Rev.* **A6**, 1070 (1972).
39. W. R. Garrett, *Phys. Rev.* **A11**, 1279 (1975).

polarizabilities. The forms (4) and (5) were established by Henry and Lane[37] through a variational procedure. They assigned $r_\perp = 1.22a_0$. The function $C(r)$ contains a single parameter, r_0, which has been chosen earlier[37] by finding a best fit to elastic scattering cross sections:

$$C(r) = \{1 - \exp[-(r/r_0)^6]\} \ . \tag{6}$$

The most probable channel for resonance structure in electron scattering below the first excitation threshold has been shown earlier[34] to be the $J = 2$ partial wave (J is the total angular momentum of system electron plus target molecule). For electron-hydrogen scattering we do indeed find a sharp resonance in the $J = 2$ partial wave in the energy region below the first rotational excitation threshold at $E = 0.0439$ eV for H_2 and $E = 0.0222$ eV for D_2. The exact position of the resonance depends strongly on the value of the parameter r_0 in the parameterized distortion potential. However, the resonance occurs for values ranging from $r_0 \sim 1.55$ to $r_0 \sim 1.8a_0$, which is consistent with the distortion potential found necessary to obtain agreement with scattering at higher energy.[37] Thus the long-standing question of whether a Feshbach resonance can occur in low-energy electron-hydrogen scattering is answered in the affirmative.

Results for the particular choice $r_0 = 1.75a_0$ are shown in Fig. 18.24. A width $\Gamma \sim 3 \times 10^{-7}$ Ry is found for the resonance. Eigenvalues of the projected Hamiltonian QHQ were obtained in separate calculations,[34] and the energy shift Δ was determined directly. Eigenvalues of QHQ are listed in Table 18.4. We obtain a value $\Delta = 0.35 \times 10^{-3}$ Ry for the energy shift. Additional calculations for $J = 0$ and $J = 1$ partial waves indicate that the electron-hydrogen interaction potential is not sufficiently attractive to sustain a resonance in either of these partial waves.

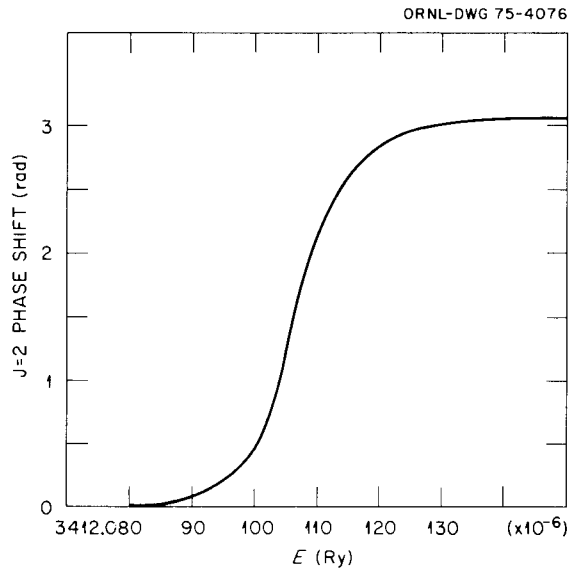

Fig. 18.24. The $J = 2$ partial-wave phase shift as a function of energy. The energy scale is marked in units of 10^{-6} Ry.

Table 18.4. Eigenvalues of QHQ for $J = 2$ states of H_2^-

R_c	E (Ry)
1.65	0.002603
1.60	0.002065
1.55	0.001125

19. Atomic Physics and Laser Research

G. S. Hurst
M. G. Payne

C. H. Chen[1] C. E. Klots W. H. Shinpaugh
W. R. Garrett M. H. Nayfeh[1] E. B. Wagner
J. P. Judish J. E. Parks[2] J. P. Young[3]

RESONANCE IONIZATION SPECTROSCOPY

Introduction

Most of the past information on the kinetics of excited states and, in general, the energy pathways following excitation of noble gases has come from time-resolved photon-emission experiments. Thus, one attempts to deduce from time-resolved emission studies the number of various kinds of atomic excited states, their lifetimes, their conversion to excimers, and the lifetimes of excimer states. We have emphasized this technique and have shown how it can be used to obtain models which could then explain more macroscopic phenomena such as Jesse effects.

Last year, we reported on a new method which we called resonance ionization spectroscopy (RIS). In this method, excited states are converted to ionization in a two-step process, one of which is resonance photon absorption; thus, the ionization signals show a resonance structure. We also showed that, in theory, pulsed dye lasers can be used in many cases to saturate the ionization. This year, we have experimental proof of RIS under saturated conditions for the singlet metastable state of helium, He(2^1S), and we discuss this accomplishment in considerable detail in this section.

For energy pathways research, RIS offers several advantages: (1) by saturating the ionization, the absolute number of excited states can be determined from sensitive ionization measurements; (2) each excited state of a given gas can be separately studied with the technique, irrespective of whether it is a resonance state or a metastable state; and (3) in cases where time-resolved emission studies give ambiguities because of the overlap of resonance lines and molecular continua (as in the case of the 1067-Å radiation of Ar), the RIS technique enables one to resolve the ambiguity, since either the atomic state or the molecular state can be photoionized.

Another very significant application of RIS was started this year and is reflected heavily in our annual report. There are many cases (e.g., the elemental metal vapors) where lasers can be used to excite from the ground state. Thus, with a laser for initial excitation followed with the RIS technique, one atom in the ground state can be converted to one ion pair, and this process can be saturated. Detection of ionization would then lead to analytical systems of unprecedented sensitivity. We expect, therefore, to be increasingly involved in new analytical methods that take advantage of resonance ionization spectroscopy.

Accelerator Modification for Resonance Ionization Spectroscopy

For the past several years, the ORNL 3-MV Van de Graaff accelerator has been an important tool for the investigation of energy pathways in noble gases. Its purpose has been the injection of proton pulses into a reaction cell containing the gas being studied. The collisions occurring when protons traverse the gas cell

[1] Postdoctoral research appointment through the University of Kentucky and supported by Los Alamos Scientific Laboratory.
[2] Consultant.
[3] Part time, Analytical Chemistry Division.

lead to the conversion of a fraction of the gaseous atoms to ion pairs and excited states. Energy pathways studies concern themselves chiefly with the observation of the evolution and decay of the various excited states as the ground-state atoms, excited atoms, ions, and deexcitation photons interact.

In these investigations the Van de Graaff accelerator is normally run at 2 MV, since this is a comfortably safe voltage for the machine and 2-MeV protons have sufficient energy to completely traverse the gas cell at the pressures employed. The protons originate as a 500-μA dc beam extracted from a duoplasmatron ion source mounted in the terminal of the accelerator. Proton beam pulses are generated by utilizing two pairs of deflector plates mounted in the terminal. The first set is driven by a 2-MHz sine-wave voltage and sweeps the dc beam across an aperture. The second set is mounted below and at right angles to the first and applies a properly phased unblanking voltage pulse. The repetition rate of the unblanking pulse is selected by adjusting a switch at the Van de Graaff's central console. Beam bursts can be repeated at a choice of intervals 1, 2, 4, 8, 16, 32, 64, 128, 256, or 512 μsec for injection into the accelerator tube. The beam burst duration can be changed from about 10 nsec to 20 nsec by controlling the sweep voltage amplitude.

For use of the accelerator in conjunction with laser experiments a new feature has been added. It allows the injection of a single proton burst into a reaction cell and also provides a trigger signal to fire a single burst of photons from a dye laser into the cell. The time interval between the creation of the excited states by the proton burst and the arrival of the photon burst from the laser can be selected by the experimenter.

Figure 19.1 depicts the apparatus. The pulsed Van de Graaff is shown at the right of the figure. A continuous

ORNL-DWG 75-6407

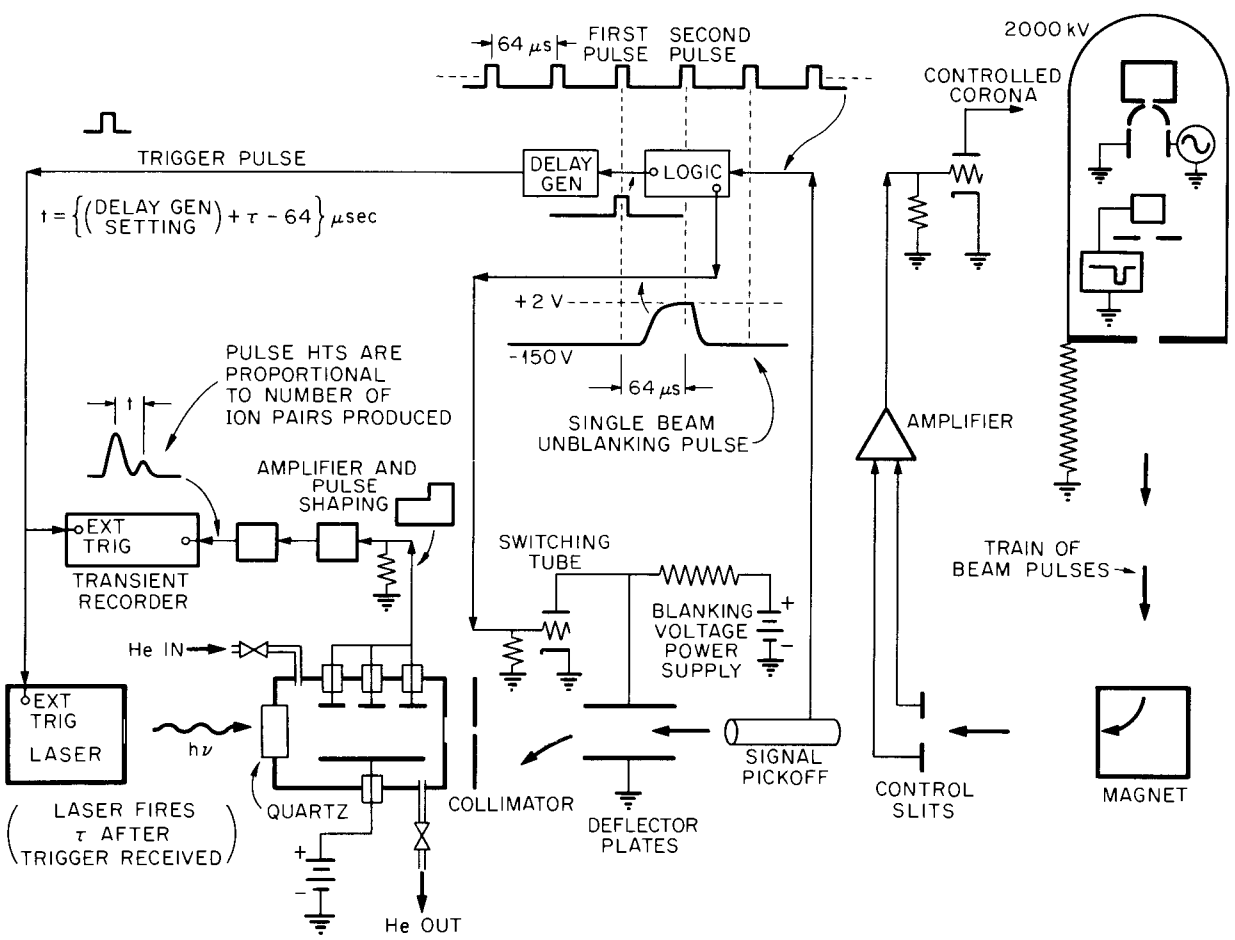

Fig. 19.1. Schematic diagram of the apparatus.

stream of proton bursts leaves the accelerator, is bent 90° by an analyzer magnet, and passes between the control slits. The setting of the magnet's field determines the energy of the analyzed proton beam. Error signals from the slits are used to lock the accelerator voltage at the value determined by the analyzer magnet setting.

With laser experiments the time between proton bursts is set at 64 μsec. This continuous stream of bursts traverses a signal pick-off which generates a continuous stream of electrical pulses and sends them to a logic circuit which normally ignores the pulses. The stream of proton bursts enters a set of deflector plates which normally deflects all the bursts from the reaction cell.

Only two proton bursts are of interest. These are the first two which arrive at the signal pick-off after a manual switch is depressed. The first of these proton bursts produces the one electrical pulse to which the logic circuit responds. This pulse is transmitted to a delay generator and also initiates the generation of an unblanking pulse which is timed to allow only the second proton burst to traverse the deflector plates and reach the reaction cell.

The pulse from the adjustable delay generator fires the laser, allowing a photon pulse to enter the reaction cell at any selected time with respect to the arrival of the proton burst. The pulse from the delay generator also triggers the sweep of a transient recorder that records the amplified electrical signals from the reaction cell.

Laser Facilities for Resonance Ionization Spectroscopy

The light source used in RIS experiments is a pulsed coaxial flash-lamp-pumped dye laser (manufactured by Phase R). The laser output can be tuned from 3500 to 11,000 Å by using various dye solutions. This region can be extended into the ultraviolet (uv) region by optical mixing in nonlinear materials. The energy output per pulse, which can reach 1 J, varies with the wavelength region according to the availability of high-gain dyes. It also varies with the cavity configuration. The maximum energy and spectral content of ~40 Å FWHM at a dye's central wavelength are produced by a flat-flat cavity configuration. As dispersive elements are introduced into the laser cavity, the spectral content is reduced and the output energy is somewhat reduced.

The dye cell is 12.5 in. long and ½ in. in diameter and is enclosed by a xenon flash lamp having slightly more than a ½-in. diameter. The flash lamp is fired by a standard spark-gap arrangement. At 20 kV, 100 J of electrical energy is stored in the capacitor. Of this, on the order of 1% is converted to the laser beam. Because the flash lamp has very low inductance, the pulse has a 100×10^{-9} sec rise time and a 300×10^{-9} sec width. The dye concentration is chosen such that a uniform circular beam of 14-mm diameter is delivered by the laser.

Figure 19.2 shows a labeled scheme of the different cavity configurations. Configuration *a* has a 600-line/mm grating (*G*) as a angle-dependent dispersive wavelength selector at one end of the cavity and a broadband plane reflector (*O*) of 70% reflectivity at the other end of the cavity. Along with the grating, a broadband plane reflector (*M*) of 60% reflectivity is inserted in the cavity. This mirror-grating combination makes the spectral selectivity interference-dependent and thus eliminates certain satellite lines. Satellite lines due to some modes that oscillate slightly askew to the beam axis have a different spectral content and in some cases mask the tuning line. At 20 kV, the measured output (at 5015 Å) of this configuration is 250 mJ with 14 Å FWHM. This energy, while not enough for performing RIS experiments under saturation conditions, is enough to damage grating coatings.

Configuration *b* is more attractive, since one can go to higher energies without damaging the components. A

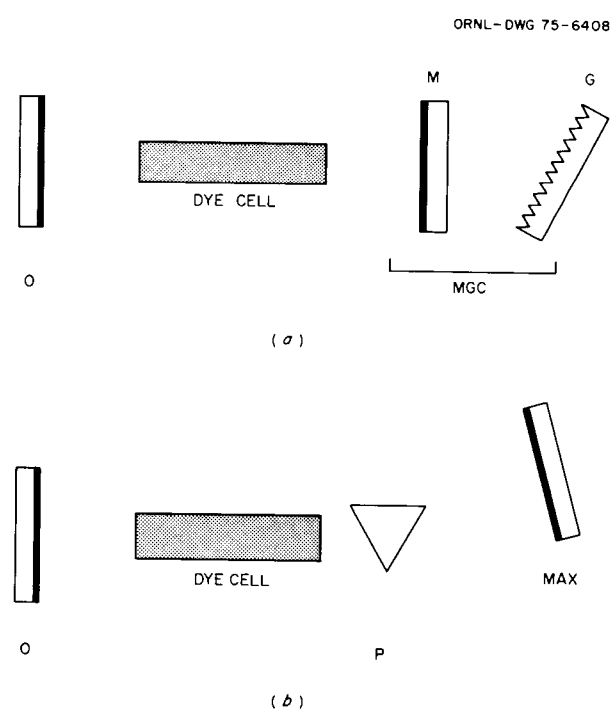

Fig. 19.2. Laser configurations. (*a*) Configuration using a grating and a mirror-grating combination as tuning elements. (*b*) Configuration using a prism as a tuning element.

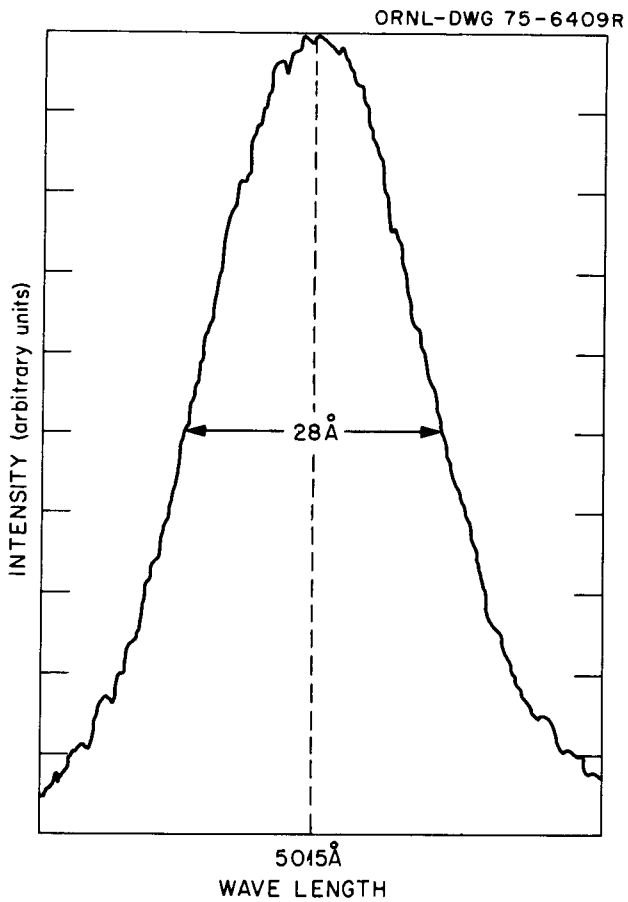

Fig. 19.3. The wavelength spectrum of the dye laser at 5015 Å recorded by an optical multichannel analyzer. The FWHM is 28 Å.

prism (*P*) (60°) is used as a wavelength-selective element. A maximum broadband reflector (*Max*) is used at one end of the cavity, and a broadband mirror of 70% reflectivity is used at the output end of the cavity. At 20 kV the measured output (at 5015 Å) of this configuration is 690 mJ with 28 Å FWHM.

The spectrum for a typical shot with coumarin 314 dye was measured with an optical multichannel analyzer and is shown in Fig. 19.3.

Reaction Cell and Ionization Measurements

The reaction cell is shown schematically in Fig. 19.4. The cell is a metal chamber through which the gas being studied can flow at a selected pressure. The chamber is electrically insulated and is isolated from the proton beam vacuum lines on the left by a 0.1-mil Havar foil. On the right, a quartz window coated with a thin, transparent conductor seals the chamber. Rectangular plates *A*, *B*, and *C* mounted parallel to rectangular plate *D* complete the essential characteristics of the cell. Each of the rectangular metal plates is electrically insulated. A wire from each plate is brought outside the vacuum system enclosing the reaction cell, allowing a choice of external electrical connections.

The Havar foil is highly transparent to the proton beam bursts, which enter on axis from the left. The coated quartz is highly transparent to laser-produced photon bursts, which enter the cell on axis from the right.

Figure 19.4 shows the electrical connections employed when measuring the *W* value of a gas. These

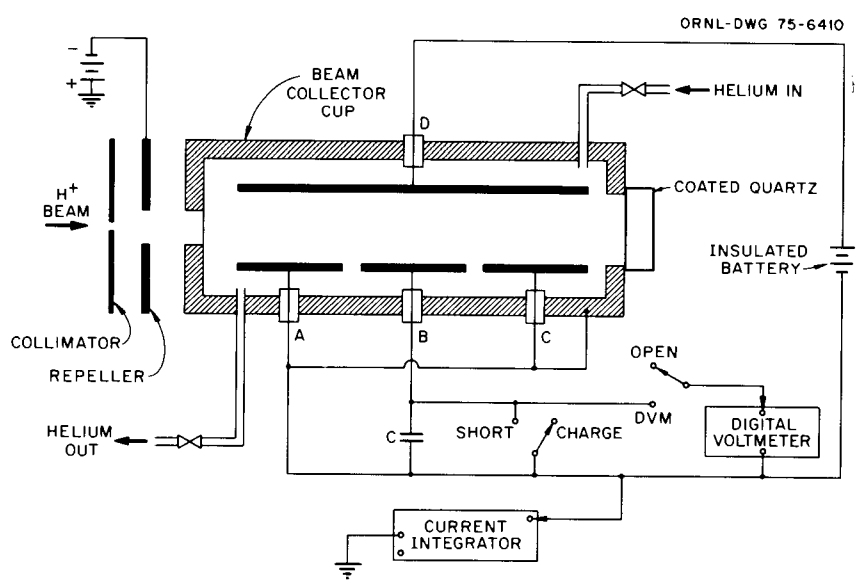

Fig. 19.4. Schematic diagram of the reaction cell for studying resonance ionization spectroscopy.

measurements are made with the proton beam alone. Versatility is achieved in allowing connections for the measurement of W, since this quantity characterizes the purity of a gas. To measure W, the number of protons traversing the cell is counted by a current integrator, while the energy loss per proton in the region above plate B is calculated by the known stopping power of the gas. The number of ion pairs created above plate B is deduced from the voltage measured and hence the charge collected on the known value of capacitor C′.

When measuring the lifetime of metastable states, both proton bursts and photon bursts are used. A positive voltage is applied to plate D. Plates A, B, and C may be connected singly or in parallel to the input of an amplifier whose output is in turn connected to the transient recorder. Both broadband and pulse-shaping amplifiers have been used. When using a broadband amplifier a small signal resistor, R, is used such that RC (C is the chamber input capacitance) is less than t_e, the electron collection time. When the pulse-shaping amplifier is used, R is large, so that RC is much greater than t_e. In both cases the output of the amplifier is proportional to the number of ion pairs created in the chamber. Pulse shaping is preferred in those cases where the expected transients generated when the laser is fired are large compared with the desired electrical signal from plates A, B, and C. On the other hand, time resolution is best when the broadband amplifier is used, for in this case the electron currents are recorded on the transient recorder.

In operation, the proton beam burst produces charged particles and excited states in the gas. The charged particles alone produced an electrical signal at A, B, and C proportional to the number of ion pairs created. At a preselected time later, a photon burst, with the photons tuned to the right wavelength, ionizes the atoms in the metastable state being studied. A second signal is produced at A, B, and C by these charged particles. It is separated in time from the proton-produced signal and is proportional to the number of atoms in the particular metastable state at the time the photons enter the reaction cell.

Theory Related to Resonance Ionization Spectroscopy

During the past year, we have investigated in considerable detail the validity of rate equations for the description of the interaction of a laser pulse with an extremely dilute population of atoms having an absorption line that overlaps in wavelength with the laser line shape. Particular attention has been given to the situation where the absorption of two photons by a single atom results in the ionization of the species in question. We have found that the more basic density-matrix formulation[4–6] of the problem can be simplified to rate equations for atomic populations if

1. the electromagnetic field amplitude changes very little within the time that either off-diagonal elements of the density matrix decay or saturation of the transition occurs;
2. the density of atoms in the state that resonates with the laser pulse is so small that attenuation or amplification of the laser pulse is negligible;
3. the laser line width is very broad compared with that of the absorption line (including pressure and power-broadening contributions to line width);
4. the off-diagonal elements of the density matrix decay in a time that is small compared with the time over which diagonal elements change appreciably. The latter situation can occur either because of the pressure-broadening effects, which rapidly destroy memory of how a state was excited, or because of the short coherence times of the laser pulse itself.

Even when conditions 1 and 4 are not satisfied, rate equations can be used to predict the yield of ion pairs, provided the laser beam is sufficiently powerful to saturate the transition in a time that is short compared with the pulse length and provided conditions 2 and 3 are satisfied.

In RIS, one is likely to use very powerful dye lasers having line widths of the order of a few angstroms and pulse lengths of the order of 10^{-7} sec. If the energy per pulse is of the order of 1 J, the above considerations lead us to believe that a rate-equation approach is appropriate for the description of RIS in almost any situation where the density of the species in question is sufficiently low. We will now use a rate-equation approach to describe the interaction of a laser pulse peaked at $\lambda \approx 5015$ Å with a small population of He(2^1S) atoms. We will generalize on the equations written and solved in last year's report by including the effect of collision processes which are important when the He(2^1S) population is accompanied by a much larger number (say a pressure of several torr) of ground-state He atoms. Under such high-pressure conditions, the He(3^1P) population not only is photoionized

4. W. E. Lamb, Jr., in *Lectures in Theoretical Physics*, vol. 2, ed. by W. E. Britten and B. W. Downs, Interscience, New York, pp. 435–88.
5. F. Bloch, *Phys. Rev.* **70**, 460 (1946).
6. J. P. Wittke and P. J. Worter, *J. Appl. Phys.* **35**, 1668 (1964).

by further photons but is also rapidly converted to He(3^1S) and He(3^1D) by two-body collisions with ground-state He atoms. Further, the He(3^1P) and He(3^1D) states undergo the process He(3^1P or 3^1D) + He (1^1S) → He_2^+ + e with a very large rate[7] at room temperature. As an aid to the formulation of the rate equations, the reader is referred to Fig. 19.5, which summarizes the appropriate energy pathways.

We define:

$g(t)$ = photon flux density,

$F(\nu)\,d\nu$ = fraction of the laser photons with frequency ν to $\nu + d\nu$,

g_u/g_l = ratio of degeneracies of the upper and lower levels (3^1P and 2^1S),

λ_0 = wavelength at the line center,

$\beta(2^1S)$ = decay rate of the 2^1S population without the laser pulse,

$C(2^1S)$, $C(2^1P)$, $C(3^1P)$, $C(3^1D)$, and $C(3^1S)$ = population of the corresponding states,

$\alpha(3^1P)$, $\alpha(3^1D)$ = rates for associative ionization out of the states in question,

7. H. F. Wellenstein and W. W. Robertson, *J. Chem. Phys.* **56**, 1077 (1972).

ORNL-DWG 75-6411

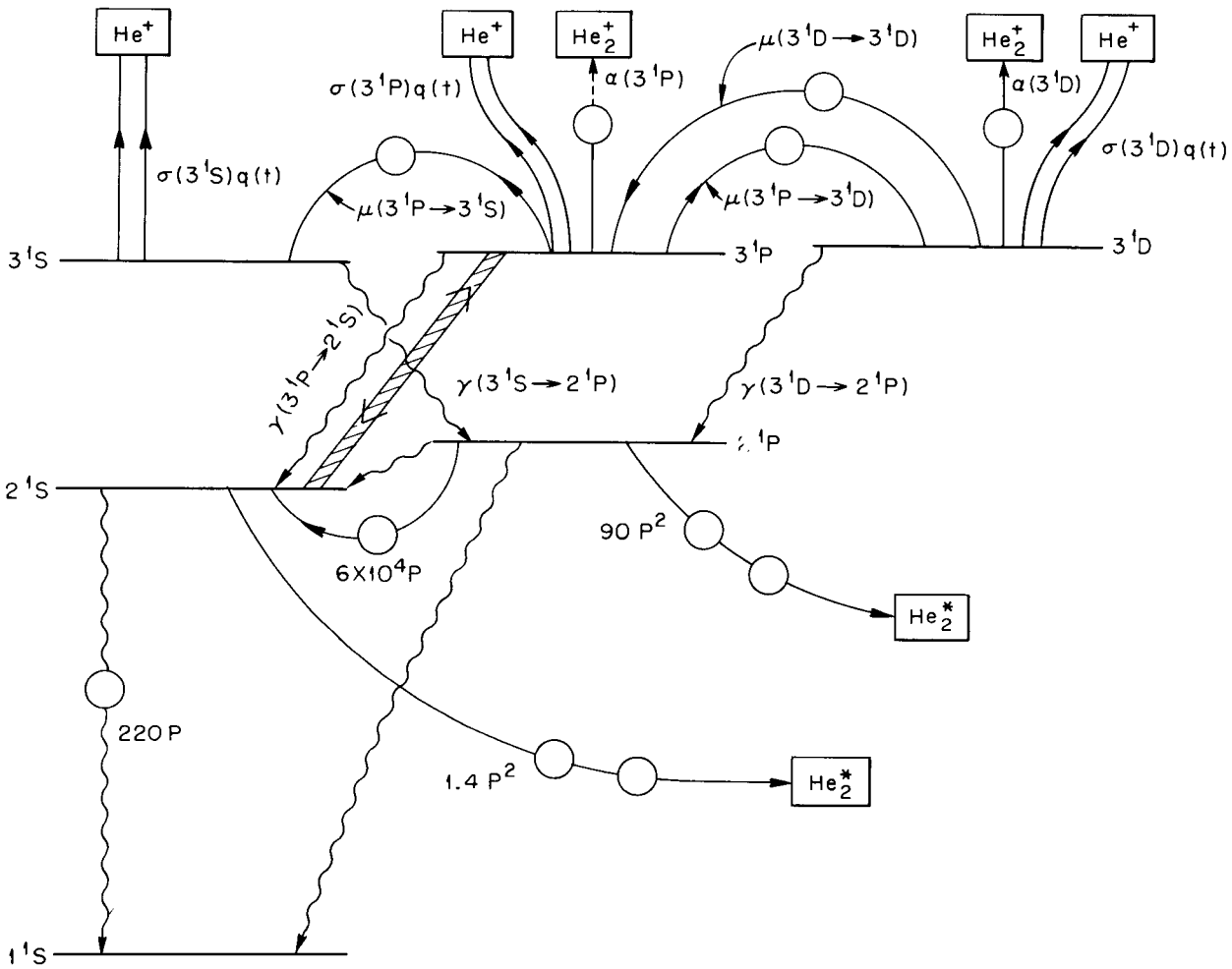

Fig. 19.5. Energy pathways diagram for RIS of the He(2^1S) state. The lines —O— represent collisional processes involving a collision with one ground-state atom, the lines —O—O— represent collisions with two ground-state atoms, the wavy lines represent spontaneous emission, ~~O~~ represents emission stimulated by a collision with a ground-state atom, and laser-induced processes are represented by double lines. In all cases, arrows represent the direction of the reaction. Only dominant mechanisms have been included.

$\mu(3^1P \to 3^1D)$, $\mu(3^1D \to 3^1P)$, $\mu(3^1P \to 3^1S)$ = rates for two-body conversion of the first population to the second,

$\gamma(3^1P \to 2^1S)$, $\gamma(3^1S \to 2^1P)$, $\gamma(3^1D \to 2^1P)$ = spontaneous decay rates,

$\lambda(2^1P \to 2^1S)$ = rate of collisional conversion of 2^1P to 2^1S,

$\beta(2^1P)$ = total rate of destruction of He(2^1P),

$\beta_0(3^1P)$ = rate of escape of resonance $3^1P \to 1^1S$ radiation to the walls,

$\sigma(3^1P)$, $\sigma(3^1S)$, $\sigma(3^1D)$ = photoionization cross sections for states in question at 5015 Å.

The rate equations for the five coupled states are:

$$\frac{dC(2^1S)}{dt} = \frac{-\lambda_0{}^2}{8\pi}\gamma(3^1P \to 2^1S)\,F(\nu_0)\,g(t)\,[3C(2^1S) - C(3^1P)] + \gamma(3^1P \to 2^1S)\,C(3^1P) - \beta(2^1S)\,C(2^1S) + \lambda(2^1P \to 2^1S)\,C(2^1P)\,, \quad (1a)$$

$$\frac{dC(3^1P)}{dt} = \frac{\lambda_0{}^2}{8\pi}\gamma(3^1P \to 2^1S)\,F(\nu_0)\,g(t)\,[3C(2^1S) - C(3^1P)] - [\sigma(3^1P)\,g(t) + \gamma(3^1P \to 2^1S) + \beta_0(3^1P) + \alpha(3^1P) + \mu(3^1P \to 3^1D) + \mu(3^1P \to 3^1S)]\,C(3^1P) + \mu(3^1D \to 3^1P)\,C(3^1D)\,, \quad (1b)$$

$$\frac{dC(3^1D)}{dt} = -[\sigma(3^1D)\,g(t) + \alpha(3^1D) + \gamma(3^1D \to 2^1S) + \mu(3^1D \to 3^1P)]\,C(3^1D) + \mu(3^1P \to 3^1D)\,C(3^1P)\,, \quad (1c)$$

$$\frac{dC(3^1S)}{dt} = -[\sigma(3^1S)\,g(t) + \gamma(3^1S \to 2^1P)]\,C(3^1S) + \mu(3^1P \to 3^1S)\,C(3^1P)\,, \quad (1d)$$

$$\frac{dC(2^1P)}{dt} = -\beta(2^1P)\,C(2^1P) + \gamma(3^1D \to 2^1P)\,C(3^1D) + \gamma(3^1S \to 2^1P)\,C(3^1S). \quad (1e)$$

Initially, all the C's are zero except $C(2^1S)$.

We can derive a lower bound on the total number of ion pairs produced by neglecting completely $\lambda(2^1P \to 2^1S)$, so that any population which was originally in 2^1S but ends up in 2^1P is lost. In actuality, about 70 to 85% of the 2^1P population eventually becomes 2^1S due to radiative transitions and collisional effects and thereby may be promoted once again to 3^1P, from which ionization can again occur. Once $\lambda(2^1P \to 2^1S)$ is set equal to zero, Eqs. (1*a*), (1*b*), and (1*c*) are uncoupled from (1*d*) and (1*e*) and can be solved separately. Further simplifications occur if for most of the laser pulse we have

$$\frac{\lambda_0{}^2}{8\pi}\,\gamma\,(3^1P \to 2^1S)\,F(\nu_0)\,g(t) \gg \text{any collisional or radiative rates.} \quad (2)$$

In the latter situation, one quickly reaches the point where $C(3^1P) \approx (g_u/g_\ell)\,C(2^1S)$. Thus, one can eliminate $C(2^1S)$ and obtain the following coupled equations for $C(3^1P)$ and $C(3^1D)$:

$$[1 + g_\ell/g_u]\,\frac{dC(3^1P)}{dt} = -[\sigma(3^1P)\,g(t) + (g_\ell/g_u)\,\beta(2^1S) + \beta_0(3^1P) + \alpha(3^1P) + \mu(3^1P \to 3^1D) + \mu(3^1P \to 3^1S)]\,C(3^1P) + \mu(3^1D \to 3^1P)\,C(3^1D)\,, \quad (3a)$$

$$\frac{dC(3^1D)}{dt} = -[\sigma(3^1D)\,g(t) + \alpha(3^1D) + \gamma(3^1D \to 2^1S) + \mu(3^1D \to 3^1P)]\,C(3^1D) + \mu(3^1P \to 3^1D)\,C(3^1P)\,. \quad (3b)$$

Once the above equations are solved, one can calculate the yield of ion pairs from the two states. Further, with $C(3^1P)$ known, $C(3^1S)$ can be determined from (1*d*), and the yield of ion pairs from that state can be calculated. With a laser beam having a 1-cm^2 beam diameter, 35 Å FWHM, 0.7 J per pulse, and pulses lasting 3×10^{-7} sec, this should be a good approximation below 10 torr He pressure, provided the energy density is spread reasonably uniformly over the beam cross-sectional area.

At much higher pressures, $\mu(3^1P \to 3^1D)$ and $\alpha(3^1D)$ as well as some other collisional rates become very large compared with the reciprocal length of the laser pulse and compared with $\sigma(3^1P)\,g(t)$, $\sigma(3^1D)\,g(t)$, and $\sigma(3^1S)\,g(t)$. In the latter case, one obtains a good approximation for the number of ion pairs produced by assuming that photoionization can be neglected compared with associative ionization and that $g(t) \approx g_0$ for $t \leqslant \tau$ and $g(t) \approx$

O for $t > \tau$. In the latter case, (1a), (1b), and (1c) have constant coefficients and are easily solved. Once they are solved, the solutions can be used to solve (1d) and (1e), and the resulting $C(2^1P)$ can be used in (1a) in order to obtain better solutions to (1a), (1b), and (1c). After obtaining accurate populations for $C(3^1D)$ and $C(3^1P)$, the total amount of associative ionization can be obtained and compared with the original population of 2^1S. With the laser pulse described previously, one finds that 90 to 95% of the initial He(2^1S) population is converted to ion pairs for 15 torr $\leqslant P \leqslant$ 100 torr.

Application of Resonance Ionization Spectroscopy to the Study of He(2^1S)

The facilities described in previous sections have been used to study the time dependence of the He(2^1S) population following the excitation of He by fast charged particles. The laser described earlier was used to generate 0.69-J pulses lasting 0.3 μsec and having a wavelength centered at 5015 Å. The line width was ~30 Å. The laser pulses were fired into a gas cell filled with He (99.9995% pure) at various times following excitation by pulses of 10^3 to 10^4 protons. Signals generated by the direct ionization of the protons and by the resonant ionization of He(2^1S) by the laser pulses were recorded by a transient recorder. From the ratio of pulse heights, the number of ion pairs due to the laser divided by the number of ion pairs produced by the protons was determined. A typical recording of the signals is shown in Fig. 19.6. It was demonstrated that (1) the laser pulse could be attenuated by a factor of $\sqrt{10}$ without appreciably reducing the ratio and (2) the laser beam could be spread by a lens (so that its radius in the interaction region was increased by a factor of ~2) without appreciably changing the ratio. Thus, as suggested by theory, it appeared that the ionization was saturated and the spatial overlap was complete, so that the measured ratio represented the ratio of the He(2^1S) population to the number of ion pairs produced during and just after the passage of the protons. Figures 19.7–19.10 show decay curves measured in the experiment at helium pressures of 15.3, 30, 60, and 100 torr respectively.

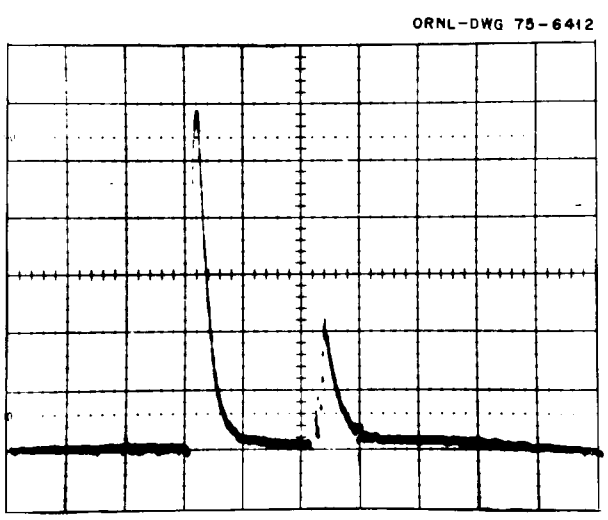

Fig. 19.6. Resonance ionization of He(2^1S) at 14.9 torr. Direct ionization by the pulsed proton beam accounts for the large pulse at the left. After 9 μsec the laser fired a sufficient number of 5015-Å photons to convert all of the He(2^1S) to ion pairs.

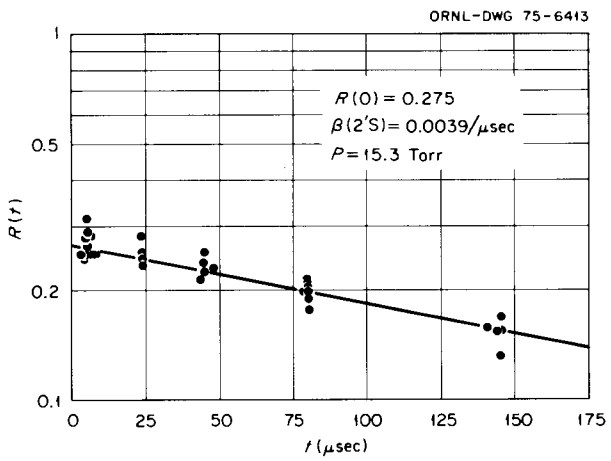

Fig. 19.7. The ratio $R(t)$ of the number of He(2^1S) states to the number of direct ion pairs surviving at a time t. The intercept gives the initial number R_0 of excited states, and the slope gives their decay rates, β. Data at 15.3 torr.

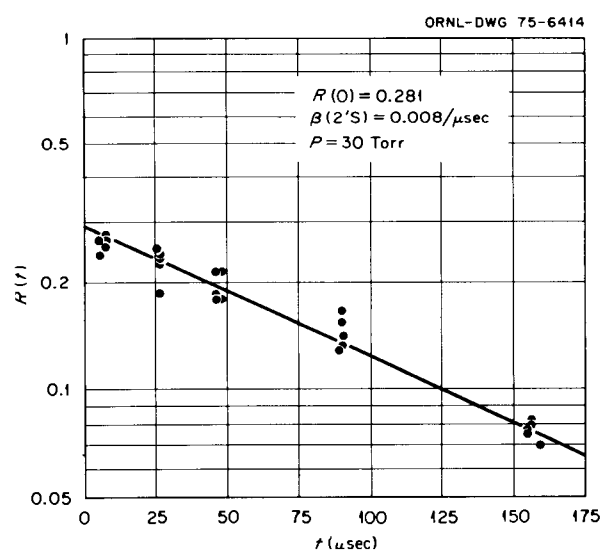

Fig. 19.8. The ratio $R(t)$ of the number of He(2^1S) states to the number of direct ion pairs surviving at a time t. The intercept gives the initial number R_0 of excited states, and the slope gives their decay rates, β. Data at 30 torr.

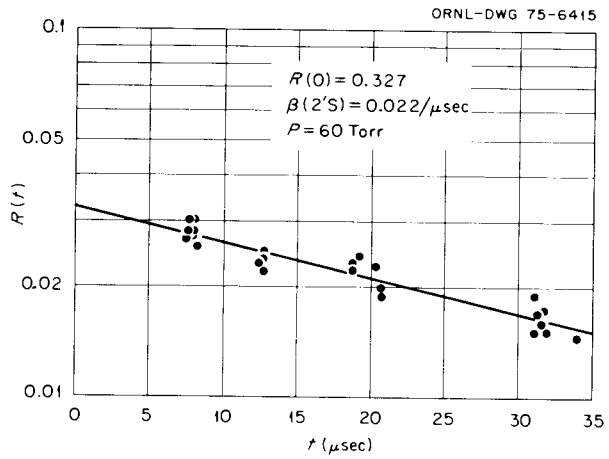

Fig. 19.9. The ratio $R(t)$ of the number of He(2^1S) states to the number of direct ion pairs surviving at a time t. The intercept gives the initial number R_0 of excited states, and the slope gives their decay rates, β. Data at 60 torr.

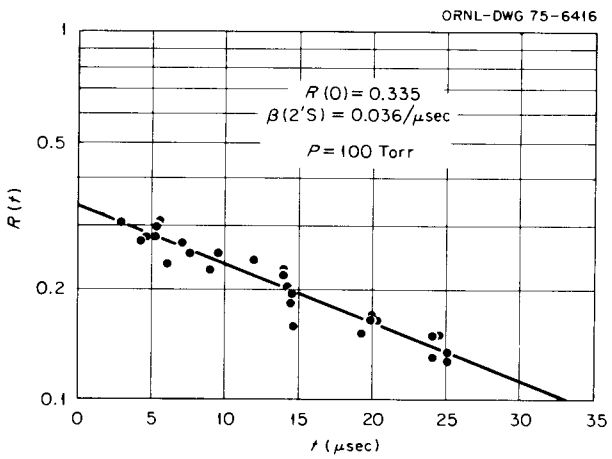

Fig. 19.10. The ratio $R(t)$ of the number of He(2^1S) states to the number of direct ion pairs surviving at a time t. The intercept gives the initial number R_0 of excited states, and the slope gives their decay rates, β. Data at 100 torr.

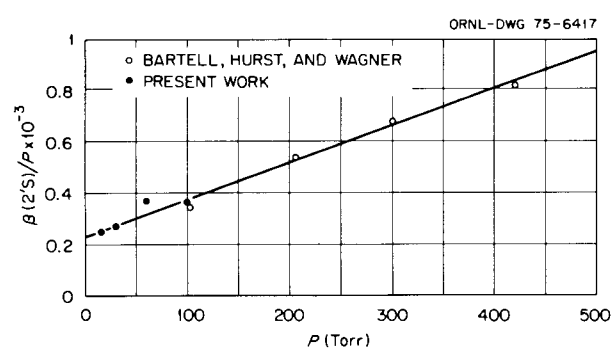

Fig. 19.11. $\beta(2^1S)/P$ vs P for decay of He(2^1S) states as determined through RIS (present work) and from time-resolved vuv emission (Bartell).

The decay rates of He(2^1S) measured by the present technique are in excellent agreement with the measurements of Bartell et al.[8] of the collision-induced emission of He(2^1S) at 601 Å. In both cases the late time decay is exponential with decay constant β,

$$\beta(2^1S) = 230P + 1.4\,P^2 \ ,$$

where $\beta(2^1S)$ has units of $\sec^{-1}$ and P is He pressure in torr. Figure 19.11 shows a graph of $\beta(2^1S)/P$ vs P with both the present data and several points from the work of Bartell.

As mentioned earlier, the intercepts of the decay curves are in agreement with theory for the population of He(2^1S), providing one assumes that (in accord with the He energy pathways model discussed earlier) most of the initial He(2^1P) population is also converted to He(2^1S).

In addition to the experiments at 15 torr $\leqslant P \leqslant$ 100 torr, we have also carried out measurements at 0.6 torr and 1.0 torr. At the latter pressures, little associative ionization occurs, yet the intercept of the decay curves is 0.2, indicating that photoionization out of the intermediate states is nearly saturated, as is expected from theory.

Further studies of excited species in inert gases following excitation by a pulse of fast charged particles are planned. In particular, we hope to obtain important information about the He(2^3S) and $He_2(a^3\Sigma_u^+)$ population as a function of time and then to look at other noble gases. These investigations will be of considerable importance for Ar, where considerable ambiguity exists in the interpretation of time-resolved emission studies.

ENERGY PATHWAYS AND JESSE EFFECTS IN HELIUM

In our FY 1974 annual report, we presented a detailed kinetic scheme for the processes which determine the time dependence of vacuum ultraviolet (vuv) emissions from helium following excitation by fast charged particles (see Fig. 19.12 for details). One of the most novel mechanisms in the model was the suggestion that the very large linear-in-pressure term in the rate constant for the decay of the 584-Å resonance line[8] represented the process He(2^1P) + He(1^1S) → He(2^1S) + He(1^1S). The latter suggestion was motivated partly by an extrapolation from information about transport of photons from resonance lines of other noble gases.

8. D. M. Bartell, G. S. Hurst, and E. B. Wagner, *Phys. Rev. A* 7, 1068 (1973).

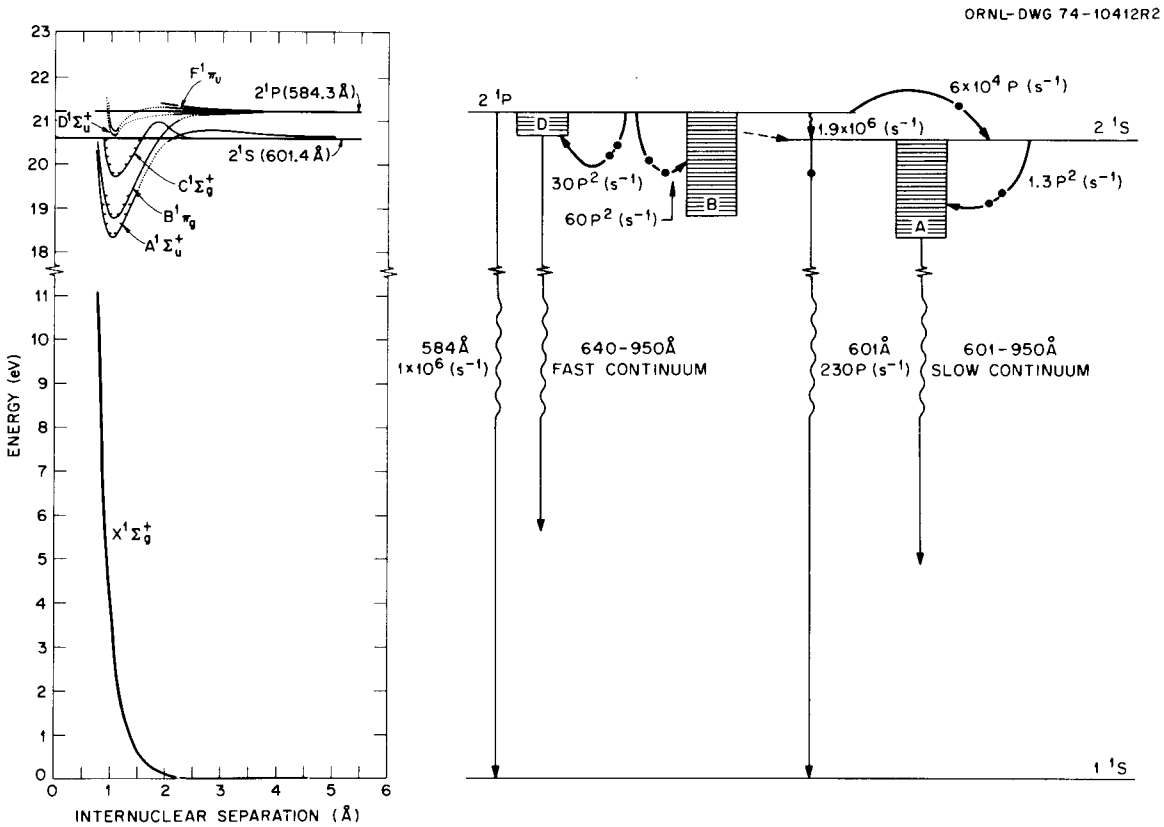

Fig. 19.12. The adiabatic potential energy curves for He_2 shown alongside a model for the kinetic processes which lead to the observed decay of the electromagnetic radiation emitted with 584 Å $\leqslant \lambda \leqslant$ 950 Å following pulsed excitation.

The information implies that such a large pressure dependence due to a breakdown of the Holstein transport theory was extremely unlikely. The other chief motivations concerned the facts that (1) due to energy considerations, the He(2^1S) state is the only one likely to result from a two-body collision with a ground-state atom and (2) our theoretical calculation of the rate yielded a value nearly equal to the one observed experimentally. We have now used our resonance ionization spectroscopy (RIS) technique[9] in order to provide further evidence concerning the existence of the mechanism.

In the RIS experiment, helium gas at various pressures was excited by a single pulse of 10^3 to 10^4 protons ($E \approx 2$ MeV) delivered in a time period of 1.5×10^{-8} sec. The protons produced 10^6 to 10^7 ion pairs and a comparable number of excited atoms. After different delay times, a pulsed laser tuned between He(2^1S) and He(3^1P) was fired and $\gtrsim 95\%$ of the He(2^1S) population remaining in the system was converted to ion pairs. The number of ion pairs arising at the time the laser was fired was measured and compared with the number produced very near the time of passage of the protons. Further experimental and theoretical details are described in a later section of the report. According to theory,[8,10] the combined population of He(2^1S) and He(2^1P) is about 34% of the number of ion pairs produced by the protons and secondary electrons, with the He(2^1P) population being about five times as large as that of He(2^1S). At pressures of a few torr, the He(2^1P) population decays at a rate $B(2^1P) \approx 3 \times 10^6$ sec^{-1}, with 2×10^6 sec^{-1} of the rate representing radiative decay to He(2^1S). Thus, at such low pressures, about two-thirds of the He(2^1P) population becomes He(2^1S), and for delay times >1 μsec, the number of ion pairs detected just after the laser pulse divided by the number detected just after the proton pulse should be about 0.23. If the large linear-in-pressure term

9. G. S. Hurst et al., *Health Phys. Div. Annu. Progr. Rep. July 31, 1974*, ORNL-4979, pp. 230–33.

10. G. D. Alkhazov, Ioffe Institute of Physics and Technology, Leningrad, Report No. FTI-108, 1969 (unpublished); Transl. Scientific Service, JTS Order No. 7926.

represented an increased rate of escape of resonant photons from the system, then the above ratio should decrease to about 0.11 at P = 100 torr. On the other hand, if the linear-in-pressure term represents a collisional conversion of He(2^1P) to He(2^1S), the ratio should increase to about 0.29 at P = 100 torr. Our experiment shows that at P = 15 torr the ratio is 0.26 and that at P = 100 torr it has reached 0.33, which is in good agreement with the interpretation of the linear-in-pressure term as a rate for converting He(2^1P) to He(2^1S).

Along the same lines, we have looked for other independent evidence related to the question of whether the large linear-in-pressure term observed in the decay of 584-Å emission might represent an increased rate of escape of radiation to the walls. Important empirical information comes from studies[11,12] of the decay of the Ar($^1P_1$), Ar($^3P_1$), and Ne($^1P_1$) populations.[13] In the first two cases, excellent agreement with the Holstein theory (with impact-broadened line shape[14]) for the rate of escape of resonance photons to the walls is obtained for $P \lesssim 50$ torr. Above 50 torr. some pressure dependence appears, and the observed decay rate is $B \approx B_H + CP^2$, where B_H is the Holstein rate. In both cases there is no observable linear-in-pressure term, and the P^2 term is believed to represent the formation of electronically excited diatomic molecules. Since the form $B \approx B_H + CP^2$ is observed to hold with excellent accuracy up to several hundred torr, it is tempting to suggest that the rate of escape of resonance photons to the container walls is pressure-independent to good accuracy up to at least 100 torr and possibly up to 200 torr. In the case of Ne($^1P_1$), theory[14] suggests that no bound molecule exists that correlates with Ne($^1P_1$) + Ne($^1S_0$) at large internuclear separation. Accordingly, experimental studies[15] show that the decay rate contains no P^2 term but that it is represented accurately by $B = B_H + C'P$. In the latter case, spin-orbit coupling leads to an avoided crossing between adiabatic potential curves corresponding to Ne($^1P_1$) + Ne($^1S_0$) and Ne($^3P_1$) + Ne($^1S_0$) at large R,[14] and theoretical estimates suggest that there should be a large rate for the collision Ne($^1P_1$) + Ne($^1S_0$) → Ne($^3P_1$) + Ne($^1S_0$). Experiments[13] show that the linear-in-pressure term is large and that the emission from Ne($^3P_1$) starts out low and builds up [over the same time scale as Ne($^1P_1$) decays] before bending over and decaying itself. The decay rate for Ne($^1P_1$) is fitted very accurately by $B = B_H + C'P$ from P = 1 torr up to pressures where the line can no longer be seen. This again suggests that the rate of escape of resonance photons to the wall is pressure-independent above a few torr and is given accurately up to rather large pressures by the Holstein theory with impact-broadened line shape.

Some insight into the reason why the Holstein theory with impact-broadened line shape may hold up to rather high pressures is gained by noting that a statistical line-shape theory[15] is valid on the far wings of the line, and if the valence forces did not come into play at small internuclear separation, the emission profile predicted by the statistical theory would be symmetrical and given by (for $^1P_1 \rightarrow {}^1S_0$ transitions)

$$P(\nu) = \frac{\gamma N \lambda_0{}^3}{24\pi^3(\nu - \nu_0)^2}, \tag{4}$$

where γ is the spontaneous decay rate for the resonance transition, N is the number density of ground-state atoms, λ_0 is the wavelength at the line center, and ν_0 is the frequency at the line center. Much nearer the line center (but still on the line wings), the impact theory of line shape is valid and is given by[14]

$$P(\nu) = 1.53\,\frac{\gamma N \lambda_0{}^3}{24\pi^3(\nu - \nu_0)^2}\,. \tag{5}$$

Thus we see that in the absence of valence forces we would have a theory that is valid on the near wings of the line and another valid on the far wings. Further, the dependence on $\nu - \nu_0$ is the same and the amplitude is sufficiently close so that if the expression which is valid on the near wings is extrapolated to the far wings, it comes rather close to joining smoothly into the correct function. Thus it would not be surprising if Eq. (5) is accurate to within 50% error all the way from the near wings to the far wing region where the statistical theory (including valence forces) begins to predict asymmetrical broadening. Whether one uses Eq. (4) or (5) in the Holstein theory is relatively unimportant, since the rate of escape to the container walls only differs by ~25% in changing from one to the other. We estimate that the transport theory will begin to sample far enough on the wings for valence forces to come into play at about 50

11. M. G. Payne, J. E. Talmage, G. S. Hurst, and E. B. Wagner, *Phys. Rev. A* **9**, 1050 (1974); J. E. Talmage, Jr., G. S. Hurst, M. G. Payne, and E. B. Wagner, *Transport of Resonance Radiation in Argon*, ORNL-TM-4368 (1973).

12. G. S. Hurst, E. B. Wagner, and M. G. Payne, *J. Chem. Phys.* **61**, 3680 (1974).

13. P. K. Leichner, to be published.

14. P. R. Berman and W. E. Lamb, *Phys. Rev.* **187**, 221 (1969).

15. Henry Margenau and William W. Watson, *Rev. Mod. Phys.* **8**, 22 (1936).

to 100 torr. Thus, at room temperature and for pressures less than 50 torr, it would be somewhat surprising if deviations from the theory were greater than 25% for the 584-Å line of He and a container of radius ~1 cm. If the linear-in-pressure term is a deviation from the Holstein transport theory, there would be a factor of 2 error at only 15 torr. We plan further investigation into this matter, since it is extremely important for the interpretation of the time dependence of escaping resonance radiation.

The Jesse effect in He[16,17] with Ar, Kr, or Xe as an impurity depends on He pressure and impurity pressure in exactly the way that would be expected if all of the effect came from the He(2^1S) population. This is consistent with our suggestion that most of the large He(2^1P) population is converted to He(2^1S). However, our recent experiment on this population indicates that, even after the conversion of the He(2^1P) to He(2^1S), the population of the latter state is only about two-thirds as big as would be required to explain the entire effect. Thus, either part of the extra ionization comes from the He(2^3S) population [as for singlet states, He(2^3P) is rapidly converted to He(2^3S)], or it must be accounted for in terms of ionization of impurities by electrons that are sub excitation in pure He. Since the pressure dependence of the latter effect is rather different from what is observed, we regard the former suggestion as being more likely to contribute a large portion of the missing extra ionization.

The pressure dependence of the effect from He(2^3S) is easily estimated from knowledge of the Penning ionization cross section and from the known decay kinetics of He(2^3S) for the pure gas. The dependence on He and impurity partial pressures is very close to what is observed for the He(2^1S) population, and this is what is required. Further, the size of the population is just about what is needed.[8,10] to explain the additional one-third of the effect. However, there is a possible difficulty with the explanation. When an He(2^3S) atom does not undergo Penning ionization, it forms a metastable molecule by the process

$$\mathrm{He}(2^3S) + 2\mathrm{He}(1^1S) \rightarrow \mathrm{He}_2(a^3\Sigma_u^+) + \mathrm{He}(1^1S)\ .$$

The $a^3\Sigma_u^+$ molecule is known to have a lifetime against radiative decay of the order of seconds (or longer). Thus, in the absence of electrons or many other excited atoms, but at rather high pressures, it is eventually quenched by encountering an impurity atom. The latter process should be the principal mode of deexcitation even in He with impurity levels less than 1 ppm. Thus, if the quenching process leads to ion pairs with unit efficiency, these ion pairs should be present and counted even in measurements of W values for pure gases. If one includes the conversion of 3^1P, 3^1D, 3^3P, and 3^3D, as well as 2^3S, 2^3P, and all other states with $n > 3$ to ion pairs (the $n \gtrsim 3$ levels are converted by the Hornbeck-Molnar process with at least 80% efficiency for He pressures greater than 50 torr), one concludes that there is a considerable discrepancy between calculated W values for the pure gas and the value that is actually measured for gases with a part per million or more of an impurity. Further, if the ionization efficiency of $\mathrm{He}_2(a^3\Sigma_u^+)$ is unity, very little of the pressure dependence of the Jesse effect will come from the triplet population. One is then left with the problem of accounting for one-third of the observed pressure dependence in terms of subexcitation electrons.

A look at the adiabatic potential curve of $\mathrm{He}_2(a^3\Sigma_u^+)$ is suggestive of an explanation for the problem. We note that with relatively small amounts of impurity and at large He pressure, the $\mathrm{He}_2(a^3\Sigma_u^+)$ is likely to be relaxed to its ground vibrational level before being quenched. Thus, if a reasonably long-range encounter resulted in energy transfer, the energy transferred from the He might be of the order of magnitude of the energy difference between the minimum of the $a^3\Sigma_u^+$ potential curve and the ground-state $X^1\Sigma_g^+$ potential curve at the same internuclear separation. This energy is about 14.5 eV, which is not sufficient to ionize Ar but might be sufficient to ionize Xe at some internuclear separations. Thus, if discrete-discrete energy transfer to a considerable number of impurities other than Ne is a possibility, one might conceivably have an ionization efficiency considerably less than unity, in which case a pressure-dependent contribution from the triplet population would occur and look very much like that from He(2^1S).

We plan to time-resolve emission from Ar as a function of Ar pressure in order to prove or disprove the existence of this mechanism (we have already shown that argon fluoresces strongly in nearly pure He excited by pulses of charged particles). In such an experiment the Ar emission should build up as He(2^3S) decays and then decay at a rate that is limited by the slow decay of $\mathrm{He}_2(a^3\Sigma_u^+)$. The latter decay rate should be proportional to Ar partial pressure.

ENERGY TRANSFER

Energy Transfer from Argon Resonance States to N_2, H_2, and NO

Previously[12] we described a time-resolved spectroscopic method for obtaining quenching rates of reso-

16. W. P. Jesse and J. Sadauskis, *Phys. Rev.* 88, 418 (1952).
17. J. E. Parks, G. S. Hurst, T. E. Stewart, and H. L. Weidner, *J. Chem. Phys.* 57, 5467 (1972).

nance excited states. These studies have proven to be of considerable interest (1) because of their scientific value in, for instance, checking theoretical calculations; (2) because they produce data for the design of energy-transfer lasers; and (3) because they suggest concepts and supply data for analysis of low-level atmospheric pollution. Consequently, we have extended[18] the measurements to some additional acceptors (quenchers). In particular, we investigated for the resonance states $Ar(^1P_1)$ and $Ar(^3P_1)$ at 1048 Å (11.82 eV) and 1067 Å (11.62 eV), respectively, the rate of energy transfer to N_2 and H_2, both examples of discrete-discrete transfer, and to NO, an example of a discrete-continuum process. In Fig. 19.13, we illustrate the time-resolved quenching data for $Ar\text{-}H_2$.

18. J. R. McNeely, G. S. Hurst, E. B. Wagner, and M. G. Payne, submitted for publication in the *Journal of Chemical Physics.*

Rate constants for energy transfer were deduced from the changes of the rate of decay of excited states corresponding to known changes of the density of the diatomic molecules. See Fig. 19.14 for a sample of the data for $Ar\text{-}H_2$. For $Ar^*\text{-}N_2$ the rate constants were 5.4×10^{-11} and 0.8×10^{-11} molecule^{-1} cm^3 sec^{-1} for $Ar(^1P_1)$ and $Ar(^3P_1)$ respectively. For $Ar^*\text{-}H_2$ the measured rate constants were 22×10^{-11} and 21×10^{-11} molecule^{-1} cm^3 sec^{-1} for $Ar(^1P_1)$ and $Ar(^3P_1)$ respectively. The results for nitric oxide were 54×10^{-11} and 32×10^{-11} molecule^{-1} cm^3 sec^{-1} for $Ar(^1P_1)$ and $Ar(^3P_1)$ respectively, compared with 59.7×10^{-11} and 32.6×10^{-11} molecule^{-1} cm^3 sec^{-1} calculated from a theory for discrete-continuum energy transfer. Table 19.1 may be consulted to see how these results compare with previous measurements. Also included in Table 19.1 are data for energy transfer from the metastable species $Ar(^3P_0)$ and $Ar(^3P_2)$. Table 19.2 provides a comparison of experiment and theory for the discrete-continuum cases.

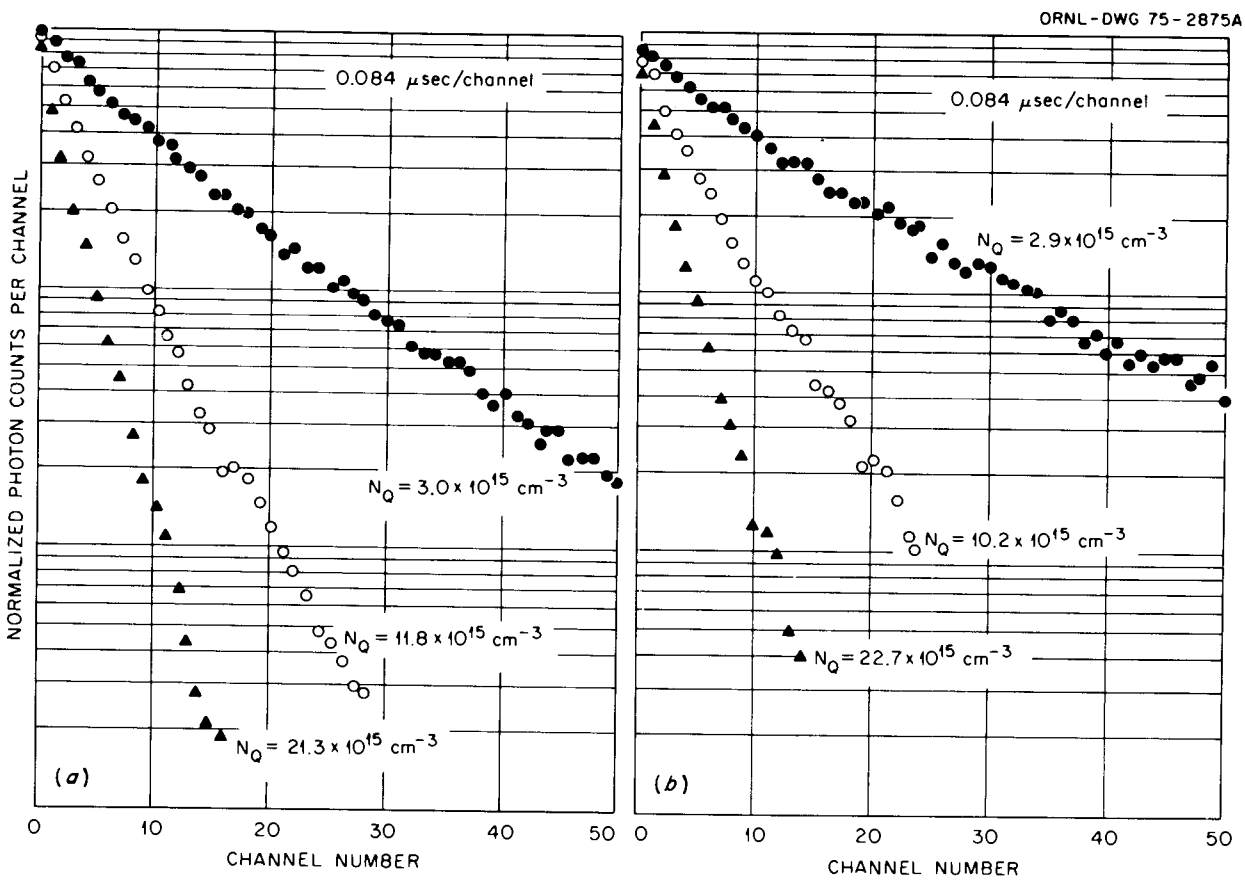

Fig. 19.13. Time distribution for resonance photons in $Ar\text{-}H_2$ mixtures at 50 torr. (*a*) 1048-Å photons, (*b*) 1067-Å photons.

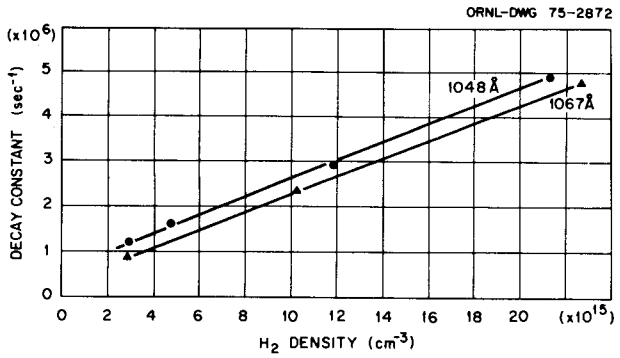

Fig. 19.14. Decay constants for 1048-Å and 1067-Å resonance radiation vs H_2 density for argon pressure equal to 50 torr.

Energy Transfer from Helium Excited States

During the past few years, electronic energy transfer from excited rare gases to foreign atoms or molecules has been the subject of many theoretical and experimental studies. Energy transfer from excited helium is amenable to theoretical calculations. A variety of experimental approaches has aroused even more interest. Measurements of Jesse effects, ionization cross sections, and Penning electron energy distributions have all been carried out. The study of excitation transfer processes for the lowest lying metastable and transition-allowed resonance states of helium will be discussed individually in the following.

The process of Penning ionization from metastable He has been discussed from two points of view by Nakamura,[19] namely, on the basis of quasi-adiabatic and adiabatic representations of electronic states. A detailed theoretical formalism of Penning ionization and associative ionization has been given by Miller[20,21] through classical, semiclassical, and quantum mechanical considerations. Bell, Dalgarno, and Kingston[22]

19. N. Nakamura, *J. Phys. Soc. Japan* **26**, 1473 (1969).
20. W. H. Miller, *J. Chem. Phys.* **52**, 3563 (1970).
21. W. H. Miller, *Chem. Phys. Lett.* **4**, 627 (1970).
22. K. L. Bell, A. Dalgarno, and A. E. Kingston, *J. Phys. B* **1**, 18 (1968).

Table 19.1. Rate constants[a] for transfer of argon excitation energy at 300°K

Quencher molecule	Rate constant when donor state is –			
	$Ar(^3P_2)$	$Ar(^3P_1)$	$Ar(^3P_0)$	$Ar(^1P_1)$
N_2	3.6×10^{-11} [b] 3×10^{-11} [d]	0.6×10^{-11} [c] 0.8×10^{-11} [e]	1.6×10^{-11} [b]	5.4×10^{-11} [e]
H_2	6.6×10^{-11} [b]		7.8×10^{-11} [b]	
NO	22×10^{-11} [b]	21×10^{-11} [e] 40×10^{-11} [c] 20×10^{-11} [f]	25×10^{-11} [b]	22×10^{-11} [e] 60×10^{-11} [f]
C_2H_4	64×10^{-11} [d]	32×10^{-11} [e] 56×10^{-11} [g]		54×10^{-11} [e] 103×10^{-11} [g]

[a]In units of $cm^3\ sec^{-1}$.
[b]L. G. Piper, J. E. Velazco, and D. W. Setser, *J. Chem. Phys.* **59**, 3323 (1973).
[c]C. J. Chapman, A. J. Masson, and R. P. Wayne, *Mol. Phys.* **23**, 979 (1972).
[d]M. Bourène and J. LeCalvé, *J. Chem. Phys.* **58**, 1452 (1973).
[e]Present work.
[f]C. E. Klots, *J. Chem. Phys.* **56**, 124 (1972).
[g]G. S. Hurst, E. B. Wagner, and M. G. Payne, *J. Chem. Phys.* **61**, 3680 (1974).

Table 19.2. Comparison of experimental and theoretical rate constants[a] for transfer of argon excitation energy in four discrete-continuum processes

Acceptor molecule	Experiment		Theory[b]	
	$Ar(^3P_1)$	$Ar(^1P_1)$	$Ar(^3P_1)$	$Ar(^1P_1)$
NO	32×10^{-11}	54×10^{-11}	33×10^{-11}	60×10^{-11}
C_2H_4	56×10^{-11} [c]	103×10^{-11} [c]	54×10^{-11}	103×10^{-11}

[a]In units of $cm^3\ sec^{-1}$.
[b]T. Watanabe and K. Katsuura, *J. Chem. Phys.* **47**, 800 (1967).
[c]G. S. Hurst, E. B. Wagner, and M. G. Payne, *J. Chem. Phys.* **61**, 3680 (1974).

assumed that the C_6/R^6 dispersion interaction at long distance is the main factor that determines the ionization cross section and calculated the reaction rate and ionization cross section of He(2^1S)-Ar through the orbiting approximation. The reaction rate and ionization cross section calculated by Bell et al.[22] are 9.95 × 10^{-10} cm^3/sec and 85.3 Å^2. Ferguson et al.[23] correelated classical momentum transfer cross sections for He(2^1S)-Ar and got results close to those obtained by Bell et al.[22] Unfortunately, the calculated results from the different groups always show an ionization cross section larger than the experimental data, some of which are not consistent.

For He(2^1S)-Ar, Benton et al.[24] obtained a cross section of 55 Å^2 from afterglow studies of pulsed helium discharges. Sholette and Muschlitz[25] used a beam technique and got 7.6 Å^2; Schmeltekopf et al.[26] and Howard et al.[27] obtained 16.4 Å^2 and 23.5 Å^2 by flowing afterglow methods and cross-beam techniques respectively. Chen et al.[28,29] measured the differential cross sections and got 22.5 Å^2 at room collision energy through a localized complex potential calculation. It was pointed out that the ionization cross section strongly depends on the interaction potential and collision energy. From the above data, it is clear that the experimental discrepancies are quite significant.

Phelps[30] did absorption studies of the decay of metastable He and obtained the decay rate $\beta = 150P$ with β in sec^{-1} and P in torr. Phelps attributed the rate to the collision-induced emission process suggested by Nickerson[31] which involved the $A^1\Sigma^+_u$ molecule created by barrier penetration into a quasi-bound vibrational level. Phelps's interpretation is supported through emission and absorption studies of Sando et al.[32] and Tanaka et al.[33] The existence of a potential barrier has been proved by theoretical calculation,[34,35] and the barrier height was accurately determined as 61 MeV by Lee et al.[36] Bartell et al.[8] used the time-resolved technique to decide the decay rate of He(2^1S) as $\beta = 150P + 1.3P^2$ with P in torr and β in sec^{-1}. The term of $1.3P^2$ comes from a three-body collision process.

Since He(2^1S) can decay through collision-induced emission, the time-resolved vacuum ultraviolet (vuv) method can be used as an accurate and sensitive tool to study energy pathways[37–40] and energy transfer processes leading from this state.

When small amounts of foreign species are added to pure He and produce ionization through the Jesse effect, the vuv radiation is quenched. Through the time-resolved vuv spectroscopic method of 601 Å, the reaction rate of energy transfer process of He(2^1S) can be obtained much more accurately than the data obtained by beam and afterglow discharge methods. The experimental data of time-resolved vuv spectroscopy for He(2^1S)-Ar, Kr, and Xe are presented in Fig. 19.15. The agreement between this result and those of Howard et al.[27] and Chen et al.[28] is good. Numerical results are given in Table 19.3, with an estimated accuracy of 10%.

From the accurate determination through the time-resolved vuv method, it is known that the long-range dispersion interaction considered by Bell et al.[22] through orbiting approximation is not adjustable. The interaction potential between He(2^1S)-Ar, He(2^1S)-Kr, and He(2^1S)-Xe should be similar to alkali-atom–rare-gas interaction potentials. If further data at different temperatures for time-resolved vuv spectroscopy become available, a detailed interaction potential and transition mechanism can be deduced.

Dipole-transition-allowed excited states of rare gases are the other important species for study of excitation energy transfer processes. The ionization process from resonance excited states was probed by Katsuura[41] from the rotating-atom approximation, which assumed

23. E. E. Ferguson, *Phys. Rev.* **128**, 210 (1962).
24. E. E. Benton, E. E. Ferguson, F. A. Matsen, and W. W. Robertson, *Phys. Rev.* **127**, 206 (1962).
25. W. P. Sholette and E. E. Muschlitz, Jr., *J. Chem. Phys.* **53**, 3173 (1970).
26. A. L. Schmeltekopf and F. C. Fehsenfeld, *J. Chem. Phys.* **53**, 3173 (1970).
27. J. S. Howard, J. P. Riola, R. D. Rundel, and R. F. Stebbings, *Phys. Rev. Lett.* **29**, 321 (1972).
28. C. H. Chen, H. Haberland, and Y. T. Lee, *J. Chem. Phys.* **61**, 3095 (1974).
29. H. Haberland, C. H. Chen, and Y. T. Lee, in *Atomic Physics*, vol. 3, Plenum Press, New York, 1973, p. 339.
30. A. V. Phelps, *Phys. Rev.* **99**, 1307 (1955).
31. J. L. Nickerson, *Phys. Rev.* **47**, 707 (1935).
32. K. M. Sando and A. Dalgarno, *Mol. Phys.* **20**, 103 (1971).
33. Y. Tanaka and K. Yoshino, *J. Chem. Phys.* **39**, 3081 (1963).
34. R. A. Buckingham and A. Dalgarno, *Proc. Roy. Soc. London A* **213**, 327 (1952).
35. S. L. Guberman and W. A. Goddard, *Chem. Phys. Lett.* **14**, 460 (1972).
36. Y. T. Lee and C. H. Chen, to be published.
37. G. S. Hurst, T. E. Bortner, and T. D. Strickler, *J. Chem. Phys.* **49**, 2460 (1968).
38. G. S. Hurst, T. E. Bortner, and T. D. Strickler, *Phys. Rev.* **178**, 4 (1969).
39. T. E. Stewart, G. S. Hurst, T. E. Bortner, J. E. Parks, F. W. Martin, and H. L. Weidner, *J. Opt. Soc. Am.* **60**, 1290 (1970).
40. N. Thonnard and G. S. Hurst, *Phys. Rev. A* **5**, 1110 (1972).
41. K. Katsuura, *J. Chem. Phys.* **43**, 3771 (1965).

that the electronic polarization of the atoms is always directed along the molecular axis during the collision. The interaction can be given as the interaction energy of the dipoles resulting from the two charge distributions. The dipole moments correspond to the dipole matrix elements associated with the transition. Watanabe and Katsuura[42] averaged all the contribution through different angular momenta without using the rotating-atom approximation. They obtained the rate constant

$$k = 14.59\,(\mu_1{}^2\mu_2{}^2/\hbar)^{2/5}\,(2k_BT/M^*)^{3/10}\ ,$$

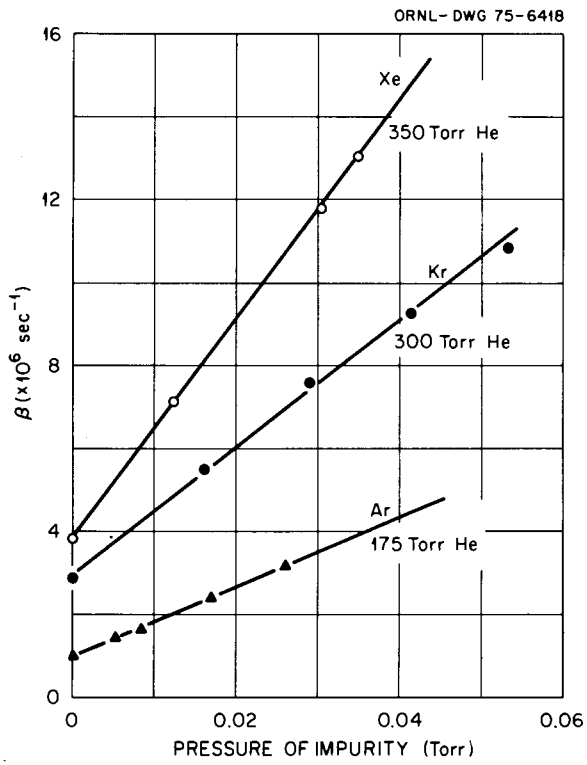

Fig. 19.15. Decay rate constant at 601 Å vs amount of impurity. Linear least-squares fitting was used to get the straight lines.

where μ_1 and μ_2 are transition dipole moments, k_B is the Boltzmann constant, M^* is reduced mass, and T is the temperature. The reaction rate of He(2^1P)-Ar from the above equation is 9.5×10^{-10} cm^3/sec.

Recently, Hurst et al.[12,18] studied energy transfer from the resonance states Ar($^1P_1$) and Ar($^3P_1$) to ethylene and to nitric oxide. It was found that the agreement between experimental data and theory was very good. A more critical experiment to check the validity of the equation by Katsuura and Watanabe[42] should be He(2^1P)-Ar. The quenching rate for He(2^1P)-Ar mixtures is given in Fig. 19.16 and was determined from vuv time-resolved measurements. Numerical data are included in Table 19.3. The experimental results are 75% larger than the calculated results. This may indicate that the long-range dipole-dipole interaction is not a good approximation for the process where resonance excited states ionize foreign atoms. In other words, the close agreement quoted above for argon may have been fortuitous.

The excited A state of He_2 can be formed through three-body collisions involving one He(2^1S). Radiation of $A \rightarrow X$ is in the region of 601 Å to 950 Å and is called "slow continuum." Rate constants for the quenching of the He "slow continuum" by Ar and Kr are presented in Fig. 19.17. The experimental results of the decay rates are essentially the same as the results from He(2^1S) since the decay of the "slow continuum" is rate-limited by the slow decay of He(2^1S) compared with the radiative decay rate of the $A^1\Sigma^+{}_u$ molecule.

Formation of the D molecular state by a three-body collision involving one 2^1P atom leads to a "fast continuum" covering the wide energy region 640 Å to 950 Å. The reaction rate of the D molecule with foreign species should be comparable with the rate of 2^1P state.

42. T. Watanabe and K. Katsuura, *J. Chem. Phys.* **47**, 800 (1967).

Table 19.3. Summary of reaction rate and cross sections for the helium mixture

	β (sec^{-1})	k (cm^3/sec)	Ionization cross section			
			This work	*a*	*b*	Calculated
He(2^1S)-Ar	8.41×10^6	2.63×10^{-10}	22.5	23.5	22.5	85.3[c]
He(2^1S)-Kr	15.3×10^6	4.79×10^{-10}	42		42.5	97.7[c]
He(2^1S)-Xe	26.2×10^6	8.2×10^{-10}	70		57	114.[c]
He(2^1P)-Ar	53.3×10^6	16.6×10^{-10}	142			81.3[d]

[a]Data obtained from J. S. Howard, J. P. Riola, R. D. Rundel, and R. F. Stebbings, *Phys. Rev. Lett.* **29**, 321 (1972).

[b]Data obtained from C. H. Chen, H. Haberland, and Y. T. Lee, *J. Chem. Phys.* **61**, 3095 (1974).

[c]Calculated from K. L. Bell, A. Dalgarno, and A. E. Kingston, *J. Phys. B* **1**, 18 (1968).

[d]Calculated from T. Watanabe and K. Katsuura, *J. Chem. Phys.* 47, 800 (1967).

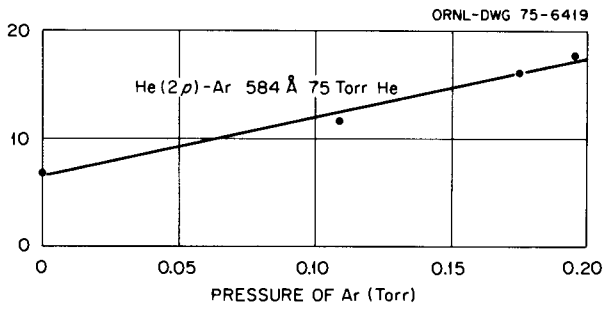

Fig. 19.16. Decay rate constant for He(2^1P) at 584 Å vs amount of impurity. Least-squares fitting was used to get the slope.

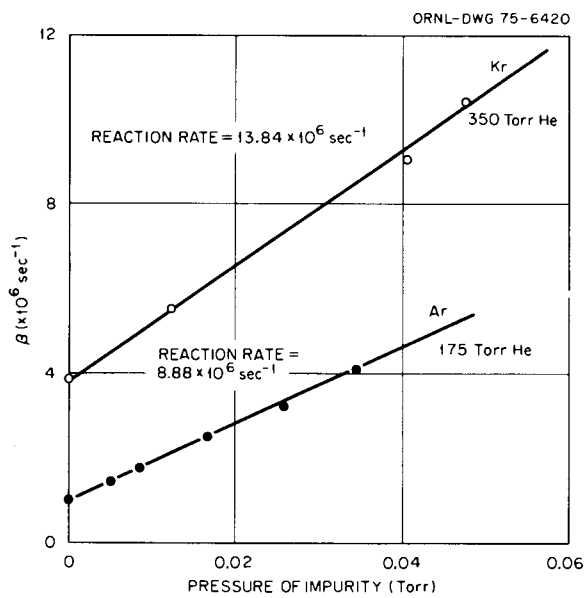

Fig. 19.17. Decay rate constants for quenching of the slow continuum in He at 800 Å bv Ar and at 615 Å by Kr.

The quenching experiments of $D^1\Sigma^+_u$ will be done in the near future.

New Energy Transfer Facility

It is well known that time-resolved vacuum ultraviolet (vuv) spectroscopy is one of the most convenient tools for studying the quenching rate of rare-gas excited states. Recently, Fink et al.[43] and McNeely et al.[18] did energy transfer studies of Ar($^1P_1$) and Ar($^3P_1$) to H_2 and N_2. The agreement for the reaction rate of discrete-discrete electronic energy transfer between experimental data and calculational results by Katsuura and Watanabe formula[42] is very poor. On the other hand, Piper et al.[44] measured the quenching cross section of metastable Ar by small molecules. Their results could not be explained by any simple theoretical model either. Therefore, detailed experimental information of energy transfer kinetics becomes increasingly important.

In addition to the theoretical interest, more information on the detailed mechanism of electronic energy transfer is needed to develop high-power ultraviolet lasers for fusion work and for laser isotope separation. Therefore, we have built a new facility for measurements of time-resolved vuv spectroscopy and time-resolved visible spectroscopy. A high-power pulsed laser will also be set up to determine, in a direct way, the atomic precursors to excimer states. In the following, we will briefly describe this new experimental setup and the work planned for the near future.

A schematic of the multipurpose rectangular reaction cell is given in Fig. 19.18. Proton beams of 2 MeV are pulsed into the cell to produce ion pairs and excited electronic states. Through direct interaction, recombination, and cascade process, many low-level metastable and resonance excited states will be produced. Vuv photons will be emitted from both excited rare-gas atoms and excimers. They will pass through a lithium fluoride window and be resolved by a vuv monochromator, with a wavelength resolution of about 3 Å. Photons of a chosen wavelength leave the monochromator through a variable-width exit slit and strike the vuv-sensitive cone of a channel electron multiplier which gives 0.5 dark count per second.

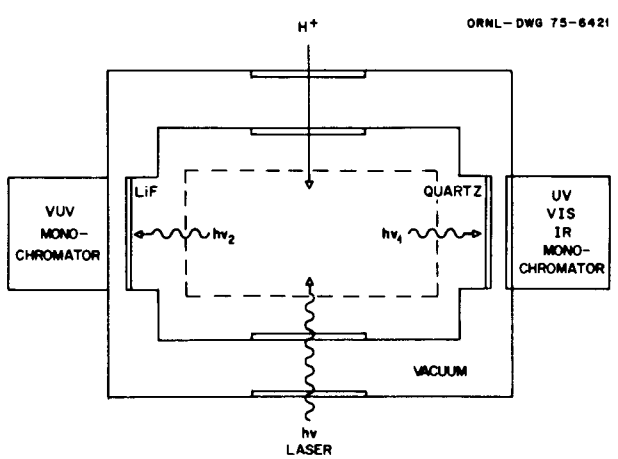

Fig. 19.18. Schematic diagram of the reaction cell for studying energy transfer.

43. E. H. Fink, D. Wallach, and C. B. Moore, *J. Chem. Phys.* **56**, 3608 (1972).

44. L. G. Piper, J. E. Velazco, and D. W. Setser, *J. Chem. Phys.* **59**, 3323 (1973).

If there are foreign gases in the reaction cell, the energy transfer process from excited rare gases to foreign species will occur. When the ionization potential of foreign gases is higher than the energy level of excited states, the process will be a discrete-discrete electronic energy transfer. Thus, there is high probability of fluorescence from the foreign molecules, mainly in the ultraviolet (uv) and visible region. Photons emitted from the fluorescence will pass through the quartz window and enter a uv–visible–near-infrared monochromator. The resolution can be set better than 0.3 Å. Photons with a selected wavelength are detected by another electron multiplier which has 0.5 dark count per second at a temperature of –20°C. Both vuv and uv-visible photons will be detected through time-resolved single-photon counting techniques.

In addition to time-resolved vuv and uv-visible spectroscopy, the ion-pair collection plates are set up to collect all the ion pairs produced by the proton beam. This *W*-vale measurement can be used to provide Jesse effect and to verify the purity of gases.

Since there are many different electronic excited states, it is helpful to know the precursor for each individual energy transfer process. A high-power tunable pulsed laser with high repetition rate can be used to remove a selected excited state of a rare gas through photoionization. Dunning et al.[45] have been successful in ionization of Ar by two-step photoionization through a pulsed dye laser. Detailed discussion on resonance ionization spectroscopy which makes use of two-photon ionization was reported above.

A brief discussion of proposed work with the new facility will be given in the following.

1. *Laser applications.* A high-power, high-efficiency laser with a wavelength in the visible or near ultraviolet would be very desirable for laser-induced fusion and isotope separation. Molecular nitrogen has excited states suitably spaced for stimulated emission in the desired wavelength range. Argon-nitrogen lasers have been built by Searles et al.[46,47] Bhaumik et al.,[48] and Basov et al.,[49] but the power is less than the 10^4 J per pulse needed for fusion work. In order to improve the efficiency, a detailed study on energy transfers is important. Hill et al.[50] studied time-resolved emission of Ar-N_2 by electron excitation and got a kinetic model to explain the energy transfer process. According to this model, the efficiency is less than 2%. However, detailed kinetic studies of energy transfer through electron excitation are difficult since recombination and electronic collision processes make the situation quite complicated. A careful study will be done through vuv and uv-visible time-resolved methods by proton-beam excitation under conditions where mainly linear processes occur.

In addition to lasing through the triplet system $N_2(C^3\pi_u \rightarrow B^3\Sigma_g)$, it may be possible to study the laser action through spin singlet excitation. For $Ar(^1P_1) + N_2$, the quenching rate of $Ar(^1P_1)$ has been found quite large by McNeely et al.[18] For $Ar(^1P_1)$, the spin conservation rule, if applicable, is against N_2 triplet excitation. Recently, Golde[51] studied vuv emission from discharges for Ar and N_2 mixtures. A strong emission of $N_2(a^1\Pi_g - {}^1\Sigma^+{}_g)$ was observed. If $N_2(a^1\Pi_g)$ comes from the $Ar(^1P_1)$ state, it might be possible to develop a new laser system through singlet discrete-discrete transition. The energy transfer from Ar* to O_2 and to Cl_2, which could lead to a very powerful dissociation-type uv laser,[52] will also be studied.

2. *High Rydberg states.* When a rare gas is excited by proton beams, some high Rydberg states are created. High-Rydberg-state atoms emit visible photons in transitions to lower excited states. Some of the high Rydberg states are converted to associative ionization through the Molnar-Hornbeck process. Time-resolved visible photon spectroscopy will give more detailed information of energy pathway of high Rydberg states.

3. *Electronic energy transfer to kinetic energy.* It is well known that $He(2^1S)$ can form $A^1\Sigma^+{}_u$ through three-body collision. The lower vibrational state of $A^1\Sigma^+{}_u$ can be converted to a discrete level of a foreign gas such as Ar, because the ground molecular state of He_2 is highly repulsive. However, because of the short lifetime of the *A* molecule, it may be more feasible to make the studies for the metastable molecule of helium.

4. *Ionization kinetics.* Richardson et al.[53] studied fluorescence of N_2, O_2, and Cl_2 ionized by $He(2^3S)$. It was found that the Franck-Condon principle does not

45. F. B. Dunning and R. F. Stebbings, to be published.
46. S. K. Searles and G. A. Hart, *Appl. Phys. Lett.* **25**, 79 (1974).
47. S. K. Searles, *Appl. Phys. Lett.* **25**, 734 (1974).
48. E. R. Ault, M. L. Bhaumik, and N. T. Olson, *IEEE J. Quantum Electron.* **QE-10**, 624 (1974).
49. N. G. Basov, V. A. Danilychev, V. A. Dolgikh, O. M. Kerimov, A. N. Dobanov, and A. F. Suchkov, *Sov. Phys. JETP Lett.* **20**, 53 (1974).
50. R. M. Hill, D. J. Eckstrom, R. A. Gutcheck, D. L. Huestis, D. C. Lorents, D. Mukherjee, and H. H. Nakarro, *Bull. Am. Phys. Soc.* **19**, 153 (1974).
51. M. F. Golde, *Chem. Phys. Lett.* **31**, 348 (1975).
52. D. W. Setser, private communication.
53. W. C. Richardson and D. W. Setser, *J. Chem. Phys.* **58**, 1809 (1973).

always hold in these collision processes. It is, therefore, interesting to compare ionization by resonance excited states with photoionization in which vertical (Franck-Condon) transitions always occur.

5. *Lifetime measurements of excited states of ions and molecules.* The time-resolved visible photon spectroscopy method should be a direct and convenient way to measure lifetimes of many excited molecules and ions.

6. *Pollution and analytical chemistry research.* Since time-resolved techniques are very sensitive to small amounts of impurities, they can be widely applied in pollution research and analytical chemistry. Detailed discussion will be given in the following sections.

Energy Transfer for Pollution Analyses

The basic ideas that have been conceived and the results obtained from energy transfer studies are being evaluated in terms of their obvious analytical applications. Materials are being procured and experiments are being designed to demonstrate the sensitivity that these measurements of energy transfer will exhibit for the determination of gaseous pollutants. Although some energy pathways of gases of environmental interest have been studied,[18] there is a need for energy pathway studies of He or Ar in the presence of a wider variety of contaminant gases of environmental interest. The first experimental studies will be with Ar-CH_3I mixtures. Also of rather immediate interest are contaminant vapors of I_2, T_2, SO_2, etc. An evaluation of competition and other complications caused by the presence of atmospheric gases – for example, O_2, N_2, H_2O – will be necessary for practical applications. Some of these competing processes will not be a problem, however, for the possible application of energy transfer methods for a determination of T_2 in the helium gas stream of gas-cooled reactors.

LASER APPLICATIONS

Introduction

During the past year, a portion of our work has been supported by the Laser Division of the Los Alamos Scientific Laboratory (LASL). Our original connection with laser development was related to our facilities for studying the kinetic processes which effect the decay of excited species in a gas excited by fast charged particles (under relatively simple conditions where nonlinear processes such as recombination and collisions between excited species are relatively unimportant). This year, we have also developed and built some facilities for the study of discrete-discrete energy transfer processes. Several high-power lasers work because of inverted populations achieved in this way. These experiments have been discussed above; see the section entitled "Energy Transfer."

Since the initiation of the resonance ionization spectroscopy (RIS) effort, our interest in lasers has increased considerably. With RIS, we want to saturate the ionization of a selected species by tuning a pulsed dye laser between the state of the population of interest and an excited state and achieving ionization due to the absorption of a second photon either from the same laser or from another laser pulse which is coincident with the first. This technique is very powerful if a sufficiently energetic laser in the wavelength region of interest can be found. At present, dye lasers which are sufficient for the first step are available at most of the wavelengths from 3900 Å to 7400 Å. It is reasonable to believe that lasers may exist within the next few years which extend this range to 2400 Å $\leqslant \lambda \leqslant$ 7400 Å. Presently, to get photons below 3400 Å, frequency doubling is usually required. In this region, then, the second photon generally must come from a second laser. Sometimes the undoubled portion of the pulse from the first laser can be used, but it is often so far above the ionization threshold in energy that saturation of the ionization is not achieved. In the latter situation, the second laser need not be tunable, but it must deliver about 1 J per pulse with a pulse length comparable with that of the first laser and a photon energy not too far above threshold. Because of the requirement of coincidence of the pulses, it may be better if the pulse lengths are fairly long. With the latter technique for RIS, the lasers required are somewhat different from those required for laser isotope separation. For isotope separation, the laser line width must be very small, but the energy per pulse requirements can be more modest. With this RIS method, the line width can be several angstroms, but the length of pulse should be long and the energy per pulse large. Tunability is required in both cases. Because our laser requirements are somewhat different from those for other ERDA programs, the involvement in laser development with LASL presents an important opportunity to stay familiar with the laser technology. Lasers which may not be important in the laser fusion or isotope separation programs may be useful for RIS.

Energy Pathways in Metal Vapors

High-power gas lasers producing photons in the range from 2000 to 4000 Å are needed for laser isotope

separation and for laser fusion. One approach to meeting the laser requirements is the use of metal vapors at high temperature and pressure, when excited atomic states are converted to molecular emission. These so-called excimer lasers which involve bound upper states and repulsive ground states have been considered for some time; yet much of the necessary energy pathways information is lacking.[54]

For several years we have studied excimers of the noble gases created by proton excitation of the gases at high pressure. By using time-resolved spectroscopic techniques, one obtains the kinetics, the excimer lifetimes, and the emission spectra. For the metal vapor experiments, we are incorporating two important new techniques into our time-resolved spectroscopy. First, the heat pipe technology[55] is employed to provide a uniform vapor temperature, and with the inert-gas buffer technique,[56] the heat pipe can be used to protect cell windows from the metal vapors. Second, a tunable dye laser will be used to excite just one state at a time, thus permitting a more definitive precursor-excimer assignment than is possible with proton excitation.

A heat pipe designed primarily for mercury vapor experiments is shown in Fig. 19.19. Considerable experience[57] with mercury as a heat pipe fluid can then be utilized. In the figure, we illustrate excitation with a tunable pulsed dye laser. We visualize a scheme in which atomic states of mercury are selectively excited as a uniform line source by detuning the laser to the wings of the absorption line. Following the ideal initial excitation (a uniform line source at $t = 0$), the time behavior of both resonance and Franck-Condon photons resulting from excimer decay will be followed. By controlling the temperature up to 260°C, mercury gas pressures can be selected up to 100 torr.

ANALYTICAL APPLICATIONS

Introduction

In our initial experiment utilizing resonance ionization spectroscopy (RIS), we measured quantitatively the number of He(2^1S) atoms remaining at different times after excitation. Depending on the pressure and time after excitation, the number of these atoms ranged from 10^6 to 10^7, while the number of ground-state atoms present was typically about 10^{18}. This extreme sensitivity was attained while using a relatively insensitive device (an ionization chamber and associated electronics) to detect the resulting ion pairs. It is not unreasonable to believe that as few as 100 (or possibly less if background effects are small) He(2^1S) atoms could have been detected and their number measured if we had used a more sensitive ion or electron detection system.

The RIS technique could also be used to detect small numbers of atoms or molecules in their ground state. The only requirement is that a tunable laser be available which is capable of saturating a transition between the ground state and an excited state and that the laser (or another one fired simultaneously) be able to saturate the yield of ion pairs. In the latter situation, essentially all atoms (or a fixed fraction of the molecules) resonating with the laser light and lying in the beam are converted to ion pairs, which can be detected with great sensitivity. (Even one ion can be detected under ideal conditions.) Thus, we see the possibility of unprecedented sensitivity for gas-phase analytical chemistry. Further, flash evaporation techniques may eventually be developed to the point where the technique could be applied to liquids as well.

One can list several promising applications for the RIS technique whose principal advantage is that it enables one to determine with great sensitivity the number of atoms or molecules present in a particular state at a particular time and in a particular region of space. A few types of studies where the technique should be useful are (1) the study of transport processes involving minute concentrations of compounds that could change either slowly or quickly with time, (2) the determination of reaction rates in cases where one of the products is in the gas phase and the rate of production of this product is very small (either because the reaction rate constant is extremely small or because one or more participants in the reaction is present in very small concentrations), (3) the study of the electronic structure of an extremely small number of atoms of a rare element (say a transuranic element). The RIS technique might also be used as a selective pump in high-vacuum

54. This work is performed for the Laser Division of Los Alamos Scientific Laboratory under the direction of K. Boyer. We are considerably indebted to Robert Carbone for his guidance on specific laser requirements and for important contacts with other laboratories.

55. Modern heat pipe technology has been highly developed at Los Alamos Scientific Laboratory, starting with the work of G. M. Grover, T. P. Cotter, and G. F. Erickson, *J. Appl. Phys.* **35**, 1990 (1964). We are indebted to the LASL Heat Pipe Group for much information privately communicated. The cooperation of W. A. Ranken, J. E. Deverall, and J. E. Kemme is gladly acknowledged.

56. C. R. Vidal and F. B. Haller, *Rev. Sci. Instrum.* **42**, 1779 (1971).

57. J. E. Deverall, *Mercury as a Heat Pipe Fluid,* LA-4300-MS (1969).

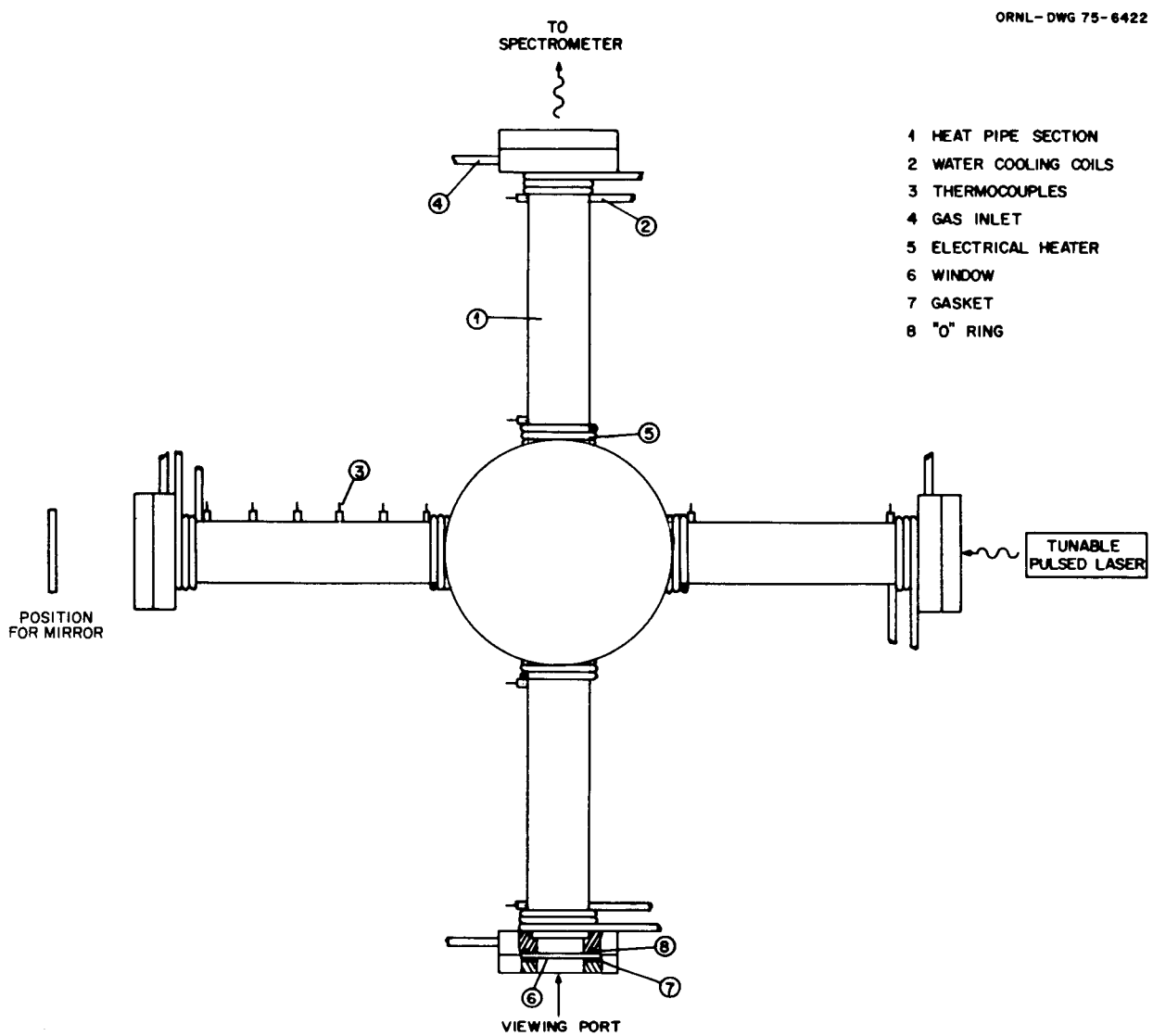

Fig. 19.19. Schematic of heat pipe experiment. (1) Typical heat pipe section, (2) water cooling coils, (3) thermocouples, (4) noble-gas inlet, (5) electric heater, (6) window, (7) gasket, (8) window O-ring seal.

work or for the purpose of removing selected impurities in the preparation of small amounts of very pure compounds. This list is not exhaustive, but it should serve to show the potential for future development.

We will describe two projects of analytical importance that are now under way.

Atom Vapor Ionization Resonance Ionization Spectroscopy

In addition to the RIS studies described above, studies of laser-excited ionization of atomic vapors are under way. Apparatus has been designed and is being assembled to study two-step photoionization using a pulsed laser beam. The apparatus is composed of a cylindrically shaped vacuum-tight optical cell fabricated of fused silicon. The cell contains a four-electrode ion-detecting system described previously for the helium studies. It will be loaded with pellets of potassium metal; the vapor pressure of the metal will be controlled from 10^{-11} to 10^{-8} torr by controlling the temperature of a cold finger appendage on the cell from 273° to 300°K. The RIS effect in potassium vapor will be demonstrated by using pulsed 4014-Å laser light derived from a flash-lamp tunable dye laser. This apparatus will be useful for RIS studies of other amenable atomic vapor species, as it is designed so that the material to be

studied can be in an inert-gas environment and the pressure of either component can be varied and controlled. The apparatus will serve as the cell to be used, or as a prototype cell to be used, in intercavity, laser-excited single-energy, two-step RIS studies and in studies involving RIS effects derived from excitation by two laser beams of different wavelengths. This latter excitation mode can lead directly to photoionization of electrons to Rydberg levels where field ionization can be applied to ultimately yield an ionization product. Obviously, in all these studies, lifetimes, kinetics, and pathways can be investigated.

Background Studies for One-Atom Detection

We are working on an experimental system with the goal of detecting very small amounts of an elemental substance. Ultimately, we may be able to detect one atom of a given element in a sample.

The basis for this method is to photoionize the sample with a tunable dye laser which is tuned between the ground state and an excited state lying more than halfway to the continuum. Under these conditions, the ionization has a resonance structure, and to a good approximation only atoms of a selected type will be photoionized. With sufficiently high laser energy (e.g., 1 J per pulse), nearly all of the selected atoms are ionized. The ultimate sensitivity of the method may be limited by various background problems. Nonresonant multiphoton processes can yield appreciable numbers of ion pairs if the number of background atoms is too large. Other background sources, such as stray photoelectrons ejected from the cell walls and windows, will also be investigated in the preliminary experiment described below.

If the background turns out to be extremely low, one can simply work with electron detectors. However, if one detects many electrons per laser pulse, positive-ion detection may be necessary. Therefore, single-ion measurements and methods of mass discrimination using a quadrupole mass analyzer, or time-of-flight discriminators, are viewed as possible extensions of this work.

The experimental apparatus, shown in Fig. 19.20, includes a chamber which can be pumped by a high-vacuum pumping station. A window is placed on the side of the chamber to allow entry of the laser beam. The chamber contains ionization electrode plates, a preaccelerator electron lens, and a nude electron multiplier.

When the laser is fired after having been tuned to produce photoionization of a given substance in the chamber, the following sequence should take place. The electrons produced by photoionization should move toward the upper electrode plate due to the negative potential on the lower plate. Electrons in the central region of the chamber should go through the grid and then, by means of the electron lens, be directed into the electron multiplier.

The first experiments will be a study of background when the chamber is evacuated to the best possible vacuum. Then, studies will be carried out introducing selected samples into the chamber. The low vapor pressures of the chosen samples will not change appreciably the vacuum conditions in the chamber. Finally, studies will be made to determine the effect of other substances present with the sample being analyzed. The apparatus discussed above has been constructed and is currently being installed in the laboratory.

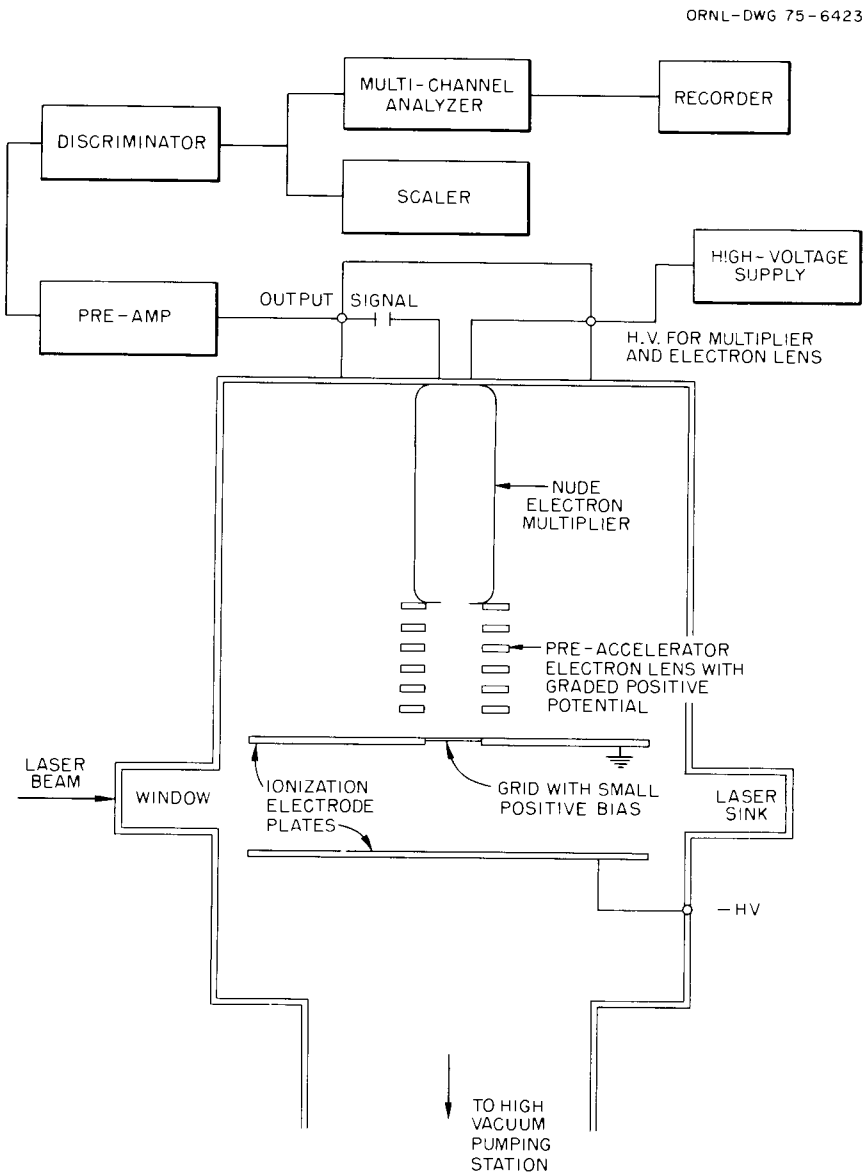

Fig. 19.20. Experimental apparatus, background studies for one-atom detection.

Part V. Medical Physics and Internal Dosimetry

J. W. Poston

20. Metabolic Models for Estimation of Internal Radiation Exposure Received by Human Subjects from the Inhalation of Noble Gases

S. R. Bernard W. S. Snyder[1]

The purpose of this chapter is to present and develop metabolic models needed for estimation of dose equivalent from exposure to noble gases. Human subjects may inhale low levels of radioactive noble gases released to the atmosphere by nuclear reactors or fuel reprocessing plants either on a regular basis or after an accidental release. Also, medical studies using radioactive noble gases are employed to obtain data on ventilation and perfusion of the lungs.[2] Estimates of radiation dose to human tissue are sometimes based on the equilibrium levels predicted from the Ostwald absorption coefficient [ratio of concentration (mass per unit volume) of gas in the tissue or fluid to the concentration in air].[3] This amounts to assuming an equilibrium between the gas present in the atmosphere and that present in tissue. Such an estimate may be valid for long-lived radioactive gases but does not appear adequate for short-lived radioactive gases. It is for this reason that a metabolic model is needed.

In 1950, Harley, Jetter, and Nelson[4] published data on the exhalation of ^{222}Rn by a human subject (actually more than one subject, but adequate data are available on only one) who inhaled ^{222}Rn at a concentration of 7×10^{-10} Ci/liter for $8\frac{1}{2}$ hr. Data on the rate of exhalation, in picocuries per minute, were measured out to 76 hr after the exposure ceased (see Fig. 20.1). We then fit a five-term exponential equation to these data:

$$\text{Rate of exhalation} = 3210e^{-1.818t} + 328e^{-0.155t} + 71e^{-0.0168t} + 25e^{-0.00342t} + 4.8e^{-0.00063t}\ \text{pCi/min}\,, \qquad (1)$$

with t in minutes. This equation is not corrected for radioactive decay, but the value of the decay constant is $\lambda_r = 0.00013\ \text{min}^{-1}$.

Equation (1) has been converted to the equation for a single intake via inhalation by the following procedure. Let $R_S(t)$ denote the fractional retention in the body at time t (in minutes) following a single intake by inhalation and assume

$$R_S(t) = \sum_{i=1}^{5} b_i e^{-\mu_i t}\,, \qquad (2)$$

where

$$\sum_i b_i = 1\,,$$

$$\mu_i = \lambda_r + \lambda_i\ \text{min}^{-1}\ ;$$

that is, the μ_i is the ith effective elimination constant, and the λ_i is the constant for removal or transfer from

1. Consultant.
2. R. Knisely and B. Tauxe (Eds.), *Dynamic Clinical Studies with Radioisotopes*, TID-7678, 1964.
3. R. Hober, *Physical Chemistry of Cells and Tissues*, Blakiston, Philadelphia, 1950.
4. J. H. Harley, E. Jetter, and N. Nelson, USAEC report HASL-32, 1958.

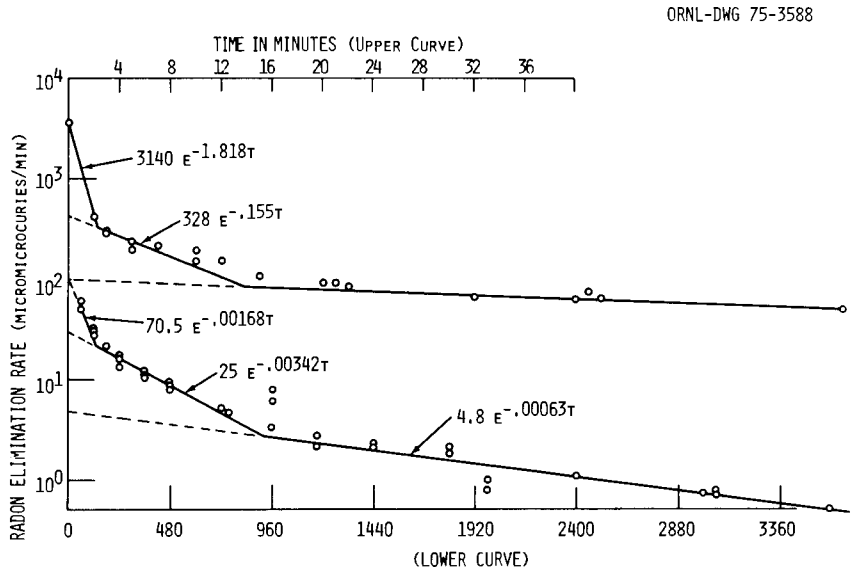

Fig. 20.1. Radon elimination rate by a human volunteer who had inhaled radon for 8½ hr. Data from Harley, Jetter, and Nelson (ref. 4).

the compartment. For an intake rate of I pCi/min, the intake in a period $d\tau$ is $Id\tau$ pCi. In the case of continuous exposure at a constant level, the retention is

$$\int_0^t d\tau\, IR_S(t-\tau) = I \sum_{i=1}^{5} \frac{b_i}{\mu_i}\left(1 - e^{-\mu_i t}\right) \text{ pCi} . \quad (3)$$

If exposure of the tissue to the gas continues for a period of E (in minutes) and then ceases, the retention at a time t (in minutes) following the cessation of exposure is given by

$$R(t) = I \sum_{i=1}^{5} \frac{b_i}{\mu_i}\left(1 - e^{-\mu_i E}\right) e^{-\mu_i t} \text{ (pCi)}, \; t \geqslant 0 . \quad (4)$$

The derivative with respect to t, assuming $t > 0$, is

$$I \sum_{i=1}^{5} \frac{b_i(\lambda_i + \lambda_r)}{\mu_i}\left(1 - e^{-\mu_i E}\right) e^{-\mu_i t} \text{ (pCi/min)} . \quad (5)$$

The term involving λ_r corresponds to radioactive decay. Thus the biological elimination which is here assumed equal to the exhalation is given by

Rate of exhalation

$$= I \sum_{i=1}^{5} \left[\frac{b_i \lambda_i}{\mu_i}\left(1 - e^{-\mu_i E}\right)\right] e^{-\mu_i t} \text{ (pCi/min)} . \quad (6)$$

This equation can be compared to the experimental equation of Harley, Jetter, and Nelson,[4] and the values of each λ_i can be identified by inspection. The expression $(1 - e^{-\mu_i E})$ can be computed, and the values of each b_i can then be obtained. The retention equation for the total body for the case of a single intake via inhalation is found to be

$$R_S(t) = 0.874e^{-1.818t} + 0.0913e^{-0.155t} + 0.0198e^{-0.01686t} + 0.00863e^{-0.00342t} + 0.00612e^{-0.00063t} \quad (7)$$

(t in minutes), without correction for radiological decay ($\lambda_r = 0.00013$ min^{-1} for ^{222}Rn).

Equation (7), corrected for radioactive decay, was then analyzed with the MAMX code described by Bernard[5] to obtain rate transfer constants λ_{ij} for a five-compartment mammillary model taken to represent the distribution of radon in the body. In ref. 5 the following equations were solved for λ_{ij} and λ_{ji} using the MAMX code:

$$g(\lambda_{1j}) = \sum_{i=1}^{5} \frac{b_i \lambda_i}{\lambda_{1j} - \lambda_i} = 0 \quad (8)$$

$$\sum_{i=1}^{5} \frac{\lambda_{j1}\lambda_{1j}}{\lambda_{1j} - \lambda_i} = \lambda_{11} - \lambda_i , \quad i = 1, \ldots 5 , \; j = 2, \ldots 5 . \quad (9)$$

$$C_{ji} = \frac{\lambda_{j1}(b_i\lambda_i)/(\sum_i b_i\lambda_i)}{\lambda_{1j} - \lambda_i} . \quad (10)$$

5. S. R. Bernard, *Bull. Math. Biol.* **35**, 129 (1973).

The biological elimination constants (λ_i), in units of reciprocal minutes, are obtained from Eq. (7). The mammillary model, together with the symbol for the rate transfer constants between compartments, appears in Fig. 20.2. The values of b_i, λ_i, λ_{1j}, and C_{ji} are listed in Tables 20.1 and 20.2. The time integrals of the activities in the various compartments, r_i, appear in Table 20.3.

Equation (7), when converted back to the case of continuous intake of 7×10^{-10} Ci/liter for a period of $8\frac{1}{2}$ hr exposure and for an inhalation rate of 5 liters/min, will recover the equation of Harley, Jetter, and Nelson within ~4% for exhalation after cessation of exposure.

For dosimetry, the compartments must be identified with the tissues of the body. Nussbaum's data[6] on the distribution of activity in rats are used here. The rats were permitted to inhale ^{222}Rn for periods ranging from 30 min up to 48 hr. Samples of tissues and organs

6. E. Nussbaum, USAEC report UR-503, 1957.

ORNL-DWG 75-4615

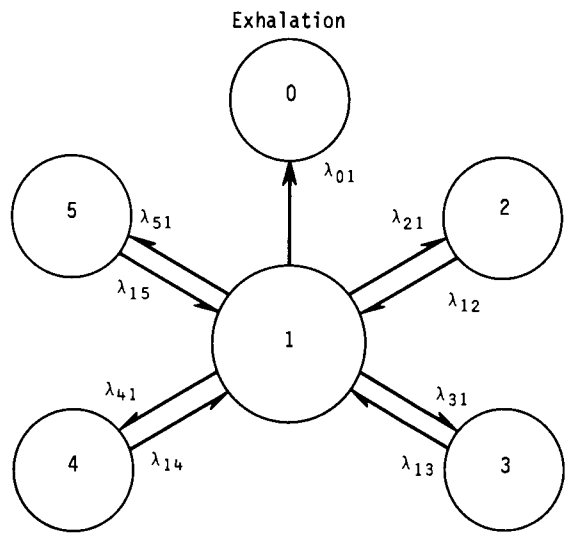

Fig. 20.2. Mammillary model for radon.

Table 20.1. Constants for the mammillary model of human retention of radon following a single inhalation by man[a]

b_1 6.12×10^{-3}	b_2 8.63×10^{-3}	b_3 1.98×10^{-2}	b_4 9.13×10^{-2}	b_5 8.74×10^{-1}
λ_1 5.00×10^{-4}	λ_2 3.29×10^{-3}	λ_3 1.67×10^{-2}	λ_4 1.55×10^{-1}	λ_5 1.82
λ_{11} 1.80	λ_{12} 5.03×10^{-4}	λ_{13} 3.32×10^{-3}	λ_{14} 1.71×10^{-2}	λ_{15} 1.70×10^{-1}
λ_{11} 1.80	λ_{21} 9.82×10^{-3}	λ_{31} 1.39×10^{-2}	λ_{41} 3.22×10^{-2}	λ_{51} 1.43×10^{-1}

[a]Units on λ's are reciprocal minutes.

Table 20.2. C_{ji} matrix for radon retention in man

j	i = 1	2	3	4	5
1	1.91×10^{-6}	1.77×10^{-5}	2.06×10^{-4}	8.83×10^{-3}	9.91×10^{-1}
2	6.10×10^{-3}	-6.24×10^{-5}	-1.25×10^{-4}	-5.61×10^{-4}	-5.36×10^{-3}
3	9.43×10^{-6}	8.62×10^{-3}	-2.14×10^{-4}	-8.10×10^{-4}	-7.60×10^{-3}
4	3.70×10^{-6}	4.13×10^{-5}	1.97×10^{-2}	-2.06×10^{-3}	-1.77×10^{-2}
5	1.62×10^{-6}	1.52×10^{-5}	1.93×10^{-4}	8.59×10^{-2}	-8.61×10^{-2}

Table 20.3. Time integrals (r_i) of retention in the ith compartment out to 50 years

$r_1 = 0.622$	$r_2 = 9.65$	$r_3 = 2.51$	$r_4 = 1.16$	$r_5 = 0.523$

were obtained and analyzed for radon concentrations. (We defer discussion of the loss of radon from the tissue sample by diffusion and escape to the atmosphere until later in this chapter.) In general, it was found that fats (such as omental fat) contained ~5 μCi/cm^3 if the inhaled air was at a level of 1 μCi/cm^3 of air, while for other nonfatty tissues the Ostwald coefficient concentrated ^{222}Rn at values down to ~$^1/_{30}$ of this value. Nussbaum lists the data for rats and also some in vitro data on fat and blood and extrapolates these to organs and total body on the basis of the percentages of organs and tissues which are fat and nonfat. These data are shown in Tables 20.4 and 20.5.

By the single intake model for retention of ^{222}Rn, one obtains by integration the time integrals of activity for each compartment. These are indicated by r_i for compartment i and are listed in Table 20.3. These values indicate the equilibrium levels that would be reached if a person were continuously breathing atmospheric ^{222}Rn at a level of 1 μCi/cm^3. It will be recalled that the basic data on which Eq. (7) is based are for an individual breathing 5 liters of air per minute, and thus the levels would be in terms of picocuries per kilogram, taking the density of the total body as essentially 1.

To make a dose calculation possible, the activity in the compartments must now be assigned to various tissues and organs of the body. The data on distribution of activity at equilibrium are taken from Nussbaum[6] and, ignoring minor differences, may be grouped into three groups: separable fat, comprising ~12.5 kg; bone, heart, muscle, skin, testes, and urinary bladder, which together comprise ~40 kg; and the other organs, which comprise the remaining 17.5 kg of reference man. On the basis of Nussbaum's data,[6] Ostwald coefficients of ~5 for fat, ~0.15 for the group containing bone, muscle, etc., and ~0.4 for the remaining organs are suggested.

On this basis, the assignments to the compartments of these three groups of tissues are

$$5 \sum_{i=1}^{5} r_i l_{ij} = L_j \times W_j \quad j = 1,2,3 , \tag{11}$$

where L_j is ~5, ~0.4, and ~0.15 for the three groups of tissues. It will quickly become apparent that the equations cannot be rigorously solved since

$$\sum_{j=1}^{3} l_{ij} = 1 \quad i = 1,2,3,4,5 , \tag{12}$$

Table 20.4. Calculation of the whole-body solubility coefficient of radon in the rat

Tissue	% of whole-body wt.	Radon solubility coefficient L	Product of $L \times$ % body wt.
Depot fat	7.08	4.83	34.20
Muscle	45.50	0.154	7.01
Liver	4.15	0.306	1.27
Heart	0.289	0.221	0.064
Kidney	0.76	0.285	0.22
Testis	0.94	0.184	0.17
Brain	0.550	0.309	0.18
Blood	4.95	0.405	2.01
Skin			
Nonfat	16.88	0.15[a]	2.53
Fat	1.22	4.83	5.41
Supportive			
Nonfat	7.38	0.15[a]	1.11
Fat	0.30	4.83	1.45
Balance	10.1	0.30[b]	3.03
	100		58.65

Whole-body solubility coefficient: 0.59

[a]Solubility estimated to be approximately equivalent to that in physiological saline.

[b]Solubility estimated to be equal to or lower than the weighted mean value in heart, kidney, brain, and liver, that is, 0.303.

Table 20.5. Nussbaum's calculation of the whole-body solubility coefficient of radon in man

Tissue	% of whole-body wt.	Radon solubility coefficient L	Product of $L \times$ % body wt.
Muscle	43	0.154	6.62
Skin (2000g) and subcutaneous tissue	8.7	0.154	1.30
Fat	14	4.83	67.62
Skeleton (less marrow)	10	0.154	1.50
Red marrow	2.1	0.43	0.90
Yellow marrow	2.1	4.83	10.14
Blood	7.7	0.43	3.31
GI tract	2.9	0.303[a]	0.88
Liver	2.4	0.306	0.73
Brain	2.1	0.309	0.65
Lungs (2)	1.4	0.303[a]	0.42
Lymphoid tissue	1.0	0.303[a]	0.30
Kidneys (2)	0.43	0.285	0.12
Heart	0.43	0.221	0.10
Spleen	0.21	0.303[a]	0.06
Urinary bladder	0.21	0.154	0.03
Testes (2)	0.057	0.184	0.01
Balance	1.263	0.303[a]	0.38
Total body	100.0		95.07

[a]Solubility is assumed to be approximately equal to the weighted mean of the values in heart, kidney, and brain.

and this requires, by addition of all the equations, that

$$5 \times \sum_{i=1}^{5} \sum_{j=1}^{3} r_i l_{ij} = 72.275 \cong \sum_{j=1}^{3} L_j W_j = 75.5 \,. \qquad (13)$$

The discrepancy is only of the order of 4%, and this seems acceptable in view of the widely different sources of the data. To avoid accumulation of errors, we reduce the right members by a factor of 1/1.044. Thus the equations to be solved are the following:

$$0.622 l_{11} + 9.65 l_{12} + 2.5 l_{13} + 1.16 l_{14} + 0.523 l_{15} = 12 \,, \qquad (14)$$

$$0.622 l_{12} + 9.65 l_{22} + 2.5 l_{23} + 1.16 l_{24} + 0.523 l_{25} = 1.34 \,. \qquad (15)$$

If the equations can be solved, Eq. (13) is automatically met, since

$$\sum_{j=1}^{3} l_{ij} = 1 \,.$$

One cannot hope for a unique solution since there are far too many unknowns. However, there is some guidance in the choice of values that reflect some facts concerning the distribution. For example, fat is known to have a high Ostwald coefficient, and it is apparent from inspection that l_{12} must be fairly close to 1. This suggests that $l_{12} = 1$, $l_{22} = l_{32} = 0$. Similarly, a few trials suggest that l_{13} is fairly large, and consequently a suggested set of values, $l_{13} = 0.6$, $l_{23} = l_{33} = 0.2$, seem acceptable. The remaining values are found by trial and error but are by no means unique. The completed set of values for the l_{ij} are given in Table 20.6.

The l_{ij} values presented above represent only one choice. There are probably others that can be obtained by iteratively seeking other sets of values. In this chapter, use will be made of the values derived above. How closely does this model determine the activity in the body at equilibrium?

For the case of equilibrium for inhalation of 1 μCi/cm^3 of air, the total activity is given by

$$\int_0^\infty \frac{1\mu\text{Ci}}{\text{cm}^3} \times \frac{2 \times 10^7 \text{ cm}^3/\text{day}}{1440 \text{ min/day}} \times \frac{R_S(\tau)d\tau}{7 \times 10^4 \text{ g}} \cong 2.8\,\mu\text{Ci/g} \,. \qquad (16)$$

Table 20.6. Fractions of compartments assigned to the tissue groups

	1	2	3	4	5
1	0.225	1	0.6	0.5	0.25
2	0.225	0	0.2	0.5	0.25
3	0.55	0	0.2	0	0.5

In Eq. (9), we are assuming 1 μCi/cm^3 as the concentration in air, 2×10^7 cm^3 of air breathed per day, and 7×10^4 g in the total mass of the body. The value obtained from Eq. (16) is approximately three times higher than Nussbaum predicts for man (Table 20.5). Reasons for the overestimates were sought, and it is believed that the minute volume of air breathed by reference man

$$\left(\frac{2 \times 10^7 \text{ cm}^3}{1.44 \times 10^3 \text{ min}} \cong 14 \times 10^3 \text{ cm}^3/\text{min}\right)$$

and used in obtaining Eq. (9) may be partly responsible for the increase. The breathing rate of the human subject in the experiment of Harley, Jetter, and Nelson was 5×10^3 cm^3/min. In addition, there may be some individual variation and possibly some species differences between the Ostwald coefficients of a tissue in a rat and in man. This discrepancy by a factor of 2.8 is well within the range of variation usually found in biological experiments. This possible overestimate of uptake and retention is accepted here because no biological data are known to the authors which might resolve the question and also because the model will be used principally to estimate retention of short-lived radionuclides. Such use may introduce another uncertainty in that, not only the activities in the various tissues, but also the time scale for their rate of buildup and removal are involved. This model, using the breathing rate for reference man, will now be extended to other inert gases, namely, xenon, krypton, and argon.

In the case of xenon, there are human data on concentration in fat and blood and plasma, but experimental data on tissue distribution have not been found (Snyder et al.[7]). The same is true of data on krypton; Ostwald coefficients for blood and oils and fats are available (Snyder et al.[7]). In the case of argon, the only data seem to be those obtained in laboratory studies by the chemists on uptake by water and olive oil (Lawrence et al.[8]). Lawrence[8] has chosen values of the Ostwald coefficients and has plotted them vs the molecular weight of the gas atoms; a version of this graph is seen in Fig. 20.3. As can be noted, the Ostwald coefficient for fat decreases more steeply with decrease in atomic weight than do the values for water or plasma. This has been known by chemists for many years, and they have expressed it in terms of the ratio of Ostwald coefficients in oil to that in water, which they called the oil-to-water partition coefficients (Lawrence et al.[8]). How should the mammillary model be modified to incorporate this effect?

Integration of Eq. (6) indicates that the equilibrium level of the gas in the total compartment system will decrease (in that the equilibrium level is given by the time integral out to 50 years) in inverse proportion to the elimination rate constants. Thus, if all the elimination constants are increased by a factor of 10, the concentration in the total body will decrease by a factor of 10. Actually, the elimination rate constants of all exponentials will be multiplied by the factor

7. W. S. Snyder et al., in *Symposium on Noble Gases, Las Vegas, Nevada, Sept. 24–28, 1973,* CONF-730915.

8. J. H. Lawrence et al., *J. Physiol. (London)* **105,** 197 (1940).

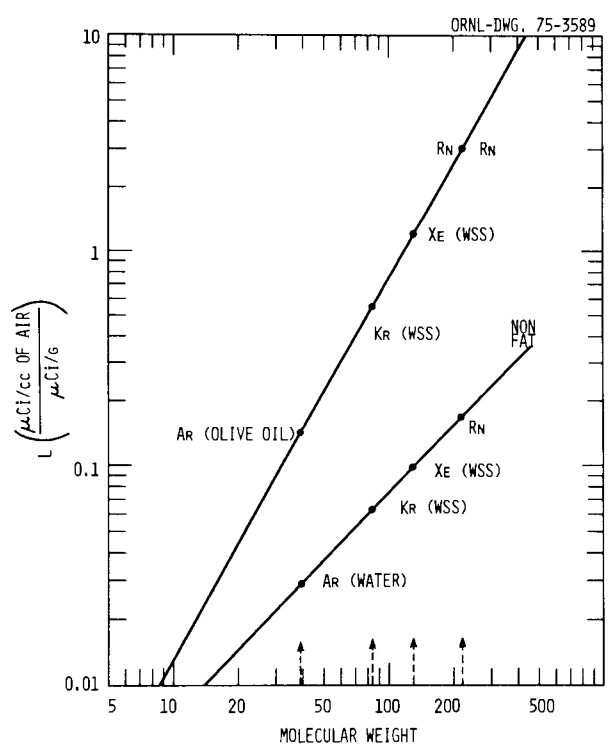

Fig. 20.3. Plot of L (the Ostwald solubility coefficient) for fatty tissues and oil and nonfat tissues vs molecular weight of the noble gas.

$(L_{Xe}/L_{Rn})_{nonfat}$, which is necessary to account for the value for nonfat tissues. The coefficients of the two longer-termed exponentials (which largely represent fat) are multiplied by the factor

$$\left(\frac{L_{Rn}}{L_{Xe}}\right)_{NF} \Big/ \left(\frac{L_{Rn}}{L_{Xe}}\right)_{F}.$$

The differences between these old and new coefficients are added to the coefficient of the shortest-term exponential. This is necessary in order that the sum of the coefficients adds to unity. For example, the ratio of L for xenon in nonfat tissue to that for radon in nonfat tissue is $\sim 0.15/0.08 \cong 2$. So, the elimination rate constants for radon are multiplied by a factor of 2. For the fatty tissue, the value of L for radon is ~5, while for xenon it is ~2 or a decrease by a factor of ~2.5 = $^5/_2$. Thus, to decrease the coefficients of the two long-term exponentials in the radon retention equation, the factor is 2/2.5 = 0.8. So, the two coefficients of the long-term exponentials of 0.005 and 0.009 are multiplied by 0.8 to obtain 0.004 and 0.0072 and the difference (0.005 − 0.004 and 0.009 − 0.0072), and these are added to the coefficient of the shortest-term exponential, whose value is 0.874, thus producing ~0.877. The general procedure is to obtain the ratio of the Ostwald coefficient for the fatty tissues, divide that ratio by the ratio of the Ostwald coefficient for the nonfatty tissues, decrease the coefficients of the two long-term exponentials by this latter factor, and place the difference in the coefficient of the shortest-term exponential. The above procedure is used to obtain retention equations for the other noble gases, xenon, krypton, and argon.

Tables 20.7 to 20.9 present the parameters of the total-body retention equations and the λ_{ij} for the mammillary model for xenon, krypton, and argon, respectively, as obtained from the radon equation for total-body retention. Tables 20.10 to 20.12 present the coefficients of the exponential terms C_{ji} for the compartments of the mammillary model for xenon, krypton, and argon, as obtained from the MAMX code. The values of l_{ij} in the three groups of tissues mentioned previously are shown for radon in Table 20.6. The equations for xenon, krypton, and argon in the three groups of tissues are not given but may be estimated similarly to the procedure that can be used to obtain the equations for radon in the three tissue groups. Thus a metabolic model is now available for internal dose estimation for a single intake, via inhalation of the radionuclides of radon, xenon, krypton, and argon. Needless to say, it must be remembered that only a limited amount of data have been found to generate these models. They need to be tested against the experimental data on man. No use of the diffusion coefficient for each of the noble gases has been made, and this might be a drawback for the above models. Further theoretical studies need to be carried out, coupled with an experimental program to provide better metabolic models for internal dose estimation.

The errors in Nussbaum's experimental data and the effect of the breathing rate on clearance of inert gas from the body need to be discussed. As regards the radon data on rats, Nussbaum did perform an experiment to estimate the loss of radon from the tissues. He estimated that on standing in the atmosphere for a period of $4^1/_2$ hr, not more than ~3% of the radon was lost from the dissected tissues. He is careful to point out that his estimates of L are probably underestimates rather than overestimates, for various reasons (Nussbaum[6]). As regards the effect of breathing rate on radon clearance and buildup in the human body, the equilibrium level is probably not affected. However, the rate of attainment of equilibrium and loss probably is slower for a slow breathing rate and higher for a high breathing rate. How the exhalation rate curve given by Harley, Jetter, and Nelson[4] for a breathing rate of 5 liters/min would be shifted to a different rate needs to be tested on man, and the effect on the deconvolution process also needs to be checked.

Table 20.7. Mammillary model for retention of xenon following a single inhalation by man[a]

b_1	b_2	b_3	b_4	b_5
3.00×10^{-3}	5.40×10^{-3}	2.00×10^{-2}	9.20×10^{-2}	8.80×10^{-1}
λ_1	λ_2	λ_3	λ_4	λ_5
7.50×10^{-4}	4.94×10^{-3}	2.53×10^{-2}	2.33×10^{-1}	2.70
λ_{11}	λ_{12}	λ_{13}	λ_{14}	λ_{15}
2.68	7.52×10^{-4}	4.97×10^{-3}	2.58×10^{-2}	2.55×10^{-1}
λ_{11}	λ_{21}	λ_{31}	λ_{41}	λ_{51}
2.68	7.18×10^{-3}	1.29×10^{-2}	4.79×10^{-2}	2.13×10^{-1}

[a]Units on λ's are reciprocal minutes.

Table 20.8. Mammillary model for retention of krypton following a single inhalation by man[a]

b_1	b_2	b_3	b_4	b_5
1.50×10^{-3}	2.70×10^{-3}	2.00×10^{-2}	9.20×10^{-2}	8.63×10^{-1}
λ_1	λ_2	λ_3	λ_4	λ_5
1.50×10^{-3}	9.87×10^{-3}	5.06×10^{-2}	4.65×10^{-1}	5.46
λ_{11}	λ_{12}	λ_{13}	λ_{14}	λ_{15}
5.41	1.50×10^{-3}	9.90×10^{-3}	5.16×10^{-2}	5.09×10^{-1}
λ_{11}	λ_{21}	λ_{31}	λ_{41}	λ_{51}
5.41	7.29×10^{-3}	1.30×10^{-2}	9.64×10^{-2}	4.29×10^{-1}

[a]Units on λ's are reciprocal minutes.

Table 20.9. Mammillary model for retention of argon following a single inhalation by man[a]

b_1	b_2	b_3	b_4	b_5
8.00×10^{-4}	1.50×10^{-3}	2.05×10^{-2}	9.20×10^{-2}	8.86×10^{-1}
λ_1	λ_2	λ_3	λ_4	λ_5
2.50×10^{-3}	1.65×10^{-2}	8.43×10^{-2}	7.75×10^{-1}	9.10
λ_{11}	λ_{12}	λ_{13}	λ_{14}	λ_{15}
1.81×10^{-1}	5.00×10^{-3}	3.29×10^{-2}	1.72×10^{-1}	1.70
λ_{11}	λ_{21}	λ_{31}	λ_{41}	λ_{51}
1.81×10^{-1}	1.38×10^{-2}	2.40×10^{-2}	3.28×10^{-1}	1.43

[a]Units on λ's are reciprocal minutes.

Table 20.10. C_{ji} matrix for xenon retention in man

9.31×10^{-7}	1.11×10^{-5}	2.11×10^{-4}	8.92×10^{-3}	9.91×10^{-1}
2.96×10^{-3}	-1.91×10^{-5}	-6.18×10^{-5}	-2.77×10^{-4}	-2.64×10^{-3}
2.87×10^{-6}	5.37×10^{-3}	-1.34×10^{-4}	-5.05×10^{-4}	-4.74×10^{-4}
1.79×10^{-6}	2.56×10^{-5}	1.98×10^{-2}	-2.07×10^{-3}	-1.77×10^{-2}
7.88×10^{-7}	9.48×10^{-6}	1.96×10^{-2}	8.59×10^{-2}	-8.61×10^{-2}

Table 20.11. C_{ji} matrix for krypton retention in man

4.62×10^{-7}	5.47×10^{-6}	2.08×10^{-4}	8.79×10^{-3}	9.91×10^{-1}
1.50×10^{-3}	-4.76×10^{-6}	-3.09×10^{-5}	-1.38×10^{-4}	-1.33×10^{-3}
7.16×10^{-7}	2.88×10^{-3}	-6.64×10^{-5}	-2.51×10^{-4}	-2.37×10^{-3}
8.89×10^{-7}	1.26×10^{-5}	1.99×10^{-2}	-2.05×10^{-3}	-1.77×10^{-3}
3.91×10^{-7}	4.70×10^{-6}	1.94×10^{-4}	8.56×10^{-2}	-8.59×10^{-2}

Table 20.12. C_{ji} matrix for argon retention in man

2.46×10^{-7}	3.03×10^{-6}	2.12×10^{-4}	8.77×10^{-3}	9.91×10^{-1}
7.98×10^{-4}	-1.41×10^{-6}	-1.68×10^{-5}	-7.36×10^{-5}	-7.07×10^{-4}
2.12×10^{-7}	1.49×10^{-3}	-3.77×10^{-5}	-1.39×10^{-4}	-1.31×10^{-3}
4.83×10^{-7}	7.16×10^{-6}	2.01×10^{-2}	-2.09×10^{-3}	-1.81×10^{-2}
2.07×10^{-7}	2.60×10^{-6}	1.98×10^{-4}	8.55×10^{-2}	-8.57×10^{-2}

21. Tabulations of Average Dose Equivalent Due to Residence of Radionuclides in Body Organs of an Adult

W. S. Snyder[1] M. R. Ford G. G. Warner[2] S. B. Watson[2]

The report ORNL-5000[3] was published to make the dosimetric data on internal emitters, which had been compiled by the authors over a period of some five years, more readily available for use in calculations of dose by health physicists. Users of the report will still need a retention model which will enable them to compute the microcurie-days, U, accumulated in the various organs. However, when such a model is given, the dose equivalent from source organ Y to target organ X is obtained as

$$\mathrm{DE}(X \leftarrow Y) = U \times S(X \leftarrow Y) \quad \text{rems},$$

where $S(X \leftarrow Y)$ is tabulated in the report. The target and source organs include most of the organs used by the National Council on Radiation Protection and Measurements (NCRP) and the International Commission on Radiological Protection (ICRP) in specifying the annual dose limits. Generally, one will require a sum of such terms over all the source organs contributing significantly to dose. In principle, the new report replaces MIRD Pamphlet No. 5 (ref. 4) but spares the user the necessity of making detailed calculations for the many particles occurring in most decay schemes. The present report contains a complete text on the methodology and, in addition, has data on 60 radionuclides. A second volume is in the final stage of publication which will have data on 100 radionuclides, and further volumes in the ORNL-5000 series are planned. Also, the Medical Internal Radiation Dose (MIRD) Pamphlet No. 11, in publication, contains similar data for about 100 radionuclides of interest in nuclear medicine. The text of the pamphlet conforms to the MIRD formulism, and it contains much less detail than the ORNL-5000 text.

The dosimetric data on photons are the results of a Monte Carlo-type calculation based on a nonhomogeneous phantom having the general form of the human body but omitting many details, for example, fingers, ears, nose, etc. The phantom is composed of three tissue types – lungs, skeletal tissue, and general soft tissue. These have densities of approximately 0.3, 1.5, and 1 g/cm^3, respectively. The skeletal tissues include the bone marrow and cartilage as well as bone per se, and these are homogenized and thus have a density less than that of bone. It is assumed the skeletal tissues absorb energy in proportion to their masses. Each absorbed fraction which is accepted is the result of a computation with a sample size of 60,000 photons and has a coefficient of variation of not more than 50%. When the absorbed fractions fail to meet the above criterion, they are replaced by an absorbed fraction calculated by use of the buildup factor for an infinite medium. Evidence is presented in the report that these are seldom, if ever, in error by more than a factor of 2 and are usually accurate to approximately 30%.

The design of the phantom has been changed since the publication of MIRD Pamphlet No. 5. The legs have been separated, thus providing for a more exposed position of the testes. The top of the head has been rounded, thus removing some excess of soft tissue. These changes are of more importance for estimation of dose from external sources than from internal sources. In addition, distributions of red and of yellow marrow are included, and calculated results are available for

1. Consultant.
2. Computer Sciences Division.
3. W. S. Snyder, Mary R. Ford, G. G. Warner, and Sarah B. Watson, *A Tabulation of Dose Equivalent per Microcurie-Day for Source and Target Organs of an Adult for Various Radionuclides*, ORNL-5000 (1974).
4. W. S. Snyder, M. R. Ford, G. G. Warner, and H. L. Fisher, Jr., "Estimates of Absorbed Fractions for Monoenergetic Photon Sources Uniformly Distributed in Various Organs of a Heterogeneous Phantom," MIRD Pamphlet No. 5, *J. Nucl. Med., Suppl. No. 3*, 10 (August 1969).

these as source and as target tissues. The skeleton has been changed to include clavicles and scapulae, since these bones contain a fair amount of red marrow. All the Monte Carlo values for photons are based on the use of this new phantom.

In addition to organs specifically designed in the phantom, results are given for a number of other tissues, for example, muscle and fat; neither is specifically designed as a portion of the phantom. However, both are of rather general distribution in the "other tissues" compartment, which consists of what is left of the phantom when all designated organs are removed. Results on this "other tissue" compartment are scaled to obtain results approximately valid for muscle and fat. The limitations of this and other procedures used for extrapolation of the direct results are discussed in a section of the report.

For most organs the dosimetry of beta particles, or electrons, amounts to complete absorption of energy in the source organ. However, there are a number of cases where source and target tissues are close enough that irradiation by electrons outside the target tissue is considered. These include the walled organs (sections of the gastrointestinal tract and bladder) with the source in the contents, as well as red and yellow marrow and bone, which are so closely intermixed that dose from electrons must be considered. For the walled organs, a surface dose is calculated. However, for the source in bone and with red marrow or endosteal cells near bone surfaces as the target, the dosimetry of Spiers[5] is used. When red or yellow marrow is the source tissue, an approximate absorbed fraction is obtained by consideration of the Spiers dosimetry. The formulas, while not highly accurate, are not expected to lead to serious difficulties for radionuclides if their decay constants are sufficiently long that the uniform distribution assumed by Spiers is valid.

For alpha particles, complete absorption of energy is assumed. However, an exception occurs when the emitter is in the contents of the gastrointestinal tract, in which case only 1% of the energy is assumed to apply to the crypt cells. This follows ICRP practice. When the alpha emitter is in bone, a factor of $n = 5$ is used, in addition to the quality factor $Q = 10$. This use is not entirely that of ICRP, although the only exception is for the isotopes of radium. Here, ICRP recommendations indicate that, if the radium isotope is the parent, $n = 1$ should be used; while, if the radium isotope is a daughter, $n = 5$ should be used for its alpha radiation. Since only one table of S values is given, one must choose which prescription will be followed; and, in this report, $n = 5$ is used for all alpha emitters in bone. The user can easily make the proper correction for his case, since the S values for photons, for electrons, for alpha radiation, and for recoil nuclei are listed separately; and the total also is given.

From the listed values of S, one can, by addition or subtraction, derive many more which represent dose to various portions of the body. It is pointed out that since the value of S is always subject to some uncertainty, for example, use of the buildup factor, results obtained in this way may sometimes give absurd results. One such example has been found and is being remedied in the volumes now in publication. In estimating the dose with red marrow as source and target organ, the term representing the dose from cortical bone to red marrow is included, although by itself it makes a small contribution to the dose. However, in some cases the other terms cancel out, and thus one needs this term to prevent acceptance of a spurious result. Such cases have only been found when the values of S are subtracted to correspond to restricted portions of the body, for example, total body minus the skeleton. Also included in the volumes in press are several radionuclides where the parent has a daughter radionuclide of physical half-life less than 5 min. In such cases, not only are S tables given for the parent and for the daughter, but also a composite table listing the S values for parent plus daughter is given. The composite table is included for convenience in these cases and should be used only when the microcurie-days of the parent and daughter are assumed to be those indicated in the table.

5. F. W. Spiers, *Radioisotopes in the Human Body, Physical and Biological Aspects,* Academic Press, New York, 1968.

22. Variation of the Absorbed Fraction with Shape and Size of the Thyroid

M. R. Ford W. S. Snyder[1] G. G. Warner[2]

The estimation of dose from internal emitters requires knowledge of the fraction of energy absorbed in the organ of interest. The authors[3] have published absorbed fractions of photon energy for a variety of body organs, including the thyroid. These estimates were all based on organs of typical size and shape, however, and it is known that the thyroid, in particular, is quite variable in size as well as in shape. In fact, in some cases the thyroid seems best described as occupying whatever space it can find.

Figure 22.1 is a plot of data from the ICRP Report on a Reference Man[4] showing the weight of the normal thyroid as a function of age and sex. The dashed lines indicate plus or minus one standard deviation of the values for the different ages. Based on these and other data, the Reference Man report gives 20 g as the weight of the thyroid for males and 17 g for females, although there are indications that these values are perhaps a little high for the U.S. population.

Some of the various shapes of the normal gland are shown in Fig. 22.2. Generally, it consists of two lateral lobes located on either side of the upper trachea and lower larynx, connected by an isthmus lying ventral to the upper trachea. The isthmus may vary in size and outline from rather voluminous, with an extension known as a pyramidal lobe that occurs in about one-third of the population,[5] to a thin band in some

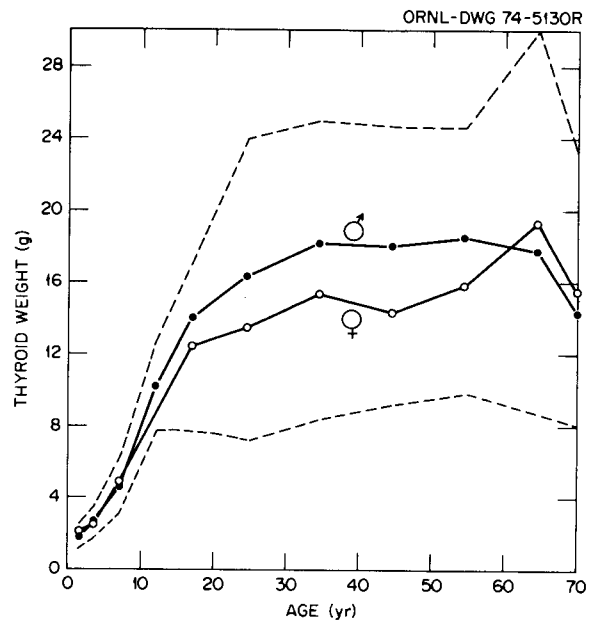

Fig. 22.1. Weight of the thyroid as a function of age and sex. Data from ICRP Reference Man report, 1975 (ref. 4).

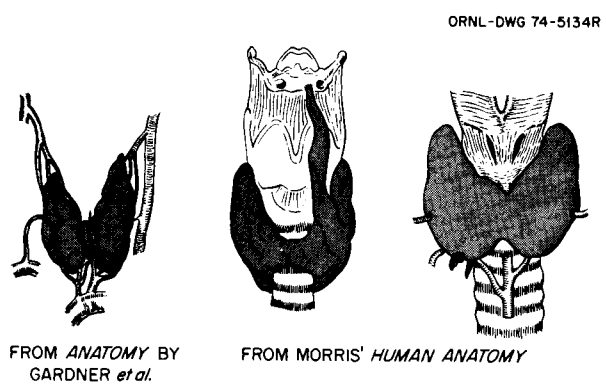

Fig. 22.2. Various shapes of the thyroid.

1. Consultant.
2. Computer Sciences Division.
3. W. S. Snyder, Mary R. Ford, G. G. Warner, and H. L. Fisher, Jr., "Estimates of Absorbed Fractions for Monoenergetic Photon Sources Uniformly Distributed in Various Organs of a Heterogeneous Phantom," MIRD Pamphlet No. 5, *J. Nucl. Med. Suppl. No. 3,* 5 (1969).
4. W. S. Snyder, chairman, *Report of the Task Group on Reference Man,* ICRP Report No. 23, Pergamon Press, 1975.
5. B. J. Anson, ed., *Human Anatomy,* 12th ed., 1966, p. 1547.

individuals; or it may be completely absent in others. The lobes may be of different lengths, or one or both may be absent.

Because of the great importance of iodine when used therapeutically and because of its importance in reactor siting, it is of interest to explore the variation of dose (or, alternately, the absorbed fraction) from the thyroid to itself in various cases.

To get an idea of the influence that the shape as well as the size might have on the absorbed fraction, we designed the models shown in Fig. 22.3. In general, each lobe is represented by half an ellipsoid of a circular cross section topped by a right circular cone, and we have used three basic shapes for each of three weights, namely, for 10, 20, and 30 g. In one of the configurations, the lobes are symmetrical; in another, the upper portion of one lobe is missing; and in the third design, one lobe is shrunken while the other is enlarged. Of course, the relative dimensions change to keep the masses constant for the three cases.

Estimates of the specific absorbed fraction (i.e., the absorbed fraction divided by the mass) were made by the buildup factor method described in previous

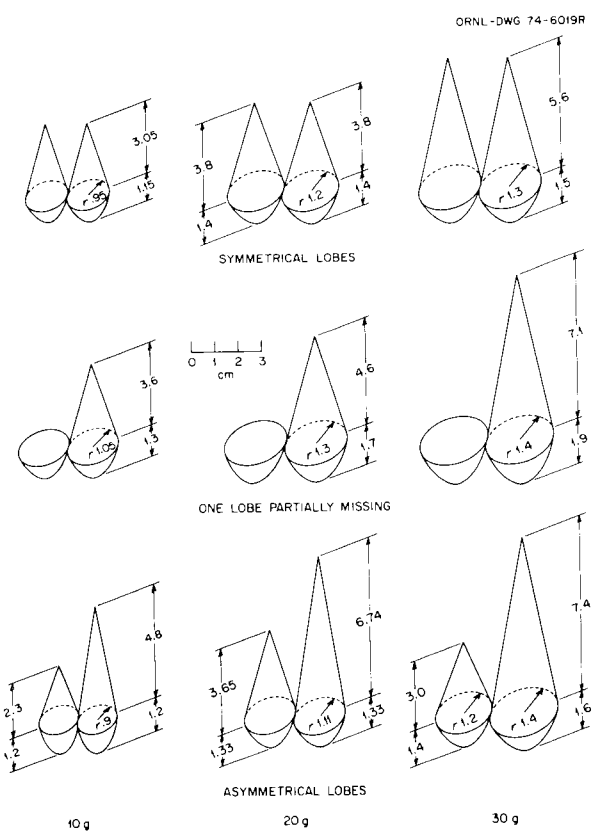

Fig. 22.3. Model thyroids of various sizes and shapes.

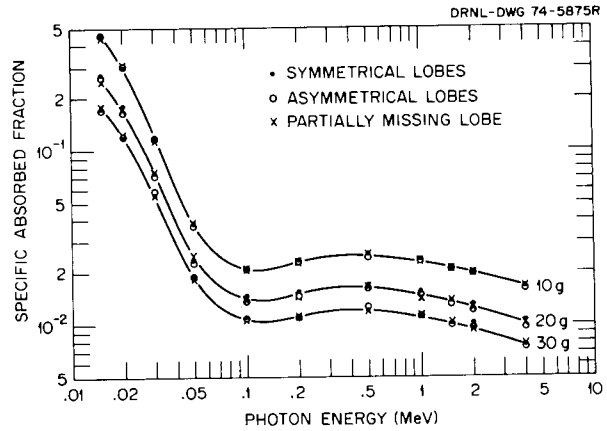

Fig. 22.4. Specific absorbed fractions as a function of photon energy and size and shape of the thyroid. Source in thyroid.

studies.[6] The estimates were made at 11 photon energies for each of the three shapes and sizes, that is, for the nine different models, and the results are displayed in Fig. 22.4. The values are distinct for the three sizes, but the shape seems to make little difference. The greatest difference to be noted, in any case, between the three shapes is 9.3%; and, generally, the difference is much less. The coefficient of variation is not shown, but it is typically about 2% and in no case exceeds 5%.

The specific absorbed fractions as a function of organ mass are presented in Fig. 22.5. It will be noted that the same general relationship reported in a previous study[7] for different age phantoms seems to hold also for organs of various size – the specific absorbed fraction (SAF) for a given energy decreases as organ size increases, the SAF for a particular size decreases as energy increases, and the ratios of SAF for a smaller to a larger organ decrease as the size increases. For example, at 0.02 MeV the ratios of the 10- and 20-g thyroids to the 30-g thyroid are, respectively, 2.5 and 1.5.

Also, as seen in Fig. 22.6, these data for the thyroid support the principle noted in previous studies[7] that for uniform deposition in an organ the absorbed fraction, except at low energies, varies with the cube root of the mass. Here the ratio of AF to $\mu_{ab}M^{1/3}$ is plotted as a

6. W. S. Snyder, M. R. Ford, and G. G. Warner, "Estimates of Absorbed Fractions for Photon Emitters within the Body," *Health Phys. Div. Annu. Progr. Rep. July 31, 1972,* ORNL-4811, p. 86.

7. M. J. C. Hilyer, W. S. Snyder, and G. G. Warner, "Estimates of Dose to Infants and Children from a Photon Emitter in the Lungs," *Health Phys. Div. Annu. Progr. Rep. July 31, 1972,* ORNL-4811, p. 91.

function of energy for the various-size thyroids. Points are plotted only for the thyroids of one shape for the three weights, but values for the other shapes are within 8% of those shown. In all cases, the ratios are approximately constant for photon energies above 0.2 MeV; and at lower energies the rule cannot be expected to hold, since the AF is approaching 1 and thus cannot continue to increase substantially. On the other hand, μ_{ab} increases rapidly as the energy decreases below 100 keV.

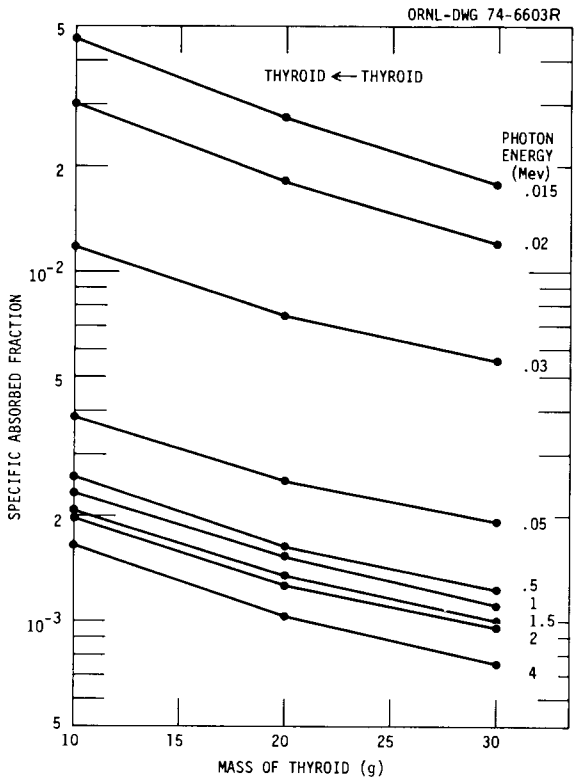

Fig. 22.5. Specific absorbed fractions as a function of photon energy and size of the thyroid. Source in thyroid.

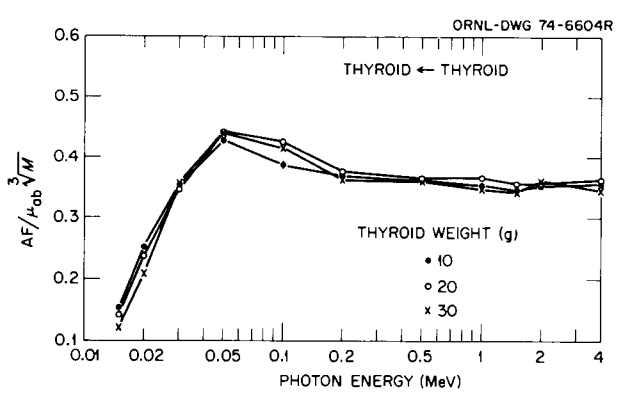

Fig. 22.6. Absorbed fractions as a function of photon energy and size of the thyroid. Source in thyroid.

The absorbed fractions discussed thus far pertain to photon emitters only. However, if one makes the usual assumption of complete absorption of electron energy in the organ containing the source, our estimates indicate that from 70 to 95% of the dose from iodine in the thyroid is due to beta radiation. We asked ourselves, How valid is the practice of assuming complete absorption of electron radiation, that is, of taking the absorbed fraction equal to 1?

To explore this question, we have made use of a Monte Carlo technique for estimating absorbed fractions of electrons by use of Berger's point-source formula given in MIRD Pamphlet No. 7 (ref. 8). The method is developed in the Appendix to this section. Integrating this formula over the source and target organs yields statistically reliable absorbed fractions for those organs. Thus, computations were made for the adult thyroids of various sizes and shapes, described earlier, at nine electron energies ranging from 0.025 to 4 MeV; and, as shown in Fig. 22.7, the results indicate practically complete absorption, that is, above 95% for energies below 0.2 MeV. The data shown here are the three estimates of absorbed fractions for thyroids of different shapes having a mass of 10 g, and only the

8. M. J. Berger, "Distribution of Absorbed Dose around Point Sources of Electron and Beta Particles in Water and Other Media," MIRD Pamphlet No. 7, *J. Nucl. Med. Suppl. No. 5* (1971).

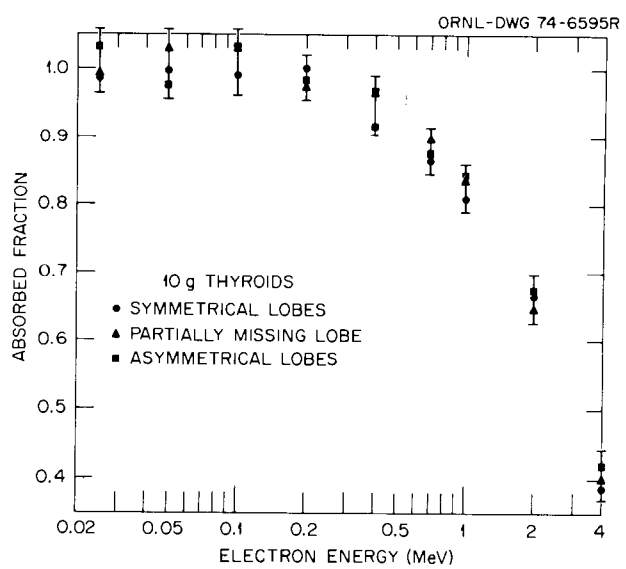

Fig. 22.7. Absorbed fractions as a function of electron energy and the shape of the thyroid. Source in thyroid.

maximum standard deviations are shown. Corresponding data for the 20- and 30-g thyroids are almost identical to these data. Above 0.2 MeV, absorption decreases as energy increases, so that the absorbed fraction at 1 MeV is about 82% and at 4 MeV about 40%. Most of the iodine isotopes, however, do not emit significant electron energy in this range.

We have computed the electron absorbed fraction in the typical adult thyroid of our reference-man phantom for the beta spectra of five iodine isotopes, namely, ^{123}I, ^{124}I, ^{125}I, ^{126}I, and ^{131}I, and find practically complete absorption of electron energies in all cases except for ^{124}I. This is not surprising, since a significant fraction of the energy of the electrons emitted by ^{124}I is in excess of 1 MeV. In the case of ^{124}I, electron absorption was found to be about 86%, which decreases the total dose by only about 10% since beta decay is a rather small fraction of the total. For all other isotopes the total dose computed, assuming complete absorption of electrons, was accurate to within 5%.

These studies are being extended to include absorbed fractions of photon and electron energies in thyroids of children. So far, taking the worst cases, we find from 70 to 80% of the total electron energies emitted by ^{124}I are absorbed in thyroids of 1 to 3 g, and absorption of the other isotopes is even greater. In the case of photons, absorbed fractions have been estimated at 12 monoenergetic photon energies with the source in the thyroids of anthropomorphic phantoms described in previous studies,[9,10] corresponding to children of various ages. The results, together with the coefficients of variation ($100\sigma_\phi/\phi$) and the masses of the phantom thyroids, are displayed in Table 22.1. For comparison, absorbed fractions for the adult phantom thyroid are also shown. It can be seen that the absorbed fractions from the smallest to the largest thyroid at any energy differ by only a factor of 2 at most. However, the thyroid masses in the child phantoms seem somewhat high compared with values noted in the literature.[4] As discussed in previous studies,[9,10] the phantoms representing the younger ages were obtained by transforming the adult phantom by scale factors selected separately for the head, trunk, and leg section of the phantom, with all internal organs being reduced by the scale factors for the section in which they lie. This procedure is only approximate, and, in fact, calculations for

9. M. J. C. Hilyer, G. S. Hill, and G. G. Warner, "Dose from Photon Emitters Distributed Uniformly in the Total Body as a Function of Age," *Health Phys. Div. Annu. Progr. Rep. July 31, 1973,* ORNL-4903, p. 119.

10. G. G. Warner, J. W. Poston, and W. S. Snyder, "Absorbed Dose in Male Humanoid Phantoms from External Sources of Photons as a Function of Age," *Health Phys. Div. Annu. Progr. Rep. July 31, 1974,* ORNL-4979, p. 40.

Table 22.1. Absorbed fractions in the thyroid as a function of age for various monoenergetic photon sources present in the thyroid

Phantom age (years)	Thyroid mass (g)	Absorbed fraction (AF) for photon energy of –											
		0.01 MeV		0.015 MeV		0.02 MeV		0.03 MeV		0.05 MeV		0.1 MeV	
		AF	CV[a]	AF	CV	AF	CV	AF	CV	AF	CV	AF	CV
Newborn	3.4	0.74	0.2	0.42	0.4	0.23	0.6	0.079	0.9	0.024	1.2	0.015	1.5
1	8.5	0.80	0.2	0.51	0.4	0.29	0.5	0.11	0.8	0.034	1.0	0.020	1.3
5	11	0.81	0.2	0.53	0.4	0.31	0.5	0.12	0.8	0.037	1.0	0.022	1.3
10	13	0.82	0.2	0.54	0.4	0.32	0.5	0.12	0.7	0.040	1.0	0.023	1.2
15	17	0.83	0.2	0.56	0.3	0.34	0.5	0.14	0.7	0.044	0.9	0.026	1.1
Adult	20	0.84	0.2	0.58	0.3	0.36	0.5	0.15	0.7	0.047	0.9	0.028	1.1

Phantom age (years)	Thyroid mass (g)	Absorbed fraction (AF) for photon energy of –											
		0.2 MeV		0.5 MeV		1.0 MeV		1.5 MeV		2.0 MeV		4.0 MeV	
		AF	CV	AF	CV	AF	CV	AF	CV	AF	CV	AF	CV
Newborn	3.4	0.017	1.7	0.018	2.1	0.017	2.4	0.015	2.7	0.014	2.8	0.012	3.2
1	8.5	0.023	1.5	0.025	1.8	0.023	2.0	0.021	2.2	0.019	2.4	0.016	2.7
5	11	0.025	1.4	0.027	1.7	0.026	1.9	0.022	2.2	0.020	2.3	0.017	2.6
10	13	0.026	1.4	0.028	1.6	0.026	1.9	0.023	2.1	0.020	2.3	0.018	2.6
15	17	0.029	1.3	0.031	1.6	0.028	1.8	0.026	2.0	0.023	2.2	0.020	2.5
Adult	20	0.030	1.3	0.033	1.5	0.030	1.8	0.029	1.9	0.026	2.1	0.021	2.4

[a]Coefficient of variation ($CV = 100\sigma_\phi/\phi$).

Table 22.2. Specific absorbed fractions of various monoenergetic photons in the thyroid and total body of a one-year-old child

Photon energy (MeV)	Specific absorbed fraction		
	Thyroid → total body or total body → thyroid	Total body → total body	Thyroid → thyroid
0.01	1.1×10^{-4}	9.2×10^{-5}	2.6×10^{-1}
0.015	1.1×10^{-4}	8.8×10^{-5}	1.4×10^{-1}
0.02	9.9×10^{-5}	8.1×10^{-5}	8.0×10^{-2}
0.03	7.5×10^{-5}	6.4×10^{-5}	2.9×10^{-2}
0.5	4.3×10^{-5}	3.7×10^{-5}	9.0×10^{-3}
0.1	2.6×10^{-5}	2.1×10^{-5}	5.2×10^{-3}
0.2	2.4×10^{-5}	2.0×10^{-5}	5.6×10^{-3}
0.5	2.5×10^{-5}	2.1×10^{-5}	6.2×10^{-3}
1.0	2.3×10^{-5}	2.0×10^{-5}	5.8×10^{-3}
1.5	2.1×10^{-5}	1.8×10^{-5}	5.4×10^{-3}
2.0	2.0×10^{-5}	1.7×10^{-5}	4.9×10^{-3}
4.0	1.7×10^{-5}	1.4×10^{-5}	3.9×10^{-3}

infants are often based on a one-year-old child with a 2-g thyroid. Therefore, it may be of some interest to give a more precise value for a thyroid of this mass (see, for example, ref. 11, p. 23). Iodine taken into the body enters the blood pool, and the subsequent metabolism is virtually independent of the original form of the compound in most instances.[12-14] However, the usual models for metabolism[15,16] all agree in assigning the iodine atoms to the thyroid or to tissues which are relatively uniformly distributed in the body. This is not to be taken to imply that the chemical form is the same, and there do exist some tissues which appear to store iodine at higher levels; but for the most part the above simplified model of a fraction of the activity in the thyroid and the remainder generally distributed throughout the body suffices.[12]

Thus, to supply the needs of dosimetry, one needs the dose for the activity in the thyroid and the dose from activity distributed throughout the total body. In both cases we neglect the microdistribution of the iodine – for example, in the follicles of the thyroid, which are important if microdosimetry is attempted – and only consider the average dose due to each of the two source distributions in the thyroid and in the total body. This average dose to an organ is the dose used in the recommendations of NCRP and ICRP.

To meet these needs of dosimetry, the specific absorbed fraction is given in Table 22.2 for a photon emitter uniformly distributed in a 2-g thyroid, and for the same emitter uniformly distributed in the total body of mass 9.1 kg. These values were obtained by Monte Carlo calculations for all the data in the table except that with total body as source and thyroid as target. In this instance, the data were statistically erratic due to the small size of the thyroid; and, consequently, the specific absorbed fractions from thyroid to total body were used by reciprocity. These values are also reasonably close to what would be obtained by use of the buildup factor.[17] For the various isotopes of iodine, the dose due to each photon emitted in the decay scheme can be obtained by an interpolation.

Appendix

ABSORBED FRACTION OF ELECTRON AND BETA ENERGIES

The absorbed fraction, ϕ, of electron energy for a target region R_2, with a distributed source in a region

11. "Estimates and Evaluation of Fallout in the United States from Nuclear Weapons Testing Conducted through 1962," Report No. 4 of the Federal Radiation Council, U.S. Government Printing Office.
12. L. Van Middelsworth, *Health Phys.* **9**, 1197 (1963).
13. E. W. Bretthauer, A. L. Mullen, and A. A. Moghissi, *Health Phys.* **22**, 257 (1972).
14. A. Morgan, D. J. Morgan, J. C. Evans, and B. A. J. Lister, *Health Phys.* **13**, 1067 (1967).
15. D. S. Riggs, *J. Clin. Endocrinol. Metab.* **11**, 1095 (1951).
16. M. Berman and R. Schoenfeld, *J. Appl. Phys.* **27***(11)*, 1361 (1956).
17. W. S. Snyder, M. R. Ford, G. G. Warner, and Sarah B. Watson, "A Tabulation of Dose Equivalent per Microcurie-Day for Source and Target Organs of an Adult for Various Radionuclides," ORNL-5000 (November 1974).

R_1, can be estimated by use of Berger's kernel for a point source of monoenergetic electrons.[8] Although the primary source of the data is L. V. Spencer,[18] it is Berger's formulation and tabulation we use. Equation (14*a*) of MIRD Pamphlet No. 7 (ref. 8) expresses the specific absorbed fraction (absorbed fraction of energy per gram) in terms of a tabulated quantity $F(\xi, E_0)$, specifically

$$F(\xi, E_0) = 4\pi\rho X^2 X_{90}\, \Phi(X, E_0)\,, \tag{1}$$

where ρ is the density (g/cm^3), X is the distance from the point source (cm), X_{90} is the 90-percentile of the energy distribution, E_0 is the initial energy, $\Phi(X, E_0)$ is the fraction of energy absorbed per gram at distance X from the point source, and $\xi = X/X_{90}$. The procedure for estimating ϕ, or alternatively Φ, for a distributed source R_1 and for a target region R_2 will be described in terms of Φ, but for calculation one will express the results in terms of $F(\xi, E_0)$.

Assuming the electron of energy E_0 originates at the origin of the coordinate system, the fraction of energy absorbed in a volume element $\mathbf{dX}$ about $\mathbf{X}$ is given by

$$d\phi(\mathbf{X}) = \rho\, \mathbf{dX}\, \Phi(\mathbf{X}, E_0)\,. \tag{2}$$

Integrating this over the target region R_2, one obtains an absorbed fraction for a point source at the origin,

$$\phi(R_2 \leftarrow \mathbf{0}) = \rho \int_{R_2} \mathbf{dX}\, \Phi(\mathbf{X}, E_0)\,. \tag{3}$$

To obtain the absorbed fraction $\phi(R_2 \leftarrow R_1)$ for the source uniformly distributed throughout R_1, say at 1 μCi/g, we need to integrate formula (3) over R_1. Using the vector $\mathbf{Y}$ to designate the position of an infinitesimal source volume $\mathbf{dY}$,

$$\phi(R_2 \leftarrow R_1) = \frac{\rho}{\rho|R_1|} \times \int_{R_1} \rho\, \mathbf{dY} \int_{R_2} \mathbf{dX}\, \Phi(|\mathbf{X} - \mathbf{Y}|, E_0)\,, \tag{4}$$

where $|\mathbf{X} - \mathbf{Y}|$ denotes the length of the position vector $\mathbf{X} - \mathbf{Y}$ and $\rho|R_1|$ is the mass of region R_1, which is proportional to the energy emitted. Since $\Phi(|\mathbf{X} - \mathbf{Y}|, E) = 0$ when $|\mathbf{X} - \mathbf{Y}| > R$ = the range of the electron, one may avoid specifying complicated limits of integration by use of the characteristic function of region R_2, $\chi_{R_2}(\mathbf{X})$, which equals 1 or 0 according as $\mathbf{X}$ is in R_2 or not.

18. L. V. Spencer, "Energy Dissipation by Fast Electrons," National Bureau of Standards Monograph No. 1, 1959.

Thus,

$$\phi(R_2 \leftarrow R_1) = \frac{\rho}{|R_1|} \times \int_{R_1} \mathbf{dY} \int_{|\mathbf{X}-\mathbf{Y}| \leqslant R} \mathbf{dX}\, \Phi(|\mathbf{X} - \mathbf{Y}|, E_0)\, \chi_{R_2}(\mathbf{X})\,. \tag{5}$$

In practice, data on Φ, or equivalently on $F(\xi, E_0)$, are available for water, although attenuation factors for some other materials are given. For example, for muscle these amount to 98.4% or more of the values for water, and this correction was made to the value computed for water. In what follows, $\rho = 1$ will be used, so that data given by the formulas are for water without correction to values for muscle.

The integral is evaluated by Monte Carlo techniques. It is well known that if N sample points are selected from a region K and if $f(\mathbf{X}_i)$ is computed for each sample point $\mathbf{X}_i$, then

$$\frac{1}{N}\sum_{i=1}^{N} f(\mathbf{X}_i) \rightarrow \frac{1}{|K|}\int_K \mathbf{dX} f(\mathbf{X})\,. \tag{6}$$

In our case the region being sampled is $R_1 \times S$, where S is a sphere of radius equal to the range of the electron, and a point of this cross-product space is given as a pair of points $(\mathbf{X}, \mathbf{Y})$, $\mathbf{Y}$ being in R_1 and $\mathbf{X}$ in the sphere $|\mathbf{X} - \mathbf{Y}| \leqslant R$. Thus,

$$\frac{1}{N}\sum_{i=1}^{N} \Phi(|\mathbf{X}_i - \mathbf{Y}_i|, E_0)\, \chi_{R_2}(\mathbf{X}_i) \rightarrow \frac{1}{|R_1|4\pi R^3/3}\int_{R_1} \mathbf{dY} \int_{|\mathbf{X}-\mathbf{Y}| \leqslant R} \mathbf{dX}\, \Phi(|\mathbf{X} - \mathbf{Y}|, E_0) \times \chi_{R_2}(\mathbf{X}) = \frac{\phi(R_2 \leftarrow R_1)}{4\pi R^3/3}\,. \tag{7}$$

Similarly, one may, for each point $\mathbf{Y}_i$ chosen in R_1, select a fixed number k of points $\mathbf{X}_{i1}, \mathbf{X}_{i2}, \ldots, \mathbf{X}_{ik}$ in $|\mathbf{Y}_i - \mathbf{X}_{ij}| < R$ and evaluate

$$\frac{1}{NK}\sum_{i=1}^{N}\sum_{j=1}^{N} \Phi(|\mathbf{X}_{ij} - \mathbf{Y}_i|, E_0)\, \chi_{R_2}(\mathbf{X}_{ij}) \rightarrow \frac{\phi(R_2 \leftarrow R_1)}{4\pi R^3/3}\,. \tag{8}$$

as an alternative.

One difficulty with this approach is that the integrand is singular, although it is an integrable singularity. Still,

it is possible that a single choice of the points $\mathbf{X}_i$ and $\mathbf{Y}_i$, if the distance $|\mathbf{X}_i - \mathbf{Y}_i|$ is close to zero, may contribute a large amount to the value of ϕ. Of course, this can happen only when R_1 and R_2 have some common portion; but it is expected that the procedure should apply even when R_1 coincides with R_2. To avoid this difficulty, the value of $\Phi(|\mathbf{X}_i - \mathbf{Y}_i|, E_0)$ is replaced by its average value over a small sphere of radius r, which is yet to be specified. Thus, if $|\mathbf{X}_i - \mathbf{Y}_i| \leqslant r$, $\Phi(|\mathbf{X}_i - \mathbf{Y}_i|, E_0)$ will be replaced by

$$\hat{\Phi}(|\mathbf{X}_i - \mathbf{Y}_i|, E_0) = \frac{3}{4\pi r^3} \int_{|\mathbf{X}-\mathbf{Y}_i|<r} \mathbf{dX}\, \Phi(|\mathbf{X} - \mathbf{Y}_i|)$$

$$= \frac{3}{4\pi r^3 X_{90}} \int_0^r \mathbf{dX}\, F\left(\frac{\mathbf{X}}{X_{90}}, E_0\right) = \frac{3\bar{F}}{4\pi r^2 X_{90}}, \quad (9)$$

where $\bar{F}$ is the average value of $F(\xi, E_0)$ over the interval $0 \leqslant \xi \leqslant r/X_{90}$. One notes that $F(\mathbf{X}/X_{90}, E_0)$ is a slowly varying function of $\mathbf{X}/X_{90}$. The use of this replacement involves some falsification of the boundary of R_2, since the entire sphere may not be contained in R_2. Therefore it is desirable to keep r small. However, values of $r = 0.1X_{90}$, $0.05X_{90}$, and $0.2X_{90}$ have not revealed any large discrepancies in the results. In the calculation, $r = 0.1X_{90}$ has been used.

A similar formula using Berger's kernel for beta emitters can be developed. Alternatively, one can use the results for monoenergetic electrons and integrate over the beta spectrum of energies emitted. It is this last alternative which is used here. The beta spectra are obtained by use of Dillman's computer code for analysis of decay schemes.[19]

19. L. T. Dillman, "Radionuclide Decay Schemes and Nuclear Parameters for Use in Radiation-Dose Estimation," MIRD Pamphlet No. 4, *J. Nucl. Med. Suppl. No. 2* (1969).

23. Dose to the Bladder

Walter S. Snyder[1] Mary R. Ford

INTRODUCTION

The size of the bladder varies greatly during a filling, and this has a marked effect on the dose per photon the bladder receives. The situation is even more complicated for electrons and beta particles, many of which often fail to penetrate the entire thickness of the bladder wall. Thus the average dose may differ greatly from the dose the surface receives. Other parameters that may affect the dose or dose rate are: (1) the rate at which radioactivity enters the bladder, (2) the rate of entry of urine into the bladder, (3) the voiding schedule, (4) the radiological half-life of the radionuclide, (5) the amount of urine in the bladder when the radionuclide is administered, and (6) the fraction of the radioactivity excreted in the urine. The dose commitment is estimated here corresponding to a model involving considerable idealizations of the parameters mentioned above.

THE BLADDER MODEL

The bladder is considered to be an oblate spheroid,

$$\left(\frac{x-x_0}{a}\right)^2+\left(\frac{y-y_0}{b}\right)^2+\left(\frac{z-z_0}{c}\right)^2=1\ ,$$

where $(x_0, y_0, z_0) = (0, -4.5, 8)$ are the coordinates of the center in a Cartesian system of coordinates as chosen in MIRD Phamplet No. 5 (ref. 2), that is, positive x axis to the left, positive y axis pointing toward the back, and positive z axis directed upward along the centerline of the trunk, with the origin at the base of the trunk. The semiaxes of the ellipsoid have the ratio $a:b:c = 4:3:3$, and this ratio is assumed to remain fixed as the bladder fills. The above equation may be considered to represent the inner wall of the bladder,

$$\left(\frac{x-x_0}{wa}\right)^2+\left(\frac{y-y_0}{wb}\right)^2+\left(\frac{z-z_0}{wc}\right)^2=1\ , \qquad (1)$$

where, assuming unit density, w is chosen so that

$$\frac{4}{3}\pi abc(w^3-1)=45\ \text{g}$$

is the mass of the bladder wall. For different volumes of urine present in the bladder, the mass remains unchanged, and the value of 45 g has been chosen as typical.[3] Schematic diagrams of the bladder with contents of 0 ml (empty), 100 ml, and 400 ml are shown in Fig. 23.1.

Define now a function $D_r(V)$ to be the average dose per photon to the bladder wall (in rads per photon)

1. Consultant.

2. W. S. Snyder, M. R. Ford, G. G. Warner, and H. L. Fisher, Jr., "Estimates of Absorbed Fractions for Monoenergetic Photon Sources Uniformly Distributed in Various Organs of a Heterogeneous Phantom," MIRD Pamphlet No. 5, *J. Nucl. Med., Suppl. No. 3* **10**, 7 (1969).

3. *Report of the Task Group on Reference Man,* ICRP Publication 23, Pergamon Press, Oxford, May 1975.

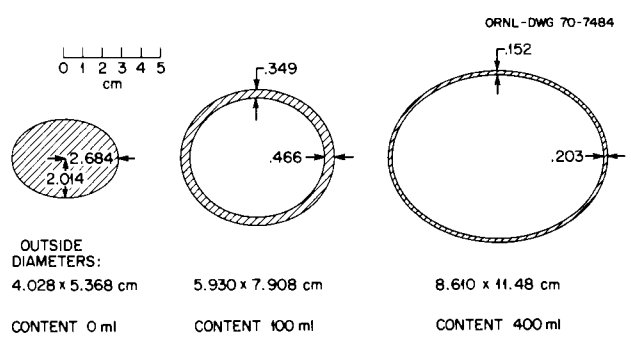

Fig. 23.1. Section of bladder for several volumes. Mass of bladder, 45 g.

when the bladder content (urine content) is V ml. No mathematical formula for $D_r(V)$ is available; rather, its values may be obtained by use of the Monte Carlo method described in MIRD Pamphlet No. 5, the only change being that the bladder content here is V ml and the dose is estimated to the wall rather than averaged over the wall and the contents.

The function $D_r(V)$ has been computed for $V = 0$, 50, 100, 200, 300, 400, and 500 ml and for the same 12 monoenergetic sources of photons given in MIRD Pamphlet No 5, namely, 0.01, 0.015, 0.02, 0.03, 0.05, 0.1, 0.2, 0.5, 1, 1.5, 2, and 4 MeV. The dose per photon at $V = 0$ is for a point source and corresponds to an infinitesimal volume of urine in the bladder. The results are displayed in Fig. 23.2(*a*) for the four lowest energies and in Fig. 23.2(*b*) for the other energies. As will be noted, the curves cross, and they are separated here to facilitate their use. This complex behavior seems to be due to the interplay of a number of factors: (1) the amount of energy released, (2) the changes in the mass absorption and mass attenuation coefficients with energy, and (3) the thickness of the wall. Where the mass absorption coefficient varies slowly (e.g., 0.1 to 4 MeV), $D_r(V)$ decreases as photon energy decreases; but at still lower energies, the increase in the mass absorption coefficient causes $D_r(V)$ to increase for small values of V. For large V, attenuation predominates, and $D_r(V)$ continues to decrease, although not regularly, as energy decreases.

The data in Figs. 23.2(*a*) and (*b*) suggest a multiexponential form for $D_r(V)$. A two-exponential formula,

$$D_r(\mathrm{v}) \approx ae^{-\alpha V} + be^{-\beta V} , \qquad (2)$$

has been found to fit the data with sufficient accuracy for practical purposes. The values of the parameters do change with photon energy to the extent that no single formula applicable for the entire energy range is practical. The errors are not significantly less for a three-exponential form than for Eq. (2). The values of a, b, α, and β and the maximum percent deviation of the formula from the estimated value of $D_r(V)$ are given in Table 23.1. An average percent deviation is also given for each energy. P. Brindza, ORAU summer student from Marquette University on assignment to the Health

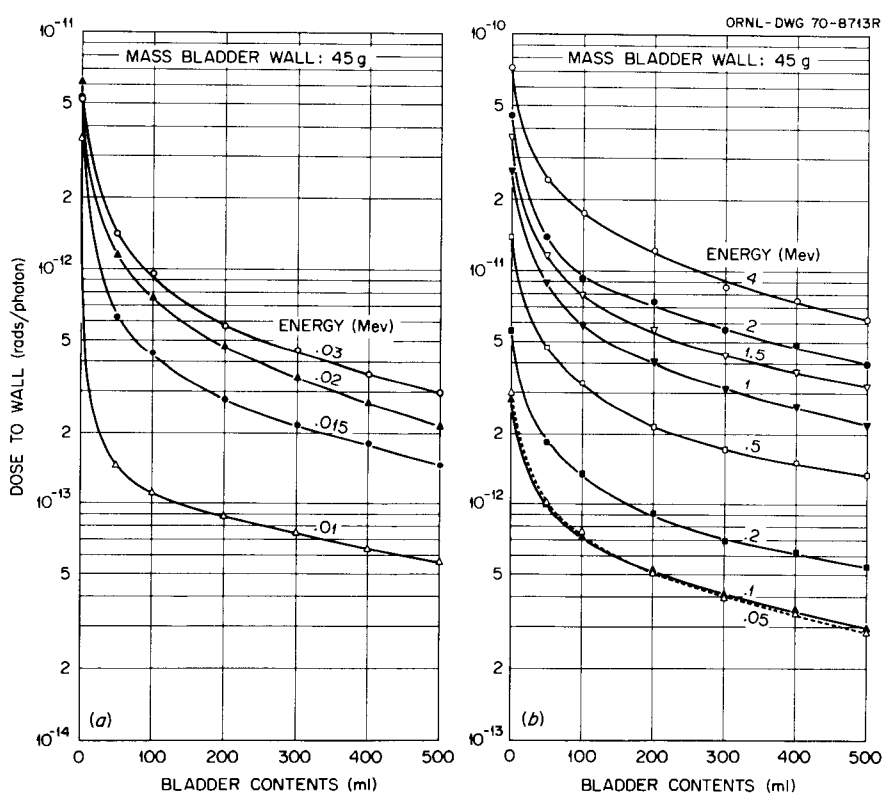

Fig. 23.2. Variation of dose to bladder wall of a photon emitter in urine as a function of photon energy and volume of bladder contents.

Table 23.1. Parameter values for dose to bladder wall:

$D_r(V) = ae^{-\alpha V} + be^{-\beta V}$ (rads/photon)

E (MeV)	a ($\times 10^{-12}$)	α	b ($\times 10^{-12}$)	β	Deviation of function and data (%)	
					Average	Maximum
0.01	0.126	0.00168	3.47	0.0953	2.51	4.8
0.015	0.479	0.00252	4.81	0.0631	4.28	8.9
0.02	0.872	0.00292	5.30	0.0507	4.44	8.7
0.03	0.977	0.00248	4.16	0.0388	3.83	10.7
0.05	0.807	0.00218	2.17	0.0390	3.65	8.6
0.1	0.766	0.00195	2.02	0.0378	2.30	−5.4
0.2	1.31	0.00187	4.12	0.0344	4.04	9.0
0.5	3.28	0.00192	10.5	0.0342	3.66	−7.8
1.0	6.14	0.00213	19.9	0.0349	2.56	−4.6
1.5	8.27	0.00199	28.3	0.0377	3.03	−6.0
2.0	10.6	0.00198	34.7	0.0414	2.04	−4.6
4.0	19.1	0.00235	53.2	0.0380	5.08	−10.9

Physics Division in 1969, is responsible for the development of Eq. (2).

ACTIVITY IN THE BLADDER

The rate W at which urine enters the bladder (in milliliters per day) probably varies somewhat during the day, and one may consider W as a function of time. If voiding occurs at times $T_1, T_2, T_3, \ldots$, days after the time 0 when the radionuclide is administered, one can consider W as a constant during the time intervals between voids, say $W_1, W_2, W_3, \ldots$; and this is the only case considered here. Moreover, it will be supposed that a void occurs at time 1 day and that the pattern of voidings during the first day is unchanged during the succeeding days.

Suppose now that retention of the radionuclide is described by

$$R(t) = I \sum_{i=1}^{n} A_i e^{-(\lambda_i + \lambda_r)t} \quad (\mu\text{Ci}) , \qquad (3)$$

where t is in days following administration, which is assumed to be at time $t = 0$, and I is the intake in microcuries. We consider here only the case where F_i, the fraction of the total excretion entering the bladder, does not vary with time. Then the activity in the bladder at time $t \leqslant T_1$ is given by

$$A_1(t) = I \int_0^t d\tau \sum_{i=1}^{n} A_i F_i \lambda_i e^{-(\lambda_i + \lambda_r)\tau} e^{-\lambda_r(t-\tau)}$$

$$= I \sum_{i=1}^{n} A_i F_i e^{-\lambda_r t} (1 - e^{-\lambda_i t}) \, \mu\text{Ci} , \qquad (4)$$

where I is the activity entering the blood at time 0, F_i is the fraction of activity in compartment i excreted in the urine, and $\exp[-\lambda_r(t - \tau)]$ represents decay (during the interval from τ to t) of the activity entering the bladder in time $d\tau$.

DOSE FROM PHOTONS

To calculate dose from photons, we need only carry out an integration, namely,

$$D_p(T_1) = I \times 3.2 \times 10^9$$

$$\times \int_0^{T_1} dt \left[\sum_{i=1}^{n} A_i F_i e^{-\lambda_r t}(1 - e^{-\lambda_i t}) \right]$$

$$\times \sum_{j=1}^{k} y_j \left(a_j e^{-\alpha_j W_1 t} + b_j e^{-\beta_j W_1 t} \right) \quad \text{rad} , \qquad (5)$$

where the first bracket, with the constant factor, represents the number of disintegrations occurring in the time interval dt, y_j is the yield of the jth photon, and a_j, α_j, b_j, and β_j are appropriate constants in the formula for dose for a photon of this energy. In practice, the values of these parameters can be obtained by interpolation from Table 23.1. Alternatively, one may compute the sum for the two neighboring energies and interpolate on the energy. It is this last alternative that is coded here since it permits ready extrapolation for photons of energy less than 0.01 MeV. The present code does not provide for extrapolation for energies above 4 MeV. The doses for the succeeding intervals are

similarly calculated, merely replacing W_1 and T_1 by W_2 and $T_2 - T_1$, W_3 and $T_3 - T_2$, etc., successively, and the appropriate sum provides the dose during the first day. Since the pattern of voids is unchanged on succeeding days, the dose commitment is the sum of a geometric series corresponding to each exponential term of the retention function. Thus, if $D_p{}^i(1)$ is the dose from photons during the first day corresponding to the term $A_i \exp -[\lambda_i + \lambda_r)t]$ in Eq. (3), the dose commitment corresponding to these terms is

$$D_p = \sum_{i=1}^{n} D_p{}^i(1)/[1 - e^{-(\lambda_i + \lambda_r)}] \text{ rad}. \tag{6}$$

A summation on i thus provides the required dose commitment. If the time intervals between voids are equal, alternatively one may compute

$$D_p = \sum_{i=1}^{n} D_p{}^i(T_1)/[1 - e^{-(\lambda_i + \lambda_r)T_1}] .$$

RESULTS FOR PHOTON DOSE

Essentially the code as described above has been run for hundreds of cases with biological half-times and radiological half-times both ranging from 1 hr to ten days, with formations of urine of 1000, 1400, and 2000 ml/day, and with voiding schedules of four, seven, and ten voids per day in each case. In addition, a further provision for incomplete emptying of the bladder, that is, the bladder retaining 10, 20, and 30% of its maximum volume at voiding, has been explored, as well as administering the radionuclide when the bladder is partly full. It appears that incomplete emptying of the bladder does not have a major effect on the dose from photons. Likewise, a change from four to ten voids per day is not a major effect, although the dose will always decrease as the number of voids increases. Major effects on the dose from photons appear to be: (1) if the urine output can be increased, the dose is diminished, a change from 1000 ml/day to 2000 ml/day, decreasing the dose from photons by 25 to 50%; (2) if the radionuclide is adminstered while the bladder is one-third to two-thirds of its capacity, there is a reduction of dose by 25 to 50% if the effective half-time, that is, $\lambda_i + \lambda_r = 0.693/T_{\text{eff}}$, is less than one day. At long effective half-times, much of this effect disappears, as might be expected.

SURFACE DOSE FROM ELECTRONS AND BETA PARTICLES

A "surface dose" from electrons and beta rays, as well as the more usual "average dose" in the wall, will be described because there are difficulties in interpreting either dose; and the doses frequently differ by an order of magnitude. The difficulties arise because one can assign only an infinitesimal layer of tissue which receives the surface dose, while if the dose is averaged over the wall, it may happen that a considerable portion of the wall does not receive any dose. If the movements of cells as the bladder wall expands were known in detail, a dose to a cell might be produced; however a description of this movement has not been found.

The activity in the bladder at time t is given by Eq. (4) above, and hence the concentration at time t during the first filling is given by

$$C_1(t) = A_1(t)/tW_1$$

$$= \frac{I}{tW_1} \sum_{i=1}^{n} A_i F_i e^{-\lambda_r t}(1 - e^{-\lambda_i t}) \, (\mu\text{Ci/ml}) . \tag{7}$$

In an infinite homogeneous medium contaminated at this level, each gram of mass must absorb the energy emitted from a gram mass, and thus the dose rate in such a medium is given by

$$51.15 C_1(t) \sum_{m=1}^{p} Y_m \bar{E}_m/\rho \quad (\text{rad/day}) , \tag{8}$$

where Y_m is the yield of the electrons or beta particles, $\bar{E}_m$ is the unique or average energy emitted, p denotes the number of such particles emitted per disintegration, and ρ is the density of the medium, which is urine in this case. Assuming the presence of a tissue wall and assuming that the activity extends a distance of the range of the electron or beta particle on only one side of the wall, the surface dose rate is just half of the estimate given in Eq. (8). This estimate is conservative in that, for very energetic electrons, the range may be a centimeter or more; and during this early period, the dose will be somewhat less. Also, one should bear in mind that usually the dose rate falls off steeply within the wall, and thus the average dose rate in the wall is generally much less than that at the surface. Nevertheless, the NCRP and ICRP have used this surface dose rate extensively in the past to estimate the dose to the

walls of the gastrointestinal tract and to the skin when the radionuclide is in the air. The surface dose rate is given by Eq. (8), and an integration over time provides an estimate of dose during the first filling. This dose is given by

$$D_e(T_1) = \frac{51.15I}{2\rho W_1} \sum_{m=1}^{p} Y_m \bar{E}_m \sum_{i=1}^{m} A_i F_i \times \int_0^{T_1} dt \frac{e^{-\lambda_r t}(1 - e^{-\lambda_i t})}{t}$$

$$= \frac{51.15I}{2\rho W_1} \sum_{m=1}^{p} Y_m \bar{E}_m \sum_{i=1}^{n} A_i F_i \left\{ \ln\left(\frac{\lambda_i + \lambda_r}{\lambda_r}\right) - E_1(\lambda_r T_1) + E_1[(\lambda_r + \lambda_i)T_1] \right\} \text{ (rad)} . \quad (9)$$

Dose during succeeding periods between voidings is calculated similarly, but if all these periods are equal, the dose from the ith term for successive periods forms a geometrical series with the ratio $\exp - [(\lambda_i + \lambda_r)T_1]$; hence the total dose from electrons and betas is given by

$$D_e = \frac{51.15I}{2\rho W_1} \sum_{m=1}^{p} Y_m \bar{E}_m \sum_{i=1}^{n} A_i F_I \left[\ln\left(\frac{\lambda_i + \lambda_r}{\lambda_r}\right) - E_1(\lambda_r T_1) + E_1(\lambda_i + \lambda_r)T_1 \right] \times \left[1 - e^{-(\lambda_i + \lambda_r)T_1}\right]^{-1} \text{ (rad)} . \quad (10)$$

This dose must be added to the dose from photons as given by Eq. (5).

A method of estimating the average dose to the wall from electrons or betas has been given in ORNL-4979.[4] Generally, the average dose is far less than the surface dose, as has been indicated. The results for electrons or betas largely parallel the results for photons, as stated above, in that if the amount of urine excreted per day can be substantially increased (e.g., doubled), the dose will be reduced by 25 to 50%; and if the radionuclide can be administered at a time when the bladder is from one-third to two-thirds full, there is again a substantial reduction of the dose. Of course, other clinical requirements may not permit the realization of this objective, but in many cases where there is no such conflict, this dose reduction may be worthy of consideration.

4. W. S. Snyder, J. W. Poston, G. G. Warner, and L. W. Owen, *Health Phys. Div. Ann. Progr. Rep. July 31, 1974*, ORNL-4979, p. 13. [*Erratum:* In the headings of Tables 4.1 and 4.2, "In rads per microcurie per cubic centimeter" should read "In rads per microcurie injected."]

24. Practical Consideration for Computing the Dose to the Bladder

E. M. Smith[1] G. G. Warner[2]

Work has recently been initiated to evaluate the various factors that will affect the dose to the wall of the bladder from representative administrations of radiopharmaceuticals to humans. These studies are based on the bladder model developed by Snyder et al.[3] (see also Chap. 23 of this report).

The factors to be studied include: (1) total daily urine output, (2) voiding schedule (frequency and volume voided at each voiding throughout the day), (3) volume of urine in bladder at time radioactivity is administered (initial conditions), and (4) stimulation of urine production. The effect on dose from urine retained in the bladder after urination will not be studied at this time since any volume of retained urine greater than 5 to 10 ml presents an abnormal condition.

The initial study was to determine the effect the voiding schedule has on the total dose to the bladder wall for a specified daily urine output of 1500 ml. Since urinary excretion data for ^{197}Hg- and ^{203}Hg-labeled chlormerodrin were available from the MIRD Committee, Society of Nuclear Medicine,[4] these data were used. Table 24.1 gives the data for this initial study. Four cases were studied, each for four voiding schedules. The two cases marked "blocked" were for patients who were preadministered a mercurial diuretic to stimulate urinary excretion of the labeled compound. The bladder was assumed empty at the time the radioactivity was administered, and the bladder was assumed completely emptied at each voiding. The radioactivity was administered immediately preceding the first voiding listed under the voiding schedule for each sequence enumerated. The first number in the parentheses is the number of hours between voidings, and the second number is the volume of urine (in

1. Consultant.
2. Computer Sciences Division.
3. W. S. Snyder, J. W. Poston, G. G. Warner, and L. W. Owen, *Health Phys. Div. Annu. Progr. Rep. July 31, 1974,* ORNL-4979, p. 13.
4. MIRD Pamphlet No. 6, to be published in *J. Nucl. Med.*

Table 24.1. Dose to bladder wall from radioactivity present in the urine administered as ^{197}Hg or ^{203}Hg chlormerodrin

Voiding schedule[a]	Rads/μCi administered			
	^{197}Hg		^{203}Hg	
	Blocked	Unblocked	Blocked	Unblocked
(4.8;300) (4.8;300) (4.8;300) (4.8;300) (4.8;300)	1.29×10^{-4}	1.65×10^{-4}	1.82×10^{-3}	3.40×10^{-3}
(2;200) (5;350) (6;350) (8;400) (3;200)	1.39×10^{-4}	1.56×10^{-4}	2.01×10^{-3}	3.76×10^{-3}
(3;250) (4;250) (3;200) (4;250) (8;400) (2;150)	1.25×10^{-4}	1.61×10^{-4}	1.83×10^{-3}	3.42×10^{-3}
(6;350) (6;400) (8;400) (4;350)	1.46×10^{-4}	1.85×10^{-4}	2.05×10^{-3}	3.82×10^{-3}

[a]The first number in the parentheses is the number of hours between voidings, and the second number is the volume of urine (in milliliters) produced during that period.

milliliters) produced during that period. The original bladder model was designed for a repetitive voiding schedule and was modified to accept a variable voiding schedule.

The results of this study are given in Table 24.2. This very limited study indicates that the voiding schedule has a minimal effect on the total dose to the bladder wall. This study is currently being expanded to evaluate six representative voiding schedules for seven clinically used radionuclides, each evaluated for ten effective biological excretion half-times ranging in binary multiples from 0.5 to 256 hr.

Table 24.2. Effect that various voiding schedules have on the dose to the bladder wall

Variation in dose for four voiding schedules	^{197}Hg		^{203}Hg	
	Blocked	Unblocked	Blocked	Unblocked
Mean dose, rad/μCi administered	1.35×10^{-4}	1.67×10^{-4}	7.71×10^{-3}	3.60×10^{-3}
Maximum variation, $\frac{x_{max} - x_{min}}{x_{min}}$	17%	19%	13%	11%
Mean variation, $\frac{\lvert \bar{x} - x \rvert_{max}}{\bar{x}}$	8%	11%	6%	6%

25. Metabolic Model for Whole-Body and Gastrointestinal-Tract Retention of ^{141}Ce in a Human Infant

S. R. Bernard

Inaba and Lengemann[1] administered single oral doses of $^{141}Ce(NO_3)_3$ via a stomach tube to nonfasted rats of ages 0, 7, 14, and 25 (weaned) days. They measured total-body retention in all pups and gastrointestinal (GI)-tract retention in the pups dosed at birth. Over an interval of one month, when there is negligible loss of ^{141}Ce from organs in the total body minus the GI tract and contents, the fractional retention in the total body is given approximately by the complement of a 20-term, cumulative, Poisson function, plus a constant. For fractional retention in the gut and contents, the formula is taken as

$$f_g(A) + \sum_{i=0}^{20} \frac{(\lambda_A t)^i}{i!} e^{-\lambda_A t} ,$$

which assumes permanent fixation of a fraction $f_g(A)$ in the gut walls. The parameters $f_g(A)$ and λ_A depend on the age at the time of administration of the $^{141}Ce(NO_3)_3$. In the formula, $(\lambda_A t)^0$ for $t = 0$ is taken as unity. The model has been extrapolated to human retention. Dose has been estimated for a single intake of 1 μCi of $^{141}Ce(NO_3)_3$, assuming uniform deposition throughout the whole infant GI tract minus the contents and assuming complete absorption of beta energy in the walls. The dose was ~6 rads if ingestion occurred at birth. The retention in the gut wall was taken as constant after 180 days, but the dose due to this retention was about 0.03 rad. The model, the dose estimate, and its uncertainties are discussed in ref. 2.

---

1. J. Inaba and F. W. Lengemann, "Intestinal Uptake and Whole-Body Retention of ^{141}Ce by Suckling Rats," *Health Phys.* 22(2), 169 (February 1972).

2. *Symposium on Population Exposures,* Proceedings of the 8th Midyear Topical Symposium of the Health Physics Society, CONF-741018, October 1974.

26. The Dosimetry of ^{241}Pu Reconsidered

J. W. Poston W. S. Snyder[1] L. W. Owen[2]

Plutonium-241 is a pure beta emitter having a radioactive half-life of 13.2 years, a maximum energy of 20.8 keV, and an average energy of 5.2 keV.[3] Its range in tissue is about 8.2 μm, which is far shorter than the range of most alpha particles. This has prompted us to consider carefully whether the dosimetry generally used for the alpha particles from ^{238}Pu or ^{239}Pu is appropriate for this beta emitter.

The retention model used for alpha-emitting radionuclides of plutonium in shown in Table 26.1. The lung model is the standard ICRP lung model, although some of the clearance constants may not be entirely familiar. A particle size of 1 μm average median aerodynamic diameter (AMAD) is used as being fairly typical, although we have means of adjusting the dose for this parameter. The model is essentially the same for ^{241}Am, the decay product of ^{241}Pu, except that we used $f_1 = 10^{-3}$ for absorption from GI tract to blood. It was agreed to assess dose from alpha particles by using a lung mass of 570 g, which omits the blood present in the large arteries and veins, which would not absorb much energy. For beta radiation, however, the lung mass was taken as 1000 g. This model was the consensus arrived at in assessing the reactor accident situation by radiobiologists representing major ERDA laboratories that work with transuranics.

In our calculations, we have considered an inhalation exposure to a class Y aerosol of pure ^{241}Pu. In addition, we shall consider the dose over 50 years post-exposure for a single intake of this radionuclide.

The microcurie-days of ^{241}Pu accumulated in the lungs and respiratory lymph nodes are shown in Table 26.2. Values for ^{241}Am produced in the body are shown also. The ICRP intends to estimate an average dose to the lung tissue, and this dose will include all the energy absorbed in lung tissue from alpha, beta, and gamma radiation released in the lung tissue. From this table, it is clear that there is a considerable accumulation, in terms of microcurie-days, in the lymph nodes – 58 μCi-days vs 98 μCi-days in the lungs. Alpha energy produced in the lymph nodes is assumed to be completely absorbed there, but most of the beta and gamma energy released is assumed to escape and to be absorbed in lung and surrounding tissue. For a beta particle with a range of only ~8μm, it seems reasonable to assume that this energy is completely absorbed in the lymph nodes. Thus, energy released by this beta particle in the lymph nodes should not be averaged in with the lung tissue, and one might argue that our dose estimate for lung should be reduced. On the other hand, if it is appropriate to omit blood in the large arteries and veins for alpha radiation, it is also appropriate to omit the energy for such a weak beta. These two adjustments offset each other; so the dose from ^{241}Pu hardly changes. However, the total dose is essentially unchanged, being mostly due to ^{241}Am.

A summary for the dose to the GI tract for the supposed intake of 1 μCi of ^{241}Pu is given in Table 26.3. The third column gives the dose as calculated under the assumptions of the ICRP. It is our belief that

Table 26.1. Retention model for inhalation of plutonium

1. Particle size AMAD = 1 μm; lung clearance classes W and Y.
2. For absorption to blood from GI tract, $f_1 = 3 \times 10^{-5}$.
3. Retention in bone is given by 0.45 exp $(-0.693t/100 \times 365)$.
4. Retention in liver is given by 0.45 exp $(-0.693t/40 \times 365)$.
5. Retention in kidney is given by 0.01 exp $(-0.693t/40 \times 365)$.
6. Retention in testes is given by 0.0005 exp $(-0.693t/T_r)$.
7. Retention in ovaries is given by 0.0001 exp $(-0.693t/T_r)$.

1. Consultant.
2. Computer Sciences Division.
3. C. M. Lederer, J. M. Hollander, and I. Perlman, *Table of Isotopes*, Sixth Edition, John Wiley and Sons, Inc., New York, 1967.

Table 26.2. Dosimetry of the lung – ^{241}Pu

	μCi-days		Lung dose	
	Lung	Respiratory lymph nodes	Dose (ICRP-rem)	New doses (rem)
^{241}Pu	98	58	0.042	0.046
^{241}Am	0.174	0.91	0.89	0.89

Table 26.3. Dosimetry of the GI tract – ^{241}Pu

Organ		Dose (ICRP-rem)	New doses (rem)
Stomach	^{241}Pu	1.3×10^{-5}	1.3×10^{-7}
	^{241}Am	8.4×10^{-5}	8.4×10^{-5}
	Total	9.6×10^{-5}	8.4×10^{-5}
Small intestine (SI)	^{241}Pu	3.2×10^{-5}	3.2×10^{-7}
	^{241}Am	6.9×10^{-5}	6.9×10^{-5}
	Total	1.0×10^{-4}	6.9×10^{-5}
Upper large intestine (ULI)	^{241}Pu	1.9×10^{-4}	1.9×10^{-6}
	^{241}Am	1.1×10^{-4}	1.1×10^{-4}
	Total	3.0×10^{-4}	1.1×10^{-4}
Lower large intestine (LLI)	^{241}Pu	5.6×10^{-4}	5.6×10^{-6}
	^{241}Am	7.5×10^{-5}	7.5×10^{-5}
	Total	6.4×10^{-4}	8.1×10^{-5}

the dose from ^{241}Pu to the radiosensitive cells of the GI tract should be drastically reduced. Many years ago, Sullivan and Thompson[4] demonstrated a complete absence of effect on the GI tract using ^{239}Pu and producing surface doses that were fantastically high. The average depth to the critical cells is ~140 μm or more, and the cells close to the surface are replaced rather rapidly. The ICRP conservatively uses a factor of 0.01 for dose to these cells from alpha particles. It should be emphasized that this factor is not used because the data indicate a 1% probability of damage, but only to allow something for unforeseen side effects, perhaps some condition of the tract which would expose these cells more than usual. This same factor is proposed for the beta dose from ^{241}Pu, which has a range much smaller than the range of the alpha particle. Thus, GI tract doses from plutonium might be reduced to 1% of the values shown, but again, the dose from ^{241}Am predominates, and curiously, the upper large intestine (ULI) is the section with the highest dose. This

4. M. F. Sullivan and R. C. Thompson, "Absence of Lethal Radiation Effects Following Massive Oral Administrations of Plutonium," *Nature* **180**, 651–652 (1957).

Table 26.4. Dosimetry of bone – ^{241}Pu

	Average dose to bone (ICRP-rem)	New dose (rem)
^{241}Pu	5.7×10^{-3}	1.2×10^{-4}
^{241}Am	14	14

due to the cross-irradiation by the gamma rays emitted in liver and in bone.

Doses to the liver and to the gonads would be unaffected since no microdosimetry is used by the ICRP for these organs. However, the distribution of plutonium in the Kupffer cells might offer a fruitful topic for further exploration, but the ICRP has not indicated a dose limit for these cells.

Finally, we consider the dose to bone (Table 26.4), and here we encounter several difficulties. The ICRP has designated the endosteal cells as the radiosensitive tissues in bone.[5] They are indicated as lying from 5 to 10 μm from the bone surface. The extent of bone surface estimated by Lloyd and Hodges[6] is 11.2 m^2. If 1 μCi of ^{241}Pu enters blood, 0.45 μCi deposits on bone surfaces; thus the surface deposition would be $1 \times 0.45/(11.2 \times 10^4) = 4 \times 10^{-6}$ μCi/cm^2. Using the point kernel given by Berger,[7] we computed the dose rate, averaged over 5 to 10 μm from such a plane distribution, and found it to be 5×10^{-7} rad/day. The plutonium has also been distributed in slabs of thickness 0.1, 0.2, . . . 1 μm fronting on the bone surface, and over this range of thicknesses, the dose rate (averaged over the distance from 5 to 10 μm) decreases by about a factor of 2. We accept the value of 5×10^{-7} rad/day as the initial dose rate due to 1 μCi of ^{241}Pu

5. *A Review of the Radiosensitivity of the Tissues in Bone,* ICRP Publication 11, Pergamon Press, New York, 1968.

6. E. Lloyd and D. Hodges, Annual National Laboratory Report, ANL-7760, Part II, U.S. Department of Commerce, 1970.

7. J. J. Berger, "Distribution of Absorbed Dose Around Point Sources of Electrons and Beta Particles in Water and Other Media," *J. Nucl. Med., Suppl. No. 5* 12 (March 1971).

entering the blood. Alternatively, merely averaging the dose rate over the bone mass of 5000 g and assuming that all the energy is absorbed, one obtains

$$\frac{51 \times 0.45 \times 0.0052}{5000} = \frac{0.12}{5000} = 2.4 \times 10^{-5} \text{ rad/day},$$

corresponding to 1 μCi entering the blood. There is little biological evidence available on redistribution in either case, and what is available tends to show that redistribution is rather small, at least in the mature animal. We will thus assume that the ^{241}Pu remains fixed until it decays; so the ratio of dose commitments is just the ratio of these initial dose rates. This assumption indicates a dose of about 1.2×10^{-4} from ^{241}Pu in bone to endosteal cells. There is a clear factor of ~50 involved in calculating the dose to bone or to endosteal cells, and if the surface distribution broadens, the discrepancy would be even greater. We know of no data now available to indicate the thickness of this surface deposition or how it might vary with time. Of course, in ICRP Publication 2 (ref. 8), an additional factor of 5 is brought in – the so-called *n* factor – and this would make the dose (in rem) averaged over bone larger by a factor of ~250 than the dose to endosteal cells. However, the doses shown in Table 26.4 were computed *without* the use of the *n* factor; so dose to endosteal cells would be less by at least a factor of 50. This might be considerably larger, depending on the thickness of the surface layer over which the activity is distributed at various times postexposure.

In short, one concludes that the doses from ^{241}Pu given in this presentation would be reduced considerably for lung, GI tract, and bone. We have not found any plausible basis for sizable reductions of dose for the liver or for the gonads, and these are undoubtedly the critical organs for ^{241}Pu. Practically, the dose from ^{241}Am is always dominant, and thus there is little change in the appropriate maximum permissible concentrations. One finds that the results are much the same if the aerosol is of inhalation class W or if the ^{241}Pu is taken orally.

---

8. *Report of Committee II on Permissible Dose for Internal Radiation*, ICRP Publication 2, Pergamon Press, New York, 1959.

27. A Computer Program for Estimating Microcurie-Days of a Radionuclide in the Organs of the Human Body

W. S. Snyder[1] M. R. Ford Sarah B. Watson[2]

Average dose equivalent in an organ of the body from an internally deposited emitter is given by

$$\mathrm{DE}(T) = \sum_i U_i(Y_i) \times S(T \leftarrow Y_i) , \qquad (1)$$

where U_i represents the microcurie-days accumulated in the various source organs, Y_i, and $S(T \leftarrow Y_i)$ represents the dose to a target organ T due to one microcurie-day (=3.2 × 10^9 disintegrations) of the emitter in the source organ. The summation extends over all the source organs Y_i; and S has been tabulated for about 60 radionuclides, assuming these are distributed uniformly in the source organ[3] for many of the organs usually considered. A second volume containing data on about 100 additional radionuclides is in preparation. In this paper we discuss a possible basis for estimating the microcurie-days per microcurie of intake when a retention model has been indicated. In principle, this is simple in that if $f(t)$ represents the fraction of activity entering the body (μCi) that is present in an organ at time t, the microcurie-days accumulated in that organ from time t_1 to t_2 (days) is given by

$$U = I \int_{t_2}^{t_1} dt\, f(t) \quad (\mu\text{Ci-days}) , \qquad (2)$$

where I is the intake in μCi.

The complexity of the problem is due partly to the fact that generally retention is described in terms of transfer rates between organs or subsystems of the body (lungs, gastrointestinal tract, blood, etc.), so that there is delay in the transfer of some of the activity, and to the presence of daughter radionuclides. A computer code has been developed that embodies a system of differential equations to represent the transfer of activity in the body, but does assume that retention can be adequately represented by a system of compartments with constant rates of transfer to other organs or out of the body.

Lungs. The differential equations, representing the lung portion of retention, embody the lung model as described in the report of the ICRP Task Group on Lung Dynamics.[4] The respiratory system consists of a nasal-pharyngeal region (N-P), a tracheo-bronchial region (T-B), a pulmonary region (P), and the lymph nodes (L), and deposition is governed by the activity median aerodynamic diameter (AMAD) of the aerosol (see ref. 4 for a more detailed discussion). Some of the deposition and transfer constants used in the computer code are not identical with the published values, but are those listed in Fig. 27.1. The appropriate pathways for each transfer constant are shown also in Fig. 27.1, which is a schematization of the model.

The differential equations appropriate for this model are given below. Taking X_a^n, X_b^n, X_c^n, X_d^n, X_e^n, X_f^n, X_g^n, X_h^n, X_i^n, X_j^n, X_k^n, X_l^n as the activities of the parent (n = 1) and daughters (n = 2, 3, . . .) in a compartment moving by the pathway with the appropriate subscript, and using $\dot{X}$ to represent the derivative with respect to time (each X or $\dot{X}$ is understood to be a function of t in what follows), the equations for the lung are the following [Eqs. (3)]:

$$\dot{X}_a^{n+1} = -X_a^{n+1}(\lambda_a^{n+1} + \lambda_r^{n+1}) + (X_a^n + X_b^n)\lambda_r^{n+1} F_a^{n+1} ,$$

1. Consultant.
2. Computer Sciences Division.
3. W. S. Snyder, Mary R. Ford, G. G. Warner, and Sarah B. Watson, *A Tabulation of Dose Equivalent per Micro-curie Day for Source and Target Organs of an Adult for Various Radionuclides*, ORNL-5000 (November 1974).
4. ICRP Task Group on Lung Dynamics, "Deposition and Retention Models for Internal Dosimetry of the Human Respiratory Tract," *Health Phys.* **12**, 173 (1966).

CLEARANCE MODEL

COMPARTMENT		CLASS D T	D F	W T	W F	Y T	Y F
N-P	a	0.01	0.5	0.01	0.1	0.01	0.01
(D_{N-P}=0.30)	b	0.01	0.5	0.40	0.9	0.40	0.99
T-B	c	0.01	0.95	0.01	0.5	0.01	0.01
(D_{T-B}=0.08)	d	0.2	0.05	0.2	0.5	0.2	0.99
	e	0.5	0.8	50	0.15	500	0.05
P	f	n.a.	n.a.	1.0	0.4	1.0	0.4
(D_P=0.25)	g	n.a.	n.a.	50	0.4	500	0.4
	h	0.5	0.2	50	0.05	500	0.15
L	i	0.5	1.0	50	1.0	1000	0.9

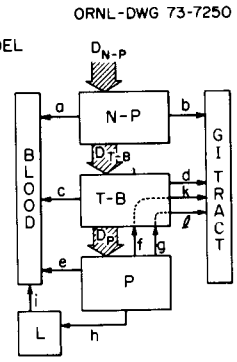

Fig. 27.1. Values for the removal half-times, T_a–T_i, and compartmental fractions, F_a–F_i, for each of the three classes of retained materials. The values given for $D_{N\text{-}P}$, $D_{T\text{-}B}$, and D_P (right column) are the regional depositions based on an aerosol with an AMAD of 1 μm. The schematic drawing identifies the various clearance pathways in the model, *a–i*, in relation to the initial depositions $D_{N\text{-}P}$, $D_{T\text{-}B}$, and D_P and the three respiratory regions, *N-P*, *T-B*, and *P*. The lymphatic clearance for class Y compounds indicates that a 90% regional fraction follows a 1000-day biological half-time. The remaining 10% is presumed to be permanently retained in the nodes and is subject only to radioactive decay.

$$\dot{X}_b^{n+1} = -X_b^{n+1}(\lambda_b^{n+1} + \lambda_r^{n+1}) + (X_a^n + X_b^n)\lambda_r^{n+1}F_b^{n+1} ,$$

$$\dot{X}_c^{n+1} = -X_c^{n+1}(\lambda_c^{n+1} + \lambda_r^{n+1}) + (X_c^n + X_d^n)\lambda_r^{n+1}F_c^{n+1} ,$$

$$\dot{X}_d^{n+1} = -X_d^{n+1}(\lambda_d^{n+1} + \lambda_r^{n+1}) + (X_c^n + X_d^n)\lambda_r^{n+1}F_d^{n+1} ,$$

$$\dot{X}_e^{n+1} = -X_e^{n+1}(\lambda_e^{n+1} + \lambda_r^{n+1}) + (X_e^n + X_f^n + X_g^n + X_h^n)\lambda_r^{n+1}F_e^{n+1} ,$$

$$\dot{X}_f^{n+1} = -X_f^{n+1}(\lambda_f^{n+1} + \lambda_r^{n+1}) + (X_e^n + X_f^n + X_g^n + X_h^n)\lambda_r^{n+1}F_f^{n+1} ,$$

$$\dot{X}_g^{n+1} = -X_g^{n+1}(\lambda_g^{n+1} + \lambda_r^{n+1}) + (X_e^n + X_f^n + X_g^n + X_h^n)\lambda_r^{n+1}F_g^{n+1} ,$$

$$\dot{X}_h^{n+1} = -X_h^{n+1}(\lambda_h^{n+1} + \lambda_r^{n+1}) + (X_e^n + X_f^n + X_g^n + X_h^n)\lambda_r^{n+1}F_h^{n+1} ,$$

$$\dot{X}_i^{n+1} = -X_i^{n+1}(\lambda_i^{n+1} + \lambda_r^{n+1}) + X_h^{n+1}\lambda_h^{n+1}F_i^{n+1} + (X_i^n + X_j^n)\lambda_r^{n+1}F_i^{n+1} ,$$

$$\dot{X}_j^{n+1} = -X_j^{n+1}\lambda_r^{n+1} + X_h^{n+1}\lambda_h^{n+1}(1 - F_i^{n+1}) + (X_i^n + X_j^n)\lambda_r^{n+1}(1 - F_i^{n+1}) ,$$

$$\dot{X}_k^{n+1} = -X_k^{n+1}(\lambda_d^{n+1} + \lambda_r^{n+1}) + X_k^n\lambda_r^{n+1} + X_f^{n+1}\lambda_f^{n+1} ,$$

$$\dot{X}_l^{n+1} = -X_l^{n+1}(\lambda_d^{n+1} + \lambda_r^{n+1}) + X_l^{n+1}\lambda_r^{n+1} + X_g^{n+1}\lambda_g^{n+1} .$$

It will be noted that the terms with a negative sign in the right member correspond to elimination by biological transfer or by radioactive decay. The terms involving a superscript n refer to the activity in μCi of the preceding radionuclide of the chain, which produces λ_r^{n+1} μCi of the following radionuclide per unit time, and these are redistributed according to the values of the F's for that radionuclide. Thus a radionuclide following pathway a in the N-P region may produce a daughter element which follows pathway b, and will do this in the ratio of $F_a^{n+1}:F_b^{n+1}$. This redistribution of the daughter radionuclide is rather essential, since the daughter may have an entirely different clearance class than does the parent. This applies also to the lymph nodes, where, for an aerosol of class Y, a fraction of 90% is supposed to be subject to transport and decay; but the remaining fraction of 10% is subject only to radioactive decay. The daughter radionuclide may be of a different class. These two pathways, symbolized by i and j, are not shown separately in the table, since the pathway j does not transfer activity to another pathway. However, both pathways i and j produce daughter radionuclides, and these are redistributed according to the clearance class of the daughter. At present, the values used for F_i^{n+1} are either 0.9 or 1, according to whether the assumed clearance model is of class Y or of class W or D. Likewise, the pathways f and g are in the pulmonary region, but to reach the gastrointestinal tract (GIT) must traverse the T-B region; here they are represented as pathways k and l. In principle, $\lambda_d = \lambda_k = \lambda_l$ for all radionuclides, since, in the present model, it is the rate of ciliary clearance and hence is expected to be relatively independent of the radionuclide. Equations (3) are written for the $(n + 1)$-st radionuclide of a chain and suppose the functions X^n are known. Thus the integration proceeds serially. The equations are valid for the case $n = 0$, that is, for the parent radionuclide, if $X_\alpha^0 \equiv 0$ for all values of t and all subscripts α representing the lungs.

These equations are valid whatever initial values are used. Generally, the microcurie-days from inhalation of

1 μCi has been computed for an aerosol of AMAD = 1 μCi, but any starting values of D_3, D_4, D_5 may be used. For the above case the initial values are

$$X_a{}^1(0) = D_3F_a{}^1 , \qquad X_e{}^1(0) = D_5F_e{}^1 ,$$
$$X_b{}^1(0) = D_3F_b{}^1 , \qquad X_f{}^1(0) = D_5F_f{}^1 ,$$
$$X_c{}^1(0) = D_4F_c{}^1 , \qquad X_g{}^1(0) = D_5F_g{}^1 ,$$
$$D_d{}^1(0) = D_4F_d{}^1 , \qquad X_h{}^1(0) = D_5F_h{}^1 ,$$
$$X_i{}^1(0) = X_j{}^1(0) = X_k{}^1(0) = X_l{}^1(0) = 0 ,$$
$$X^n(0) = 0 \text{ for } n > 1 \text{ and for all subscripts.}$$

This last provision ensures that only the parent radionuclide is inhaled, although daughters produced in the lung are taken into account. Of course, other initial conditions could be used.

Although the equations are stated in terms of X, one really is more interested in the microcurie-days accumulated in each region. If we set

$$Y_\alpha{}^n = \int_0^{t_1} dt\, X_\alpha{}^n , \tag{4}$$

where t_1 defines any desired initial period of time, one has the microcurie-days accumulated by each of the pathways. Other time periods may be obtained from these. The microcurie-days for each subregion of the respiratory system is then

$$\begin{aligned} U_{NP}{}^n &= Y_a{}^n + Y_b{}^n , \\ U_{TB}{}^n &= Y_c{}^n + Y_d{}^n + Y_k{}^n + Y_l{}^n , \\ U_P{}^n &= Y_e{}^n + Y_f{}^n + Y_g{}^n + Y_h{}^n , \\ U_L &= Y_i{}^n + Y_j{}^n , \\ B^n &= Y_a{}^n\lambda_a{}^n + Y_c{}^n\lambda_c{}^n + Y_e{}^n\lambda_e{}^n + Y_i{}^n\lambda_i{}^n , \\ G^n &= Y_b{}^n\lambda_b{}^n + Y_d{}^n\lambda_d{}^n + Y_k{}^n\lambda_d{}^n + Y_l{}^n\lambda_d{}^n . \end{aligned} \tag{5}$$

Here $U_\alpha{}^n$ is the microcurie-days accumulated in region α of the respiratory system, while B^n and G^n represent the total microcuries going to blood and to the GIT, respectively, during the period $0 \leqslant t \leqslant t_1$. While these last two values are not directly used in the subsequent models, it is convenient to have them available.

Gastrointestinal tract. The differential equations for the GIT are similar for oral intake or for activity entering from the lung, and it will be convenient to combine them. Letting $X_S{}^n$, $X_{SI}{}^n$, $X_{UL}{}^n$, and $X_{LL}{}^n$ be the activities present at time t in the contents of the stomach (S), of the small intestine (SI), of the upper large intestine (UL), and of the lower large intestine (LL), respectively, the equations are the following:

$$\begin{aligned} \dot{X}_S{}^{n+1} &= -X_S{}^{n+1}(\lambda_S{}^{n+1} + \lambda_r{}^{n+1}) + X_b{}^{n+1}\lambda_b{}^{n+1} \\ &\quad + X_d{}^{n+1}\lambda_d{}^{n+1} + X_k{}^{n+1}\lambda_d{}^{n+1} \\ &\quad + X_l{}^{n+1}\lambda_d{}^{n+1} + X_S{}^n\lambda_r{}^{n+1} , \\ \dot{X}_{SI}{}^{n+1} &= -X_{SI}{}^{n+1}(\lambda_{SI}{}^{n+1} + \lambda_r{}^{n+1} + \lambda_{ab}{}^{n+1}) \\ &\quad + X_S{}^{n+1}\lambda_S{}^{n+1} + X_{SI}{}^n\lambda_r{}^{n+1} , \\ \dot{X}_{UL}{}^{n+1} &= -X_{UL}{}^{n+1}(\lambda_{UL}{}^{n+1} + \lambda_r{}^{n+1}) \\ &\quad + X_{SI}{}^{n+1}\lambda_{SI}{}^{n+1} + X_{UL}{}^n\lambda_r{}^{n+1} , \\ \dot{X}_{LL}{}^{n+1} &= -X_{LL}{}^{n+1}(\lambda_{LL}{}^{n+1} + \lambda_r{}^{n+1}) \\ &\quad + X_{UL}{}^{n+1}\lambda_{UL}{}^{n+1} + X_{LL}{}^n\lambda_r{}^{n+1} . \end{aligned} \tag{6}$$

These equations provide for a constant percentage of elimination of the activity present in each segment of the GIT and are, perhaps, more physiological than the model which considers a bolus of activity (food) moving at a constant rate through each section.[5] Likewise, they provide for a constant rate of absorption to blood from the contents of the SI, $\lambda_{ab}{}^n$. In practice, if f_1 is the fraction of the material ingested which is absorbed to blood, one has

$$\int_0^\infty dt\, \lambda_{ab} e^{-(\lambda_{ab}+\lambda_{SI})t} = \frac{\lambda_{ab}}{\lambda_{ab} + \lambda_{SI}} = f_1 \tag{7}$$

if the material is stable. If the material is radioactive, f_1 is the amount absorbed to blood, corrected for radioactive decay to the time of entry into the SI. Since $\lambda_{SI} = 6 \text{ day}^{-1}$, Eq. (7) is equivalent to

$$\lambda_{ab} = \frac{6f_1}{1 - f_1} , \tag{8}$$

where λ_{ab} represents the fraction of the activity present in the SI which is absorbed to blood per unit time, that is, per day. If $f_1 = 1$, no solution exists; yet experimenters occasionally report $f_1 = 1$. In this context we usually set $f_1 = 0.95$, believing that the experimental data are not highly accurate and that some small

5. R. L. Hayes, J. E. Carlton, and W. R. Butler, Jr., "Radiation Dose to the Human Intestinal Tract from Internal Emitters," *Health Phys.* 9, 915 (1963).

amount of material will be present in the GIT. It is assumed that f_1^{n+1} is not necessarily the same as f_1^n, although there is generally only scanty experimental data available on this point. Clearly, the initial conditions for the GIT following an intake by inhalation are that $X_\alpha^n(0) = 0$ for all n and all subscripts α representing a section of the tract. This is easily adapted for oral intake.

The calculation of the microcurie-days in the contents of the GIT is quite analogous to that in the lung, but is even simpler here, since only one retention function exists for a given section of the GIT for each radionuclide of the chain.

Blood and other organs. The activity transferred to blood from the lungs or from the GIT will probably deposit in some other organs. The computer code provides for such other organs, each of which may have a retention equation consisting of five exponential terms. The form and the values of the constants in each formula must be prescribed on the basis of experimental data. Thus for a simple intake of 1 μCi to blood,

$$\sum_{s=1}^{q_j^n} a_{js}^n \, e^{-(\lambda_{js}^n+\lambda_r^n)t} , \quad j=1, 2, \ldots k , \tag{9}$$

represents retention in the jth organ of the nth radionuclide. The coefficients a_{js}^n and the exponential constants λ_{js}^n and λ_r are supposedly known, and t represents time in days following the intake to blood. It is noted that

$$\sum_{j=1}^{k} \sum_{s=1}^{q_j^n} a_{js}^n = 1 ,$$

which simply means that these functions are normalized to a unit intake to blood for every value of n. By allowing for nearly instantaneous excretion, we may relax this condition and assume that the above sum is $\leqslant 1$.

Let X_{js}^n represent retention of the nth radionuclide in the compartment which corresponds to the sth term in the sum for the jth organ. Then

$$\begin{aligned}\dot{X}_{js}^{n+1} = &-X_{js}^{n+1}(\lambda_{js}^{n+1} + \lambda_r^{n+1}) \\ &+ a_{js}^{n+1}(X_a^{n+1}\lambda_a^{n+1} \\ &+ X_c^{n+1}\lambda_c^{n+1} + X_e^{n+1}\lambda_e^{n+1} \\ &+ X_i^{n+1}\lambda_i^{n+1} + X_{\mathrm{SI}}^{n+1}\lambda_{\mathrm{ab}}^{n+1}) \\ &+ a_{js}^{n+1} \sum_{l=1}^{k} \sum_{m=1}^{q_l^n} X_{lm}^n \lambda_r^{n+1} I_{lm}^n \\ &+ \left[\sum_{m=1}^{q_j^n} X_{jm}^n \lambda_r^{n+1}(1 - I_{jm}^n)\right] \frac{a_{js}^{n+1}}{\sum_{p=1}^{q_j^{n+1}} a_{jp}^{n+1}} .\end{aligned} \tag{10}$$

In Eq. (10) the first term on the right side represents elimination, and the second term, with the lengthy parentheses, represents the various pathways by which activity is transferred to blood from the lung or from the GIT. The last two terms represent activity of the (n + 1)-st daughter produced in the various organs. In the first term (terms containing I_{lm}^n), the activity circulates to the blood pool and hence is redeposited, while in the last sum (terms containing $1 - I_{lm}^n$), the radionuclide is assumed to remain in the organ where it is produced subject to transfer, as would activity of the (n + 1)-st daughter which is freshly deposited. Of course, the total activity produced must be preserved, and consequently

$$I_{lm}^n + (1 - I_{lm}^n) = 1 ,$$

I_{lm}^n being the fraction of activity of the (n + 1)-st daughter produced in compartment m which recirculates to blood, and $1 - I_{lm}^n$ the fraction of the activity remaining fixed in the organ. It will be noticed that the activity in the terms containing $(1 - I_{lm}^n)$ is distributed among the compartments represented in the retention function for the organ in the same proportion as is freshly deposited material, the renormalization merely emphasizing that this organ is not competing with other organs for this material. It will also be noted that the terms involving I_{lm}^n are, except for the constant a_{js}^{n+1} which precedes them, independent of j and s. This means that this activity is available to all the organs in the same proportions as activity just entering blood from the lungs or the GIT. Indeed, a similar term will appear in every retention function if I_{lm}^n are not all equal to zero. Actually, there are very scanty biological data available to indicate how the daughter radionuclides are distributed; thus the code allows for considerable flexibility in that for each problem the values of I_{lm}^n are part of the input and must be prescribed. The integration of the X_{js}^n to obtain microcurie-days is straightforward. The computer code contains a provision to handle a chain of radionuclides

with various kinds of branching, but these are not described here.

Integration of the equations. These equations generally are what are termed "stiff" equations, which means, in this context, that the transfer constants vary widely. For example, for ^{226}Ra the biological and radioactive decay constants will both be very small for certain components. In the same problem, one has ^{222}Rn for which the constants are many orders of magnitude larger. Special methods have been developed for integration of such equations, and these are presented by Gear.[6] The procedure used here is an adaptation of the Gear method for stiff differential equations. The computer code implementing Gear's method was originally written by Hindmarch at Lawrence Livermore Laboratory and was modified for use at ORNL by Arnurius.[7]

The ^{226}Ra chain has been used as a test case. Integration of the equations for the chain of eight radionuclides for the time period 50 years after intake required a computer execution time of only 9 sec.

---

6. C. William Gear, *Numerical Initial Value Problems in Ordinary Differential Equations,* Prentice Hall, Englewood Cliffs, N.J., 1971.

7. D. E. Arnurius, Computer Sciences Division, private communication.

28. A Semitheoretical Approach to Excretion and Retention of Various Ions

L. C. Henley[1]

The properties of ions to form complexes and to be absorbed on or in a solid medium are related to the ionic charge and radius of the ion. Hydrolysis can be considered a special case of complex-ion formation; one may use either the hydrolytic properties or the ionic potential as a basis for comparison of the retention and excretion of different ions, assuming that the medium in which the ions exist is exactly the same. Reference man is assumed to be such a medium.

With the possible exception of certain large, singly charged ions such as Rb^+ and Cs^+, positively charged ions in aqueous solutions tend to be associated with water or other coordinating groups. This tendency is proportional to the charge and inversely proportional to the radius of the ion. This principle, which may be expressed in terms of the ionic potential, Z/r, where Z is the net charge on the ion and r is its radius in angstrom units, provides a useful basis for comparison of the complex-forming tendencies of ions.[2]

The difficulties in applying this concept directly to such mechanisms as absorption or migration of ions within a medium arise mainly because of the uncertainty in evaluating the dielectric constant of the medium. For this work, two assumptions have been made: (1) that the dielectric constant of the extracellular fluid in man and the absorption properties of his cellular tissue are constant, and (2) that plutonium in man exists in only the tetrapositive state. These assumptions were combined with Langham's plutonium excretion equation,[3]

$$\frac{Y_u(t)}{q_0} = 0.002t^{-0.74} ,$$

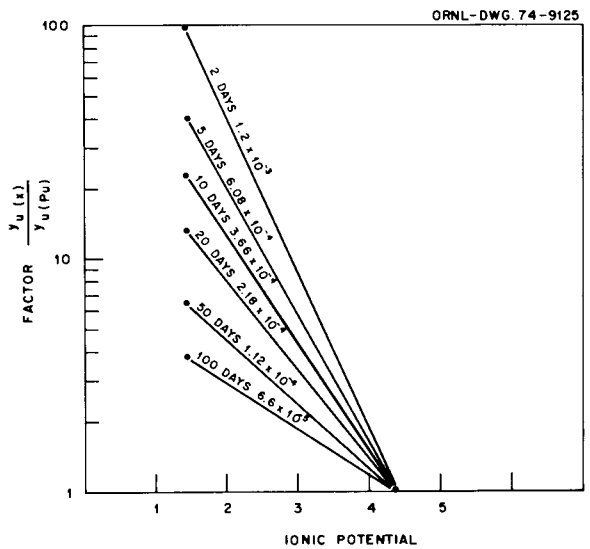

Fig. 28.1. Variation in urinary excretion of ions relative to ionic potential.

and Spiers' radium excretion equation,[4]

$$\frac{Y_u(t)}{q_0} = 0.28t^{-1.52} ,$$

to obtain the series of curves shown in Fig. 28.1.

The top curve is for $t = 2$ days after intake of ionized material. The fraction of q_0 excreted on the second day was calculated for radium using Spiers' equation and for

1. Radiation Monitoring Section.
2. *The Actinide Elements,* ed. by Glenn T. Seaborg and Joseph J. Katz, McGraw-Hill, New York, 1954.
3. Wright H. Langham, "The Application of Excretion Analyses to the Determination of Body Burden of Radioactive Isotopes," *The Measurement of Body Radioactivity,* British Journal of Radiology, suppl. 7, p. 95, 1957.
4. F. W. Spiers and P. R. J. Burch, "Measurements of Body Radioactivity in a Radium Worker," *The Measurement of Body Radioactivity,* British Journal of Radioactivity, suppl. 7, p. 81, 1957.

plutonium using Langham's equation. The ratio of these values, as shown on the ordinate, is plotted at the ionic potential of radium, as shown on the abscissa, then connected with a straight line on the semilog scale to the point for a ratio value of 1 at the ionic potential of plutonium. The curves for other times after exposure were obtained similarly.

The fraction excreted for another material may be predicted by use of these curves if the ionic potential of the material is known.

Figure 28.2 shows a comparison between the estimated strontium excretion using this technique and that obtained with the power function equation given in ICRP Publication 2; $^{90}Sr^{2+}$ has an ionic potential of 1.77.

Figure 28.3 shows an estimated americium excretion curve compared with the experimental excretion values reported by Rosen, Cohen, and Wren.[5]

Values for ^{147}Pm activity in the first postexposure urine samples of three persons were used with this technique to plot predicted excretion rates (Fig. 28.4); the predicted and actual results are shown.

The equation for excretion in urine of an ion having an ionic potential denoted by i is

$$\text{Exc rate} = 5.54t^{-1.82+0.182i}\, e^{-1.429}\ \text{day}^{-1}\ ,$$

assuming the power function describes the excretion from and retention in the body. When hydrolysis is assumed as the basis, then the equation is

$$\text{Exc rate} = 1.1t^{-0.095-0.047\text{pK}_h}\, e^{-0.059\text{pK}_h}\ ,$$

5. J. C. Rosen, N. H. Cohen, and M. E. Wren, *Health Phys.* **22**, 621 (1972).

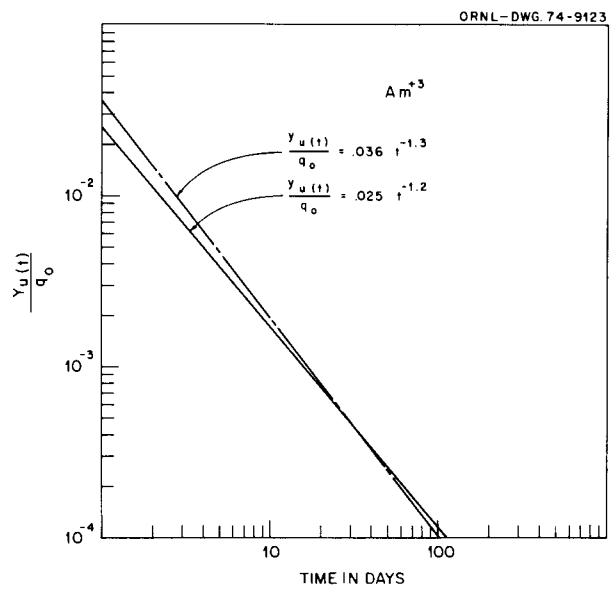

Fig. 28.3. Comparison of derived and experimental Am excretion rates.

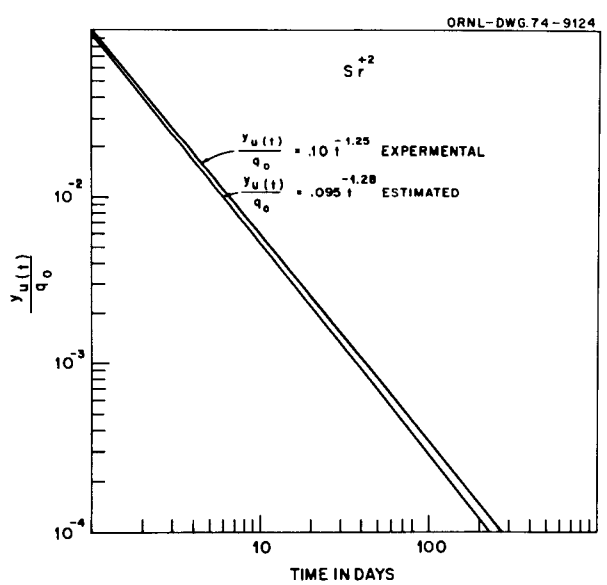

Fig. 28.2. Comparison of derived and experimental ^{90}Sr excretion rates.

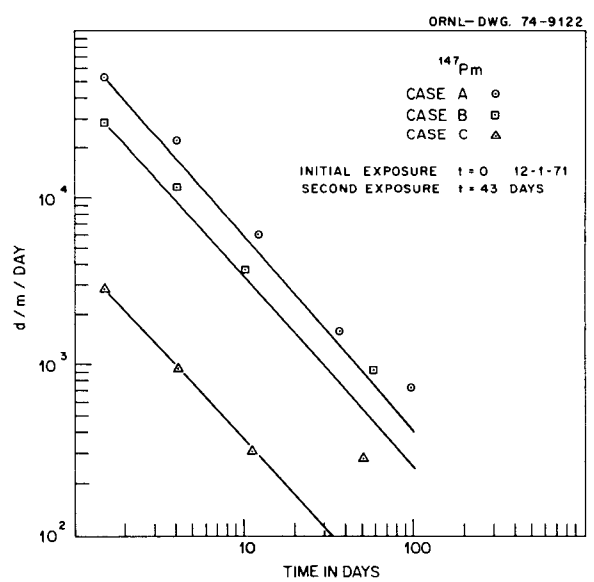

Fig. 28.4. Comparison of predicted and actual excretion of ^{147}Pm.

where pK_h is the negative log of the hydrolysis constant.

We anticipated and have found that the excretion rates for elements of the rare-earth transition series are predictable, because the electrons of the inner shell of this series are not involved in chemical bond formation, and because their chemical properties primarily are functions of charge and size. We have found, also, on the basis of actual excretion data, that the excretion rates of several other materials may be predicted rather well by use of this ionic potential technique.

29. Absorbed Dose During Breast X-Ray Therapy

G. G. Warner[1] J. W. Poston

The computer code BRHGAM[2] was modified to obtain computations of absorbed doses to various organs during radiotherapy for breast cancer. Four exposure situations (Fig. 29.1) were suggested by R. J. Cloutier of ORAU, with ^{60}Co as the source nuclide.[3] A new target region for each exposure was inserted in the phantom (Fig. 29.1) to determine the absorbed dose in the useful beam. Each region had a finite thickness with beam dimensions and was placed at a specified depth. Skin-to-source distance for all exposures was 70 cm. Some results, expressed as rads relative to 1 rad in the useful beam, for selected organs are found in Table 29.1.

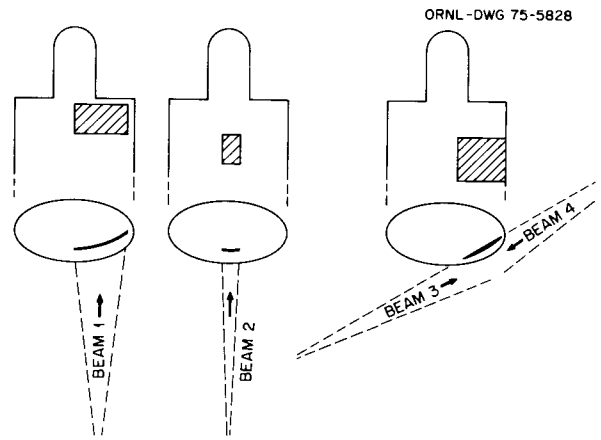

Fig. 29.1. Four exposures for breast x-ray therapy.

1. Computer Sciences Division.
2. G. G. Warner, *BRHGAM: A Medical X-Ray Dose Estimation Program,* ORNL-TM-4393 (October 1973).
3. Letter to J. W. Poston, May 31, 1974.

Table 29.1. Absorbed dose during breast x-ray therapy

Exposure	(1) A/P	(2) A/P	(3) LA/31.5°	(4) RA/31.5°
Beam size, cm	10 × 18	6 × 10	10 × 15	10 × 15
Depth, cm	4.0	3.0	2.9	2.9
Organs	rads/rad			
Adrenal glands	*a*	0.0073	0.0016	*a*
Heart	0.010	0.50	0.0029	0.011
Left lung	0.21	0.021	0.035	0.022
Pancreas	0.0027	0.0036	0.0024	0.0031
Left arm bone	0.13	0.0013	0.073	0.11
Clavicles	0.25	0.0017	*a*	0.0018
Ribs	0.14	0.037	0.10	0.058
Scapula	0.18	0.0048	0.0039	0.0013
Spine	0.095	0.088	0.0010	0.0014
Skin	0.057	0.016	0.059	0.044
Spleen	0.0034	0.0025	0.0040	0.0017
Thymus	0.16	0.076	*a*	0.0058
Thyroid	0.012	0.0017	*a*	0.0022
Total body	0.041	0.016	0.012	0.0099

[a] Less than 0.001 rad/rad.

30. Effect of Source Organ Size on Absorbed Fraction Distribution

N. H. Mei[1] G. G. Warner[2] P. S. Stansbury[3] J. W. Poston

A program of measurements was performed to determine if the size of a source organ affected the absorbed fraction in various target organs. Measurements were made in the MR. ADAM phantom[4] in a manner similar to that of Garry et al.[5] for a set of five bladders filled with ^{137}Cs, a set of five bladders filled with ^{60}Co, and a set of five stomachs filled with ^{137}Cs (see Figs. 30.1 and 30.2 and Tables 30.1 and 30.2).

Estimates of absorbed fraction based on the measurements were compared with Monte Carlo estimates for similar source organ–target organ configurations.

Many of the techniques of measurement were similar to those reported by Garry et al. Absorbed dose measurements were made with the Phil detector at representative locations within the target organs. All of the 20 target organs studied were within the soft-tissue equivalent parts of the phantom. Source organs were filled with aqueous solutions containing the radionuclides. In order to ensure a uniform distribution of source material by preventing precipitation, sodium hydroxide was added to the ^{137}Cs solutions (0.25 *N*) and hydrochloric acid was added to the ^{60}Co solutions (1 *N*).

1. Foreign guest, Republic of China.
2. Computer Sciences Division.
3. ORAU Laboratory Graduate Participation Grant, School of Nuclear Engineering, Georgia Institute of Technology.
4. P. S. Stansbury and J. W. Poston, *Health Phys. Div. Annu. Progr. Rep. July 31, 1974*, ORNL-4979, p. 73.
5. S. M. Garry, P. S. Stansbury, and J. W. Poston, *Health Phys. Div. Annu. Progr. Rep. July 31, 1974*, ORNL-4979, p. 33.

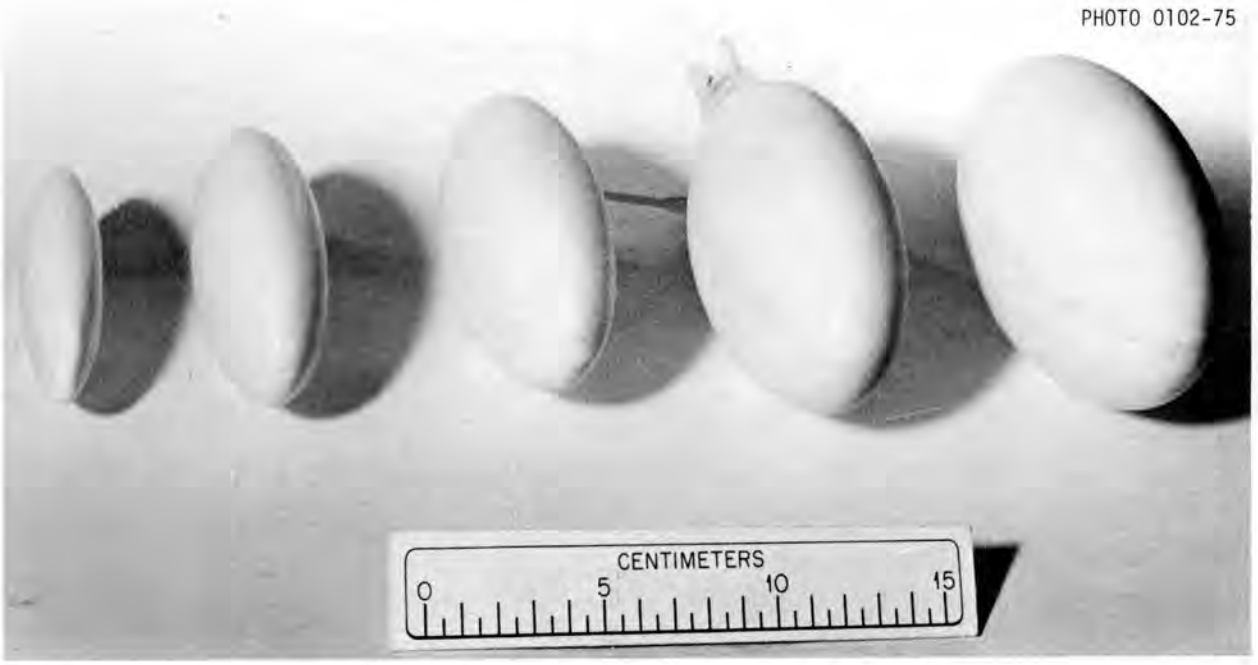

Fig. 30.1. Molded polystyrene stomach source organs of varying size.

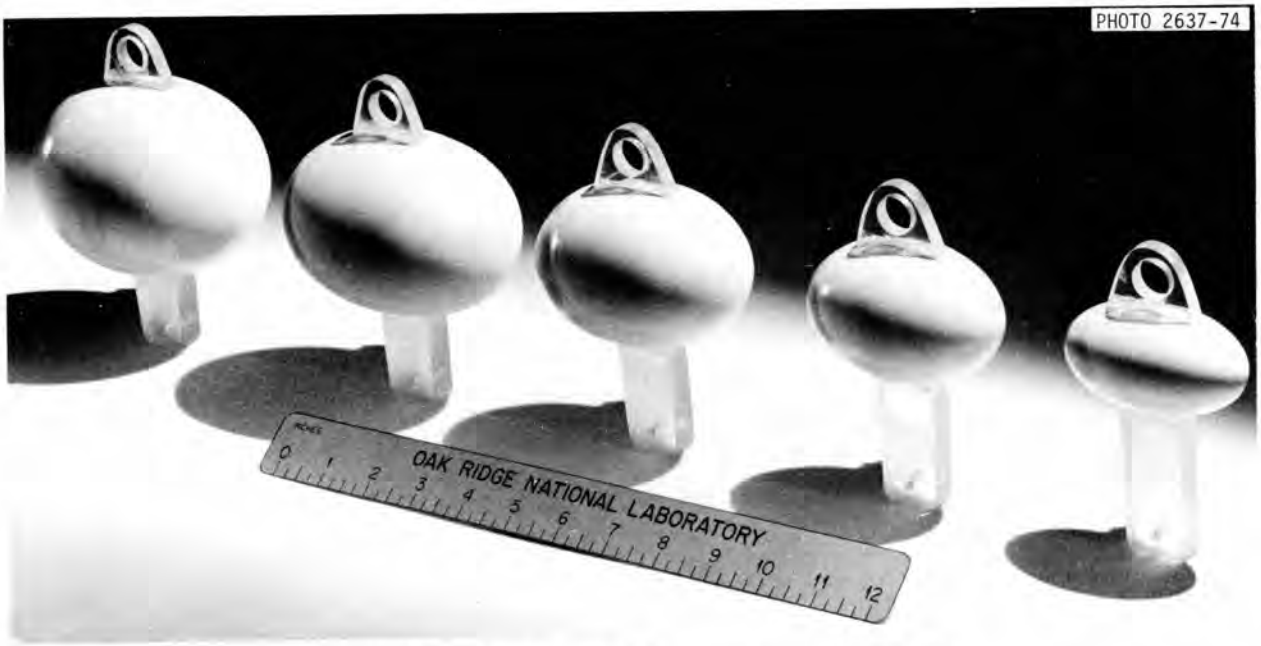

Fig. 30.2. Molded polystyrene bladder source organs of varying size.

Table 30.1. Comparison of physical stomach contents (cm^3) with mathematical stomach contents (cm^3)

Stomach	Physical stomach contents	Mathematical stomach contents	Percent difference	Percent difference (compared with normal stomach)
I	568.9	573.1	−0.73	+127.38
II	371.2	381.1	−2.60	+48.36
III	236.0	250.2	−5.68	−5.68
IV	117.2	156.8	−6.12	−41.17
V	59.9	68.1	−12.04	−76.06

Table 30.2. Comparison of physical bladder contents (cm^3) with mathematical bladder contents (cm^3)

Bladder	Physical bladder contents	Mathematical bladder contents	Percent difference	Percent difference (compared with normal bladder)
I	454.0	463.7	−2.09	+124.08
II	316.4	308.1	+2.69	+56.17
III	206.4	202.6	+1.88	+1.88
IV	121.3	127.3	−4.71	−40.13
V	53.3	55.1	−3.27	−73.69

Several improvements over previous techniques were made. The source organs were molded of polystyrene, mechanically a much stronger plastic than Lucite. Instead of immobilizing the radioactive contents with a jelling material, the organs were coated with an approximately 1-mm-thick layer of latex. Testing, by dropping a coated water-filled organ a height of 2 m, showed that the latex maintained its own mechanical integrity, while the polystyrene beneath shattered from the impact. Personnel of the Isotopes Division performed the organ loading, sealing, and coating with latex. The coating procedure saved time and personnel exposure during loading.

A further safety technique was the use of phenolphthalein. One gram of this indicator was added per liter of tissue-equivalent fluid. The acid-base nature of the tissue-equivalent fluid was adjusted slightly to be the opposite of the contents of each source organ. Because of the sensitivity of this system, it was felt that very small leaks could be detected easily. However, no leaks were detected; as previously, no traces of contamination due to these experiments were found.

Other improvements included a better detector positioning device and better source organ mounting apparatus. The detector positioning device shown in Fig. 30.3 allowed greater flexibility in choosing measurement locations and provided an optically determined repeatability of better than 1 mm. The organ mounting apparatus, some of the male ends of which are shown in Figs. 30.1 and 30.2, provided easy-to-use, stable organ mounts.

The experimentally determined absorbed fractions compare favorably with the Monte Carlo estimates. A tabulation of the results along with a more complete description of the methods and data analysis is given by Mei et al.[6] The overall experimental error was estimated to be 12%. The error estimates for the calculated absorbed fractions are based on the calculated coefficients of variation. If the sum of both errors is used as the criterion for judgment, both estimates of absorbed fractions agree for all target organs except those in the gastrointestinal tract. In these cases, it is believed that the measured absorbed fractions are in error due to the difficulty in measuring the absorbed fraction in target organs of complicated geometry in close proximity to the source organs.

The data from experiment and from calculations were analyzed to assess the effect of source organ size on absorbed fraction in a few selected target organs. Over the range of source organ sizes chosen, the absorbed fractions did not change significantly for either ^{60}Co or ^{137}Cs. The measured absorbed fractions tended to vary less than the calculated absorbed fractions. In fact, for the target organs analyzed, all variations of absorbed fraction with source organ size were less than 5%. Figures 30.4 and 30.5 show results which are typical of the data.

Similar experiments need to be done at other energies, particularly lower energies, before it can be said that a symmetric distribution can be accurately approximated by a point source. An improvement suggested by this work is the development of a smaller dosimeter in order that better assessments of absorbed fraction may be made in organs of complicated geometry close to a source organ.

6. N. H. Mei, G. G. Warner, P. S. Stansbury, and J. W. Poston, *Measurements of Absorbed Fractions as a Function of Source Organ Size for Selected Source Organs in a Heterogeneous Phantom*, ORNL-TM-4916 (June 1975).

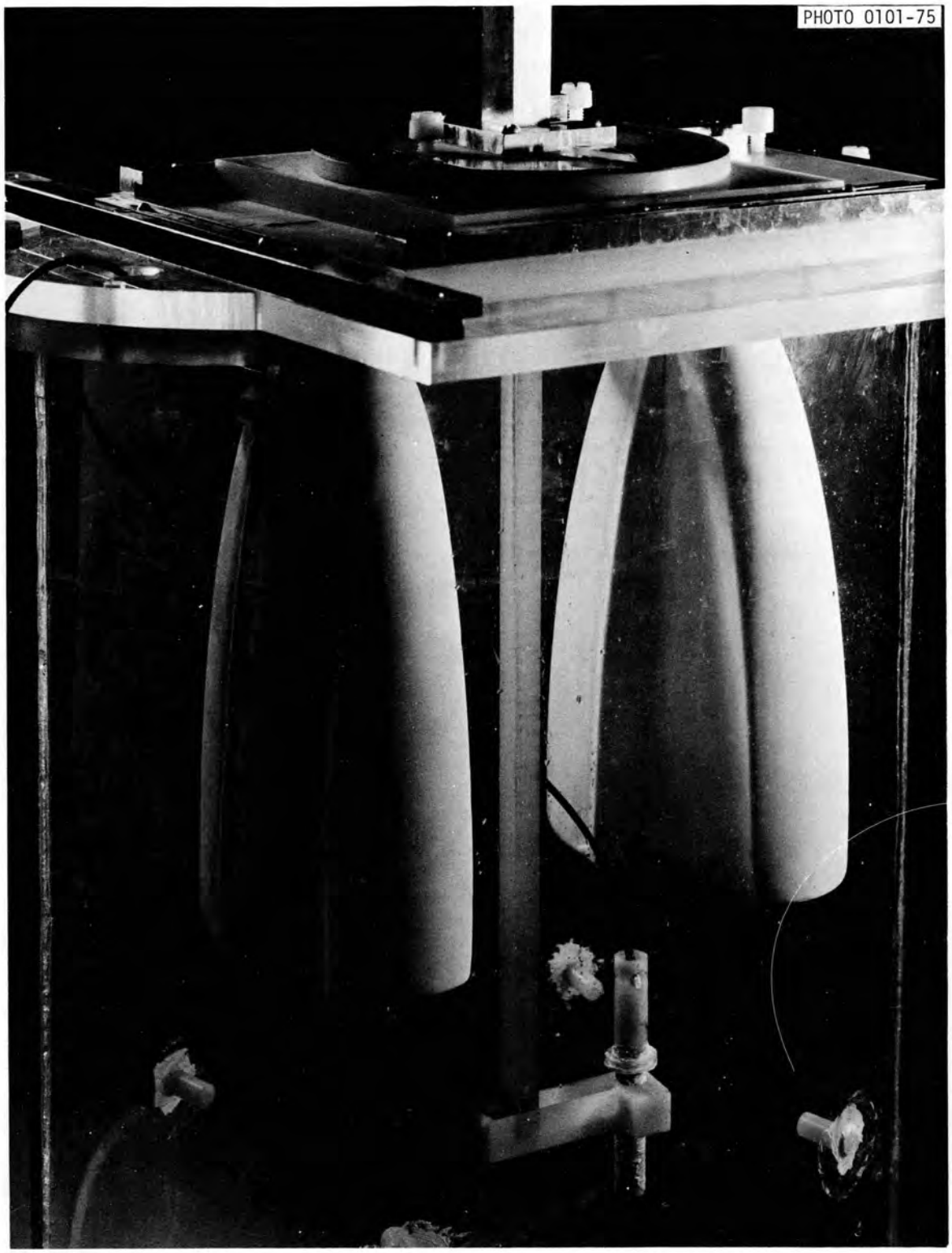

Fig. 30.3. Detector position device holding Phil detector inside the MR. ADAM phantom.

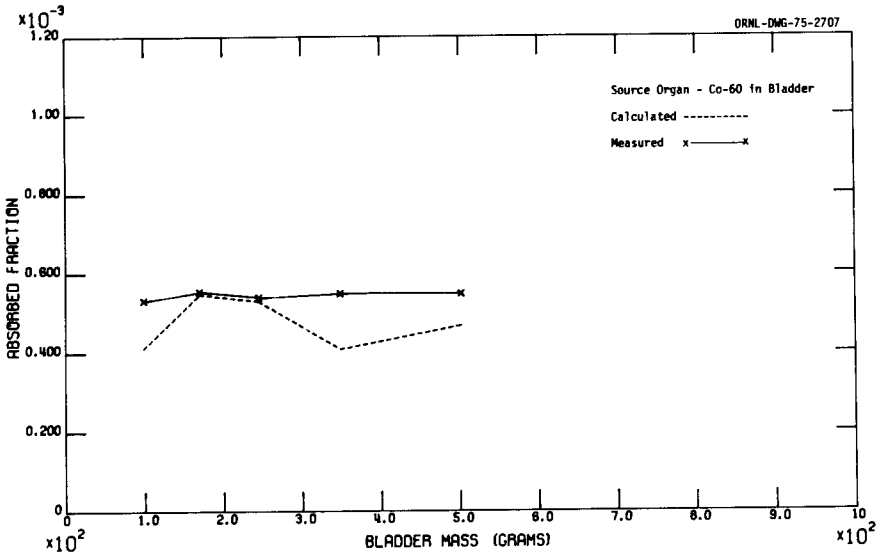

Fig. 30.4. Absorbed fractions in the stomach as a function of the mass of the ^{60}Co bladder.

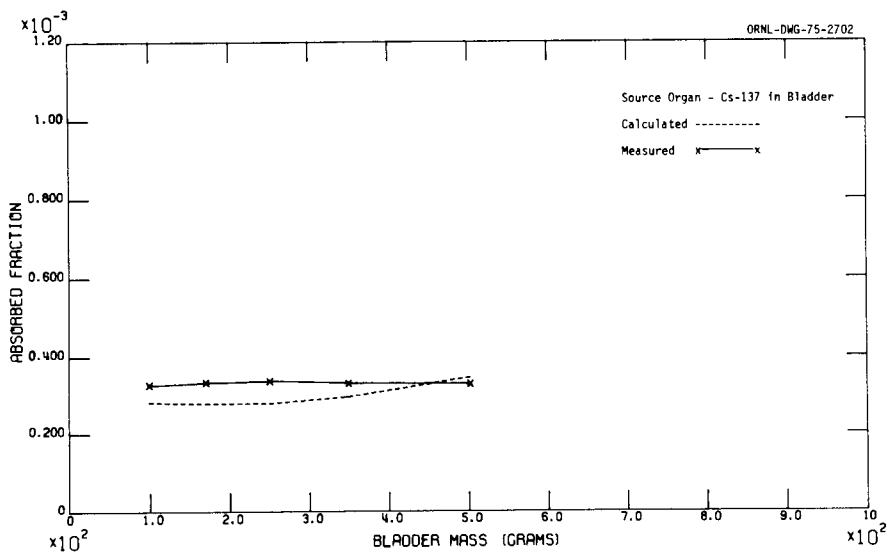

Fig. 30.5. Absorbed fractions in the kidneys as a function of the mass of the ^{137}Cs bladder.

31. Nuclear-Powered Cardiac Pacemakers

R. L. Shoup

The cardiac pacemaker is the first prosthetic device powered by nuclear energy to achieve practical application in man. Several manufacturers have developed ^{238}Pu-powered pacemakers. Since plutonium is, by definition, "special nuclear material," pacemakers containing ^{238}Pu are subject to Nuclear Regulatory Commission (NRC) regulations in Title 10, Code of Federal Regulations, Part 70 (10 CFR 70). Prior to licensing plutonium-powered pacemakers for routine use, the NRC is required to write an environmental statement discussing aspects of their impact on the environment. This program in the Health Physics Division of ORNL is to provide NRC with technical assistance in completing this environmental assessment. This assistance primarily includes performing an environmental risk assessment and a benefit analysis.

BACKGROUND

Several tens of thousands of cardiac patients in the United States have been restored to normal and useful lives with the implantation of cardiac pacemakers. Pacemaker implantations are indicated for patients suffering from certain forms of cardiac arrhythmias. In most cases, these disturbances are associated with a lack of effective, coordinated contraction of the heart's lower chamber in synchrony with its upper chambers.

Conventional pacemakers are powered by mercury batteries (mercuric oxide–zinc) and require periodic surgical replacement of the entire pacemaker upon the loss, or impending loss, of battery output. The present expected service lifetime of conventional pacemakers including new improved batteries ranges from 1½ to 6 years (service lifetimes based on the period of time the manufacturer will grarantee the unit). A rechargeable pacemaker using a nickel–cadmium battery has recently been developed with a lifetime of 10 years. The expected lifetimes of plutonium-powered cardiac pacemakers range from 10 to 20 years.

The NRC is currently licensing the implantation of plutonium-powered pacemakers under a limited investigational program until it can be established that (1) nuclear-powered pacemakers are safe and reliable, (2) routine use will not subject the public to any undue risk, and (3) the benefits derived from the use of nuclear-powered units will outweigh the risk to the public.

Pursuant to NRC's responsibilities under the National Environmental Policy Act of 1969 (Public Law 91-190), the Council of Environmental Quality's guidelines of August 1, 1973 (38 F.R. 20550), and 10 CFR 51 of the Commission's regulations, environmental statements are required to be prepared prior to taking major Federal actions that may affect the quality of the human environment. Authorizing the routine use of nuclear-powered pacemakers (beyond the present investigational use) is considered to be a major Federal action. Therefore, an environmental statement has been written which describes and evaluates the environmental consequences of use of plutonium fuel in cardiac pacemakers.

Three major subjects are identified from the 10 CFR 51 guidelines as being pertinent to this environmental statement. These are (1) potential impacts on the environment, (2) a cost-benefit and benefit-risk balance, and (3) available alternatives to such use. With respect to environmental impacts, three are identified: (1) radiation exposure to the patients from implanted pacemakers, (2) exposure to the public from normal use, and (3) release of plutonium from accidental or abnormal events.

ENVIRONMENTAL ASSESSMENT

The radiation doses from a Medtronics model 9000 pulse generator containing 173.2 mg of plutonium of 90% by weight ^{238}Pu and 0.26 ppm ^{236}Pu were determined by Battelle Pacific Northwest Labora-

tories.[1] Integrated total dose equivalents to various organs for 5-, 10-, 15-, and 20-year periods are shown in Table 31.1 for a subcutaneous pacemaker implant above the left pectoral muscle (implant location shown in Fig. 31.1).

The radiation level at the skin surface of a patient with an implanted pacemaker is 1 to 2 millirems/hr, and at a distance of 20 cm from a patient's body the radiation from a pacemaker is less than the ambient background radiation.

Spouses of pacemaker patients will receive the largest radiation exposure. This is because their contact with the patients is more frequent and at closer distances than contacts by other persons. The average annual exposure to a spouse from a patient was calculated by Battelle Pacific Northwest Laboratories to be 5 to 15 millirems/year,[2] and most of this exposure is received during the sleeping hours, when the spouse is usually within a few feet of the patient.

All other individuals associating with pacemaker patients will be exposed to much lower levels of radiation. Dose calculations for various categories of people with whom pacemaker patients are likely to come into contact during their daily activities are shown in Table 31.2. With respect to the general public, the radiation dose attributable to pacemaker patients will be negligible.

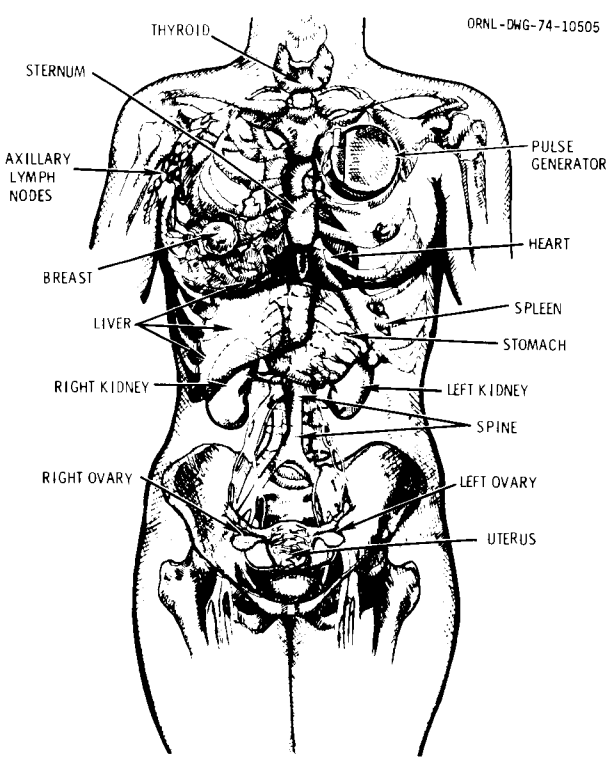

Fig. 31.1. Location for normal implantation of a pacemaker above left (or right) pectoral muscle.

Pacemakers are required to be designed to high standards such that they can withstand hypothetical credible accidents. Also, requirements are placed on the fuel form to assure that its physical and chemical form be such that it will be as nondispersible and nontransportable as is practicable. Plutonium dioxide, a chemically unreactive form of plutonium, is compressed and fired into a hard, glossy ceramic pellet to reduce the likelihood of wide-scale fuel dispersion in the event of an accidental capsule breach. To provide a high degree of assurance that the plutonium fuel will be contained under any accident condition, the fuel pellets are clad with two or three layers of refractory metals. Manufacturers are required to demonstrate that their pacemaker model will be able to maintain fuel capsule integrity over a spectrum of mechanical, thermal, and environmental stresses.

The possibility that stresses may be sufficient to breach the fuel capsule does exist. For this reason, a risk assessment of credible events and their probability of occurrence was performed. A probabilistic model was developed to establish probabilities of and potential hazards from a capsule breach. A block diagram of this analysis is shown in Fig. 31.2.

Radiological consequences are calculated by combining accident statistics from mortality tables with probabilities of capsule breach by different stresses and source-term information in the event of a breach.

The cremation of a deceased patient's body with his pacemaker still intact is deemed to be the most likely incident to result in the dispersion of plutonium fines into the environment. The probability of a pacemaker's fuel capsule rupturing in a crematory furnace is dependent upon a number of factors. These are the probability of a patient death per year, the probability of a body being cremated after death, the probability that the pacemaker will not be removed prior to cremation, and the probability that the cremation furnace may exceed the prototype test temperature for a sufficiently long time to rupture the fuel capsule. These four probabilities combine to an overall expecta-

1. L. W. Brackenbush, G. W. R. Endres, and B. I. Griffin, "Radiation Doses from the Medtronic Laurens-Alcatel Model 9000 Pulse Generator," Battelle Pacific Northwest Laboratories Report 2211201653, Amendment 2 (October 1973).

2. R. W. McKee, L. C. Clark, B. M. Cole, and R. A. Libby, "Dose to the Population: Estimates for Use of Radioisotope Powered Cardiac Pacemakers," BNWL-1858 (draft) Battelle Pacific Northwest Laboratories (September 1974).

Table 31.1. Integrated dose equivalents to organs for 5-, 10-, 15-, and 20-year periods

Pulse generator above left pectoral muscle

Organ location	Integrated dose equivalent, neutron and gamma (rems)			
	5 years	10 years	15 years	20 years
Thyroid	2.7	5.5	8.9	12
Left axillary lymph nodes	2.4	5.1	8.1	11
Right axillary lymph nodes	0.33	0.88	1.2	1.7
Sternum	2.3	4.7	7.8	10
Left pectoral muscle (base of breast)	0.76	1.8	2.7	3.6
Right pectoral muscle (base of breast)	0.31	0.82	1.2	1.7
Heart	0.70	1.7	2.5	3.2
Liver	0.23	0.64	0.97	1.4
Spleen	0.30	1.3	1.9	2.4
Stomach	0.29	0.80	1.2	1.6
Left kidney	0.20	0.52	0.81	1.2
Right kidney	0.19	0.48	0.75	1.1
Left ovary	0.11	0.25	0.41	0.60
Right ovary	0.11	0.24	0.40	0.58
Uterus	0.10	0.23	0.38	0.54
Testes	0.09	0.20	0.32	0.43
Spine (average)	0.70	1.6	2.4	3.3
Torso (average)	0.70	1.7	2.5	3.3
Whole body (average)	0.36	0.95	1.3	1.8

Table 31.2. Radiation doses to critical groups from cardiac pacemakers

Assuming 10,000 implanted cardiac pacemakers with plutonium batteries

Critical group	Group population	Individual dose (millirems per person per year)			Total dose to group (man-rems/year)	
		Dose from pacemaker[a]	Average dose		Dose from pacemaker[b]	Natural background radiation
			Medical X rays	Natural background radiation		
Spouses	6,340	6–15	73	102	84	646
Household members	8,950	1–3	73	102	24	912
Work associates[c]	72,000	0.1–0.3	73	102	21	7,344
Nonwork associates[c]	218,000	0.05–0.15	73	102	29	22,378
Total in U.S. populace not included above		$\ll 0.01$	73	102	98	21,400,000
Total[d]					256	

[a]Dose will vary depending upon the plutonium content and fuel characteristics of a particular pacemaker model.
[b]Integrated dose using 8 Ci of plutonium, which is maximum plutonium used in any battery.
[c]A patient is predicted to associate with approximately 30 persons during his daily activities.
[d]Total dose to U.S. population of 210,000,000 excluding dose to patients.

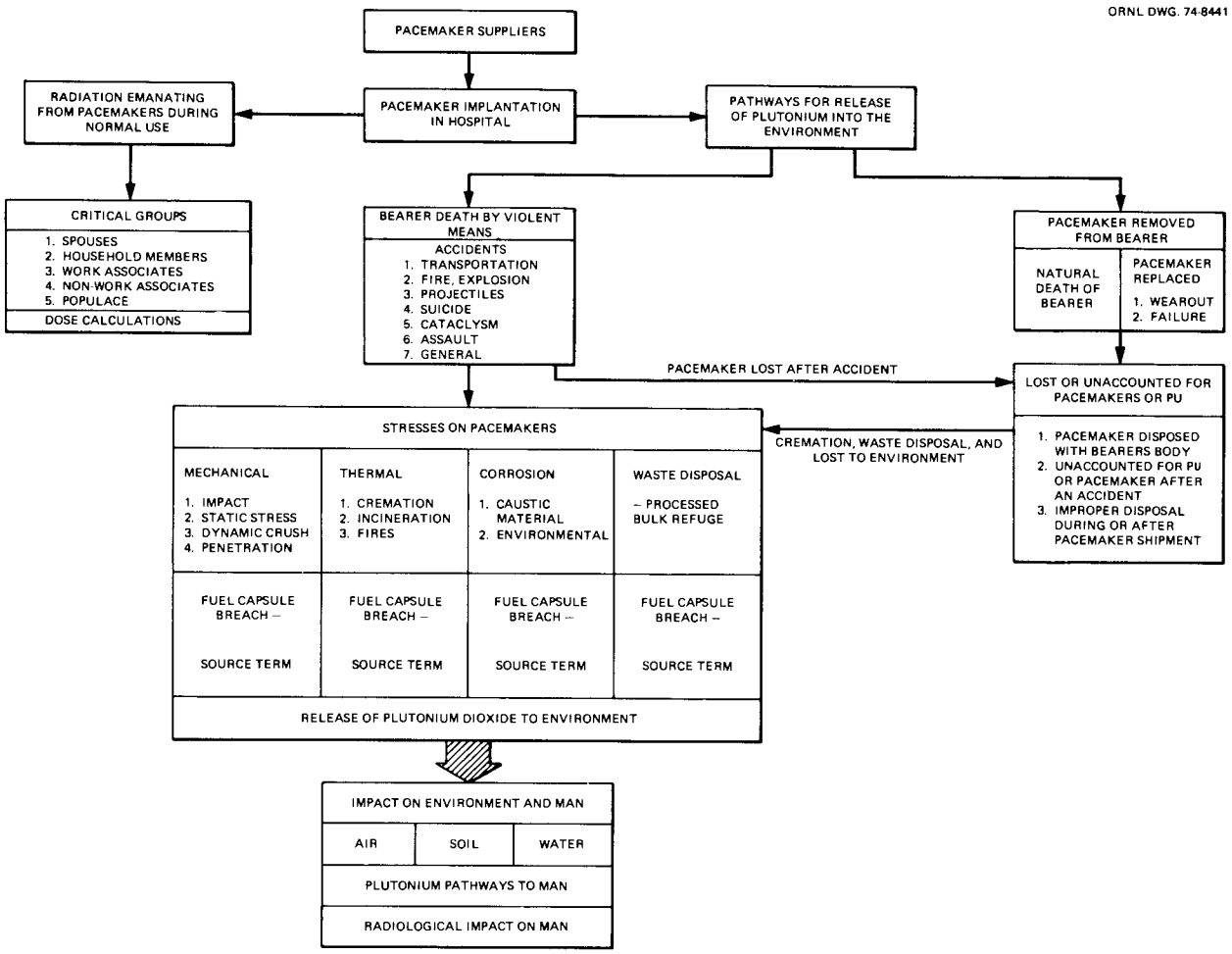

Fig. 31.2. Plutonium-powered cardiac pacemaker risk logic model.

tion of one breach in 20 years from a pacemaker population of 10,000 patients. Figure 31.3 shows the risk-logic progression for a fuel-capsule breach during cremation.

If a fuel capsule were to be breached in a crematory furnace, most of any plutonium fines would remain in the retort or entrainment system of the furnace. By assuming that all of the respirable-size particles ($\leqslant 10$ μm from source-term information) leave the furance stack, the maximum dose commitment to an individual in the vicinity of a crematorium is calculated to be 420 millirems (50-year dose commitment). The average 50-year dose commitment to individuals exposed to plutonium particles in the gaseous plume out to 2000 m from a crematorium is 7.5 millirems.

These dose commitments are calculated from a computer code given settling velocities and release rate of plutonium fines. Near-neutral weather stability and a 4-m/sec wind velocity are used in the calculation, for they are reasonably representative of average U.S. meteorological conditions. The inhalation model employed to calculate absorbed dose is a representation of the lung model developed by the International Commission on Radiological Protection Task Group on Lung Dynamics. The results of these calculations are shown in Fig. 31.4. Data from Fig. 31.4 on individual dose commitments are combined with data on population densities to calculate the total radiological impact within the area of the plume. An average metropolitan population density (1760 persons/km^2) is chosen as representative of population densities of cities in which crematoria are located. The total 50-year dose commitment to an average metropolitan population exposed in the downwind sector from a crematorium out to a radius of 20,000 m is 410 man-rems per postulated breach. The population in

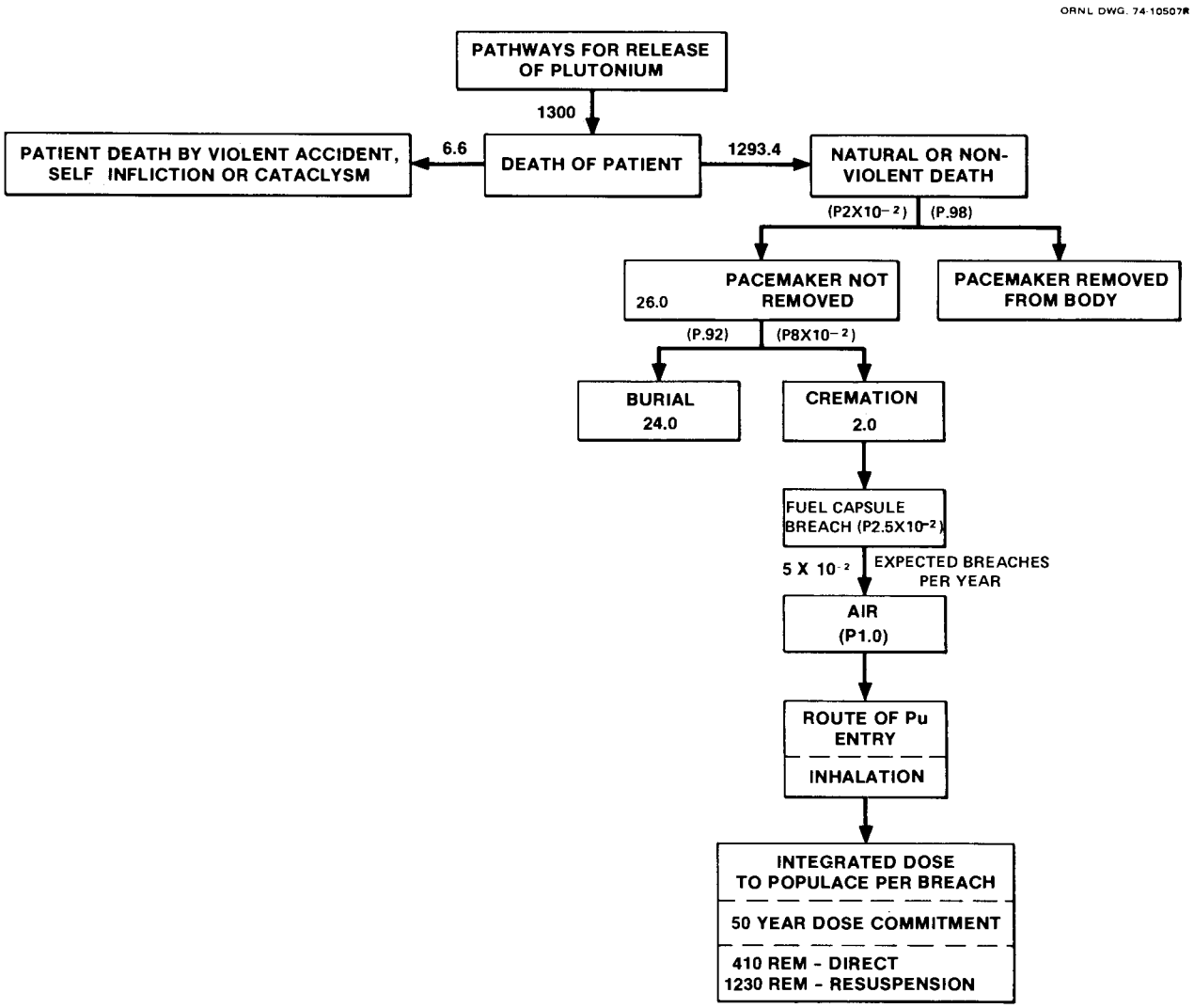

Fig. 31.3. Risk logic for a postulated fuel capsule breach during cremation.

such a sector is 4500 persons, which is approximately 0.002% of the U.S. population. The dose commitment over 50 years to this group of 4500 persons from a breach would be approximately 2% of their ambient background absorbed dose.

BENEFIT ASSESSMENT

The benefits that can be realized from the use of plutonium-powered cardiac pacemakers are related to the long lifetime of the plutonium-powered battery, which results in the reduction or elimination of the need for pacemakers to be replaced because of battery depletion. The principal benefit derived from the use of plutonium-powered pacemakers is the number of lives saved by the decreased surgical mortality associated with decreased need for replacement operations, the attendant reduction in surgical and medical complications, and the reduction of patient pain, suffering, and anxiety.

Mortalities from surgical procedures including post-operative follow-up vary from 1 to 4%, with a mean value of approximately 3%. A surgical mortality rate of 1% is used for reimplantation operations because they involve a reduced risk due to simpler procedures. (More recent statistics indicate that these mortalities are much lower.)

These mortality rates were used in a computer program which was developed to compare expected patient mortalities for groups of patients using various

Table 31.3. Surgical deaths per 10,000 pacemaker patients (equilibrium patient population size) wearing pacemakers with various replacement (service life) intervals

At end of year –	Deaths per 10,000 patients for pacemaker replacement interval of –					
	1½–3 years	5 years	6 years	8 years	10 years	20 years
5	665	528	500	489	489	489
10	1100	822	785	750	727	712
15	1545	1118	1066	1002	973	938
20	1980	1413	1342	1260	1218	1162

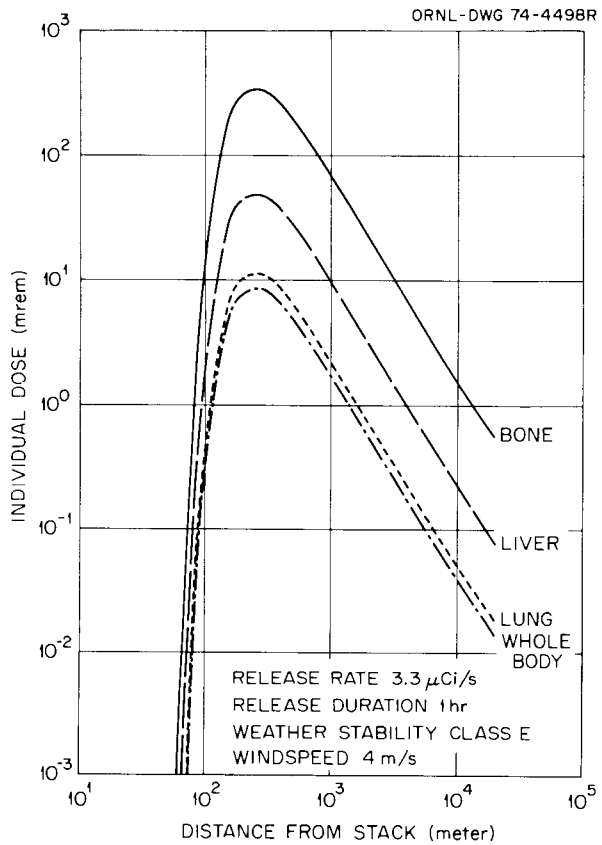

Fig. 31.4. Dose for $^{238}PuO_2$ particle size ≤10 μm as a function of distance.

pacemaker replacement intervals. The results of these calculations can be used to determine the lives saved by pacemakers with one replacement interval as compared with pacemakers with a different replacement period. Results of these calculations are shown in Table 31.3. For example, for an equilibrium population of 10,000 pacemaker patients, the use of plutonium-powered pacemakers with an expected service life of 10 years would save, in 10 years, an estimated 373 lives (1100 – 727) when compared with conventional pacemakers with a 1½- to 3-year service life. The lives saved for other combinations of expected pacemaker service lives may be obtained from Table 31.3.

Data for these computations were abstracted from literature references. This literature represents experience with approximately 20,000 patients with conventional-powered pacemakers. The input data for the computation included (1) estimated mortality of pacemaker patients from causes not pacemaker-related, (2) replacement of pacemakers due to battery depletion at a distribution of times over 1½ to 3 years as reported in the literature and at the other designated replacement intervals, (3) pacemaker replacements because of random failures at the rate of 2% annually for all types, (4) a patient mortality rate due to pacemaker system failures of 0.1% annually, (5) mortality rates due to initial implantation surgery of 3% and due to reimplantation surgery of 1%, and (6) the addition of new patients to the groups to replace patients lost from the groups by death.

Pacemaker patient populations are not representative of the U.S. populace with respect to age distribution. The age distribution of patients submitted by Medtronics, Inc.,[3] was used in this study since their data cover the largest statistical population of patients (1989 patients) and are similar to other reported age distributions.

Each patient group was subdivided into five-year age subgroups. The mortality rate from natural attrition for each age subgroup was assumed to be the same as the U.S. mortality rate for the subgroup. The patient age distribution, U.S. populace mortality rates, and expected patient deaths from natural attrition per age subgroup are presented in Table 31.4.

3. Medtronics, Inc., "Benefits Resulting from the Use of the Isotopic Pulse Generator," Dec. 17, 1973, with enclosure "Long-Term Survival of the Bearers of Cardiac Stimulators," Marie-Francoise LeFebvre, Attachee au Centre Hospitalier Regional de Lille, January 1963–July 1972.

Table 31.4. Pacemaker patient mortality estimates

From natural attrition. Does not include pacemaker-related mortality

Age group[a]	Percent of patients in age group[b]	Percent of Patient deaths per year[c]	Average remaining lifetime (years)	Expected % patient deaths per year
0–5	0.16	2.44	71.0	0.004
6–10	0.16	0.21	67.2	0.0003
11–15	0.16	0.20	62.3	0.0003
16–20	0.17	0.56	57.5	0.0009
21–25	0.15	0.71	52.8	0.0011
26–30	0.15	0.69	48.1	0.0010
31–35	0.25	0.83	43.5	0.0021
36–40	0.25	1.19	38.8	0.0030
41–45	1.45	1.78	34.3	0.0258
46–50	1.45	2.62	29.9	0.0380
51–55	4.4	3.88	25.7	0.1707
56–60	4.4	5.61	21.8	0.2468
61–65	15.5	7.75	18.1	1.2013
66–70	15.5	10.19	14.8	1.5795
71–75	19.5	12.78	11.8	2.4921
76–80	19.5	13.80	9.3	2.6910
81–85	7.5	13.94	7.0	1.0455
86–90	7.5	35.32	5.0	2.6490
81–95	0.3	68.95	5.0	0.2069
96 up	0.3	100.00		0.3000
				12.66

[a]Mean patient age, 66.8 years.

[b]Based on information from Medtronics, Inc., on age distribution of pacemaker patients.

[c]Based on average U.S. mortality rate for each age group. This assumes the life expectancy of pacemaker patients to be the same as the life expectancy of other persons of the same age.

The patient population within each subgroup was adjusted yearly in this computer study for 20 years. These adjustments included subtracting yearly the total number of patient deaths in each group from the patient population of that age group and then promoting an appropriate fraction of the remaining patients into the next older subgroups. The total number of patient mortalities per age subgroup is a sum of patient deaths from natural attritions, deaths due to risk of surgery, and deaths caused from pacemaker failures.

The above procedures for adjusting the patient populations yearly assume that pacemaker patient mortality rates due to natural attrition are the same as those of the U.S. populace of the same ages. This appears to be valid, for physicians have reported that many patients for whom pacemakers are implanted return to a relatively normal life, that is, to activities considered appropriate for their age; and they enjoy normal longevity patterns.

SUMMARY

The medical benefits (reduction of patients' surgical risk of death, complications, pain, suffering, and anxiety) and the environmental risks (radiation exposure to the population and patients) of using plutonium-powered cardiac pacemakers are difficult to quantify on a basis that can be directly compared.

For a pacemaker population of 10,000 patients, plutonium-powered pacemakers with a 10- to 20-year service life would save six to nine lives annually when compared with conventional pacemakers with a 6-year service life. The total radiation exposure to the U.S. population from 10,000 plutonium-powered pacemaker implants would be 258 man-rems/year. Exposures to others from pacemakers implanted in patients accounts for 256 man-rems/year of this total, with approximately 2 man-rems resulting from postulated breaches of fuel capsules. The total-body exposure to 10,000 patients will exceed 1000 man-rems/year, but this is a voluntary risk.

The NRC has not yet issued its final position on the use of plutonium-powered cardiac pacemakers. There appears to be an alternative pacemaker, the rechargeable nickel–cadmium battery-powered pacemaker, which offers a postulated service lifetime similar to that of the plutonium-powered unit. However, rechargeable pacemakers are not suitable for all patients requiring a long-lived pacemaker. (Up to about 25% of patients requiring pacemakers can fully use a unit's lifetime of 10 to 20 years.)

There is a small population of pacemaker patients which can benefit from the use of plutonium-powered cardiac pacemakers, and the benefits to these patients are substantially greater than the risks to the environment, which are comparatively small. Future authorized use of these units will most likely be selective with respect to patients and subject to strict requirements on accountability, recovery, and disposal.

32. Variation of Calculated Organ Dose Rates from a Pacemaker as a Function of Body Size

W. S. Snyder[1] G. G. Warner[2]

Estimates of dose rate to individual cardiac patients who might use a nuclear-powered pacemaker are usually based on an "average" individual. There is reason to suppose the dose rate to some organs would be greater if a smaller sized individual had been hypothecated. This study was undertaken to provide estimates of the amount of such variation within a reasonable range of body sizes.

The ICRP Report on Reference Man[3] provides average values of mass of 70 kg for the male and 58 kg for the female. One standard deviation each way about the mean suggests limits of 82 kg to 61 kg for the male and 65 kg to 48 kg for the female. Similar data on height or length of the total body would be of the order of 175 cm as the mean for the male and 161 cm as the mean for the female, and the corresponding range of plus or minus one standard deviation about the mean is 168 cm to 180 cm for the male and 158 cm to 168 cm for the female. These lengths of the total body are in approximately the ratio required if the 70-kg phantom is shrunk by a common factor to produce the required mass. Thus the ratio of the mass of the total body (kg) to 70 kg was used to produce phantoms by shrinking all dimensions by a common factor

$$f = (M_{TB}/70)^{1/3} . \qquad (1)$$

Calculated neutron dose rates are reported here for a number of organs for M_{TB} = 70 kg, M_{TB} = 58 kg, and M_{TB} = 48 kg for a pacemaker implanted in the right pectoral position.

The problem is being explored at present, and possibly other positions of the pacemaker and other body masses and sizes may be considered. No computer estimate has been made for the 82-kg body size, as the dose rate to the various organs would be expected to be less than those reported here. These values are of interest principally because they indicate the ratios of increase of the dose rates to organs which are localized (thyroid, kidneys, etc.) and for those of more general distribution (skeleton, red bone marrow, etc.).

The phantom used is that described in ORNL-5000 (ref. 4) and has a mass of 69.88 kg. To produce the smaller sizes, all dimensions were shrunk by the factor f indicated by Eq. (1). The phantom and organs will have the same shapes as in the original phantom, and the masses will be shrunk by the factor f^3. A coordinate system is used as described in ORNL-5000 with the origin at the center of the base of the elliptical trunk, the z axis extending upward, the y axis toward the back of the phantom, and the x axis to the left. The pacemaker is positioned with center at (−10, −7.90, 64). This is equivalent to a subcutaneous implantation of the pacemaker, which is fastened to the pectoral muscle.

A kernel was used to represent the dose rate at various distances within the body. The particular kernel used here is that derived by Dillman,[5] and it appeared to fit several of the published neutron dose curves for pacemaker. This kernel is given by

$$k(X) = 2.87e^{-0.07536X}/X^2 , \qquad (2)$$

1. Consultant.
2. Computer Sciences Division.
3. W. S. Snyder, chairman, *Report of the Task Group on Reference Man,* ICRP Report No. 23, Pergamon Press, 1975.
4. W. S. Snyder, Mary R. Ford, G. G. Warner, and S. B. Watson, *A Tabulation of Dose Equivalent per Microcurie-Day for Source and Target Organs of an Adult for Various Radionuclides,* ORNL-5000 (November 1974).
5. L. T. Dillman and T. D. Jones, "Internal Dosimetry of Spontaneously Fissioning Nuclides," *Health Phys. Div. Annu. Progr. Rep. July 31, 1974,* ORNL-4979, p. 17.

Table 32.1. Variation of dose rates to various organs as a function of body mass for a pacemaker

Organ	Dose rate (10^4 millirads/hr) for body mass of –		
	70 kg	58 kg	48 kg
Thyroid	66.00	85.00	100.00
Lungs	51.00	56.00	66.00
Heart	26.00	30.00	36.00
Red bone marrow	28.00	42.00	41.00
Skeleton	21.00	24.00	41.00
Liver	5.00	6.00	7.60
Kidney, right	1.80	2.30	3.00
Kidney, left	1.20	1.50	2.00
GI, stomach	2.00	2.50	3.30
GI, upper large intestine	0.69	0.89	1.20
GI, small intestine	0.58	0.76	1.00
GI, lower large intestine	0.17	0.23	0.33
Ovaries	0.24	0.33	0.46
Testes	0.041	0.060	0.091

where the kernel gives the dose rate in millirads per hour approximately for the LASL-1 source.[6] The data for a number of target organs are listed in Table 32.1.

Inspection of the dose rates in Table 32.1 reveals that generally the variation is within a factor of 2. Of course, these are not the extremes of size variation in the population. The increase is clearest for small organs which are localized. For larger organs such as skeleton, red bone marrow, and lungs, there are regions of higher dose rates averaged with regions of lower dose rates; and thus a trend for the average is not as clearly evident. It should be remembered that in the large phantom and in the smaller ones the higher dose rates are very nearly equal, but these are not necessarily composed of the same tissue. For example, some of the red marrow will be located quite close to the pacemaker, and the dose rate to these portions of the red bone marrow will be high both in the larger and in the smaller phantom. However, the same fraction of the active marrow may not be included in the region between two isodose curves. The active marrow at greater distances will have a smaller dose rate; but, again, the fraction of the red bone marrow may be different in the two cases. This study is of interest principally to determine approximate bounds for the doses usually considered in radiation protection. However, these average doses may not be the only ones to consider, since the doses received by tissues close to the pacemaker over a ten-year period are fairly high; but, when averaged over a distributed organ such as muscle or red bone marrow, they do not greatly raise the average. Thus, both points of view need to be considered – the higher doses and dose rates received by portions of tissue close to the pacemaker and, also, the average doses and dose rates received by the various organs of the body.

6. F. T. Cross and J. C. Sheppard, "In-Phantom Dosimetry of Plutonium-238 Circulatory Support Heat Sources," *Nucl. Technol.* **13,** 83–94 (January 1972).

33. Age Factors for Dose Rates from an Infinite Cloud of a Photon Emitter

J. W. Poston W. S. Snyder[1] G. G. Warner[2]

Immersion in a cloud of radioactive gas is an important pathway of exposure for the population around nuclear reactors or fuel processing plants. However, the estimates of the dose rate due to a cloud source are based usually on the adult and, in many cases, are only for a dosimeter exposed to the cloud, that is, a dosimeter representing a small mass of tissue. Recently, the authors[3] discussed a more realistic model for dose rate to body organs of an adult which gave estimates of dose rate from 12 monoenergetic cloud sources of photons for 21 body organs as well as an estimate of the whole-body dose. In this paper, the dose rates to children, or persons of smaller body size, are considered to see whether the dose estimates for the cloud are reasonably valid for the population as a whole. It should be emphasized that the data given below, and also those data published previously for the adult, apply only for dose rates received from the external cloud and not to the absorption of the gas within the tissues of the body.

The phantoms used to represent the children are those which have been studied for internal sources for a number of years at the Oak Ridge National Laboratory.[4] They are obtained by shrinking the head, the trunk, and the leg section of the adult phantom by three independent linear transformations. This permits the size of the head, trunk, and legs to be varied independently. The dimensions chosen for the phantoms are based on a study of data presented in the Report on a Reference Man[5] and are chosen to represent possible median values of the distribution of dimensions for the specified age groups namely, the newborn child and children of ages 1, 5, 10, and 15 years. These dimensions together with the adult are listed in Table 33.1, and an outline of the phantoms is shown to scale in Fig. 33.1.

When the transformations are applied to the adult phantom, a phantom having the dimensions of the specified child phantom is obtained for the head, the trunk, and the legs. However, other internal organs may be somewhat distorted. No attempt has been made to redesign the child phantoms to give them the approximate size and shapes of organs as is desirable, and from this point of view the results obtained here are preliminary. Experience thus far has indicated that the dose is reasonably insensitive to small changes in mass and shape when the source is outside the target organ,[6] as it is in this case since it is exterior to the body.

Each of the 12 monoenergetic sources has been processed by the computer code of Dillman[7] to produce the energy spectrum of the scattered photons incident on the surface of the phantom. In fact, the spectrum used for each calculation was identical to that used for the adult phantom, although the sample selection was random, being 60,000 photons in each case. These photons were allowed to impinge on the exterior surface of the phantoms, and doses were recorded as usual in the tissues where the interactions take place.

---

1. Consultant.
2. Computer Sciences Division.
3. J. W. Poston and W. S. Snyder, *Health Phys.* **26**, 287 (1974).
4. W. S. Snyder et al., "Internal Dosimetry," *Health Phys. Div. Annu. Progr. Rep. July 31, 1971,* ORNL-4720, p. 116.
5. *Report of the Task Group on Reference Man,* ICRP-23, Pergamon Press, 1975.
6. W. S. Snyder, "Estimation of Absorbed Fraction of Energy from Photon Sources in Body Organs," in *Medical Radionuclides: Radiation Dose and Effects,* CONF-691212 (1970).
7. L. T. Dillman, *Health Phys.* 27, 571 (1974).

Table 33.1. Phantom dimensions and dose regions

Age (yr)	Weight (kg)	H_1 (cm)	H_2 (cm)	H_3 (cm)	A_1 (cm)	B_1 (cm)	A_2 (cm)
0	3.148	23	13	16	5.5	5	4.5
1	9.112	33	16	28.8	8	7	6.5
5	18.12	45	20	46	11	7.5	6.5
10	30.57	54	22	64	14	8	6.5
15	53.95	65	23	78	18	9	7
Adult	69.88	70	24	80	20	10	7

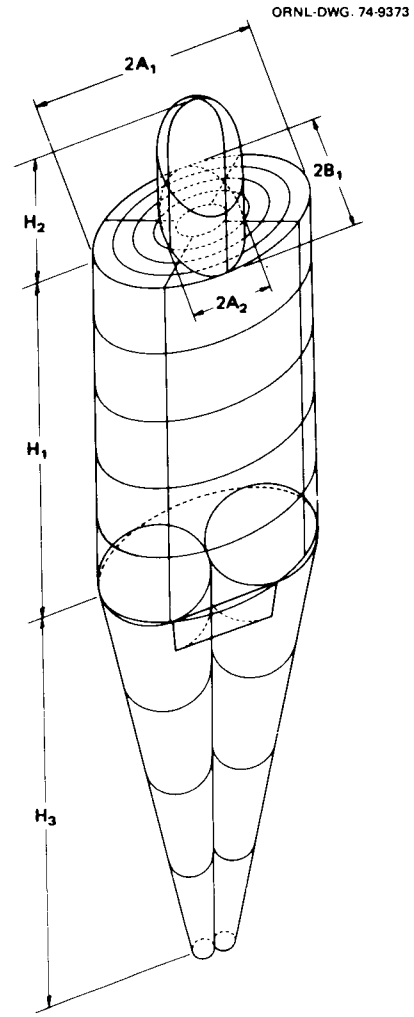

Results were adjusted for each phantom after considering differences in the surface area of each smaller phantom and the photon flux density incident on the surface of the phantoms. Figures 33.2–33.4 show the results for three parts of the body chosen to represent typical results of the calculations. The ratio of absorbed dose (in rads per day) to each phantom to that of the adult is plotted as a function of age (body size) for several monoenergetic photon clouds. Figure 33.2 shows the dose ratios for the skin for energies of 0.01, 0.1, and 1 MeV. The skin was chosen since it represents essentially the surface dose to an individual exposed to the cloud. Many dose estimates given today give only this surface dose. For the lowest energy shown, the dose ratio increases as the phantom age decreases; however, for more energetic photons, little change in the ratio is shown. For photons of about 0.01 MeV the mean free path in tissue is about 0.2 cm; thus most of the energy is deposited in the skin. For photons of higher energy the mean free path is much greater (~6.5 cm for 0.1-MeV photons), and the dose to the skin remains essentially constant.

The dose ratios for the red bone marrow are shown in Fig. 33.3 for the same three energies. The red marrow can be considered as a distributed organ since all parts of the skeleton except the lower arms and the lower legs contain red bone marrow. Here, the dose ratios for low-energy photons increase dramatically as the age of the phantom decreases (about a factor of 7 for the newborn). As the photon energy increases, there is a

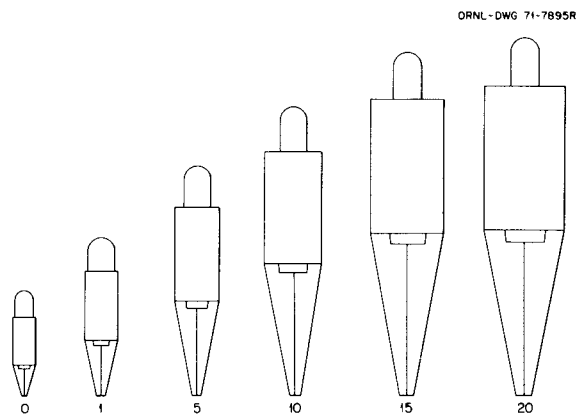

Fig. 33.1. Relative sizes of phantoms for 0, 1, 5, 10, 15, and 20 years.

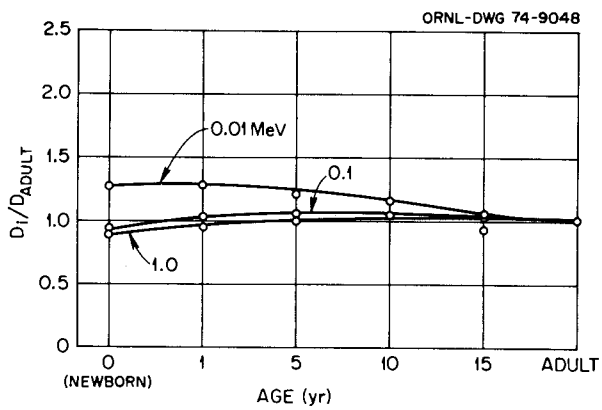

Fig. 33.2. Ratio of dose to child to dose to adult. Mono-energetic photon cloud, skin.

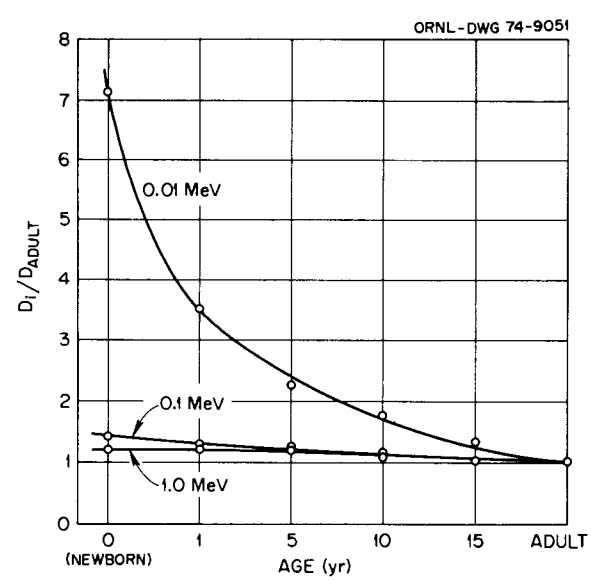

Fig. 33.3. Radio of dose to child to dose to adult. Mono-energetic photon cloud, red bone marrow.

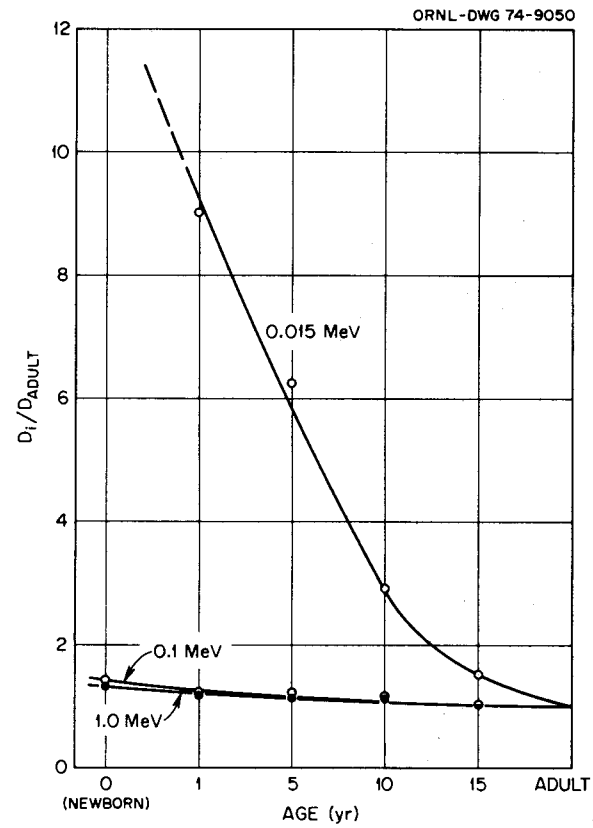

Fig. 33.4. Ratio of dose to child to dose to adult. Mono-energetic photon cloud, liver.

leveling of the dose ratio curve. Note, however, that the newborn is still about 20% higher than the adult at 1.0 MeV.

Figure 33.4 shows the dose ratio values for the liver, a rather large organ (1809 g in the adult) occupying a significant volume on the right side of the phantom. Here again the results are quite similar to those for the red bone marrow – that is, a large increase in the dose ratio for the low-energy photon cloud with little change in the dose ratio as the photon energy is increased.

Table 33.2 illustrates the manner in which these dose ratios might be used. From our previous data on the adult[3] the absorbed doses to the skin, liver, red bone marrow, and the total body due to immersion in a cloud of ^{85}Kr or ^{133}Xe have been estimated by interpolation. In addition, the dose ratios for these two radionuclides for the younger phantoms are given. Thus, by simple multiplication, the dose to these organs can be estimated for the five smaller phantoms. Due to space limitations a comprehensive set of dose ratios cannot be published here. However, these data can serve to illustrate their usefulness in the estimation of dose to population groups.

Table 33.2. Absorbed dose and dose ratios for selected organs in various sized phantoms when exposed to clouds of ^{85}Kr and ^{133}Xe

Radionuclide	Organ	Absorbed dose to adult (rads/day)	Ratio to adult value				
			15 years	10 years	5 years	1 year	Newborn
Kr-85	Skin	9.28×10^{-3}	1.031	1.073	1.078	1.009	0.904
	Liver	6.65×10^{-3}	1.058	1.186	1.223	1.395	1.357
	Red marrow	8.94×10^{-3}	1.060	1.117	1.132	1.157	1.204
	Total body	7.72×10^{-3}	1.055	1.120	1.144	1.171	1.108
Xe-133	Skin	1.40×10^{-3}	1.022	1.040	1.056	1.044	0.942
	Liver	8.55×10^{-4}	1.073	1.225	1.314	1.363	1.656
	Red marrow	1.96×10^{-3}	1.063	1.214	1.338	1.418	1.639
	Total body	1.19×10^{-3}	1.060	1.172	1.232	1.289	1.293

34. Joint Research with the Comparative Animal Research Laboratory

J. W. Poston

During the past year the Comparative Animal Research Laboratory (CARL), in concert with the Medical Physics and Internal Dosimetry Section, proposed to the Division of Biomedical and Environmental Research a research program entitled "Metabolism of Internally Deposited Emitters." This program was funded, and initial experiments with ^{144}Ce were begun at CARL, while experiments involving ^{238}Pu and ^{239}Pu were conducted in existing facilities of the Chemical Technology Division at Oak Ridge National Laboratory. The results of these experiments will be published in forthcoming CARL progress reports.

In addition, much effort was devoted to the design of a facility, to be established at CARL, for further experiments involving the metabolism of selected actinides in small animals. The design included modifications of an existing laboratory space, the selection and placement of glove-box units, and the preparation of a document describing the proposed facility. This document also contained extensive operating procedures as well as general health physics, safety, and emergency procedures for use in the laboratory. The staff of the Section as well as other members of the Health Physics Division made major contributions to this work.

35. Some Operating Characteristics of Tissue-Equivalent Proportional Counters

J. J. Shonka[1] C. M. Gritzinger[2] J. W. Poston

In connection with an experimental program in neutron dosimetry, the Medical Physics and Internal Dosimetry Section has made some investigations of operating characteristics of commercially available tissue-equivalent proportional counters (TEPC).[3] Our initial investigations indicated that common misconceptions exist in the literature which affect all methods of neutron dosimetry employing tissue-equivalent plastic. This material, available from the Physical Sciences Laboratory,[4] is known variously as A-150, Shonka plastic, or muscle-equivalent conducting plastics.

One of these misconceptions arises from an error in the assumed composition of the plastics. This material was first developed by the late Dr. F. R. Shonka in the 1950's.[5] A later refinement in plastic altered the composition slightly while improving physical properties, as well as simplifying the mixture. While this refinement in the midsixties was never reported by Shonka in the open literature, at least one publication[6] lists the composition of A-150. Table 35.1 compares these two compositions. A-150 refers only to the newer composition, and it has been the only muscle-equivalent plastic available from the Physical Sciences Laboratory since the midsixties.[7] Fast neutrons deposit most of their dose through recoil hydrogen nuclei. Although the differences are slight, the choice of a wrong value of hydrogen content in the plastic can result in an underestimation of dose to tissue by a few percent.

Table 35.1. Composition of muscle-equivalent plastic

Composition (% by weight)	A-150 (Marshall et al.)	TE plastic (F. R. Shonka et al.)
H	9.94	10.25
C	77.14	76.08
N	4.36	3.49
O	4.98	5.16
Ca	1.84	2.05
F	1.74	1.95
Si		1.03

The paper by Marshall et al.[6] which gave the composition of A-150 concerned itself with quantifying diffusion and absorption of various gases in the plastic. Other authors have qualitatively noticed this. Bewley has suggested that absorbed oxygen is present at times and can be chemically bound to the plastic by preirradiation to 50 kilorads.[8] Our initial experiments with the TEPC showed the following. After evacuating the TEPC for long periods of time, then refilling with

1. Oak Ridge Associated Universities Participant, Georgia Institute of Technology, School of Nuclear Engineering, Atlanta, Georgia.

2. Great Lakes Colleges Association Participant, Wooster College, Wooster, Ohio.

3. Available from E. G. and G., Inc., Goleta, Claif.

4. Physical Sciences Laboratory, Illinois Benedictine College, Lisle, Ill. 60532.

5. F. R. Shonka, J. E. Rose, and G. Failla, "Conducting Plastic Equivalent to Tissue, Air and Polystyrene," *Proceedings of the 2nd International Conference on the Peaceful Uses of Atomic Energy, Geneva, 1958,* p. 753.

6. J. H. Marshall, R. J. Lari, and J. Kastner, *Health Phys.* **10,** 331 (1964).

7. Private communication, J. J. Spokas, director, PSL.

8. D. K. Bewley, F. C. McCullough, B. C. Page, and S. Sakata, "Determination of Absorbed Dose in a Fast Neutron Beam by Ionization and Calorimetry Methods," *First Symposium on Neutron Dosimetry in Biology and Medicine, 1972,* p. 159.

tissue-equivalent gas, approximately a 10% drop in gas pressure was found to occur over 24 hr. Moreover, the gain and resolution of the counter appeared to vary over the first several hours after refilling. We feel a reasonable explanation for this behavior can be found in considering the Marshall paper. The drop in pressure is caused by the absorption of the gas by the wall of A-150 plastic. The TE gas has three components, which have differeing diffusion coefficients and solubilities in the plastic. The changing resolution and gain are probably the result of preferential absorption of gas components and decreasing pressure. To avoid these problems, we initiated a filling regime which evacuated the chamber for short periods relative to diffusion times of the gas, then refilled with fresh gas. This allowed the wall to equilibrate with the gas mixture. Following this procedure, no change in gain, resolution, or pressure was observed.

36. Human Phantom Plotting Routine

J. L. Hwang[1] R. L. Roswell[2] R. L. Shoup

Phantoms, mathematical representations of human bodies, have been developed to calculate absorbed doses from internally deposited radionuclides and external photon fields. Three phantoms, representing an adult, an infant, and a five-year old child, are described by geometrical shapes. Trunks are specified as a solid elliptical cylinder which includes arms and hip bones from the point where the separation of the legs begins. Head sections are right elliptical cylinders topped by half ellipsoids, and the legs consist of frustums of two circular cones. Twenty-two geometrical organs and skeletal systems are designed to fit within these phantoms.

The maternal, fetal, and pediatric phantoms were constructed recently. (The adult phantom was developed by W. S. Snyder and H. Fisher.) In the construction of the one-year- and five-year-old phantoms, it is imperative that the internal organs and bones do not intersect each other. To assure that this would not happen, a computer plot routine was developed to construct cross-sectional plots of the phantoms. Plots of the *X-Y*, *X-Z*, and *Y-Z* planes can be generated.

The plot routine simply scans diagonally back and forth in a specified plane of a phantom using the mathematically encoded geometries of the organs. When the routine locates an interface between two different organs or media, it plots a point at that position. Examples generated by this plot routine are presented in Figs. 36.1–36.5. This program has been instrumental in avoiding organ overlap and in developing organ shapes, sizes, and orientations.

1. Physics Department, University of Tennessee, Knoxville, Tenn.

2. Great Lakes Colleges Association Participant, Denison University, Granville, Ohio.

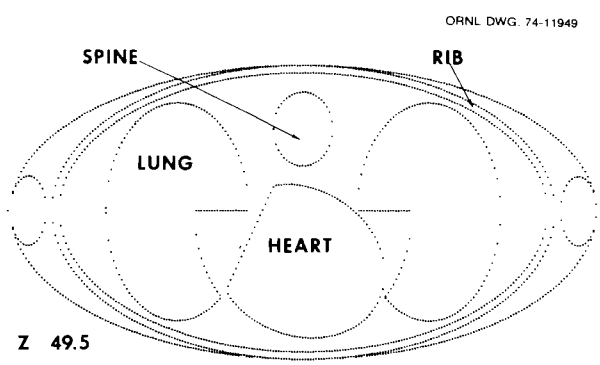

Fig. 36.1. Adult phantom. *X-Y* plot of chest.

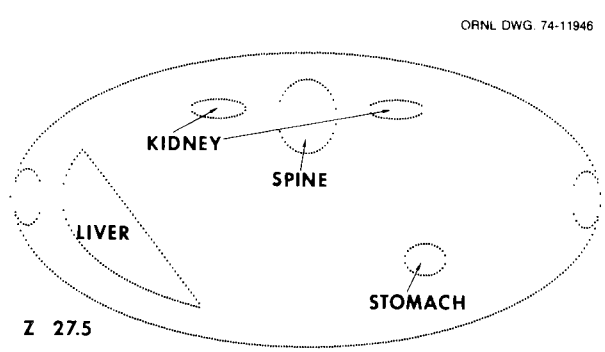

Fig. 36.2. Adult phantom. *X-Y* plot of abdomen.

Fig. 36.3. One-year-old phantom. *X-Y* plots of chest.

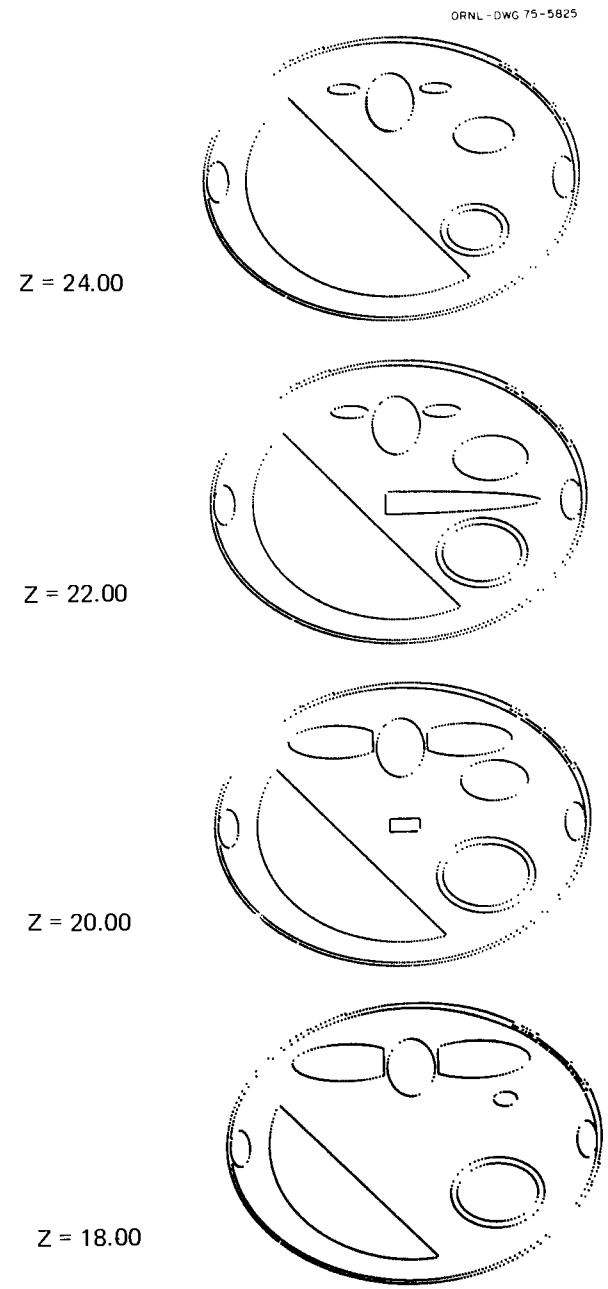

Fig. 36.4. Five-year-old phantom. *X-Y* plots of upper abdomen.

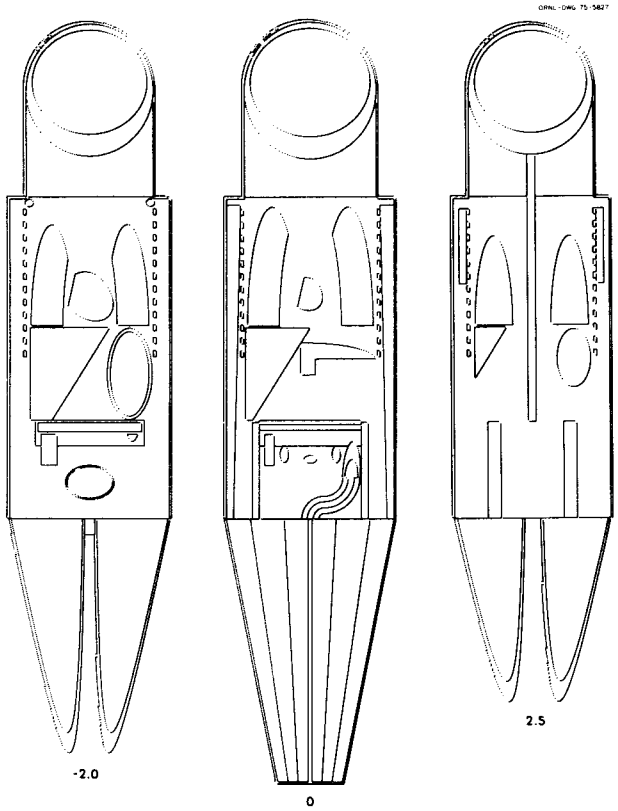

Fig. 36.5. One-year-old phantom. *X-Z* plots.

37. Maternal, Fetal, and Pediatric Phantoms

J. L. Hwang[1] J. W. Poston
R. L. Shoup G. G. Warner[2]

Estimates of the absorbed dose due to internally deposited radionuclides published by the Section have formed the basis for exposure guidelines in most nuclear energy programs throughout the world. These estimates are derived through the use of a standard individual, or reference man. He is considered to be an adult human weighing 70 kg and standing 170 cm tall. However, estimates of dose to other population groups are now required for reactor siting evaluations (including accidental releases) and in nuclear medicine. Of special interest in many of these evaluations are children. The child is not merely an adult shrunk isotropically by a constant factor. The sizes and shapes of many organs are not those of the adult reduced by some factor, and this undoubtedly affects the dose to the various organs from a source in any one of them. Preliminary studies done in the Section indicate large differences which apply for different ages. For example, dose to the total body will be higher for the child by a factor of 10 or more if the same source is present in the body of the child and of an adult.

Mathematical representations of one-year-old and five-year-old children have been developed. The exteriors of these phantoms have approximately the form of human pediatric bodies. These phantoms are shown in Figs. 37.1 and 37.2 with the gross dimensions as indicated (see Table 37.1). Representations of internal organs with approximate geometries, positions, and densities were also determined using information from the Reference Man report and other anatomical literature. A summary of organ masses and weights is presented in Table 37.2.

The exteriors of the one-year- and five-year-old phantoms are similar to the exterior of the adult phantom. Trunks are specified as a solid elliptical cylinder which includes arms and hip bones from the point where the separation of the legs begins. Head sections are right elliptical cylinders topped by half ellipsoids, and the leg regions consist of frustums of two circular cones. The gross dimensions of these exterior geometries were derived by taking into consideration heights, weights, and general exterior dimensions of infants and small children.

The geometrical shapes of the internal organs resemble those of the adult phantom but are not merely the adult organs scaled down to size. Twenty-two organs and the skeletal systems were constructed to fit within the phantoms, with the skeletons being developed first. The major organs were added next, prior to fitting other organs around them. For example, the lungs were designed to fit inside the rib cage, and then the heart was adjusted to fit into the cavity between the lungs. Anatomical references were used to check sizes, orientations, and configurations of various organs.

The pediatric phantoms will form the basis for dosimetric studies as has been done for the adult. These phantoms will be used to calculate absorbed dose due to the internally deposited radionuclides that are most common in children.

---

1. Physics Department, University of Tennessee.
2. Computer Sciences Division.

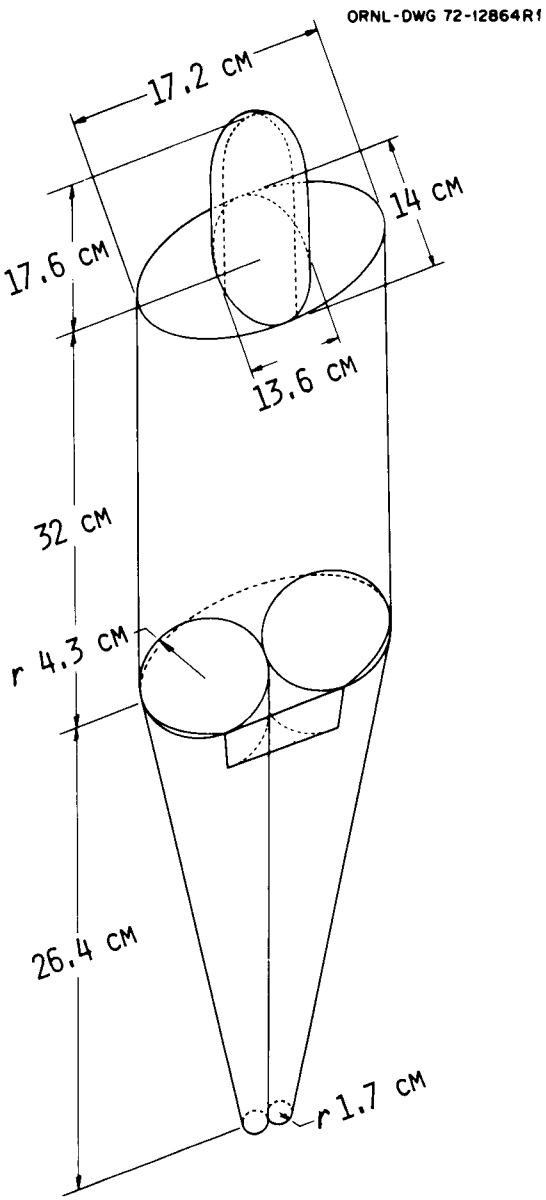

Fig. 37.1. The one-year-old phantom.

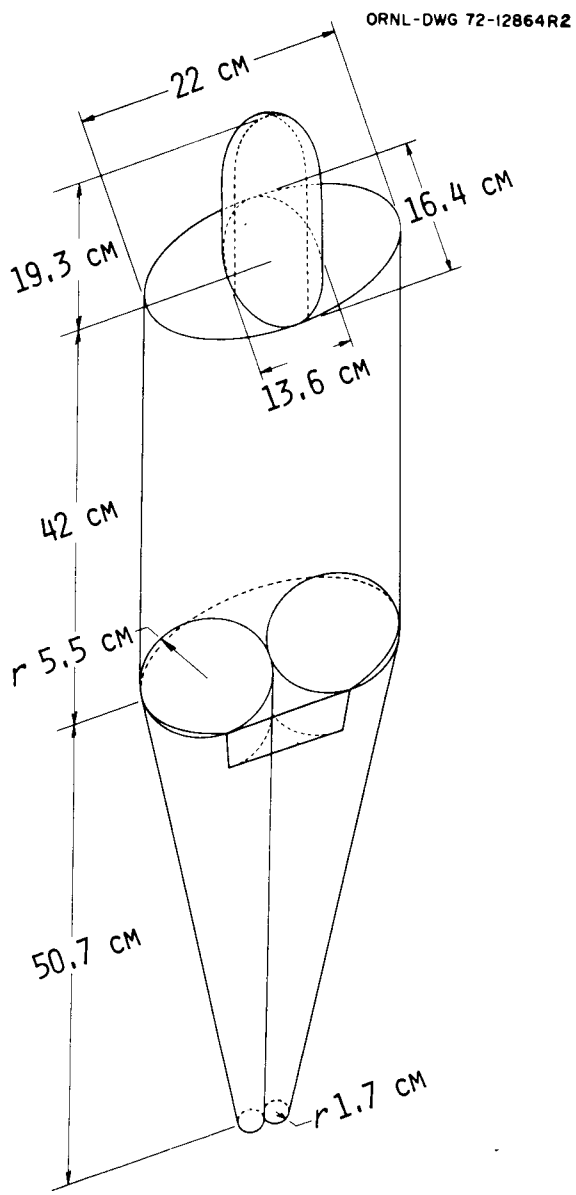

Fig. 37.2. The five-year-old phantom.

Table 37.1. Weights and volumes of one-year- and five-year-old phantoms

	One year	Five year
Weight (g)	10,400	20,000
Specific gravity	1.017	1.019
Volume (cm^3)		
Total	10,226	19,627
Head	2608	3180
Arms and trunk	6033	11,933
Legs	1585	4514

Table 37.2. Summary of organs for one-year- and five-year-old phantoms

Organ	Mass (g)		Volume (cm^3)	
	One year	Five year	One year	Five year
Adrenals	4.04	6.12	3.94	5.97
Bladder	8	14	12.04	17.96
Brain	1005.5	1179.3	977.2	1146.1
G.I. tract				
Stomach	27.27	52.18	25.99	49.69
S.I.[a]	75.90	175.95	76.92	178.32
U.L.I.	26.35	46.46	25.26	44.55
L.L.I.	21.45	40.02	20.56	38.37
Heart	48.17	91.16	46.78	88.52
Kidneys	68.00	115.51	64.95	110.22
Lungs	128.82	255.10	429.40	850.32
Liver	303.64	608.14	289.54	575.89
Ovaries	0.65	1.90	0.62	1.81
Pancreas	8.99	18.93	8.58	18.07
Spleen	27.30	49.62	25.71	46.72
Skeleton	1612.50	2785.15	1151.79	1989.39
Red bone marrow	150.0	400.0		
Yellow bone marrow	0	48.0		
Thymus	21.88	30.61	21.32	29.84
Thyroid	2.38	4.85	2.26	4.62
Testes	1.47	1.60	1.41	1.53
Uterus	1.53	2.60	1.45	2.47

[a]Includes small intestine contents.

38. An Outline of Experimental Programs Using the MR. ADAM Phantom

P. S. Stansbury[1] J. W. Poston

In addition to the absorbed fraction measurements described elsewhere,[2,3] the MR. ADAM phantom is being used currently in three other areas. One program involves the whole-body counting of ^{239}Pu in the lungs. Another program pertains to the dosimetry of ^{99m}Tc in the liver and spleen. The third program area is spectrometry in the phantom exposed to X rays typical of medical diagnostic radiology. These projects are in varying stages of completion.

A minor study of the whole-body counting of ^{239}Pu in the lungs of the MR. ADAM phantom is in progress. The major objectives of this study are: (1) to show the limits of detection in a complex but standard geometry and (2) to assess the importance of the effect of source distribution on geometric efficiency and, hence, calibration factors.

This program is being undertaken jointly with the Internal Dose Group of the Radiation Monitoring Section. Measurements will be made using the ORNL whole-body counting facility, and the results will be intercompared with Monte Carlo calculations.

Research concerning the dosimetry of the radiopharmaceutical isotope ^{99m}Tc has been performed. This research was done in support of a larger project undertaken by researchers associated with Vanderbilt University. One of the purposes of this study is to determine the calibration factors by which an estimate of the organ doses to an individual patient administered ^{99m}Tc may be assessed from thermoluminescent dosimetry (TLD) measurements made on the exterior of his thorax.

Both theoretical and experimental techniques have been used in this study. Monte Carlo estimates of calibration factors for ^{99m}Tc uniformly distributed in a cubical phantom and in the liver and spleen of the Snyder-Fisher phantom have been made. Hollow liver and spleen models were constructed (see Fig. 38.1). These were filled with 5 mCi and 10 mCi, respectively, of ^{99m}Tc, and TLD measurements of exposure on the anterior thoracic surface were made. The amounts of ^{99m}Tc placed in the liver and spleen are typical of particular radiopharmaceutical techniques. At the time of preparation of this report, final analysis of the data had not been completed.

The program of spectrometry and dosimetry of medical diagnostic X rays, described previously,[4] is in progress; although major delays have been encountered in the procurement of detectors, it is believed that the detectors received after a process of rejection, cancellation, and reprocurement are suitable. Similarly, the x-ray facility in Building 2008[5] has undergone delays in construction. However, its construction is complete, and the necessary extensive calibrations and check-out are under way. It is hoped that useful data will be realized shortly. Further, plans have been made for the construction and use of one-year-old and five-year-old children phantoms. These new phantoms will be built according to the mathematical models developed by Hwang et al.[6]

---

1. Oak Ridge Associated Universities, School of Nuclear Engineering, Georgia Institute of Technology.

2. N. H. Mei, G. G. Warner, P. S. Stansbury, and J. W. Poston, "The Effect of Source Organ Size on the Absorbed Fraction Distribution," this report.

3. N. H. Mei, G. G. Warner, P. S. Stansbury, and J. W. Poston, *Measurements of Absorbed Fractions as a Function of Source Organ Size for Selected Source Organs in a Heterogeneous Phantom,* ORNL-4916 (June 1975).

4. P. S. Stansbury, J. W. Poston, and G. G. Warner, *Health Phys. Div. Annu. Progr. Rep. July 31, 1974,* ORNL-4979, pp. 70–72.

5. P. S. Stansbury and J. W. Poston, *Health Phys. Div. Annu. Progr. Rep. July 31, 1974,* ORNL-4979, pp. 68–69.

6. J. L. Hwang, R. L. Shoup, J. W. Poston, and G. G. Warner, "Maternal, Fetal, and Pediatric Phantoms," this report.

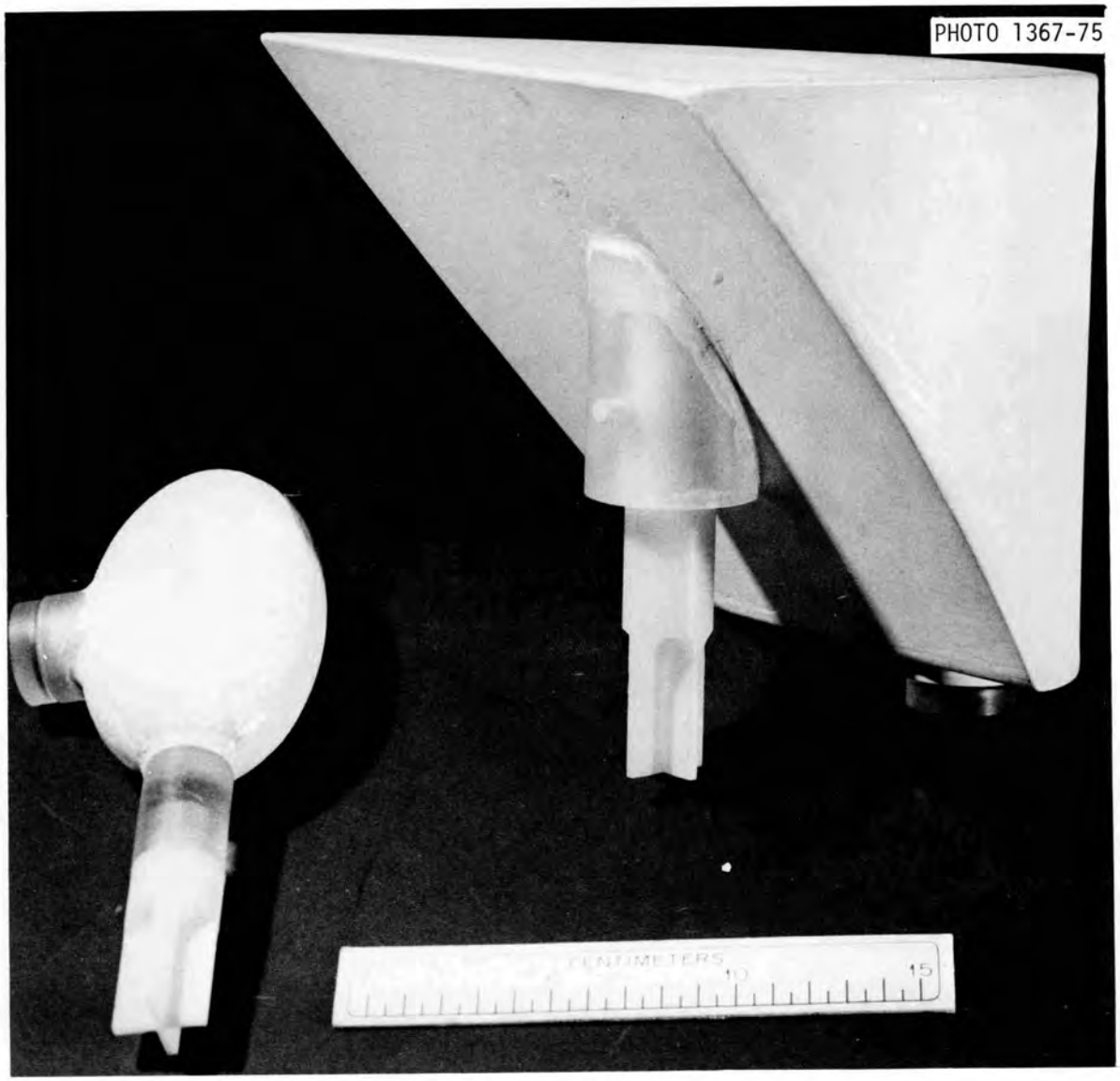

Fig. 38.1. Posterior-anterior view of liver model (right) and spleen model (left). Note the four-finned rods, which are part of the mounting apparatus.

Part VI. Office of Education and Information

J. E. Turner

The Office of Education and Information plans and coordinates the Division's educational programs and operates the Health Physics Information System, which assists the staff of the Division and parts of ERDA and other organizations in obtaining, compiling, and analyzing information in fields of health physics.

39. Education and Vocational Training

M. F. Fair J. E. Turner

The Faculty Institute in Applied Health Physics started in the summer of 1974 in response to the nation's needs for persons trained at the bachelor's level in health physics technology. Surveys, such as WASH-1281,[1] and our own forecasts (summarized in last year's Annual Report[2]) indicate that between 3300 and 6000 new trained technologists will be needed by 1985. They will be required for nuclear power reactors, fuel-cycle operations, nuclear medicine, regulatory activities, and to replace currently employed workers. The Faculty Institute program provides support for contacting college officials, making them aware of these forecasts, and interesting them in instituting undergraduate health physics course work at their institutions. In addition, the program provides support for ten faculty participants from different universities to spend approximately ten weeks during the summer in the Health Physics Division. These participants have access to the staff and the diverse research and field facilities of the Division.

Instructors from nine different colleges participated in the Institute during the summer of 1974. These schools were Southwest Texas State University, Purdue University, the University of Virginia, Vanderbilt University, Carson-Newman College, the University of Florida, Memphis State University, Appalachian State University, and West Virginia Wesleyan College. These schools have indicated an interest in having suitable undergraduate courses for health physics technologists. Several of these schools have already been involved extensively in graduate training programs in health physics. The first year's experience indicates that the Faculty Institute was quite successful – seven of the nine schools either now have or expect to have ongoing courses by September 1975.

A staff member from this group spent three weeks at the Instituto Nacional de Energia Nuclear in Mexico City teaching a course in health physics under the sponsorship of the Organization of American States.

The Health Physics Division provided assistance to the University of Tennessee, through the Ford Foundation Program, whereby five staff members taught courses in the Department of Physics. Also, a

1. *The Nation's Energy Future,* U.S. Government Printing Office, Stock No. 5210-00363, Washington, D.C. (1973).
2. *Health Phys. Div. Annu. Progr. Rep. July 31, 1974,* ORNL-4979, p. 253.

number of graduate students worked on their theses for advanced degrees under the supervision of Division staff members and using Division facilities.

Assistance was given to Oak Ridge Associated Universities in the presentation of ten-week courses in health physics. Three student trainees from ORAU spent the summer of 1974 in the Division as research participants. One student trainee from the Southern Colleges Universities Union spent a semester in the Division.

Tours were provided for various college groups visiting the Division facilities.

40. Information Activities and Dissemination

J. E. Turner
K. Becker R. B. Gammage B. L. Houser
C. M. Dixon C. F. Holoway A. S. Loebl[1]

HEALTH PHYSICS INFORMATION SYSTEM

The Health Physics Information System (HPIS) was established to serve as a focal point to which technical questions may be directed to assist researchers in the Division as well as persons outside the Division. Ready access to the entire Division staff enables the group to respond to a wide variety of needs within the broad interdisciplinary areas associated with health physics. The group also functions in a core operation of gathering information, compiling bibliographies, and adding critical judgment on various subjects to assist the Division's research programs. This activity, which parallels responding to specific questions, provides the opportunity to review various problems and to synthesize and evaluate what is known about them.

The group responded to a number of inquiries throughout the past year. Examples of the subjects addressed and the sources seeking information include:

1. radiation safety of accelerators (Health Physics Division staff member),
2. contribution of tobacco radioactivity to cancer in the human population (Division staff member),
3. metabolism and dosimetry for G.I. tract (Lowell Technological Institute staff),
4. Title 10 CFR (Central Michigan University),
5. behavioral effects of radiation on animals (University of Florida),
6. radiation waste handling at different stages in the fuel cycle (Idaho Falls contractor),
7. packaging and transportation of high-level waste (ERDA staff),
8. nuclear safety and legal aspects of thermal pollution (Rutgers University Law School).

The group answered numerous other requests from inside and outside the Division for information on plutonium. In many instances, the assembled material was abstracted and added to the HPIS data base. These activities involved about 100 searches on RECON and 150 on ORLOOK.

The *Health Physics* journal (1967 to date) has been made accessible in the HPIS data base. This file begins where the Public Health Service left off with its index of the journal from 1958 to 1966. Information appearing in the author, abstract, and publication fields is retrievable; the key-word field will be added early in FY 1976. A KWOC index (key word out of context) by author and title is available in the HPIS office.

This year's experience has shown that the group can be most effective by limiting its efforts to relatively few studies, done in depth. The main subjects emphasized this year were tritium (a working computer bibliography is available), environmental monitoring (for both nuclear and nonnuclear pollutants), radioactivity in water, waste management, uranium mill tailings, and copper and selenium metabolism in mammals. A card file on krypton is available in the HPIS office.

The final structuring of data bases and formats for the long-term needs of HPIS has been resolved dur-

1. Energy Division.

ing this year's operation in conjunction with the development of long-range cooperative plans with the Energy and Information divisions. The system is general and tailored to the needs of the Division to maintain and make available data files, some of which may need to be documented and organized properly before being abstracted for computerization by the group.

SOLID-STATE DOSIMETRY INFORMATION DISSEMINATION

As in previous years, a substantial percentage of time was devoted to activities of a general nature, such as training IAEA students from Bangladesh, Korea and Egypt and giving lectures at ORNL and ORAU. In the field of information collection and dissemination, a pocket textbook version of our solid-state dosimetry monograph has been prepared,[2] and critical state-of-the-art reviews on personnel and environmental dosimetry are being published.[3–5] We also participated extensively in reviews of research proposals, manuscripts, and other technical papers.

---

2. K. Becker and A. Scharmann, *Introduction into Solid-State Dosimetry,* Thiemig, Munich, 1975.
3. K. Becker, "Quo Vadis, Personnel Monitoring?" *Nucl. Safety,* in press.
4. K. Becker, "The Future of Personnel Monitoring in Tropical Countries," Proceed. First Asian Reg. Congress Radiat. Protect., Bombay, 1974.
5. K. Becker, "Integrating Dosimeter for Environmental Radiation Assessment," ibid.

Theses, Papers, Publications, and Lectures

Theses

Q. A. Huynh
Photophysical Studies of Organic Molecules in Liquid Media (University of Tennessee) (in preparation)

J. P. Johnson
The Formation and Lifetimes of Negative Ions Resulting from the Impact of Low Energy Electrons with Selected Organic Molecules (University of Tennessee) (in preparation)

S. I. Juan
Optical Properties of Nucleic Acid Bases in the Soft X-Ray Region, ORNL-TM-4773 (University of Tennessee) (February 1975)

J. R. McNeely
Time Resolved Quenching of Argon Resonance Radiation by Nitrogen Molecules, ORNL-TM-4697 (University of Tennessee) (1974)

N. H. Mei
Measurements of Absorbed Fractions as a Function of Source Organ Size for Selected Source Organs in a Heterogeneous Phantom (University of Tennessee) (June 1975)

V. N. Neelavathi
Theoretical Studies of Some Plasma Effects in Condensed Matter, ORNL-TM-4833 (University of Tennessee) (1974)

I-lan Tang
Optical Properties of Nucleic Acid Bases, ORNL-TM-4559 (University of Tennessee) (September 1974)

C. J. Tung
Electron Transport Properties in Solids (University of Tennessee) (in preparation)

R. J. Warmack
D.C. Conductivity and Optical Properties of TTF-Halides (University of Tennessee) (in preparation)

C. E. Wheeler, Jr.
Excitation of Surface Plasmons in Grating Surfaces (University of Tennessee) (in preparation)

J. M. Younkin
π-Electron Affinities of Conjugated Molecules (University of Tennessee) (in preparation)

Papers

S. A. Abdullah, H. W. Dickson, F. F. Haywood, and G. D. Kerr
"Environmental Gamma Radiation Measurements," Health Physics Society Annual Meeting, Buffalo, N.Y., July 13–17, 1975

E. T. Arakawa, A. J. Braundmeier, M. W. Williams, R. N. Hamm, and R. D. Birkoff
"Electron Attenuation Lengths in Carbon Films," IEEE Annual Conference on Nuclear and Space Radiation Effects, Fort Collins, Colo., July 15–18, 1974

"Electron Attenuation Lengths in Carbon Films," Fourth International Conference on Vacuum-Ultraviolet Radiation Physics, Hamburg, Germany, July 22–26, 1974

E. T. Arakawa and M. W. Williams
"Radiation Induced Changes in the Soft X-Ray Emission from LiF and NaCl," International Conference on X-Ray Processes in Matter, Helsinki, Finland, July 29–Aug. 1, 1974

J. C. Ashley and L. C. Emerson
"Scattering of Electromagnetic Radiation from Cylinders," American Physical Society, Atlanta, Ga., Dec. 5–7, 1974

J. K. Baird
"Parabolic Lithium Mirror for a Laser Driven Pellet Fusion Reactor," Sixteenth Annual Meeting of Division of Plasma Physics, American Physical Society, Albuquerque, N.M. Oct. 28–31, 1974

"Reflection and Transmission of a Traveling Unit Impulse Voltage at a Power Line–Power Transformer Junction," 1975 Winter Meeting of the IEEE Power Engineering Society, New York, N.Y., Jan. 26–31, 1975

K. Becker
"Integrierende Dosimeter zur Umberwachung der Umwelt Strahlenbelastung," Annual Meeting, German-Swiss Radiation Protection Association, Helgoland, Germany, Sept. 23–28, 1974

"Some Advances in Solid-State Fast Neutron Dosimetry," Second Symposium on Neutron Dosimetry, Neuherberg, Germany, Sept. 30–Oct. 4, 1974

"Integrating Dosimeters for Environmental Radiation Assessment," First Asian Regional Congress on Radiation Protection, Bombay, India, Dec. 15–20, 1974

"The Future of Personnel Monitoring in Areas with Hot and Humid Climates," First Asian IRPA Congress, Bombay, India, Dec. 15–20, 1974

"Improved Track Etching and TSEE Detectors for Biomedical Dosimetry and Neutron Source Intercomparisons," IAEA Symposium on Advances in Biomedical Dosimetry, Vienna, Austria, Mar. 10–14, 1975

"Fast Neutron Dosimetry at ORNL – Progress and Problems," ERDA Workshop on Neutron Personnel Monitoring, Washington, D.C., May 6–7, 1975

"Measurement of ^{239}Pu in the Presence of U_{nat} by NIAR," Radiation Research Society Annual Meeting, Miami, Fla., May 11–15, 1975

"Are There TLD Phosphors with Abnormal LET Responses?" Health Physics Society Annual Meeting, Buffalo, N.Y., July 13–17, 1975

K. Becker and J. S. Jun
"Transfer Dosimeters for Fast Neutron Sources," Health Physics Society Annual Meeting, Buffalo, N.Y., July 13–17, 1975

K. Becker and A. Moreno y Moreno
"Some Applications of Thermoluminescence Measurements in Ancient Ceramics," Fourth International Conference on Luminescence Dosimetry, Krakow, Poland, August 27–31, 1974

S. R. Bernard
"A Metabolic Model for Aluminum and Estimates of Permissible Occupational Exposure Levels for ^{26}Al," Health Physics Society Annual Meeting, Buffalo, N.Y., July 13–17, 1975

"A Metabolic Model for Lead in Man Used in Internal Dose Estimation," Health Physics Society Annual Meeting, Houston, Tex., July 7–11, 1974

S. R. Bernard and L. C. Henley
"A Semi-Theoretical Approach to Excretion and Retention of Various Ions," 20th Annual Conference on Bioassay, Environmental, and Analytical Chemistry, Cincinnati, Ohio, Sept. 24–25, 1974

S. R. Bernard and W. S. Snyder
"Metabolic Models for Estimation of Internal Radiation Dose Recieved by Human Subjects from the Inhalation of Radioactive Noble Gases," Eleventh Symposium on Biomathematics and Computer Science in the Life Sciences, Houston, Tex., Apr. 3–5, 1975

L. G. Christophorou
"Electrons in Very High Pressure Gases," Fifth International Congress of Radiation Research, Seattle, Wash., July 14–20, 1974

L. G. Christophorou, D. L. McCorkle, and J. G. Carter
"Electron Capture by Organic Molecules," Fifth International Congress of Radiation Research, Seattle, Wash. July 14–20, 1974

R. N. Compton, C. D. Cooper, and P. W. Reinhardt
"Collisional Ionization of Alkali Metal Atoms by Molecules: Electron Affinities of CO_2, COS, and CS_2," 1974 Annual Meeting of Division of Electron and Atomic Physics, Chicago, Ill. Dec. 2–4, 1974

R. N. Compton and J. A. D. Stockdale
"Some Ionic Properties of Atmospheric Constituents," Radiological and Chemical Contractors' Meeting, Menlo Park, Calif., Jan. 27–28, 1975

C. D. Cooper, R. N. Compton, and P. W. Reinhardt
"Abnormally Large Electron Affinities for Some Hexafluoride Molecules," 9th International Conference on the Physics of Electronic and Atomic Collisions, Seattle, Wash., July 24–30, 1975

H. W. Dickson and W. D. Cottrell
"A Procedure for Evaluation of Personnel Exposures at Nuclear Facilities," Health Physics Society Annual Meeting, Buffalo, N.Y., July 13–17, 1975

H. W. Dickson, G. D. Kerr, P. T. Perdue, and S. A. Abdullah
"Environmental Radiation Measurements Using *In Situ* and Core Sampling Techniques," Health Physics Society Eighth Midyear Topical Symposium, Knoxville, Tenn., Oct. 21–24, 1974

L. C. Emerson and R. D. Birkoff
"Electron Slowing Down Spectrum in an Insulator," American Physical Society, Atlanta, Ga., Dec. 5–7, 1974

M. R. Ford and W. S. Snyder
"Variation of the Absorbed Fraction with Shape and Size of the Thyroid," Health Physics Society Annual Meeting, Houston, Tex., July 7–11, 1974

M. R. Ford, W. S. Snyder, L. T. Dillman, and S. B. Watson
"Maximum Permissible Concentration (MPC) Values for Spontaneously Fissioning Radionuclides," Health Physics Society Annual Meeting, Buffalo, N.Y., July 13–17, 1975

R. B. Gammage, J. S. Cheka, and N. P. Saheli
"Long-Term Testing of TSEE Dosimeters for Personnel Dosimetry," Health Physics Society Midyear Symposium on Population Exposures, Knoxville, Tenn., Oct. 21–24, 1974

R. B. Gammage and A. K. Garrison
"EPR, TLD, and TSEE with BeO Ceramic," Fourth International Conference on Luminescence Dosimetry, Krakow, Poland, Aug. 27–31, 1974

R. B. Gammage and D. R. Glasson
"The Effect of Grinding on the Polymorphs of Calcium Carbonate," 49th National Colloid Symposium, Clarkson College of Technology, Potsdam, N.Y., June 16–18, 1975

R. B. Gammage and H. F. Holmes
"Blocking of the Alteration Reaction between Water and Lunar Fines," Sixth Lunar Science Conference, NASA, Johnson Space Center, Houston, Tex., Mar. 17–21, 1975

"Alteration of Apollo 17 Orange Fines by Adsorbed Water Vapor," 49th National Colloid Symposium, Clarkson College of Technology, Potsdam, N.Y., June 16–18, 1975

R. B. Gammage, G. D. Kerr, and Linda Huskey
"Exploratory Study of the Use of TSEE Dosimeters in Radon Monitoring," Health Physics Society Annual Meeting, Buffalo, N.Y., July 13–17, 1975

K. Gant, L. G. Christophorou, and J. K. Baird
"Slowing-Down of Subexcitation Electrons in Polyatomic Gases," Radiation Research Society, Miami Beach, Fla., May 11–15, 1975

W. R. Garrett
"Rotational Resonances in Molecular Scattering of Ultra-Low-Energy Electrons," 1974 Annual Meeting of the Division of Electron and Atomic Physics, Chicago, Ill., Dec. 2–4, 1974

"Rotational Resonance in Low Energy H_2 Scattering," 9th International Conference on the Resonance of Electronic and Atomic Collisions, Seattle, Wash., July 24–30, 1975

T. F. Gesell, G. deP. Burke, and K. Becker
"An International Intercomparison of Environmental Dosimeters under Field and Laboratory Conditions," Health Physics Society Annual Meeting, Buffalo, N.Y., July 13–17, 1975

R. N. Hamm, H. A. Wright, and J. E. Turner
"Treatment of Multiple Coulomb Scattering in Monte Carlo Radiation Transport Calculations," American Physical Society, Atlanta, Ga., Dec. 5–7, 1974

J. M. Heller, Jr., R. D. Birkoff, and L. R. Painter
"Experimental Evidence for Collective Oscillations in Molecular Liquids," American Physical Society, Atlanta, Ga., Dec. 5–7, 1974

H. F. Holmes and R. B. Gammage
"Surface Properties of a North Ray Crater Soil (Apollo 16)," Sixth Lunar Science Conference, NASA, Johnson Space Center, Houston, Tex., Mar. 17–21, 1975

G. S. Hurst, J. P. Judish, M. H. Nayfeh, J. E. Parks, M. G. Payne, and E. B. Wagner
"Use of a 3-MV Proton Accelerator for Study of Noble Gases, Including Laser Ionization of Excited States," Third Conference on Application of Small Accelerators, Denton, Tex., Oct. 21, 1974

G. S. Hurst, M. G. Payne, M. H. Nayfeh, J. P. Judish, and E. B. Wagner
"Resonance Ionization Spectroscopy of He(2^1S), American Physical Society, Knoxville, Tenn., June 16–18, 1975

T. Inagaki and E. T. Arakawa
"Optical Constants of Lithium and Sodium between 0.6 and 3.8 eV," American Physical Society, Denver, Col., Mar. 31–Apr. 3, 1975

T. Inagaki, R. N. Hamm, E. T. Arakawa, and L. R. Painter
"Optical and Dielectric Properties of Biomolecules in the Extreme Ultraviolet – Study on DNA, Polypeptides and Carotene," Fourth International Conference on Vacuum-Ultraviolet Radiation Physics, Hamburg, Germany, July 22–26, 1974

J. P. Johnson, L. G. Christophorou, J. G. Carter, and D. L. McCorkle
"Long-Lived Parent Negative Ions of NO_2 - Containing Benzene Derivatives," American Physical Society, Chicago, Ill., Dec. 2–4, 1974

T. D. Jones
"Critical Human Organ Radiation Dosimetry – the CHORD Concept," Health Physics Society Annual Meeting, Buffalo, N.Y., July 13–17, 1975

S. I. Juan, M. W. Williams, L. C. Emerson, and E. T. Arakawa
"Optical Properties of Adenine," American Physical Society, Atlanta, Ga., Dec. 5–7, 1974

G. D. Kerr and T. D. Jones
"Importance of *In Vivo* Dose Estimates in the Analysis of Epidemiological Data for Atomic Bomb Survivors of Hiroshima and Nagasaki, Japan," Health Physics Society Annual Meeting, Buffalo, N.Y., July 13–17, 1975

C. E. Klots
"New Mechanisms for the Jesse Effect," 5th International Congress of Radiation Research, Seattle, Wash., July 14–20, 1974

"Kinetic Energy Distributions from Unimolecular Dissociations," American Society for Mass Spectrometry, Houston, Tex., May 25–30, 1975

M. G. Payne, G. S. Hurst, and C. E. Klots
"Rate Processes Related to the Jesse Effect in He," 27th Annual Gaseous Electronics Conference, Houston, Tex., Oct. 22–25, 1974

J. W. Poston and W. S. Snyder
"The Dosimetry of ^{241}Pu Reconsidered," 20th Annual Conference on Bioassay, Environmental and Analytical Chemistry, Cincinnati, Ohio, Sept. 24–25, 1974

J. Rademacher, L. G. Christophorou, and R. P. Blaunstein
"Electron Attachment to SO_2 in High Pressure Gases," Sixth Annual Meeting of the Division of Electron and Atomic Physics of the American Physical Society, Chicago, Ill., Dec. 2–4, 1974

R. H. Ritchie, V. E. Anderson, and J. C. Ashley
"Electron Slowing-Down-Cascade Spectra in Solids," American Physical Society, Atlanta, Ga., Dec. 5–7, 1974

R. H. Ritchie, L. C. Emerson, R. D. Birkoff, J. C. Ashley, V. E. Anderson, and Dayashankar
"Electron Slowing-Down-Spectra in Al_2O_3," IEEE Annual Conference on Nuclear and Space Radiation Effects, Fort Collins, Colo., July 15–18, 1974

H. C. Schweinler
"Interaction Potential Energy of Excited Noble Gas Atom and One or More Like Atoms," 9th International Conference on the Physics of Electronic and Atomic Collisions, Seattle, Wash., July 24–30, 1975

J. J. Shonka
"The Stopping of Charged Particles in a Disk," American Nuclear Society Student Conference, Georgia Institute of Technology, Atlanta, Ga., Apr. 11, 1975

W. S. Snyder and L. T. Dillman
"Dose to Endosteal Cells from a Surface Distribution of a Beta Emitter," Health Physics Society Annual Meeting, Buffalo, N.Y., July 13–17, 1975

W. S. Snyder and M. R. Ford
"Tables of Average Dose to an Organ per Microcurie-Day Accumulated by a Radionuclide in a Source Organ," First Asian Regional Congress on Radiation Protection, Bombay, India, Dec. 15–20, 1974

"Physical Principles of Photon Dosimetry," International Symposium on Radiation Physics, Bose Institute, Calcutta, India, Nov. 30–Dec. 4, 1974

"Average Dose to an Organ Per Microcurie-Day Accumulated by a Radionuclide in a Source Organ," Third European Congress of the International Radiation Protection Association, Amsterdam, May 13–16, 1975

P. S. Stansbury
"An In-Phantom Spectrometer for 10–130 keV Photons," Student Session, Health Physics Society Annual Meeting, Houston, Tex., July 7–11, 1974

"MR. ADAM and His Environmental Implications," American Nuclear Society Student Conference, Georgia Institute of Technology, Atlanta, Ga., Apr. 11, 1975

J. A. Stockdale, V. E. Anderson, A. E. Carter, and Liliana Deleanu
"Dissociative Ionization of O_2 by Electron Impact," 1974 Fall Meeting of the American Physical Society, Atlanta, Ga., Dec. 5–7, 1974

J. A. Stockdale and L. Deleanu
"Vibrational Structure in Kinetic Energy Spectra of O^+ Ions from Electron Impact Dissociative Ionization of O_2: Predissociation of the $B^2\Sigma^-_g$ State of O_2^+," 27th Annual Gaseous Electronics Conference, Houston, Tex., Oct. 22–25, 1974

J. A. Stockdale, B. P. Pullen, and A. E. Carter
"Electron Impact Dissociative Ionization of CO_2," 1975 Spring Meeting of the American Physical Society, Washington, D.C., Apr. 28–May 1, 1975

C. J. Tung and R. H. Ritchie
"Electron Mean Free Paths in Solids," American Physical Society, Atlanta, Ga., Dec. 5–7, 1974

R. J. Warmack, T. A. Callcott, C. R. Watson, and C. K. Johnson
"Reflectance of TTF-I_{II} Single Crystals," American Physical Society, Denver, Colo., Mar. 31–Apr. 3, 1975

G. G. Warner, J. W. Poston, and W. S. Snyder
"Absorbed Dose in Phantoms Which Represent Various Aged Male Humans from External Sources of Photons as a Function of Age," Health Physics Society Annual Meeting, Houston, Tex., July 7–11, 1974

M. W. Williams, E. T. Arakawa, R. D. Birkoff, R. N. Hamm, H. C. Schweinler, and R. A. MacRae
"Optical Properties of Chloroplasts and Red Blood Cells in the Vacuum UV," Fourth International Conference on Vacuum-Ultraviolet Radiation Physics, Hamburg, Germany, July 22–26, 1974

M. W. Williams, R. N. Hamm, and E. T. Arakawa
"Collective Electron Oscillations in Molecular Liquids," American Physical Society, Atlanta, Ga., Dec. 5–7, 1974

Publications

J. C. Ashley, T. L. Ferrell, and R. H. Ritchie
"X-Ray Excitation of Surface Plasmons in Metallic Spheres," *Phys. Rev. B* **10**, 554 (1974)

J. C. Ashley, R. H. Ritchie, and Werner Brandt
"Z_1^3-Dependent Range Contributions," *Phys. Rev. A* **10**, 737 (1974)

"Z_1^3-Dependent Stopping Power and Range Contributions," in *Atomic Collisions in Solids,* vol. 1, Plenum Press, New York, 1975

J. A. Auxier
"Preliminary Studies of the Effects of Sealants on Radon Emanation from Concrete," *Health Phys.* **27**, 390–91 (1974)

"Physical Dose Estimation: Studies of Oak Ridge Group," to be published in *Japanese Journal of Radiation Research,* October 1975

J. K. Baird and J. H. Marable
"Reflection and Transmission of a Traveling Unit Impulse Voltage at a Power-Line Transformer Junction," *Proceedings of the IAEE Power Engineering Society Winter Meeting,* New York, N.Y., Jan. 26–31, 1975

P. R. Barnes and R. W. Manweiler
The Effects of Nuclear EMP on Nuclear Power Plants, ORNL-5029 (July 1975)

K. Becker
"Integrierende Dosimeter zur Uberwachung der Umwelt-Strahlenbelastung," *Proceedings of the Annual Meeting, German-Swiss Radiation Protection Association, Helgoland, Germany, Sept. 23–28, 1974*

"Some Advances in Solid-State Fast Neutron Dosimetry," *Proceedings of the Second International Symposium on Neutron Dosimetry in Biology and Medicine, Neuherberg, Germany, Sept. 20–Oct. 4, 1974*

"The Future of Personnel Monitoring in Areas with Hot and Humid Climates," and "Integrating Dosimeters for Environmental Radiation Assessment," *Proceedings of the First Asian IRPA Regional Congress on Radiation Protection, Bombay, India, Dec. 15–20, 1974*

"A Glow from the Distant Past – Thermoluminescence in Ancient Pottery," *ORNL Rev.*, Fall 1974, p. 11

"Conferences on Exoelectron Emission and Dosimetry", news item, *Health Phys.* **26**, 377 (1974)

"On the Discovery of Thermoluminescence," *Health Phys.* **27**, 321 (1974)

"Progress in Luminescence Dosimetry," *Health Phys.* **28**, 309–10 (1975)

"A Comment Concerning the Assessment of Population Exposures to External Environmental Radiation," letter to the editor, *Health Phys.*, in press

"First Asian Regional Congress on Radiation Protection," conference report, *Health Phys.*, in press

"Quo Vadis Personnel Monitoring," *Nucl. Safety*, in press

"A Simple Method for the Automatic Evaluation of Particle Tracks in Mica," *Nucl. Instrum. Methods*, in press

K. Becker and M. M. Abd El Razek
"Automatic Spark Counting of Fast Neutron-Induced Recoil Particle Tracks in Polymer Foils," *Nucl. Instrum. Methods* **124**, 557–61 (1975)

K. Becker and J. S. Jun
"Transfer Dosimeters for Fast Neutron Sources," technical note, *Phys. Med. Biol.*, in press

S. R. Bernard
"A Metabolic Model for Whole Body and GI Tract Retention in a Human Infant Deduced from Experimental Data on Suckling Rats Administered a Single Oral Dose of Cerium-141 at Different Ages" *Proceedings of the Eighth Midyear Topical Symposium of the Health Physics Society, Knoxville, Tenn., Oct. 21–24, 1974*, CONF-741018, pp. 267–74

Werner Brandt, V. N. Neelavathi, and R. H. Ritchie
"Spectra of Wake-Riding Electrons Emerging from Solids," *Phys. Lett. A* (to be published)

Werner Brandt, Anthony Ratkowski, and R. H. Ritchie
"Energy Loss of Swift Proton Clusters in Solids," *Phys. Rev. Lett.* **33**, 1325 (1974)

T. A. Callcott and E. T. Arakawa
"Ultraviolet Optical Properties of Li," *J. Opt. Soc. Am.* **64**, 839 (1974)

"Volume and Surface Photoemission Processes from Plasmon Resonance Fields" *Phys. Rev. B*, accepted for publication

C. V. Chester, R. O. Chester, G. A. Cristy, and C. M. Haaland
National Security Considerations of Nuclear Energy Centers, ORNL-5036 (July 1975)

C. V. Chester and E. P. Wigner
"Population Vulnerability: The Neglected Issue in Arms Limitation and the Strategic Balance," *ORBIS*, Fall 1974

R. O. Chester
Biological Dose and Radiological Activity from Nuclear Reactor or Nuclear Reactor Weapon Fission Products, ORNL-4996 (December 1974)

L. G. Christophorou
"Electrons in High Pressure Gases," *Proceedings of the Fifth International Congress of Radiation Research* (in press).

"Mobilities of Slow Electrons in Low- and High-Pressure Gases and Liquids," *Int. J. Radiat. Phys. Chem.* (R. L. Platzman Memorial Issue) **7**, 205 (1975)

L. G. Christophorou, R. P. Blaunstein, and D. Pittman
"Mobilities of Thermal Electrons in π-Electron Containing Organic Gases," *Chem. Phys. Lett.* **22**, 41–46 (1974).

L. G. Christophorou, K. Gant, and J. K. Baird
"Slowing-Down of Subexcitation Electrons in Polyatomic Gases," *Chem. Phys. Lett.* **30**, 104–8 (1975)

L. G. Christophorou and R. E. Goans
"Low-Energy (< 1 eV) Electron Attachment to Molecules in Very-High Pressure Gases: C_6H_6," *J. Chem. Phys.* **60**, 4244–50 (1974)

L. G. Christophorou, D. L. McCorkle, and J. G. Carter
"Compound-Negative-Ion Resonant States and Threshold-Electron Excitation Spectra of Monosubstituted Benzene Derivatives." *J. Chem. Phys.* **60**, 3779–86 (1974)

"Resonant States of Organic Molecules," *Proceedings of International Congress of Excited States of Biological Molecules,* Wiley-Interscience (in press)

R. N. Compton, P. W. Reinhardt, and C. D. Cooper
"Collisional Ionization of Na, K, and Cs by CO_2, COS, and CS_2: Molecular Electron Affinities" submitted for publication in the *Journal of Chemical Physics*

C. D. Cooper, W. T. Naff, and R. N. Compton
"Negative Ion Properties of *p*-Benzoquinone: Electron Affinity and Compound States," submitted for publication in the *Journal of Chemical Physics*

G. A. Cristy

Best Shelter for Critical Industry Workers, ORNL-5022 (March 1975)

G. A. Cristy, ed.
Civil Defense (Moscow, 1974), ORNL-tr-2845 (Russian translation) (July 1975)

G. A. Cristy and C. H. Kearny
Expedient Shelter Handbook, ORNL-4941 (August 1974)

Liliana Deleanu and J. A. Stockdale
"Dissociative Ionization of Molecules by Electron Impact. II. Kinetic Energy and Angular Distributions of N^+ and N^{++} Ions from N_2," submitted for publication in the *Journal of Chemical Physics*

H. W. Dickson, W. F. Fox, and F. F. Haywood
1974 Intercomparison of Personnel Dosimeters, ORNL-TM-4786, in preparation

H. W. Dickson, F. F. Haywood, and K. Becker
Tenth Dosimetry Intercomparison Study, ORNL-TM-4566 (March 1975)

H. W. Dickson and G. D. Kerr
"Dose Rates from Plane Sources of Gamma Rays," *Health Phys.,* in press

H. W. Dickson, G. D. Kerr, P. T. Perdue, and S. A. Abdullah
"Environmental Radiation Measurements Using *In Situ* and Core Sampling Techniques," *Proceedings of the Health Physics Society Eighth Midyear Topical Symposium on Population Exposures, Knoxville, Tenn., Oct. 21–24, 1974*

"Environmental Gamma-Ray Measurements Using *In Situ* and Core Sampling Techniques," *Health Phys.*, in press

L. T. Dillman
"Absorbed Gamma Dose Rate for Immersion in a Semi-Infinite Radioactive Cloud," *Health Phys.* **27**, 571–80 (December 1974)

L. T. Dillman and T. D. Jones
"Internal Dosimetry of Spontaneously Fissioning Nuclides" *Health Phys.* (in press)

C. E. Easterly and L. G. Christophorou
"Fluorescence Emission from the First- and the Second-Excited π-Singlet States of Aromatic Hydrocarbons in Solution and Their Temperature Dependences," *J. Chem. Soc., Faraday Trans. II,* **70**, 167–73 (1974)

L. C. Emerson, M. W. Williams, I-Ian Tang, R. N. Hamm, and E. T. Arakawa
"Optical Properties of Guanine from 2 to 82 eV," accepted for publication in *Radiation Research*

E. M. Engler, F. B. Kaufman, D. C. Green, C. E. Klots, and R. N. Compton
"Ionization Potentials and Donor Properties of Selenium Analogues of Tetrathiofulvalene," *J. Amer. Chem. Soc.* (in press)

M. R. Ford and W. S. Snyder
"A Tabulation of Specific Effective Energies for Dose Calculations," *Proceedings of the Third Congress of the International Radiation Protection Association, Washington, D.C., Sept. 9–14, 1973* (February 1974)

J. S. Gailar
"Soviet Shelter Building," *Survive* 7(2) (September–October 1974)

R. B. Gammage
"The Effect of Grinding on the Polymorphs of Calcium Carbonate," *J. Colloid Interface Sci.*, in press

R. B. Gammage and J. S. Cheka
"Measuring Tritium with Exoelectron Dosimeters," *J. Nucl. Instrum. Methods,* in press

R. B. Gammage, J. S. Cheka, and N. Saheli
"Field Testing of TSEE Dosimeters for Personnel Monitoring," *Proceedings of the Health Physics Society Eighth Midyear Topical Symposium on Population Exposures, Knoxville, Tenn., Oct. 21–24, 1974*

R. B. Gammage and K. W. Crase
"Improvements in the Use of Ceramic BeO for TLD," *Health Phys.*, in press

R. B. Gammage and A. K. Garrison
"Investigation of EPR, TLD, and TSEE of BeO Ceramic," *Proceedings of the Fourth International Conference on Luminescence Dosimetry, Krakow, Poland, August 27–31, 1974,* vol. I, pp. 263–82

R. B. Gammage and D. R. Glasson
"The Effect of Grinding on the Polymorphs of Calcium Carbonate." *Proceedings of the 49th National Colloid Symposium, Potsdam, N.Y., June 16–18, 1975*

R. B. Gammage, F. F. Haywood, M. H. Lee, and J. S. Cheka
Fast Neutron Monitoring with Exoelectron Emitting BeO Dosimeters, ORNL-TM-4624 (June 1974)

R. B. Gammage and H. F. Holmes
"Alteration of Apollo 17 Orange Fines by Adsorbed Water Vapor," *J. Colloid Interface Sci.*, in press

"Blocking of the Alteration Reaction between Water and Lunar Fines," *Lunar Sci.*, **6**, Part 1, 384–86 (1975)

"Surface Properties of a North Ray Crater Soil (Apollo 16)," *Lunar Sci.* **6**, Part 1, 387–89 (1975)

"Blocking of the Water–Lunar Fines Reaction by Air and Water Concentration Effects," *Proceedings of the Sixth Lunar Science Conference, Houston, Tex., March 17–21, 1975*

"Specific Surface Area as a Maturity Index of Lunar Fines," *Earth Planet. Sci. Lett.*, in press

R. B. Gammage, G. D. Kerr, and L. Huskey
"Exploratory Study of the use of TSEE Dosimeters in Radon Monitoring." *Health Phys.*, in press

W. R. Garrett
"Rotational Resonances in Molecular Scattering of Ultra-Low-Energy Electrons." *Phys. Rev. A* **11**, 509–15 (February 1975)

"Molecular Scattering: Convergence of Close-Coupling Expansions in the Presence of Many Open Channels," *Phys. Rev. A* **11**, 1297–1302 (April 1975)

S. M. Garry, P. S. Stansbury, and J. W. Poston
"Measurement of Absorbed Fractions for Photon Sources Distributed Uniformly in Various Organs of a Heterogeneous Phantom," *Proceedings of the Eighth Midyear Topical Symposium of the Health Physics Society, Knoxville, Tenn., October 21–24, 1974,* CONF-741018

"Measurement of Absorbed Fractions for Photon Sources Distributed Uniformly in Various Organs of a Heterogeneous Phantom," *Health Phys.* (to be published)

T. F. Gesell, G. deP. Burke, and K. Becker
An International Intercomparison of Environmental Dosimeters under Field and Laboratory Conditions, ORNL-TM-4887, in press

R. E. Goans and L. G. Christophorou
"Electron Attachment to C_2H_5Br in High Pressure Gases," *J. Chem. Phys.* (submitted for publication)

M. Grant, D. L. McCorkle, and L. G. Christophorou
"Interactions of Slow Electrons with Benzene and Benzene Derivatives" (in preparation)

C. M. Haaland
"On Rowland K. Hawkes' 'Spatial Patterning of Urban Population Characteristics,'" *Am. J. Sociol.* (March 1975)

"The Changing Strategic Balance," *Survive* (July–August 1975)

C. M. Haaland, M. M. Williams, and M. T. Heath
Computer Mapping: Social Data for St. Louis, ORNL-TM-4849 (June 1975)

J. C. Hart, R. H. Ritchie, and B. S. Varnadore, eds.
Proceedings of the Eighth Midyear Topical Symposium of the Health Physics Society, CONF-741018 (October 1974)

J. M. Heller, Jr., R. D. Birkhoff, and L. R. Painter
"Collective Oscillation in Liquid Normal Tetradecane and Normal Heptadecane," *J. Chem. Phys.,* accepted for publication

J. M. Heller, Jr., R. N. Hamm, R. D. Birkhoff, and L. R. Painter
"Collective Oscillations in Liquid Water," *J. Chem. Phys.* **60**, 3483–86 (1974)

M. J. Hilyer, G. S. Hill, and G. G. Warner
"Dose from Photon Emitters Distributed Uniformly in the Total Body as a Function of Age," *Proceedings of the Third Congress of the International Radiation Protection Association, Washington, D.C., Sept. 9–14, 1973* (February 1974)

H. F. Holmes, E. L. Fuller, Jr., and R. B. Gammage
"Some Surface Properties of Apollo 17 Soils," *Proceedings of the Fifth Lunar Conference* (Supplement 5, *Geochimica et Cosmochimica Acta)* **3**, 2275–85 (1974)

D. Y. Hsia and R. O. Chester
A Study of the Fission Product Release from a Badly Damaged Water-Cooled Reactor, ORNL-TM-4702 (June 1974)

H. H. Hubbell, Jr., Wei-Li Chen, W. H. Shinpaugh, and T. D. Jones
"Measured and Calculated Dose Distributions from Neutrons Incident on a Tissue-Equivalent Phantom," *Health Phys.* **27**, 289–97 (1974)

G. S. Hurst
"Energy Pathways, Including the Jesse Effect, in Noble Gases," *Radiat. Res.* **59**, 350–55 (August 1974)

G. S. Hurst, J. P. Judish, M. H. Nayfeh, J. E. Parks, M. G. Payne, and E. B. Wagner
"Use of a 3-MV Proton Accelerator for Study of Noble Gases, Including Laser Ionization of Excited States," *Proc. Third Conference on Application of Small Accelerators, Denton, Tex., Oct. 21–23, 1974* (in press)

G. S. Hurst and C. E. Klots
"Elementary Processes in Irradiated Noble Gases," to be published in vol. 5 of *Advances in Radiation Chemistry,* ed. by M. Burton and J. L. Magee, Wiley-Interscience, New York

G. S. Hurst, M. G. Payne, M. H. Nayfeh, J. P. Judish, and E. B. Wagner
"Saturated Two-Photon Resonance Ionization of He(2^1S)," submitted for publication in *Physical Review Letters*

G. S. Hurst, E. B. Wagner, and M. G. Payne
"Energy Transfer from the Resonance States $Ar(^1P_1)$ and $Ar(^3P_1)$ to Ethylene," *J. Chem. Phys.* **61**, 3680–85 (November 1974)

T. Inagaki, R. N. Hamm, E. T. Arakawa, and R. D. Birkhoff
"Optical Properties of Bovine Plasma Albumin between 2 and 82 eV," accepted for publication in *Biopolymers*

T. Inagaki, R. N. Hamm, E. T. Arakawa, and L. R. Painter
"Optical and Dielectric Properties of DNA in the Extreme Ultraviolet," *J. Chem. Phys.* **61**, 4246–50 (1974)

D. G. Jacobs
"Management of Radioactive Wastes – Programs of the International Atomic Energy Agency," *Nucl. Technol.* **24**, 300 (December 1974)

J. P. Johnson, D. L. McCorkle, L. G. Christophorou, and J. G. Carter
"Long-Lived Parent Negative Ions Formed via Nuclear Excited Feshbach Resonances: Part IV. A Systematic Study of NO_2-Containing Benzene Derivatives," *J. Chem. Soc., Faraday Trans. II* (in press)

T. D. Jones
"Distributions for the Design of Dosimetric Experiments in a Tissue-Equivalent Medium," *Health Phys.* **27**, 87–96 (1974)

"Particle Current to Fluence Conversion for Instruments of Detection and for Monte Carlo Simulated Radiation Transport," *Health Phys.* **28**, 451 (1975)

"Monte Carlo Irradiation in a Spatially Dependent Field," *Health Phys.*, in press

T. D. Jones, J. A. Auxier, J. S. Cheka, and G. D. Kerr
"*In Vivo* Dose Estimates for A-Bomb Survivors in Hiroshima and Nagasaki," *Health Phys.* **28**, 367–81 (April 1975)

T. D. Jones and F. F. Haywood
"Transmission of Photons through Common Shielding Media," note, *Health Phys.*, in press

Transmission of Photons through Common Shielding Media, ORNL-TM-4728 (January 1975)

J. S. Jun and K. Becker
"TLD with Terbium-Activated Magnesium Orthosilicate," note, *Health Phys.* **28**, 459–61 (1975)

C. H. Kearny
Expedient Shelter Construction and Occupancy Experiments, ORNL-5039 (July 1975)

G. D. Kerr
Report of Liaison Studies with the Atomic Bomb Casualty Commission, Hiroshima, Japan, ORNL-TM-4830 (February 1975)

C. E. Klots
"Theory of Ionic Fragmentations: Recent Developments," *Adv. Mass Spectrom.* **6**, 969–74 (1974)

C. E. Klots and L. W. Sieck
"Argon Sensitized Formation of Xe_2^+: A New Mechanism for the Jesse Effect," *Chem. Phys. Lett.* **27**, 71 (1974)

"Long-Lived Molecular Rydberg States," *J. Chem. Phys.* **62**, 741–42 (January 1975)

R. A. MacRae, M. W. Williams, and E. T. Arakawa
"Optical Properties of Some Aromatic Liquids in the Vacuum Ultraviolet," *J. Chem. Phys.* **61**, 861–65 (1974)

J. H. Marable, P. R. Barnes, and D. B. Nelson
Power System EMP Protection, ORNL-4958 (March 1975)

J. R. McNeely, G. S. Hurst, E. B. Wagner, and M. G. Payne
"Energy Transfer from Argon Resonance States to Nitrogen, Hydrogen, and Nitric Oxide," *J. of Chem. Phys.* (submitted for publication)

V. N. Neelavathi and R. H. Ritchie
"Surf-Riding Electron States: Polarization Charge Density Effects Associated with Ion Motion in Solids," *Atomic Collisions in Solids,* vol. 1, Plenum Press, New York, 1975

D. B. Nelson, P. R. Barnes, J. H. Marable, and G. L. Ragan
Electromagnetic Pulse (EMP) Protection Requirements for the 487L Transmitter Facility at Silver Creek, Nebraska (U), ORNL-4983 (January 1975) (classified)

M. Oberhofer
Safe Handling of Radiation Sources, Verlag Karl Thiemig, Munich (1974), English translation by J. E. Turner and R. G. Turner

G. Östrom, F. Schmidt-Bleek, R. N. Compton, and S. Datz
"Electron-Induced Sputtering Reactions from Alkali Halide Crystals," *Phys. Rev. B,* submitted for publication

L. R. Painter, R. D. Birkhoff, and J. M. Heller, Jr.
"Electrons Dance in Water," accepted for publication in *The Physics Teacher*

M. G. Payne
"Transport of Resonance Radiation," *Radiat. Res.* **59**, 405–07 (August 1974)

M. G. Payne and W. R. Garrett
"Application of Microdosimetry to Models of Cell Survival. Part I," *Radiat. Res.* (in press)

"Models for Cell Survival with Low LET Radiation," *Radiat. Res.* (in press)

"Some Relations between Cell Survival Models Having Different Inactivation Mechanisms." *Radiat. Res.* (in press)

M. G. Payne, Cornelius E. Klots, and G. S. Hurst
"Kinetic Processes Determining the Time Dependence of vuv Emissions in He," submitted for publication in the *Journal of Chemical Physics*

J. W. Poston, W. S. Snyder, and G. G. Warner
"Age Factors for Dose Rates from an Infinite Cloud of a Photon Emitter," *Proceedings of the Eighth Midyear Topical Symposium of the Health Physics Society, Knoxville, Tenn., Oct. 21–24, 1974,* CONF-741018

J. W. Poston and G. G. Warner
"Absorbed Dose to Selected Internal Organs from Typical Diagnostic Exposures," *Proceedings of the Third Congress of the International Radiation Protection Association, Washington, D.C., Sept. 9–14, 1973* (February 1974)

J. W. Poston, G. G. Warner, and P. S. Stansbury
Medical X-Ray Dose Estimation Program Progress Report for Period Ending August 31, 1974, ORNL-TM-4722 (September 1974)

J. Rademacher, L. G. Christophorou, and R. P. Blaunstein
"Electron Attachment to SO_2 in High Pressure Gases," *J. Chem. Soc., Faraday Trans. II* (in press)

R. H. Ritchie
"Theoretical Aspects of Channeling," *Proceedings of Conference on Channeling and Blocking Phenomena, Saclay, France, May 1974*

R. H. Ritchie and Werner Brandt
"Primary Processes and Track Effects in Irradiated Media," *Radiat. Res.* (to be published)

W. S. Snyder
"Estimates of Dose Rate to Gonads of Infants and Children from a Photon Emitter in Various Organs of the Body," *Proceedings of the Third Congress of the International Radiation Protection Association, Washington, D.C., Sept. 9–14, 1973* (February 1974)

"Dosimetry of Internal Emitters for Population Exposures." *Proceedings of the Eighth Midyear Topical Symposium of the Health Physics Society, Knoxville, Tenn., October 21–24, 1974,* CONF-741018

Report on Reference Man, ICRP Publication 23, Pergamon Press Great Britain, ICRP Task Group (W. S. Snyder, chairman) (April 1975)

W. S. Snyder, M. R. Ford, G. G. Warner, and S. B. Watson
A Tabulation of Dose Equivalent per Microcurie-Day for Source and Target Organs of an Adult for Various Radionuclides, ORNL-TM-5000 (November 1974)

J. A. D. Stockdale, V. E. Anderson, A. E. Carter, R. N. Compton, and Liliana Deleanu
"Dissociative Ionization of Molecules by Electron Impact. I. Apparatus and Kinetic Energy Distributions of D^+ Ions from D_2," submitted for publication in the *Journal of Chemical Physics*

J. A. Stockdale, F. J. Davis, R. N. Compton, and C. E. Klots
"Production of Negative Ions From CH_3X ($X = NO_2$, CN, I, Br) Molecules by Electron Impact and by Collisions with Atoms in Excited Rydberg States," *J. Chem. Phys.* **60**, 4279–85 (June 1, 1974)

J. A. Stockdale and L. Deleanu
"Vibrational Structure in Kinetic Energy Spectra of O^+ Ions from Electron Impact Dissociative Ionization of O_2: Predissociation of the $B^2\Sigma^-_g$ State of O_2^+," *Chem. Phys. Lett.* **28**, 588–89 (Oct. 15, 1974)

J. A. D. Stockdale, B. P. Pullen, and A. E. Carter
"A Simple Method of Obtaining Excitation Functions in Digital Form," *Int. J. Mass Spectrom. Ion Phys.* **17**, 241–44 (1975)

J. H. Thorngate
" 'Though It's Been Said Many Times, Many Ways . . . ,' " letter to the editor, *Health Phys.* **28**, 633 (May 1975)

J. H. Thorngate, D. J. Christian, and G. K. Sumner
The Spectrum of Gamma Rays with Energies Greater than 1.8 MeV Produced by Fissions and Short-Lived Fission Products in the Health Physics Research Reactor, ORNL-TM-4636 (October 1974)

R. N. Thurmer
"Revitalization of Soviet Civil Defense," *Survive* 8(1) (January–February 1975)

"Soviet Civil Defense: Full Speed Ahead!," *Survive* 8(3) (May–June 1975)

J. E. Turner
"Symposium on Population Exposures," news item, *Health Phys.* **28**, 310 (1975)

J. E. Turner and W. S. Nichols
"Final Report – Symposium on Population Exposures," *Proceedings of the Eighth Midyear Topical Symposium of the Health Physics Society, Knoxville, Tenn., Oct. 21–24, 1974,* CONF-74018 (February 1975)

J. E. Turner, H. A. Wright, and R. N. Hamm
"Calculations for High-Energy Radiations," *Radioprotection* **9**, 131 (1974)

"Estimated *W*-Values for Negative Pions in Nitrogen and Argon," *Health Phys.* (in press)

G. G. Warner, J. W. Poston, and W. S. Snyder
"Absorbed Dose in Phantoms Which Represent Various Aged Male Humans from External Sources as a Function of Age," *Health Phys.*, in press

E. P. Wigner and J. S. Gailar
"The Russian Evacuation Plans – the Fears They Create," *Survive,* 7(5) (September–October 1974)

M. W. Williams, E. T. Arakawa, R. D. Birkhoff, R. N. Hamm, H. C. Schweinler, and R. A. MacRae
"Optical Properties of Chloroplasts and Red Blood Cells in the Vacuum UV," *Radiat. Res.* **61**, 185 (1975)

M. W. Williams, R. N. Hamm, E. T. Arakawa, L. R. Painter, and R. D. Birkhoff
"Collective Electron Effects in Molecular Liquids," *Int. J. Radiat. Phys. Chem.* (Platzman Memorial Issue) 7, 95 (1975)

J. F. Wilson, F. J. Davis, D. R. Nelson, and R. N. Compton
"Electron Transport and Ion Clustering Reactions in Water Vapor and Deuterated Water Vapor," *J. Chem. Phys.* **62**, 4204–12 (1975)

H. A. Wright, R. N. Hamm, and J. E. Turner
"Estimation of Dose Equivalent and Average Quality Factors for π^- and π^+ Beams." *Health Phys.* 27, 3 (1974)

Lectures

J. A. Auxier
"Health Protection Aspects of Fusion Power," presented at meeting with CTR and BER Management (Division of Biomedical and Environmental Research, ERDA, Headquarters) on Fusion Power and the Environment, Jan. 15, 1975

"Plutonium Toxicity: Environmental and Public Health Impacts of Energy Production," presented before the Illinois Commission on Atomic Energy, Mar. 27, 1975 (at ORNL)

"Environmental and Public Health Impact of Energy Production," given before the University of Pennsylvania College of Thematic Course on Energy Management," Apr. 7, 1975 (at ORNL)

Talk on current research in health physics given before a meeting of the medical directors, ORAU, Apr. 15, 1975

"Effects of Low Levels of Radiation, Including Plutonium," guest speaker at American Nuclear Society banquet, Blacksburg, Va., Apr. 23, 1975

J. K. Baird
"A Parabolic Lithium Mirror for a Laser Driven Pellet Fusion Reactor" Lawrence Livermore Laboratory, Livermore, Calif., July 31, 1974

"The Emergence of a New Branch of Nuclear Engineering – Laser Driven Pellet Fusion," School of Nuclear Engineering, Georgia Institute of Technology, Atlanta, Ga., Sept. 26, 1974

"The Emergence of a New Branch of Nuclear Engineering – Laser Driven Pellet Fusion," Department of Nuclear Engineering, University of Tennessee, Knoxville, Tenn., Oct. 15, 1974

"Laser Fusion," Department of Physics, University of Tennessee Knoxville, Tenn., Nov. 12, 1974

"Prospects for Electric Power Generation by Laser Fusion," Department of Physics, Western Kentucky University, Bowling Green, Ky., Nov. 22, 1974

P. R. Barnes
"Effects of EMP on a PWR," Civil Defense Research Section Review, Oak Ridge National Laboratory, Oct. 16, 1974

K. Becker
"Current Developments in Solid-State Dosimetry," Oak Ridge Associated Universities, Mar. 27, 1975

"Fast Neutron Dosimetry at ORNL – Progress and Problems," ERDA Workshop on Neutron Personnel Monitoring, Washington, D.C., May 6–7, 1975

K. Becker, J. S. Cheka, R. B. Gammage, F. F. Haywood, J. S. Jun, A. M. Moreno, and M. M. Abd El Razek
"Solid-State Dosimeters and Their Applications," Seminars: University of Giessen, Germany, and Centre d'Etudes Nucléaires, Fontenay-aux-Roses, France, September 1974

R. D. Birkhoff
"Research in Vacuum Ultraviolet Surface Physics at ORNL," Livermore Laboratory, Livermore, Calif., Aug. 1, 1974

"Measurements of Electron Slowing Down Spectra," National Bureau of Standards, Washington, D.C., Aug. 9, 1974

C. V. Chester
"Nuclear Power and Post-Attack Recovery," Oak Ridge Civil Defense Society Meeting, Oak Ridge, Tenn., May 14, 1975

"Nuclear Terrorism in Perspective," Civil Defense Research Section Review, Oak Ridge National Laboratory, Oct. 16, 1974

"Population Vulnerability," Civil Defense Research Section Review, Oak Ridge National Laboratory, Oct. 16, 1974

R. O. Chester

"Consequences of an Uncontained Meltdown," Civil Defense Research Section Review, Oak Ridge National Laboratory, Oct. 16, 1974

"Planning for Nuclear Emergencies," Harvard School of Public Health, Harvard University, Boston, May 20, 1975

"Post Accident Recovery," Radiation Accident Management Course for State Radiological Health Personnel, Oak Ridge Associated Universities, Oak Ridge, Tenn., May 13, 1975

L. G. Christophorou

"When Slow Electrons Collide with Molecules," Virginia Polytechnic Institute and State University, Blacksburg, Va., Oct. 3, 1974

"Electrons in High Pressure Gases," Argonne National Laboratory, Argonne. Ill., Dec. 5 1974

"Radiation and Chemical Physics," Department of Physics, University of Tennessee, Knoxville, Nov. 26, 1974

"Electrons in Fluids," Department of Physics, University of North Carolina, Chapel Hill, Feb. 14, 1975

"Electrons in Dense Gases," Brookhaven National Laboratory, Brookhaven, N.Y., Mar. 21, 1975

R. N. Compton

"Electron Affinities of Complex Molecules," California Institute of Technology, Pasadena, Calif.. Jan. 31, 1975

"Negative Ions of Complex Molecules." Stanford University, Stanford, Calif.. Jan. 29, 1975

"Negative Ion Formation in Some Hexafluoride Molecules," Los Alamos Scientific Laboratory, Los Alamos N.M., Oct. 30, 1974

G. A. Cristy

"Shelter for Critical Industry Workers," Civil Defense Research Section Review, Oak Ridge National Laboratory, Oct. 16, 1974

H. W. Dickson

"Conventional Reactors," Oak Ridge Associated Universities, Aug. 12, 1974

"Power Reactor Effluents," Oak Ridge Associated Universities, Aug. 12, 1974

"Principles of Reactors and Potential Reactor Accidents," Oak Ridge Associated Universities, Dec. 12, 1974

"Reactor Effluents," presented to ORAU health physics course participants, Oak Ridge National Laboratory, Apr. 18, 1975

"Reactors and Potential Reactor Accidents," Medical Management of Radiation Accidents Seminar conducted by ORAU, June 12, 1975

"Types of Reactors," Oak Ridge Associated Universities, Apr. 15, 1975

R. B. Gammage

"Understanding and Using BeO Ceramic for TSEE and TLD," Institut für Strahlenschutz, MBH, Munich, W. Germany, Aug. 23, 1974; EURATOM, Ispra, Italy, Sept. 2–3, 1974; Physics Department, University of Giessen, Giessen, W. Germany, Sept. 4, 1974; USAEC Health and Safety Laboratory, New York, Aug. 14, 1974

W. R. Garrett

"Electron Scattering Phenomena Involving Polar Molecules." Physics Division Seminar, Oak Ridge National Laboratory, Nov. 14, 1974

C. M. Haaland

"Post-Crisis Shelter Program," Civil Defense Research Section Review, Oak Ridge National Laboratory, Oct. 16, 1974

F. F. Haywood
"New Options in Health Protection Research," Georgia Institute of Technology, Atlanta, Ga., Feb. 20, 1975

G. S. Hurst
"Laser Ionization of Excited States of the Noble Gases," Centre for Interdisciplinary Studies in Chemical Physics, University of Western Ontario, London, Ontario, Nov. 5, 1974

T. Inagaki
"Optical Responses of Organic Macromolecules in the Region from Infrared to X-Ray and Precise Measurement of the Optical Constants," National Institute of Health, Bethesda, Md., Oct. 25, 1974

D. G. Jacobs
"Impact in Groundwater of Effluents Arising in the Nuclear Industry," course in Environmental Analysis and Environmental Monitoring for Nuclear Power Generation, University of California Extension, Berkeley, Calif., Sept. 9–13, 1974

"Waste Management," course on The Energy Crisis and Its Effect on the Environment, Georgia Institute of Technology, Atlanta, Ga., June 17–21, 1974

"Waste Management" and "Environmental Monitoring," Technical Fundamentals for New Technicians, ORNL, Oak Ridge, Tenn., Mar. 6 and Apr. 24, 1975

"Environmental Monitoring at HNL," Ten-Week Health Physics and Radiation Protection Course, ORAU, Oak Ridge, Tenn., Apr. 17, 1975

"Environmental Monitoring," Health Physics Certification Review, East Tennessee Chapter of Health Physics Society, Oak Ridge, Tenn., April 17, 1975

C. H. Kearny
"Experimental Studies of Expedient Shelters," Civil Defense Research Section Review, Oak Ridge National Laboratory, Oct. 16, 1974

G. D. Kerr
"*In Vivo* Dose Estimates for Atomic Bomb Survivors in Hiroshima and Nagasaki," Atomic Bomb Casualty Commission, Hiroshima, Japan, Aug. 22, 1974

"Health Physics Research at the Oak Ridge National Laboratory," Research Institute for Nuclear Medicine and Biology, Hiroshima University, Hiroshima, Japan, Sept. 11, 1974

C. E. Klots
"Unimolecular Decompositions," Department of Chemistry, Purdue University, Lafayette, Ind., Aug. 29, 1974

M. G. Payne
"Kinetic Processes in Inert Gases," Department of Physics, University of Kentucky, Lexington, Ky., Dec. 6, 1974

J. W. Poston
"Medical X-Ray Dose Estimation," Physics Department, Appalachian State University, Boone, N.C., Feb. 12, 1975

R. H. Ritchie
"Monte Carlo Calculations of Electron Slowing-Down Spectra," National Bureau of Standards, Washington, D.C., Aug. 9, 1974

W. S. Snyder
"A Personal View of ICRP Recommendations," "ORNL-5000 as an Aid to Better Dose Evaluation," "The Variation of Dose with Size and Shape of the Thyroid," and "On Dose to the Bladder from an Emitter Excreted in Urine," Boris Kidric Institute of Nuclear Sciences, Vinca, Beograd, Yugoslavia, Apr. 15, 1975

J. A. Stockdale
"Dissociative Ionization of Diatomic Molecules," Department of Chemistry, Florida State University, Tallahassee, Fla., Mar. 6, 1975

J. A. Stockdale and Liliana Deleanu

"A Crossed Beams Study of Dissociative Ionization by Electron Impact: Recent Results of O_2 and N_2," Department of Physics and Astronomy, University of Georgia, Athens, Ga., Jan. 16, 1975

R. N. Thurmer

"Developments in Soviet Civil Defense," Civil Defense Research Section Review, Oak Ridge National Laboratory, Oct. 16, 1974

J. E. Turner

"Research in Health Physics at ORNL," Cancer Foundation, Winnepeg, Manitoba, Canada, July 26, 1974

Miscellaneous Staff Activities

Academic Appointments

K. Becker
Adjunct Professor, University of Tennessee

R. D. Birkhoff
Ford Professor, University of Tennessee

L. G. Christophorou
Ford Professor, University of Tennessee

M. F. Fair
Visiting Assistant Professor of Physics, University of Tennessee

G. S. Hurst
Adjunct Professor, University of Kentucky

M. G. Payne
Adjunct Associate Professor, University of Kentucky

R. H. Ritchie
Ford Professor, University of Tennessee
Senior Visiting Fellow, 1974–75, Cavendish Laboratory, Cambridge University, Cambridge, England

H. C. Schweinler
Ford Professor, University of Tennessee

Service in Professional Organizations

J. A. Auxier
National Academy of Science Advisory Committee on Civil Defense; National Academy of Sciences Subcommittee on Radiation Shielding; ICRU Task Group on Neutron Instrumentation; USASI Subcommittee N-13.8; NCRP Subcommittee 28; IAEA Panel on Nuclear Accident Dosimetry Systems; ERDA-DBER Cf-252 Biomedical Advisory Panel; ICRP Task Group on Emergency and Accidental Exposures; Joint SNS/BER Biomedical Working Group; and Managing Editor, *Health Physics*

K. Becker
Chairman, Standing Committee on International Conferences on Luminescence Dosimetry; Vice President and Program Committee Member, Fourth International Conference on Luminescence Dosimetry, Krakow, Poland, 1974; IAEA Working Group on Neutron Transfer Dosimeters; Vice Chairman, ICRP Task Group on External Radiation Exposures; ICRU Task Group on Radiation Protection Instrumentation

S. R. Bernard
ICRP Task Group on Dose Calculations for the Report of Committee 2

C. E. Easterly
Review Committee for Government Grant to St. Mary's College, Winona, Minnesota

Mary R. Ford
ICRP Task Group on Dose Calculations for the Report of Committee 2; NCRP Scientific Committee 32: Administered Radioactivity; NCRP Scientific Committee 33: Dose Calculations

G. S. Hurst
Report Committee on Average Energy Required to Produce an Ion Pair, ICRU

F. F. Haywood
Subcommittee on Radiation Shielding, National Academy of Sciences Advisory Committee on Civil Defense; Standards Committee N-16, American National Standards Institute (Alternate Member); Chairman, Standards Subcommittee N13.3, American National Standards Institute; IAEA Panel on Nuclear Accident Dosimetry; Annual Meeting Place Committee, Health Physics Society

D. G. Jacobs
Consultant to IAEA for preparation of a booklet on Waste Management; Consultant to Department of Environmental Conservation, State of New York, on subject of commercial waste burial; Program Committee of Health Physics Society; NCRP Subcommittee on Tritium; Assistant Editor for *Nuclear Safety*, Section V, Consequences of Effluent Release

G. D. Kerr
Editor, *Health Physics*

D. B. Nelson
Technical Advisory Committee for Air Force Weapons Laboratory's C^3 Program; Advisory Committee on Civil Defense and EMP Subcommittee, National Academy of Sciences

J. W. Poston
ICRP Task Group on Dose Calculations for the Report of Committee 2; NCRP Ad Hoc Committee on the Experimental Verification of Internal Dosimetry Calculations; MIRD Task Group on Pediatric Phantoms; MIRD Task Group on a Cardiac Model; ANSI Committee on the Internal Dosimetry of Fission Products and Corrosion Products; Secretary, Health Physics Society

R. L. Shoup
Section Editor, *Nuclear Safety*

J. E. Turner
Editor, *Health Physics*

Guests and Trainees

FACULTY INSTITUTE PARTICIPANTS

James H. Barker, *St. Louis University*

Edward B. Barnes, *West Virginia State College*

Homer E. Holloway, *West Virginia Wesleyan College*

Harold T. Larson, *Grand Valley State College*

Ernest L. Madsen, *Pembroke State University*

Robert C. McIlhenny, *Louisiana State University*

T. M. S. Namboodiri, *Texas College*

Sarah A. Smith, *University of North Alabama*

Keith G. Walker, *Bethany Nazarene College*

Thomas M. Willard, *Florida Southern College*

FACULTY RESEARCH PARTICIPANT

J. L. Beach, *University of Kansas*

STUDENTS

GLCA Participants

C. M. Gritzinger, *Wooster College*

R. L. Roswell, *Denison University*

ORAU Trainees

J. M. Baraza, *Vanderbilt University*

S. A. Brown, *University of North Carolina*

M. W. Cortner, *Austin Peay State College*

J. Karras, *University of Wisconsin*

H. R. Petty, *Manchester College*

D. J. Simpkin, *University of Wisconsin*

L. J. Smith, *Southwestern University*

B. R. Thomas, *Oklahoma State University*

Graduate Students

Liliana Deleanu, *University of Tennessee*

K. S. Gant, *University of Tennessee*

Q. A. Huynh, *University of Tennessee*

J. P. Johnson, *University of Tennessee*

S. I. Juan, *University of Tennessee*

J. R. McNeely, *University of Tennessee*

V. N. Neelavathi, *University of Tennessee*

J. J. Shonka, *Georgia Institute of Technology*

P. S. Stansbury, *Georgia Institute of Technology*

I-Ian Tang, *University of Tennessee*

C. J. Tung, *University of Tennessee*

R. J. Warmack, *University of Tennessee*

C. E. Wheeler, Jr., *University of Tennessee*

J. M. Younkin, *University of Tennessee*

Exceptional Students Program

James E. Phillips, *University of North Carolina*

FOREIGN GUESTS

M. M. Abd El Razek, *Atomic Energy Establishment, Cairo, Egypt*

S. A. Abdullah, *Atomic Energy Center, Dacca, Bangladesh*

H. T. Chen, *Chinese Atomic Energy Council, Taiwan*

W. L. Chen, *Chinese Atomic Energy Council, Taiwan*

Kei-Den Chou, *Taiwan*

Q. A. Huynh, *South Vietnam*

T. Inagaki, *Osaka Kyoiku University, Osaka, Japan*

Sung-I Juan, *Taiwan*

M. P. Kanduc, *IAEA Fellow, Yugoslavia*

N. H. Mei, *Taiwan*

M. F. K. Miah, *Atomic Energy Center, Dacca, Bangladesh*

V. N. Neelavathi, *Bhabha Atomic Research Centre, Bombay, India*

I-Ian Tang, *Taiwan*

C. J. Tung, *Taiwan*

H. Yamada, *Atomic Bomb Casualty Commission, Hiroshima, Japan*

HEALTH PHYSICS DIVISION

JUNE 30, 1975

J. A. AUXIER, DIRECTOR
D. L. ANDERSON, SECRETARY

J. E. TURNER*, ASSOCIATE DIRECTOR
W. S. NICHOLS*, SECRETARY

D. M. DAVIS, ASSISTANT DIRECTOR
C. J. MILLER*, SECRETARY

ADMINISTRATIVE ASSISTANT
J. S. CARVER[2]

FINANCE OFFICER
D. J. ROOK

ENGINEERING AND MAINTENANCE
W. CAREY[13]
S. R. LARKINS
E. T. LOY
J. L. MALONE[4]

SPECIAL ASSIGNMENT
K. E. COWSER

SENIOR RESEARCH ADVISORS
K. Z. MORGAN
E. P. WIGNER*

ASSESSMENT AND TECHNOLOGY
D. G. JACOBS
F. F. HAYWOOD

SECRETARIAL STAFF
L. J. BROWN
D. S. HIBBEN
S. S. STOCKSTILL
A. R. WEBB

TECHNICAL SUPPORT
L. A. LEE[6]
C. P. LITTLETON[7]

EVALUATION OF HEALTH EFFECTS
G. D. KERR
T. D. JONES*
H. YAMADA[5]

HEALTH PHYSICS RESEARCH REACTOR
D. R. WARD[8]
W. F. FOX*
J. E. JACKSON

MEASUREMENT OF POLLUTANTS AND ASSESSMENT OF IMPACTS
W. D. COTTRELL
H. W. DICKSON
C. E. EASTERLY
S. A. ABDULLAH[5]
J. M. DAVIS
W. A. GOLDSMITH
C. R. HENSON
J. P. HICKEY*
M. F. K. MIAH[5]
W. H. SHINPAUGH
R. L. SHOUP*
J. P. SPRAIN
W. B. TOWNS

TECHNOLOGY AND DEVELOPMENT
K. BECKER
R. B. GAMMAGE
J. H. THORNGATE
D. J. CHRISTIAN
P. T. PERDUE

CONSULTANTS
J. S. CHEKA
D. J. WILHOIT

BIOLOGICAL AND RADIATION PHYSICS
H. A. WRIGHT*
R. N. HAMM*

SECRETARIAL STAFF
A. L. McCRAY*
B. S. VARNADORE

TECHNICAL SUPPORT
H. L. BARNAWELL[7]*
A. E. CARTER*
J. T. COX*

ATOMIC AND MOLECULAR PHYSICS
L. G. CHRISTOPHOROU
J. K. BAIRD
J. G. CARTER
K. S. GANT[3]
O. A. HUYNH[3]
D. R. JAMES[1]
J. P. JOHNSON[3]
D. L. McCORKLE
D. PITTMAN

PHYSICS OF SOLIDS AND MACROMOLECULES
E. T. ARAKAWA
R. N. HAMM*
T. INAGAKI[1]
C. E. WHEELER[2]
M. W. WILLIAMS

LIQUID AND SURFACE PHYSICS
R. D. BIRKHOFF

GENERAL PHYSICS
R. H. RITCHIE[14]
J. C. ASHLEY
R. N. HAMM*
C. J. TUNG[3]
J. E. TURNER*
H. A. WRIGHT*

MATHEMATICAL ANALYSIS
V. E. ANDERSON[9]*

CONSULTANTS
G. BASBAS
J. B. BIRKS
A. J. BRAUNDMEIER
T. A. CALLCOTT*
C. CHEN
T. L. FERRELL
R. A. MacRAE
J. NEUFELD
M. PACE
L. R. PAINTER
M. SILVER
P. W. TODD

EMERGENCY TECHNOLOGY
C. V. CHESTER*

SECRETARIAL STAFF
M. A. CHRISMON
K. D. PRUETT

LIBRARIAN
R. N. THURMER*

STRATEGIC DEFENSE
G. A. CRISTY
P. R. BARNES*
S. A. BROWN[11]
C. V. CHESTER*
C. M. HAALAND
C. H. KEARNY
P. M. LANTZ[12]
R. N. THURMER*
E. P. WIGNER*

ENERGY SYSTEMS VULNERABILITY
C. V. CHESTER*
P. R. BARNES*
R. O. CHESTER
K. D. CHOU[5]
R. R. DAVIS
M. E. FISH

INDUSTRIAL SAFETY AND SPECIAL PROJECTS
A. D. WARDEN*

SECRETARIAL STAFF
E. M. RUCKART

BALANCE AREA REPRESENTATIVE
T. J. BURNETT*

SAFETY
D. C. GARY[1]
R. E. MILLSPAUGH*
E. M. ROBINSON
J. W. SHUEY

ORIENTATION AND TRAINING
R. E. MILLSPAUGH*

PROGRAM AND FACILITIES REVIEWS
T. J. BURNETT*

X-RAY AND MICROWAVE REVIEW
W. F. OHNESORGE*

STANDARDS AND PROCEDURES
A. D. WARDEN*

TRANSURANIUM HEALTH PHYSICS AND SAFETY PROCEDURES
C. E. HAYNES*

MEDICAL PHYSICS AND INTERNAL DOSIMETRY
J. W. POSTON
S. R. BERNARD*
H. T. CHEN[3,5]
W. L. CHEN[2,5]
M. R. FORD
J. P. HICKEY*
M. L. HWANG[3,5]
T. D. JONES*
J. J. SHONKA[3]
P. S. STANSBURY[3]
R. L. SHOUP*
G. G. WARNER[8]
S. B. WATSON[8]

SECRETARIAL STAFF
N. L. BARRINGER
K. M. BRANAM

CONSULTANTS
L. T. DILLMAN
E. M. SMITH
W. S. SNYDER
F. C. VONDER LAGE

CHEMICAL PHYSICS AND SPECTROSCOPY
W. R. GARRETT*

SECRETARIAL STAFF
N. E. BRASHIER
A. L. McCRAY*

TECHNICAL SUPPORT
H. L. BARNAWELL[7]*
A. E. CARTER*
J. T. COX*

CHEMICAL PHYSICS
R. N. COMPTON
M. W. CORTNER[3]
W. R. GARRETT*
C. E. KLOTS
P. W. REINHARDT
H. C. SCHWENLER
L. J. SMITH[3]
J. A. STOCKDALE
R. J. WARMACK[3]
J. M. YOUNKIN[3]

ATOMIC PHYSICS AND LASER RESEARCH
G. S. HURST
T. L. BULLER[3]
C. H. CHEN[1]
C. W. CHOI[3]
J. P. JUDISH
M. H. NAYFEH[1]
M. G. PAYNE
W. H. SHINPAUGH
E. B. WAGNER
J. P. YOUNG[10]

MATHEMATICAL ANALYSIS
V. E. ANDERSON[9]*

CONSULTANTS
T. A. CALLCOTT*
C. D. COOPER
W. F. FREY
J. E. PARKS
B. P. PULLEN
J. G. SKOFRONICK

RADIATION MONITORING
E. D. GUPTON*

SECRETARIAL STAFF
D. W. GADDIS

INSTRUMENTATION
E. D. GUPTON*
D. R. CLARK*
G. L. ARTHUR
C. Y. CHILDRESS
I. T. FANN
S. W. NICHOLS

DOSE DATA
J. R. MUIR
M. C. BENTLEY
D. M. SOARD
J. H. WILLIAMS

INTERNAL DOSE
W. W. PARKINSON
R. E. GOANS
W. M. GOOD

PERSONNEL METERS
D. R. CLARK*
G. L. DOWNS
E. W. JOHNSON
M. R. MATTHEWS
R. C. WOOD

RADIOCHEMISTRY
L. C. HENLEY
J. C. ANDERSON
M. W. JOHNSON
A. J. SOARD

RADIATION AND SAFETY SURVEYS
R. L. CLARK

SECRETARIAL STAFF
C. J. MILLER*

Y-12 OPERATIONS
D. E. ARTHUR
A. CARDWELL
H. R. CRAFT
R. P. WARD

BLDG. SURVEYS GP. 1
B. T. WALTERS

CENTRAL
A. J. SMITH
B. C. BURRELL
W. T. MARTIN
R. D. PARTEN

SOUTH CENTRAL
C. A. GOLDEN
W. A. ALEXANDER
A. C. BUTLER
J. V. HILYER
J. H. SPENCE

EAST
H. M. BUTLER[1]
J. S. ADDISON
J. F. ALEXANDER
W. D. CARDEN
R. C. COOPER
P. E. COX
A. B. ELDRIDGE
C. E. HAYNES*
C. F. JACKSON
W. M. JOHNSON
S. B. LUPICA
W. F. OHNESORGE*

SOUTH EAST
E. L. SHARP
T. G. CLARK
J. C. DAVIS
R. S. HOWELL

BLDG. SURVEYS GP. II
L. C. JOHNSON

NORTH WEST
C. H. MILLER
J. BURDEN
M. L. CONNER
W. A. McLOUD
G. R. PATTERSON
C. F. ZAMZOW

NORTH CENTRAL
J. A. WORTH
J. H. PEMBERTON

MELTON VALLEY
R. E. COLEMAN
W. F. FOX*
J. C. RICHTER
R. L. WALKER

SHIFT AND AREA SURVEYS
C. R. GUINN

SHIFT SUPERVISORS
R. L. JEFFERS
R. E. KENY
R. B. MALCOLM
D. G. NOE

SHIFT SURVEYS
R. E. HALLIBURTON
C. F. JACKSON
R. L. JEFFERS

AREA SURVEYS
J. R. SLATEN
C. F. SMITH
I. H. WIGGINS

*DUAL CAPACITY
*RADIATION CONTROL OFFICER
[1]DIVISION SAFETY OFFICER
[2]POSTDOCTORAL FELLOW
[3]ALTERNATE FINANCE OFFICER
[5]STUDENT
[4]QUALITY ASSURANCE COORDINATOR
[5]ALIEN GUEST
[6]PLANT AND EQUIPMENT DIVISION
[7]INSTRUMENTATION AND CONTROLS DIVISION
[8]NEUTRON PHYSICS DIVISION
[9]COMPUTER SCIENCES DIVISION
[10]ANALYTICAL CHEMISTRY DIVISION
[11]ORAU RESEARCH TRAINEE
[12]ON LOAN TO CHEMICAL TECHNOLOGY DIVISION
[13]ON LOAN TO FINANCE AND MATERIALS DIVISION
[14]SENIOR VISITING FELLOW, CAVENDISH LABORATORY, UNIVERSITY OF CAMBRIDGE, ENGLAND

OFFICE OF EDUCATION AND INFORMATION
J. E. TURNER*
S. R. BERNARD*
M. N. DIXON
M. F. FAIR
C. F. HOLLOWAY
B. L. HOUSER

HEALTH PHYSICS JOURNAL EDITORIAL OFFICE
J. A. AUXIER*
G. D. KERR*
W. S. NICHOLS*
J. E. TURNER*

HEALTH PHYSICS DIVISION LONG-RANGE PLANNING COMMITTEE
J. W. POSTON, CHAIRMAN
G. A. CRISTY
C. E. EASTERLY
R. N. HAMM
G. S. HURST
C. H. MILLER
R. E. MILLSPAUGH
D. M. SOARD
J. A. STOCKDALE
J. H. THORNGATE
J. E. TURNER, EX OFFICIO

HEALTH PHYSICS DIVISION ADVISORY COMMITTEE
WERNER BRANDT
NEW YORK UNIVERSITY
NEW YORK CITY, NEW YORK

GEORGE COWPER
ATOMIC ENERGY OF CANADA
CHALK RIVER, ONTARIO
CANADA

L. V. SPENCER
NATIONAL BUREAU OF STANDARDS
WASHINGTON, D.C.

ORNL-5046
UC-41 — Health and Safety

INTERNAL DISTRIBUTION

1. V. E. Anderson
2. E. T. Arakawa
3. D. E. Arthur
4. R. E. Baker
5. J. C. Ashley
6. S. I. Auerbach
7–16. J. A. Auxier
17. J. K. Baird
18. J. A. Barker
19. P. R. Barnes
20. S. E. Beall
21. K. Becker
22. S. R. Bernard
23. D. S. Billington
24. Biology Library
25. R. D. Birkhoff
26. W. J. Boegley
27. C. J. Borkowski
28. F. R. Bruce
29. T. H. J. Burnett
30. H. M. Butler
31. G. C. Cain
32. A. E. Carter
33. H. P. Carter
34. J. G. Carter
35–36. Central Research Library
37. C. V. Chester
38. R. D. Chester
39. K. D. Chou
40. L. G. Christophorou
41. R. L. Clark
42. R. E. Coleman
43. W. C. Colwell
44. R. N. Compton
45. W. B. Cottrell
46. W. D. Cottrell
47. K. E. Cowser
48. J. A. Cox
49. J. T. Cox
50. G. A. Cristy
51. F. L. Culler
52. D. M. Davis
53. R. R. Davis
54. H. W. Dickson
55. C. E. Easterly
56. Emergency Technology Library
57. L. C. Emerson
58–59. M. F. Fair
60. D. E. Ferguson
61. M. E. Fish
62. M. R. Ford
63. J. Gailar
64. R. B. Gammage
65. D. C. Gary
66. W. R. Garrett
67. J. H. Gillette
68. R. E. Goans
69. C. A. Golden
70. W. Good
71. C. R. Guinn
72. E. D. Gupton
73. C. M. Haaland
74. R. N. Hamm
75. W. O. Harms
76. F. F. Haywood
77. Health Physics Information System
78. L. C. Henley
79. R. F. Hibbs
80. J. V. Hilyer
81. L. B. Holland
82. C. F. Holoway
83. G. S. Hurst
84. T. Inagaki
85. D. G. Jacobs
86. L. C. Johnson
87. P. L. Johnson
88. T. D. Jones
89. P. R. Kasten
90. C. H. Kearny
91. G. D. Kerr
92. C. E. Klots
93. G. Kyker
94. Laboratory Shift Supervisor
95–112. Laboratory Records Department

113. Laboratory Records, ORNL R.C.
114. T. A. Lincoln
115. R. S. Livingston
116. T. F. Lomenick
117. F. C. Maienschein
118. R. W. Manweiler
119. J. H. Marable
120. W. C. McClain
121. D. L. McCorkle
122. H. F. McDuffie
123. C. H. Miller
124. R. E. Millspaugh
125. MIT Practice School
126. D. B. Nelson
127. D. J. Nelson
128–157. W. S. Nichols
158. ORNL – Y-12 Technical Library Document Reference Section
159. W. W. Parkinson
160. Patent Office
161. C. H. Patrick
162. G. R. Patterson
163. M. G. Payne
164. P. T. Perdue
165. D. Pittman
166. H. Postma
167. J. W. Poston
168. M. E. Ramsey
169. M. L. Randolph
170. P. W. Reinhardt
171. C. R. Richmond
172. L. P. Riordan
173. R. H. Ritchie
174. E. M. Robinson
175. P. S. Rohwer
176. M. W. Rosenthal
177. H. C. Schweinler
178. H. E. Seagren
179. R. B. Setlow
180. J. J. Shonka
181. R. L. Shoup
182. A. J. Smith
183. W. S. Snyder
184. P. S. Stansbury
185. P. Stelson
186. J. A. Stockdale
187. J. B. Storer
188. E. G. Struxness
189. D. A. Sundberg
190. E. H. Taylor
191–192. Technical Publications
193. J. H. Thorngate
194. M. L. Tobias
195. J. R. Totter
196. D. B. Trauger
197. J. E. Turner
198. E. B. Wagner
199. B. T. Walters
200. D. R. Ward
201. A. D. Warden
202. J. R. Weir
203. J. C. White
204. M. K. Wilkinson
205. M. W. Williams
206. J. A. Worth
207. H. A. Wright
208. J. P. Young

EXTERNAL DISTRIBUTION

209. F. Abeles, Institut D'Optique, 3, Blvd. Pasteur, Paris, France
210. Harold M. Agnew, Director, Los Alamos Scientific Laboratory, Los Alamos, New Mexico 87544
211. R. E. Alexander, NRC, Washington, D.C.
212. G. A. Andrews, Medical Division, Oak Ridge Associated Universities, Oak Ridge, Tennessee 37830
213. Army, Aberdeen Proving Ground, Technical Library, Aberdeen Proving Ground, Md. 21010
214. Army War College, Library, Ft. McNair, Washington, D.C. 20315
215. Assistant Secretary of the Air Force (R&D), Room 4E968, The Pentagon, Washington, D.C. 20330
216. Assistant Secretary of the Army (R&D), Attn: Assistant for Research, Washington, D.C. 20310
217. R. E. Baker, NRC, Washington, D.C. 20555
218. R. J. Barbuti, Deputy Director, Office of Natural Disaster and Civil Defense, N.Y. State Department of Transportation, Bldg. 22, State Office Bldg. Campus, Albany, N.Y. 12226
219. J. H. Barker, Physics Dept., St. Louis University, St. Louis, Mo. 63103
220. E. B. Barnes, West Virginia State College, Institute, West Va. 25112
221. N. F. Barr, U.S. ERDA, Division of Biomedical and Environmental Research, Washington, D.C. 20545

222. R. L. Butenhoff, U.S. ERDA, Division of Biomedical & Environmental Research, Washington, D.C. 20545
223. J. W. Baum, Health Physics Division, Brookhaven National Laboratory, Upton, L.I., N.Y. 11973
224. D. W. Bensen, Re(HV), Defense Civil Preparedness Agency, Washington, D.C. 20301
225. H. W. Berk, Dept. of Nuclear Engineering, Reactor Facility, University of Virginia, Charlottesville, Va. 22901
226. D. A. Bettge, Research Directorate, DCPA, Washington, D.C. 20301
227. J. Billheimer, Systan, Inc., 343 Second Street, P.O. Box U, Los Altos, Ca. 94022
228. G. F. Bing, Lawrence Livermore Laboratory, P.O. Box 808, Livermore, Calif. 94550
229. R. P. Blaunstein, Division of Biomedical and Environmental Research, U.S. ERDA, Washington, D.C. 20545
230. W. Brandt, Physics Department, New York University, New York, N.Y. 10003
231. J. E. Brantley, Civil Defense Office, 94 Arkansas Avenue, Oak Ridge, Tennessee 37830
232. A. J. Braundmeier, Faculty of Physics, Southern Illinois University, Edwardsville, Illinois 62025
233. C. E. Breckinridge, Jr., Department of Radiological Science, University of Arkansas Medical Center, Little Rock, Arkansas 72201
234. D. G. Brennan, Hudson Institute, Quaker Ridge Road, Croton-on-Hudson, N.Y. 10520
235. M. A. Bricka, Commissariat A L'Energie Atomique, Centre D'Etudes Nucleaires De Cadarache, Service D'Etudes De Surete Radiologique, Boite Postale No. 1, Saint-Paul-Lez-Durance, France
236. J. J. Broerse, Radiobiological Institute Tno, 151 Tange Kleiweg, Rijswijk, The Netherlands
237. W. M. Brown, Research Consultant, 19709 West Horseshoe Drive, Topanga, Calif. 90290
238. G. L. Brownell, Physics Research Laboratory, Massachusetts General Hospital, Fruit Street, Boston, Massachusetts 02114
239. A. Broyles, Department of Physics, University of Florida, Gainesville, Florida 32601
240. J. O. Buchanan, DCPA, Washington, D.C. 20301
241. W. M. Bugg, Physics Dept., University of Tenn. 37916
242. P. R. J. Burch, Department of Medical Physics, University of Leeds, General Infirmary, Leeds I, England
243. G. Burger, Gesellschaft Fur Strahlen-Und, Umweltforschung MBH Munich, Institut Fur Strahlenschutz, 8042 Neuherberg, Post Oberschleissheim, Ingolstadter Landstrasse 1, Munich, Germany
244. E. A. Burke, Radiation Effects Branch, Solid State Sciences Laboratory, Air Force Cambridge Research Lab., L. G. Hanscom Field, Bedford, Massachusetts 01730
245. T. E. Burlin, Department of Mathematics and Physics, The Polytechnic, 309 Regent Street London W.I., England
246. Z. Burson, EG&G, P.O. Box 1912, Las Vegas, Nevada 89109
247. T. Callcott, Physics Department, University of Tennessee, Knoxville, Tennessee 37916
248. P. Candes, Chef Du Service, D'Etudes De Surete Radiologique, Commissariat A L'Energie Atomique, Centre D'Etudes Nucleaires De Saclay, Boite Postale No. 2, Gif-Sur-Yvette, Saclay, France
249. M. W. Carter, School of Nuclear Engineering, Georgia Institute of Technology, Atlanta, Georgia 30332
250. J. S. Cheka, 4710 Middlebrook Pike, Knoxville, Tennessee 37921
251. T. Chin-Jones, Room 5443-ACDA, Department of State, 320 21st Street, N.W., Washington, D.C. 20451
252. W. K. Chipman, Deputy Assistant Director, Plans Po(DP), Defense Civil Preparedness Agency, Washington, D.C. 20301
253. B. C. Clarke, Jr., Director, Office of Strategic Research, CIA, Washington, D.C. 20505
254. R. J. Cloutier, Special Training Div., Oak Ridge Associated Universities, Oak Ridge, Tennessee 37830
255. F. E. Coffman, DCTR, USERDA, Washington, D.C.
256. C. E. Collins, TVA, 604 Power Building, Chattanooga, Tennessee 37401
257. Commander, Field Command, Defense Nuclear Agency, Sandia Base, Albuquerque, N.M. 87100
258. C. D. Cooper, University of Georgia, Athens, Georgia 30601
259. R. D. Cooper, Division of Biomedical and Environmental Research, U.S. ERDA, Washington, D.C. 20545
260. G. Cowper, Radiation Dosimetry Branch, Atomic Energy of Canada Limited, Chalk River, Ontario, Canada
261. R. W. Crompton, Research School of Physical Science, The Australian National University, Ion Diffusion Unit, Box 4, G.P.O., Canberra A.C.T., Australia
262. F. T. Cross, Battelle-Northwest, P.O. Box 999, Richland, Washington 99352
263. W. G. Cross, Atomic Energy of Canada, Ltd., Chalk River Nuclear Laboratories, Chalk River, Ontario, Canada

264. J. Crowell, Department of Physics and Mathematics, St. Andrews College, Laurinburg, N.C. 28352
265. A. M. Cruze, Research Triangle Institute, P.O. Box 12194, Research Triangle Park, N.C. 27709
266. L. B. Czech, Emergency Plans and Special Projects Unit, Department of Health, State of New York, 845 Central Avenue, Albany, New York 12206
267. D. R. Davy, A.A.E.A., Research Establishment, Private Mail Bag, Sutherland, N.S.W., Australia
268. L. J. Deal, Division of Operational Safety, USERDA, Washington, D.C. 20545
269. P. N. Dean, Lawrence Livermore Laboratory, P.O. Box 808, Livermore, Ca. 94550
270. Defense Supply Agency, Defense Logistics Services Center, Battle Creek Federal Center, Attn: Librarian, Battle Creek, Michigan 49016
271. H. J. Delafield, Atomic Energy Research Establisment, Health Physics and Medical Division, Harwell, Didcot, Berks., United Kingdom
272. J. Dennis, Head, Health Physics Department, National Radiological Protection Board, Harwell, Didcot, Berks., England
273. Department of the Army, Office, Chief of Engineers, Attn: Daen-Rdm, Washington, D.C. 20314
274. The Dikewood Corporation, 1009 Bradbury Drive, S.E., University Research Park, Attn: Librarian, Albuquerque, New Mexico 87106
275. L. T. Dillman, Ohio Wesleyan Univ., Deleware, Ohio 43015
276. Director of Defense Research and Engineering, Department of Defense, Washington, D.C. 20310
277. G. W. Dolphin, Radiological Protection Division, U. K. Atomic Energy Authority, Harwell, Didcot, Berks., England
278. G. A. Dorofeev, USSR State Committee on the Utilization of Atomic Energy, Staromonetny Pereulok 26, Moscow, USSR
279. M. Dousset, Department De La Protection Sanitaire, Centre D'Etudes Nucleaires, Fontenay-Aux-Roses (Seine), B.P. No. 6, France
280. J. Downing, Nuclear Materials Security, U.S. ERDA, Washington, D.C. 20545
281. C. W. Eddington, Division of Biomedical and Environmental Research, US ERDA, Washington, D.C. 20545
282. G. G. Eichholz, School of Nuclear Engineering, Georgia Institute of Technology, Atlanta, Ga. 30332
283. C. Eisenhauer, National Bureau of Standards, Washington, D.C. 20234
284. W. Porter Ellis, 10632 Seneca Ridge Drive, Gaithersburg, Maryland 20760
285. F. M. Empson, USNRC, Washington, D.C. 20545
286. The Engineer School Library, Fort Belvoir, Virginia 22060
287. U. Fano, Department of Physics, University of Chicago, 1118 East 58th Street, Chicago, Illinois 60637
288. F. S. Feer, Central Intelligence Agency, Washington, D.C. 20505
289. W. L. Fite, Department of Physics, University of Pittsburgh, Pittsburgh, Pennsylvania 15213
290. J. Fowler, Postgraduate Medical School, Hammersmith Hospital, London, England
291. W. F. Frey, Department of Physics, Davidson College, Davidson, N.C. 28036
292. J. C. Frye, Executive Secretary, Geological Society of America, 3300 Penrose Place, Boulder, Colorado 80301
293. F. Gabbard, Department of Physics, University of Kentucky, Lexington, Kentucky 40506
294. C. C. Gamertsfelder, Dir. of Regulatory Standards, USNRC, 5650 Wall Lane, North Bethesda, Md. 20314
295. S. M. Garry, TVA-ROB, Muscle Shoals, Ala. 35630
296. B. J. Garrick, Holmes and Narver, Inc., 400 East Orangethorpe Ave., Anaheim, California 92801
297. J. C. Garth, Radiation Effects Branch, Solid State Sciences Laboratory, Air Force Cambridge Research Lab., L. G. Hanscom Field, Bedford, Massachusetts 01730
298. E. Gerjuoy, Department of Physics, University of Pittsburgh, Pittsburgh, Pennsylvania 15213
299. J. C. Greene, Greenewood, Box 85A, Route 4, McKinney Cove, Bakersville, N.C. 28705
300. H. P. Harrenstien, Dean, School of Engineering, University of Miami, Miami, Florida 33124
301. C. F. Heddleson, Room 3102, General Electric Company, 3198 Chestnut Street, Philadelphia, Pa. 19101
302. W. R. Hendee, University of Colorado Medical Center, 4200 East Ninth Avenue, Denver, Colorado 80220
303. E. L. Hill, Research Triangle Institute, P.O. Box 12194, Research Triangle Park, N.C. 27709
304. H. E. Holloway, West Virginia Wesleyan College, Buckhannon, West Va. 26201
305. J. E. Hoy, Radiological Sciences Division, Savannah River Laboratory, Aiken, S.C. 29802
306. H. H. Hubbell, 248 Outer Drive, Oak Ridge, Tennessee 37830
307. D. S. Hudson, Re(Se), Defense Civil Preparedness Agency, Washington, D.C. 20301
308. R. H. Huebner, Physics Division, Argonne National Laboratory, 9700 South Cass Avenue, Argonne, Illinois 60439

309. Illinois Institute of Technology, Institute Library, Chicago, Illinois 60616
310. Institute for Energy Analysis, P.O. Box 117, Oak Ridge, Tennessee 37830
311. International Atomic Energy Agency, Wien A-1011, Austria
312. L. B. Jackson, 6912 Floyd Avenue, University Extension, University of Wisconsin, Madison, Wisconsin 53706
313. W. Jacobi, Gesellschaft Fur Strahlenund Umwel Tforschung, Ingolstadter Land Str. 1, D-8042 Neuherberg/Munich, Federal Republic of Germany
314. R. E. Johnston, Dept. of Radiology, Div. of Nuclear Medicine, Univ. of North Carolina, Chapel Hill, N.C. 27514
315. Chief, Joint Civil Defense Support Group, Office, Chief of Engineers, Department of the Army, Attn: ENGMC-D, Washington, D.C. 20314
316. B. Kahn, Environmental Resources Center, Georgia Institute of Technology, Atlanta, Georgia 30332
317. H. Kahn, Hudson Institute, Croton-on-Hudson, New York 10520
318. M. Kasha, Department of Chemistry, Florida State University, Tallahassee, Florida 32306
319. J. Kastner, U. S. NRC, Bethesda, Maryland 20014
320. J. R. Kelso, Defense Atomic Support Agency, Department of Defense, Washington, D.C. 20305
321. R. P. Kennedy, Holmes and Narver, Inc., 400 East Orangethrope Avenue, Anaheim, California 92801
322. C. D. Kepple, Springfield, Va. 22150
323. V. Klener, Dept. of Radiation Hygiene, Institute of Hygiene and Epidemiology, Uinohrady, Srobarova 48; Praha 10, C.S.S.R.
324. H. A. Knapp, Institute for Defense Analysis, 400 Army-Navy Drive, Arlington, Va. 22202
325. P. Krenkel, Director, Division of Environmental Planning, TVA, 268 401 Building, Chestnut Street, Chattanooga, Tennessee 37401
326. R. A. Krupka, Hudson Institute, Croton-on-Hudson, N.Y. 10520
327. H. A. Lamonds, EG&G, Inc., P. O. Box 98, Goleta, California 93717
328. H. T. Larson, Grand Valley State College, Physics Dept., Allendale, Michigan 49401
329. R. K. Laurino, System Sciences, Inc., 750 Welch Road, Palo Alto, California 94304
330. F. K. Levochkin, Head of Sector 46, Zhiropisnaja Ulitza, Institute of Biophysics, USSR Ministry of Health, D-98 Moscow, USSR
331. Library, University of Tennessee, Knoxville, Tennessee 37916
332. Bo Lindell, National Inst. of Radiation Protection, Stockholm 60, Sweden
333. J. Lindhard, Institute of Physics, Aarhus University, Aarhus, Denmark
334. J. Gordon Lindsay, Jr., Physics Dept., Appalachian State University, Boone, N.C. 28608
335. J. Liniecki, Instytut Medycyny Pracy, Lodz, Teresy 8, Poland
336. J. L. Liverman, Assistant Administrator for Environment and Safety, U.S. ERDA, Washington, D.C. 20545
337. A. Longinow, IIT Research Institute, 10 West 35th Street, Chicago, Ill. 60616
338. S. H. Lott, Radiation Safety Office, U-0209 Medical Center, Vanderbilt University, Nashville, Tennessee 37232
339. R. J. Lovell, University of Tennessee, Department of Physics, Knoxville, Tennessee 37916
340. R. A. MacRae, Physics Dept., Jacksonville State University, Jacksonville, Ala. 36265
341. R. P. Madden, National Bureau of Standards, Gaithersburg, Maryland 20760
342. E. L. Madsen, Dept. of Physical Science, Pembroke State University, Pembroke, N.C. 28372
343. J. L. Magee, Dept. of Chemistry, University of Notre Dame, Notre Dame, Indiana 46556
344. Sigismond Makra, Department of Health Physics, Central Research Inst. for Physics, Hungarian Academy of Sciences, P.O.B. 49, Budapest 114, Hungary
345. A. M. Marko, Director, Biology and Health Physics Division, Atomic Energy of Canada Limited, Chalk River, Ontario, Canada
346. W. G. Marley, Radiological Protection Division, U.K. Atomic Energy Authority, Harwell, Didcot, Berks., England
347. C. A. Mawson, Atomic Energy of Canada Limited, Chalk River, Ontario, Canada
348. C. W. Mays, Jr., Radiobiology Laboratory, University of Utah, Salt Lake City, Utah 84112

349. R. C. McIlhenny, Nuclear Science Center, Louisiana State University, Baton Rouge, Louisiana 70803
350. C. R. Mehl, Sandia Corporation, P.O. Box 5800, Albuquerque, N.M. 87115
351. T. T. Mercer, University of Rochester, School of Medicine and Dentistry, Rochester, N.Y. 14620
352. W. A. Mills, EPA, Room 635, Waterside Mall East, 401 M. Street, SW, Washington, D.C. 20460
353. Mr. and Mrs. Petar Miric, Radiation Protection Laboratory, Boris Kidric Institute of Nuclear Sciences – Vinca, P.O. Box 522, 11001 Belgrade, Yugoslavia
354. K. Z. Morgan, School of Nuclear Engineering, Georgia Institute of Technology, Atlanta, Georgia 30332
355. R. H. Morgan, Johns Hopkins School, Hygiene and Public Health, 615 North Wolfe Street, Baltimore, Maryland 21205
356. P. E. Morrow, The University of Rochester School, Medicine and Dentistry, Rochester, N.Y. 14620
357. P. Moulthrop, Lawrence Livermore Laboratory, P.O. Box 808, Livermore, California 94550
358. W. Murphey, Editor, Survive, P.O. Box 910, Starke, Florida 32091
359. M. Y. Nakai, Osaka Laboratory, Japan Atomic Energy Research Institute, 508 MII, Neyagawa-City, Osaka, Japan
360. D. L. Narver, Jr., Holmes and Narver, 400 East Organethrope Avenue, Anaheim, Ca. 92801
361. Nat. Radiological Protection Board, Attn: The Library, Harwell, Didcot, Berkshire OX11 Orq, England
362. V. N. Neelavathi, Directorate of Radiation Protection, Bhabha Atomic Research Centre, Trombay, Bombay 400 085, India
363. D. R. Nelson, 9025 Willow Valley Drive, Potomac, Md. 20854
364. J. Neufeld, 113 Cedar Lane, Oak Ridge, Tennessee 37830
365. W. R. Ney, Executive Director, Nat. Coun. on Rad. Prot. and Measurements, 7910 Woodmont Ave. (Suite 1016), Washington, D.C. 20014
366. A. H. Nielsen, Dean, College of Liberal Arts, Department of Physics, University of Tennessee, Knoxville, Tennessee 37916
367. W. E. Nischan, Division of Reactor Licensing, USNRC, Washington, D.C. 20545
368. Yasushi Nishiwaki, International Atomic Energy Agency, A-1010, Vienna, Karntnerring 11–13, Austria
369. G. M. Obaturov, Institute of Physics and Power Eng., Obninsk, USSR
370. M. Oberhofer, Health Physics Division, Euratom, Ispra, Italy
371. L. B. O'Kelly, Physics Dept., Memphis State University, Memphis, Tennessee 38152
372. J. S. Olson, Dber, USERDA, Washington, D.C. 20545
373. L. R. Painter, Physics Dept., University of Tennessee, Knoxville, Tennessee 37916
374. C. C. Palmiter, Radiation Office, Environmental Protection Agency, 5600 Fishers Lane, Rockland, Maryland 20852
375. P. Pards, Bureau of Radiological Health, Food & Drug Administration, 5600 Fishers Lane Hex300, Rockville, Md. 20852
376. R. Park, National Academy of Sciences, Washington, D.C. 20418
377. H. M. Parker, 2030 Harris Street, Richland, Washington 99352
378. E. Parsons, System Sciences, Inc., P.O. Box 2345, Chapel Hill, N.C. 27514
379. D. A. Patterson, Budget and Planning Staff, Tennessee Valley Authority, 410 New Sprankle Bldg., Knoxville, Tennessee 27902
380. Physics Library, Vanderbilt University, Nashville, Tennessee 37203
381. E. K. A. Piesch, Radiation Protection & Safety Dept., Karlsruhe Nuclear Research Center, Postfach 3640, 75 Karlsruhe 1, Fed. Rep. of Germany
382. Colonel William H. Pietsch (Retired), 4205 Saul Road, Chevy Chase, Maryland 20015
383. E. E. Pochin, Department of Clinical Research, Univ. College Hospital Medical School, London, W.C.1., England
384. C. Polvani, Division of Radiation Protection, Comitato Nazionale, Per L'Energia Nucleare, Casella Postale 2358 – 00100 Roma A.D.
385. C. J. Powell, Electron Physics Section, National Bureau of Standards, Washington, D.C. 20234
386. R. D. Present, Physics Department, University of Tennessee, Knoxville, Tennessee 37916

387. S. B. Pretre, Head, Section for Protection of Persons and Environment, Safety Inspectorate of Nuclear Installations, Ch-5305 Wurenlingen, Switzerland
388. B. P. Pullen, Chemistry & Physics Dept., College Station, Southeastern Louisiana University, Hammond, La. 70401
389. R. Rabin, Biomedical & Environmental Research, USERDA, Washington, D.C. 20545
390. Radiation Physics Division, Health and Safety Laboratory, New York Operations Office, U.S. ERDA, New York, N.Y. 10014
391. H. Raether, Institute for Applied Physics, University of Hamburg, Hamburg, West Germany
392. Barbara Reed, Riverview High School, 4850 Lords Lane, Sarasota, Florida 33581
393. Research & Technical Support Division, ORO
394. B. Rideout, Office of Civil Defense, Statehouse, Augusta, Maine 04330
395. H. Roback, Staff Administrator, Subcommittee for Military Operations, U.S. House of Representatives, Washington, D.C. 20515
396. C. J. Roberts, School of Nuclear Engr., Georgia Institute of Technology, Atlanta, Ga. 30352
397. S. Robin, Spectroscopy Laboratory, University of Rennes, Rennes, France
398. J. D. Rockefeller, IV, President, W. Virginia Wesleyan College, Buckhannon, W. Virginia 26201
399. R. Rodden, Operations Evaluation Department, Stanford Research Institute, Menlo Park, Calif. 94025
400. C. E. Roessler, 525 N.E. 4th St., Gainesville, Fla. 32601
401. W. C. Roesch, Battelle Northwest, P.O. Box 999, Richland, Washington 99352
402. R. H. Rohrer, Department of Physics, Emory University, Atlanta, Georgia 30322
403. J. Romm, Systems Sciences, Inc., 4720 Montgomery Lane, Bethesda, Md. 20014
404. M. Rosenstein, Bureau of Radiological Health, Food & Drug Administration, 12720 Twinbrook Parkway, Rockville, Md. 20852
405. J. H. Rust, University of Chicago, Section of Nuclear Medicine, Chicago, Ill. 60637
406. A. Sachs, Institute for Defense Analyses, 400 Army-Navy Drive, Arlington, Va. 22202
407. J. A. R. Samson, Experimental Physics Department, Geophysics Corporation of America, Bedford, Massachusetts 01730
408. R. Schneider, Bureau of Radiological Health, Food & Drug Administration, 12720 Twinbrook Parkway, Rockville, Md. 20852
409. W. W. Schroebel, Analysis and Evaluation Branch, Division of Biomedical and Environmental Research, U.S. Atomic Energy Commission, Washington, D.C. 20545
410. G. J. Schulz, Department of Physics, Yale University, New Haven, Connecticut 06520
411. J. Schwibach, Federal Health Office, 8042 Neuherberg Bei Munchen, Ingolstadter Landstr. 1 West Germany
412. F. Seitz, President, Rockefeller University, New York, N.Y. 10021
413. J. Servant, IAEA, P.O. Box 590, Karntner Ring 11, A-1011, Vienna, Austria
414. S. Y. Shieh, Physics Department, University of Tennessee, Knoxville, Tennessee 37916
415. G. N. Sisson, Shelter Research Division, Defense Civil Preparedness Agency, Washington, D.C. 20301
416. R. G. Siwicki, Health Physics Division, Institute for Nuclear Research, Swierk K/Otwocka, Poland
417. R. Sleeper, University of Tennessee Space Institute, Tullahoma, Tennessee 33778
418. B. L. Sloan, Biology Dept., Carson-Newman College, Jefferson City, Tennessee 37760
419. E. M. Smith, P.O. Box 128, Walland, Tennessee 37886
420. S. A. Smith, University of North Alabama, Florence, Alabama 35630
421. A. W. Spear, Physics Dept., SWTSU, San Marcos, Texas 78666
422. L. V. Spencer, National Bureau of Standards, Washington, D.C. 20234
423. Z. Spurny, Academy of Sciences, Nuclear Research Institute, Dosimetry Department, Na Truhlarce 39/2A, Praha 8, Czechoslovakia
424. J. N. Stannard, Univ. of Rochester School of Med. & Den., P.O. Box 287, Station 3, Rochester, New York 14620

425. Stanford Research Institute Library, Menlo Park, California 94025
426. G. Stattin, Swedish State Power Board, S-162 87 Vallingby, Sweden
427. W. Steinmann, II Physikalisches Ins. Der Univ. Munchen, Munchen 13, Germany
428. A. G. Steinmayer, Advanced Missile Systems, General Electric Company, 3198 Chestnut Street, Philadelphia, Pennsylvania 19101
429. C. G. Stewart, Director, Medical Division, Atomic Energy of Canada Limited, Chalk River, Ontario, Canada
430. D. R. Stone, Chattanooga State Technical Institute, Amnicola Highway, Chattanooga, Tennessee 37406
431. G. F. Stone, 719 Edney Building, Chattanooga, Tennessee 37401
432. H. A. Strack, Northrup Corporation, 1701 N. Fort Myer Drive, Arlington, Va. 22209
433. E. A. Straker, Suite 700, Science Applications, Inc., 2109 Clinton Avenue, Huntsville, Alabama 35805
434. C. P. Straub, University of Minnesota, College of Medical Sciences, School of Public Health, Minneapolis, Minnesota 55455
435. W. E. Strope, Stanford Research Institute, 1611 North Kent Street, Arlington, Va. 22209
436. J. B. Swan, University of Western Australia Nedlands, Western Australia
437. F. P. Szabo, Defense Research Establishment, Ottawa, Ontario, Canada KIA Oz 4
438. J. Tadmor, Director, Nuclear Safety, Israel Atomic Energy Commission, Soreq Nuclear Research Center, Yavne, Israel
439. Lauriston Taylor, National Council on Radiation Protection and Measurements, 7910 Woodmont Avenue, Washington, D.C. 20014
440. E. Teller, Lawrence Livermore Laboratory, P.O. Box 808, Livermore, Ca. 94550
441. G. E. Thoma, St. Louis University Hospital, 1462 South Grand Boulevard, St. Louis, Missouri 63104
442. R. C. Thompson, Battelle-Northwest, P.O. Box 999, Richland, Washington 99352
443. I. H. Tipton, Star Rt. 2, P.O. Box 780, Southport, North Carolina 28461
444. C. Tobias, University of California, Lawrence Radiation Laboratory, Berkeley, California 94720
445. U. S. Army Engineer Research and Development Laboratories Library, Fort Belvoir, Va. 22060
446. U.S. Naval Civil Engineering Laboratory Library, Port Hueneme, Ca. 93041
447. E. S. Vasquez, Acting Chief, Joint Civil Defense, Support Group, Directorate of Military Construction, Department of the Army, Office of the Chief of Engineers, Washington, D.C. 20314
448. J. Vennart, Radiological Protection Service, Clifton Avenue, Belmont Sutton, Surrey, England
449. R. J. Vetter, Bionucleonics Dept., Purdue University, West Lafayette, Indiana 47907
450. M. Vidmar, Boris Kidrich Institute, Vinca, Yugoslavia
451. J. Villforth, Bureau of Radiological Health, U.S. Public Health Service, 5600 Fisher Lane, Parklawn Building, Rockville, Maryland 20852
452. W. H. Von Aulock, Bell Telephone Laboratory, Whippany, N.J. 07981
453. L. Vortman, Sandia Corporation, Albuquerque, N.M. 87115
454. C. L. Wakamo, EPA, Region IV, 1421 Peachtree St. N.E. Atlanta, Ga. 30309
455. N. Wald, University of Pittsburgh, Graduate School of Public Health, Pittsburgh, Pennsylvania 15213
456. K. G. Walker, Bethany Nazarene College, Physics Dept., Bethany, Oklahoma 73008
457. Captain Arnold S. Warshawsky, U.S. Army Nuclear Agency, Attn: ATCN-W, Fort Bliss, Texas 79916
458. Shiqued Watanabe, Instituto De Energia Atomica, Cidade Univ., Cx. Postal, 11.049- Pinheiros; Sao Paulo, Brazil
459. L. E. Weaver, School of Nuclear Engineering, Georgia Institute of Technology, Atlanta, Georgia 30332
460. Lee Webster, Advanced Ballistic Missile Defense Agency, Huntsville Office, ABH-S, P.O. Box 1500, Huntsville, Alabama 35807
461. A. M. Weinberg, Institute for Energy Analysis, P.O. Box 117, Oak Ridge, Tennessee 37830
462. G. L. Weissler, Department of Physics, University of Southern California, Los Angeles, California 90007
463. J. E. Wiest, Dept. of Physical Science, West Virginia Wesleyan College, Buckhannon, West Virginia 26201

464. C. S. White, President and Scientific Director, Oklahoma Medical Research Foundation, 825 N.E. 13th Street, Oklahoma City, Oklahoma 73141
465. Carl-Olds Widell, Health and Safety Section, AB Atomenergi, Studsvik, S-611 01 Nykoping, Sweden
466. E. P. Wigner, 8 Ober Road, Princeton, New Jersey 08540
467. W. H. Wilkie, TVA-ROB, Muscle Shoals, Alabama 35630
468. T. M. Willard, Chemistry Dept., Florida Southern College, Lakeland, Florida 33802
469. R. W. Wood, Division of Biology and Medicine, U.S. ERDA, Washington, D.C. 20545
470. World Health Organization, Palais Des Nations, Geneve, Switzerland
471. C. N. Wright, Radiological Sciences Division, Savannah River Laboratory, Aiken, South Carolina 29802
472. M. D. Wright, P.O. Box 1219A, Research Triangle Park, Raleigh, N.C. 27709
473. H. O. Wyckoff, 4108 Montpelier Road, Rockville, Maryland 20853
474. W. R. Yucker, Radiation Physics Corporation, 17322 Whetmore Lane, Huntington Beach, Ca. 92647
475. P. L. Ziemer, Bionucleonics Department, Purdue University, West Lafayette, Indiana 47907
476. R. L. Zimmerman, Phoenix Technology Corporation, 1949 Silva Stone Drive, Decatur, Ga. 30033

477–721. Given distribution as shown in TID-4500 under Health and Safety category (25 copies – NTIS)

U. S. GOVERNMENT PRINTING OFFICE: 1975-748-189/57